New Zealand's bold plan to snuff out smoking p. 1268

Cooling with solvated ions pp. 1275 & 1344

Counting cell divisions to restrain cancer p. 1276

Science

$15
23 DECEMBER 2022
science.org

AAAS



BLENDING IN

Tissue transparency in glassfrogs pp. 1272 & 1315

VISIT…

LANZAROTE Caliente.com

TRILLIONS OF MICROBES

ONE ESSAY

The NOSTER *Science* Microbiome Prize is an international prize that rewards innovative research by investigators who have completed their terminal degree in the last 10 years and are working on the functional attributes of microbiota. The research can include any organism with the potential to contribute to our understanding of human or veterinary health and disease, or to guide therapeutic interventions. The winner and finalists will be chosen by a committee of independent scientists chaired by a senior editor of *Science*. The top prize includes a complimentary membership to AAAS, an online subscription to *Science*, and USD 25,000. Submit your research essay today.



Jennifer Hill, Ph.D.
2022 Winner

NOSTER | Science
MICROBIOME
PRIZE

Apply by 24 January 2023 at www.science.org/noster

Sponsored by Noster, Inc



Prof. Liu, Prof. Kuang, and their team members have developed a high-throughput 3D-nanometer resolution laser direct writing machine for sensor printing.

Adding intelligence to sensing

Advanced combinations of new sensor technology and signal processing underway at Zhejiang Lab integrate human-like perception into sensing devices.

Making sense of the five senses—sight, hearing, touch, smell, and taste—remains a forefront field in neuroscience. To explore these processes, researchers often try to model nature.

In the 1950s, for example, the late Cornell University psychologist Frank Rosenblatt mimicked the wiring and processing in a fly's eye to build a device filled with a maze of wires and electronics called a perceptron. Studies like this, now powered by advanced computation, are creating a new field of study called intelligent sensing, which many scientists explore at Zhejiang Lab in Hangzhou, China.

"Intelligent sensing is an imitation and approximation of the perception mode through which humans perceive surrounding objects and the environment," says Xu Liu, dean of the Research Institute of Intelligent Sensing at Zhejiang Lab. "Human vision, hearing, smell, taste, and touch all have their own neural networks, and they all compute in a particular way. It is not only the mechanical sensing process, but also a combination of physical sensing, neural information processing, and brain cortex recognition that forms a human's cognition of their surroundings."

Making smarter sensors

Advances in intelligent sensing rely heavily on more advanced sensors, such as so-called smart sensors created from a conventional digital sensor combined with signal-processing circuits and computing memory. "These kinds of sensors will soon enter the market, but they can only be regarded as preliminary types of intelligent sensors," Liu says, because even smarter sensors are in development.

Scientists at Zhejiang Lab are developing a range of low-cost and energy-efficient sensors, plus advanced intelligent-sensing technologies. "On the basis of powerful artificial intelligence research here at Zhejiang Lab, we will focus on developing intelligent visual, auditory, olfactory, gustatory, and tactile sensors that mimic the five senses of human beings, which can provide transformative technologies and devices such as future humanoid robots, convergent media technology, and new human–computer interaction interfaces. Additionally, these sensors will drive the development of information technology to a higher level," Liu explains.

Mimicking auditory sensing, for example, these scientists created a 20 MHz–120 MHz ultrasonic transducer integrated within a microscope that can image a sample 1 cm in depth and provide resolution of less than 10 μm. In the area of visual sensing, scientists at Zhejiang Lab are making progress on technologies that can be applied to in vivo subcellular pathology research and multiorgan diagnosis and treatment. Lastly, in their efforts to replicate touch, these scientists have also developed an intelligent tactile-sensing system based on micro/nano fibers that reacts accurately to pressure, sliding, temperature, humidity, and angle.

Building even better sensors

While acknowledging the breakthroughs that stimulated the development of existing sensors, such as charge-coupled devices (CCDs) and complementary metal-oxide semiconductor (CMOS) chips, researchers can be confident that tomorrow's sensors will be much more advanced.

"We call the current CCD and CMOS image sensors the vision sensors of the industrial age, and we hope to develop new types of visual, olfactory, gustatory, and tactile sensors that we define as biomimetic intelligent sensors," Liu says. "Therefore, we have designed and constructed the Zhejiang Lab IntelliSense Facility, which is a large-scale science and technology infrastructure for the research and development of intelligent sensors."

This R&D facility will allow scientists at Zhejiang Lab to work on all aspects of intelligent sensing. As Liu explains, "Building a full-chain intelligent sensor research and development platform will enable us to take five-sense sensing materials, large-scale array high-speed readout circuits, and intelligent chips based on human-like neural networks and merge them to support the creation of human-like five-sense devices, to form a new intelligent sensing system, and to serve more efficient and robust machine intelligence."

Sponsored by

之江实验室
ZHEJIANG LAB

PHOTO: PROVIDED BY ZHEJIANG LAB



From left: Wu Xiangdong*, Michael I. Jordan, Dirk Görlich, Roger Kornberg**, Randy Schekman

What the World Laureates Association Prize means for science

Since its establishment in 2017, the World Laureates Association (WLA) has acted as a hub for first-class scientific achievement. Each year, WLA has brought together prize-winning scientists from multiple fields to exchange ideas, develop opportunities for innovative collaboration, and focus on how science and technology can help solve the challenges facing our world.

In 2021, the WLA went one step further and decided to publicly recognize prominent scientists for their work through the annual World Laureates Association Prize, which is awarded in two categories, each with a RMB 10 million ($1.4 million) gift. According to Randy Schekman, chair of the WLA Prize Selection Committee and winner of the 2013 Nobel Prize in Physiology or Medicine for his role in revealing the machinery that regulates the transport and secretion of proteins in our cells, these prizes are intended to go to individuals whose work is critically important to our future yet hasn't been fully recognized. "I have served on many awards committees and been the beneficiary of many big prizes, and many prize [committees] end up picking the same people over and over again," he says. "Our goal is to find those people who have made fundamental achievements in basic science or medical science who have not yet been recognized and deserve that recognition."

In 2022, the WLA Prize's inaugural year, the two prizes go to Dirk Görlich and Michael I. Jordan for their respective contributions to cellular logistics and machine learning.

"What's wonderful about these prizes is that they recognize people who've made fundamental contributions to critical areas that are sculpting so much of our future," says John Hennessy, chair of the WLA Prize Selection Committee and recipient of the 2017 Turing Award, often referred to as the "Nobel Prize for Computing." Adds Hennessy, "For example, the Nobel Prize was created before computer science was even a field."



Meeting the winners: Michael I. Jordan

For the past four decades, Michael I. Jordan has helped lead and shape the field of statistical machine learning. His work at the University of California, Berkeley, spans computing, statistics, economics, and other social sciences—all subjects that, he says, must be understood and woven together to form the structural underpinning for fully realized machine learning–based systems that help drive human progress.

To Jordan, computer science remains a young discipline that acts as a bridge between science and engineering. "It has computational principles, it has mathematics, and it then builds artifacts that people use in the real world, such as search engines."

In the future, Jordan believes that humans will need to become the object of this area of study. So, rather than simply looking for ways for machines to

PHOTOS: PROVIDED BY WLA

*Executive director, World Laureates Association and chair, WLA Prize Management Committee
**2006 Nobel laureate in chemistry; chair, World Laureates Association; chair, WLA Prize Management Committee and WLA Prize Awards Committee

imitate human behavior in areas such as computer vision, robotics, and speech recognition, we should look at how algorithms can support human interaction and liberate us to do new things.

As an example, he highlights his recent work with the company United Masters, which has used machine learning to build a digital marketplace for music—a platform that empowers musicians by connecting them to brands and listeners, allowing them to earn an income from the music they create. "It's an example of technology, data analysis, and social science coming together to design a system that brings income to cultural creators. There are over 2 million young people who are participating and gaining an income, which is the kind of cultural impact you'd like to have."



PHOTO: PROVIDED BY WLA

Meeting the winners: Dirk Görlich

Biochemist Dirk Görlich's work focuses on transport processes in cell logistics. As a director at the Max Planck Institute for Multidisciplinary Sciences in Göttingen, Germany, Görlich is particularly interested in the question of how nuclear pore complexes function as highly efficient transport machines.

"Nuclear pore complexes are fascinating. They are one of the human cell's largest molecular machines. We have found that in one second, a single nuclear pore can translocate 1,000 protein molecules." In cells, nuclear pore complexes operate as selective barriers, he says, and his team has worked to reconstitute those barriers from native or designed synthetic components: "It is a new state of matter in biology, which we call an FG phase," where 'FG' refers to the amino acids phenylalanine and glycine that are found in repeating motifs in certain nuclear pore proteins. "We have demonstrated that this reconstituted phase behaves exactly like a nuclear pore complex that can keep out unwanted material and allow a rapid influx of transport receptors along with their cargoes."

While Görlich's findings are fascinating, the work is also inherently challenging for future research, as the material they are working with has an intrinsically disordered structure. This material looks and feels "like a gummy bear," remarks Görlich, explaining that the "domains are highly flexible, and they can probably interact in many, many different ways. Capturing this in a structural sense is just very challenging, and we will need to develop new methods and techniques to do this."

What awards mean for the future of science

For both Jordan and Görlich, scientific awards such as the WLA Prize act as lightning rods for future research endeavors. While they are immensely honored to be recognized for their work, both researchers are aware of how useful such moments can also be in raising the profile of their respective fields, celebrating their colleagues, and inspiring early-career researchers.

"Such awards can call attention to an emerging field, such as computer science, and give value to it. They also make younger people aspire to do something similar. And that's, I think, probably the biggest thing that I can think of in terms of the significance of important prizes," says Jordan.

For Görlich, the award is an opportunity to raise the profile of his team and make their findings and insights more visible. He adds that scientists go through many periods of frustration during which things just don't work, and that we should keep in mind that we learn as much from experiences of failure as we do from breakthroughs: "Learning from failed experiments sometimes—in fact often—gives more insights than [we receive from] those that work as expected. I've had many of those moments in my career."

The prizewinners' comments certainly reflect the WLA's three primary missions: to promote basic science, to advocate for international cooperation, and to support the development of young scientists.

Moving forward

The first winners of the WLA Prize—with Sequoia China as its exclusive sponsor—will act as a benchmark for future selection, and WLA is looking forward to the selection for the 2023 awards.

The details of the selection process will be released soon, and the selection committee will be receiving nominations from across the globe.

Hennessy says he told the organizers early on that prizes become distinguished by the people who have won them, rather than any other measure: "I think what I found interesting about the nominees for the WLA Prize is how broad a range of fields they span. Fields are intersecting more and more, and at those intersections we've seen some incredible research."

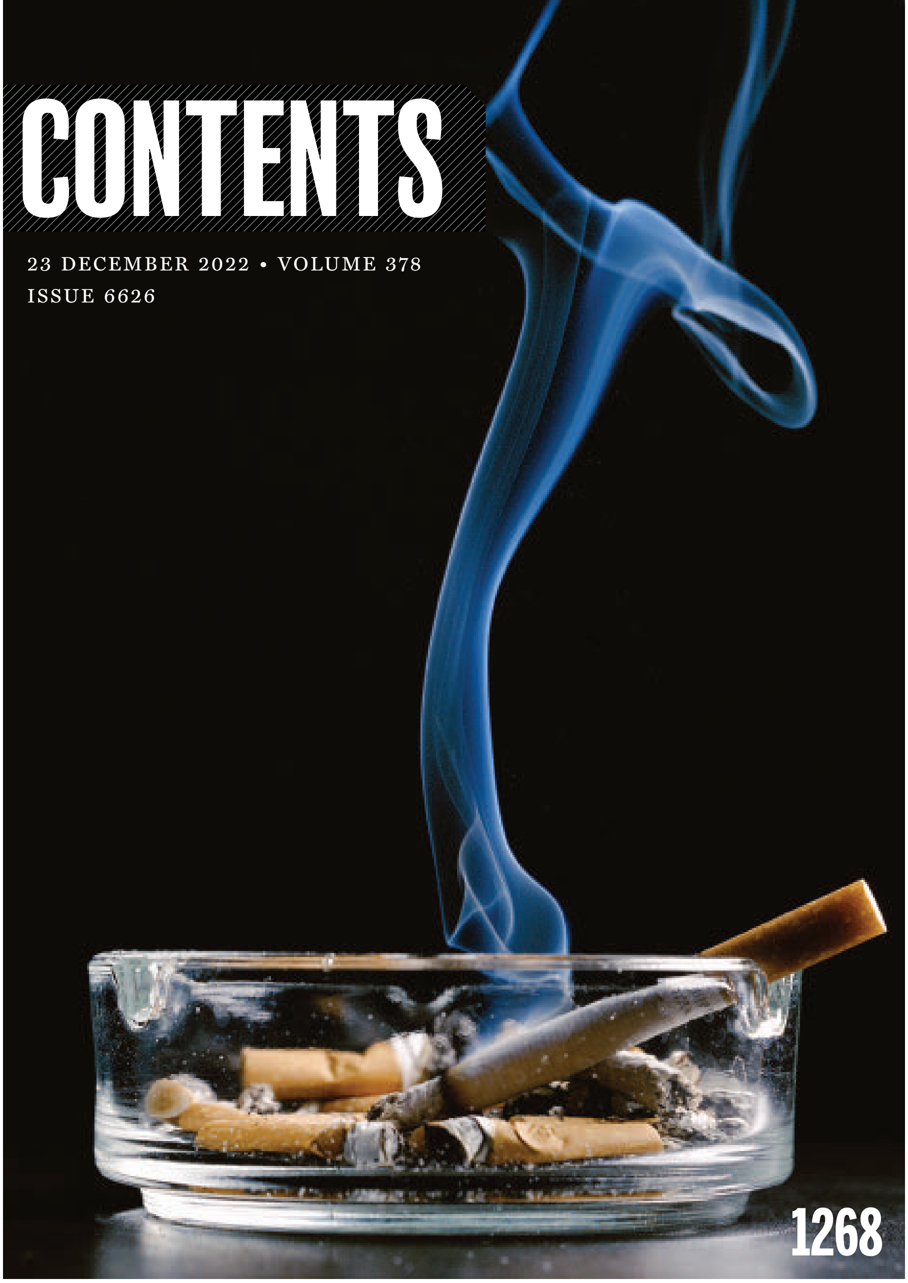
Sponsored by

WLA PRIZE
世界顶尖科学家协会奖

www.thewlaprize.org

CONTENTS

23 DECEMBER 2022 • VOLUME 378
ISSUE 6626



FEATURES

1268 The final puff
Public health officials have drawn on a decade of research to craft a plan to make New Zealand smoke-free *By D. Normile*

INSIGHTS

PERSPECTIVES

1272 Lessons on transparency from the glassfrog
Transparency in glassfrogs has potential implications for human blood clotting
By N. M. Cruz and R. M. White
REPORT p. 1315

1273 Embracing disorder in solid-state batteries
Enhanced ion transport is achieved by chemically induced structural distortion
By M. Botros and J. Janek
REPORT p. 1320

1275 Cool it, with a pinch of salt
Melting a solvent with a salt and then desalinating it enables a reversible cooling cycle *By E. Defay*
REPORT p. 1344

1276 Epigenetic clocks, aging, and cancer
Global methylation changes in aging cells affect cancer risk and tissue homeostasis *By S. E. Johnstone* et al.

POLICY FORUM

1278 Data blind: Universities lag in capturing and exploiting data
Study finds a pervasive void of infrastructure thinking
By C. L. Borgman and A. Brand

BOOKS *ET AL.*

1282 The art of aquarium science
Aquarist knowledge is an often overlooked but vital part of marine research
By P. K. Hardy

1283 Making modern medicines
The business side of drug development comes to the fore in a tale of two blockbuster blood cancer therapeutics
By A. Woolfson

LETTERS

1284 Editorial Expressions of Concern
By H. H. Thorp

1284 Retraction
By C. Fischer et al.

NEWS

IN BRIEF

1260 News at a glance

IN DEPTH

1262 Mars's magnetic field was long-lived, reversible
Study of famed meteorite by quantum microscope hints at planet's prolonged habitability *By Z. Savitsky*

1263 Research gets a boost in final 2023 spending agreement
Budgets of many civilian science agencies will grow, but not always by as much as White House had requested *By Science News Staff*

1264 Can peer reviewing preprints catch on?
As unreviewed studies proliferate online, researchers are eyeing ways to boost critiques *By J. Brainard*

1265 NIH can't deny chimps sanctuary retirement
Agency violated federal law when it prevented former lab primates from entering Chimp Haven, federal judge rules *By D. Grimm*

1266 Ocean geoengineering scheme aces field test
Alkaline lime powder spread in Florida estuary drew down carbon and reduced acidification *By P. Voosen*

1267 Moms' mitochondria may refresh cells in sick kids
Technique is designed to treat mitochondrial disease *By M. Leslie*

PHOTO: CHRISTIAN ZACHARIASEN/GETTY IMAGES

1285 Accessing the Loss and Damage climate fund
By B. Dahiya and M. Okitasari

1285 Remote opportunities for scholars in Ukraine
By K. Chhugani et al.

RESEARCH

IN BRIEF

1290 From *Science* and other journals

RESEARCH ARTICLES

1293 Neurodevelopment
Coordinated control of neuronal differentiation and wiring by sustained transcription factors *M. N. Özel* et al.
RESEARCH ARTICLE SUMMARY; FOR FULL TEXT: DOI.ORG/10.1126/SCIENCE.ADD1884

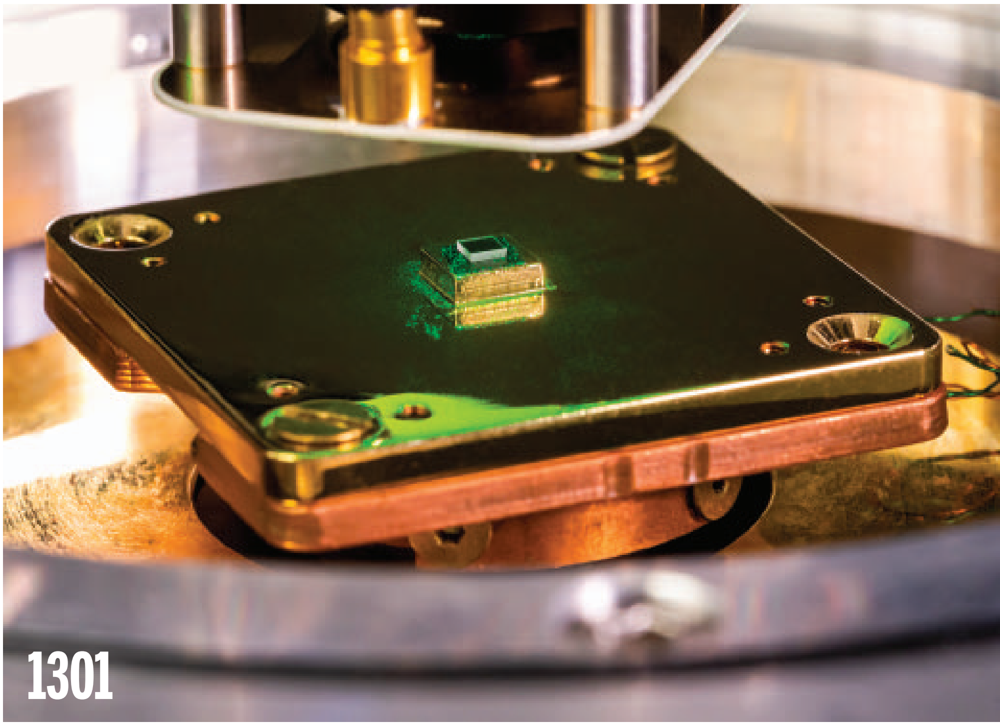
1294 Neuroscience
Mesolimbic dopamine release conveys causal associations *H. Jeong* et al.
RESEARCH ARTICLE SUMMARY; FOR FULL TEXT: DOI.ORG/10.1126/SCIENCE.ABQ6740

1295 Solar cells
Compositional texture engineering for highly stable wide-bandgap perovskite solar cells
Q. Jiang et al.

1301 Quantum sensing
Nanoscale covariance magnetometry with diamond quantum sensors *J. Rovny* et al.

1305 Development
Zygotic genome activation by the totipotency pioneer factor Nr5a2 *J. Gassler* et al.





A diamond with near-surface nitrogen vacancy defect centers rests in a cryostat illuminated by green laser light from a microscope objective lens.

REPORTS

1315 Physiology
Glassfrogs conceal blood in their liver to maintain transparency *C. Taboada* et al.
PERSPECTIVE p. 1272

1320 Batteries
High-entropy mechanism to boost ionic conductivity *Y. Zeng* et al.
PERSPECTIVE p. 1273

1325 3D printing
Three-dimensional nanofabrication via ultrafast laser patterning and kinetically regulated material assembly *F. Han* et al.

1331 Organic chemistry
Transition metal–free ketene formation from carbon monoxide through isolable ketenyl anions *M. Jörges* et al.

1336 Neuroscience
Layer-specific pain relief pathways originating from primary motor cortex
Z. Gan et al.

1344 Calorics
Ionocaloric refrigeration cycle
D. Lilley and R. Prasher
PERSPECTIVE p. 1275

DEPARTMENTS

1257 Editorial
Appoint a new NIH director, now
By H. H. Thorp

1354 Working Life
A break for my health
By J. Forson

ON THE COVER

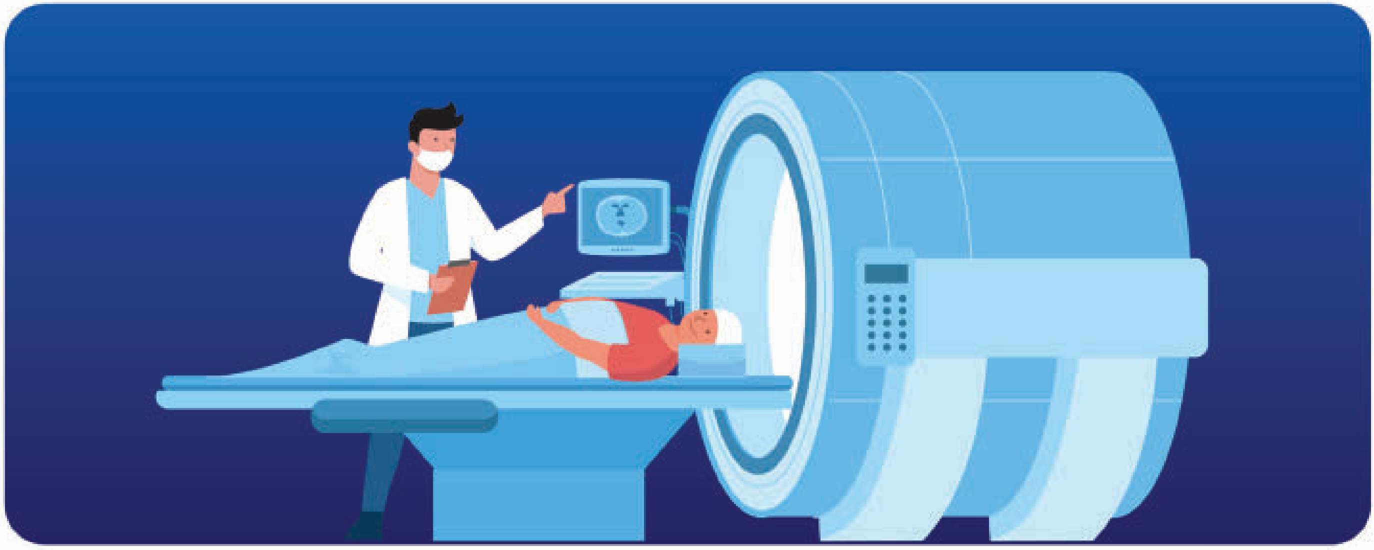
In this backlit photograph, a camouflaged glassfrog is shown sleeping on a leaf. The leaf-like appearance of glassfrogs results from highly transparent muscle and belly skin tissue in combination with their translucent green dorsal skin. To maintain tissue transparency, these frogs remove most light-absorbing red blood cells from circulation and hide them in their mirrored livers. See pages 1272 and 1315. *Photo: Jesse Delia*



Science Staff 1254
AAAS News & Notes 1288
Science Careers 1349

SCIENCE (ISSN 0036-8075) is published weekly on Friday, except last week in December, by the American Association for the Advancement of Science, 1200 New York Avenue, NW, Washington, DC 20005. Periodicals mail postage (publication No. 484460) paid at Washington, DC, and additional mailing offices. Copyright © 2022 by the American Association for the Advancement of Science. The title SCIENCE is a registered trademark of the AAAS. Domestic individual membership, including subscription (12 months): $165 ($74 allocated to subscription). Domestic institutional subscription (51 issues): $2212; Foreign postage extra: Air assist delivery: $98. First class, airmail, student, and emeritus rates on request. Canadian rates with GST available upon request, GST #125488122. Publications Mail Agreement Number 1069624. **Printed in the U.S.A.**
Change of address: Allow 4 weeks, giving old and new addresses and 8-digit account number. **Postmaster:** Send change of address to AAAS, P.O. Box 96178, Washington, DC 20090–6178. **Single-copy sales:** $15 each plus shipping and handling available from backissues.science.org; bulk rate on request. **Authorization to reproduce** material for internal or personal use under circumstances not falling within the fair use provisions of the Copyright Act can be obtained through the Copyright Clearance Center (CCC), www.copyright.com. The identification code for *Science* is 0036-8075. *Science* is indexed in the *Reader's Guide to Periodical Literature* and in several specialized indexes.

CREDITS: (ILLUSTRATION) STEPHAN SCHMITZ/ISPOT; (PHOTO) DAVID KELLY CROW



Patients implanted with DBS can now safely receive MRI scans for diagnosis.

New neurostimulation technology to advance Parkinson's disease research and treatment

PINS Medical and Tsinghua University researchers have spent the past decade developing the first magnetic resonance imaging (MRI)-compatible deep brain stimulation device. The stimulator enables Parkinson's disease patients to undergo diagnostic MRI scans safely. But it also offers new opportunities in neuroscience, as researchers can now use MRI to observe the brain while the device is operating and acting on the brain's functions.

Deep brain stimulation (DBS) is a highly effective surgical therapy for tremor, rigidity, and bradykinesia symptoms caused by Parkinson's disease. DBS involves the surgical implantation of one or more electrodes into specific brain areas, which then modulate or disrupt abnormal neural signaling patterns within the targeted region. The stimulator generates an electrical pulse train and sends it to the targeted cells in the brain through cables infiltrated into brain tissue. The pulse train parameters can be adjusted based on the disease, the individual circumstances, and the desired outcome.

The presence of these electrodes in patients' brains could make MRI unsafe because the metal components of the electrodes interact with the magnetic fields used during an MRI scan. Only under very strict conditions can patients implanted with a DBS device could undergo scanning with a 1.5T MRI—a scanner with a magnet that can produce a magnetic field of 1.5 Tesla (approximately 30,000 times more than the average gravity on the surface of the Earth), explains Changqing Jiang from Tsinghua University, Beijing. But he argues that more than half of patients implanted with a DBS device will require an MRI scan at some point in their lives. With the advancement of MRI technology, high-field 3.0T MRI equipment is gradually replacing older 1.5T MRI machines and becoming the standard in clinical practice, allowing higher signal-to-noise ratio, shorter scan time, and improved image quality. "That is why MRI compatibility of DBS devices is critical for patients."

A new device makes MRI scans safe during DBS

Led by Jiang, a key member of the National Engineering Research Center of Neuromodulation (directed by Luming Li from Tsinghua University), researchers at PINS Medical and Tsinghua University have engineered a series of new stimulators featuring 3.0T MRI compatibility with all current clinical scanning modalities. Patients implanted with the new stimulators, which can be rechargeable or non-rechargeable, can undergo whole-body 3.0T and 1.5T MRI scans without turning off or adjusting the device's parameters. The allowed radio frequency intensity can reach 3.4 μT as indicated by the effective amplitude B_{1+rms} for a continuous scan of 1 hour.

One of the primary safety concerns with old DBS devices was the heating of the conductive cables that connected the stimulator to the brain caused by the high radio frequency (RF) of the MRI magnetic fields. "The brain tissue surrounding cables is heated and can be damaged," says Jiang.

To solve this problem, researchers shielded the cables to reduce heating caused by the RF field and added RF protection diodes to the stimulator to block the energy. "The RF energy absorbed, and thus the RF-induced temperature rise, is significantly reduced," Jiang says. The RF protection also prevents the waves from entering the stimulator and damaging the device.

They also used fewer magnetic materials to prevent interaction with MRI magnetic fields, by replacing the stainless-steel battery casing with titanium and using an air core coil instead of an inductor with a ferrite core in the wireless communication circuit. Jiang says the team spent more than 10 years developing a 3.0T-compatible DBS device that is fully functional and safe. Now, the device promises to improve treatment for patients with Parkinson's disease and help researchers better understand how DBS works.

IMAGE: PROVIDED BY PINS

A powerful research tool

MRI is not only an effective diagnostic technique, but also a powerful and widely used tool to study the brain. Many neuroscience hypotheses can only be investigated with high-intensity MRI fields. As a result, a 3.0T MRI-compatible DBS device is extremely valuable in research, explains Jiang. "It could help us learn more about how the brain works and the effects of modulating neuronal signaling using DBS."

Jiang and his colleagues used the MRI-compatible stimulator in a recent study to better understand how DBS treats the motor symptoms of Parkinson's disease. Due to a lack of techniques that can reveal DBS-induced activity at the whole-brain level, DBS neuromodulatory effects on large-scale brain networks still need to be elucidated. In collaboration with Harvard University researchers, Jiang used functional MRI (fMRI) to investigate the neurological basis of patients with Parkinson's disease receiving DBS.

During the year-long, multi-center clinical trial, which started in 2016, researchers implanted the 3.0T MRI-compatible stimulator in 14 patients and collected a wealth of MRI images of their brains during DBS. At each appointment, researchers set patients' DBS devices to turn on and off in specific sequences while performing fMRI blood oxygenation level dependent (BOLD) scans, observing changes in brain function. The scan time totaled about 4 hours, during which scanning protocols in addition to BOLD were also performed, including T1- and T2-weighted structural imaging, diffusion-weighted imaging, and arterial spin label imaging.

Jiang and the team identified two neural circuits closely related to improving motor symptoms in patients with Parkinson's disease. According to Jiang, the study provides novel insight into the neural mechanism of DBS, which will help optimize treatment plans and improve the quality of life of patients. "We will continue using the 3.0T MRI-compatible stimulator for additional studies to better understand how DBS works not just in treating Parkinson's disease, but also other neurological disorders."

Given the positive responses of patients with Parkinson's disease to DBS, it is now being investigated to treat a variety of other disorders, including Alzheimer's disease, major depression, epilepsy, addiction, and pain. "We expect to understand these diseases better and develop new effective treatments with the novel paradigms provided by this new device."

PINS: fighting neurological disorders

Established in 2008, Beijing PINS Medical is now at the forefront of neuromodulation research in China, providing cutting-edge treatments for patients suffering from neurological disorders such as Parkinson's disease, epilepsy, chronic pain, and overactive bladder. "Neuromodulation, a technology that brings about the alteration—or modulation—of nerve activity by delivering electrical or pharmaceutical agents directly to a target area, is an interdisciplinary field that grew out of a clinical need," says Luming Li, director of the National Engineering Research Center of Neuromodulation at Tsinghua University. PINS Medical collaborates closely with Li's center at Tsinghua University as well as other affiliated clinical centers. They have developed a variety of clinical products, including stimulators for deep brain, vagus nerve, spinal cord, and sacral nerve, which are now available in both China and other major regions around the world.

PINS Medical's primary mission as a high-tech health care corporation is to provide patients with innovative, high-quality products and services that improve their quality of life. PINS stands for "Programmable Implanted Neuromodulation Stimulator" and is also an acronym for "Patient Is Number 1 alwayS," which speaks to their goals of improving patient well-being and restoring hope, with a focus that extends beyond business to improving society for all citizens. "The application of DBS ranges from a variety of movement disorders to psychiatric disorders. There is also a huge potential for using neuromodulation for the treatment of lifestyle diseases such as obesity and diabetes. Many diseases will be treated, and more patients will benefit from neuromodulation therapy," says Li. "It is an exciting new field that is still evolving."



The only rechargeable DBS device now that is 3.0T MRI compatible.

Sponsored by

PINS

IMAGE: PROVIDED BY PINS

Science AAAS

Editor-in-Chief Holden Thorp, hthorp@aaas.org

Executive Editor Valda Vinson

Editor, Research Jake S. Yeston **Editor, Insights** Lisa D. Chong **Managing Editor** Lauren Kmec

DEPUTY EDITORS Gemma Alderton (UK),Stella M. Hurtley (UK), Phillip D. Szuromi, Sacha Vignieri SR. EDITORS Caroline Ash (UK), Michael A. Funk, Brent Grocholski, Pamela J. Hines, Di Jiang, Priscilla N. Kelly, Marc S. Lavine (Canada), Mattia Maroso, Yevgeniya Nusinovich, Ian S. Osborne (UK), L. Bryan Ray, Seth Thomas Scanlon (UK), H. Jesse Smith, Keith T. Smith (UK), Jelena Stajic, Peter Stern (UK), Valerie B. Thompson, Brad Wible ASSOCIATE EDITORS Bianca Lopez, Madeleine Seale (UK), Corinne Simonti, Yury V. Suleymanov, Ekeoma Uzogara LETTERS EDITOR Jennifer Sills LEAD CONTENT PRODUCTION EDITORS Chris Filiatreau, Harry Jach SR. CONTENT PRODUCTION EDITOR Amelia Beyna CONTENT PRODUCTION EDITORS Julia Haber-Katris, Nida Masiulis, Abigail Shashikanth, Suzanne M. White SR. EDITORIAL MANAGERS Carolyn Kyle, Beverly Shields SR. PROGRAM ASSOCIATE Maryrose Madrid EDITORIAL ASSOCIATE Joi S. Granger SR. EDITORIAL COORDINATORS Aneera Dobbins, Jeffrey Hearn, Lisa Johnson, Jerry Richardson, Hilary Stewart (UK), Alice Whaley (UK), Anita Wynn EDITORIAL COORDINATORS Maura Byrne, Alexander Kief, Ronmel Navas, Isabel Schnaidt, Qiyam Stewart, Brian White RESEARCH & DATA ANALYST Jessica L. Slater ADMINISTRATIVE COORDINATOR Karalee P. Rogers ASI DIRECTOR, OPERATIONS Janet Clements (UK) ASI SR. OFFICE ADMINISTRATOR Jessica Waldock (UK)

News Editor Tim Appenzeller

NEWS MANAGING EDITOR John Travis INTERNATIONAL EDITOR Martin Enserink DEPUTY NEWS EDITORS Shraddha Chakradhar, Elizabeth Culotta, Lila Guterman, David Grimm, Eric Hand (Europe), David Malakoff SR. CORRESPONDENTS Daniel Clery (UK), Jon Cohen, Jeffrey Mervis, Elizabeth Pennisi ASSOCIATE EDITORS Jeffrey Brainard, Michael Price, Kelly Servick NEWS REPORTERS Adrian Cho, Jennifer Couzin-Frankel, Jocelyn Kaiser, Rodrigo Pérez Ortega (Mexico City), Robert F. Service, Erik Stokstad, Paul Voosen, Meredith Wadman INTERNS Zack Savitsky, Viviana Flores, Katherine Irving CONTRIBUTING CORRESPONDENTS Warren Cornwall, Andrew Curry (Berlin), Ann Gibbons, Sam Kean, Eli Kintisch, Kai Kupferschmidt (Berlin), Andrew Lawler, Mitch Leslie, Eliot Marshall, Virginia Morell, Dennis Normile (Tokyo), Elisabeth Pain (Careers), Charles Piller, Gabriel Popkin, Michael Price, Joshua Sokol, Richard Stone, Emily Underwood, Gretchen Vogel (Berlin), Lizzie Wade (Mexico City) CAREERS Rachel Bernstein (Editor), Katie Langin (Associate Editor) COPY EDITORS Julia Cole (Senior Copy Editor), Morgan Everett, Cyra Master (Copy Chief) ADMINISTRATIVE SUPPORT Meagan Weiland

Creative Director Beth Rakouskas

DESIGN MANAGING EDITOR Chrystal Smith GRAPHICS MANAGING EDITOR Chris Bickel PHOTOGRAPHY MANAGING EDITOR Emily Petersen MULTIMEDIA MANAGING PRODUCER Kevin McLean WEB CONTENT STRATEGY MANAGER Kara Estelle-Powers DESIGN EDITOR Marcy Atarod DESIGNER Christina Aycock SENIOR SCIENTIFIC ILLUSTRATOR Valerie Altounian SCIENTIFIC ILLUSTRATORS Austin Fisher, Kellie Holoski, Ashley Mastin INTERACTIVE GRAPHICS EDITOR Kelly Franklin SENIOR GRAPHICS SPECIALISTS Holly Bishop, Nathalie Cary SENIOR PHOTO EDITOR Charles Borst SENIOR PODCAST PRODUCER Sarah Crespi VIDEO PRODUCER Meagan Cantwell SOCIAL MEDIA STRATEGIST Jessica Hubbard SOCIAL MEDIA PRODUCER Sabrina Jenkins WEB DESIGNER Jennie Pajerowski

Chief Executive Officer and Executive Publisher Sudip Parikh

Publisher, Science Family of Journals Bill Moran

DIRECTOR, BUSINESS SYSTEMS AND FINANCIAL ANALYSIS Randy Yi DIRECTOR, BUSINESS OPERATIONS & ANALYSIS Eric Knott DIRECTOR OF ANALYTICS Enrique Gonzales MANAGER, BUSINESS OPERATIONS Jessica Tierney MANAGER, BUSINESS ANALYSIS Cory Lipman BUSINESS ANALYSTS Kurt Ennis, Maggie Clark FINANCIAL ANALYST Isacco Fusi BUSINESS OPERATIONS ADMINISTRATOR Taylor Fisher SENIOR PRODUCTION MANAGER Jason Hillman SENIOR MANAGER, PUBLISHING AND CONTENT SYSTEMS Marcus Spiegler CONTENT OPERATIONS MANAGER Rebecca Doshi SENIOR CONTENT & PUBLISHING SYSTEMS SPECIALIST Jacob Hedrick SENIOR PRODUCTION SPECIALIST Kristin Wowk PRODUCTION SPECIALISTS Kelsey Cartelli, Audrey Diggs DIGITAL PRODUCTION MANAGER Lisa Stanford CONTENT SPECIALIST Kimberley Oster ADVERTISING PRODUCTION OPERATIONS MANAGER Deborah Tompkins DESIGNER, CUSTOM PUBLISHING Jeremy Huntsinger SR. TRAFFIC ASSOCIATE Christine Hall SPECIAL PROJECTS ASSOCIATE Sarah Dhere

ASSOCIATE DIRECTOR, BUSINESS DEVELOPMENT Justin Sawyers GLOBAL MARKETING MANAGER Allison Pritchard DIGITAL MARKETING MANAGER Aimee Aponte JOURNALS MARKETING MANAGER Shawana Arnold MARKETING ASSOCIATES Aaron Helmbrecht, Ashley Hylton, Mike Romano, Lorena Chirinos Rodriguez, Jenna Voris SENIOR DESIGNER Kim Huynh

DIRECTOR AND SENIOR EDITOR, CUSTOM PUBLISHING Sean Sanders ASSISTANT EDITOR, CUSTOM PUBLISHING Jackie Oberst PROJECT MANAGER Melissa Collins

DIRECTOR, PRODUCT & PUBLISHING DEVELOPMENT Chris Reid DIRECTOR, BUSINESS STRATEGY AND PORTFOLIO MANAGEMENT Sarah Whalen ASSOCIATE DIRECTOR, PRODUCT MANAGMENT Kris Bishop PRODUCT DEVELOPMENT MANAGER Scott Chernoff PUBLISHING TECHNOLOGY MANAGER Michael Di Natale SR. PRODUCT ASSOCIATE Robert Koepke PRODUCT ASSOCIATE Caroline Breul, Anne Mason SPJ ASSOCIATE MANAGER Samantha Bruno Fuller SPJ ASSOCIATE Casey Buchta

MARKETING MANAGER Kess Knight BUSINESS DEVELOPMENT MANAGER Rasmus Andersen SENIOR INSTITUTIONAL LICENSING MANAGER Ryan Rexroth INSTITUTIONAL LICENSING MANAGER Marco Castellan, Claudia Paulsen-Young SENIOR MANAGER, INSTITUTIONAL LICENSING OPERATIONS Judy Lillibridge SENIOR OPERATIONS ANALYST Lana Guz SYSTEMS & OPERATIONS ANALYST Ben Teincuff FULFILLMENT ANALYST Aminta Reyes

DIRECTOR, GLOBAL SALES Tracy Holmes US EAST COAST AND MID WEST SALES Stephanie O'Connor US MID WEST, MID ATLANTIC AND SOUTH EAST SALES Chris Hoag US WEST COAST SALES Lynne Stickrod ASSOCIATE DIRECTOR, ROW Roger Goncalves SALES REP, ROW Sarah Lelarge SALES ADMIN ASSISTANT, ROW Victoria Glasbey DIRECTOR OF GLOBAL COLLABORATION AND ACADEMIC PUBLISHING RELATIONS, ASIA Xiaoying Chu ASSOCIATE DIRECTOR, INTERNATIONAL COLLABORATION Grace Yao SALES MANAGER Danny Zhao MARKETING MANAGER Kilo Lan ASCA CORPORATION, JAPAN Rie Rambelli (Tokyo), Miyuki Tani (Osaka)

DIRECTOR, COPYRIGHT, LICENSING AND SPECIAL PROJECTS Emilie David RIGHTS AND PERMISSIONS ASSOCIATE Elizabeth Sandler LICENSING ASSOCIATE Virginia Warren CONTRACT SUPPORT SPECIALIST Michael Wheeler

MAIN HEADQUARTERS
Science/AAAS
1200 New York Ave. NW
Washington, DC 20005

SCIENCE INTERNATIONAL
Clarendon House
Clarendon Road
Cambridge, CB2 8FH, UK

SCIENCE CHINA
Room 1004, Culture Square
No. 59 Zhongguancun St.
Haidian District, Beijing, 100872

SCIENCE JAPAN
ASCA Corporation
Sibaura TY Bldg. 4F, 1-14-5
Shibaura Minato-ku
Tokyo, 108-0073 Japan

EDITORIAL
science_editors@aaas.org

NEWS
science_news@aaas.org

INFORMATION FOR AUTHORS
science.org/authors/science-information-authors

REPRINTS AND PERMISSIONS
science.org/help/reprints-and-permissions

MEDIA CONTACTS
scipak@aaas.org

MULTIMEDIA CONTACTS
SciencePodcast@aaas.org
ScienceVideo@aaas.org

INSTITUTIONAL SALES AND SITE LICENSES
science.org/librarian

PRODUCT ADVERTISING & CUSTOM PUBLISHING
advertising.science.org/products-services
science_advertising@aaas.org

CLASSIFIED ADVERTISING
advertising.science.org/science-careers
advertise@sciencecareers.org

JOB POSTING CUSTOMER SERVICE
employers.sciencecareers.org
support@sciencecareers.org

MEMBERSHIP AND INDIVIDUAL SUBSCRIPTIONS
science.org/subscriptions

MEMBER BENEFITS
aaas.org/membership/benefits

AAAS BOARD OF DIRECTORS
CHAIR Susan G. Amara
PRESIDENT Gilda A. Barabino
PRESIDENT-ELECT Keith Yamamoto
TREASURER Carolyn N. Ainslie
CHIEF EXECUTIVE OFFICER Sudip Parikh
BOARD Cynthia M. Beall, Ann Bostrom, Janine Austin Clayton, Kaye Husbands Fealing, Maria M. Klawe, Jane Maienschein, Robert B. Millard, Babak Parviz, William D. Provine, Juan S. Ramírez Lugo, Susan M. Rosenberg

Science serves as a forum for discussion of important issues related to the advancement of science by publishing material on which a consensus has been reached as well as including the presentation of minority or conflicting points of view. Accordingly, all articles published in *Science*—including editorials, news and comment, and book reviews—are signed and reflect the individual views of the authors and not official points of view adopted by AAAS or the institutions with which the authors are affiliated.

BOARD OF REVIEWING EDITORS (Statistics board members indicated with **S**)

Erin Adams, *U. of Chicago*
Takuzo Aida, *U. of Tokyo*
Leslie Aiello, *Wenner-Gren Fdn.*
Deji Akinwande, *UT Austin*
Judith Allen, *U. of Manchester*
Marcella Alsan, *Harvard U.*
James Analytis, *UC Berkeley*
Paola Arlotta, *Harvard U.*
Delia Baldassarri, *NYU*
Nenad Ban, *ETH Zürich*
Christopher Barratt, *U. of Dundee*
Nandita Basu, *U. of Waterloo*
Franz Bauer, *Pontificia U. Católica de Chile*
Ray H. Baughman, *UT Dallas*
Carlo Beenakker, *Leiden U.*
Yasmine Belkaid, *NIAID, NIH*
Philip Benfey, *Duke U.*
Kiros T. Berhane, *Columbia U.*
Joseph J. Berry, *NREL*
Alessandra Biffi, *Harvard Med.*
Chris Bowler, *École Normale Supérieure*
Ian Boyd, *U. of St. Andrews*
Malcolm Brenner, *Baylor Coll. of Med.*
Emily Brodsky, *UC Santa Cruz*
Ron Brookmeyer, *UCLA* (**S**)
Christian Büchel, *UKE Hamburg*
Dennis Burton, *Scripps Res.*
Carter Tribley Butts, *UC Irvine*
György Buzsáki, *NYU School of Med.*
Mariana Byndloss, *Vanderbilt U. Med. Ctr.*
Annmarie Carlton, *UC Irvine*
Simon Cauchemez, *Inst. Pasteur*
Ling-Ling Chen, *SIBCB, CAS*
Wendy Cho, *UIUC*
Ib Chorkendorff, *Denmark TU*
Karlene Cimprich, *Stanford U.*
James J. Collins, *MIT*
Robert Cook-Deegan, *Arizona State U.*
Virginia Cornish *Columbia U.*
Carolyn Coyne, *Duke U.*
Roberta Croce, *VU Amsterdam*
Christina Curtis, *Stanford U.*
Ismaila Dabo, *Penn State U.*
Jeff L. Dangl, *UNC*
Chiara Daraio, *Caltech*
Nicolas Dauphas, *U. of Chicago*
Frans de Waal, *Emory U.*
Claude Desplan, *NYU*
Sandra Díaz, *U. Nacional de Córdoba*
Samuel Díaz-Muñoz, *UC Davis*
Ulrike Diebold, *TU Wien*
Stefanie Dimmeler, *Goethe-U. Frankfurt*
Hong Ding, *Inst. of Physics, CAS*
Dennis Discher, *UPenn*
Jennifer A. Doudna, *UC Berkeley*
Ruth Drdla-Schutting, *Med. U. Vienna*
Raissa M. D'Souza, *UC Davis*
Bruce Dunn, *UCLA*
William Dunphy, *Caltech*
Scott Edwards, *Harvard U.*
Todd Ehlers, *U. of Tübingen*
Nader Engheta, *UPenn*
Karen Ersche, *U. of Cambridge*
Beate Escher, *UFZ & U. of Tübingen*
Barry Everitt, *U. of Cambridge*
Vanessa Ezenwa, *U. of Georgia*
Toren Finkel, *U. of Pitt. Med. Ctr.*
Gwenn Flowers, *Simon Fraser U.*
Natascha Förster Schreiber, *MPI Extraterrestrial Phys.*
Peter Fratzl, *MPI Potsdam*
Elaine Fuchs, *Rockefeller U.*
Jay Gallagher, *U. of Wisconsin*
Daniel Geschwind, *UCLA*
Ramon Gonzalez, *U. of South Florida*
Sandra González-Bailón, *UPenn*
Gillian Griffiths, *U. of Cambridge*
Nicolas Gruber, *ETH Zürich*
Hua Guo, *U. of New Mexico*
Taekjip Ha, *Johns Hopkins U.*
Daniel Haber, *Mass. General Hos.*
Sharon Hammes-Schiffer, *Yale U.*
Wolf-Dietrich Hardt, *ETH Zürich*
Louise Harra, *UCL*
Carl-Philipp Heisenberg, *IST Austria*
Janet G. Hering, *Eawag*
Christoph Hess, *U. of Basel & U. of Cambridge*
Heather Hickman, *NIAID, NIH*
Hans Hilgenkamp, *U. of Twente*
Janneke Hille Ris Lambers, *ETH Zürich*
Kai-Uwe Hinrichs, *U. of Bremen*
Deirdre Hollingsworth, *U. of Oxford*
Randall Hulet, *Rice U.*
Auke Ijspeert, *EPFL*
Gwyneth Ingram, *ENS Lyon*
Darrell Irvine, *MIT*
Akiko Iwasaki, *Yale U.*
Stephen Jackson, *USGS & U. of Arizona*
Erich Jarvis, *Rockefeller U.*
Peter Jonas, *IST Austria*
Johanna Joyce, *U. de Lausanne*
Matt Kaeberlein, *U. of Wash.*
William Kaelin Jr., *Dana-Farber*
Daniel Kammen, *UC Berkeley*
Kisuk Kang, *Seoul Nat. U.*
Sabine Kastner, *Princeton U.*
V. Narry Kim, *Seoul Nat. U.*
Robert Kingston, *Harvard Med.*
Nancy Knowlton, *Smithsonian Institution*
Etienne Koechlin, *École Normale Supérieure*
Alex L. Kolodkin, *Johns Hopkins U.*
LaShanda Korley, *U. of Delaware*
Julija Krupic, *U. of Cambridge*
Paul Kubes, *U. of Calgary*
Chris Kuzawa, *Northwestern U.*
Laura Lackner, *Northwestern U.*
Gabriel Lander, *Scripps Res.* (**S**)
Mitchell A. Lazar, *UPenn*
Hedwig Lee, *Duke U.*
Luis Liz-Marzán, *CIC biomaGUNE*
Omar Lizardo, *UCLA*
Jonathan Losos, *Wash. U. in St. Louis*
Ke Lu, *Inst. of Metal Res., CAS*
Christian Lüscher, *U. of Geneva*
Jean Lynch-Stieglitz, *Georgia Inst. of Tech.*
David Lyons, *U. of Edinburgh*
Fabienne Mackay, *QIMR Berghofer*
Zeynep Madak-Erdogan, *UIUC*
Anne Magurran, *U. of St. Andrews*
Ari Pekka Mähönen, *U. of Helsinki*
Asifa Majid, *U. of Oxford*
Oscar Marín, *King's Coll. London*
Charles Marshall, *UC Berkeley*
Christopher Marx, *U. of Idaho*
David Masopust, *U. of Minnesota*
Geraldine Masson, *CNRS*
C. Robertson McClung, *Dartmouth*
Rodrigo Medellín, *U. Nacional Autónoma de México*
C. Jessica Metcalf, *Princeton U.*
Baoxia Mi, *UC Berkeley*
Tom Misteli, *NCI, NIH*
Alison Motsinger-Reif, *NIEHS, NIH* (**S**)
Danielle Navarro, *U. of New South Wales*
Daniel Nettle, *Newcastle U.*
Daniel Neumark, *UC Berkeley*
Thi Hoang Duong Nguyen, *MRC LMB*
Beatriz Noheda, *U. of Groningen*
Helga Nowotny, *Vienna Sci. & Tech. Fund*
Pilar Ossorio, *U. of Wisconsin*
Andrew Oswald, *U. of Warwick*
Isabella Pagano, *Istituto Nazionale di Astrofisica*
Elizabeth Levy Paluck, *Princeton U.*
Jane Parker, *MPI Cologne*
Giovanni Parmigiani, *Dana-Farber* (**S**)
Daniel Pauly, *U. of British Columbia*
Ana Pêgo, *U. do Porto*
Samuel Pfaff, *Salk Inst.*
Julie Pfeiffer, *UT Southwestern Med. Ctr.*
Philip Phillips, *UIUC*
Matthieu Piel, *Inst. Curie*
Kathrin Plath, *UCLA*
Martin Plenio, *Ulm U.*
Katherine Pollard, *UCSF*
Elvira Poloczanska, *Alfred-Wegener-Inst.*
Julia Pongratz, *Ludwig Maximilians U.*
Philippe Poulin, *CNRS*
Lei Stanley Qi, *Stanford U.*
Trevor Robbins, *U. of Cambridge*
Joeri Rogelj, *Imperial Coll. London*
Amy Rosenzweig, *Northwestern U.*
Mike Ryan, *UT Austin*
Miquel Salmeron, *Lawrence Berkeley Nat. Lab*
Nitin Samarth, *Penn State U.*
Erica Ollmann Saphire, *La Jolla Inst.*
Joachim Saur, *U. zu Köln*
Alexander Schier, *Harvard U.*
Wolfram Schlenker, *Columbia U.*
Susannah Scott, *UC Santa Barbara*
Anuj Shah, *U. of Chicago*
Vladimir Shalaev, *Purdue U.*
Jie Shan, *Cornell U.*
Beth Shapiro, *UC Santa Cruz*
Jay Shendure, *U. of Wash.*
Steve Sherwood, *U. of New South Wales*
Brian Shoichet, *UCSF*
Robert Siliciano, *JHU School of Med.*
Lucia Sivilotti, *UCL*
Emma Slack, *ETH Zürich & U. of Oxford*
Richard Smith, *UNC* (**S**)
John Speakman, *U. of Aberdeen*
Tara Spires-Jones, *U. of Edinburgh*
Allan C. Spradling, *Carnegie Institution for Sci.*
V. S. Subrahmanian, *Northwestern U.*
Ira Tabas, *Columbia U.*
Eriko Takano, *U. of Manchester*
A. Alec Talin, *Sandia Natl. Labs*
Patrick Tan, *Duke-NUS Med. School*
Sarah Teichmann, *Wellcome Sanger Inst.*
Rocio Titiunik, *Princeton U.*
Shubha Tole, *Tata Inst. of Fundamental Res.*
Maria-Elena Torres Padilla, *Helmholtz Zentrum München*
Kimani Toussaint, *Brown U.*
Barbara Treutlein, *ETH Zürich*
Jason Tylianakis, *U. of Canterbury*
Wim van der Putten, *Netherlands Inst. of Ecology*
Matthew Vander Heiden, *MIT*
Ivo Vankelecom, *KU Leuven*
Judith Varner, *UC San Diego*
Henrique Veiga-Fernandes, *Champalimaud Fdn.*
Reinhilde Veugelers, *KU Leuven*
Bert Vogelstein, *Johns Hopkins U.*
Julia Von Blume, *Yale School of Med.*
David Wallach, *Weizmann Inst.*
Jane-Ling Wang, *UC Davis* (**S**)
Jessica Ware, *Amer. Mus. of Natural Hist.*
David Waxman, *Fudan U.*
Chris Wikle, *U. of Missouri* (**S**)
Terrie Williams, *UC Santa Cruz*
Ian A. Wilson, *Scripps Res.* (**S**)
Hao Wu, *Harvard U.*
Li Wu, *Tsinghua U.*
Wei Xie, *Tsinghua U.*
Benjamin Youngblood, *St. Jude*
Yu Xie, *Princeton U.*
Jan Zaanen, *Leiden U.*
Kenneth Zaret, *UPenn School of Med.*
Lidong Zhao, *Beihang U.*
Bing Zhu, *Inst. of Biophysics, CAS*
Xiaowei Zhuang, *Harvard U.*
Maria Zuber, *MIT*

YOUR RESEARCH HAS ITS REWARDS.



Submit an essay by 3/15/23 to enter to win $25K.

The prestigious international *Science* & PINS Prize is awarded annually to outstanding early-career researchers in the emerging field of neuromodulation. Findings already show improved outcomes in several neurological disorders. To enter, just write a 1000-word essay about your research performed in the last three years. The Grand Prize winner will be presented a US$25,000 award, as well as have their essay published in *Science* magazine and on *Science* Online. A runner-up will have their essay published online. For additional inquiries, email SciencePINSPrize@aaas.org.

SCIENCE-PINS PRIZE FOR NEUROMODULATION

SCIENCE-PINS

SCIENCE.ORG/PINS

CALL FOR PAPERS

SCIENCE PARTNER JOURNALS



Journal of Remote Sensing

The *Journal of Remote Sensing* is an online-only Open Access Science Partner Journal published in affiliation with **Aerospace Information Research Institute, Chinese Academy of Sciences (AIR-CAS)** and distributed by the **American Association for the Advancement of Science (AAAS)**. Like all partners participating in the Science Partner Journal program, the *Journal of Remote Sensing* is editorially independent from the *Science* family of journals and AIR-CAS is responsible for all content published in the journal. This journal covers multiple research areas that include theory, science, technology of remote sensing, and interdisciplinary research with earth science and information science. Particular topics of interest within the journal include radiative transfer modeling, biogeosciences remote sensing, remote sensing of energy, and more.

Submit your research to the *Journal of Remote Sensing* today!

Learn more at **spj.sciencemag.org/remotesensing**

The Science Partner Journal (SPJ) program was established by the American Association for the Advancement of Science (AAAS), the nonprofit publisher of the *Science* family of journals. The SPJ program features high-quality, online-only, Open Access publications produced in collaboration with international research institutions, foundations, funders and societies. Through these collaborations, AAAS furthers its mission to communicate science broadly and for the benefit of all people by providing top-tier international research organizations with the technology, visibility, and publishing expertise that AAAS is uniquely positioned to offer as the world's largest general science membership society.

Visit us at **spj.sciencemag.org**

@SPJournals @SPJournals

OPEN ACCESS

ARTICLE PROCESSING CHARGES WAIVED UNTIL JULY 2023

Appoint a new NIH director, now



H. Holden Thorp
Editor-in-Chief,
Science journals.
hthorp@aaas.org;
@hholdenthorp

Why has President Biden's administration been staggering when it comes to key scientific appointments? Most noticeably, there has been a failure to confirm a new director of the National Institutes of Health (NIH) since Francis Collins stepped down a year ago. It took nearly a year to nominate the Commissioner of the Food and Drug Administration (FDA), Robert Califf. And regrettably, Biden began his presidency with the nomination of geneticist Eric Lander as the first science adviser to the president and director of the White House Office of Science and Technology Policy (OSTP). A year later, Lander resigned in disgrace because of abusive behavior toward staff. Although recent appointments provide some confidence [including Monica Bertagnolli as director of the National Cancer Institute (NCI), Joni Rutter as director of the National Center for Advancing Translational Sciences, and Arati Prabhakar as the new director of OSTP], the most high-profile biomedical job in the United States—NIH director—remains unfilled.

Although he faced criticism on some fronts (policies that protect researchers from harassment; equity in funding) toward the end of his tenure, Francis Collins had more impact than any previous director, serving three presidents and presiding over substantial increases in research funding. Filling the directorship after his tenure was always going to be a challenge. But many good candidates are known to have been vetted, and then dropped out after prolonged delays and inaction. This is inexcusable. The administration came in with great fanfare about the value of science, and it can count some major accomplishments (such as the Creating Helpful Incentives to Produce Semiconductors and Science Act) as well as giving some relief from 4 years of nonsense in the Trump administration. Still, with the failure to carry out a highly visible appointment, the conviction rings hollow.

The lack of a confirmed director raises some problems. Lawrence Tabak has done a commendable job as interim NIH director, but it is time for some new faces after the lengthy Collins administration. (Tabak was an NIH deputy director and the deputy ethics counselor under Collins.) Furthermore, there are key appointments still to be made within the agency, most visibly, a successor to Anthony Fauci, who will leave the directorship of the National Institute of Allergy and Infectious Diseases at the end of the year. Recruiting into this and possibly other roles (including head of the new Advanced Research Projects Agency for Health, located at NIH) without a permanent NIH director will be a big challenge.

"...the delay is taking a toll on morale across the biomedical science community."

In addition, a confirmed NIH director has much greater influence in Congress. Although well-known projects like the Cancer Moonshot will likely thrive, a permanent director is needed to lobby for other priorities. The problem of opioid addiction is an area that needs more initiatives and advocacy. And policy issues—minimum salaries for postdoctoral associates, grant requirements in the pandemic era, stem cell regulations, data policies, and compliance with OSTP's memorandum on public access to research—must be addressed. Ned Sharpless, former director of the NCI and interim FDA commissioner, confirmed that the delay is taking a toll on morale across the biomedical science community. "There are so many problems and opportunities that require the leadership of a Senate-confirmed director," he told me, "and it's getting harder to understand why a nomination hasn't been made when there are outstanding individuals willing to take on the job."

It's unclear who or what is holding up the nomination. Is the White House simply incapable of deciding whom to nominate, or more likely, has it been distracted by other matters? Either is possible, but both are indefensible. Perhaps, the White House is just comfortable with a de facto continuation of the Collins era, pushing off a decision until the next presidential term. Alternatively, it could be that the Secretary of Health and Human Services, Xavier Becerra, who is responsible for enhancing public health through both policy and research, is not sufficiently interested in research to focus on the appointment. The failure to make a nomination is a broken promise from an administration that proudly proclaimed that "the people have chosen science."

The Biden campaign leveraged the support of the scientific community to win the presidency. Leaving the most visible science position open for a year is a betrayal of that support. President Biden must personally intervene to correct this now.

–H. Holden Thorp

Published online 16 December 2022; 10.1126/science.adg3034

PHOTO: CAMERON DAVIDSON



The MBZUAI Knowledge Center on the university's Masdar City campus in Abu Dhabi.

Collaborations without borders

Scientific collaboration is a foundational aspect of translational research, with interactions between researchers in different countries now common. Ongoing collaborations between Mohammed bin Zayed University of Artificial Intelligence (MBZUAI) and the Weizmann Institute of Science (WIS) are capitalizing on the concept of "science diplomacy" to drive progress in fields applying artificial intelligence (AI) to biomedical research.

Within one year of its inauguration as the world's first graduate, AI-focused, research university, MBZUAI signed a memorandum of understanding with WIS to establish the MBZUAI-WIS Joint Program for AI Research. The collaboration involves not only joint research projects and training programs but also AI conferences and workshops, as well as staff and student exchange programs, that emphasize their commitment to driving AI utilization in healthcare and biomedical research.

"MBZUAI represents a tightly integrated, interdisciplinary team prepared to apply their AI expertise to any number of science-related problems," says Dr. Le Song, department chair of machine learning at MBZUAI. "MBZUAI-WIS is advancing the presence of AI in the Middle East, but its impact can be potentially societal and broadly transformative."

Leveraging AI to drive basic and translational research

Generation of novel therapies is both time- and resource-intensive, with an extremely low success rate of drug candidates going from discovery to development. Nevertheless, the unprecedented scale of biological and clinical data generated during these activities demands methods capable of transforming these types of "big data" into clinically actionable discoveries.

Machine learning techniques have given rise to AI applications that enable clinicians and researchers to exploit large-scale, heterogeneous datasets and identify patterns connecting disease phenotype to patient physiology and characteristics. AI offers the ability to transform data into tailored, patient-specific therapeutic strategies. Three of the MBZUAI-WIS Joint Program for AI Research projects emphasize the potential impact of AI-driven, cross-disciplinary biomedical research in precision medicine.

1 Predicting disease onset and prognosis

In his TED talk from 2016, Eran Segal, a professor in the Department of Computer Science and Applied Mathematics at WIS, presented data illustrating the fallacy of a one-size-fits-all diet for humans. The findings demonstrated that responses to food are personal, and that a generalized approach to nutrition and diet results in wildly variable outcomes across populations. Providing personalized dietary advice required machine learning techniques to process large amounts of clinical data. The result was a model capable of not only accurately predicting a person's response to a given diet but also optimizing that diet to achieve beneficial changes in the gut microbiome.

In 2018, Dr. Segal expanded this concept into Project 10K (https://www.project10k.org.il/), a long-term observational study of 10,000 Israeli volunteers with the goal of compiling an extremely comprehensive phenotype (medical history, lifestyle, and nutritional habits) and molecular profile (including transcriptome, gut and oral microbiome, metabolome) for each individual.

Dr. Segal says they ultimately enrolled over 20,000 people, with approximately 10,000 having already undergone baseline profiling and another 2,500 completing a second round after 2 years. "We have identified novel gut bacteria with therapeutic potential for weight loss, diabetes, hypertension, and several other indications, as

PHOTO: PROVIDED BY MBZUAI

well as made discoveries related to models for biological aging," says Dr. Segal. "These findings offer opportunities to perhaps treat and improve people's health by interventions directed at reducing their biological age."

Discussions are currently underway with researchers in other countries to collect similar data in order to enhance model robustness and generalization. Dr. Segal emphasizes the importance of his MBZUAI collaborators in this process. "Drs. Le Song and Eric Xing bring novel methodologies that can handle the complex and heterogeneous nature of these extremely large datasets."

2 Elucidating cellular function and dynamics in native tissue



Left to right: Eran Segal, Nir Yosef, Le Song

Single-cell RNA sequencing allows assessment and comparison of transcriptional activity at single-cell resolution, enabling novel insights into cellular processes and their regulation and variability among cells. Understanding how transcriptomes influence and are influenced by the cell's tissue environment under different physiological states requires their analysis within intact tissue (i.e., spatial transcriptomics). Although spatial transcriptomics enables high-resolution assessment in this context, limitations exist regarding data quality. Machine learning techniques are instrumental in addressing these shortcomings to enable the generation of models that approximate tissue-specific cellular networks.

Nir Yosef, an associate professor in the Department of Systems Immunology at WIS, together with Michael I. Jordan, a laureate professor at MBZUAI, is leading a project to optimize applications of these methods to more accurately define the function of specific tissues and their disease-specific alterations. "Supplementing genome-scale cell profiling with information about tissue context can offer a better understanding of the emergence of tissue function," says Dr. Yosef. "Such realizations can be leveraged for translational applications, including identifying patient-specific therapeutic targets and stratification for medical diagnosis and treatment."

This project also involves establishment of the MBZUAI-WIS Center of AI for Spatial Transcriptomics. "We expect to become a hub for software solutions that address challenges in data analysis and the development of applications to identify spatial features capable of predicting clinical outcomes," explains Yosef.

3 Designing new cancer immunotherapy strategies

The tumor microenvironment (TME) comprises both cancer and immune cells that dynamically interact to determine disease status and therapeutic response, with the efficacy of cancer immunotherapy— which harnesses a patient's immune system to recognize disease-specific characteristics and thereby target care—largely dictated by patient-specific differences in this area. In the TME, the heterogeneous state of T-cells (tumor-infiltrating lymphocytes, or TILs) is particularly important from a therapeutic standpoint.

MBZUAI-WIS collaborators are targeting the TME-specific landscape of T-cell heterogeneity and dynamics using both AI and in vivo experiments to develop models capable of tracking T-cells and identifying changes in their status as functional (exhibiting antitumor activity) or dysfunctional. Given that the state of TIL populations differs between tumor type and patient, determining TME-specific changes can ultimately facilitate precision immunotherapy.

"Our aim is to perform model pretraining using public datasets to establish gene-expression patterns across different cell types and perturbations, followed by adaption of these models to supplement data from in vivo perturbations," explains MBZUAI's Song. "The pretrained model both reduces the number of necessary in vivo perturbations and increases its predictive accuracy upon inclusion of the experimental results."

This project also aims to use these models to predict optimal combination therapies to overcome cases of acquired resistance, the concept being that generation of a patient-specific TME model will allow a rapid and targeted response to resistance, as well as predict patient response.

Driving AI innovation in biomedicine

In the press release for the joint program, leaders of both institutions emphasized the importance of empowering scientists by sharing resources and knowledge to foster a culture of international partnership and capitalize on the enormous possibilities of AI in scientific research.

"Given the broad applications of AI across disciplines, a focused understanding of traditional computational approaches is no longer sufficient for young researchers to facilitate interdisciplinary research," notes Song. "AI research now requires an integrated and collaborative approach to addressing problems across all areas of science."

Segal also emphasizes the mutually beneficial aspects of the MBZUAI-WIS partnership. "We are very excited to join forces with world-leading AI expert researchers at MBZUAI, and I believe in the power of such collaborations."

Sponsored by

MBZUAI

PHOTO: PROVIDED BY MBZUAI

NEWS

“I always had it in my mind, yeah, one of these days I’m going to be a patient. We all are.”

National Cancer Institute Director Monica Bertagnolli, quoted by *The Washington Post* after she revealed she was recently diagnosed with breast cancer.

IN BRIEF

Edited by **Michael Price**



PUBLIC HEALTH

Ebola vaccine trial on hold

Ebola treatment centers such as this one in Mubende, Uganda, remain empty.

A planned clinical trial of vaccines against the Sudan ebolavirus likely will not go forward, after traditional containment methods appear to have stamped out the outbreak of Ebola that surfaced in Uganda on 20 September. An international effort moved at record speed to deliver two experimental vaccines against the virus, which differs from the Zaire ebolavirus that caused the massive West Africa outbreak in 2014–16. The vaccines arrived in Uganda last week, and a third is on the way. But the planned “ring trial” depended on vaccinating recent contacts of people with confirmed Sudan ebolavirus infections. The last known case in Uganda left the hospital 3 weeks ago, and the number of contacts still eligible for the trial has dwindled. As of 15 December, Uganda had recorded 77 confirmed and probable deaths from the outbreak. A statement from the World Health Organization (WHO) said Makerere University is ready to lead the ring trial if new cases emerge. WHO plans to consult with experts in January 2023 on other potential studies of the vaccines.

HHMI funds education reform

PHILANTHROPY | The Howard Hughes Medical Institute (HHMI) is spending $60 million to create seven networks, totaling 104 colleges and universities, that will work together to improve U.S. undergraduate science education. Last month, HHMI announced that the third round of funding under its Inclusive Excellence program will be used to build decentralized “learning communities,” each with about 15 institutions, that will work on course content, faculty teaching, and helping students transfer from community colleges to 4-year degree programs. David Asai, HHMI’s education guru, says he hopes those in the consortia will “hold themselves accountable” for making the changes in academic culture needed to create a larger, diverse scientific workforce.

PHOTO: BADRU KATUMBA/AFP/GETTY IMAGES



The mason wasp uses the twin barbs of its genitalia as "pseudostingers."

BIOLOGY

Male wasps have protective privates

When a Japanese entomologist got stung by a male wasp earlier this year, she was shocked. Only females should be able to deliver such a painful prick, as their stingers are modified egg-laying organs known as ovipositors. Males are generally considered harmless. But looking closer at the mason wasp (*Anterhynchium gibbifrons*), the scientist realized it had pierced her skin using its sharp, two-pronged genitalia, she and colleagues reported this week in *Current Biology*. To test whether these males' pseudostingers might deter attackers, the researchers enclosed male mason wasps with one of their predators, a tree frog. The wasps fought hungry frogs with their piercing penises—and got spat out about one-third of the time. Males who had their pseudostingers removed all became frog food. The findings are the first evidence of male genitalia playing a defensive role in the animal kingdom.

Oppenheimer's name cleared

HISTORY OF SCIENCE | In 1954, the U.S. Atomic Energy Commission (AEC) revoked the security clearance of J. Robert Oppenheimer, the theoretical physicist who during World War II led the development of the first atomic bomb. Last week, the Department of Energy, AEC's successor, vacated that decision, stating the process that led to it was manifestly unfair. AEC leaders suspected Oppenheimer, who died in 1967, sympathized with communism and the Soviet Union. However, historians argue that records show he served the United States faithfully and he was sanctioned because of his opposition to developing the more powerful hydrogen bomb.

Chemical society fires editors

SCIENCE JOURNALISM | Chemists reacted with outrage after the American Chemical Society (ACS) fired two senior editors from its weekly magazine, *Chemical & Engineering News* (*C&EN*). In March 2021, ACS transferred *C&EN* from the society's publications division to its communications arm, and last week, Bibiana Campos Seijo, the magazine's editor-in-chief, and Jyllian Kemsley, an executive editor, were let go. Susan Morrissey, ACS communications vice president, noted in an editorial this week that the reorganization is meant to "strengthen [*C&EN*'s] role as the official organ" of the society. After the firings, 13 current and former members of *C&EN*'s advisory board posted an open letter questioning whether ACS officials had "revoked" the magazine's long-standing editorial independence. "What good is that subscription if *C&EN* primarily becomes a newsletter of ACS activities?" they wrote. Since the transfer, several staff journalists have left.

An old coffee bean returns

BOTANY | Recently, droughts have doubled the price of the world's most popular coffee bean, *Coffea arabica*. Global warming may soon make it impractical for many plantations to grow it. So, coffee growers in Africa have begun to resurrect a long-forgotten variety, *C. liberica*, researchers reported this week in *Nature Plants*. Botanists at the Royal Botanic Gardens, Kew, report that *C. liberica* was widely grown in the 1870s, but its walnut- to plum-size fruits and tough skin were harder to process than the cherry-size fruits of other varieties. The bean fell out of favor at the turn of the 20th century. In recent years, Ugandan farmers have started to ramp up cultivation of a *C. liberica* subspecies known as "excelsa," which is resistant to wilt and other diseases. It produces bold, sweet coffee and doesn't need chilly high altitudes to thrive. Thus, excelsa and other little-used coffee varieties may help keep coffee cups full as the planet warms, researchers note.

Kick-starting carbon capture

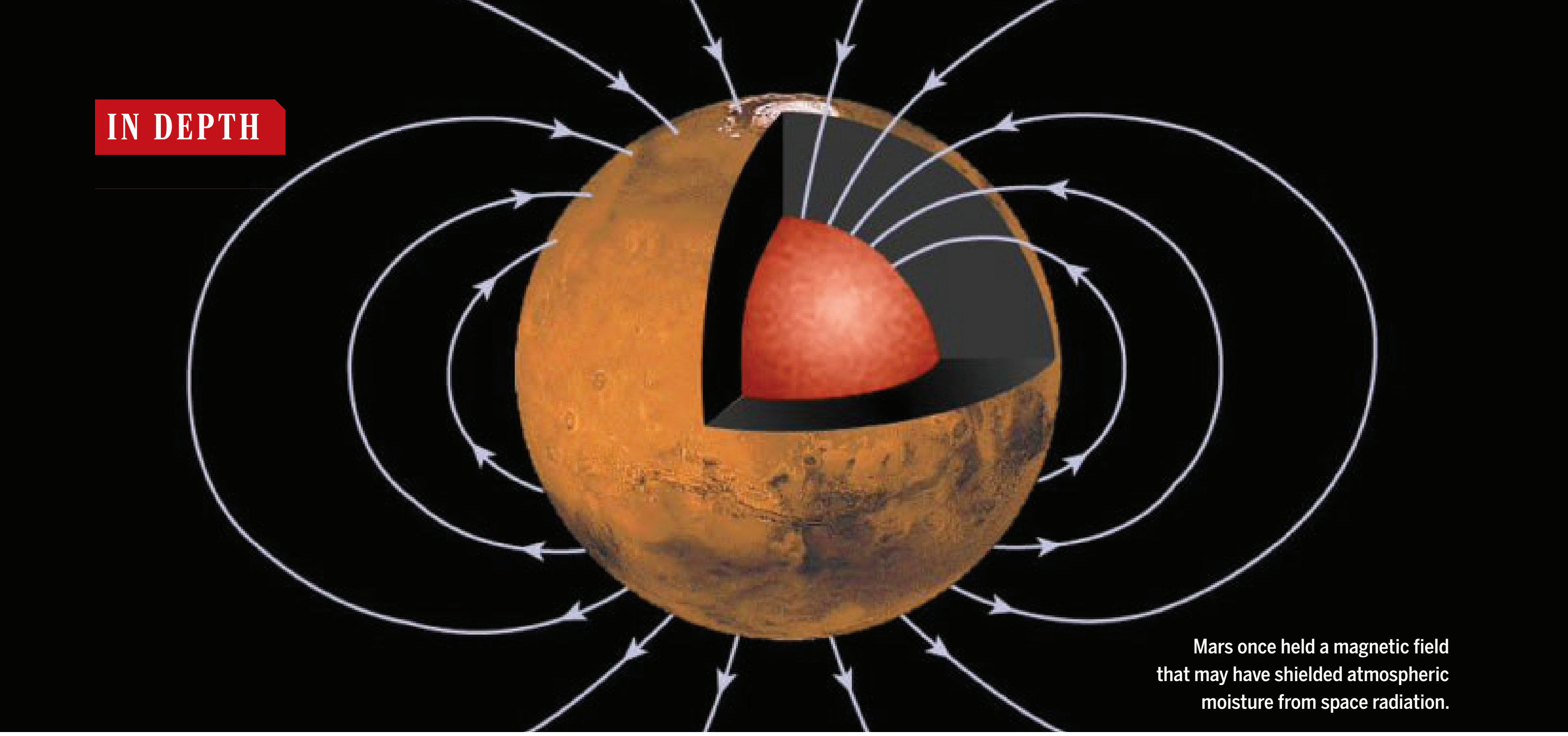
CLIMATE CHANGE | Last week, the U.S. Department of Energy (DOE) announced a $3.7 billion plan to kick-start commercial efforts to remove carbon dioxide (CO_2) from the atmosphere. DOE officials say such efforts will be critical to the U.S. meeting its goal of net-zero greenhouse gas emissions by 2050. According to the Intergovernmental Panel on Climate Change, between 100 gigatons and 1000 gigatons of CO_2 need to be removed from the atmosphere this century to limit global warming to 1.5°C. Funded by the recently passed Bipartisan Infrastructure Law, the program includes $3.5 billion for four regional facilities to demonstrate different direct air capture technologies, each capable of removing and storing at least 1 million tons of CO_2 from the atmosphere each year. Another $115 million will pay for a prize for novel direct air capture technologies. The remaining money will support state and local CO_2 capture efforts and commercial partnerships.

A vow to protect biodiversity

CONSERVATION | More than 190 nations this week agreed to new global goals for protecting nature by 2030. Two weeks of negotiations, which ended on 19 December, yielded numerous commitments including pledges to protect 30% of Earth's land and sea, and to equitably share any benefits derived from sequencing the genomes of wild organisms. Realizing the goals will be a challenge, observers warn. Nations failed to meet goals from previous versions of the biodiversity pact, and finding adequate funding is an issue. Negotiators also left many details unresolved. "Now we have to go into the nitty gritty" of implementation, says David Obura, a sustainability scientist who directs CORDIO East Africa, a conservation think tank.

PHOTO: SHINJI SUGIURA; S. SUGIURA *ET AL.*, *CURENT BIOLOGY*, 32, R1336, 2022

IN DEPTH



Mars once held a magnetic field that may have shielded atmospheric moisture from space radiation.

PALEOMAGNETISM

Mars's magnetic field was long-lived, reversible

Study of famed meteorite by quantum microscope hints at planet's prolonged habitability

By **Zack Savitsky**, *in Chicago*

Once upon a time, scientists believe, Mars was far from today's cold, inhospitable desert. Rivers carved canyons, lakes filled craters, and a magnetic field may have fended off space radiation, keeping it from eating away the atmospheric moisture. As the martian interior cooled, leading theories hold, its magnetic field died out, leaving the atmosphere undefended and ending this warm and wet period, when the planet might have hosted life. But researchers can't agree on when that happened.

Now, fragments from a famous martian meteorite, studied with a new kind of quantum microscope, have yielded evidence that the planet's field persisted until 3.9 billion years ago, hundreds of millions of years longer than many had thought. The clues in the meteorite, a Mars rock that ended up on Earth after an impact blasted it from its home planet, could extend Mars's window of habitability and reconcile conflicting timelines of the planet's early history. Discussed last week at a meeting of the American Geophysical Union (AGU), the findings also support the idea that, as on Earth, Mars's field sometimes flipped around—behavior that could shed light on the molten dynamo in the outer core that once powered it.

"They are able to paint a pretty good picture of what might have happened," says Jennifer Buz, a paleomagnetist at Northern Arizona University who was not involved in the study. "The work they did was just not possible with the technology before."

When certain kinds of iron-bearing minerals crystallize out of molten rock, their internal fields align with the planet's field like tiny compasses, preserving a stamp of its orientation. Subsequent impact events can heat up parts of a rock, glazing it with fields from later times and creating a magnetic palimpsest.

Orbiters around Mars have mapped these remnant magnetic signatures in rocks on the surface of Mars. But some of the planet's largest, most ancient scars—the Hellas, Argyre, and Isidis asteroid impact basins—don't appear to contain magnetized rocks at all. Most researchers think that's because the magnetic dynamo had subsided by the time these craters formed, about 4.1 billion years ago. Strangely, though, orbiters have detected magnetic signatures in lavas a few hundred million years younger, from other parts of Mars, suggesting the field had somehow survived longer than the basins let on.

"It's hard to ever say you really understand what's happened in the past on another planet if you have these two fundamentally opposing timelines," says Sarah Steele, a graduate student in earth and planetary sciences at Harvard University.

Steele wondered whether Allan Hills 84001, a martian meteorite retrieved from Antarctica in 1984, might have something to say on the question. Debunked claims from the 1990s that the meteorite contained fossilized bacteria made the 2-kilogram rock notorious, but researchers study it even today because at 4.1 billion years old, it is the only known pristine sample to record this critical era of Mars's history.

Steele and Harvard planetary scientist Roger Fu imaged three paper-thin slices of a 0.6-gram Allan Hills sample with Fu's state-of-the-art quantum diamond microscope. One of only a handful in the world, it relies on the sensitivity of atomic impurities in diamond to tiny changes in magnetic fields; it can map these changes across grains as small as a human hair. The enhanced resolution revealed something surprising: three distinct populations of iron-sulfide minerals. Two were strongly magnetized in different directions, whereas one lacked a significant magnetic signature.

In a paper now under review, Steele and Fu propose that these groupings reflect three known impact events recorded by the meteorite—which radioactive dating had placed at about 4 billion, 3.9 billion, and 1.1 billion years ago. Because the two older mineral populations are highly magnetized, Fu says, a global mag-

ILLUSTRATION: NASA/JPL/GSFC

netic field must still have been present at 3.9 billion years ago. The 3.9-billion-year-old field appears to be relatively strong: about 17 microtesla (about one-third the average strength of Earth's field).

At that strength, the field could have helped deflect harmful cosmic rays, protecting potential early life forms, says Ben Weiss, a planetary scientist at the Massachusetts Institute of Technology. It could have also shielded the atmosphere from the solar wind, a stream of particles that can accelerate the loss of water vapor and other constituents to space. "The longer the dynamo stays around, the longer you can have a period on Mars that's potentially habitable," Weiss says.

Rob Lillis, a planetary geophysicist at the University of California, Berkeley, is more cautious about that line of reasoning. He says a field could also accelerate atmospheric losses by funneling more solar wind to the poles.

The minerals also hold a clue to the planet's internal workings: The two magnetized populations record fields pointed in nearly opposite directions—138° apart. The researchers say there's little chance the rock simply rotated between impacts. Rather, they propose the martian dynamo must have flipped its poles, as Earth's does every few hundred million years. Computer simulations have shown dynamos only reverse within a narrow range of convection conditions in a planet's molten outer core, so the martian reversals could help constrain the history and nature of its dynamo, Lillis says.

A reversing dynamo could also help explain why many large, ancient basins lack a magnetic signal. In an AGU presentation, Steele used computer simulations to show layers of alternating magnetic fields could essentially cancel out the net magnetic field of the basins—making them appear to be demagnetized. The reversals may "allow us to tie all the strings together once and for all," Steele says.

As a bonus, magnetic reversals could provide a common time marker for rocks from different locations. "It's exciting to me to hear that there's evidence for a reversal in a meteorite," says Weiss, who proposed using reversals to date Mars rocks in a separate AGU presentation. "If [Mars's dynamo] is reversing, that plan we have in mind here is suddenly a lot more feasible."

Fu says he is in debt to the Allan Hills meteorite, which sparked his love for science as a child when he first learned of the famous rock on TV. "Early Mars is such a black box in many ways," Fu says. "The fact that we're taking a rock that's been analyzed to death … and can still get new information out of it, I think that's really cool." ■

U.S. BUDGET

Research gets a boost in final 2023 spending agreement

Budgets of many civilian science agencies will grow, but not always by as much as White House had requested

By ***Science*** **News Staff**

Congress did the best it could this week for basic research, unveiling a belated $1.7 trillion spending bill that keeps the U.S. government running for the next 9 months. But legislators' desire to increase the defense budget kept them from delivering a major promised boost for the National Science Foundation (NSF) and held several other civilian agencies to small increases.

The bill, expected to be finalized as *Science* went to press, will give the National Institutes of Health another solid year of growth. Its $2.5 billion, 5.6% increase will raise its 2023 budget—by far the largest of any federal research agency—to $47.5 billion. That increase is 10 times larger than President Joe Biden had requested. But Congress approved just $1.5 billion of his $5 billion request for the new Advanced Research Projects Agency for Health, a modest $500 million increase for its second year of operations.

NSF will get an 8% boost, to $9.54 billion. The additional $700 million is less than half the 20% increase that Biden had requested and that legislators had promised NSF earlier this year in a massive bill to boost the U.S. semiconductor industry.

Thanks to a budget gimmick, Congress is actually giving NSF an additional $1 billion over 2 years, classifying the boost as mandatory spending that falls outside the normal spending cap. The research account received $818 million more and education programs get $210 million, with most of the money coming in the current fiscal year.

Although NASA's overall budget will rise by 6%, to $25.4 billion, its science division will grow by only 2%, to $7.8 billion. Earth sciences will increase by 6%, with lawmakers requesting plans for the first four satellites in NASA's Earth System Observatory, a multibillion-dollar fleet that will monitor clouds, aerosols, and other phenomena that affect climate change. Congress also allowed NASA to shutter its Stratospheric Observatory for Infrared Astronomy, a telescope carried on a Boeing 747, giving NASA $30 million for "an orderly close-out."

Animal welfare advocates notched a victory when legislators gave the Food and Drug Administration the power to approve new drugs and biologics that have not been tested in animals. The legislation suggests alternative methods, including using organ chips and cell-based assays. "Removing the mandate for these tests opens the door to a more modern approach that reflects the current science," says Kathy Guillermo, senior vice president at People for the Ethical Treatment of Animals, one group that lobbied for the change.

The National Oceanic and Atmospheric Administration's budget grows by 17%, to $6.35 billion, less than the $6.9 billion that Biden requested. Its climate science budget would increase by 12%, to $224 million. The extra money would help fund a $12 million initiative to study water in the western United States, which is gripped by drought.

Lawmakers doubled Biden's requested increase for the Department of Energy's (DOE's) Office of Science, the nation's largest funder of physical science. The 8.4% boost, to $8.1 billion, will mostly go into research grants and activities in the office's six major disciplinary areas. A separate bill passed in the summer funneled $1.5 billion to more than a dozen construction projects for new large user facilities at DOE's national laboratories.

The U.S. Geological Survey gets a 7% increase, to $1.5 billion, as does the Environmental Protection Agency's science arm, putting it at $802 million. The agriculture department's competitive research grants program goes up 2%, to $455 million.

The massive spending bill also contains billions for projects—many of them at universities—chosen by individual legislators but not requested by agencies. Those earmarks can come at the expense of growing an agency's regular research activities. At the National Institute of Standards and Technology, for example, the earmarks consume more than half of the $103 million increase the agency received for its in-house research account, and nearly one-quarter of NIST's overall budget of $1.6 billion. ■

Reporting by Adrian Cho, Warren Cornwall, Eric Hand, Jocelyn Kaiser, Jeffrey Mervis, Erik Stokstad, and Meredith Wadman.

SCHOLARLY PUBLISHING

Can peer reviewing preprints catch on?

As unreviewed studies proliferate online, researchers are eyeing ways to boost critiques

By **Jeffrey Brainard**

For decades, peer reviewing technical manuscripts before they were published in a journal has been a regular duty for senior scientists. But James Fraser, a structural biologist at the University of California, San Francisco (UCSF), says he hasn't reviewed a paper for a journal in years. Instead, Fraser and members of his lab focus on reviewing preprint studies that are posted online whenever authors like, bypassing a journal's peer-review process.

Critiquing preprints offers big advantages over traditional, journal-based peer review, Fraser argues. Authors can get expert feedback more quickly—sometimes in days instead of months—and from a bigger and more diverse pool of reviewers. The process can also be more efficient: Reviewers can focus solely on the quality of the science without worrying about whether a paper is a good fit for a particular journal. And the reviews can be shared with everyone, not just authors and editors. "This is valuable stuff that's often locked up" in the traditional review process, which at most journals is confidential, Fraser notes.

He isn't alone in seeing promise in preprint reviews, which represent a radical shift in scholarly communication. Some regard preprint reviews as valuable input for journals that might ultimately publish a paper. Others hope reviewed preprints could ultimately take the place of journal publications. But the widespread adoption of preprint reviewing faces some thorny obstacles. This month, Fraser joined more than 200 scientists, journal editors, and research funders at a workshop that explored ways to overcome them.

Although preprints have long been common in some fields, especially physics, the COVID-19 pandemic prompted many life scientists to embrace them to quickly communicate potentially critical research findings. But many researchers worried these preprints were too often rushed and they needed at least some rapid vetting. Although the pandemic's surge of preprints has now leveled off, the overall number of life sciences preprints has grown 100-fold since 2014, to 150,000 a year. Preprints now represent 7% of all articles in the U.S. National Institutes of Health's PubMed database, up from 0.2% in 2015.

Although preprint servers have mechanisms to allow researchers to critique papers, relatively few scientists use them. As of October, for example, researchers had posted comments on just 5% of nearly 180,000 preprints posted on the bioRxiv biomedical research site.

Such lackluster numbers highlight the "massive cultural barriers" in the scientific community to the wider adoption of preprint reviews, said Catriona MacCallum, a former journal editor who is now director of open science at the publisher Hindawi. Some academic scientists, for example, are reluctant to review preprints because that labor isn't counted in tenure or promotion decisions, unlike journal reviews.



A website called PREreview tries to make reviewing more appealing by acting as a kind of message board for preprint authors and reviewers. Launched in 2017 with support from the Wellcome Trust and others, PREreview allows authors to post a preprint and request a review, as long as the preprint has a digital object identifier (DOI), a code that eases citation and indexing. Would-be reviewers must establish their identity by entering their open researcher and contributor ID (ORCID) number, a tracking system used by many academic scientists.

To date, volunteers have posted more than 300 full reviews. They also penned about 400 less-intensive "rapid reviews" by answering 12 yes-or-no questions, such as "Are the principal conclusions supported by the data and analysis?" PREreview is now working to broaden its reach, by setting up agreements with preprint sites to relay author requests for reviews.

The platform also gives preprint reviewers a means to claim credit for their work. Scientists who participate in traditional peer review often burnish their CVs by listing the journals that have asked them to serve as reviewers. For some, that is a key step toward becoming an editor at a journal, earning a promotion, or strengthening a funding proposal.

PREreview provides those incentives for preprint reviewers via the DOIs, which enables them to cite the work in their portfolios when applying for jobs, promotions, or grants. (PREreview and other platforms allow reviewers to stay anonymous, as at most journals, but are mulling ways to let preprint reviewers unmask their authorship if desired.)

PREreview and similar services do not directly address another issue, however: whether a preprint reviewer is qualified and free of potential conflicts of interest. At many journals, editors vet reviewers, although they often rely on the honor system by simply asking them to declare potential conflicts.

Other preprint review services—such as the 4-year-old Review Commons, run by EMBO Press—screen reviewers before sharing the reviews with partner journals. At one partner, the PLOS family of journals, editors were initially wary of letting others do the vetting, said Marcel LaFlamme, the publisher's manager of open research. But many of the editors have been satisfied with the results, which have reduced the workload for PLOS's own reviewers, he said. To date, PLOS has published 150 of the 400 manuscripts it has received from Review Commons, although it sought further review for some.

ILLUSTRATION: FEODORA CHIOSEA/ISTOCKPHOTO, ADAPTED BY M. ATAROD/*SCIENCE*

Some workshop speakers argued preprint reviews shouldn't only be seen as a way to get a paper published in an established journal. If the goal is simply to feed preprints into journals, said Michael Eisen, editor-in-chief of *eLife*, "we're going to get a system that doesn't appeal to the people who are enthusiastic about [reviewing preprints]." Instead, Eisen and others envision a world in which some preprints and their reviews are, in essence, the final product. The preprint receives no label summarizing quality—no "accept" or "reject"—leaving it to the reader to judge.

In October, *eLife* announced it would pilot this approach by abandoning traditional acceptance decisions and focusing instead on providing peer-review services. Eisen hopes the move will loosen academia's reliance on tying tenure, promotion, and other rewards to publishing in for-profit, selective journals with elite brand names and high impact factors.

Expanding preprint review also faces technical and financial challenges. Some workshop speakers faulted the buttons used for commenting on bioRxiv preprints as complicated and cumbersome. And most preprint reviews lack DOIs, making it difficult to find those associated with a specific preprint or know when a new one has been posted. There is also no clear business model for supporting preprint reviews; many platforms are now supported by philanthropies. One option, speakers said, is for university libraries to subscribe to services that provide reviews, much as libraries now do for packages of journals.

Advocates of preprint reviews believe they will spread as more researchers see their value to the scientific enterprise. Not that long ago, they note, many researchers resisted even the notion of posting a preprint. Now, the discussion has shifted to how best to review them.

"We've seen time and time again in publishing that when you offer up something that challenges people's assumptions, they're almost instinctively opposed to it," said Eisen, who co-founded the PLOS journals in 2003. "Trying to be guided by [those existing] opinions is a fool's errand."

For the practice to take off, however, "we need to generate many more preprint reviews so the community can start to see momentum and change," said Ron Vale, an organizer of the workshop and a professor emeritus in cell biology at UCSF.

"We know [preprint reviewing] needs to be the future of science," said Dario Taraborelli, science program officer with the Chan Zuckerberg Initiative philanthropy. The challenge, he added, is how "to figure out how to make it work." ■

ANIMAL RESEARCH

NIH can't deny chimps sanctuary retirement

Agency violated federal law when it prevented former lab primates from entering Chimp Haven, federal judge rules

By **David Grimm**

A U.S. federal judge has ruled against the nation's largest biomedical agency in a long-running battle over the fate of dozens of former research chimpanzees. On 13 December, a Maryland court declared that the U.S. National Institutes of Health (NIH) violated federal law by not moving the animals out of biomedical facilities to a government sanctuary. The decision could force the agency to transfer the great apes.

"We're elated that now we can finally move forward on getting the chimpanzees out of the laboratory," says Kathleen Conlee, vice president of animal research issues at the Humane Society of the United States (HSUS), one of the plaintiffs in the case.

Still, the judge who issued the ruling acknowledged the main concern NIH veterinarians had raised—that transporting old and sick chimps to a new location could jeopardize their health—and requested more information from it and other parties before she directs the agency on how to proceed.

> **"Congress recognized that older and sicker chimpanzees ... would enter the federal sanctuary system."**
> **Lydia Kay Griggsby**, U.S. district judge

In 2000, the U.S. Congress passed the Chimpanzee Health, Improvement, Maintenance, and Protection (CHIMP) Act, which created the only federal chimpanzee sanctuary, Chimp Haven, in Keithville, Louisiana. It also mandated retirement of NIH-owned chimps no longer needed in biomedical research.

When biomedical research on chimpanzees ended in 2015, NIH pledged to retire all of its chimps to the sanctuary. The agency has since retired more than 200 of the approximately 300 chimps it owns or supports at three facilities. But in 2019, it announced that many of the others would stay put. A panel of NIH veterinarians concluded that all 44 of the chimps that remained in the Alamogordo Primate Facility in New Mexico were too old and sick to move. The agency later stated the same applied to 49 of the chimpanzees at the MD Anderson Cancer Center in Bastrop, Texas. (NIH has since retired all of the chimps it owns from the Texas Biomedical Research Institute in San Antonio.)

"The NIH veterinary panel of experts didn't make the decision to retire these chimps in place lightly," says Cindy Buckmaster, a spokesperson for Americans for Medical Progress, a pro–animal research group that has followed the issue closely. "They would face a world of strangers and uncertain social groupings—intensely stressful to old chimps with established conspecific and human families—before they could even think about enjoying life in their new home, if they survived that long."

As of October, 30 chimps remained at Alamogordo (the rest have died) and 46 at MD Anderson—all owned by NIH. One hundred and fifty remain at Texas Biomed and other facilities, but none of these animals is owned by NIH.

Chimp Haven and HSUS have lamented NIH's decision, arguing that the great apes deserve to live out their lives in a more natural setting. Several lawmakers introduced language into spending bill reports to try to compel the agency to change its mind. But NIH held firm.

So in 2021, HSUS—along with Animal Protection of New Mexico and several other plaintiffs—sued the agency. In her decision last week, U.S. District Judge Lydia Kay Griggsby says NIH's stance violates the CHIMP Act. "Congress recognized that older and sicker chimpanzees ... would enter the federal sanctuary system," she wrote. The judge said she shared NIH's concern about the frailty of the animals. But she ruled that the agency does not have the discretion to determine which chimps should not be moved to a sanctuary.

HSUS says it wants the animals transferred as soon as possible. NIH says it doesn't comment on litigation. All parties will meet with the judge in January 2023 to try to hash out next steps. ■



A nontoxic dye tracked a plume of lime that neutralized acidic waters in a Florida estuary.

CLIMATE CHANGE

Ocean geoengineering scheme aces field test

Alkaline lime powder spread in Florida estuary drew down carbon and reduced acidification

By **Paul Voosen**, *in Chicago*

The balmy, shallow waters of Apalachicola Bay, off Florida's panhandle, supply about 10% of U.S. oysters. But the industry has declined in recent years, in part because the bay is warming and its waters are acidifying because of rising carbon dioxide (CO_2) levels. Things got so bad that in 2020, the state banned oyster harvesting for 5 years. Soon afterward, state officials encouraged climate scientists to perform an unusual experiment to see whether they could reverse the changes in the water.

In May, at an Apalachicola estuary, the researchers injected some 2000 liters of seawater enriched with lime, an alkaline powder and a primary ingredient in cement that's derived from chalk or limestone. They showed it neutralized some of the acidity and, in the process, drew CO_2 out of the atmosphere.

It is the first field demonstration of the technique, called ocean liming, that they know of. "It is precious getting this response in a real system," says Wade McGillis, an engineer and climate scientist at the University of Notre Dame who helped lead the work, which was presented this week at a meeting of the American Geophysical Union.

The experiment is also a rare test of geoengineering, the controversial proposition of artificially altering the atmosphere or ocean to counteract the effects of rising CO_2. For ocean geoengineering, "normalizing doing these experiments is really good," says Ken Caldeira, a climate scientist at the Carnegie Institution for Science. Such demonstrations can allay fears by showing small-scale perturbations do not cause lasting environmental or ecological damage, he says.

The ocean already blunts the effects of climate change, naturally absorbing 30% of annual carbon emissions. But as it dissolves in the water, the CO_2 combines with calcium and other ions, depleting them. As a result, the pH of the waters drops, harming marine life, and CO_2 uptake slows. "Alkaline enhancement" aims to reset the water chemistry.

Liming is one approach. The added calcium hydroxide, or lime, raises the water's pH and enables it to sequester more CO_2 in the form of calcium bicarbonate or as carbonate deposited in the shells of sea creatures. In effect, the liming enhances the way the ocean naturally removes CO_2, says Harald Mumma, an environmental engineering graduate student at Notre Dame. "We just speed up natural processes and make it happen not on geological time scales, but on human time scales."

A 2021 report from the National Academies of Sciences, Engineering, and Medicine (NASEM) called for $2.5 billion in ocean geoengineering research in the next decade, including field tests of alkaline enhancement. Researchers are facing limits to what can be learned in the lab, says Débora Iglesias-Rodriguez, a biological oceanographer at the University of California, Santa Barbara, and co-author of the NASEM report. Lab tests can't show how a plume of alkali spreads through ocean waters, how added particles might clump up, or how the chemicals might affect marine life. For all these reasons, she says, "We desperately need to go in the field."

McGillis had worked with officials at the Apalachicola National Estuarine Research Reserve for several years, studying the oyster decline. When he mentioned the possibility of a trial, they readily agreed. The Notre Dame–led team conducted several releases, using a nontoxic dye to follow the plume. Sampling the water, they first found that pH levels did not increase too drastically, a relief for researchers who feared it might disrupt marine life. "We got a really nice small perturbation," McGillis says. They conducted one release deeper in the estuary, off a long

PHOTO: WADE MCGILLIS

pier, where microbial activity had already reduced levels of dissolved CO_2 to about 200 parts per million, compared with more than 400 ppm in the atmosphere. The lime lowered CO_2 levels by another 70 ppm, allowing the water to take up more. They also monitored oyster and microbial metabolisms during the trial and saw no red flags.

Liming is only one possible technique for increasing ocean carbon storage. In April, researchers from the Centre for Climate Repair at the University of Cambridge, along with India's Institute of Maritime Studies, spread iron-coated rice husks across the Arabian Sea. Iron, a nutrient, is scarce in much of the ocean; the researchers hoped adding it would fertilize a bloom of photosynthetic algae, which would soak up carbon and sequester it when the algae die and sink. Unfortunately, a storm hit soon after the deployment, stirring up the husks and making their effect difficult to track. "The result was inconclusive," says Hugh Hunt, a climate engineer with the Cambridge team. Since February, researchers have also sought to capture carbon by cultivating giant kelp off the coast of Namibia—in effect creating a carbon-hungry submarine forest.

The Florida trial is not the first field test of ocean alkaline enhancement. In 2014, Caldeira and colleagues added sodium hydroxide—also known as lye and an ingredient in many soaps and detergents—to a part of Australia's Great Barrier Reef. They found it raised pH levels nearly to preindustrial levels, allowing the natural calcification of the reef to increase. But the great advantage of lime is that it is already produced at enormous scales for the cement industry, McGillis says.

Caldeira's team wrote that its approach would be "infeasible" as a global solution. That's because it's difficult to make alkaline additives without emitting CO_2, he says. Heating limestone to make lime, for example, releases so much of the gas that it partially offsets the increased uptake by the ocean. Even if low-emission lime could be made, it would probably be too costly to dump into the ocean.

But as CO_2 continues to rise and geoengineering a climate solution grows more tempting, ocean liming has a key advantage over other geoengineering proposals, such as schemes to release sunlight-reflecting particles in the atmosphere. "Altering the chemistry of seawater is much more controllable than throwing particles in the air," McGillis says. Particles can stay in the stratosphere for months or years. Ocean additives tend to only last a month before being diluted and dispersed, he says. "There's much greater control if it goes south." ■

BIOMEDICINE

Moms' mitochondria may refresh cells in sick kids

Technique is designed to treat mitochondrial disease

By **Mitch Leslie**

A gift from their mothers might reenergize the cells of children who carry faulty mitochondria, the organelles that serve as cells' power plants. A research team is testing a strategy that involves soaking patients' blood cells in a broth of healthy mitochondria from their mothers and then reinfusing them. Early signs suggest the intervention is safe and may improve the children's health and development, and the researchers are planning a follow-up clinical trial.

This approach "is different from what anyone else is doing," says Mary Kay Koenig, a pediatric neurologist at the University of Texas Health Science Center, Houston, who wasn't connected to the study, reported this week in *Science Translational Medicine*. Although the results are at a very early stage, they are "very exciting," she says. But Michael Hanna, a clinical neurologist at the University College London Queen Square Institute of Neurology, believes "it's important to be cautious. This is highly preliminary data."

> **"[This] is different from what anyone else is doing."**
> **Mary Kay Koenig**, UTHealth Houston

Mitochondria, which originated early in eukaryotic evolution as symbiotic bacteria within other organisms, generate most of the adenosine triphosphate (ATP) that fuels cells. But about one in 5000 babies is born with mitochondrial defects that cause sometimes-lethal disorders.

Elad Jacoby, a pediatric hematology and oncology physician at Sheba Medical Center, and colleagues knew that when isolated mitochondria are mixed with cells, the organelles slip into the cells and start working. Jacoby and colleagues realized they might be able to harness this behavior to boost the number of healthy mitochondria in patients' cells.

The team decided to target hematopoietic stem and progenitor cells (HSPCs), stem cells found in bone marrow that give rise to a range of blood cells. HSPCs also disperse throughout the body and may suppress disease effects in other tissues, Jacoby says.

Under compassionate use, a regulatory path for testing experimental approaches in people with untreatable illnesses, the researchers studied six children with Pearson syndrome or Kearns-Sayre syndrome, conditions caused by a missing chunk of mitochondrial DNA. The children's cells "were working on low battery," Jacoby says, resulting in problems such as kidney disease, diabetes, abnormal heart rhythms, and weakness. Impaired growth had left them shorter than about 97% of their peers.

The researchers extracted healthy mitochondria from the mothers' blood and HSPCs from the patients, then mixed them. "You put them in a tube, shake it, and leave it for a while," Jacoby says. The team returned the cells to the patients' bloodstream after 24 hours of incubation.

Mitochondrial activity in the cells suggested at least some of them had absorbed the organelles. A year after reinfusion, the patients' blood cells held 30% more mitochondrial DNA and produced one-third more ATP than before. Five of the children gained weight, and two patients tested for strength and endurance showed improvements. All are still alive, including one child who underwent the treatment nearly 5 years ago, the team reported.

Koenig says she is encouraged by "the fact that they are showing some improvements." But confirming the treatment was responsible is difficult, she cautions. The study did not have a control group for comparison, and scientists don't understand how the symptoms of the diseases typically evolve as children age. Still, Koenig says, "We [normally] expect every patient to decline."

Hanna, however, says he doubts HSPCs with healthy mitochondria would have much of an impact outside the blood because they would be vastly outnumbered by cells with faulty mitochondria.

The researchers are now analyzing results from a clinical trial of the treatment on five more patients with the two syndromes and plan to start another trial that will try to establish that the reinfused cells settle down and survive. If further research confirms the benefits, Koenig says, "There's a whole bunch of mitochondrial disorders this could work for." ■

FEATURES



THE FINAL PUFF

Public health officials have drawn on a decade of research to craft a plan to make New Zealand smoke-free

By **Dennis Normile**

Smoking kills. Ayesha Verrall has seen it up close. As a young resident physician in New Zealand's public hospitals in the 2000s, Verrall watched smokers come into the emergency ward every night, struggling to breathe with their damaged lungs. Later, as an infectious disease specialist, she saw how smoking exacerbated illness in individuals diagnosed with tuberculosis and HIV/AIDS. She would tell them: "The best thing you can do to promote your health, other than take your pills, is to quit smoking."

Verrall is still urging citizens to give up cigarettes—no longer just one by one, but by the thousands. As New Zealand's associate minister for health, she led the development of the Smokefree Aotearoa 2025 Action Plan, which could make New Zealand the first country in the world to achieve smoke-free status—typically defined as an adult smoking rate of no more than 5%. (*Aotearoa*, loosely "Land of the Long White Cloud," is the country's name in the language of its indigenous people, the Māori.) On 13 December, New Zealand's Parliament approved the law based on the plan, which Chris Bostic, Washington, D.C.–based policy director at Action on Smoking & Health (ASH), calls "a huge deal. This will be the most comprehensive antitobacco policy in history."

Taking effect on 1 January 2023, the law features three radical interventions. One, called the smoke-free generation strategy, will make it illegal to ever sell combustible tobacco products to those born in 2009 or later. The goal is to create a growing cohort that never picks up the smoking habit. A second provision calls for reducing the number of licensed tobacco retailers from 6000 now to a maximum of 600, to make cigarettes harder to get. The boldest proposal in the eyes of experts is reducing cigarettes' nicotine content to below addictive levels. This "cuts right at the heart of why people smoke in the first place," says Geoffrey Fong, head of the International Tobacco Control Policy Evaluation Project at the University of Waterloo in Canada. It's potentially a "true game changer in the battle against smoking."

Verrall emphasizes the importance of all three measures. "It's not a matter of one

PHOTO: ALPTRAUM/ISTOCKPHOTO

magic bullet that will fix our tobacco control," she says. But each measure, she says, is buttressed by science. "The effectiveness of denicotinization is well proven in clinical trials," she says. Research has also shown that reversing the current clustering of tobacco retailers in poor neighborhoods will reduce smoking among young people and make it easier for smokers to quit. Verrall believes those two strategies will get New Zealand to the smoke-free goal, and preventing young people from purchasing cigarettes will keep it there.

Skeptics warn the measures will fuel an underground market. The plan is "likely to fail as a result of numerous unintended consequences, including illicit markets and a poor understanding of how it will work in practice," says Clive Bates, a tobacco control expert at London-based Counterfactual Consulting, which does not accept tobacco funding. Critics also say it will criminalize smokers, although only retailers who sell and individuals who give tobacco products to those of the smoke-free generation will face penalties.

The legislation easily passed New Zealand's House of Representatives, with support from community leaders of the Māori, who are among New Zealand's heaviest smokers. "Thousands of people will live longer, healthier lives," Verrall said in reaction to the vote.

FROM LOW TO ZERO

New Zealand is already a leader in controlling tobacco, which kills 8 million worldwide annually. It was among the first countries to ban smoking in indoor workplaces, in 1990, and in bars and restaurants, in 2004. Taxes on cigarettes have risen 165% since 2010. In Auckland, a pack of Marlboros costs the equivalent of $21; in New York City, $14. Gruesome pictures of diseased lungs and hearts and dire warnings plaster cigarette packages. There is extensive support for quitting and tolerance of vaping as an alternative nicotine source. These efforts have given New Zealand one of the lowest smoking rates among industrialized nations: 10.9% of adults. (In the United States the rate was about 12.5% in 2020.) Yet tobacco use is still New Zealand's leading cause of preventable death and disease; smoking-related cancer, stroke, and heart disease claims 5000 lives annually in a country of 5.1 million.

The health burden falls disproportionately on the Māori, 22.3% of whom smoke. The gap in smoking leads to stark health inequities. Māori life expectancy is 73.4 years for men and 77.1 years for women; for Kiwis of European descent, the numbers are 81 and 84.5, respectively. Tobacco was introduced to the islands by Europeans in the late 1700s, and the lingering impacts of colonialism and racism mean Māori still have fewer of the social, institutional, and economic resources available to help citizens trying to quit smoking, says Andrew Waa, a public health specialist at University of Otago, Wellington.

In the mid-2000s, Māori leaders came to believe "the solution to addressing these inequities was to get rid of tobacco altogether," says Waa, a Māori who belongs to the Ngāti Hine tribe. Their concerns led to an earlier antismoking effort, launched in 2011. Like the new plan, it aimed to reduce smoking prevalence to below 5%, relying on higher taxes, public education, and support for those trying to give up smoking through a toll-free Quitline that offers expert advice and access to nicotine substitutes. Smoking rates trailed downward, but it was evident more had to be done.

IT'S THE NICOTINE, STUPID!

The seductive power of cigarettes and other tobacco products comes from nicotine—a compound as addictive as cocaine and heroin. Smokers get hooked on the rush of pleasure they feel when a drag from a cigarette sends nicotine through their bloodstream to the brain, where it triggers the release of dopamine. Other cues can also trigger that dopamine rush. "There are behavioral aspects of smoking—opening the packet, the crinkling of the wrapper, the smell of the tobacco, all those hand-to-mouth things can be very strong for some people," says Natalie Walker, a public health scientist at the University of Auckland. Contrary to widespread belief, nicotine itself has little, if any, role in causing cancer. "It is the 4000-plus chemicals in tobacco smoke that cause these horrendous diseases," Walker says.

That's not to say nicotine isn't injurious: It raises the pulse rate and blood pressure and hardens blood vessels, increasing the long-term risk of hypertension and heart disease. But the most harmful thing about nicotine in cigarettes is that it makes it hard for smokers to give up the habit. Quitting cold turkey leaves people restless and grouchy, unable to concentrate, anxious, or depressed.



Ayesha Verrall, New Zealand's minister for research, science, and innovation, says the government's antismoking initiative is founded on the latest research.

PHOTO: ROBERT KITCHIN/STUFF LIMITED

Scientists have suggested since the 1990s that limiting nicotine in cigarettes to a level that would be nonaddictive might discourage smoking. "The assumption is that if you reduce dependence and addiction, people will choose not to use [tobacco]," says Eric Donny, a tobacco expert at Wake Forest University.

But until recently, there was little hard evidence to support that assumption. Walker launched one of the earliest trials to test it, in 2009 and 2010. She split 1410 New Zealand Quitline callers randomly into one group getting nicotine replacements and behavioral support calls from trained advisers, and a second group getting the same

interventions plus cigarettes with a nicotine content of about 5% of the standard level. Most of those in the second group reported that smoking urges decreased over the 2-month treatment period. At a checkup call 6 months later, one-third of them reported not smoking at all in the prior week, compared with 28% of those getting only support. Significantly, 90% of those given the low-nicotine cigarettes said they would recommend them to others wanting to quit. Adding low-nicotine cigarettes to standard cessation support “may help some smokers to become abstinent,” Walker and colleagues wrote in the March 2012 issue of *Addiction*.

In the United States, related research got a boost in 2009, when Congress gave the Food and Drug Administration (FDA) authority to regulate the nicotine in tobacco products, provided it not be reduced to zero. Needing scientific evidence to guide regulatory decisions, the agency provided funding for studies, and its National Institute on Drug Abuse started to make cigarettes with varying levels of nicotine for research use. (Nicotine in tobacco can be reduced by treating the leaves with solvents, steam, microbes, or gases in a process akin to decaffeinating coffee beans; or by genetically modifying the plant.)

Donny’s Wake Forest team took advantage of the opportunity with a 6-week, double-blind trial that randomized smokers to receive cigarettes with standard nicotine content, about 15.8 milligrams per gram of tobacco, or cigarettes with four different nicotine levels ranging from 5.2 to 0.4 mg of nicotine per gram. Because the cigarettes were free, all 780 participants were lighting up more than usual at first. But 6 weeks later, those given standard cigarettes were smoking even more, 21 or 22 times a day; whereas groups puffing cigarettes with nicotine concentrations of 2.4 mg or less had cut their daily habit to 15 to 16. One month later, one-third of those who smoked the lowest nicotine cigarettes were trying to quit, even though they had not previously intended to do so; only 17% of those who smoked standard cigarettes were making the attempt. “Reducing nicotine content in cigarettes could lead to less smoking, less nicotine dependence and improved public health,” Donny and colleagues wrote in *The New England Journal of Medicine* in October 2015.



Cigarettes will become harder to buy under New Zealand’s new policy, which will greatly reduce the number of outlets allowed to sell tobacco products.

PHOTO: MONIQUE FORD/STUFF LIMITED

Donny and other researchers have considered the possibility that people might just smoke more low-nicotine cigarettes to get their fix. But the evidence from his studies and others lays that concern to rest, he says. “The clinical data don’t bear that out.”

Some research also supports another pillar of New Zealand’s antismoking plan. Research had shown that people living near retail tobacco outlets smoked more, more easily picked up the habit, and found it more difficult to quit. Frederieke Petroviç-van der Deen, a public health scientist at Otago, built on those data with a modeling study based on New Zealand’s demographics that found cutting the number of tobacco retailers by 90% over 10 years and limiting their locations would drive smoking prevalence down.

Hopes for the third strategy, the ban on tobacco sales to a new generation, rest on evidence that more than 80% of smokers start by 18, and virtually all by 26, and most later regret it. Parents approve of the idea. “If you ask even the most hardened smoker, ‘When would you like your kids to start smoking?’ the answer is invariably ‘Never!’” says Marita Hefler, a tobacco control specialist at Charles Darwin University in Australia. Also, “It’s politically palatable, because it doesn’t take anything away from adults who are addicted to nicotine,” Bostic says.

By the late 2010s, New Zealand researchers could “put forward a case to the government saying this is the evidence we have about what sort of policies would make a difference,” Walker says. And Verrall, a first-term parliamentarian, stepped up to craft a plan.

A STRAIGHT-TALKING DOC

From her early years as a student, Verrall showed a knack for leadership. She was elected president of the Otago students’ association as an undergrad and while in medical school led a group that founded the *New Zealand Medical Student Journal*. After joining the Otago faculty, she also worked as an infectious disease physician for the Wellington regional public health service and was elected to the service’s board in 2019.

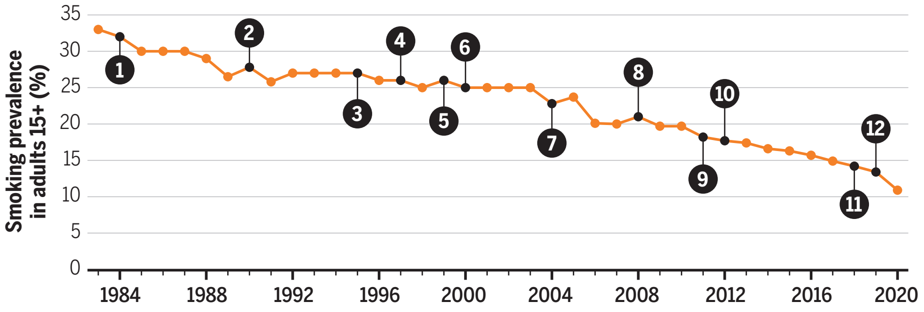
She gained national attention by criticizing the government’s early handling of the COVID-19 outbreak. “Our contact tracing capacity is a fire extinguisher, we need a fire engine,” she tweeted in April 2020. The government acted on Verrall’s advice, dramatically expanding and speeding up contact tracing and testing as part of its successful effort to keep case numbers near zero during the early phase of the pandemic. “She was the perfect person to directly engage the politicians at that time, as she understood both [the scientific and political] worlds,” says Philip Hill, an international health specialist at Otago who was Verrall’s thesis adviser.

Subsequently, Verrall made the rounds of TV news shows and gave newspaper interviews explaining the importance of contact tracing. Audiences recognized that “she is empathetic and cares about making a difference to the health of New Zealanders,” Walker says. Her popularity led the Labour Party to nominate Verrall for a seat in the House of Representatives in the October 2020 election.

She won and was made minister of COVID-19 response as well as research, sci-

Nicotine's weakening grip

Increasingly strict restrictions on smoking and bans on tobacco advertising have driven New Zealand's smoking prevalence down to 10.9%. Now, the Smokefree Aotearoa 2025 Action Plan, passed into law this month, could make New Zealand the first country in the world to become smoke-free.



A long road

1. **1984** New Zealand launches first tobacco control program.
2. **1990** Smoking is banned in many indoor workplaces and on public transport.
3. **1995** Tobacco product signs are removed from retail outlets. Tobacco company sponsorships are ended.
4. **1997** Legal age to purchase tobacco products is raised to 18.
5. **1999** National Quitline service is launched.
6. **2000** Subsidized nicotine patches and gum to aid quitters are made available.
7. **2004** All schools, restaurants, bars, cafés, sports clubs, offices, factories, and warehouses are made smoke-free.
8. **2008** Graphic health warnings covering most of a cigarette pack are introduced.
9. **2011** New Zealand adopts the goal of being smoke-free by 2025.
10. **2012** Tobacco retail displays are banned.
11. **2018** Plain packaging is mandated for all tobacco products.
12. **2019** Smoking in vehicles carrying children is prohibited. Ad campaign is launched to raise awareness of how secondhand smoke affects pets. Vaping is presented as a way to quit smoking.

CREDITS: (GRAPHIC) K. FRANKLIN/SCIENCE; (DATA) TE HIRINGA HAUORA/HEALTH PROMOTION AGENCY

ence, and innovation. Verrall asked Prime Minister Jacinda Ardern to put her in charge of realizing the smoke-free goal. Among Labour's public health commitments, "[It] was the most bold and inspiring one and I really wanted to take it forward," she says.

After a year of reviewing strategies, issuing proposals, and soliciting public feedback, the action plan was unveiled in December 2021. Verrall's "amazing" effort is "why this bundle of policies has come through," Walker says.

New Zealand may be the perfect test bed for the plan Verrall is rolling out. Smoking rates are already low. Surveys indicate 74% of the public supports the 2025 smoke-free goal and more than 70% of smokers and recent quitters favor denicotinization and the restrictions on tobacco retailers.

Not everyone is happy, though. The measures are expected to be particularly hard on mom-and-pop convenience stores called "dairies." Giving oral comments to the parliamentary committee considering the bill in September, an unnamed representative of the Dairy and Business Owners Group begged the lawmakers to "avoid 'dairygeddon'" by delaying implementing the plan until 2025 to allow "time to re-engineer dairies."

Others have argued the low-nicotine cigarette policy will backfire. It will fuel "a 'booming' black market" in normal cigarettes, British American Tobacco New Zealand warned in a submission to the committee. A May 2020 report by the consulting firm KPMG for Imperial Tobacco New Zealand estimated that illicit tobacco already accounted for 11.5% of total New Zealand consumption in 2019. And some critics point to the experience of Bhutan, a tiny Himalayan kingdom that banned the sale of tobacco products in 2004, albeit without offering cessation support or addressing adolescent tobacco use, except in a small media campaign. A 2014 survey found more than 20% of Bhutanese teens and adults were still smoking and using snuff, relying on "robust" smuggling, says Michael Givel, a political scientist and Bhutan scholar at the University of Oklahoma, Norman. In 2021, Bhutan gave up and allowed tobacco imports again. The government is now running antitobacco public education campaigns and offering cessation support.

Tobacco interests exaggerate the black market problem "to scare off policymakers," says Nick Wilson, a public health scientist at Otago. To check smuggled cigarette prevalence, Wilson and 10 colleagues picked up nearly 1600 littered tobacco packs around the country and counted how many were foreign. (Wilson, worried people might think he was scavenging discarded cigarettes, says he "pretended to be doing up a shoelace.") Just 5.4% of the packs were foreign, mostly from China and South Korea. Most of the contraband arrives in shipping containers, which suggests more targeted inspections could further dent the illicit trade, Wilson says.

Control advocates believe history is on their side. Once, Hefler says, "Smoke-free public places were considered impossible." Yet California, despite fierce opposition, made workplaces and restaurants smoke-free in 1995; other states have followed. Ireland became the first country to ban smoking in indoor public spaces—including its iconic pubs—in 2004. In 2021, the World Health Organization (WHO) reported that 67 countries had made public indoor spaces completely smoke-free. A similar pattern has been seen with pictorial health warnings, plain packaging, and stiff taxation. Again and again, one country has led the way, and "all of these innovations were followed by other countries," Hefler says.

The impact grew with each restriction. The number of cigarettes smoked in the European and American WHO regions decreased by 33% and 44%, respectively, between 1980 and 2016, according to the U.K. branch of ASH. (Cigarette consumption increased by more than 50% in WHO regions covering mainly low-income countries.) For advanced nations, the New Zealand plan "seems like the next logical step," Hefler says.

So far, the United States is the only other country considering regulating nicotine. FDA in June announced it plans to set a maximum level for cigarettes; the move will be opened for public comment in May 2023.

Bostic worries the tobacco industry's influence will delay any substantive action in the United States. He is more optimistic about progress at the local level. Beverly Hills and Manhattan Beach, both in California, halted all tobacco sales in January 2021; and Brookline, Massachusetts, in November 2020 approved a law that bans sales to those born after 1 January 2000. However, Bostic points out, smokers can just go to neighboring towns to make a purchase.

At least a half-dozen countries are now studying tobacco-free generation policies. And the once fringe idea of a tobacco endgame—explicitly aiming to permanently end, rather than simply minimize, tobacco use—"is being taken very seriously," Bostic says.

New Zealand is setting the pace. "We will be very happy to share our experience as we go," Verrall says. ■

INSIGHTS

PERSPECTIVES



PHOTO: PETE OXFORD/MINDEN PICTURES

PHYSIOLOGY

Lessons on transparency from the glassfrog

Transparency in glassfrogs has potential implications for human blood clotting

By **Nelly M. Cruz**[1] *and* **Richard M. White**[1,2]

An obvious feature of life on Earth is that most animals and plants can be seen. This visualization is important for predation, feeding, and mating but does not apply to all animals, some of which are transparent. The origins of this phenomenon and how it has been evolutionarily selected are unclear. One such species is glassfrogs, so called because of their transparent bodies and translucent skin. These nocturnal arboreal frogs sleep during the day on green leaves. Previous work (*1*) found that they exhibit dynamic transparency, camouflaging themselves against the leaves where they sleep, likely to escape from predators. On page 1315 of this issue, Taboada *et al*. (*2*) report the distinct optical properties of the glassfrog *Hyalinobatrachium fleischmanni* and uncover the surprising physiological mechanism behind their transparency. This finding provides insights into mechanisms of camouflage but also could lead to development of new anticoagulant drugs.

Taboada *et al*. found that the extent of transparency in the glassfrog changes depending on activity, with highest levels of transparency achieved during sleep. One of the barriers to transparency in vertebrates is the presence of respiratory pigments such as hemoglobin. Transmittance and reflectance measurements using optical spectroscopy confirmed that light attenuation during the active state can be attributed to changing concentrations of hemoglobin. The authors used three modalities of photoacoustic microscopy (PAM)—high-resolution, deep-penetrating, and high-speed—to noninvasively measure red blood cell (RBC) perfusion of the whole body and specific tissues during rest and exercise. This allowed them to capture dynamic changes in RBC circulation in real time with precision and high resolution, and to measure oxygenation by measuring saturation of hemoglobin (sO_2). They found that the glassfrog "hides" RBCs in its liver during sleep, allowing the animal to achieve a high level of transparency on its ventral side. As the glassfrog wakes and becomes active, the amount of RBCs in circulation increases considerably. Remarkably, the glassfrog can pack ~89% of its RBCs at high density in the liver without signs of detrimental effects, such as clotting.

The distinct properties of the glassfrog make it an important model for understanding the general phenomenon of organismal transparency. In land animals, transparency is extremely rare, making the glassfrog an exception to the rule. By contrast,

[1]Cancer Biology and Genetics, Memorial Sloan Kettering Cancer Center, New York, NY, USA. [2]Ludwig Cancer Research, University of Oxford, UK. Email: cruzestn@mskcc.org; richard.white@ludwig.ox.ac.uk

The glassfrog "hides" red blood cells in its liver during sleep, thereby appearing transparent on its ventral side.

transparency is surprisingly common in aquatic species, especially in pelagic (open sea) regions. In a comprehensive review of this phenomenon (*3*), it was noted that transparent animals cover a wide range of aquatic species, ranging from *Amphogona apicata* (hydromedusa) to *Amphitretus pelagicus* (octopus) to many different species of fish, such as the *Ambassidae* (glassfish). This observation raises the question of what binds these various transparent species together. From an ecological standpoint, the range of transparent species is quite diverse, and it appears that transparency has evolved many times over. This suggests that the physiological function of transparency is likely highly adapted to local conditions. A clue to this evolution is that many (but certainly not all) transparent aquatic species are found at specific depths called euphotic or dysphotic zones, where light can penetrate reasonably well, and animals cannot hide easily. Unlike other forms of camouflage (such as pigmentation and mirroring), transparency is distinct in that it successfully hides animals from nearly all viewpoints and depths.

"In land animals, transparency is extremely rare, making the glassfrog an exception to the rule."

How does transparency arise? Generally, transparent substances neither absorb nor scatter light. Thus, one mechanism of opacity is the production of molecules such as melanin or hemoglobin that strongly absorb certain wavelengths of light. These pigments tend to be concentrated in specific cell types: melanin in melanocytes of the skin and hemoglobin in RBCs. Alternatively, light scattering can be attributed to structural proteins such as collagen, which is concentrated in tissues such as the sclera. This accounts for the white part of the eye. Other animals such as fish have reflective cells in their skin called iridophores, which are packed with guanine crystals that scatter light (*4*). Lack of these crystals makes the skin transparent, as seen in the zebrafish mutant *casper* (*5*). These two phenomena—absorption and scattering—have been overcome in a distinct way by the glassfrog to allow transparency. The ability to concentrate nearly its entire blood volume while sleeping effectively removes the light-absorbing hemoglobin from circulation. The glassfrog also lacks melanin pigmentation and reflective structures in its ventral skin, further improving transparency. But it is not fully transparent, because the animal retains some dorsal pigmentation, raising the question of whether it should be called translucent rather than transparent (*1*).

Regardless, the adaptations described by Taboada *et al*. make a strong case that RBC "hiding" is the predominant mechanism underlying the glassfrog's unusual optical properties. To further demonstrate how exceptional this really is, the authors investigated whether other opaque tropical frogs can store RBCs in their livers during sleep. They examined three additional species, including the most closely related opaque species *Allophryne ruthveni*. This frog did not store RBCs in its liver to a great extent, suggesting that the ability to conceal RBCs is specific to the glassfrog. One of the opaque species, *Agalychnis callidryas,* has reflective guanine crystals throughout its body, precluding imaging of its vasculature. Interestingly, the authors were able to examine a translucent mutant of this species that lacks pigment and guanine crystal layers. This mutant still transmits much lower levels of visible light compared to the glassfrog, demonstrating that transparent skin is not enough to endow organism-level transparency.

The mechanism that drives RBC redistribution in glassfrogs is not understood. It is unclear if the glassfrog can actively manipulate the changes in RBC circulation—for example, in the presence of a predator. Future studies might also investigate how this behavior is influenced by environmental and behavioral factors such as its mating season or food availability. Another intriguing question is how sequestration of RBCs in the liver affects cellular respiration and whether the glassfrog has a special metabolism that adapts to the drastic changes in RBC circulation. Such studies might also have implications for understanding human vascular disorders. In particular, there might be anticoagulant factors that allow the glassfrog to redistribute RBCs. The development of genomic and molecular tools will be critical for the successful use of the glassfrog as an unconventional model system for studying why and how transparency evolves in nature. ■

REFERENCES AND NOTES

1. J. B. Barnett *et al*., *Proc. Natl. Acad. Sci. U.S.A.* **117**, 12885 (2020).
2. C. Taboada *et al*., *Science* **378**, 1315 (2022).
3. S. Johnsen, *Biol. Bull*. **201**, 301 (2001).
4. S. Hozumi, M. Shirai, J. Wang, S. Aoki, Y. Kikuchi, *Biochem. Biophys. Res. Commun*. **502**, 104 (2018).
5. R. M. White *et al*., *Cell Stem Cell* **2**, 183 (2008).

10.1126/science.adf7524

BATTERIES

Embracing disorder in solid-state batteries

Enhanced ion transport is achieved by chemically induced structural distortion

By **Miriam Botros**[1] *and* **Jürgen Janek**[1,2,3]

Batteries have become indispensable devices of modern society (*1*). Lithium-ion batteries are the most utilized electrochemical storage technology, but they have several challenges, including sustainability of material production, high cost per kilowatt-hour, and flammability of the organic liquid electrolyte (*2*). Solid electrolytes that can replace the liquid electrolyte are now being designed. The key target when designing a solid electrolyte is high ionic conductivity. All-solid-state batteries that have a solid electrolyte that electronically separates both electrodes and is mixed into the cathode composite for better interfacial contact may offer high energy density and power density, allowing for fast charging and improved safety (*3*, *4*). On page 1320 of this issue, Zeng *et al*. (*5*) report that intentionally introducing chemical disorder to inorganic solid electrolytes can increase ionic conductivity by orders of magnitude, which in turn reduces the overall battery-cell resistance, leading to enhanced performance.

Many inorganic solid electrolytes show low ionic conductivity, which is most commonly due to high migration barriers and a small charge-carrier concentration. Sufficient electrochemical stability against both alkali-metal anodes as well as high-voltage cathode materials is another key challenge of solid-electrolyte design. Trying to overcome these limitations, Zeng *et al*. consider two widely studied groups of highly stable solid electrolytes: Na superionic conductor (NASICON)–type electrolytes for lithium and sodium ions and garnet-type electrolytes for lithium-ion transport. Ionic conductivity can be increased by inducing disorder that introduces fast ion percolation pathways in an otherwise "slow" ordered lattice and by increasing the charge-carrier concentration (*6*). The latter strategy is effective in many cases, but it is

associated with several drawbacks, including complicated synthesis and increased alkali-metal loss during heat treatment (*7*, *8*).

Zeng *et al.* introduced controlled lattice distortions and small structural changes around lithium-ion sites. This is achieved by substituting several elements of the surrounding sites and thereby changing the energy landscape involved in the ionic diffusion pathway. In the best-case scenario, this change in the local energy landscape leads to an energetic overlap of neighboring lithium-ion sites, thereby increasing the possibility of the ion occupying either site. In addition to simulations that support this scenario, experimental results confirm that mixing suitable immobile ions on one rigid sublattice of a solid electrolyte, that is, increasing the configurational entropy, changes the alkali-metal occupancy of otherwise unoccupied sites and increases the ionic conductivity.

Zeng *et al.* chose the following solid solutions for experimental verification: $Li(Ti,Zr,Sn,Hf)_2(PO_4)_3$, $Na(Ti,Zr,Sn,Hf)_2(PO_4)_3$, and $Li_3(La,Pr,Nd)_3(Te,W)_2O_{12}$. They identified an optimal degree of distortion around the metal-site (M-site) of the NASICON structure and around both sites available in the garnet-type structure (Ln-site and M-site), leading to enhanced ionic conductivity. Both the observed enhancement of the ionic conductivity and the change in site occupancy determined by neutron diffraction support the predicted reduction of the site-energy difference compared with systems with a single M-site. The degree of distortion needed for better percolation pathways in the garnet structure is higher than that for the NASICON-type systems. This prediction has implications for element selection to achieve optimal distortion, initiating vast possibilities for further experimental studies that include ions that have not been combined in the garnet structure to date. Additionally, there is no experimental differentiation between element substitution on the Ln-site or M-site in the garnet structure. This also calls for further experiments and calculations.

It should be noted that pathways with a low site-energy difference and others with a high energy difference might coexist in the same solid electrolyte. Zeng *et al.* emphasize that this does not affect the macroscopic ionic conductivity because the ions take the pathway with the lowest energy barriers, avoiding severe coordination changes. Structural distortions, specifically changes in bond lengths, can be altered not only by elemental substitution but also through defects, especially at grain boundaries in polycrystalline ionic conductors. Therefore, the microstructure of the material has considerable influence on percolation pathways, because the conductivity of the grains in many cases is different from that of the grain boundaries. The choice of a suitable synthesis and processing route is crucial for successful enhancement of ionic conductivity by optimizing the grain size as well as the grain boundary composition, especially at the interfaces to electrode materials to enhance charge transfer.

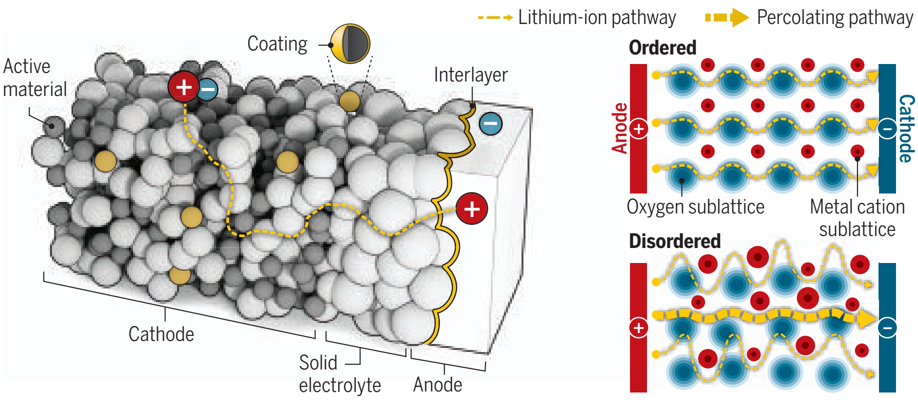
The calculations and experiments presented by Zeng *et al.* suggest a substantial enhancement of ionic conductivity, provided suitable elements are combined. However, the reported conductivities are below those of the best-known solid electrolytes. It remains to be seen whether current superionic conductors can be improved by introducing disorder, which might enhance their electrochemical stability by optimizing the constituent elements. Electrochemical stability against the electrodes is also an important requirement for solid electrolytes, because high-voltage cathodes are needed to increase the energy density of all-solid-state battery cells. The design of homogeneous and electrochemically stable high-entropy materials, as exemplified by Zeng *et al.*, leads to modified properties without changes in crystal structure, which opens possibilities for structurally aligned coatings and interlayers in solid-state batteries even with mixed ionic-electronic conductivity (see the figure).

The structural distortion depends not only on the size of the chosen immobile ions but also on their Coulomb interactions with nearest neighbors and alkali ions. The site energies that were calculated by Zeng *et al.* were determined by inserting a single alkali ion at different sites of the framework, which is a good approximation for determining the influence of distortion but can be different when the Coulomb interaction between all mobile alkali ions is considered (*9*). This needs further consideration when optimizing the degree of distortion to enhance conductivity, especially for multivalent charge carriers that exhibit low diffusion rates (*10*).

Enhancement of ionic conductivity through disorder can apply to a large range of crystal structures with two- and three-dimensional percolation networks, which opens new possibilities for a variety of charge carriers such as, for example, proton- or oxygen-ion conductors. It is an important, exciting, and open question whether the concept of fast percolation along energetically favorable routes in high-entropy lattices can ultimately lead to superior solid electrolytes that outperform conventional "low-entropy" solid electrolytes. ■

A high-entropy solid-state battery design

An all-solid-state battery cell composed of high-entropy materials as electrolytes, coatings, and interlayers with potentially enhanced ionic conductivity is shown (left). The variation of the ion pathway produced by combining different elements in the high-entropy material induces disorder (right), which opens percolating pathways for fast ion motion in otherwise low-mobility lattices. This can improve conductivity and battery performance.



REFERENCES AND NOTES

1. A. A. Kebede, T. Kalogiannis, J. Van Mierlo, M. Berecibar, *Renew. Sustain. Energy Rev.* **159**, 112213 (2022).
2. M. Balaish *et al.*, *Nat. Energy* **6**, 227 (2021).
3. J. Janek, W. G. Zeier, *Nat. Energy* **1**, 16141 (2016).
4. K. G. Gallagher *et al.*, *J. Electrochem. Soc.* **163**, A138 (2016).
5. Y. Zeng *et al.*, *Science* **378**, 1320 (2022).
6. Y. Xiao *et al.*, *Adv. Energy Mater.* **11**, 2101437 (2021).
7. A. Paolella *et al.*, *ACS Appl. Energy Mater.* **3**, 3415 (2020).
8. B. Ouyang *et al.*, *Nat. Commun.* **12**, 5752 (2021).
9. X. He, Y. Zhu, Y. Mo, *Nat. Commun.* **8**, 15893 (2017).
10. Y. Chen *et al.*, *Chem. Mater.* **34**, 128 (2022).

ACKNOWLEDGMENTS

M.B. acknowledges the European Union's Horizon 2020 project EPISTORE with grant agreement no. 101017709 and the German Research Foundation (DFG) for project nos. SE 1407/4-2 and 424789449. J.J. acknowledges financial support from the Bundesministerium für Bildung und Forschung (BMBF) within the Cluster of Competence FESTBATT (project 03XP0431).

10.1126/science.adf3383

[1]Institute of Nanotechnology, Karlsruhe Institute of Technology (KIT), Eggenstein-Leopoldshafen, Germany. [2]Institute of Physical Chemistry, Justus Liebig University, Giessen, Germany. [3]Center for Materials Research, Justus Liebig University, Giessen, Germany. Email: miriam.botros@kit.edu; juergen.janek@phys.chemie.uni-giessen.de

GRAPHIC: V. ALTOUNIAN/*SCIENCE*

MATERIALS SCIENCE

Cool it, with a pinch of salt

Melting a solvent with a salt and then desalinating it enables a reversible cooling cycle

By **Emmanuel Defay**

In countries with harsh winters, putting salt on roads transforms ice into slush. Adding salt depresses the freezing point of water. In other words, ice gets colder when salt is added. How much colder? The surface of ice cubes covered with kitchen salt reaches -10°C after a few seconds, whereas ice cubes of pure water remain at 0°C. Lilley and Prasher (*1*) revisited this cooling principle, and on page 1344 of this issue, they describe how to make it reversible. The idea behind this "ionocaloric" refrigeration is to take advantage of the large temperature change—and therefore the large heat absorption—obtained by melting a "special ice" when put in contact with a specific salt. The authors made this cooling process reversible to achieve an efficient cycle with potential wide applications in refrigeration.

Ionocaloric refrigeration could be considered electrochemical cooling. The latter occurs in liquids containing mobile ions that can be displaced with an external voltage. However, the variation of temperature obtained with electrochemical cooling is limited to a fraction of degrees because there is no accompanying phase transition, such as melting ice (*2*). Triggering a phase transition with an external stimulus to induce cooling is the essence of caloric materials (*3*). Such materials could make cooling more efficient without requiring greenhouse gases, contrary to most refrigerators. Most gases used as refrigerants are hydrofluorocarbons, which are much more potent greenhouse gases than carbon dioxide. Hence, magnetocaloric (*4*), electrocaloric (*5*), elastocaloric (*6*), and barocaloric (*7*) effects are temperature changes activated by the application of, respectively, a magnetic field, voltage, mechanical stress, and pressure. In the study by Lilley and Prasher, the ions of a salt trigger the melting of another material (called the solvent). Aptly, the authors called this the ionocaloric effect.

The solvent used by Lilley and Prasher is ethylene carbonate [$(CH_2O)_2CO$], and the salt is sodium iodide (NaI). The cooling cycle starts by mixing the solid form of the solvent with the salt close to the pure solvent's melting temperature, around 35°C. Similar to ice cubes and salt, the temperature of the mix decreases through the solid-to-liquid phase transition of ethylene carbonate. The temperature of the mixture can decrease to 6.4°C with 23% NaI. At such a temperature, heat absorption transforms the solvent into a liquid. This is the cooling step of a refrigerator. The next step is key to this cycle, which is the separation of NaI from ethylene carbonate. To achieve this, the authors used electrodialysis, which is essentially a desalination process. An external voltage is applied to separate the salt's ions from the solvent across membranes, similar to what is done in fuel cells and batteries. This desalination purifies ethylene carbonate, which in turn causes an increase in temperature. Then, the cooling cycle can start again.

Lilley and Prasher found that variations of entropy (the physical entity used to estimate how effective a cooling principle is) as large as 500 J K^{-1} kg^{-1} could be generated, which is close to that of today's refrigerants; larger than that of magnetocaloric, elastocaloric, and electrocaloric materials; and similar to that of the best barocaloric material (plastic crystals of neopentylglycol) (*7*). During the solvent-salt mixing process, the authors observed a maximum temperature decrease of 28°C, which is an excellent value.

> **"This is a serious contender for the future of cooling."**

Another asset of the ionocaloric approach is its large energy efficiency, which is the ratio of the power needed to run the cooling cycle with respect to the cooling power generated. This achievement stems from the low voltage applied during the electrodialysis process (0.22 V). Generally, efficiency (more accurately called the coefficient of performance for a device) is compared with that of the Carnot cycle (which represents the ideal thermodynamic cycle with ultimate efficiency). The ratio is called second-law efficiency. Lilley and Prasher claimed a maximum second-law efficiency of 29% with a cycle exhibiting a temperature span ΔT_{span} of 26°C. In more advanced caloric devices, it is customary to report second-law efficiency, for which extrinsic losses are often disregarded. Reported values reach 11% in elastocalorics (*8*), 12% in electrocalorics (*9*), and 40% in magnetocalorics (*10*). A fair comparison of efficiency between caloric systems is difficult because of the different levels of maturity of the respective technologies. But the results on ionocalorics are very encouraging. It is also notable that the ethylene carbonate–NaI system has no global warming effect.

The main drawback of ionocaloric refrigeration is that it is slow. It takes time to combine the solvent and salt and to desalinate the mixture. One cycle can take between 5 minutes and several hours. The longer the time, the better the efficiency. The main consequence is that cooling power is limited to 60 W kg^{-1} with a ΔT_{span} of 15 K. This is less than the best cooling power reported for electrocalorics [2800 W kg^{-1} with a ΔT_{span} of 1.4 K (*11*)], magnetocalorics [210 W kg^{-1} with ΔT_{span} of 10 K (*10*)], or elastocalorics [4400 W kg^{-1} with a ΔT_{span} of 10 K (*8*)].

One way to improve cooling power in this system is to enhance ion-exchange membrane conductivity in the electrodialysis cell. Indeed, in aqueous systems, conductivity can be two orders of magnitude larger than that obtained with ethylene carbonate. Additionally, the ionocaloric approach is not limited to one solvent. Lilley and Prasher suggest other solvent-ion couples. The main criteria to fulfill are a large entropy change of the solvent when it melts, a melting temperature in the 30° to 50°C range for cooling applications, a high solubility of the salt in the solvent, and high associated ionic conductivity.

The findings of Lilley and Prasher point to a new member in the caloric material family. It exhibits large efficiency and could be environmentally benign. This is a serious contender for the future of cooling. ■

Department of Materials Research and Technology, Luxembourg Institute of Science and Technology, 4422 Belvaux, Luxembourg. Email: emmanuel.defay@list.lu

REFERENCES AND NOTES

1. D. Lilley, R. Prasher, *Science* **378**, 1344 (2022).
2. A. Rajan, I. S. McKay, S. K. Yee, *Nat. Energy* **7**, 320 (2022).
3. X. Moya, N. D. Mathur, *Science* **370**, 797 (2020).
4. A. Kitanovski *et al.*, *Magnetocaloric Energy Conversion: From Theory to Applications* (Springer, 2015).
5. A. Torelló *et al.*, *Science* **370**, 125 (2020).
6. J. Tušek *et al.*, *Nat. Energy* **1**, 16134 (2016).
7. P. Lloveras *et al.*, *Nat. Commun.* **10**, 1803 (2019).
8. Ž. Ahčin *et al.*, *Joule* **6**, 2338 (2022).
9. Y. Meng *et al.*, *Nat. Energy* **5**, 996 (2020).
10. M. Masche, J. Liang, K. Engelbrecht, C. R. H. Bahl, *Appl. Therm. Eng.* **204**, 117947 (2022).
11. R. Ma *et al.*, *Science* **357**, 1130 (2017).

10.1126/science.adf5114

HYPOTHESIS

Epigenetic clocks, aging, and cancer

Global methylation changes in aging cells affect cancer risk and tissue homeostasis

By Sarah E. Johnstone[1,2,3], Vadim N. Gladyshev[3,4], Martin J. Aryee[2,3,5], Bradley E. Bernstein[2,3,6,7]

Cancer and aging are accompanied by stereotyped changes to the epigenetic landscape, including progressive loss of DNA methylation over gene-poor genomic regions (*1*, *2*). Global hypomethylation arises in cells that have undergone many divisions, likely owing to imperfect maintenance. Evidence suggests that global hypomethylation represents a "mitotic clock" that counts divisions in somatic cells and functions to restrain aging cells and limit malignant progression. Therapies that modulate the pace of methylation loss or eliminate hypomethylated cells could alleviate aging-associated diseases or cancers.

Several lines of evidence indicate that hypomethylation represents a general mitotic clock (*3*, *4*). In tumors, hypomethylation affects megabase-sized intervals that are CpG-poor, gene-poor, and late-replicating. Tissues from older individuals also exhibit widespread hypomethylation of the same regions as in cancer, albeit of lesser magnitude. Hypomethylation is more pronounced in proliferative epithelial tissues, compared with brain tissue and other compartments that largely comprise postmitotic cells. Moreover, primary cells become progressively hypomethylated with increasing passages in culture, but their methylation stabilizes when they exit the cell cycle (*5*). In cancer cells, the degree of hypomethylation correlates with somatic mutational burden, which is established to have mitotic clock–like properties because the number of mutations increases as cells accumulate divisions (*6*).

DNA methylation loss associated with cell divisions is likely a consequence of inefficient epigenetic maintenance (see the figure). Methylation is copied during DNA replication by DNA methyltransferases (DNMTs). However, maintenance is less efficient in CpG-poor regions that replicate late in S phase, particularly in rapidly dividing cells. A study of replicating embryonic stem and HeLa cells showed that although methylation was copied to daughter DNA strands, it was delayed and error prone in late-replicating regions (*7*). Thus, global hypomethylation is a shared feature of aging and malignant cells rooted in inefficient maintenance and gradual methylation loss as somatic cells accumulate divisions.

The mitotic hypomethylation clock is distinct from clocks that predict chronological age from methylation in tissues. These organismal aging clocks have attracted considerable attention for their accuracy and potential to predict morbidity and mortality (*8*). Machine-learning algorithms identify and integrate sets of CpGs whose methylation status correlates with age. Although aging clocks have been developed for a range of tissues and organisms, different algorithms for the same tissue type incorporate different CpGs. This inconsistency has hindered interpretation of the methylation changes.

Organismal aging clocks presumably incorporate multiple inputs, including cell type composition, environmental influences, mitotic clock features, and other disruptions that arise over time. The mitotic clock input likely includes global hypomethylation as well as focal hypermethylation of specific CpG islands, which can also accumulate as cells divide. Global hypomethylation and focal hypermethylation both loosely correlate with chronological age (*3*, *9*). A relationship between mitotic and aging clocks is also supported by the observation that telomerase reverse transcriptase (TERT) variants that increase telomere length are associated with increased epigenetic age predictions, on the basis of measurements of DNA methylation in human peripheral blood mononuclear cells (*8*). Because these variants allow cells to undergo more divisions before telomere crisis (when telomeres become too short and cells arrest), a potential explanation is that more division increases mitotic methylation changes, which accelerates the aging clock.

The relationship between mitotic and aging-associated methylation changes is confounded by cell type heterogeneity. The pace of mitotic hypomethylation varies across cell types, with embryonic stem cells representing an extreme because they remain stably methylated (*3*, *10*). Epigenetic age also varies between individual cells in a tissue, proceeding slowly in certain progenitor populations (*11*). Although the precise relationship between mitotic and aging clocks remains obscure, the cell-intrinsic properties and mechanistic underpinnings of the DNA hypomethylation clock provide a complementary framework for the study of human biology and aging.

What is the impact of hypomethylation? Its prominence in cancer prompted extensive exploration of potential oncogenic functions, yet decades of study have failed to clarify such roles. Hypomethylation in tumor cells may alternatively represent a scar of having undergone many divisions rather than being a driving feature of malignancy. The recognition that hypomethylation is a consequence of accumulated divisions suggests that it might instead prune aging cells, protecting them from malignant progression and affecting aging tissue homeostasis.

Substantial evidence supports several such restrictive functions for hypomethylation. DNA methylation plays a fundamental role in the transcriptional silencing of transposable elements (TEs) such as endogenous retroviruses (ERVs) and long interspersed nuclear elements (LINEs), which are inserted at high copy numbers throughout mammalian genomes (*12*). The expression of TEs is strongly up-regulated across a range of tumors, particularly in hypomethylated regions. In support of a causal role for methylation loss, the DNMT inhibitor 5-azacytidine induces LINE and ERV expression in vitro and in vivo (*13*).

TE reactivation triggers innate immunity through viral mimicry (*13*). The derepressed elements produce double-stranded RNAs, which are sensed by cytosolic sensors that trigger a type I interferon (IFN) response. DNMT inhibitors activate TEs in cancer cells, increase immune infiltration, and sensitize tumors to immunotherapy. LINE reactivation has also been documented in senescent cells, where it triggers IFN responses and may promote inflammaging, a chronic inflammatory state linked to aging-associated diseases (*12*).

Global hypomethylation also alters chromatin topology, which can affect the phenotypes of neoplastic and aging cells. Late-replicating genomic regions localize to the nuclear periphery and lamina in healthy cells but relocate to the interior and gain repressive histone modifications in hypomethylated tumor cells (*5*, *14*). These architectural changes are accompanied by transcriptional

[1]Department of Pathology, Dana-Farber Cancer Institute, Boston, MA, USA. [2]Department of Pathology, Harvard Medical School, Boston, MA, USA. [3]Broad Institute, Cambridge, MA, USA. [4]Division of Genetics, Department of Medicine, Brigham and Women's Hospital, Harvard Medical School, Boston, MA, USA. [5]Department of Data Science, Dana-Farber Cancer Institute, Boston, MA, USA. [6]Department of Cancer Biology, Dana-Farber Cancer Institute, Boston, MA, USA. [7]Department of Cell Biology, Harvard Medical School, Boston, MA, USA. Email: bradley_bernstein@dfci.harvard.edu

changes likely to affect tumor and aging phenotypes. In contrast to TEs, the expression of most protein-coding genes in the reorganized regions is down-regulated in association with DNA methylation loss and chromatin changes. The deregulated genes are enriched for functions related to stem cell proliferation, epithelial-mesenchymal transition, and invasion (*14*). Their repression may restrain the proliferative and invasive potential of aging cells and hinder malignant progression.

Additional evidence suggests links between global hypomethylation and senescence, a conserved program that limits the proliferation of damaged cells (*5*). Senescent cells exhibit global hypomethylation and profound chromatin architecture changes, including the formation of senescence-associated heterochromatin foci (SAHFs). Key features of SAHFs, including their spatial redistribution and their association with repressive histone modifications, are reminiscent of reorganized chromatin in hypomethylated aging and malignant cells. These parallels raise the possibility that hypomethylation and associated chromatin changes also promote senescence.

DNA methylation is also critical for nuclear and genome integrity. Global hypomethylation could contribute to tumor initiation and evolution by promoting chromosomal instability (*4*). At the same time, p53-dependent DNA damage responses associated with hypomethylation consequent to DNMT inhibition or haploinsufficiency may cause cell cycle arrest or apoptosis. Aging cells also harbor cytoplasmic chromatin fragments enriched for markers of DNA damage and heterochromatin that are capable of activating the inflammatory stimulator of interferon genes (STING) pathway (*12*). Hence, although hypomethylation may contribute to the evolution of tumors, its net impact is more likely to restrain the proliferative capacity and plasticity of aging cells and to promote their immune clearance. In addition to checking malignant progression, effects of these sequelae on tissue homeostasis may confer other adaptive or detrimental aging phenotypes.

To the extent that global hypomethylation enacts barriers to proliferation and malignant progression, tumor cells must adopt strategies to overcome them. Certain tumors arise from stem cells unaffected by hypomethylation, whereas others acquire hypermethylating phenotypes that may slow or reverse mitotic hypomethylation (*3*). Activation of TEs and downstream sensing pathways may be muted by chromatin regulators or immune factors, which are frequently altered in cancer. Cancer cells may also benefit from the derepression of certain TEs, such as the ERVs that activate oncogenes in colorectal tumors (*12*). These competing forces allude to a battle between organismal evolution and tumor evolution, with the former yielding tumor-suppressive features of the hypomethylation clock and the latter enabling malignant cells to overcome or exploit those features.

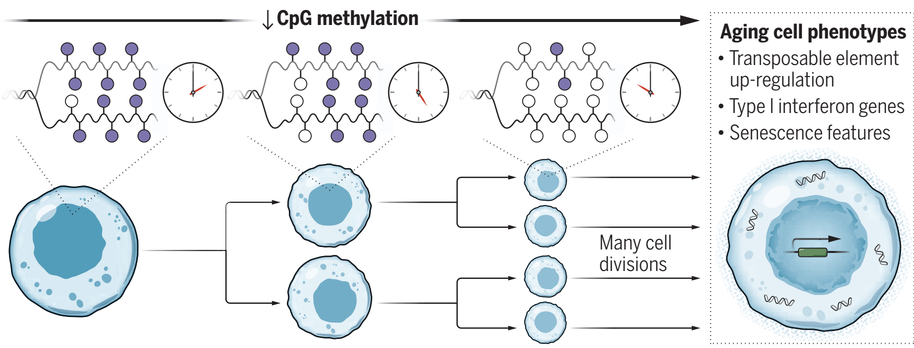
Although hypomethylation is conserved across mammals, its pace varies between organisms and cell types. Accelerated global hypomethylation was proposed to explain the rarity of tumors in blind mole rats, a species notable for longevity and cancer resistance (*15*). So although hypomethylation may reflect an inherent feature of mammalian genomes, it may be "tunable" across species and tissues. This is reminiscent of the heterochromatin-based mitotic clock in the yeast *Saccharomyces cerevisiae*, whose modulation alters life span (*5*). There are also parallels to somatic mutational rates, whose variability across mammals scales with life span (*6*). Moreover, the extent to which hypomethylation primes downstream expression changes and phenotypes may represent an additional tunable component of the mitotic clock. Even to the extent that hypomethylation is an intrinsic feature of mammalian genomes predicated in imperfect maintenance, its pace and downstream integration by chromatin and transcriptional machinery have likely evolved to balance cancer resistance and aging phenotypes.

It should be recognized that this model of mitotic hypomethylation and its impact on cell phenotypes remains nascent and largely inferential. The hypomethylation landscape has been defined from profiles of tumors, heterogeneous tissues, and cultured cell lines, but the patterns and pace of methylation loss will vary according to cell lineage, developmental stage, and environment. New tools are needed to resolve methylation patterns across single cells in heterogeneous tissues and to track methylation loss in real time. Furthermore, downstream functional consequences have been largely inferred from correlations with chromatin states and TE expression. They are supported by genetics and the effects of DNMT inhibitors, but these do not fully recapitulate the hypomethylation in aging and malignant cells. Other key questions relate to the ubiquity of hypomethylation in tumors and how cancer cells overcome the associated barriers.

A more detailed understanding of the hypomethylation clock could reveal biomarkers that predict disease risk or stratify tumors. It could yield new therapeutic modalities that prune aging or premalignant cells by exploiting vulnerabilities associated with hypomethylation. Alternatively, therapies that slow or reverse cell-intrinsic DNA hypomethylation might alleviate inflammation or other aging-associated deficits. Interventions will need to strike a balance to improve aging tissue homeostasis without potentiating cancer risk. ■

The mitotic hypomethylation clock restrains aging cells

DNA hypomethylation arises from inefficient maintenance of CpG methylation in late-replicating genomic regions with low CpG density. The baseline methylation of these regions (purple circles) can gradually be lost (empty circles) as cells divide. Eventually, global hypomethylation may arise, which restrains aging cells and hinders tumor progression through the induction of transposable element expression, innate immunity (interferon responses), and senescence-associated chromatin alterations.



GRAPHIC: A. FISHER/*SCIENCE*

REFERENCES AND NOTES

1. M. Ehrlich, *Epigenomics* **1**, 239 (2009).
2. A. P. Feinberg *et al.*, *Nat. Rev. Genet.* **17**, 284 (2016).
3. W. Zhou *et al.*, *Nat. Genet.* **50**, 591 (2018).
4. M. Dmitrijeva *et al.*, *Nucleic Acids Res.* **46**, 7022 (2018).
5. P. Sen *et al.*, *Cell* **166**, 822 (2016).
6. A. Cagan *et al.*, *Nature* **604**, 517 (2022).
7. X. Ming *et al.*, *Cell Res.* **30**, 980 (2020).
8. S. Horvath, K. Raj, *Nat. Rev. Genet.* **19**, 371 (2018).
9. Z. Yang *et al.*, *Genome Biol.* **17**, 205 (2016).
10. Z. Shipony *et al.*, *Nature* **513**, 115 (2014).
11. A. Trapp *et al.*, *Nat. Aging* **1**, 1189 (2021).
12. V. Gorbunova *et al.*, *Nature* **596**, 43 (2021).
13. P. A. Jones *et al.*, *Nat. Rev. Cancer* **19**, 151 (2019).
14. S. E. Johnstone *et al.*, *Cell* **182**, 1474 (2020).
15. Y. Zhao *et al.*, *Nat. Immunol.* **22**, 1219 (2021).

ACKNOWLEDGMENTS

B.E.B. has financial interests in Fulcrum Therapeutics, HiFiBiO, Arsenal Biosciences, Chroma Medicine, Cell Signaling Technologies, and Design Pharmaceuticals. M.J.A. has financial interests in SeQure Dx.

10.1126/science.abn4009

POLICY FORUM

HIGHER EDUCATION

Data blind: Universities lag in capturing and exploiting data

Study finds a pervasive void of infrastructure thinking

By **Christine L. Borgman**[1] and **Amy Brand**[2]

Research universities are large, complex organizations that generate vast amounts of administrative and research data. If exploited effectively, these data can aid in addressing myriad challenges. Yet universities lag behind industry, business, and government in deriving strategic value from their data resources (*1*). We recently conducted interviews on the state of data-informed decision-making with university leaders who were highly attuned to how well their institutional data systems and organizational structures are serving them and to the kinds of data capture and exploitation most needed. Findings from this exploratory study shed light on ways in which universities are data rich, data poor, and—sometimes—intentionally data blind. They point toward the need for leadership that supports a panoramic view of the data infrastructure and policies at play within individual universities, whether realized by creating a new senior role with relevant authority and budget or through greater multistakeholder coordination.

The cost of poor data management and the lack of data governance is an invisible tax on an organization's efficiency. Despite sporadic initiatives in recent years to grow interoperability and reduce redundancies in academic data management, most institutions still lack needed coordination and expertise. Over the past two decades, a commercial market has emerged for expensive systems that manage information about instruction, scholarship, grants, human resources, finance, and operations. Our engagement with university administrators revealed both concerns about commercial control of their internal systems and continuing tensions about local capacity for data-informed planning. Many felt handicapped by the lack of databases of record, coordinated information management strategies, and administrators with data science training and skills. Faculty, students, and administrators alike have concerns—some legitimate, some not—about who has access to data, decisions that may result, and potential commercial exploitation of their information. So too, universities have been slower than other economic sectors in creating senior positions such as chief data officers to coordinate data quality, strategy, governance, and privacy matters (*2*). Our study sought to identify sources of these tensions along with innovative solutions adopted or under development within the academy. We unexpectedly found a pervasive void of infrastructure thinking and a relatively limited set of data-informed planning successes.

Although our study did not address the COVID-19 pandemic per se, this unprecedented crisis heightened the salience and urgency of many data considerations. The onset of the pandemic found university administrators scrambling to make data-informed decisions about remote access to services such as health care, instruction, and libraries; about security of buildings, laboratories, and technology; and about the effectiveness of various infrastructures. Myriad privacy issues became apparent as administrators sought aggregated or identifiable information about activities on campuses, networks, and systems.

We interviewed a dozen university leaders selected to represent a balance of perspectives on data management, with roles including provost or vice provost; vice president (or vice chancellor) for research (VPR) or institutional research; university librarian; and chief information officer (CIO) or chief technology officer. Several participants had multiple job titles. Although we interviewed these leaders about their current institutional roles, most of them also commented from their perspectives as current or former faculty. The sample was diversified by type of institution, public or private; by gender and ethnicity; and by geography, with respondents from east and west coasts of North America and midwestern US states (see supplementary materials). We conducted interviews by Zoom, which we recorded and transcribed, averaging about 45 minutes in length, from April through August of 2021.

Our interview questions addressed the participant's role in university data, what key business decisions are data-informed, where they lack data for decision-making, which information systems are most important in making critical management decisions, who is responsible for what kinds of data, what are their criteria for outsourcing or insourcing data systems, what integrative views of university data they need, and where sensitivities about data access and use arise on their campuses. These questions led to wide-ranging discussions that addressed many kinds of data, decisions, strategies, and concerns. Because the United States lacks the centralized models for tracking research outputs and academic productivity common in the UK, Europe, and many Latin American countries, our findings will apply differently by region and institutional arrangements. Similarly, comparisons to government and industry are inherently limited. University infrastructures must accommodate a complex array of stakeholders, missions, data resources, and time horizons.

URGENT CHALLENGES

Participants spoke to the urgency of the data governance and exploitation challenges faced by universities. In coding the long lists of data elements mentioned in our interviews, three general categories of data emerged, varying by origin, application, and policy sensitivity (see the box). Various interdependencies arise among these three categories of data, often requiring interoperability between systems. For example, for library collections to support the teaching and research missions of the university effectively, their systems incorporate telemetric and administrative data from internal systems for learning management, registrar, identity management, and finance and may interoperate with external systems of publishers, community repositories, and other agencies.

Data for strategic decisions

The ability to monitor activity related to teaching, research, telecommunications, building services, and operations proved crucial in transitioning to remote work at the height of the COVID-19 pandemic. Crisis experience also revealed where data to inform decisions were lacking. Valuable

[1]Department of Information Studies, University of California, Los Angeles, Los Angeles, CA, USA. [2]The MIT Press, Massachusetts Institute of Technology, Cambridge, MA, USA. Email: amybrand@mit.edu

data may be inaccessible because of data governance practices or friction between stakeholder groups, or be technically accessible but not exploited because of a lack of staff expertise. One VPR told us, "I don't think we made very good use of our data, in part because the people we had in our office were not used to using data to make decisions."

Provosts, librarians, VPRs, deans, and faculty all want better control over records of scholarly products such as publications, research data, materials, and software. In some universities, faculty productivity data are held centrally in "research information management systems" or "current research information systems"; many of these are commercial products (*3*). In other universities, faculty productivity information is decentralized, held by deans and departments.

Provosts told us that they could make more strategic hiring and curricular decisions if they had more comprehensive data on faculty research areas, career interests of prospective students, research funding patterns, higher-education policy trends, and competitive intelligence about other universities. Librarians could target their collections and services more strategically with current data about faculty scholarship and curriculum decisions. VPRs could grow their university's funding and scholarship portfolios more effectively with fuller data on current and emerging research areas, faculty and staff expertise, and tools to match talent to funding opportunities. Faculty members, per our participants, could benefit from tools that reduce their administrative burden to produce data for populating personnel files, institutional repositories, and university reports. In STEM fields, faculty also seek data about potential collaborators.

Most participants sought more transparent and coordinated approaches to their university's data resources. Our overall findings supported the value of chief data officers, although only a few participants explicitly expressed a need for such a leadership role. Arguments for taking an infrastructure approach to university technology investments include more effective use of data for strategic decision-making; decreased duplication of systems and labor; and policy oversight for privacy, data protection, and cybersecurity.

Barriers to access, control, and use

One clear point of unanimity among participants was that tensions exist among stakeholders regarding who has access to particular data, appropriate uses of data, and mechanisms for data governance, privacy, and integration. We highlight key issues here.

Data governance and privacy

In policy contexts, data governance spans privacy, security, data protection, boundaries, ownership, authority, stewardship, and degrees of centralization versus decentralization. Participants offered a variety of opinions about who should control which kinds of data, systems, and uses. One provost commented that "COVID has changed our practices and expectations about control over data, such as Zoom, and who has access to transcripts and recordings." Faculty and other stakeholders are concerned about the surveillance capabilities of centralized systems and how integrated data might be used for resource allocation.

Categories of data

Telemetry data
Functional administrative data—the signals generated by systemic transactions, wireless networks, security cameras, sensors, and similar information produced in day-to-day operations.

Academic administrative data
Information about students, faculty, staff, visitors, collaborators, funding, and academic outputs such as publications. These data span university operations such as personnel, research information management, and learning management systems.

Research data
Products of scholarly activity. These data require local infrastructure and may be subject to sharing requirements by funding agencies and journals.

Decentralization has advantages of local control by individual data stewards who know their data, sources, and users well. Administrators often acquire systems to serve their own needs, with little university-wide oversight for interoperability or data sharing. When local data stewards have sole authority over system access, they can constrain data release to other internal units on grounds of privacy, labor requirements for extracting data, technical incompatibilities, or administrative reasons. We found that data stewards seek to protect their own data: Libraries control patron records, research offices control grant proposals and financial data, provosts control personnel data, and so on. Several participants commented on how decentralized control by strong deans and schools can make coordination across the university "a big problem." One provost said they have many "data czars and czaresses" over their data. Another provost opined that the idea of trying "to have a single personnel system at [our university] … is a fool's errand." Entrenched decentralization constrains an institution's appetite for integration and coordinated planning.

Many governance concerns we encountered were framed as privacy issues, often conflating complex conceptual, technical, and legal aspects of privacy, anonymity, confidentiality, security, and surveillance (*4*). Privacy can be a blunt instrument—or "talisman," as a university librarian said—to assert control over data about individuals. Rarely did we find broad campus engagement in governing privacy matters. Rather, diffused governance of data about individuals was the norm, delegated to offices of the CIO, chief information security officer (CISO), or legal affairs; few universities had chief privacy officers.

Data integration

The difficulty of integrating data across campus was noted by almost every participant. Some integration issues were technical, such as duplicate data in incompatible systems from competing commercial providers. Others were conceptual, such as lack of agreement on data elements, and situations in which too much data integration might impinge on academic freedom. One director of institutional research noted a recent agreement on defining a "gateway course" as a big win. Some integration issues are territorial, such as when one office refuses to share data with another; others were framed as data quality issues, such as inconsistent reporting across units. Administrators need better data rather than more data.

Some integration issues involve claims of intellectual property rights that conflate ownership, licensing, and educational policy. An example given by provosts and librarians was access to course syllabi. Databases of syllabi would give students a broad view of course offerings and the ability to sample readings, enable provosts and deans to identify duplication and gaps in instructional offerings, and strengthen librarians' ability to match collections to curriculum. Whereas individual faculty may claim ownership of syllabi in principle, in practice these syllabi are available in campus learning management systems—but accessible only by currently enrolled students. A change in policy could open syllabi to the university community. Integration barriers often involve governance more than technology.

Of the six job categories in our study, university librarians were most explicit about their goals for integrating data sources across their campuses. These librarians



ILLUSTRATION: SABELSKAYA/ISTOCK.COM AND OLGA_ROM/ISTOCK.COM. ADAPTED BY C. AYCOCK/*SCIENCE*

want to tailor collections and services to their university's academic strategy and faculty research trajectories (*5*) but report that they rarely are granted access to those data. One university librarian commented that "collection management remains an artisanal practice," for reasons such as the ways in which "collection purchasing is atomized into autonomous budgets, making it difficult to grasp the big picture." As a consequence, library collection decisions do not depend on data as much as they could.

CIOs, and individuals in other roles, often said that the desire for data integration was greater than the local expertise and political will to invest accordingly. Data integration was particularly complex for universities implementing multiple, often incompatible, corporate solutions. Rather than exporting and exploiting their data resources, they found themselves being forced to "buy back" their own data from vendors, or devoting weeks or months of staff time to merge data manually. Meanwhile, these same vendors are mining and combining university data and open-access data to offer competitive intelligence services to the academic market.

Although no one expected seamlessly interoperable systems across campus, our participants did seek sufficient systems integration to increase efficiency and reduce redundancy, while not forcing interoperability between incompatible systems or across institutional boundaries.

In response to growing concerns about corporate control of academic platforms and analytics (*6*, *7*), institutions are taking great care in negotiating terms for data ownership, control over data migration and integration, documentation, privacy, security, and risk management. More of the private research universities than public universities in our small sample are contracting for systems to manage faculty profiles, library content, teaching and learning services, grants, and institutional research.

Several participants noted that new interoperability platforms improve the ability to exchange data between commercial systems. Others commented that universities cannot compete with business interests in the marketplace for technical talent, making it difficult to maintain and document open-source software or locally built systems. Research universities with medical centers mentioned data integration as a substantial source of friction. Maintaining separate technology operations for central campuses and medical campuses is expensive but often necessary to comply with regulations on health data.

Research data management

Researchers in all disciplines, and especially those who rely on extramural funding, may be subject to requirements for maintaining, releasing, and sharing scholarly products such as publications, data, software, and documentation (*8*–*10*). Despite more than two decades of data-sharing requirements by funding agencies and journals, none of our participants reported coordinated university approaches to research data management (RDM). Much of the infrastructure required for RDM involves workflows throughout the university. One respondent commented, "You need a vice president of research, … CIO, and … a library that's completely on board" to stake out territory between these three entities and "to convince the faculty we can put their data in the safest place." Our participants generally agreed that "difficult conversations among stakeholders are necessary."

VPRs, librarians, and provosts alike deferred RDM responsibility to principal investigators (PIs), disciplinary repositories, and funding agencies. One university librarian commented that it is "hard to justify the high costs of data preservation and stewardship." One VPR in our sample was deeply concerned about funding agency mandates for maintaining access to data: "Agencies are not realistic in what they are expecting of PIs, especially for short-term projects … Maintaining software necessary to use older data (also) is infeasible."

University librarians, to whom several of the provosts, CIOs, and VPRs also deferred, had nuanced explanations of RDM challenges. They now have enough experience to assess methods and costs. Rather than store datasets locally, for example, one library is indexing university datasets that are deposited elsewhere. Another library is developing "workflow wizards" to automate some data management tasks. A VPR is addressing policy to identify data sources worthy of local stewardship and those sources better diverted to disciplinary repositories. Medical libraries have greater oversight of research datasets than occurs in most domains. These are important steps toward addressing the data-sharing requirements of government agencies in the United States, Europe, and elsewhere. However, full compliance remains a daunting challenge to the universities studied, not least because RDM has the classic economic characteristics of a "commons," subject to competition and free riders (*11*). Shared governance models for research data stewardship remain elusive.

LESSONS LEARNED

Academic leaders have legitimate concerns about economic constraints, lack of data expertise, being locked into commercial

solutions, and creating surveillance states on their campuses. Even when their universities are "data rich," they may also be "data poor" in that they are struggling to exploit data resources to their strategic advantage, or "data blind" in being reluctant to initiate stakeholder discussions necessary to build consensus for data governance. Lessons learned from the experiences of these major research universities can help to inform institutions with fewer resources.

Invest in knowledge infrastructures

To improve data access, intelligence, and integration, universities can make greater investments in knowledge infrastructures (KIs): robust networks of people, artifacts, and institutions that generate, share, and maintain various kinds of knowledge—including, crucially, data (*12*). These infrastructures incorporate systems managed by administrative units and their interactions with other technologies and institutions. By mapping existing infrastructure components and points of interaction, universities can identify duplications of effort, sources of friction, and means to improve information flows throughout the institution.

Local and national investments in KI are a matter of strategic competition [for example, (*11*)]. Research data involve more stakeholders than may be immediately apparent, given the many hands, technologies, and university offices touching them: faculty investigators, student and staff researchers, computer centers, grants administration, finance, libraries, institutional repositories, legal and technology transfer offices, and laboratory and building services. These entities in turn interact with their counterparts at partner institutions and with funding agencies, journals, data and software repositories, publishers, professional societies, and other stakeholders in scholarly communication. Small datasets may reside locally on campus but still require complex infrastructure to maintain data, software, code, and documentation. Large datasets, such as climate models, may require multi-institution infrastructure for stewardship (*9*).

Identity management is an essential component of university KIs. As one provost summarized, "without a common identification system, all of this [data integration work] is futile." Universities assign personal identifiers for various privileges, services, access, and finances. An individual might have multiple university identifiers and multiple external identifiers, such as an ORCID and a social security number. In addition to technical and political challenges, mapping identifiers between systems has high stakes for scholarly attribution and credit.

Invest in data management capacity

New data science programs are producing professionals for all economic sectors while also developing data-management expertise in traditional disciplines. As universities begin to employ more of this new crop of professionals, invest in training existing personnel, and develop new career paths for them, they will gain capacity for managing telemetry, academic administrative, and research data. Another benefit of data-management capacity is the ability to mine these data to yield strategic, policy, social, cultural, and technical insights.

Our interviews surfaced many examples of low-hanging fruit, in which small investments can yield large payoffs in data exploitation. These include interoperability tools that extract data from university databases to produce customized information feeds, portals for self-service access to university databases, indices to internal and external resources, and application-programming interfaces (APIs) to access university data. APIs can support search, download, and data visualization capabilities for myriad systems and purposes, such as institutional research, institutional repositories, course materials, and library content. Other APIs are being deployed at universities to index research data, aggregate newsfeeds, populate academic personnel files, and integrate internal websites with external resources such as grant databases. These innovations often arose from seed grants for pilot projects or prizes for student competitions.

Develop FAIR and just data resources

Rarely are data simply "facts." Data collection of all kinds is based on models, assumptions, and methods, whether explicit or implicit. Thus, data-informed decision-making is only as good as the data on which decisions are based. Scholarly research on sources of data bias, and on ways to address them, offers valuable guidance on paths forward (*13*). Engaging the university community in governing data resources in ways that are transparent is an important step toward institutional goals for equity and justice.

The FAIR principles (findable, accessible, interoperable, reusable) (*14*), although adopted widely for research data, also offer aspirational guidelines for KIs. For data to be findable and interoperable, they need to be documented with consistent metadata. For data to be accessible, they must be searchable and retrievable. To be reusable, data need to be associated with sufficient documentation, methods, software, and other tools for others to use them. Although the FAIR principles may be a high bar for telemetry and academic administrative data, the emphasis on interoperability is key to campus data integration.

CONCLUSIONS

National and international policy for data sharing, management, reuse, privacy, and security are advancing rapidly (*11*, *15*). To remain competitive, universities will partner in these initiatives and respond to new policy requirements. As the COVID-19 pandemic has reminded us, good hygiene begins at home. Similarly, good data hygiene begins on campus. Data-informed decision-making provides opportunities to promote transparent governance; advance fairness and equity for faculty, students, and staff; and save money. We encourage university leaders to embrace more objective and transparent data-informed models for decision-making. ■

REFERENCES AND NOTES

1. K. L. Webber, H. Y. Zheng, Eds., *Big Data on Campus: Data Analytics and Decision Making in Higher Education* (Johns Hopkins Univ. Press, 2020).
2. K. Ilkani, "The role of the chief data officer in higher education" (The Tambellini Group, 2020); https://www.thetambellinigroup.com/the-role-of-the-chief-data-officer-in-higher-education.
3. M. Givens, "Keeping up with... research information management systems" (Association of College & Research Libraries, 2016); https://www.ala.org/acrl/publications/keeping_up_with/rims.
4. C. L. Borgman, *Berkeley Technol. Law J.* **33**, 365 (2018).
5. D. Cooper, C. B. Hill, R. C. Schonfeld, "Aligning the research library to organizational strategy" (Ithaka S+R, 2022); https://doi.org/10.18665/sr.316656.
6. C. Aspesi, A. Brand, *Science* **368**, 574 (2020).
7. A. Posada, G. Chen, *ELPUB* 2018, (2018).
8. C. L. Borgman, *Big Data, Little Data, No Data: Scholarship in the Networked World* (MIT Press, 2015).
9. C. L. Borgman, P. E. Bourne, *Harvard Data Science Review* (2022).
10. National Academies of Sciences, *Reproducibility and Replicability in Science* (National Academies Press, 2019).
11. P. E. Bourne *et al.*, *Science* **377**, 256 (2022).
12. P. N. Edwards, *A Vast Machine: Computer Models, Climate Data, and the Politics of Global Warming* (MIT Press, 2010).
13. C. O'Neil, *Weapons of Math Destruction: How Big Data Increases Inequality and Threatens Democracy* (Crown, 2016).
14. M. D. Wilkinson *et al.*, *Sci. Data* **3**, 160018 (2016).
15. National Academies of Sciences, *Open Scholarship Priorities and Next Steps: Proceedings of a Workshop–In Brief* (National Academies Press, 2022).

ACKNOWLEDGMENTS

We are grateful to our participants for their generous contributions of time and expertise. We thank colleagues who served as pilot testers of our interview protocol, provided advice on research design, and commented on prior drafts of this article, including P. E. Bourne, P. Courant, S. Garfinkel, M. L. Kennedy, C. Lynch, and M. Smith.

SUPPLEMENTARY MATERIALS

science.org/doi/10.1126/science.add2734

10.1126/science.add2734

BOOKS *et al.*



Samantha Jaworski monitors corals at the Australian Institute of Marine Science in October 2019.

MARINE SCIENCE

The art of aquarium science

Aquarist knowledge is an often overlooked but vital part of marine research

By **Penelope K. Hardy**

For the public, aquariums provide a window into an ocean they may never otherwise see. Part of the magic of aquariums is that the work that sustains them is largely invisible. This is intentional. It allows a glass box to become the ocean, whether to the camera's lens or the public eye.

As Samantha Muka demonstrates in her thoughtful new book, *Oceans Under Glass: Tank Craft and the Sciences of the Sea*, both the ways in which the technical knowledge of aquarium keeping developed and the ways in which that knowledge spreads are also largely invisible. This obscures the substantial roles hobbyists, technologists, and public aquarists have played and continue to play in producing this knowledge, as well as their contribution to the scientific knowledge developed in academic aquariums.

The popular aquarium's history starts with the introduction of new technologies of plate glass manufacture in the 19th century. Fishkeeping, for both aquaculture and pleasure, dates back millennia. Muka concentrates on specialist aquariums of the past century or so. Over the course of five chapters, she considers the broad evolution of aquarium craft, as well as the specific histories of photography tanks, kreisel (jellyfish) tanks, reef tanks, and breeding tank systems.

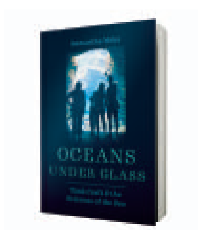
The development of tank systems for specialized purposes involved tinkering with nonstandard—and, Muka shows, often nonstandardizable—technology and required tacit knowledge accumulated through painstaking, hands-on trial and error. All these efforts were in service to the goal of reproducing nature in a glass box, although what one meant by "nature" depended on the particular aquarist's goals. These included taking photographs that clearly illustrated fish species, providing conditions that would support fragile jellyfish throughout their complicated life cycles, and encouraging highly coveted tropical species to reproduce in captivity on a commercial scale.

The tacit knowledge required to create such conditions filtered through hobbyist, professional, and academic communities along paths that are often difficult to trace. Muka uses the tools of both historian and sociologist to illuminate these roles, following patents, mentions, and citations through scientific and hobbyist literature. She also shadows and interviews practitioners in various aquarium settings to uncover the wide array of contributors to marine-biological knowledge production and to follow that knowledge through the "permeable boundaries" of the aquarium's various communities. The result provides a fascinating and thoughtful elucidation of the history of aquariums as an environmental technology and of public aquarists as "knowledge couriers" between communities.

The book also suggests broader questions that Muka does not address as directly as she might have. Because of the complicated constellation of skills and interests involved in tank craft, aquariums provide an excellent lens for interrogating our notions of where knowledge comes from and of what counts as science—what it is, who does it, what role technology plays in it, and even its purpose. These are suggested but largely left to the reader to ponder.

The important question that Muka leaves us with instead is how the aquarium influences our understanding of the ocean at a moment when the latter is being profoundly affected by anthropogenic climate change. Aquariums, she notes, have served as a "slice of the environment" through which viewers can consider, for research or pleasure, the broader ocean. This has been important scientifically, as an ocean in miniature lets us focus on and experiment with parameters that are difficult or impossible to isolate in the actual sea.

Muka predicts that, as widespread destruction of marine habitat continues, aquariums will form the basis for "building better and more resilient marine worlds." Those species that aquarists can coax into reproducing in tanks and those that might be bred to withstand disease or other challenges may someday replace dying species in the wild. Alternatively, aquariums themselves—scaled up as our technological capabilities allow—may eventually be all we have left. Either way, that meticulous craftwork and tacit knowledge painstakingly acquired by aquarists who have gone largely uncited in scientific literature will likely be critical to the future of marine life. ■



Oceans Under Glass
Samantha Muka
University of Chicago Press, 2022. 240 pp.

The reviewer is at the Department of History, University of Wisconsin–La Crosse, La Crosse, WI 54601, USA. Email: phardy@uwlax.edu

10.1126/science.adf4079

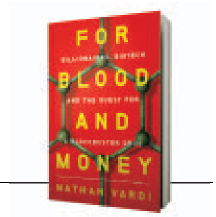
PHOTO: JONAS GRATZER/LIGHTROCKET VIA GETTY IMAGES

DRUG DEVELOPMENT

Making modern medicines

The business side of drug development comes to the fore in a tale of two blockbuster blood cancer therapeutics

For Blood and Money; Billionaires, Biotech, and the Quest for a Blockbuster Drug
Nathan Vardi
Norton, 2023. 288 pp.



By **Adrian Woolfson**

Big pharma companies have in the past decade begun to focus their efforts on what they do best: late-stage clinical development, medical and regulatory affairs, sales, and marketing. As a result, they have become increasingly dependent on licensing early-stage drug candidates developed by smaller companies to bolster their pipelines. Two drugs developed to treat blood cancers by fledgling companies and brought to market by big pharma—the small-molecule Bruton's tyrosine kinase (BTK) inhibitors Imbruvica and Calquence—are canonical examples of licensed therapeutic agents that have emerged via this mechanism. In his new book, *For Blood and Money*, Nathan Vardi narrates the intriguing and improbable tale of how these two small-molecule compounds were rescued from obscurity and transformed lead investors into billionaires overnight.

In 2006, Pharmacyclics CEO Richard Miller fortuitously picked up Imbruvica (ibrutinib)—or CRA-032765, as it was then known—along with two other early-stage drug candidates from Craig Venter's failed genome sequencing company Celera, for just $6.6 million. Preliminary data from 16 patients presented by Pharmacyclics at the 2009 American Society of Hematology meeting provided the first evidence that the drug was efficacious.

This flicker of a signal, missed by many, caught the attention of one of Pharmacyclics' lead investors, Wayne Rothbaum, as well as the American investment firm OrbiMed, who avidly bought up Pharmacyclics stock. Their optimism was vindicated by a 2013 study published in the *New England Journal of Medicine*, which detailed a 71% overall response rate in patients with chronic lymphocytic leukemia that translated into extended survival (*1*). Two years later, in 2015, Pharmacyclics was acquired by AbbVie in a transaction valuing the company at an astronomical $21 billion, netting its largest shareholder and executive chairman, Bob Duggan—an eccentric investor and fervent scientologist with no prior experience in biopharma—an unprecedented $3.5 billion.

Meanwhile, a more selective and potentially safer BTK inhibitor (*2*), Calquence (acalabrutinib, then known as SCH 2046835), was licensed in 2012 for a paltry $1000, with 5% royalties by Acerta—headed by Rothbaum—from Organon, a small Dutch outpost of Merck that the company had obtained in 2009 as part of its acquisition of Schering-Plough. Rothbaum, Vardi reveals, had—in a moment of weakness—divested more than half his position in Pharmacyclics before Imbruvica's full potential had been realized. While still making a handsome profit, Rothbaum's panic selling ensured that the return on his investment was a fraction of what it would have been had he maintained his original position.



ILLUSTRATION: STEPHAN SCHMITZ/ISPOT

According to Vardi, Rothbaum was desperate to correct what was, undoubtedly, "the worst trading error of his career." He received his opportunity when he founded Acerta in 2012 with a group of former Pharmacyclics employees, including the company's former chief medical officer Ahmed Hamdy, whom Duggan had unceremoniously fired in 2011 when the pair disagreed on how best to approach regulatory strategy. By this time, however, the promise of BTK inhibitors had become more obvious, making a breakthrough more challenging for newcomers.

By the winter of 2014, Imbruvica had received two regulatory approvals, whereas Acerta had not yet even commenced its first-in-human study. To Acerta's great relief, however, the first patients treated with acalabrutinib had a pronounced clinical response. It later also became evident that the new drug's improved selectivity prevented some of the side effects that had led select patients to stop taking Imbruvica. Rothbaum's decision to form a new BTK inhibitor company turned out to be life-changing, both for blood cancer patients and for himself. In February 2016, Acerta was acquired by AstraZeneca in a deal worth up to $7 billion, securing Rothbaum a $2.8 billion windfall.

Vardi reminds readers that historical accounts are by necessity subjective, noting that key individuals are often omitted from such narratives for a variety of reasons. He attempts to address this by calling out some of the unsung heroes of this story, including the Chinese chemist Zhengying Pan, who designed and synthesized CRA-032765, as well as key clinical investigators such as Daniel Pollyea and Susan O'Brien, who helped design and secure patients for the clinical studies and interpret the data. Most importantly, Vardi acknowledges the critical role played by the patients who risked their lives by participating in the early BTK inhibitor clinical studies.

In the hands of big pharma, Imbruvica and Calquence have joined the hallowed pantheon of the most successful drugs of all time. In detailing the fascinating story of how this happened, Vardi has delivered a master class in the machinations of modern drug development. ■

The reviewer is the executive chairman, president, and cofounder of Replay Holdings Inc., San Diego, CA, USA, and the author of *Life Without Genes* (HarperCollins, 2000). Email: adrianwoolfson@yahoo.com

REFERENCES AND NOTES

1. J. C. Byrd *et al.*, *N. Engl. J. Med.* **369**, 32 (2013).
2. J. C. Byrd *et al.*, *J.Clin. Oncol.* **39**, 3441 (2021).

10.1126/science.ade4644

LETTERS

Edited by **Jennifer Sills**

Editorial Expressions of Concern

In 2001, *Science* published the Report "Binding of DCC by netrin-1 to mediate axon guidance independent of adenosine A2B receptor activation" by E. Stein *et al.* (*1*). In 2015, the authors made us aware of issues with Western blot images in Figures 1 and 3, which were caused by tiling with overlap of adjacent columns and combining blot images to standardize panel sizes. The authors provided corrected images, but due to an error on our part, *Science* never posted an Erratum. We regret this error and apologize to the scientific community. Both we and the authors are aware that additional concerns have been raised since 2015. We are therefore not proceeding with a correction at this point but are alerting readers to the concerns while the authors and the authors' institution investigate further.

H. Holden Thorp
Editor-in-Chief

REFERENCES AND NOTES

1. E. Stein, Y. Zou, M.-M. Poo, M. Tessier-Lavigne, *Science* **291**, 1976 (2001).

Published online 15 December 2022
10.1126/science.adg2852

In 2001, *Science* published the Research Article "Hierarchical organization of guidance receptors: Silencing of netrin attraction by Slit through a Robo/DCC receptor complex" by E. Stein and M. Tessier-Lavigne (*1*). In 2015, the authors made us aware of issues with Western blot images in Figures 4, 5, and 6, which were caused by tiling with overlap of adjacent columns and combining blot images to standardize panel sizes. The authors provided corrected images for those Western blots. In addition, images were duplicated in Figure 2D (micrographs) and in Figure 4B (blank Western blots), and an incorrect blank panel was used in Figure 5E (top right). The original data for these figures could not be accessed, so not all specific conclusions related to these panels are supported by these figures. *Science* agreed to the publication of an Erratum; however, due to an error on our part, it was not posted. We regret this error and apologize to the scientific community. In light of the delay, we are not proceeding with a correction at this point but are alerting readers to the concerns while the authors and the authors' institution investigate further.

H. Holden Thorp
Editor-in-Chief

REFERENCES AND NOTES

1. E. Stein, M. Tessier-Lavigne, *Science* **291**, 1928 (2001).

Published online 15 December 2022
10.1126/science.adg2860

Retraction

In the Research Article "Gradual emergence followed by exponential spread of the SARS-CoV-2 Omicron variant in Africa" (*1*), we reported data from retrospective characterization of viral genomes of putative ancestors of the SARS-CoV-2 Omicron variant from western Africa months before the first detection of Omicron. After several social media posts suggested that these putative early Omicron ancestor sequences may have been false positives, we reanalyzed our data and the residual samples. We found a mixture of different SARS-CoV-2 genomic fragments contaminating some of the samples and sequence data on which we based our analysis. The residual samples are now exhausted, and the reconstruction of evolutionary intermediates cannot be replicated. Therefore, we are retracting our Research Article. The epidemiological data are not called into question and will be made available.

Carlo Fischer[1], Tongai Gibson Maponga[2], Anges Yadouleton[3], Nuro Abílio[4], Emmanuel Aboce[5], Praise Adewumi[3], Pedro Afonso[6], Jewelna Akorli[7], Soa Fy Andriamandimby[8], Latifa Anga[9], Yvonne Ashong[7], Mohamed Amine Beloufa[10], Aicha Bensalem[10], Richard Birtles[11,12], Anicet Luc Magloire Boumba[13,14], Freddie Bwanga[5,15], Mike Chaponda[16], Paradzai Chibukira[17], R. Matthew Chico[18], Justin Chileshe[16], Gershom Chongwe[16], Assana Cissé[19], Umberto D'Alessandro[20], Xavier Nicolas de Lamballerie[21], Joana F. M. de Morais[6], Fawzi Derrar[10], Ndongo Dia[22], Youssouf Diarra[23], Lassina Doumbia[23], Christian Drosten[1,24], Philippe Dussart[8], Richard Echodu[11], Yannik Eggers[25,26], Abdelmajid Eloualid[9], Ousmane Faye[22], Torsten Feldt[25,26], Anna Frühauf[1], Afiwa Halatoko[27], Pauliana-Vanessa Ilouga[28], Nalia Ismael[4], Ronan Jambou[29], Sheikh Jarju[20], Antje Kamprad[1], Ben Katowa[30,31], John Kayiwa[32], Leonard King'wara[33], Ousmane Koita[23], Vincent Lacoste[8], Adamou Lagare[29], Olfert Landt[34], Sonia Etenna Lekana-Douki[35], Jean-Bernard Lekana-Douki[35], Etuhole Iipumbu[36], Hugues Loemba[37,14], Julius Lutwama[32], Santou Mamadou[29], Issaka Maman[27], Brendon Manyisa[17], Pedro A. Martinez[6], Japhet Matoba[30,31], Lusia Mhuulu[36], Andres Moreira-Soto[1], Judy Mwangi[11,12], Nadine N'dilimabaka[35], Charity Angella Nassuna[32], Mamadou Ousmane Ndiath[20], Emmanuel Nepolo[36], Richard Njouom[28], Jalal Nourlil[9], Steven Ger Nyanjom[38], Eddy Okoth Odari[38], Alfred Okeng[5], Jean Bienvenue Ouoba[19], Michael Owusu[39], Irene Owusu Donkor[7], Karabo Kristen Phadu[2], Richard Odame Phillips[39], Wolfgang Preiser[2,40], Vurayai Ruhanya[17], Fortune Salah[27], Sourakatou Salifou[41], Amadou Alpha Sall[22], Augustina Angelina Sylverken[39,42], Paul Alain Tagnouokam-Ngoupo[28], Zekiba Tarnagda[19], Francis Olivier Tchikaya[14], Tafese Beyene Tufa[25,26], Jan Felix Drexler[1,24]*

[1]Charité–Universitätsmedizin Berlin, corporate member of Freie Universität Berlin and Humboldt Universität zu Berlin, Institute of Virology, Berlin, Germany. [2]Division of Medical Virology, Stellenbosch University Faculty of Medicine and Health Sciences, Cape Town, South Africa. [3]Laboratoire dés fievres hemorragiques virales de Cotonou, Akpakpa, Benin. [4]Instituto Nacional de Saúde, Maputo, Mozambique. [5]MBN Clinical Laboratories, Kampala, Uganda. [6]Instituto Nacional de Investigação em Saúde (INIS), Luanda, Angola. [7]Noguchi Memorial Institute for Medical Research, University of Ghana, Legon, Ghana. [8]Institut Pasteur de Madagascar, Antananarivo, Madagascar. [9]Institut Pasteur du Maroc, Casablanca, Morocco. [10]Institut Pasteur of Algeria, National Influenza Centre, Sidi-Fredj, Algeria. [11]Gulu University Multifunctional Research Laboratories, Gulu, Uganda. [12]School of Science, Engineering and Environment, University of Salford, Salford, UK. [13]Faculty of Health Sciences, Marien Ngouabi University, Pointe-Noire, Congo. [14]Molecular Diagnostic Laboratory HDL, Pointe-Noire, Congo. [15]Makerere University College of Health Sciences, Kampala, Uganda. [16]Tropical Diseases Research Centre, Ndola Teaching Hospital, Ndola, Zambia. [17]National Virology Laboratory, Faculty of Medicine and Health Sciences, University of Zimbabwe, Avondale, Zimbabwe. [18]London School of Hygiene and Tropical Medicine, London, UK. [19]Laboratoire National de Référence-Grippes, Ouagadougou, Burkina Faso. [20]Medical Research Council Unit at London School of Hygiene and Tropical Medicine, Banjul, Gambia. [21]Unité des Virus Émergents, Aix Marseille Université, Marseille, France. [22]Institut Pasteur de Dakar (IPD), Dakar, Senegal. [23]Université des Sciences, des Techniques et des Technologies de Bamako (USTTB), Bamako, Mali. [24]German Centre for Infection Research (DZIF), associated Partner Charité-Universitätsmedizin Berlin, Berlin, Germany. [25]Hirsch Institute of Tropical Medicine, Asella, Ethiopia. [26]Department of Gastroenterology, Hepatology and Infectious Diseases, University Hospital Düsseldorf, Heinrich Heine University Düsseldorf, Düsseldorf, Germany. [27]Institut National d'Hygiène, Lomé, Togo. [28]Centre Pasteur du Cameroun, Yaounde, Cameroon. [29]Centre de Recherche Médicale et Sanitaire (CERMES), Niamey, Niger. [30]Macha Research Trust, Choma, Zambia. [31]School of Veterinary Medicine, University of Zambia, Lusaka, Zambia. [32]Uganda Virus Research Institute, Entebbe, Uganda. [33]National Public Health Reference Laboratory, Ministry of Health, Nairobi, Kenya. [34]TiB-Molbiol GmbH, Berlin, Germany. [35]Centre Interdisciplinaire de Recherches Médicales de Franceville (CIRMF), Franceville, Gabon. [36]School of Medicine, University of Namibia, Windhoek, Namibia. [37]Faculty of Medicine, University of Ottawa, Ottawa, Ontario, Canada. [38]School of Biomedical Sciences, Jomo Kenyatta University of Agriculture and Technology, Nairobi, Kenya. [39]Kumasi Centre for Collaborative Research in Tropical Medicine (KCCR), Kwame Nkrumah University of Science and Technology (KNUST), Kumasi, Ghana. [40]National Health Laboratory Service Tygerberg Business Unit, Cape Town, South Africa. [41]Ministère de la Santé, Akpakpa, Benin. [42]Department of Theoretical and Applied Biology, KNUST, Kumasi, Ghana.

*Corresponding author.
Email: felix.drexler@charite.de

REFERENCES AND NOTES

1. C. Fischer *et al.*, *Science* 10.1126/science.add8737 (2022).

Published online 20 December 2022
10.1126/science.adg2821

Accessing the Loss and Damage climate fund

The 2022 United Nations Climate Change Conference, or Conference of the Parties (COP27), held in Sharm el-Sheikh, Egypt, in November, produced a long-awaited agreement to set up a global "Loss and Damage" fund (*1*). Under negotiation since the early 1990s, the fund's primary purpose is to provide financial assistance to developing countries that are vulnerable to and suffering from the adverse effects of climate change (*2*), such as the destruction of physical and social infrastructure. The new funding arrangements will "focus on addressing loss and damage by providing and assisting in mobilizing new and additional resources" (*2*). Now that a decision to establish the fund has been made, the question of how vulnerable groups can access the money must be addressed.

People who live in developing countries, many of whom are already climate refugees (*3*), are particularly vulnerable to climate change (*4*). Those who live below the poverty line often reside in precarious housing, haphazard settlements, underserviced neighborhoods, and environmentally hazardous locations, such as steep slopes, riverbanks, and low-lying areas. These populations suffer disproportionately relative to more affluent communities from extreme weather events, such as tropical cyclones, fluvial floods, and landslides (*4*). For example, the 2022 flood in Pakistan caused damages and economic losses of about US$30 billion (*5*). In addition, people in developing countries are affected by slow-onset processes, such as sea level rise (*4*), and noneconomic losses and damages, such as loss of territory, cultural heritage, sense of place, and Indigenous knowledge (*6*).

The transitional committee responsible for the operationalization of the new funding arrangements (*2*) must assure that the most vulnerable and affected groups can access this critical financial support. The deliberations ought to focus on making financing inclusive. Flexible finance governance architecture, such as a database tracking social protection of vulnerable populations in each country, could mitigate inequalities. Proactive measures could ensure that the money reaches even those communities who lack internet connections and the expertise required to make requests. For example, social security numbers, bank accounts, and smart (mobile) technologies could be linked to enable direct benefit transfers, similar to the system used in India to provide support during the COVID-19 pandemic (*7*). Contingency funds should be established to provide rapid financial support to the affected groups in the immediate aftermath of future disasters. The Loss and Damage fund should also include long-term financing to support alternative, climate-resilient livelihoods. This provision could help address financing gaps in the case of slow-onset events and noneconomic losses. The litmus test for a fair and just Loss and Damage fund will be whether it serves those who need it the most.



PHOTO: BAY ISMOYO/STRINGER/GETTY IMAGES

A new fund will support impoverished communities vulnerable to climate change, such as this one in Jakarta.

Bharat Dahiya[1]* and Mahesti Okitasari[2]
[1]School of Global Studies, Thammasat University, Rangsit, Pathum Thani, Thailand. [2]United Nations University Institute for the Advanced Study of Sustainability, Shibuya, Tokyo, Japan.
*Corresponding author. Email: bharat@sgs.tu.ac.th

REFERENCES AND NOTES

1. UN Framework Convention on Climate Change, "Sharm el-Sheikh implementation plan, draft decision -/CMA.4" (2022); https://unfccc.int/documents/621908.
2. UN Framework Convention on Climate Change, "Funding arrangements for responding to loss and damage associated with the adverse effects of climate change, including a focus on addressing loss and damage, draft decision -/CP.27 -/CMA.4" (2022); https://unfccc.int/documents/624440.
3. V. Clement *et al.*, "Groundswell part 2: Acting on internal climate migration" (World Bank, 2021); https://openknowledge.worldbank.org/handle/10986/36248.
4. Intergovernmental Panel on Climate Change, "Climate change 2022: Impacts, adaptation and vulnerability. Contribution of Working Group II to the Sixth Assessment Report of the Intergovernmental Panel on Climate Change," H.-O. Pörtner *et al.*, Eds. (2022); https://report.ipcc.ch/ar6/wg2/IPCC_AR6_WGII_FullReport.pdf.
5. World Bank, "Pakistan: Flood damages and economic losses over USD 30 billion and reconstruction needs over USD 16 billion—new assessment" (2022); https://www.worldbank.org/en/news/press-release/2022/10/28/pakistan-flood-damages-and-economic-losses-over-usd-30-billion-and-reconstruction-needs-over-usd-16-billion-new-assessme.
6. UN Framework Convention on Climate Change, "Side event of the ExCom at SB44. Shining the light on non-economic losses. Challenges, risks & lessons for addressing them. Summary Note, June 2016" (2016); https://unfccc.int/files/adaptation/groups_committees/loss_and_damage_executive_committee/application/pdf/nels_side_event_summary_note.pdf.
7. Ministry of Finance [Government of India], "Pradhan Mantri Jan Dhan Yojana (PMJDY)—National Mission for Financial Inclusion, completes eight years of successful implementation", (2022); https://www.pib.gov.in/PressReleasePage.aspx?PRID=1854909.

10.1126/science.adf9670

Remote opportunities for scholars in Ukraine

Russia's unprovoked attack on Ukraine has destroyed civilian infrastructure, including universities, research centers, and other academic infrastructure (*1*). Many Ukrainian scholars and researchers remain in Ukraine, and their work has suffered from major setbacks (*2–4*). We call on international scientists and institutions to support them.

The global research community has offered research opportunities and



Russian shelling damaged this Kharkiv National University building in March 2022. As Russia's invasion continues, scientists who remain in Ukraine would benefit from international support and remote opportunities.

fellowships to Ukrainian academic faculty and students who were forced to leave the country due to the war (*5*, *6*). Science diplomacy (*7*) has resulted in opportunities like the Polish Academy of Sciences–US National Academy of Sciences Scientists and Engineers in Exile or Displaced (PAS-NAS SEED) initiative, which helps to place Ukrainian researchers in an institute of the Polish academy and supplies grants that provide up to 6 months of support (*8*). The Institute for International Education (IIE) emergency student fund provides financial support to Ukrainian students studying at US colleges and universities (*9*). The Resources to Help Displaced Scholars from Ukraine program mobilizes short-term stipends in support of displaced Ukrainian scholars.

Despite the success of those initiatives, little support has been made available to scientists who have not left the country. Men between the ages of 18 and 60 are not allowed to leave the country under martial law (*10*). Many scholars, both male and female, have volunteered to fight on the front lines. Others have families to take care of and are not willing to leave them behind (*11*).

Supporting the researchers who remain in Ukraine through short-term and long-term opportunities can help the current situation and prevent a potential disconnect with the global research community that could lead to lost opportunity for a generation. Remote opportunities are especially important, but they need to come in tandem with proper training on state-of-the-art skills including coding, data analytics, and scientific writing. Computational data–driven fields are particularly suitable to remote work, but other fields could also participate through collaboration, training, and data sharing. The beneficiaries of these opportunities will be able to increase their international collaborations and research output and facilitate the postwar recovery. Institutions across the world should fund training initiatives for scientists in Ukraine.

Engaging Ukrainian scholars and students in scientific conferences is another remote opportunity. Many conferences are now hosted in a hybrid format, allowing in-person as well as remote attendance (*12*). Organizations that hold scientific conferences could waive fees for scientists located in Ukraine to participate virtually. Scientific societies can also help by waiving the registration fees for Ukrainians, allowing them to participate in international scientific life without leaving the country.

Supporting and engaging Ukrainian scholars remaining in the country could have benefits that span generations. Making remote opportunities available will strengthen the Ukraine's scientific landscape and expedite the postwar reconstruction of the country.

Karishma Chhugani[1], Alina Frolova[2,3], Yuriy Salyha[4], Andrada Fiscutean[5], Oksana Zlenko[6], Sanita Reinsone[7], Walter W. Wolfsberger[8], Oleksandra V. Ivashchenko[9], Megi Maci[10], Dmytro Dziuba[11], Andrii Parkhomenko[12], Eric Bortz[13], Fyodor Kondrashov[14], Paweł P. Łabaj[15], Veronika Romero[16], Jakub Hlávka[17], Taras K. Oleksyk[18,19]*, Serghei Mangul[1,20]

[1]Department of Clinical Pharmacy, University of Southern California Alfred E. Mann School of Pharmacy and Pharmaceutical Sciences, Los Angeles, CA 90089, USA. [2]Institute of Molecular Biology and Genetics of National Academy of Sciences of Ukraine, Kyiv, Ukraine. [3]Kyiv Academic University, Kyiv, Ukraine. [4]Institute of Animal Biology NAAS, 79034 Lviv, Ukraine. [5]Faculty of Journalism and Communication Studies, University of Bucharest, Bucharest, Romania. [6]National Scientific Center, "Institute of Experimental and Clinical Veterinary Medicine," Kharkiv, Ukraine. [7]Institute of Literature, Folklore, and Art, University of Latvia, Riga LV-1004, Latvia. [8]Department of Biological Sciences, Oakland University, Rochester, MI 48309–4479, USA. [9]Medical Imaging Center, University Medical Center Groningen, 9713GZ Groningen, Netherlands. [10]Stritch School of Medicine, Loyola University Chicago, Maywood, IL 60153, USA. [11]Department of Anesthesiology and Intensive Care, P.L. Shupyk National Healthcare University, Kyiv, Ukraine. [12]Department of Finance and Business Economics, Marshall School of Business, University of Southern California, Los Angeles, CA 90089, USA. [13]Department of Biological Sciences, University of Alaska Anchorage, Anchorage, AK 99508, USA. [14]Institute of Science and Technology Austria, 3400 Klosterneuburg, Austria. [15]Małopolska Centre of Biotechnology, Jagiellonian University, Kraków, Poland. [16]Department of Neurobiology, University of Utah, Salt Lake City, UT 84112, USA. [17]Price School of Public Policy, University of Southern California, Los Angeles, CA 90089–3333, USA. [18]Department of Biological Sciences, Oakland University, Rochester, MI 48309–4479, USA. [19]Department of Biology, Uzhhorod National University, 88000 Uzhhorod, Ukraine. [20]Department of Quantitative and Computational Biology, University of Southern California Dornsife College of Letters, Arts, and Sciences, Los Angeles, CA 90089, USA.
*Corresponding author.
Email: oleksyk@oakland.edu

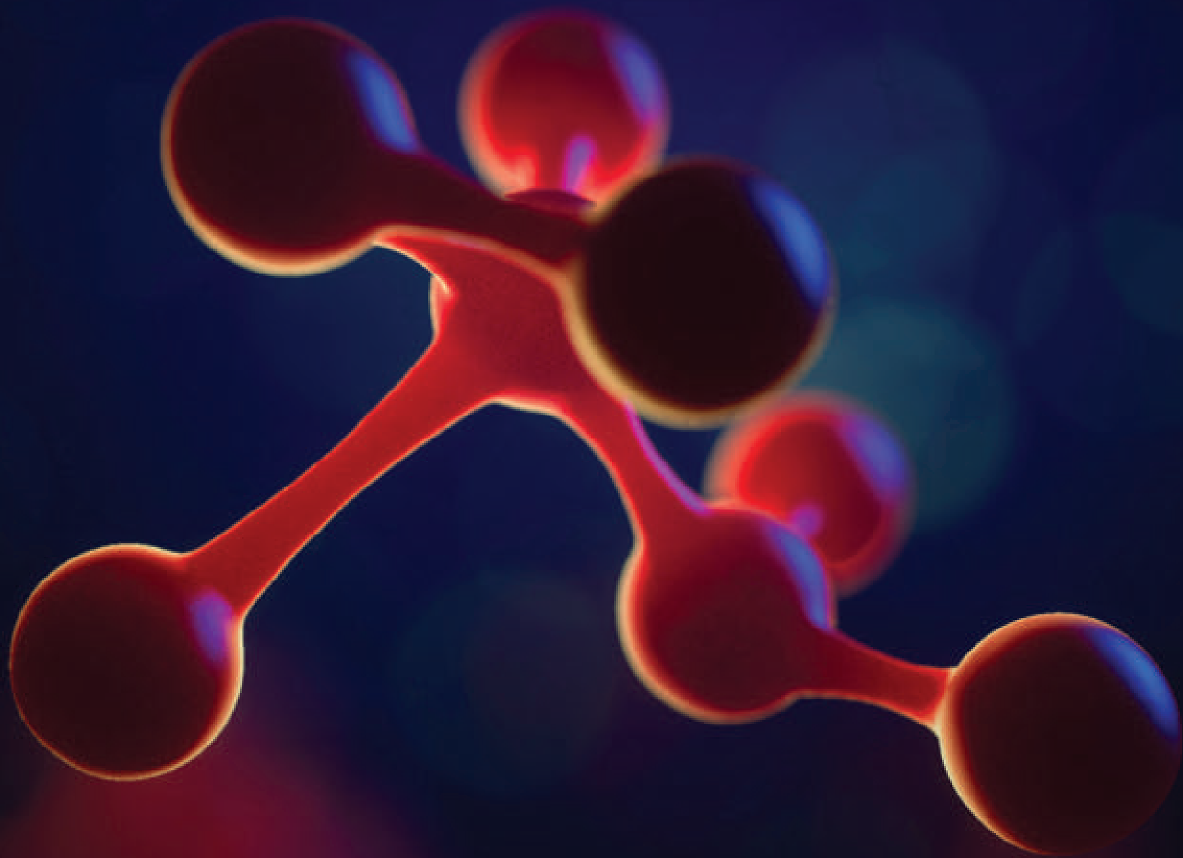
REFERENCES AND NOTES

1. N. Petrić Howe, N. Gaind, R. Van Noorden, "*Nature*'s Take: How the war in Ukraine is impacting science," *Nature* Podcast 10.1038/d41586-022-03155-z (2022).
2. N. Gaind, *Nature* **605**, 414 (2022).
3. M. Maryl *et al.*, *Nat. Hum. Behav*. **6**, 746 (2022).
4. D. Boglaienko, *Science* **377**, 1354 (2022).
5. M. E. Rose *et al.*, "#ScienceForUkraine: an initiative to support the Ukrainian academic community. '3 months since Russia's invasion in Ukraine,' February 26–May 31, 2022" (Max Planck Institute for Innovation and Competition Research Paper No. 22-13, 2022); https://doi.org/10.2139/ssrn.4139263 (2022).
6. *Nature* **609**, 7 (2022).
7. N. V. Fedoroff, *Cell* **136**, 9 (2009).
8. "NAS launches effort to help support Ukrainian researchers as they resettle in Poland," National Academies (2022); https://www.nationalacademies.org/news/2022/03/nas-launches-effort-to-help-support-ukrainian-researchers-as-they-resettle-in-poland.
9. "IIE Statement on the War in Ukraine" (2022); https://www.iie.org:443/Why-IIE/Announcements/2022/02/IIE-Statement-on-Crisis-in-Ukraine.
10. "President signed a decree on the imposition of martial law in Ukraine, the Verkhovna Rada approved it," Official website of the President of Ukraine (2022); https://www.president.gov.ua/en/news/prezident-pidpisav-ukaz-pro-zaprovadzhennya-voyennogo-stanu-73109.
11. R. Stone, *Science* 10.1126/science.adb1726 (2022).
12. J. Wu *et al.*, *Nat. Biotechnol*. **40**, 133 (2022).

10.1126/science.adg0797

PHOTO: OLEKSANDR LAPSHYN/REUTERS IMAGES

Science
JOURNALS AAAS



Publish your research in the *Science* family of journals

The *Science* family of journals (*Science, Science Advances, Science Immunology, Science Robotics, Science Signaling*, and *Science Translational Medicine*) are among the most highly-regarded journals in the world for quality and selectivity. Our peer-reviewed journals are committed to publishing cutting-edge research, incisive scientific commentary, and insights on what's important to the scientific world at the highest standards.

Submit your research today!

Learn more at **Science.org/journals**

AAAS NEWS & NOTES



California oil fields were at the center of one award-winning piece.

AAAS Kavli Science Journalism Award winners named

2022 awards recognized reporting on citizen science, climate change, and more

By **Earl Lane**

Stories exploring the behavior of small animals at the edge of the visible world and others dealing with world-changing forces of climate change are among the winners of the 2022 AAAS Kavli Science Journalism Awards. A trio of stories on aspects of the ongoing COVID-19 pandemic also were honored.

The awards, administered by the American Association for the Advancement of Science (AAAS), recognize distinguished science reporting for a general audience. The program, endowed by The Kavli Foundation and open to journalists worldwide, drew entries from a record 63 countries this year. Winners included journalists in India, China, Australia, South Korea, Germany, and the United Kingdom.

The awards go to individuals rather than institutions, publishers, or employers. There is a Gold Award ($5000) and Silver Award ($3500) for each of the eight categories. Independent panels of science journalists select the winners, who will receive their awards in a virtual ceremony held in conjunction with the 2023 AAAS Annual Meeting in March.

The Deep Look digital video series, created by KQED San Francisco and distributed by PBS Digital Studios, won a Gold Award in the Video Spot News/Feature Reporting category for a close-up look at the activities of tiny creatures such as honeypot ants, water bugs, and acorn barnacles. The Gold Award in the Video In-Depth Reporting category went to a PBS Nature documentary on "My Garden of a Thousand Bees," an exercise in citizen science by British filmmaker and bee enthusiast Martin Dohrn, who spent the pandemic lockdown investigating the behavior of more than 60 species of bees he found in his garden.

Kendra Pierre-Louis won the Gold Award in the Magazine category for a piece in *MIT Technology Review* on how rising groundwater, an overlooked aspect of climate change, could devastate coastal communities. Lois Parshley won a Silver Award in the same category for a piece in Grist, an online magazine, on the impact of climate-driven thawing of permafrost in Alaska.

Pandemic-related winners included a team from Germany's *Süddeutsche Zeitung* that used an online format to show the structure and behavior of the coronavirus at the atomic level; a report for AJ+, an Al Jazeera outlet, on a side effect of COVID-19 that causes the sense of smell to go haywire; and an in-depth piece, also for *MIT Technology Review*, by Beijing-based freelancer Jane Qiu on the scientist at the center of the COVID-19 lab leak controversy. It is the second time Qiu has won the award.

The Gold Award in the Science Reporting – Small Outlet category went to Ankur Paliwal in India for a piece for FiftyTwo, an online outlet, on a rare genetic disease called spinocerebellar ataxia and the work of a small group of scientists and doctors to better understand the disorder. A writer for FiftyTwo won the Gold Award in this category last year as well.

"Congratulations to this year's winners of the AAAS Kavli award," said Sudip Parikh, CEO of AAAS and executive publisher of the *Science* family of journals. "The media universe is diverse and changing, but these winners show a commitment to the best traditions of science journalism that digs below the surface for stories that matter."

CREDIT: LIZA GROSS

The full list of winners of the 2022 AAAS Kavli Science Journalism Awards follows. For a description of the winning entries, with comments from the judges and the winners, go to https://sjawards.aaas.org.

Science Reporting – Large Outlet

Gold Award: Juliet Eilperin and Salwan Georges, *The Washington Post*, This tree has stood here for 500 years. Will it be sold for $17,500? December 30, 2021

Silver Award: Christoph von Eichhorn, Sandra Hartung, Christian Helten, and Sarah Unterhitzenberger, SZ.de (*Süddeutsche Zeitung*, Germany), Anatomy of a killer, January 7, 2022

Science Reporting – Small Outlet

Gold Award: Ankur Paliwal, FiftyTwo (India), Off Balance, April 15, 2022

Silver Award: Liza Gross and Anne Marshall-Chalmers, Inside Climate News, A California Water Board Assures the Public That Oil Wastewater Is Safe for Irrigation, But Experts Say the Evidence Is Scant, February 6, 2022

Science Reporting – In-Depth (more than 5000 words)

Gold Award: Lulu Ramadan, Ash Ngu, Maya Miller, and Nadia Sussman, *The Palm Beach Post* and ProPublica, "Black Snow: Big Sugar's Burning Problem" — thematic series
The Smoke Comes Every Year. Sugar Companies Say the Air Is Safe. July 8, 2021
"A Complete Failure of the State": Authorities Didn't Heed Researchers' Calls to Study Health Effects of Burning Sugar Cane, August 19, 2021
Burning Sugar Cane Pollutes Communities of Color in Florida; Brazil Shows There's Another Way. December 29, 2021

Silver Award: Jane Qiu, *MIT Technology Review,* Meet the scientist at the center of the covid lab leak controversy, February 9, 2022

Audio

Gold Award: Arielle Duhaime-Ross, Julia Nutter, Pran Bandi, Annie Avilés, and Pete Lang-Stanton, VICE News — A Show About Animals
A Talking Gorilla, November 3, 2021
A Gorilla Who Lied, November 10, 2021
Uptown Chimp, November 17, 2021

Silver Award: Ann Jones, Petria Ladgrove, Joel Werner, and Jo Khan, ABC Science (Australian Broadcasting Corporation), Does It Fart?, July 1, 2022

Magazine

Gold Award: Kendra Pierre-Louis, *MIT Technology Review,* How rising groundwater caused by climate change could devastate coastal communities, Dec. 13, 2021

Silver Award: Lois Parshley, Grist, Don't Look Down – As permafrost thaws, the ground beneath Alaska is collapsing. April 20, 2022

Video Spot News/Feature Reporting (20 minutes or less)

Gold Award: Josh Cassidy, Gabriela Quirós, Lesley McClurg, Elyse DeFranco, Teodros Hailye, Kia Simon, and Seth Samuel; KQED and PBS Digital Studios,
Deep Look: Honeypot Ants Turn Their Biggest Sisters into Jugs of Nectar, April 5, 2022
Deep Look: Barnacles Go To Unbelievable Lengths To Hook Up, April 26, 2022
Deep Look: Don't Go Chasing Water Bugs, June 28, 2022

Silver Award: Yara Elmjouie, Adrienne Blaine, Shadi Rahimi, Matias Sesti, and Michael Bendeck, AJ+ (Al Jazeera Media Network), The bizarre COVID side effect no one is talking about, August 7, 2021

Video In-Depth Reporting (more than 20 minutes)

Gold Award: David Allen, Martin Dohrn, Gaby Bastyra, David Guy Elisco, Sean B. Carroll, and Fred Kaufman, PBS Nature, My Garden of a Thousand Bees, October 20, 2021

Silver Award: Bella Falk and David Dugan, A NOVA Production by Windfall Films, Ltd. (part of the Argonon Group) for GBH, Ice Age Footprints, May 25, 2022

Children's Science News

Gold Award: Sarah Zielinski, Maria Temming, and JoAnna Wendel, *Science News Explores*
Cockatoos learn from each other how to open garbage bins, October 26, 2021
A panda stands out at the zoo but blends in the wild, December 15, 2021
Goldfish driving 'cars' offer new insight into navigation, February 16, 2022

Silver Award: Dasol Lee, *Kids Donga Science* (South Korea)
On a journey to finding a happy zoo, November 15, 2021
Home for lost animals, Sanctuary, December 1, 2021

NEWS FROM Science
AAAS

Subscribe to **News from Science** for unlimited access to authoritative, up-to-the-minute news on research and science policy.

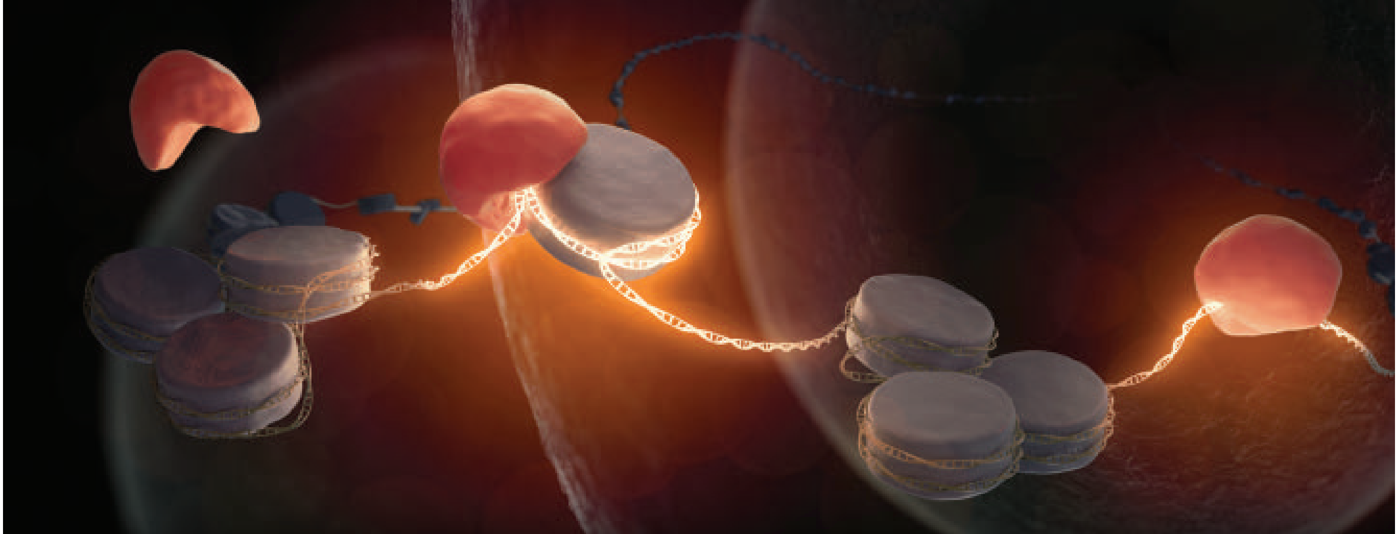


bit.ly/NewsFromScience

RESEARCH

IN *SCIENCE* JOURNALS

Edited by
Michael Funk



DEVELOPMENT

Switching on the genome in mouse embryos

Life begins with a transcriptionally silent embryo that initially relies on maternal RNAs and proteins. To enable subsequent development, the genome of totipotent embryos is transcriptionally "awakened." Despite the importance of this process, the essential transcription factors that trigger zygotic genome activation (ZGA) remain largely unidentified in mammals. Gassler *et al.* discovered that Nr5a2 and potentially related orphan nuclear receptors activate transcription of most ZGA genes in mouse embryos. Nr5a2 binds to retrotransposable elements of the *short interspersed nuclear element B1* family that are upstream of ZGA genes. Developmental, genomics, and biochemical data support a model in which ZGA is triggered by Nr5a2 pioneering activity to open chromatin. —DJ and BAP

Science, abn7478, this issue p. 1305

Artist's illustration of the process of transcriptional "awakening" that occurs in early embryos

QUANTUM SENSING

Covariance magnetometry

Color defect centers in diamond, such as the nitrogen vacancy center effect, behave as miniature compass needles. Their optical signature is sensitive to local magnetic fields with nanoscale resolution. To date, these sensing modalities have been largely limited to detecting static magnetic fields or sensing an ensemble average, providing access to dynamical behavior only indirectly. Rovny *et al*. developed a theoretical framework and demonstrate a new sensing modality for detecting spatiotemporal correlations from simultaneous measurements of two nitrogen vacancy defect centers in diamond. Covariance measurements open a window for sensing spatiotemporal dynamics through nanoscale magnetometry. —ISO

Science, ade9858, this issue p. 1301

NEUROSCIENCE

Motor cortex modulates pain perception

The main function of the primary motor cortex is to initiate movements and to control voluntary motor behavior. Unexpectedly, the perception of pain also evokes motor cortical responses. However, very little is known about the neurobiological basis for this unconventional role of the motor cortex in modulating pain perception. Gan *et al*. investigated the neuronal pathways and mechanisms involved in the modulation of sensory and affective components of pain after selective stimulation of the mouse motor cortex. Extensive viral tracing and mouse genetics, combined with chemo- and optogenetic approaches, revealed that although activation of layer 5 neurons reversed allodynia in neuropathic mice, the specific activation of neurons in layer 6 of the primary motor cortex reduced the aversive component of pain. —PRS

Science, add4391, this issue p. 1336

ORGANIC CHEMISTRY

Ketenes from ylides

Most chemical reactions that build complex molecules from carbon monoxide rely on transition metal catalysis. Jörges *et al*. found that carbon monoxide also reacts cleanly with potassium ylides by phosphine displacement. The

IMAGE: © MPIB

resulting negatively charged ketenyl compounds could be isolated and crystallographically characterized, manifesting a bent structure poised for downstream reactivity at the carbon rather than oxygen site. This behavior was borne out in a variety of reactions of the anions with electrophiles to produce ketenes and their derivatives. —JSY

Science, ade4563, this issue p. 1331

RSV VACCINE

Function follows form

Respiratory syncytial virus (RSV) can cause severe infection in infants and older adults, but no vaccine for RSV is currently approved. Candidate vaccines that target the RSV fusion (F) protein have been developed. Older vaccines use the postfusion, or Post-F, version of the protein, whereas newer vaccines use a prefusion-stabilized, or Pre-F, immunogen. Chang *et al*. directly compared immune responses elicited by a Post-F vaccine, MEDI7510, and a Pre-F vaccine, DS-Cav1. The authors found that DS-Cav1 elicited antibodies that more potently neutralized RSV A and B than MEDI7510 did. This enhanced response was mediated by the presence of antibodies that could bind sites on the F protein and were only present in the Pre-F state. These data highlight the value of structure-based vaccine design. —CSM

Sci. Transl. Med. **14**, eade0424 (2022).

CELL DEATH

PANX1 pulls the trigger on pyroptosis

Instead of apoptosis, chemotherapy can induce pyroptosis, a form of lytic cell death that can trigger antitumor immune responses through the pore-forming protein gasdermin E. Zhou *et al*. found alternate pathways to chemotherapy-induced pyroptosis mediated by the channel PANX-1. PANX-1 mediated pyroptosis either through a gasdermin D–dependent pathway or independently of gasdermins. In blood and bone marrow biopsies from leukemia patients, the relative levels of gasdermin E, gasdermin D, and PANX-1 predicted the pathway that mediated doxorubicin-induced pyroptotic cell death. —LKF

Sci. Signal. **15**, eabl6781 (2022).

SOLAR CELLS

Rapid quenching maintains the mix

Tandem perovskite solar cells require stable, efficient wide-bandgap perovskites with mixed bromide and iodide anions, but these anions are prone to segregation during crystallization that can then limit the device voltage and operational stability. Jiang *et al*. determined that a gentle gas-quench method produced a bromine-rich surface layer, and that subsequent columnar growth created films with reduced defect density. Solar cells based on these films maintained 90% of their efficiency at 65°C for more than 2200 hours. All-perovskite tandem cells exhibited 27.1% efficiency resulting from a high open-circuit voltage of 2.2 volts. —PDS

Science, adf0194, this issue p. 1295

3D PRINTING

Making many tiny things

Fabricating high-resolution and complex objects with additive manufacturing across a wide range of materials is challenging. Han *et al*. synthesized very finely detailed objects from a wide range of materials using femtosecond light sheets and nanoparticle-laden hydrogels. The strategy works for ceramics, polymers, metals, semiconductors, and other materials while still maintaining fine feature sizes. This technique could enable nanofabrication across different classes of materials. —BG

Science, abm8420, this issue p. 1325

IN OTHER JOURNALS

Edited by **Caroline Ash** *and* **Jesse Smith**



The anatomy of the voice box of the Daubenton's bat (*Myotis daubentonii*) allows it to have a seven-octave vocal range.

PHOTO: HUGH CLARK/FLPA/SCIENCE SOURCE

ANATOMY

A versatile singer

Dolphins and bats find locations of objects by reflected sound. Bats produce very diverse sound signals for echolocation that span seven octaves. For comparison, most humans can claim only four octaves. To understand the extraordinary vocal range of bats, Håkansson *et al.* excised voice boxes from Daubenton's bats and applied airflow to them to mimic breathing. Ultra-high-speed video recording of the vibrations showed that the different parts of the vocal box produce different ranges of sounds. The vocal membrane generates 10- to 70-kHz high frequencies for echolocation and social calls, whereas the ventricular folds produce 1- to 5-kHz low frequencies—lower than the most talented human bass singer. —DJ

PLOS Biol. 10.1371/journal.pbio.3001881 (2022).

NEUROSCIENCE

From perception to categorization

How does the brain transform the encoding of visual features into abstract categorical representations? We already know that the middle temporal (MT) area shows strong directional encoding but not abstract categorical encoding. By contrast, the lateral intraparietal (LIP) area plays a causal role in categorical decisions about visual motion stimuli. Recording neural activity from monkeys, Zhou *et al.* directly compared the

roles of the LIP and the media superior temporal (MST) area, a motion-processing region that is reciprocally connected with both the LIP and the MT in visual motion categorization. MST neurons showed significant motion category encoding during presentation of a stimulus and memory delay periods. These results indicate that the MST area encodes abstract task-related factors such as categorical decisions and working memory, going beyond its traditionally recognized role in visual motion processing. —PRS

J. Neurosci. **42**, 9069 (2022).



SCIENTIFIC WORKFORCE

Choose your supervisor—and peers—wisely

As the academic job market continues to tighten, research into what constitutes a "quality" graduate education continues. Corsini *et al.* analyzed data from 77,143 doctoral students in STEM who graduated from French institutions to investigate how the characteristics of supervisors and peers influenced their publication quantity, quality, and co-author network. Three findings stand out: (i) a female supervisor is associated with a higher number of citations and a larger collaboration network, (ii) a supervisor's mentorship experience is negatively associated with the student's productivity, and (iii) having productive freshman peers or at least one female peer is positively associated with the student's productivity. Collectively, these results can inspire students to leverage supervisor and peer factors and directors of doctoral programs to find new levers for designing policies that benefit students. —MMc *Res. Policy* **51**, 104561 (2022).

BRAIN CIRCUITS

Exciting withdrawal

Withdrawal from chronic alcohol consumption alters neuronal circuits involved in the regulation of fear and anxiety in rats. Sizer *et al.* used a rat model of alcohol withdrawal and showed enhanced glutamate release from neurons in the basolateral amygdala (BLA) as a result of strengthening of cholinergic transmission between the nucleus basalis magnocellularis (NBM) and the BLA. The results suggest that alterations in the NBM-BLA circuit might contribute to the behavioral changes associated with alcohol withdrawal. —MM

eNeuro 10.1523/ENEURO.0164-22.2022 (2022).

NANOMATERIALS

Potentially changing nanoparticle sizes

The interaction of metal nanoparticles with their metal oxide supports can dictate their stability at the high temperatures needed for many catalytic reactions. Kim *et al*. controlled the size and stability of gold nanoparticles on metal oxides by electrochemically tuning the formation of oxygen ion vacancies. For mixed ionic-electronic conducting oxides such as $La_{0.8}Ca_{0.2}MnO_{3\pm\delta}$ and $Pr_{0.1}Ce_{0.9}O_{2-\delta}$, applying a cathodic potential created high concentrations of oxygen vacancies. Small gold nanoparticles (7 to 13 nanometers) formed that were stable up to 770°C as long as the potential remained applied. Switching to anodic potentials oxidized the surface and drove the formation of larger nanoparticles. —PDS

J. Am. Chem. Soc. **144**, 21926 (2022).

MANUFACTURING

Mass-producing complex patterned surfaces

The roll-to-roll technique allows for the processing of large sheets of material in a compact space and can include steps for patterning, printing, or coating onto the substrate sheet. A challenge in the use of flexible molds is that they typically degrade in just tens of cycles, causing a loss of fidelity in the transferred patterns. Kim *et al.* describe a two-step curing process that does not necessitate a change in the chemistry of the resins, so it can overcome this limitation. They used silicone-based materials for the molds because these permit the permeation of oxygen, and show that this slows down the curing at the mold interface. As the substrate is removed from the mold, there is less adhesion and abrasion, thus minimizing damage between the mold and the printed substrate, which is then fully cured in a second step. —MSL

Adv. Mater. 10.1002/adma.202207257 (2022).

LIFE HISTORY

Legacy of stress

Research on telomere length has found that a mother's exposure to stress is associated with accelerated cellular aging of the child. However, the timing of the mother's stressors, the type of stressors, and the impact of the mother's race are often neglected in studies. Using a sample of the youngest child of Black and white mothers, Mayer *et al.* measured telomere length from saliva samples. They also measured mothers' self-reported stressors (including financial and social) at three stages: during adolescence, during pregnancy, and across their life span. Only financial stress (e.g., job loss or difficulty paying bills) during pregnancy significantly predicted shorter telomere length in the children of white mothers but not Black mothers. More research is needed to understand these results because shorter telomere length is associated with earlier death and earlier onset of diabetes and heart disease. —EEU

Psychol. Med. 10.1017/S0033291722003397 (2022).

ILLUSTRATION: ROBERT NEUBECKER

ALSO IN *SCIENCE* JOURNALS

Edited by **Michael Funk**

CANCER

Rethinking DNA methylation

Cells that undergo many division cycles, such as cancer cells, exhibit a "mitotic clock" in which DNA methylation is progressively lost with each division. This leads to large regions of DNA hypomethylation in cancer cells, as well as in aged cells. In a Perspective, Johnstone *et al.* discuss how considering this progressive hypomethylation as a mitotic clock affects how we think about aging and cancer. This framework allows for inactivation of aged cells and represents a hurdle that is overcome in the progression to malignancy. Further understanding of the mitotic clock could be informative for predicting risk of disease progression and may reveal vulnerabilities that could be targeted therapeutically. —GKA

Science, abn4009, this issue p. 1276

NEURODEVELOPMENT

Generating neuronal diversity

Neurons in the brain seem to come in a dizzying array of diversity. Özel *et al*. found that the identities of nearly 200 different neurons in *Drosophila* fruit flies are set from a combinatorial code of only about 10 transcription factors. Modified expression of certain transcription factors drives predictable changes on neuronal cell fates, and these transcription factors intersect with hormone signaling to control brain wiring. —PJH

Science, add1884, this issue p. 1293

NEUROSCIENCE

A framework for associative learning

How do animals learn to associate environmental cues with delayed outcomes such as rewards? Temporal difference reinforcement learning (TDRL) is the most widely accepted model of reward learning. Jeong *et al*. now challenge this view by introducing a formal account and model of dopamine's role in learning. They present an algorithm that supports retrospective causal learning, allowing animals to infer the causes of an event. To directly compare the two competing hypotheses, the authors devised eight experimental tests. In each of the eight tests in every animal tested, they challenge the TDRL signaling model and show that every observation is consistent with their causal inference algorithm. These findings provide a fresh physiological and theoretical framework for associative learning in the brain. —PRS

Science, abq6740, this issue p. 1294

CALORICS

Ionic cooling

Solid- or liquid-state cooling strategies often rely on caloric effects in which materials are taken through some sort of phase change. Lilley and Prasher found that ions in solution can be used to control the melting and crystallization of a material, creating what the authors refer to as an ionocaloric cycle (see the Perspective by Defay). This cycle could drive refrigeration that is competitive with other caloric cooling strategies. —BG

Science, ade1696, this issue p. 1344; see also adf5114, p. 1275

BATTERIES

High entropy by design

A key property for solid-state battery electrolytes is the ability to rapidly transport lithium ions. This property can be achieved by developing a percolating pathway or by increasing the mobility of the carrier ions in the electrolyte. However, standard design methods limit the selection of dopants and complicate the synthesis. Zeng *et al*. adapted some of the concepts of high-entropy materials to the development of solid electrolytes (see the Perspective by Botros and Janek). The addition of a mixture of high-entropy metal cations induces local disorder, thus creating overlapping site energy distributions for charge-carrying ions. This approach results in a percolating network of connected sites with a reduced energy difference and correspondingly fast lithium ion transport, as demonstrated for lithium- and sodium-based batteries. —MSL

Science, abq1346, this issue p. 1320; see also adf3383, p. 1273

PHYSIOLOGY

Hiding in plain sight

Transparency provides a form of camouflage that is particularly useful for increasing crypsis in motionless animals. Many taxa have evolved transparency, but it is particularly challenging for vertebrates because red blood cells attenuate light. Taboada *et al*. found that glass frogs are able to maintain a high level of transparency because a large proportion of their red blood cells are "hidden" in the liver (see the Perspective by Cruz and White). This strategy allows the frogs to attain transparency when they are the most vulnerable. Understanding this liver-packing process may inform our understanding of hemodynamics more broadly. —SNV

Science, abl6620, this issue p. 1315; see also adf7524, p. 1272

CYTOKINES

IL-37, proinflammatory after all

Interleukin-37 (IL-37), like other members of the extended IL-1 family, contains an N-terminal prodomain that requires proteolytic cleavage for its activity. Although the full activity of IL-37 remains unknown, prior work has demonstrated that IL-37 cleaved by caspase-1 can suppress inflammatory cytokine production. Sullivan *et al.* show that IL-37 can also be cleaved by neutrophil elastase and cathepsin S, generating an active form that stimulates robust proinflammatory cytokine production in human keratinocytes. IL-37 truncated at the cathepsin S cleavage site induced a similar proinflammatory response in the murine peritoneal cavity and required the IL-36 receptor, identifying IL-37 as a putative ligand. These results show that when cleaved at specific sites, IL-37 can also stimulate proinflammatory responses consistent with other IL-1 family member proteins. —CO

Sci. Immunol. **7**, eade5728 (2022).


science.org/journal/stm
PUT HUMAN HEALTH AT THE HEART OF YOUR RESEARCH
Submit your research:
cts.ScienceMag.org
Science Translational Medicine
AAAS
Twitter: @ScienceTM
Facebook: @ScienceTranslationalMedicine

RESEARCH ARTICLE SUMMARY

NEURODEVELOPMENT

Coordinated control of neuronal differentiation and wiring by sustained transcription factors

Mehmet Neset Özel*, Claudia Skok Gibbs, Isabel Holguera, Mennah Soliman, Richard Bonneau*, Claude Desplan*

INTRODUCTION: Neurons are by far the most diverse of all cell types in animals, to the extent that "cell types" in mammalian brains are still mostly heterogeneous groups, and there is no consensus definition of the term. The *Drosophila* optic lobes, with approximately 200 well-defined cell types, provides a tractable system with which to address the genetic basis of neuronal type diversity. We previously characterized the distinct developmental gene expression program of each of these types using single-cell RNA sequencing (scRNA-seq), with one-to-one correspondence to the known morphological types.

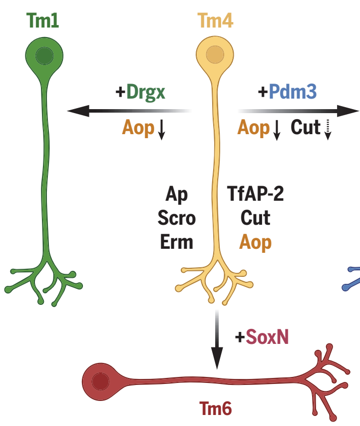
RATIONALE: The identity of fly neurons is determined by temporal and spatial patterning mechanisms in stem cell progenitors, but it remained unclear how these cell fate decisions are implemented and maintained in postmitotic neurons. It was proposed in *Caenorhabditis elegans* that unique combinations of terminal selector transcription factors (TFs) that are continuously expressed in each neuron control nearly all of its type-specific gene expression. This model implies that it should be possible to engineer predictable and complete switches of identity between different neurons just by modifying these sustained TFs. We aimed to test this prediction in the *Drosophila* visual system.

RESULTS: Here, we used our developmental scRNA-seq atlases to identify the potential terminal selector genes in all optic lobe neurons. We found unique combinations of, on average, 10 differentially expressed and stably maintained (across all stages of development) TFs in each neuron. Through genetic gain- and loss-of-function experiments in postmitotic neurons, we showed that modifications of these selector codes are sufficient to induce predictable switches of identity between various cell types. Combinations of terminal selectors jointly control both developmental (e.g., morphology) and functional (e.g., neurotransmitters and their receptors) features of neurons.

The closely related Transmedullary 1 (Tm1), Tm2, Tm4, and Tm6 neurons (see the figure) share a similar code of terminal selectors, but can be distinguished from each other by three TFs that are continuously and specifically expressed in one of these cell types: Drgx in Tm1, Pdm3 in Tm2, and SoxN in Tm6. We showed that the removal of each of these selectors in these cell types reprograms them to the default Tm4 fate. We validated these conversions using both morphological features and molecular markers. In addition, we performed scRNA-seq to show that ectopic expression of *pdm3* in Tm4 and Tm6 neurons converts them to neurons with transcriptomes that are nearly indistinguishable from that of wild-type Tm2 neurons. We also show that Drgx expression in Tm1 neurons is regulated by Klumpfuss, a TF expressed in stem cells that instructs this fate in progenitors, establishing a link between the regulatory programs that specify neuronal fates and those that implement them. We identified an intronic enhancer in the *Drgx* locus whose chromatin is specifically accessible in Tm1 neurons and in which Klu motifs are enriched. Genomic deletion of this region knocked down *Drgx* expression specifically in Tm1 neurons, leaving it intact in the other cell types that normally express it. We further validated this concept by demonstrating that ectopic expression of Vsx (visual system homeobox) genes in Mi15 neurons not only converts them morphologically to Dm2 neurons, but also leads to the loss of their aminergic identity.

Our results suggest that selector combinations can be further sculpted by receptor tyrosine kinase signaling after neurogenesis, providing a potential mechanism for postmitotic plasticity of neuronal fates. Finally, we combined our transcriptomic datasets with previously generated chromatin accessibility datasets to understand the mechanisms that control brain wiring downstream of terminal selectors. We built predictive computational models of gene regulatory networks using the Inferelator framework. Experimental validations of these networks revealed how selectors interact with ecdysone-responsive TFs to activate a large and specific repertoire of cell surface proteins and other effectors in each neuron at the onset of synapse formation. We showed that these network models can be used to identify downstream effectors that mediate specific cellular decisions during circuit formation. For instance, reduced levels of *cut* expression in Tm2 neurons, because of its negative regulation by *pdm3*, controls the synaptic layer targeting of their axons. Knockdown of *cut* in Tm1 neurons is sufficient to redirect their axons to the Tm2 layer in the lobula neuropil without affecting other morphological features.

CONCLUSION: Our results support a model in which neuronal type identity is primarily determined by a relatively simple code of continuously expressed terminal selector TFs in each cell type throughout development. Our results provide a unified framework of how specific fates are initiated and maintained in postmitotic neurons and open new avenues to understanding synaptic specificity through gene regulatory networks. The conservation of this regulatory logic in both *C. elegans* and *Drosophila* makes it likely that the terminal selector concept will also be useful in understanding and manipulating the neuronal diversity of mammalian brains. ■



Terminal selectors enable predictive cell fate reprogramming. Tm1, Tm2, Tm4, and Tm6 neurons of the *Drosophila* visual system share a core set of TFs continuously expressed by each cell type (simplified). The default Tm4 fate is overridden by the expression of a single additional terminal selector to generate Tm1 (*Drgx*), Tm2 (*pdm3*), or Tm6 (*SoxN*) fates.

The list of author affiliations is available in the full article online.
*Corresponding author. Email: no24@nyu.edu (M.N.Ö.); rb133@nyu.edu (R.B.); cd38@nyu.edu (C.D.)
Cite this article as M. N. Özel *et al.*, *Science* **378**, eadd1884 (2022). DOI: 10.1126/science.add1884

READ THE FULL ARTICLE AT
https://doi.org/10.1126/science.add1884

RESEARCH ARTICLE

NEURODEVELOPMENT

Coordinated control of neuronal differentiation and wiring by sustained transcription factors

Mehmet Neset Özel[1]*, Claudia Skok Gibbs[2,3], Isabel Holguera[1], Mennah Soliman[1], Richard Bonneau[1,2,3]*, Claude Desplan[1,4]*

The large diversity of cell types in nervous systems presents a challenge in identifying the genetic mechanisms that encode it. Here, we report that nearly 200 distinct neurons in the *Drosophila* visual system can each be defined by unique combinations of on average 10 continuously expressed transcription factors. We show that targeted modifications of this terminal selector code induce predictable conversions of neuronal fates that appear morphologically and transcriptionally complete. Cis-regulatory analysis of open chromatin links one of these genes to an upstream patterning factor that specifies neuronal fates in stem cells. Experimentally validated network models describe the synergistic regulation of downstream effectors by terminal selectors and ecdysone signaling during brain wiring. Our results provide a generalizable framework of how specific fates are implemented in postmitotic neurons.

Neurons are by far the most diverse of all cell types in animals. Understanding the molecular mechanisms that produce this diversity is a central goal of neurobiology. The *Drosophila* brain provides a tractable system to approach this challenge because of its manageable size and genetically hardwired development. The optic lobes constitute two-thirds of the fly brain, and each of their neuropils—the lamina, medulla, lobula, and lobula plate (Fig. 1A)—is divided into ~800 columns, corresponding to the same number of ommatidia (unit eyes) in the retina. Because of this retinotopic organization with multiple repeats of the same circuits, most neuronal types are present in high numbers of cells per brain. We previously completed a large single-cell RNA sequencing (scRNA-seq) atlas of the optic lobes, resolving ~200 cell types that we consistently tracked across six time points from the early pupal stages to adult (*1*). Almost all annotated clusters in this atlas corresponded to a distinct neuronal type with unique morphology (*2*). This strongly suggests that most of our clusters represent biologically homogeneous groups, giving us access to the cell-type-specific transcriptome of every neuron throughout its development.

The identity of optic lobe neurons is specified deterministically by their progenitors during neurogenesis, which occurs from late larval stages (L3) until ~20% of pupal development (P20) (*3*). Neurons from the medulla neuropil are produced from a neuroepithelium called the outer proliferation center, which is progressively converted into neuroblasts that asymmetrically divide multiple times, each time self-renewing and producing an intermediate progenitor that divides once to generate two different neurons (*4*). Neurons are diversified by the intersection of three patterning mechanisms: (i) compartmentalization of the neuroepithelium into at least eight spatial regions by transcription factors (TFs) and signaling molecules (*5*), (ii) sequential expression of at least 11 temporal TFs (tTFs) in neuroblasts (*6*), and (iii) Notch signaling between sister neurons (*7*). Similar patterning mechanisms are also used in other parts of the fly brain, as well as mammalian neural stem cells to generate diversity [reviewed in (*8*)]. However, most spatial and tTFs are not maintained in neurons (*6*), so it is not clear how these cell fate decisions are implemented and maintained in postmitotic neurons.

Much of our knowledge about neuronal identity control originates from *Caenorhabditis elegans*. The terminal selector hypothesis (*9*) posits that type-specific gene expression in neurons is controlled by combinations of TFs that are continuously maintained in each neuron throughout its life. Terminal selectors control both developmental features such as synaptic connectivity (*10*) and functional features such as neurotransmitter identity (*11*), but they are largely not required for pan-neuronal gene expression programs (*12*). This model also implies that individual selectors do not specialize in distinct phenotypic features of a neuron. Although a few TFs that could function as terminal selectors have been identified in mammalian neurons (*13*–*15*), it remains unclear how generally applicable this regulatory logic is beyond the relatively simple nervous system of worms. Moreover, the ultimate test of this model, i.e., the predictive and complete transformation of one neuronal type into another through targeted modification of its selector code, has been difficult to assess, even in *C. elegans* (*16*).

Results

Terminal selectors of optic lobe neurons

To determine whether a sustained code of TFs maintains the identity of each neuron throughout development, we sought to identify the combinations of candidate terminal selectors expressed in each of the 174 neuronal clusters in our scRNA-seq atlas (*1*). We determined the sets of TFs continuously expressed in each cluster throughout all six stages of development (P15 to adult), excluding those expressed in all clusters (pan-neuronal or ubiquitous genes; see the materials and methods). We found, on average, unique combinations of 10 such genes per cluster, representing 95 TFs in total (fig. S1A and table S1); 72 of these TFs were expressed in fewer than 25 clusters (fig. S1B). Homeobox genes were enriched in this list (fig. S1C), but unlike in the *C. elegans* nervous system (*17*), they were not sufficient to uniquely define every neuron. Furthermore, whereas the selectors could delineate developmentally related lineages, e.g., from lamina or the inner proliferation center (fig. S2A), homeobox genes alone could not (fig. S2B).

The terminal selector hypothesis predicts that if continuously maintained TFs are primarily responsible for cell-type-specific neuronal differentiation, then it should be possible to engineer complete switches of identity between different neurons by modifying these TFs alone. All genes that were previously reported to interfere with neuronal type identity in the optic lobe, including *bsh*, *hth*, *drifter* (*vvl*), *Lim1*, *erm*, *SoxN*, and *Sox102F* (*18*–*22*), were indeed candidate selectors for the respective neurons (fig. S1A). However, these studies generally reported disruptions rather than switches of morphological identity; for example, loss of *hth*/*bsh* in Mi1 results in an incomplete conversion to "Tm1-like" neurons (*19*), likely because Tm1 differs from Mi1 by the expression of the additional selectors *Drgx* and *TfAP-2*. It remains challenging to simultaneously perturb more than one or two genes at once using classical genetic methods. To provide definitive evidence for the sufficiency of terminal selectors in determining neuronal type identity, we looked for groups of closely related neurons with selector codes that differed only by one or two genes, in which complete conversions from one cell type to another may be feasible.

Transmedullary (Tm) neurons 1, 2, and 4 and an unidentified cluster (#62) have nearly indistinguishable transcriptomes shortly after their terminal division at P15 (*1*), suggesting a

[1]Department of Biology, New York University, New York, NY 10003, USA. [2]Flatiron Institute, Center for Computational Biology, Simons Foundation, New York, NY 10010, USA. [3]Center for Data Science, New York University, New York, NY 10003, USA. [4]New York University Abu Dhabi, Saadiyat Island, Abu Dhabi, United Arab Emirates.
*Corresponding author. Email: no24@nyu.edu (M.N.Ö.); rb133@nyu.edu (R.B.); cd38@nyu.edu (C.D.)

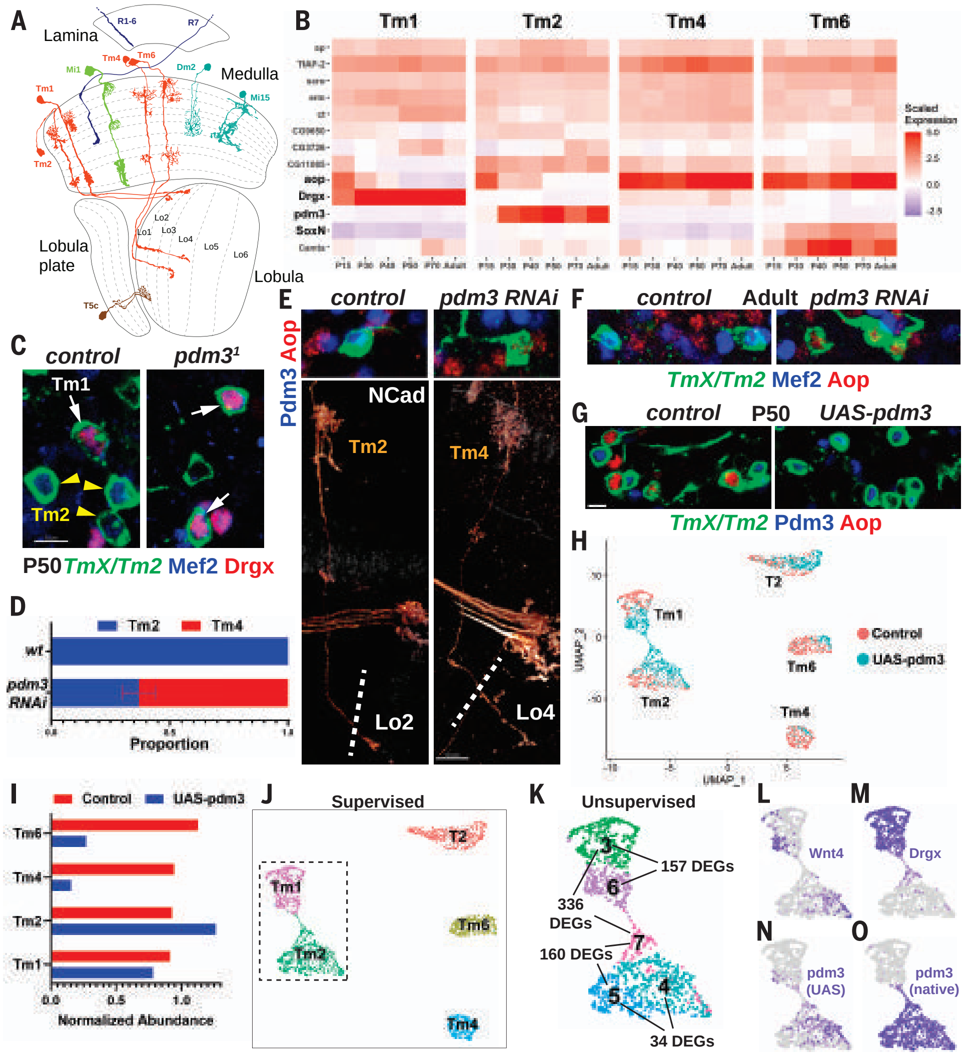


Fig. 1. *Pdm3* instructs complete switches of neuronal fates. (**A**) *D. melanogaster* optic lobe in cross section, with drawings of select cell types. Image was adapted in part from (*2*). (**B**) Developmental (scaled) expression patterns (*1*) of all genes that are candidate selectors in any of the displayed cell types. (**C**) FRT40A and *pdm3*[1] MARCM clones labeled with *TmX/Tm2-Gal4* and CD4-tdGFP in P50 brains (maximum projection), with anti-Mef2 shown in blue and anti-Drgx in red. *n* = 8 control and *n* = 4 mutant brains. (**D** to **F**) *TmX/Tm2-Gal4* driving *pdm3* RNAi and CD4-tdGFP (flip-out). (D) Quantification of (E) and (F). *n* = 54/6 control and *n* = 96/8 RNAi neurons/brains, *P* < 0.0001. Error bar indicates SEM. (E) Three-dimensional (3D) reconstructions of GFP (bottom) or maximum projections (top) for the same representative adult neurons in each condition, with anti-NCad shown in white, anti-Pdm3 in blue, and anti-Aop in red. The dashed lines indicate the border of the lobula neuropil based on NCad staining. (F) Same as (E), top, but with anti-Mef2 instead of Pdm3. (**G**) *TmX/Tm2-Gal4* driving *UAS-pdm3* and CD4-tdGFP (flip-out). Maximum projections of somas in P50 medulla cortex, with anti-Pdm3 shown in blue and anti-Aop shown in red. *n* = 129 control and *n* = 118 pdm3 neurons. Scale bars: (C) and (E), top, (F), and (G), 5 μm; (E), bottom, 10 μm. (**H** to **O**) scRNA-seq of FACSed neurons [same experiment as in (G)]. UMAP visualizations were calculated using top six principal components (PCs). Cells are colored according to library (condition) of origin (H), supervised classifications (J), unsupervised clustering [(K) inset only, see also fig. S4A], and the log-normalized expression of indicated genes [(L) to (O)]. (I) Numbers of Tm neurons in each library divided by the numbers of T2 neurons.

very close developmental relationship. We annotated cluster 62 as being composed of Tm6 neurons on the basis of its expression of the unique combination of *aop*, *SoxN*, and *Wnt10* (fig. S3, A to C). Although these Tms share similar overall morphology, adult neurons are readily distinguishable from one another by their distinct dendritic shapes, as well as the different target layers of their axons in the lobula (Fig. 1A). Analysis of candidate selector expression in these clusters across development (Fig. 1B) revealed that the four neurons indeed share a similar code: *ap*, *TfAP-2*, *scro*, *erm*, and *ct* are continuously expressed in all four clusters. *CG9650*, *CG3726*, *CG11085*, and *aop* could also be found in all four Tm neurons at some point during development, although they were only transiently expressed in some of them. *Camta* is expressed at much higher levels in Tm6 but is also detected in the others. Among these four neurons, *Drgx* is specific to Tm1, *pdm3* to Tm2, and *SoxN* to Tm6, whereas there are no candidate selectors exclusive to Tm4. Therefore, these TFs that are each continuously and specifically expressed in one of these types are strong candidates to differentially specify their fates.

Pdm3 instructs transcriptionally complete neuronal fate conversions

Because *pdm3* is the only TF that continuously distinguishes Tm2 from Tm4 (Fig. 1B), the terminal selector code predicts that its loss should reprogram Tm2 neurons to Tm4 fate. *R71F05-Gal4* is expressed in all four Tm neurons (1, 2, 4, and 6) until P50; however, it is only maintained in Tm2 in adults (fig. S3D, *TmX/Tm2-Gal4*). Using this driver, we generated MARCM (*23*) clones of a *pdm3*-null allele (*24*). No mutant Tm neurons were recovered in adult brains, suggesting that Tm2 were not specified properly (fig. S3E). *Mef2* is an effector (downstream) TF that is normally expressed specifically in both Tm1 and Tm2 after P40 (Fig. 1C and fig. S7J). At P50, we observed that the only remaining Mef2[+] Tm neurons in *pdm3*[1] clones were Tm1 that expressed Drgx (Fig. 1C), indicating that Tm2 were either lost or converted to another fate. Unlike the mutant, upon RNA interference (RNAi) knockdown of *pdm3* using *TmX/Tm2-Gal4*, 65% of Tm2s that retained the expression of the driver in adult brains were converted to neurons with Tm4 morphology, as characterized by wider dendritic arbors that were symmetrical around the main fiber of the neuron and axons targeting the deeper lobula layer 4 (Fig. 1, D and E; compare with Fig. 1A). It is likely that the knockdown retains low levels of Pdm3 in Tm2 that are sufficient to maintain expression of *TmX/Tm2-Gal4* but are insufficient for instructing the Tm2 fate. These Tm4-looking neurons did not express Mef2 and instead expressed the putative Tm4 selector Aop (Fig. 1, E and F).

We then investigated whether ectopic expression of *pdm3* in Tm4 and Tm6 could be sufficient to convert them to Tm2 fate. We used *TmX/Tm2-Gal4* to express *UAS-pdm3.short* (25) and found that >90% of Aop$^+$ neurons (Tm4 and Tm6) were eliminated at P50 (Fig. 1G), suggesting that they had been lost or converted. To address the completeness of these conversions at P50, when the neurons have not fully acquired their adult morphology but display the greatest transcriptomic diversity (1), we analyzed their gene expression with scRNA-seq. Because the driver weakly labels several other cell types (fig. S4A and see the materials and methods), we only retained the cells classified as Tm1, Tm2, Tm4, or Tm6 by a neural network trained on our reference atlas (1), in addition to those classified as T2 that are also strongly labeled by *TmX/Tm2-Gal4* (Fig. 1, H and J). T2 neurons, like Tm2, natively express *pdm3*, and thus they should not be affected by this perturbation and serve as an internal control. We observed a depletion of Tm4 and Tm6 in the UAS-pdm3 library compared with control and an increase in the number of Tm2s (Fig. 1I), indicating that ectopic *pdm3* converts Tm4 and Tm6 to Tm2. We noted that the increased number of Tm2s upon *pdm3* overexpression was not sufficient to fully account for the lost Tm4s and Tm6s. Some optic lobe neurons are known to be generated in excess, followed by widespread apoptosis in the first half of pupal development (26). Staining against cleaved Dcp-1, an activated caspase that marks dying cells (27), indeed showed a significantly increased rate of apoptosis in brains overexpressing *pdm3* at P25 (fig. S4, B and C), whereas no Tm2 somas (GFP$^+$Pdm3$^+$) were stained with Dcp-1 in the control brains. Together, these results suggest that when excess Tm2s are produced through conversions from Tm4 and Tm6, this is compensated for by increased cell death. This mechanism potentially helps to ensure that only one Tm neuron of each type is present per column in wild-type brains.

To distinguish the wild-type Tm2 neurons from those converted from another cell type, we performed unsupervised clustering on the dataset. This revealed heterogeneous populations among the cells classified as Tm1 and Tm2 (fig. S4D and Fig. 1K). Tm2 subclusters 4 and 5 were extremely similar, with only 34 significant differentially expressed genes (DEGs). Most of these differences were consistent with markers of the control Tm4 and Tm6 clusters (fig. S4E), including the strongest one, *Wnt4*, which was found in cluster 4 (Fig. 1L). We recently showed that *Wnt4* is expressed in ventral Tm4 and Tm6, but not in Tm2 (1), suggesting that cells in cluster 4 were converted neurons that had retained these markers from their initial specification as Tm4 or Tm6. Nevertheless, these differences between the converted and "original" Tm2s were minimal compared with the >700 DEGs observed between wild-type Tm2 and Tm4 at this stage (Table S2). We therefore conclude that conversion from Tm4 or Tm6 fate to Tm2 fate induced by ectopic *pdm3* appears complete.

The third subgroup of the cells classified as Tm2, cluster 7, consisted entirely of cells from the UAS-pdm3 library and expressed the Tm1 selector *Drgx* (Fig. 1M), suggesting that they were originally Tm1s converted to a Tm2-like state. These were still significantly different from cluster 5 (wild-type Tm2), with 160 DEGs (Fig. 1K). The cells classified as Tm1 were clustered into two groups: cluster 6, which was made entirely of cells from the UAS-pdm3 library and was significantly different from the second group, cluster 3, which consisted essentially of wild-type Tm1s (Fig. 1, H and K). Thus, both clusters 6 and 7 contained Tm1s with ectopic *pdm3*. Uniform manifold approximation and projection (UMAP) visualization showed a thin stripe of cells bridging the Tm1-like (cluster 6) and Tm2-like (cluster 7) states. We observed that although both clusters 6 and 7 displayed reads coming from the *UAS-pdm3* construct, as expected (Fig. 1N), cluster 7 also expressed *pdm3* from the native locus (Fig. 1O). We thereby conclude that the amount of protein produced from the UAS construct is insufficient for conversion into Tm2, and instead Pdm3 must autoactivate above a certain threshold. Once this threshold is reached, Pdm3 quickly drives Tm1, Tm4, and Tm6 to a Tm2-like state; however, this conversion is incomplete in Tm1 (cluster 7) because *Drgx* remains expressed. Morphologically, Tm1s overexpressing *pdm3* appeared normal in adults (fig. S3F), suggesting that the 157 DEGs between clusters 3 and 6 are not important for morphology.

In summary, *pdm3* is necessary and sufficient to instruct the fate choice between Tm2 and Tm4 neurons, as predicted by the terminal selector code. Its loss results in morphological conversion of Tm2 into Tm4, and its ectopic expression can induce essentially complete transcriptomic conversions of Tm4 and Tm6 to Tm2 fate. It is also an upstream repressor of the Tm4 and Tm6 selector *aop* (Fig. 1, E and G).

The Tm1 selector Drgx is regulated by Klumpfuss

Similar to *pdm3* in Tm2, Drgx is the only TF that continuously distinguishes Tm1 from Tm4 (Fig. 1B). We ectopically expressed *Drgx* using *R35H01-Gal4*, which is expressed in all four Tm neurons until P50 but is only maintained in Tm4 and Tm6 in adults (fig. S5, A and B, *TmX/Tm4,6-Gal4*). In these adult brains, the proportion of Tm6 remained unchanged, but most Tm4s were converted into Tm1s, characterized by much narrower dendritic arbors and axons terminating in the first layer of the lobula (Fig. 2, A and B, and see Fig. 1A). The converted neurons also lost Aop expression and instead expressed Mef2 (a Tm1 and Tm2 marker) (Fig. 2C). Some of the converted neurons displayed morphological features atypical of Tm1, such as targeting to the Lo2 layer instead of Lo1 (fig. S5C). We suspect that this partial expressivity is caused by low Gal4 expression from *TmX/Tm4,6-Gal4*. Moreover, the fact that this driver is expressed at even weaker levels in Tm6 compared with Tm4 (fig. S5B) might explain our failure to affect Tm6 fate. Loss of *Drgx* (described below) resulted in conversion of Tm1s into Tm4s (Fig. 2, G and H). Thus, *Drgx* specifies the Tm1 fate: It can repress *aop* and mediate the conversion of Tm4 into Tm1, as predicted by the selector code.

Neither *Drgx* nor *pdm3* is expressed in the progenitors (neuroblasts) of Tm neurons (6), implying that their postmitotic expression in specific neurons is instructed by tTFs in the neuroblasts. To investigate how this is controlled, we used a single-nucleus assay for transposase-accessible chromatin sequencing (snATAC-seq) dataset of the developing *Drosophila* brain (28). We identified the cells belonging to optic lobe neurons at adult, P48, and P24 stages, and then reclustered and annotated them using our scRNA-seq atlas (1) as a reference (fig. S6, A to D, and materials and methods). We found a putative enhancer in the fourth intron of *Drgx* that was specifically accessible in Tm1 throughout development (fig. S6E) but was not accessible in the other Tm neurons or in T2, T3, T4, or T5 neurons, which also express *Drgx* (Fig. 2D). We found that the only enriched binding motifs for any of the TFs expressed in the optic lobe (E-value < 100; see the materials and methods) within this 700 base-pair region belonged to the tTF Klumpfuss (Klu). Klu is expressed at higher levels in neuroblasts during early temporal windows, when Tm1s are generated, and its overexpression in neuroblasts can expand Runt$^+$ neurons (29) that are likely born in the same temporal window as Tm1 (Fig. 2E) (6). Thus, Klu might also regulate *Drgx* expression. Indeed, *Klu* overexpression using *pxb-Gal4*, which is expressed in the central region of the neuroepithelium (Fig. 2, E and F, dashed lines), resulted in the expansion of Drgx$^+$ neurons (i.e., Tm1) in this region, similar to Runt (Fig. 2F). We therefore conclude that Klu expression in neuroblasts helps to specify Tm1 from an early temporal window by activating the selector *Drgx* in their neuronal progeny.

Next, we investigated whether *Drgx* expression is regulated by this enhancer element by engineering a CRISPR deletion ($Drgx^{\Delta Tm1}$; see the materials and methods), which should function as a conditional mutant specifically

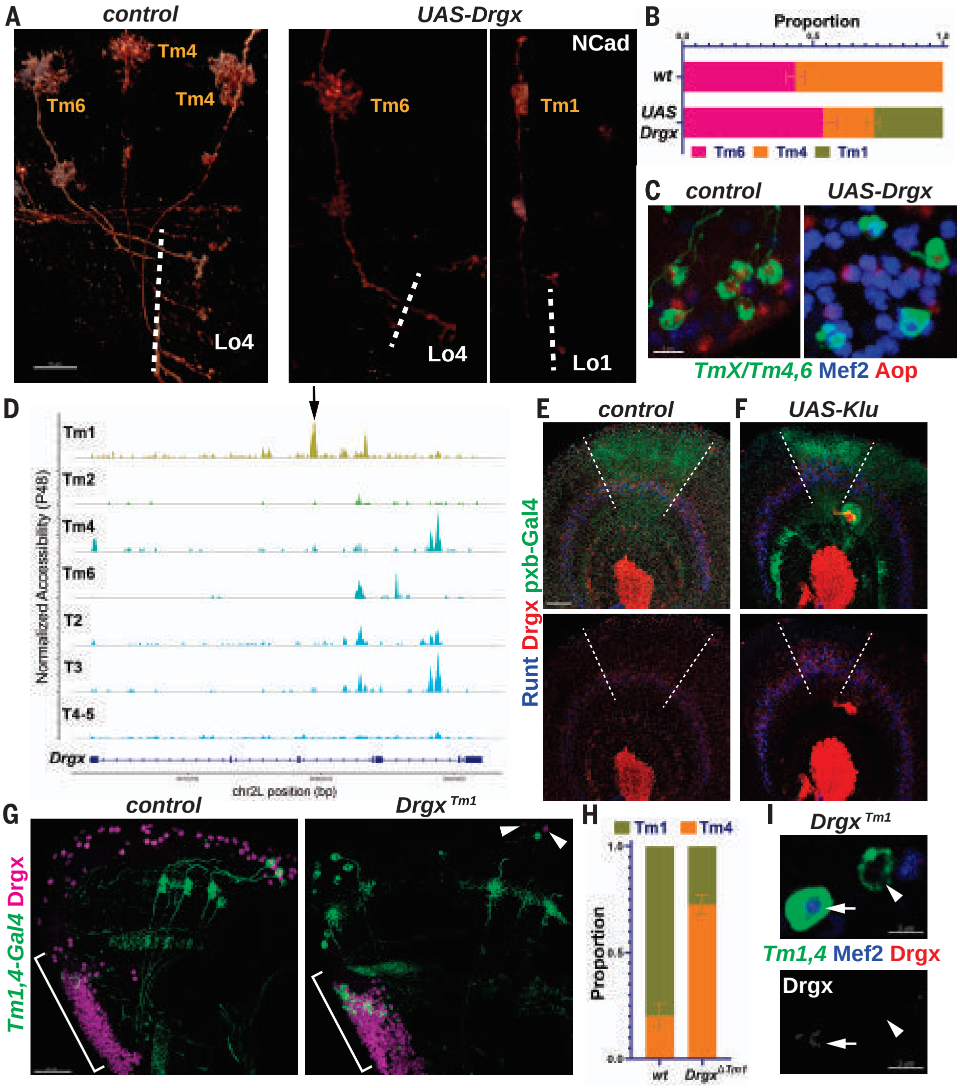


Fig. 2. The Tm1 selector Drgx is regulated by Klumpfuss. (**A** to **C**) *TmX/Tm4,6-Gal4* driving UAS-Drgx and CD4-tdGFP (flip-out). (A) 3D reconstructions of GFP for representative adult neurons, with anti-NCad shown in white. Dashed lines mark the border of lobula neuropil. (B) Quantification of (A). n = 92/4 control and n = 45/6 Drgx neurons/brain, P = 0.0003. (C) Same as (A) but with maximum projections of somas. anti-Mef2 is shown in blue and anti-Aop is shown in red. (**D**) Aggregated accessibility tracks of *Drgx* locus from the normalized snATAC-seq data at P48 (*28*). Arrow indicates the Tm1-specific enhancer deleted in (G) to (I). (**E** and **F**) *pxb-Gal4* driving CD8-GFP and UAS-Klu [(F), n = 5 brains] in L3 optic lobes, with anti-Runt shown in blue and anti-Drgx shown in red. Dashed lines mark the borders of driver expression. (**G** to **I**) *Tm1,4-Gal4* driving CD4-tdGFP (flip-out) in heterozygous (control) or homozygous *Drgx*$^{\Delta Tm1}$ mutants. (G) Maximum projections of adult optic lobes. Anti-Drgx is shown in magenta. Brackets mark the location of the lobula plate cortex (T2 to T5 neurons). Arrowheads indicate glia (see also fig. S5E) that maintain Drgx expression in the mutants. (H) Quantification of (G) (see also fig. S5D). Tm1 were normally observed more frequently than Tm4 because the driver expression is much lower in Tm4. n = 57/6 control and n = 181/10 *Drgx*$^{\Delta Tm1}$ neurons/brains, P < 0.0001. (I) Same as (G), but with somas. Anti-Mef2 is shown in blue and anti-Drgx is shown in red, or only anti-Drgx in grayscale (bottom). The arrow indicates a Tm1 nucleus, and the arrowhead indicates a Tm4 nucleus. Scale bars: (A), (E), and (F), 15 µm; (C), 5 µm; (G), 20 µm; and (I), 3 µm. Error bars indicate SEM.

in Tm1. *27b-Gal4* (*30*) is expressed in Tm1 and much more weakly in Tm4 (fig. S5D, *Tm1,4-Gal4*) throughout development. In *Drgx*$^{\Delta Tm1}$ mutant adults, Drgx expression in the medulla cortex (where all Tm somas are located) was almost completely lost (Fig. 2G), but it was still normally present in Repo$^+$ perineurial glia (fig. S5E) at the surface of the brain (Fig. 2G, arrowheads) and in T neurons originating from the lobula plate (Fig. 2G, brackets). The observed ratio of Tm1 to Tm4 labeled by *Tm1,4-Gal4* decreased significantly in the mutant brains (Fig. 2H). This was not caused by the death of Tm1s because we could observe no apoptotic Tm1s at P25 in either condition (fig. S5, F and G), suggesting instead that most Tm1s were converted to Tm4s. Furthermore, 69% of the few remaining Tm1s displayed abnormal morphological features such as disrupted dendritic arbors and/or axons reaching to deeper layers in the lobula (fig. S5D). Close examination of somas revealed that these neurons that maintained Mef2 (a Tm1 and Tm2 marker) still expressed Drgx at very low levels (Fig. 2I, arrow). In addition, Drgx expression was normal in *Drgx*$^{\Delta Tm1}$ mutants at the L3 stage (fig. S5H). These results suggest that there are other, partially redundant enhancers regulating *Drgx* that control its initial activation in newborn neurons, whereas the robust maintenance of expression in Tm1 requires this specific enhancer. Even though it is not maintained later, Klu could be priming this enhancer in newborn Tm1s to ensure the sustained expression of *Drgx*.

Selectors jointly control developmental and functional features

Similar to *Drgx* in Tm1 and *pdm3* in Tm2, *SoxN* is the sole candidate selector distinguishing Tm6 from Tm4 (Fig. 1B). In control MARCM clones marked with *TmX/Tm4,6-Gal4*, we observed roughly equal numbers of adult Tm4 and Tm6. By contrast, only Tm4s could be observed in the *SoxN*-null mutant (*31*) clones (Fig. 3A). All four Tm neurons are unicolumnar neurons produced by all neuroblasts; therefore, a given column should contain one Tm4 and one Tm6 generated from the same neuroblast (*5*). We consistently observed Tm4 and Tm6 neurites occupying the same column in sparse control MARCM neuroblast clones (Fig. 3B). However, these clones consisted of two Tm4s in *SoxN* mutants (Fig. 3B), indicating that the loss of *SoxN* converted Tm6 to Tm4 rather than eliminating them. However, columns with these pairs were rare, suggesting that the extra Tm4s often undergo apoptosis, as shown above for Tm2. Overexpressing *SoxN* using *TmX/Tm4,6-Gal4* did not convert Tm4s to Tm6 fate (fig. S7A). This is again likely caused by the weak Gal4 driver, because the amount of SoxN protein detected in these Tm4 nuclei was an order of magnitude lower than in wild-type Tm6 nuclei (fig. S7A, insets). Thus, we could engineer predictable switches of type identity between all four Tm neurons guided solely by a code of sustained transcription factors.

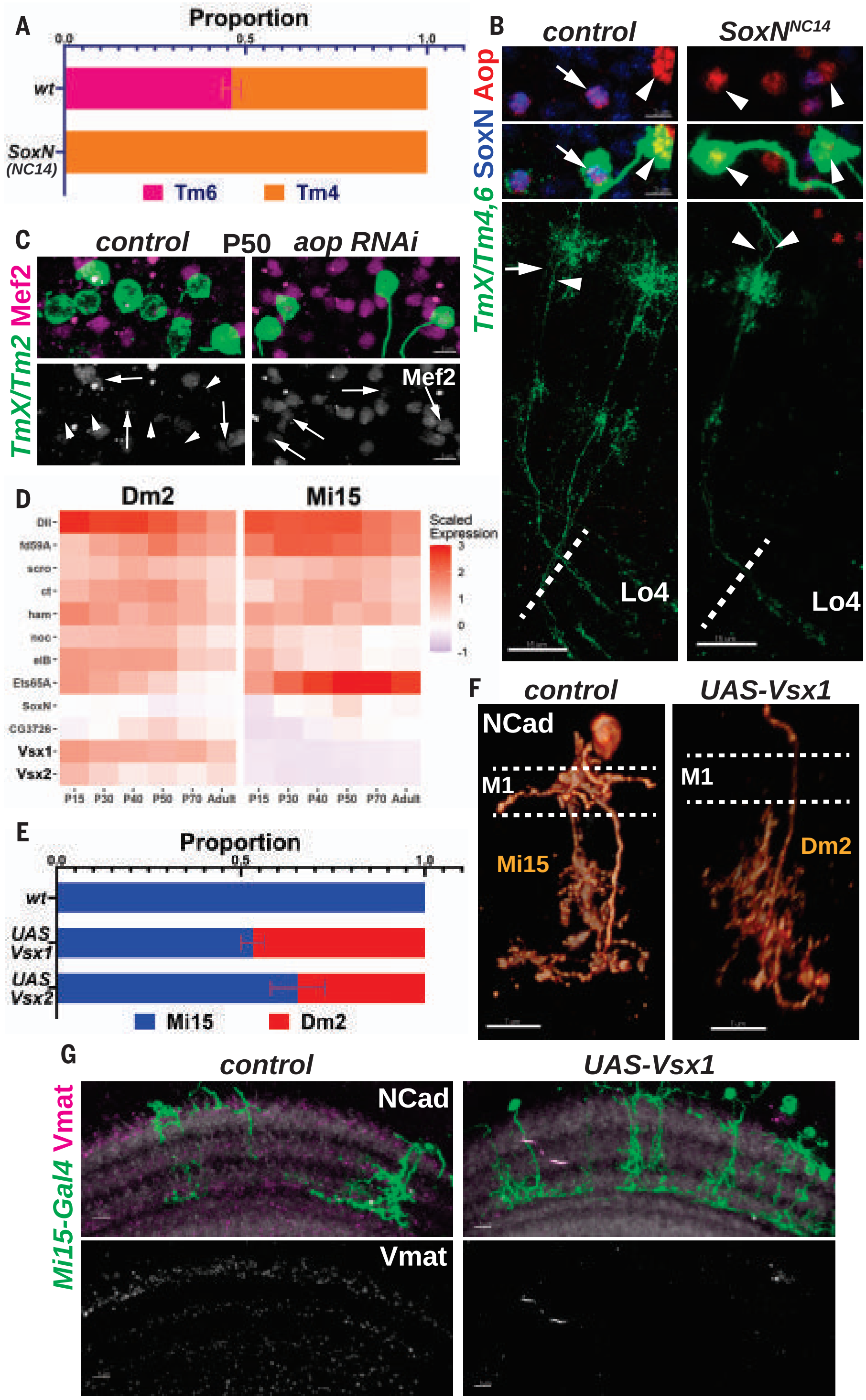


Fig. 3. Selectors jointly control developmental and functional features. (**A** and **B**) FRT40A and *SoxN*^{NC14} MARCM clones labeled with *TmX/Tm4,6-Gal4* and CD4-tdGFP in adult brains. (A) Quantification of (B) based on Aop-only (Tm4) and Aop+SoxN (Tm6) neurons. *n* = 225/9 control and *n* = 258/10 SoxN^{NC14} neurons/brains, $P < 0.0001$. No neurons with Tm6 morphology were observed in the mutant clones. (B) Maximum projections, with anti-SoxN shown in blue and anti-Aop shown in red, displaying the neurites (bottom) and the somas (top) of the same two neurons. Arrows indicate Tm6, and arrowheads indicate Tm4. (**C**) *TmX/Tm2-Gal4* driving *aop* RNAi (*n* = 6 brains) and CD4-tdGFP (flip-out). Maximum projections of somas at P50 with anti-Mef2 (top: magenta, bottom: white). Arrows indicate GFP$^+$Mef2$^+$ Tm neurons, and arrowheads indicate GFP$^+$Mef2$^-$ Tm neurons. (**D**) Developmental (scaled) expression patterns (*1*) of all genes that are candidate selectors in either of the displayed cell types. (**E**) Quantification of (F) and fig. S7D. Cells labeled by *Mi15(R76F01)-Gal4* were identified on the basis of their morphology in each condition. *n* = 104/11 wild-type, *n* = 108/11 UAS-Vsx1, and *n* = 24/4 UAS-Vsx2 neurons/brains, $P < 0.0001$ for change in Dm2 proportions in both conditions. Error bars indicate SEM. (**F** and **G**) *Mi15-Gal4* driving UAS-Vsx1 and CD4-tdGFP (flip-out). (F) 3D reconstructions of GFP for representative adult neurons in each condition (see also Fig. 1A), with anti-NCad shown in white. Dashed lines mark the M1 layer where Mi15 arborizes but Dm2 does not. Also note that Mi15 has two descending branches, whereas Dm2 has one. (G) Maximum projections of adult optic lobes, with anti-NCad shown in white and anti-Vmat shown in magenta (top) and white (bottom). *n* = 4 control brains and *n* = 7 UAS-Vsx1 brains. Scale bars: (B), 15 μm; (C) and (G), 5 μm; (F), 7 μm.

Combined, our results suggest that Tm4 is the default fate among these Tm neurons, which is overridden by *Drgx* in Tm1, by *pdm3* in Tm2, and by *SoxN* in Tm6. *aop* is expressed in both Tm4 and Tm6, but it is repressed by *Drgx* in Tm1 and by *pdm3* in Tm2. To address whether Aop also functions as a selector, we generated *aop*-null MARCM clones (*32*) and also performed RNAi knockdown using *TmX/Tm4,6-Gal4*; in both cases, the driver was turned off (fig. S7, B and C). When we instead used *TmX/Tm2-Gal4* to express *aop* RNAi, we observed that all Tm neurons at P50 (when this driver normally labels all four Tms) expressed the Tm1 and Tm2 marker Mef2 (Fig. 3C), indicating that *aop* is necessary for Tm4 and Tm6 identity. However, we could not determine the exact fate of these neurons, i.e., whether they were eliminated or transformed to Tm1 or Tm2 fate, because both were labeled by the driver.

To further validate the terminal selector concept for functional features of neurons, we sought other neuronal types with selector codes that differ only by a few genes, and that also use different neurotransmitters. Dm2 and Mi15 are both cholinergic, but Mi15 are also the

only aminergic neurons in the optic lobe (*33*), expressing the vesicular monoamine transporter (*Vmat*). Both of these neurons express the candidate selectors *Dll*, *fd59A*, *scro*, *ct*, *ham*, *noc*, *eIB*, and *Ets65A*, but *Vsx1* and *Vsx2* are specific to Dm2 and are the only TFs that continuously distinguish the two cell types (Fig. 3D). Ectopic expression of either *Vsx1* or *Vsx2* using an Mi15-specific (early) driver was sufficient to convert them to Dm2 morphology (Fig. 3, E and F; fig. S7D; and see Fig. 1A). *Vsx1* and *Vsx2* could function redundantly because of their sequence similarity or they could cross-activate each other's expression. However, we did not observe Vsx2 protein in Mi15s ectopically expressing Vsx1 (fig. S7E), suggesting redundancy.

Next, we evaluated these conversions for more terminal features that are likely to be important for neurotransmission. We observed a drastic reduction in Vmat protein levels in the medulla upon *Vsx1* overexpression in Mi15 (Fig. 3G). In addition, we investigated four neurotransmitter or modulator receptor genes that are differentially expressed between Mi15 and Dm2 clusters: *5-HT7*, *Octβ1R*, *Or63a*, and *Dh44-R1* (fig. S7I). Using in situ hybridization, we observed that Mi15s overexpressing Vsx1 down-regulated *Or63a* and *Dh44-R1* and they up-regulated *5-HT7* and *Octβ1R* (fig. S7, F to H), as expected. These results show that Vsx genes function as terminal selectors in Dm2, controlling both morphological and functional features.

RTK signaling stabilizes the Tm selector network

Even though the mRNA of the Tm4/6-specific selector *aop* could be found in all four Tm neurons up to P40 (fig. S7J), Aop protein was no longer localized to Tm1 nuclei already by P25 (fig. S5F). This could be explained by a well-known posttranslational regulatory mechanism: Aop is exported from the nucleus and degraded after phosphorylation by mitogen-activated protein kinase (MAPK) (*34*). This regulation is essential for specification of R7 photoreceptors in the developing eye through receptor tyrosine kinase (RTK) signaling (*35*). We could not detect phosphorylated MAPK in Tm4 and Tm6 somas that strongly expressed Aop, but P-MAPK was present in Tm1 and Tm2, in which Aop protein could sometimes be observed as a "ring" outside the nucleus at P30 (fig. S7K, arrows), suggestive of nuclear export. This suggests that Drgx and Pdm3 initially repress Aop protein indirectly in Tm1 and Tm2, respectively, by rendering them sensitive to RTK signaling.

After P40, *aop* mRNA is also down-regulated in Tm1 and Tm2; this coincides with *Mef2* up-regulation in these cell types (fig. S7J) downstream of Pdm3 and Drgx (Figs. 1F and 2C). Knocking down *Mef2* using *TmX/Tm2-Gal4* resulted in a very rare (one out of 38 neurons observed) conversion of Tm2 into Tm4 in adults, and 18% of Tm neurons observed were morphologically unrecognizable (Fig. 4, A and D). Aop could be detected in some of these cells, but only outside the nucleus (Fig. 4E), similar to wild-type Tm1 and Tm2 at P30 (fig. S7K). This indicates that *aop* was transcriptionally derepressed without Mef2, but its posttranslational repression through MAPK remained intact, even in adult brains. Therefore, *aop* appears to be down-regulated in Tm1 and Tm2 through two independent mechanisms (Fig. 4H): degradation of the protein through MAPK at all stages and transcriptional suppression by *Mef2* after P40. Drgx and Pdm3 could control the first mechanism by regulating the expression of RTK genes such as *InR*, *Ror*, and *Alk*, which are differentially expressed between Tm1/2 and Tm4/6 clusters (fig. S7L).

Because *pdm3* and *Drgx* both negatively regulate Aop expression (Figs. 1G and 2C), we investigated whether the opposite was also true. Overexpression of wild-type *aop* with *TmX/Tm2-Gal4* did not convert Tm2 to either Tm4 or Tm6, but 25% of Tm neurons were morphologically unrecognizable (Fig. 4, A and D), similar to those observed with *Mef2* RNAi, in which *aop* transcription was derepressed. These neurons still maintained Pdm3 (Fig. 4F), the coexpression of which with Aop might create a confused state. The signal for the ectopic Aop protein was weak (Fig. 4F), suggesting that it was being degraded by the active MAPK pathway in Tm2. We therefore overexpressed a constitutively active form of Aop (*aop.ACT*) that cannot be phosphorylated and degraded (*34*). In these brains, 40% of Tm2s were converted to Tm4s (Fig. 4, C and D) that had lost Pdm3 expression (Fig. 4G). This indicates that whereas Aop can suppress *pdm3* and promote Tm4 fate (Fig. 4H, dashed arrow), this regulation is not relevant with wild-type *aop* because of RTK signaling, which ensures that *pdm3* acts upstream.

The apparent destabilization of the fate choice between Tm2 and Tm4 with the postmitotic expression of *aop.ACT* (but not *aop.WT*) implies that neuronal identity remains dependent on the signaling conditions even after the initial specification events. Similar mechanisms in organisms with larger and more complex brains could be exploited to further diversify the neurons that are generated from the same stem cell pool with a common identity but then migrate to distinct brain regions where different signals might be available (*36*).

Decoding neuronal gene regulation through network inference

Cell-type identity encoded by terminal selectors represents only one aspect of neuronal gene regulation. Neuronal transcriptomes are dynamic throughout differentiation, typically in response to external signals such as the steroid hormone ecdysone (*37*–*39*). It remains unclear how these two top-level regulatory programs, i.e., the identity and developmental state, interact to combinatorially determine the expression of downstream genes in each neuron.

We implemented the Inferelator 3.0 framework (*40*) to build gene regulatory network (GRN) models with the goal of gaining a more complete understanding of the regulatory programs used by developing optic lobe neurons. A key feature of this method is its use of transcription factor activity (TFA) that allows Inferelator to estimate the underlying activity of each TF using the expression levels of its known targets from prior information ("priors") (Fig. 5A). Calculating TFA before fitting a linear regression model to infer a GRN circumvents the issue that mRNA levels are often not a good substitute for a TF's latent activity (*41*), which may vary with posttranscriptional modifications or the presence of cofactors. We modeled GRNs in Tm1, Tm2, Tm4, and Tm6, as well as in the five types of lamina monopolar neurons (L1 to L5), which provide a useful benchmark for our models. For inference, we used single-cell transcriptomes from both our atlas (*1*) and one generated by another group (*42*) between the stages P24 and P50, when optic lobe neurons acquire most of their morphological features and begin to form synapses. We constructed priors for each network using the corresponding P48 clusters (fig. S6C) in the snATAC-seq dataset described above (*28*). Figure 5C displays the entire GRN inferred from the Tm neurons, highlighting the top 10 TFs with the highest number of targets predicted, which includes *Mef2*; the selectors *pdm3*, *cut*, and *ap*; as well as the ecdysone-responsive TFs *Hr3*, *Hr39*, *Eip74EF*, and *Eip93F*.

The scarcity of ground-truth networks presents a challenge when benchmarking inferred GRNs in complex multicellular organisms. To assess the predictive power of our models, we exploited available RNA-seq datasets collected from perturbed neurons. For lamina neurons, we used two relevant datasets: knockdown of *Hr3* in all five lamina neurons at P48 (*39*) and L3 neurons at P40 mutant for *erm* (*21*). For Tm neurons, we used the UAS-*pdm3* scRNA-seq experiment that we performed at P50 (Fig. 1H). For each experiment, TFA was calculated using the same corresponding priors used for inference. We then applied matrix multiplication (dot product) between the estimated TFA and the learned weights between TFs and targets (betas) to generate a predicted expression matrix (fig. S8C). Even though these betas were determined from the completely independent, wild-type datasets discussed above, the real and predicted transcriptomes aligned

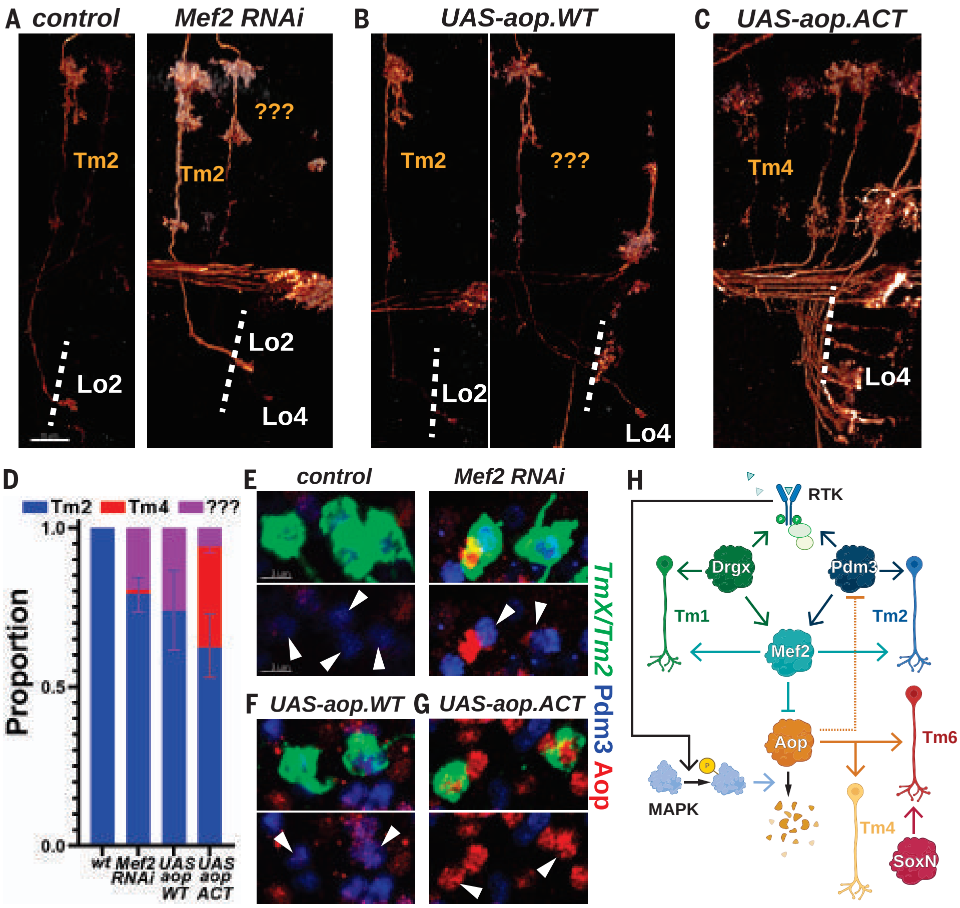


Fig. 4. RTK signaling stabilizes the Tm selector network. (**A** to **G**) *TmX/Tm2-Gal4* driving CD4-tdGFP (flip-out) and Mef2 RNAi [(A) and (E)], UAS-aop.WT [(B) and (F)], or UAS-aop.ACT [(C) and (G)]. (A) to (C) 3D reconstructions of GFP for the representative adult neurons in each condition, with anti-NCad shown. "???" marks neurons that typically target to Lo4 but could not be recognized as any known optic lobe neuron on the basis of their morphology. Dashed lines mark the border of lobula neuropil. (D) Quantification of (A) to (C). *n* = 54/6 control, *n* = 38/8 Mef2 RNAi, *n* = 16/6 aop.WT, and *n* = 75/5 aop.ACT neurons/brains. *P* = 0.03 (Mef2 RNAi), *P* = 0.02 (aop.WT), and *P* = 0.005 (aop.ACT) for change in cell-type proportions. Error bars indicate SEM. (E) to (G) Same as (A) to (C), with maximum projections of somas with anti-Pdm3 shown in blue and anti-Aop shown in red. Arrowheads indicate GFP^{+} neurons. Scale bars: (A) to (C), 10 μm; (E) to (G), 3 μm. (**H**) Summary of the experimentally validated regulatory interactions between Drgx, Pdm3, Mef2, and Aop in Tm neurons. Negative regulation of Pdm3 by Aop (dashed line) is only applicable when Aop cannot be degraded through the MAPK pathway.

nearly perfectly according to their cell type and condition of origin (Fig. 5, D to F) after Seurat integration (*43*). However, we also observed that before integration (fig. S8E-G), the differences between control and perturbed conditions were much smaller in predicted clusters. Consistently, we found that the predicted transcriptomes recapitulated only a small proportion (10 to 30%) of the real DEGs between the control and perturbed conditions (low recall), but the predicted DEGs were mostly (>50%) correct (high precision) (fig. S8, H to J). Thus, our benchmarks suggest that the interactions learned by our models are largely accurate, although they represent only a snippet of the true underlying GRNs.

Selectors and ecdysone signaling regulate downstream targets

We found that nearly all of the regulatory relationships that we experimentally validated in the previous sections (Fig. 4H) were also captured by our GRN model (Fig. 5G), such as the regulation of *Mef2* by *Drgx* and *pdm3*. Drgx and Pdm3, although required, are not sufficient to activate *Mef2* expression, which does not occur until P40 despite the continuous expression of the selectors. Ecdysone-responsive *Hr3* emerged as a candidate for this temporal trigger because its activation around P30 precedes *Mef2* (fig. S7J). We tested this prediction by generating *Hr3* mutant MARCM clones using *TmX/Tm2-Gal4*. In adult brains, Mef2 expression was not affected, and Tm2 appeared morphologically normal (fig. S9A). However, at P50, Mef2 could not be detected in mutant clones (Fig. 5H), indicating that *Mef2* expression was delayed but not abolished in *Hr3* mutants. This implies that there are redundant temporal mechanisms regulating *Mef2* expression and/or that *Hr3* acts indirectly to control *Mef2*. Among the predicted downstream targets of *Hr3* (Fig. 5I), *Hr4*, *Eip74EF*, and *Blimp-1* were all shown to be regulated by *Hr3* in lamina neurons, the knockdown of which delays the downregulation of *Blimp-1* (*39*), which normally occurs around P40 (fig. S7J). Indeed, overexpression of *Blimp-1* using *TmX/Tm2-Gal4* also repressed Mef2 at P50 (Fig. 5J), suggesting that Hr3 acts through Blimp-1 for this function. Our results show that the combinatorial action of the selectors *Drgx*/*Pdm3* and the ecdysone-responsive TFs *Hr3*/*Blimp-1* enables *Mef2* to be expressed specifically in Tm1 and Tm2 and only after P40.

Another inferred edge in this subnetwork (Fig. 5G), the negative regulation of *cut* (*ct*) by *pdm3*, was consistent with the lower levels of *ct* expression in Tm2 cluster compared with other Tm neurons (fig. S9B). Because different Cut expression levels in larval "da" sensory neurons regulate the size of their dendritic arborizations (*44*), this difference could be functionally significant. Indeed, we found that 73% of Tm1s targeted to the Lo2 layer instead of Lo1 upon *ct* knockdown (Fig. 5K). Thus, the level of *ct* expression controls a specific subroutine during brain wiring downstream of *pdm3*. However, overexpression of *ct* in Tm2 did not lead to their axons projecting to Lo1 instead of Lo2 (fig. S9C), suggesting that there are redundant mechanisms allowing Tm2 to arborize in this layer.

Finally, we inspected the GRN model of the Tm neurons (Fig. 5C) to assess whether different types of TFs specialize on different types of targets. We previously reported that TFs and cell surface proteins (CSPs) are overrepresented in DEGs between optic lobe neurons. CSPs are particularly up-regulated at P40 to P50 (*1*) during synaptogenesis. Accordingly, CSPs that may be involved in cell-cell recognition (*45*) were strongly enriched among the network targets (fig. S9D). However, we did not see a clear bias for any TF class to regulate more or fewer CSPs than others. We also performed Gene

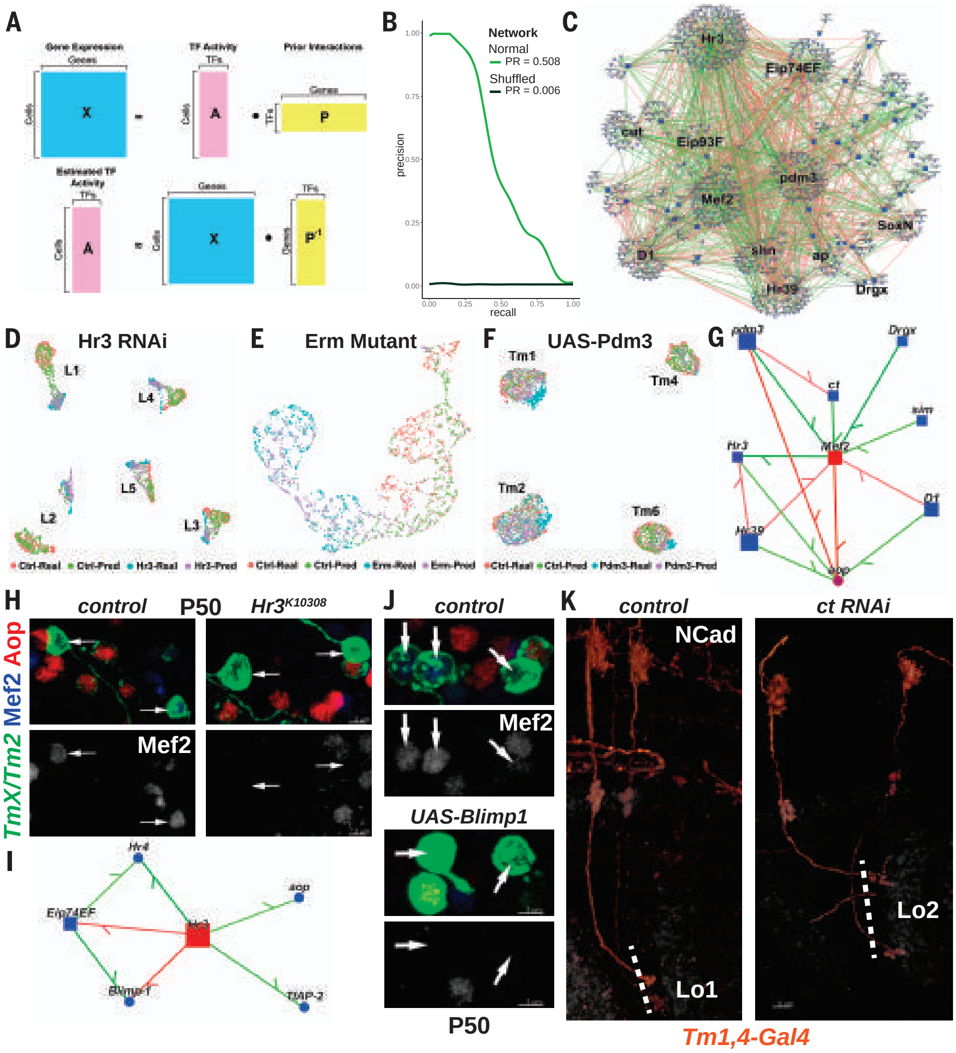


Fig. 5. Computational inference of gene regulatory networks. (**A**) Gene expression in each cell is assumed to be a linear product of latent TF activities and the connectivity matrix (prior) between TFs and their targets (top). TFA is estimated as the dot product of the expression matrix and the pseudoinverse of the prior matrix (bottom). (**B**) Area under the precision-recall (AUPR) curves for the Tm network built using the MergedDA prior (see also fig. S6A). (**C**) Visualization of the network in (B), displaying all interactions with a minimum of 80% confidence (combined) and variance explained of 1%. Top 10 TFs that had the highest number of target genes in the network are highlighted in addition to SoxN and Drgx. (**D** to **F**) Single-cell transcriptomes of L1 to L5 at P48 expressing *Hr3* RNAi (*39*) (D); simulated single L3 neurons (fig. S8D) at P40 mutant for *erm* (*21*) (E); and Tm1, Tm2, Tm4, and Tm6 at P50 overexpressing *pdm3* (Fig. 1) (F). UMAPs were calculated using 30 PCs [(D) and (F)] or three PCs (E) on the integrated gene expression. (see also fig. S8, E to G). (**G**) Network visualization displaying all TFs predicted to regulate *Mef2* or *aop* with confidence > 95%, and all inferred interactions between the displayed genes in the Tm network. Green indicates a positive correlation and red a negative correlation between mRNA levels of the gene pairs. (**H**) FRT42D and *Hr3*^{K10308} MARCM clones labeled with *TmX/Tm2-Gal4* and CD4-tdGFP in P50 medulla cortex (maximum projection), with anti-Mef2 shown in blue and anti-Aop shown in red. Arrows indicate Aop^{-} Tm neurons that should normally be Mef2^{+} (n = 6 brains). (**I**) Same as (G), displaying all TFs predicted to be regulated by Hr3 (confidence > 95%). (**J**) *TmX/Tm2-Gal4* driving CD4-tdGFP (flip-out) and UAS-Blimp1 (n = 5 brains). Maximum projection is the same as in (H). (**K**) *Tm1,4-Gal4* driving CD4-tdGFP (flip-out) and *ct* RNAi (n = 40/6 neurons/brains). 3D reconstructions of GFP for the representative adult neurons in each condition, with anti-NCad shown in white. Dashed lines mark the border of lobula neuropil. Scale bars: (H) to (J), 3 μm; (K), 5 μm.

Ontology (GO) term enrichment analysis on the predicted targets of the top three regulators in the network: ecdysone TF Hr3, the terminal selector Pdm3, and the effector TF Mef2. The same general terms were enriched for all of them: ion channels, cell adhesion, and signaling molecules (fig. S9E). These results further highlight the combinatorial nature of neuronal gene regulation, and they are consistent with other findings that most targets of the ecdysone-responsive TFs are cell-type specific (*39*) despite the uniform expression of these TFs in all neurons.

Discussion

We set out to test whether neuronal type identity is primarily encoded by unique and sustained combinations of TFs in each cell type. The terminal selector hypothesis has been extensively supported in *C. elegans*, and a few selectors have also been described in mice, such as Fezf2 (homolog of Erm), the expression of which in cortical progenitors induces corticospinal motor neuron–like fates (*15*). However, the previous studies focused on the roles of individual selector genes and did not systematically test the sufficiency of a continuously expressed TF code in instructing all type-specific gene expression in neurons. We explicitly addressed this prediction by determining the selector codes of every neuron in the fly visual system using a developmental scRNA-seq atlas and by engineering predictable transformations between different neurons using only these TFs. This has so far been difficult to demonstrate, even in *C. elegans*, likely because neurons typically diverge by multiple selectors (*46*). Our results suggest that effector genes are controlled by different permutations of available selectors in each neuron, which implies that every effector might not be regulated by all selectors. Similar selector combinations generally resulted in similar transcriptomes and vice versa (fig. S1D), but this relationship was not strict, reflecting the combinatorial nature of TF action. For instance, during brain wiring (P50), we observed a distinct branch (fig. S2C, red circle) in which all annotated clusters corresponded to neurons that connect to the central brain irrespective of their developmental origin and the similarity of selector expression.

We defined terminal selectors broadly to satisfy two key criteria: continuous expression in postmitotic neurons and involvement in the control of neuronal type identity. It has also been proposed that selectors directly regulate most effector genes by binding to their cis-regulatory enhancers (*47*). In our GRN models (table S3), the interactions that were present in our prior network ("gold_standard=1")

represent those that were directly supported by cis-regulatory evidence, i.e., enrichment of motifs in differentially accessible regions near the target gene, and thereby indicate direct regulation. For instance, 27 of the 120 high-confidence targets of Pdm3 (fig. S9, D and E) have been supported by snATAC-seq to be direct interactions. This does not imply that all other interactions are indirect, because the Inferelator-Prior pipeline was designed to favor accuracy by only retaining the highest confidence targets for TFA calculation (*40*). These direct targets include several wiring molecules such as *Dscam4* and the Netrin receptor *frazzled*, as well as effector TFs *NK7.1* and *CG9932*. Consistently, overexpression of *fra* in Tm4s led to 54% of these neurons forming dendritic branches that split into a "fork" in the M2 layer, which is normally characteristic of Pdm3-expressing Tm2 (fig. S9F, arrowhead, compare with fig. S9C). Nevertheless, extensive utilization of effector TFs (such as Mef2 in Tm1 and Tm2) makes it likely that many targets are also regulated indirectly. Such transcriptional subroutines may be more prevalent in flies and higher organisms, in which neuronal differentiation occurs over several days or weeks, in contrast to worm neurons, which are typically functional within a few hours after their terminal division. Another feature that has been commonly, but not universally, associated with terminal selectors is autoregulation (*47*). Our results support that Pdm3 indeed autoactivates (Fig. 1, N and O), but this is unlikely to be the case for Drgx, SoxN, and Vsx1/2 given the lower efficiency of their overexpression (Fig. 2B and 3E and fig. S7A).

The apparent conservation of this regulatory logic in both *C. elegans* and *Drosophila*, the last common ancestor of which lived >600 million years ago (*48*), makes it likely that the terminal selector concept will also be useful for understanding and manipulating the neuronal diversity of mammalian brains. This could have large implications for the emerging field of cell replacement therapy. The usage of lineage-specific TFs for the generation of specific neuronal types in vitro have significantly improved the efficiency of these protocols (*49*). Some of these TFs, such as *Pet1* and *Lmx1b* for serotonergic neurons (*50*) or *Lmx1a* and Nurr1 for dopaminergic neurons (*51*), are also likely to be terminal selectors. However, the protocols used still tend to produce heterogeneous populations of related cell types (*52*). We propose that more specific combinations of such reprogramming TFs could be identified in specific cell types of interest by virtue of their sustained postmitotic expression.

We found that the tTF *Klu* from neuroblasts activates the selector *Drgx* in newborn Tm1s, but we still know little about how the combined action of temporal, spatial, and Notch patterning (*5*) activates a unique set of selectors in every neuronal type, and subsequently how the selector combination enacts precise gene batteries over the course of development. There are also some limitations of this framework. We and others previously reported that a few neuronal types have distinct transcriptomes during development but then converge to a common state in adult brains (*1*, *53*). These are generally very similar (sub)types that only differ in their connectivity, so the TFs that encode their differences do not need to be maintained after their wiring is complete. In addition, TFs can be posttranscriptionally regulated by, e.g., the RNA-binding proteins Imp and Syp, which are widely used in *Drosophila* nervous system to generate neuronal diversity (*54*). This could complicate the identification of correct selector combinations from RNA-seq data alone.

Both this work and other previous efforts to decipher gene regulation in the fly brain (*28*) have now made it possible to study the molecular mechanisms of synaptic specificity within the framework of gene-regulatory mechanisms that encode neuronal type identity. We propose a "top-down" approach in which terminal selectors that cause broad changes in neuronal fates are identified first, followed by the dissection of downstream mechanisms aided by GRN modeling. Perhaps the most promising targets are effector TFs (e.g., *cut*) that still regulate many other genes but have more limited functions (subroutines) than the selectors. Nevertheless, the current models still have limitations, imposed mainly by the quality of snATAC-seq priors. Single-nucleus multiome studies that simultaneously profile gene expression and chromatin accessibility could remove many of these limitations in the near future.

Methods summary

Candidate terminal selectors

We selected for each neuronal cluster in our developmental scRNA-seq atlas (*1*) the TFs that were found as a consistent marker of that cluster or were continuously expressed at all stages according to binarized expression. We discarded all TFs that were expressed in >150 clusters (likely pan-neuronal).

Genetics

The precise genotypes and temperatures used for experiments in each figure panel are detailed in table S4. Source details for all fly strains are specified in table S5. Full names of all genes referred to in the manuscript are listed in table S6.

Immunohistochemistry and RNA-FISH

Immunohistochemistry and RNA-fluorescence in situ hybridization (RNA-FISH) experiments were performed according to previously described protocols. New polyclonal antibodies were generated against Drgx, Pdm3, SoxN, Mef2, Vsx2, Brp, and Repo by Genscript. Source details for all other antibodies are specified in table S5. Custom FISH probes were designed by Molecular Instruments against the transcripts of *5-HT7*, *Octβ1R*, *Or63a*, and *Dh44-R1*. All samples were imaged using a Leica SP8 confocal microscope with a 63× (numerical aperture 1.3) glycerol objective. Images were analyzed using Imaris (for details, see the supplementary materials). Parametric, two-sided *t* tests were used for all pairwise comparisons. $Drgx^{\Delta Tm1}$ deletion was produced by WellGenetics through CRISPR-mediated mutagenesis.

scRNA-seq

We labeled all four Tm neurons (*TmX/Tm2-Gal4*) with nuclear green fluorescent protein, crossed to either *UAS-pdm3* or *yw* (control), isolated the labeled cells using fluorescence-activated cell sorting (FACS), prepared libraries using the 10x Genomics 3′ kit (v3.1), and then sequenced them on the Illumina NovaSeq 6000 platform. The data were analyzed with CellRanger v5 and Seurat v4.

Network inference

We used a published snATAC-seq dataset (*28*) to identify differentially accessible regions between the Tm1, Tm2, Tm4, and Tm6 clusters (the Tm network) and L1 to L5 clusters (the lamina network) at P48. We then used the Inferelator-Prior v0.2.3 faf5e47 package to scan and score these regions within 10 kb of every gene for TF-binding motifs. The scores were then clustered to retain only the highest confidence targets of each TF for TFA calculation. For inference, we used single-cell transcriptomes from (*1*) at stages P30, P40, and P50 and from (*42*) at stages P24, P36, and P48. The networks were modeled only on the genes that displayed differential expression between either the cell types or the time points analyzed using Inferelator 3 (v0.5.6 dd532f4). The network performances were evaluated against the respective priors using four different metrics (fig. S8 and materials and methods). We additionally compared the performance of each network with negative control networks that were built with shuffled priors.

REFERENCES AND NOTES

1. M. N. Özel *et al*., Neuronal diversity and convergence in a visual system developmental atlas. *Nature* **589**, 88–95 (2021). doi: 10.1038/s41586-020-2879-3; pmid: 33149298
2. K. F. Fischbach, A. P. M. Dittrich, The optic lobe of *Drosophila melanogaster*. I. A Golgi analysis of wild-type structure. *Cell Tissue Res.* **258**, 441–475 (1989). doi: 10.1007/BF00218858
3. K. T. Ngo, I. Andrade, V. Hartenstein, Spatio-temporal pattern of neuronal differentiation in the *Drosophila* visual system: A user's guide to the dynamic morphology of the developing optic lobe. *Dev. Biol.* **428**, 1–24 (2017). doi: 10.1016/j.ydbio.2017.05.008; pmid: 28533086
4. F. Yu, C. T. Kuo, Y. N. Jan, *Drosophila* neuroblast asymmetric cell division: Recent advances and implications for stem cell biology. *Neuron* **51**, 13–20 (2006). doi: 10.1016/j.neuron.2006.06.016; pmid: 16815328

5. T. Erclik *et al*., Integration of temporal and spatial patterning generates neural diversity. *Nature* **541**, 365–370 (2017). doi: 10.1038/nature20794; pmid: 28077877
6. N. Konstantinides *et al*., A complete temporal transcription factor series in the fly visual system. *Nature* **604**, 316–322 (2022). doi: 10.1038/s41586-022-04564-w; pmid: 35388222
7. X. Li *et al*., Temporal patterning of *Drosophila* medulla neuroblasts controls neural fates. *Nature* **498**, 456–462 (2013). doi: 10.1038/nature12319; pmid: 23783517
8. I. Holguera, C. Desplan, Neuronal specification in space and time. *Science* **362**, 176–180 (2018). doi: 10.1126/science.aas9435; pmid: 30309944
9. O. Hobert, "Terminal selectors of neuronal identity," in *Current Topics in Developmental Biology*, P. M. Wassarman, Ed. (Academic, 2016), vol. 116, pp. 455–475.
10. E. G. Berghoff *et al*., The Prop1-like homeobox gene *unc-42* specifies the identity of synaptically connected neurons. *eLife* **10**, e64903 (2021). doi: 10.7554/eLife.64903; pmid: 34165428
11. L. Pereira *et al*., A cellular and regulatory map of the cholinergic nervous system of C. elegans. *eLife* **4**, e12432 (2015). doi: 10.7554/eLife.12432; pmid: 26705699
12. N. Stefanakis, I. Carrera, O. Hobert, Regulatory Logic of Pan-Neuronal Gene Expression in C. elegans. *Neuron* **87**, 733–750 (2015). doi: 10.1016/j.neuron.2015.07.031; pmid: 26291158
13. E. Serrano-Saiz, E. Leyva-Díaz, E. De La Cruz, O. Hobert, BRN3-type POU homeobox genes maintain the identity of mature postmitotic neurons in nematodes and mice. *Curr. Biol.* **28**, 2813–2823.e2 (2018). doi: 10.1016/j.cub.2018.06.045; pmid: 30146154
14. L. Remesal *et al*., PBX1 acts as terminal selector for olfactory bulb dopaminergic neurons. *Development* **147**, dev.186841 (2020). doi: 10.1242/dev.186841; pmid: 32156753
15. S. Lodato *et al*., Gene co-regulation by Fezf2 selects neurotransmitter identity and connectivity of corticospinal neurons. *Nat. Neurosci.* **17**, 1046–1054 (2014). doi: 10.1038/nn.3757; pmid: 24997765
16. P. Arlotta, O. Hobert, Homeotic transformations of neuronal cell identities. *Trends Neurosci.* **38**, 751–762 (2015). doi: 10.1016/j.tins.2015.10.005; pmid: 26596501
17. M. B. Reilly, C. Cros, E. Varol, E. Yemini, O. Hobert, Unique homeobox codes delineate all the neuron classes of C. elegans. *Nature* **584**, 595–601 (2020). doi: 10.1038/s41586-020-2618-9; pmid: 32814896
18. E. Hasegawa, M. Kaido, R. Takayama, M. Sato, Brain-specific-homeobox is required for the specification of neuronal types in the *Drosophila* optic lobe. *Dev. Biol.* **377**, 90–99 (2013). doi: 10.1016/j.ydbio.2013.02.012; pmid: 23454478
19. E. Hasegawa *et al*., Concentric zones, cell migration and neuronal circuits in the *Drosophila* visual center. *Development* **138**, 983–993 (2011). doi: 10.1242/dev.058370; pmid: 21303851
20. T. Suzuki *et al*., Formation of neuronal circuits by interactions between neuronal populations derived from different origins in the *Drosophila* visual center. *Cell Rep.* **15**, 499–509 (2016). doi: 10.1016/j.celrep.2016.03.056; pmid: 27068458
21. J. Peng *et al*., *Drosophila* Fezf coordinates laminar-specific connectivity through cell-intrinsic and cell-extrinsic mechanisms. *eLife* **7**, e33962 (2018). doi: 10.7554/eLife.33962; pmid: 29513217
22. T. Schilling, A. H. Ali, A. Leonhardt, A. Borst, J. Pujol-Martí, Transcriptional control of morphological properties of direction-selective T4/T5 neurons in *Drosophila*. *Development* **146**, dev169763 (2019). doi: 10.1242/dev.169763; pmid: 30642835
23. T. Lee, L. Luo, Mosaic analysis with a repressible cell marker (MARCM) for *Drosophila* neural development. *Trends Neurosci.* **24**, 251–254 (2001). doi: 10.1016/S0166-2236(00)01791-4; pmid: 11311363
24. C.-K. Chen, W.-Y. Chen, C.-T. Chien, The POU-domain protein Pdm3 regulates axonal targeting of R neurons in the *Drosophila* ellipsoid body. *Dev. Neurobiol.* **72**, 1422–1432 (2012). doi: 10.1002/dneu.22003; pmid: 22190420
25. A. L. Tichy, A. Ray, J. R. Carlson, A new *Drosophila* POU gene, *pdm3*, acts in odor receptor expression and axon targeting of olfactory neurons. *J. Neurosci.* **28**, 7121–7129 (2008). doi: 10.1523/JNEUROSCI.2063-08.2008; pmid: 18614681
26. Y. Togane *et al*., Spatio-temporal pattern of programmed cell death in the developing *Drosophila* optic lobe. *Dev. Growth Differ.* **54**, 503–518 (2012). doi: 10.1111/j.1440-169X.2012.01340.x; pmid: 22587328
27. Z. Song, K. McCall, H. Steller, DCP-1, a *Drosophila* cell death protease essential for development. *Science* **275**, 536–540 (1997). doi: 10.1126/science.275.5299.536; pmid: 8999799
28. J. Janssens *et al*., Decoding gene regulation in the fly brain. *Nature* **601**, 630–636 (2022). doi: 10.1038/s41586-021-04262-z; pmid: 34987221
29. T. Suzuki, M. Kaido, R. Takayama, M. Sato, A temporal mechanism that produces neuronal diversity in the *Drosophila* visual center. *Dev. Biol.* **380**, 12–24 (2013). doi: 10.1016/j.ydbio.2013.05.002; pmid: 23665475
30. J. Morante, C. Desplan, The color-vision circuit in the medulla of *Drosophila*. *Curr. Biol.* **18**, 553–565 (2008). doi: 10.1016/j.cub.2008.02.075; pmid: 18403201
31. A. T. Chao, W. M. Jones, A. Bejsovec, The HMG-box transcription factor SoxNeuro acts with Tcf to control Wg/Wnt signaling activity. *Development* **134**, 989–997 (2007). doi: 10.1242/dev.02796; pmid: 17267442
32. M. Schober, I. Rebay, N. Perrimon, Function of the ETS transcription factor Yan in border cell migration. *Development* **132**, 3493–3504 (2005). doi: 10.1242/dev.01911; pmid: 16014514
33. F. P. Davis *et al*., A genetic, genomic, and computational resource for exploring neural circuit function. *eLife* **9**, e50901 (2020). doi: 10.7554/eLife.50901; pmid: 31939737
34. I. Rebay, G. M. Rubin, Yan functions as a general inhibitor of differentiation and is negatively regulated by activation of the Ras1/MAPK pathway. *Cell* **81**, 857–866 (1995). doi: 10.1016/0092-8674(95)90006-3; pmid: 7781063
35. E. M. O'Neill, I. Rebay, R. Tjian, G. M. Rubin, The activities of two Ets-related transcription factors required for *Drosophila* eye development are modulated by the Ras/MAPK pathway. *Cell* **78**, 137–147 (1994). doi: 10.1016/0092-8674(94)90580-0; pmid: 8033205
36. C. Mayer *et al*., Developmental diversification of cortical inhibitory interneurons. *Nature* **555**, 457–462 (2018). doi: 10.1038/nature25999; pmid: 29513653
37. K. P. White, P. Hurban, T. Watanabe, D. S. Hogness, Coordination of *Drosophila* metamorphosis by two ecdysone-induced nuclear receptors. *Science* **276**, 114–117 (1997). doi: 10.1126/science.276.5309.114; pmid: 9082981
38. L. M. Riddiford, J. W. Truman, A. Nern, Juvenile hormone reveals mosaic developmental programs in the metamorphosing optic lobe of *Drosophila melanogaster*. *Biol. Open* **7**, bio034025 (2018). doi: 10.1242/bio.034025; pmid: 29618455
39. S. Jain *et al*., A global timing mechanism regulates cell-type-specific wiring programmes. *Nature* **603**, 112–118 (2022). doi: 10.1038/s41586-022-04418-5; pmid: 35197627
40. C. Skok Gibbs *et al*., High-performance single-cell gene regulatory network inference at scale: The Inferelator 3.0. *Bioinformatics* **38**, 2519–2528 (2022). doi: 10.1093/bioinformatics/btac117; pmid: 35188184
41. T. Schacht, M. Oswald, R. Eils, S. B. Eichmüller, R. König, Estimating the activity of transcription factors by the effect on their target genes. *Bioinformatics* **30**, i401–i407 (2014). doi: 10.1093/bioinformatics/btu446; pmid: 25161226
42. Y. Z. Kurmangaliyev, J. Yoo, J. Valdes-Aleman, P. Sanfilippo, S. L. Zipursky, Transcriptional programs of circuit assembly in the *Drosophila* visual system. *Neuron* **108**, 1045–1057.e6 (2020). doi: 10.1016/j.neuron.2020.10.006; pmid: 33125872
43. T. Stuart *et al*., Comprehensive integration of single-cell data. *Cell* **177**, 1888–1902.e21 (2019). doi: 10.1016/j.cell.2019.05.031; pmid: 31178118
44. W. B. Grueber, L. Y. Jan, Y. N. Jan, Different levels of the homeodomain protein cut regulate distinct dendrite branching patterns of *Drosophila* multidendritic neurons. *Cell* **112**, 805–818 (2003). doi: 10.1016/S0092-8674(03)00160-0; pmid: 12654247
45. M. Kurusu *et al*., A screen of cell-surface molecules identifies leucine-rich repeat proteins as key mediators of synaptic target selection. *Neuron* **59**, 972–985 (2008). doi: 10.1016/j.neuron.2008.07.037; pmid: 18817735
46. P. Kratsios *et al*., An intersectional gene regulatory strategy defines subclass diversity of *C. elegans* motor neurons. *eLife* **6**, e25751 (2017). doi: 10.7554/eLife.25751; pmid: 28677525
47. O. Hobert, P. Kratsios, Neuronal identity control by terminal selectors in worms, flies, and chordates. *Curr. Opin. Neurobiol.* **56**, 97–105 (2019). doi: 10.1016/j.conb.2018.12.006; pmid: 30665084
48. T. A. Holton, D. Pisani, Deep genomic-scale analyses of the metazoa reject Coelomata: Evidence from single- and multigene families analyzed under a supertree and supermatrix paradigm. *Genome Biol. Evol.* **2**, 310–324 (2010). doi: 10.1093/gbe/evq016; pmid: 20624736
49. M. Fitzgerald, N. Sotuyo, D. J. Tischfield, S. A. Anderson, Generation of cerebral cortical GABAergic interneurons from pluripotent stem cells. *Stem Cells* **38**, 1375–1386 (2020). doi: 10.1002/stem.3252; pmid: 32638460
50. Z. Xu *et al*., Direct conversion of human fibroblasts to induced serotonergic neurons. *Mol. Psychiatry* **21**, 62–70 (2016). doi: 10.1038/mp.2015.101; pmid: 26216300
51. M. Caiazzo *et al*., Direct generation of functional dopaminergic neurons from mouse and human fibroblasts. *Nature* **476**, 224–227 (2011). doi: 10.1038/nature10284; pmid: 21725324
52. N. Konstantinides, C. Desplan, Neuronal differentiation strategies: Insights from single-cell sequencing and machine learning. *Development* **147**, dev193631 (2020). doi: 10.1242/dev.193631; pmid: 33293292
53. H. Li *et al*., Classifying *Drosophila* olfactory projection neuron subtypes by single-cell RNA sequencing. *Cell* **171**, 1206–1220.e22 (2017). doi: 10.1016/j.cell.2017.10.019; pmid: 29149607
54. A. M. Rossi, C. Desplan, Extrinsic activin signaling cooperates with an intrinsic temporal program to increase mushroom body neuronal diversity. *eLife* **9**, e58880 (2020). doi: 10.7554/eLife.58880; pmid: 32628110

ACKNOWLEDGMENTS

We thank all members of the Desplan and Bonneau laboratories; O. Hobert, R. Mann, and D. Jabaudon for helpful discussions; C. Doe, S. Aerts, J. Blau, E. Mazzoni, R. Hiesinger, N. Konstantinides, D. Chen, R. Loker, and S. Mukherjee for critical reading of the manuscript; D. Krantz, I. Rebay, C.-T. Chien, W. Grueber, and J. Rister for reagents; Y.-C. Chen for help with plotting; J. Janssens and S. Aerts for sharing the snATAC-seq data ahead of publication; and G.-A. Saldi for help with network inference. **Funding:** This work was supported by the National Institutes of Health (NIH grants EY13010 and EY017916 to C.D. and R01HD096770, R01CA229235, and RM1HG011014 to R.B.) and the Simons Foundation. M.N.O. was a Leon Levy Neuroscience Fellow and is supported by the National Institute of Neurological Disorders and Stroke (NIH grant K99NS125117). C.S.G. is supported by National Science Foundation award 1922658 to the New York University Center for Data Science. I.H. has been supported by Human Frontier Science Program Postdoctoral Fellowship LT000757/2017-L and by a senior postdoctoral fellowship from the Kimmel Center for Stem Cell Biology. **Author contributions:** M.N.O., R.B., and C.D. conceived the project. M.N.O. designed all experiments. C.S.G. developed and optimized the Inferelator workflows. M.N.O., I.H., and M.S. performed the experiments. M.N.O. and C.S.G. analyzed the data. M.N.O., C.S.G., and C.D. wrote the manuscript. All authors edited the manuscript. **Competing interests:** The authors declare no competing interests. **Data availability:** All data supporting the conclusions in this manuscript can be found in the main text or the supplemental materials. Raw and processed scRNA-seq data are publicly accessible on GEO with identifier GSE199734). Newly created materials from this study may be requested from the corresponding authors. **License information:** Copyright © 2022 the authors, some rights reserved; exclusive licensee American Association for the Advancement of Science. No claim to original US government works. https://www.science.org/about/science-licenses-journal-article-reuse

SUPPLEMENTARY MATERIALS

science.org/doi/10.1126/science.add1884
Materials and Methods
Figs. S1 to S9
Tables S1 to S6
FACS Gating Strategy
References (*55*–*66*)
MDAR Reproducibility Checklist

Submitted 25 May 2022; accepted 17 November 2022
Published online 8 December 2022
10.1126/science.add1884

RESEARCH ARTICLE SUMMARY

NEUROSCIENCE

Mesolimbic dopamine release conveys causal associations

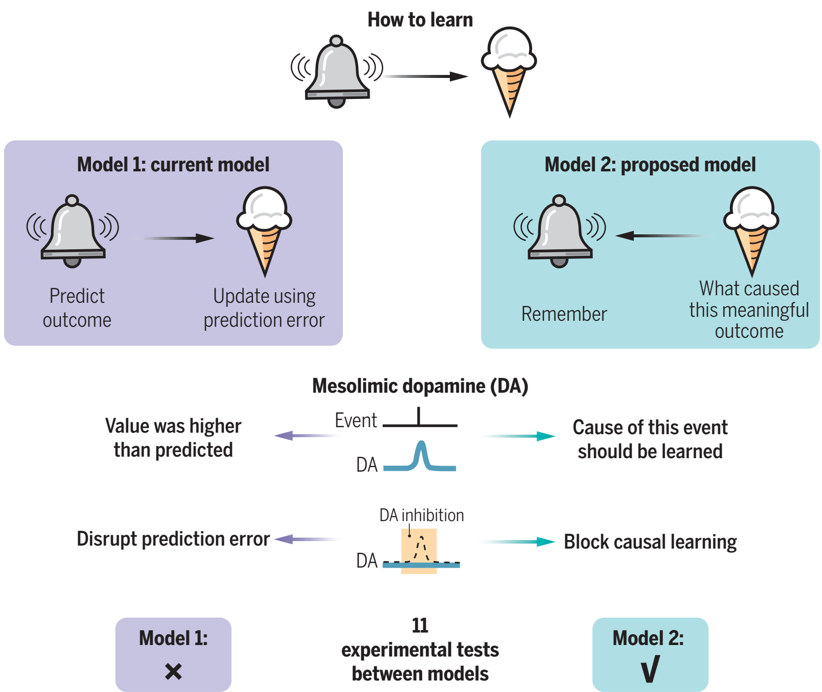
Huijeong Jeong, Annie Taylor, Joseph R Floeder, Martin Lohmann, Stefan Mihalas, Brenda Wu, Mingkang Zhou, Dennis A Burke, Vijay Mohan K Namboodiri*

INTRODUCTION: How do animals learn to prospectively predict delayed outcomes such as rewards from environmental cues? Considerable evidence shows that the neuromodulator dopamine is critical for such associative learning. This evidence has supported the hypothesis that midbrain dopamine neurons and nucleus accumbens dopamine release signal a temporal difference (TD) reward prediction error (RPE)—the difference between received and predicted reward. Hence, it is widely believed that animals use the TD algorithm to learn reward predictions. Recent results, however, suggest that dopamine signaling may not be fully consistent with RPEs. Despite this, the TDRPE hypothesis remains the best explanation of associative learning in the brain because no alternate model exists that successfully explains experimental observations inconsistent with TDRPE while also capturing experimental phenomena currently best explained by TDRPE.

RATIONALE: Here, we propose a new theory of associative learning. Since causes must precede outcomes, we propose that animals learn associations by looking back in memory to infer causes of meaningful outcomes such as rewards. For instance, imagine a child learning that the bell of an ice cream van predicts ice cream. Learning what cues precede ice cream (retrospective) is simpler than learning the future outcome of a near-infinite number of cues, only a few of which may result in ice cream (prospective). Thus, once a meaningful outcome such as ice cream is realized, the child can look back in memory to infer that the bell causes ice cream. Such learning only requires a memory of the previous bell when ice cream is received, and not active maintenance of predictions of ice cream prior to its receipt. We developed a model based on this concept—adjusted net contingency for causal relations (ANCCR, pronounced "anchor")—and tested whether this model is capable of learning reward predictions and explaining nucleus accumbens dopamine release better than TDRPE. In this model, a current event is considered a "meaningful causal target" (i.e., an event whose cause should be learned) when it is either innately meaningful (e.g., ice cream) or when it has been learned to be a cause of other meaningful causal targets (e.g., bell of ice cream van after it has been learned to be a cause of ice cream). Our central hypothesis is that mesolimbic dopamine conveys the learned meaningfulness of events by signaling ANCCR and guides causal learning of the current event.

RESULTS: We first showed using simulations that ANCCR identifies relationships between events spread in time (e.g., cues and rewards) better than TD without loss of generality across timescales. Next, we showed that many classic experimental results supporting TDRPE coding are also consistent with ANCCR signaling. Thus, we sought to test dopamine activity during experiments that distinguish these two hypotheses. To this end, we devised eleven experimental tests that are capable of qualitatively distinguishing between both hypotheses. We performed these tests by using fiber photometry of an optical dopamine sensor (dLight1.3b) to measure nucleus accumbens dopamine release. We did so across tasks including repeated exposure to random rewards, variations of cue-reward learning, and sequential conditioning with and without optogenetic inhibition of dopamine release. In all cases, we observed that the results were inconsistent with TDRPE but consistent with ANCCR.

CONCLUSION: Collectively, these results demonstrate that dopamine function can be better understood as providing a signal to initiate learning of causes of a meaningful stimulus. These results reshape current understanding of the algorithms and neural mechanisms of associative learning in the brain. ■



Retrospective causal learning of meaningful outcomes. How do we learn that environmental stimuli (e.g., bell of ice cream van) predict rewards (e.g., ice cream)? The standard model learns prospectively using prediction errors. Here, we present an alternative that learns predictions using retrospective identification of causes of meaningful outcomes. These models make different predictions about mesolimbic dopamine, a critical controller of learning. Our data support retrospective causal learning.

The list of author affiliations is available in the full article online.
*Corresponding author. Email: vijaymohan.knamboodiri@ucsf.edu

Cite this article as H. Jeong *et al.*, *Science* 378, eabq6740 (2022). DOI: 10.1126/science.abq6740

READ THE FULL ARTICLE AT https://doi.org/10.1126/science.abq6740

RESEARCH ARTICLE

NEUROSCIENCE

Mesolimbic dopamine release conveys causal associations

Huijeong Jeong[1], Annie Taylor[2]†, Joseph R Floeder[2]†, Martin Lohmann[4], Stefan Mihalas[4,5], Brenda Wu[1], Mingkang Zhou[1,2], Dennis A Burke[1], Vijay Mohan K Namboodiri[1,2,3]*

Learning to predict rewards based on environmental cues is essential for survival. It is believed that animals learn to predict rewards by updating predictions whenever the outcome deviates from expectations, and that such reward prediction errors (RPEs) are signaled by the mesolimbic dopamine system—a key controller of learning. However, instead of learning prospective predictions from RPEs, animals can infer predictions by learning the retrospective cause of rewards. Hence, whether mesolimbic dopamine instead conveys a causal associative signal that sometimes resembles RPE remains unknown. We developed an algorithm for retrospective causal learning and found that mesolimbic dopamine release conveys causal associations but not RPE, thereby challenging the dominant theory of reward learning. Our results reshape the conceptual and biological framework for associative learning.

How do animals learn to associate environmental cues with delayed outcomes such as rewards? It is widely believed that they learn a prospective prediction of how often reward follows a given cue. A simple way to learn such prospective predictions is to update one's prediction every time the outcome following a cue deviates from the prediction (Fig. 1, A and B). Such violations of reward predictions are commonly called reward prediction errors (RPEs). The simplest model in this family is the Rescorla-Wagner model (*1*). Temporal difference reinforcement learning (TDRL) models extend the Rescorla-Wagner model to account for cue-outcome delays and are the most widely accepted models of reward learning (*2*, *3*). To account for delays, these models typically propose that a sequential pattern of neural activities ("states") tiles temporal delays and propagates predictions from the cue to the reward (Fig. 1B). TDRL RPE has been successful at explaining the activity dynamics of dopaminergic cell bodies and release in the nucleus accumbens (*4*–*13*). Hence, TDRL RPE has become the dominant theory regarding dopamine's role as the critical regulator of behavioral learning (*14*–*17*).

An alternative approach to learning cue-reward associations is to infer the cause of meaningful outcomes such as rewards (*18*–*20*) (Fig. 1, A and C). Because causes must precede outcomes, a viable approach to infer whether a cue causes a reward is to learn whether the cue consistently precedes a reward. Predicting the future is highly demanding in a cue-rich environment but inferring the cause of a rarer meaningful outcome simply requires a memory of previous experience. If an animal knows that a stimulus it just received is meaningful (e.g., a reward), it can look back in memory to infer its cause. Given the central role of dopamine in learning, we hypothesized that dopamine may guide retrospective causal learning instead of conveying RPEs. Though the differences between prospective and retrospective learning may not be apparent at first glance, we show that these models make highly divergent predictions about mesolimbic dopamine dynamics. We directly test between these models regarding the role of dopamine in associative learning.

A retrospective causal learning algorithm

Although some stimuli are innately meaningful, others acquire meaning after it is learned that they cause other meaningful stimuli (e.g., a cue that predicts a reward becomes meaningful). We denote stimuli whose cause should be learned by the animal as a "meaningful causal target" and propose that mesolimbic dopamine signals whether a current event is a meaningful causal target (Fig. 1C and figs. S1 and S2). We propose a causal inference algorithm that infers whether a cue is a cause of reward by measuring whether it precedes the reward more than that expected by chance (Fig. 1C and fig. S2), then converting this to a prospective prediction signal using Bayes' rule (fig. S3) (supplementary note 1), and finally using the net contingency between a cue and reward to build a cognitive map of causal associations (*20*) (Fig. 1C and fig. S4).

We developed this algorithm to address problematic temporal assumptions that are foundational to common conceptions of TDRL, which result in a nonscalable representation of time (*21*). We tested whether this new algorithm learns causal relationships without loss of generality across timescales. Consistent with this and unlike TDRL, our algorithm learns the underlying causal structure of a variety of complex environments across two orders of magnitude of timescales and explains well-established behavioral observations of the timescale invariance of learning (figs. S5 and S6). The algorithm proposes that meaningful causal targets are signaled by an adjusted net contingency for causal relations (ANCCR, pronounced "anchor") (fig. S4). The ANCCR-based causal learning model is consistent with simulations of classical results supporting the RPE coding hypothesis including dopaminergic responses to reward magnitude and probability, blocking, unblocking, overexpectation, conditioned inhibition, and trial-by-trial update of action probabilities (Fig. 2). It is also consistent with the observation that apparent negative RPEs in dopamine responses are not as strong as positive RPEs of the same magnitude, even without assuming a floor effect in dopamine responses. Therefore, we reasoned that mesolimbic dopamine release has been tested only under conditions in which the ANCCR and RPE hypotheses make similar predictions, and that dopamine release may convey ANCCR instead of RPE.

In most behavioral tasks, prospective and retrospective associations are highly correlated and difficult to separate. To distinguish between the two hypotheses (RPE or ANCCR signaling by mesolimbic dopamine release), we performed eleven experimental tests. To maximize our ability to distinguish the models for strong inference (*22*), we designed the experiments such that the predictions of the two hypotheses are qualitatively different and often opposing. Because it has been proposed that distinct dopaminergic systems exist in the midbrain and that only some faithfully signal RPE (*23*–*30*), we tested these predictions by optically measuring sub-second mesolimbic dopamine release in the nucleus accumbens core (NAcc), a projection widely believed to encode RPE and shown to mediate Pavlovian learning (*8*–*10*, *12*, *31*–*33*) [by contrast, see (*34*)] (Fig. 3A and fig. S7). We did so in mice using fiber photometry of the dopamine sensor dLight 1.3b expressed in NAcc (*7*, *35*).

Tests 1 and 2 (unpredicted rewards)

We first tested between the two hypotheses in a simple experiment with divergent predictions. We presented naïve head-fixed mice with no experience in any laboratory behavior task with random unpredicted drops of a 15%

[1]Department of Neurology, University of California, San Francisco, CA, USA. [2]Neuroscience Graduate Program, University of California, San Francisco, CA, USA. [3]Weill Institute for Neuroscience, Kavli Institute for Fundamental Neuroscience, Center for Integrative Neuroscience, University of California, San Francisco, CA, USA. [4]Allen Institute for Brain Science, Seattle, WA, USA. [5]Department of Applied Mathematics, University of Washington, Seattle, WA, USA.
***Corresponding author. Email: vijaymohan.knamboodiri@ucsf.edu**
†These authors contributed equally to this work.

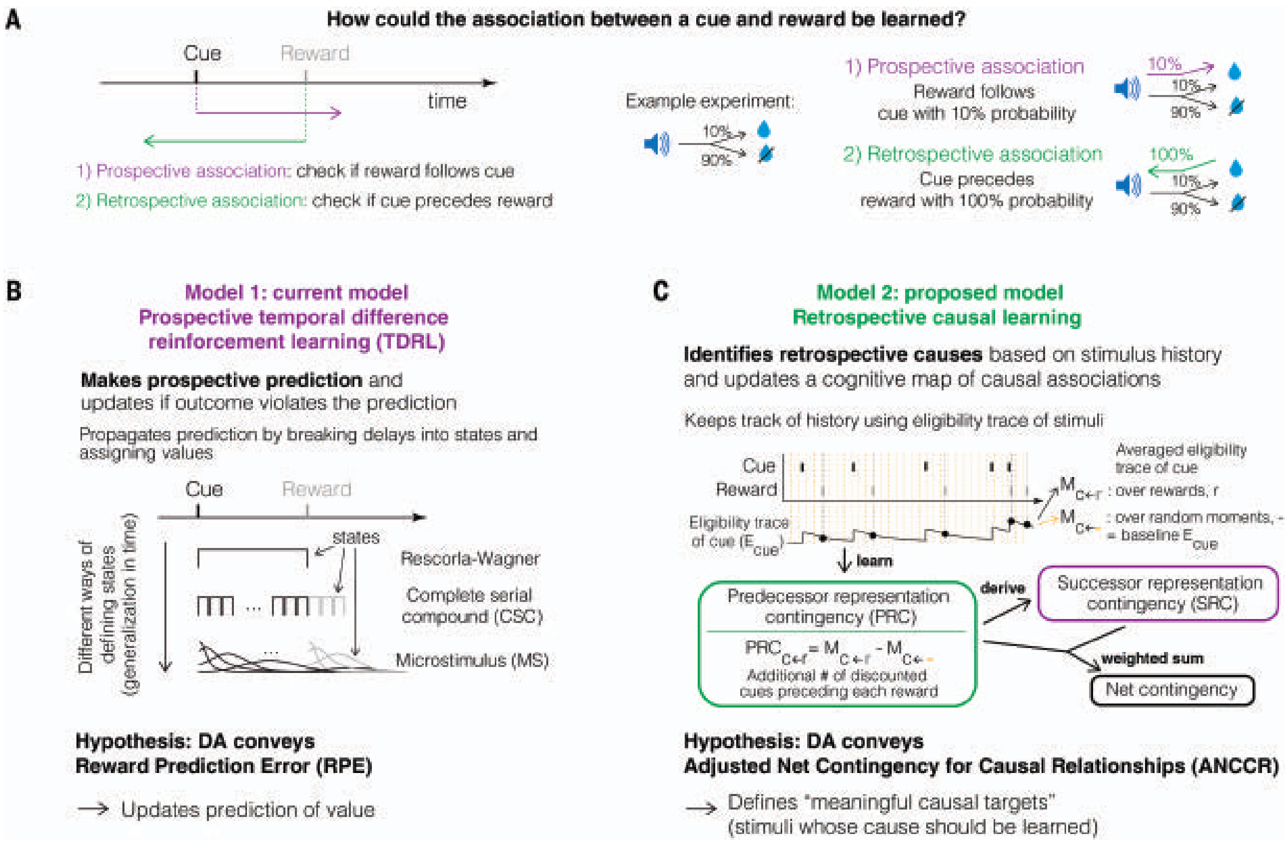


Fig. 1. An algorithm for uncovering causal associations in an environment. (**A**) Animals can learn cue-reward associations either prospectively ("does reward follow cue?") or retrospectively ("does cue precede reward?"). (**B**) The dominant model for cue-reward learning is temporal difference reinforcement learning, in which the prospective association between a cue and reward is learned, i.e., a measure of how often the reward follows the cue (cue value). To this end, the algorithm looks forward from a cue to predict upcoming rewards. When this prediction is incorrect, the original prediction is updated using a reward prediction error (RPE). The simplest of this family of models is the Rescorla-Wagner model which does not consider the delay between cue and reward. Temporal difference reinforcement learning (TDRL) algorithms extend this simple model to account for the cue-reward delay by modeling it as a series of states that measure time elapsed since stimulus onset. Two such examples are shown. (**C**) Here, we propose an algorithm which retrospectively learns the causes of meaningful stimuli such as rewards (figs. S1 to S4). Because causes precede outcomes, causal learning only requires a memory trace of the past. In our mechanistic model, a memory trace of prior stimuli is maintained using an exponentially-decaying eligibility trace for a stimulus (*77*), which allows the online calculation of the experienced rate of this stimulus (*78*). We hypothesized that mesolimbic dopamine activity signals ANCCR, a quantity that allows measurement of whether an experienced stimulus is a meaningful causal target.

sucrose solution delivered with an exponential inter-reward interval (IRI) distribution (mean 12 seconds), while recording mesolimbic dopamine release in NAcc. In this task, the timing of individual sucrose deliveries cannot be anticipated based on the previous delivery but the average rate of sucrose delivery is fixed (once every 12 seconds on average). Because the animal is experimentally naïve with no history of receiving sucrose before the onset of the experiment, the RPE hypothesis predicts high dopamine response to sucrose during early exposures. This is because the sucrose is highly unpredicted initially. With repeated exposure to the context, the RPE is predicted to decrease slightly as the context becomes a predictor of the reward. More formally, the internal IRI "states" in TDRL acquire positive value with experience (see supplementary note 2 for a consideration of a semi-Markov state space in TDRL) (*36*). Since RPE is the difference between the value of sucrose and the value of the IRI state that preceded the sucrose delivery, RPE will reduce at sucrose delivery with repeated experience (Fig. 3, B and C).

By contrast, the ANCCR hypothesis predicts that the response to sucrose will increase with repeated experience. This is because the predicted sucrose response is proportional to the difference between the average rate of previous sucrose deliveries calculated at a given sucrose delivery (including the current sucrose delivery) and the baseline average rate of previous sucrose deliveries (Fig. 3B). Because both of these quantities are initially low in naïve animals that have no experience with sucrose, ANCCR of sucrose is low early in this task. ANCCR eventually reaches an asymptote of ~1 times the incentive value of sucrose (see methods) because the rate of sucrose calculated just before a sucrose delivery (i.e., excluding the current sucrose) is equal to the baseline average rate of sucrose. Thus, the RPE hypothesis predicts that the dopamine response to sucrose will decrease over repeated experiences whereas the ANCCR hypothesis predicts that the response will increase. Testing these differential predictions formed Test 1 (Fig. 3, B and C).

Observed mesolimbic dopamine release was consistent with ANCCR but not RPE (Fig. 3, D and E). Every animal showed an increasing sucrose response that reached a high positive asymptote. This is entirely inconsistent with RPE—because RPE is the difference between a received and predicted reward, it cannot be higher than that for an unpredicted reward. These results also cannot be explained by RPE based on a slower learning of the incentive

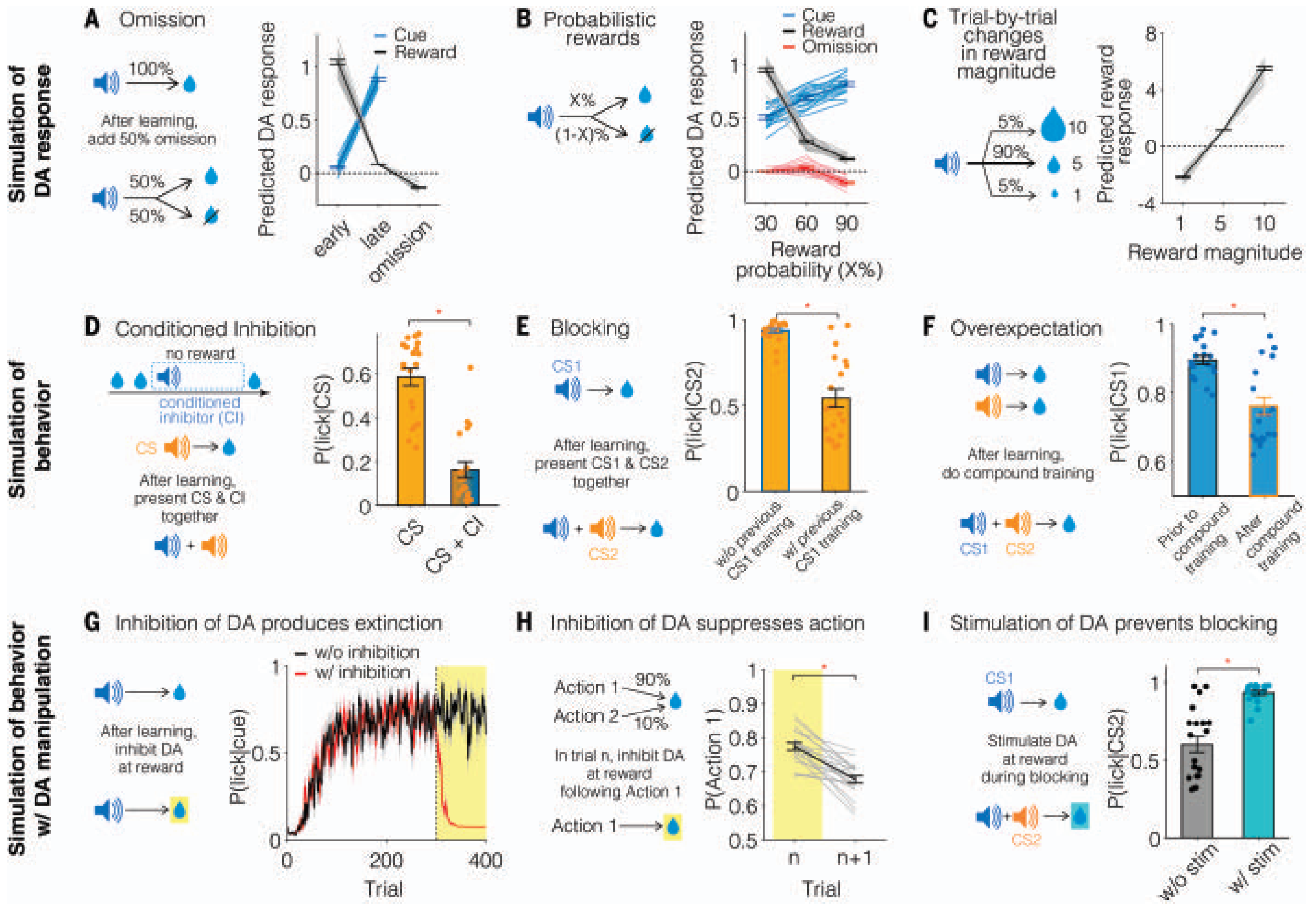


Fig. 2. The retrospective causal algorithm produces a signal similar to that of temporal difference reward prediction error (RPE) in simulations of previous experiments. (**A**) During simple conditioning of a cue-reward association, ANCCR appears qualitatively similar to an RPE signal, being low before and high after learning for the cue, whereas being high before and low after learning for the reward, and negative after omission of an expected reward. All error bars are standard error of the mean throughout the manuscript. (**B**) For probabilistic rewards, ANCCR produces qualitatively similar responses as RPE for cue, reward, and omission. Note that in (B) animals were never trained on a fully predicted reward. Slight differences in omission responses from [(A) to (B)] result from this difference. (**C**) For trial-by-trial changes in reward magnitude, ANCCR produces reward responses similar to that of positive and negative RPEs [similar to (*79*)]. (**D** to **F**) Simulations of ANCCR learning produces behavior consistent with conditioned inhibition (D), blocking (E), and overexpectation (F). (**G**) Simulated inhibition of dopamine at reward time in cue-reward conditioning produces extinction of learned behavior [similar to (*55*)]. (**H**) Simulation of dopamine inhibition at reward time produces trial-by-trial changes in behavior [similar to (*80*)]. (**I**) Simulation of unblocking due to dopamine activation at reward during blocking [similar to (*14*)].

value of sucrose; animals actively licked to consume sucrose at high rates starting from the first delivery, demonstrating that sucrose had high value (Fig. 3D and fig. S8). Such high motivation for sucrose from the onset of the experiment is consistent with well-known results that sugar is innately rewarding to mice (*37*). We also ruled out alternative hypotheses such as stress (supplementary note 3, fig. S8) or a nonspecific increase in responses to the consummatory action (lick bout onset) (fig. S8).

We next tested a "trial-by-trial" prediction in this experiment by measuring the correlation between the dopamine response to a sucrose delivery and the previous IRI. Getting the next reward sooner than predicted would produce a larger RPE than getting the next reward later. Hence, the RPE hypothesis predicts a negative correlation between the dopamine response to a sucrose delivery and the previous IRI (*36*) (Fig. 3, B and F) (supplementary note 4). However, ANCCR predicts a positive correlation because the ANCCR of reward involves the subtraction of the baseline reward rate. Because the baseline reward rate declines with longer IRI, ANCCR should increase with longer IRI (Fig. 3, B and F). This was Test 2.

The experimentally observed correlation between dopamine response to sucrose and the previous IRI was positive and was thereby consistent with ANCCR but not RPE. We also ruled out the hypothesis that this positive correlation is simply a result of an inability of animals to learn the mean IRI. This is because (i) the correlation was consistently positive for more than 800 experiences of sucrose (8 sessions) (fig. S8), (ii) mice learn the average IRI within at most two sessions (fig. S8), (iii) rodents can be as fast as Bayesian ideal observers in detecting changes in the rate of exponentially scheduled rewards (*38*), and (iv) even the original experiments that inspired the Rescorla-Wagner model showed that animals learn the mean inter-reinforcer interval despite unpredictable timing (*39*, *40*) [see (*41*) for a detailed discussion].

Tests 3 to 7 (Cue-reward learning)

Next, we studied dopamine response dynamics during cue-reward learning. We measured behavioral learning using anticipatory licking before the delivery of sucrose 3 seconds following onset of an auditory cue. Anticipatory licking reflects the prediction of an upcoming

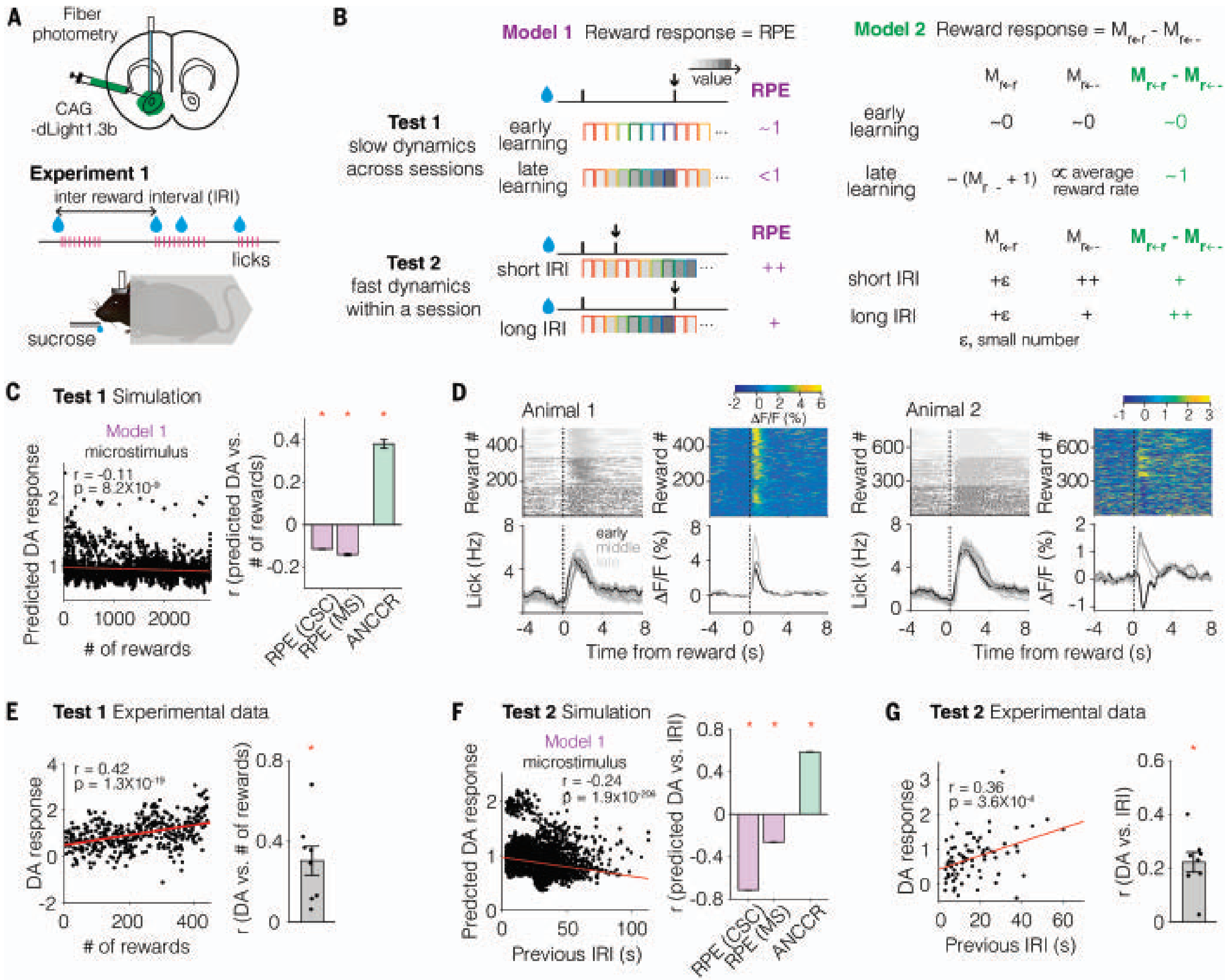


Fig. 3. The dynamics of dopamine responses to unpredicted rewards are consistent with ANCCR but not TDRL RPE. (**A**) For the first two tests, we gave experimentally naïve mice random unpredictable sucrose rewards immediately following head-fixation while recording subsecond dopamine release in NAcc using the optical dopamine sensor, dLight 1.3b (Methods). Animals underwent multiple sessions with 100 rewards each (n = 8 mice). (**B**) Theoretical predictions for both models. Test 1: As a naïve animal receives unpredicted rewards, the RPE model predicts high responses since the rewards are unpredicted. Nevertheless, since the inter-reward interval (IRI) states acquire value over repeated experience, the RPE at reward will be reduced with repeated experience. By contrast, ANCCR predicts low reward responses early since an experimentally naïve animal will have no prior expectation/eligibility trace of sucrose early in the task but will subsequently approach a signal that is ~1 times the incentive value of sucrose. Test 2: The reward response following a short IRI will be larger in the RPE model because the reward was received earlier than expected, thereby resulting in a negative correlation between dopamine reward response and the previous IRI. However, since ANCCR has a subtractive term proportional to the baseline reward rate ($M_{r\leftarrow-}$, in the figure), and baseline reward rate reduces with longer IRI, ANCCR predicts a positive correlation between dopamine reward response and the previous IRI. (**C**) Simulations confirming the intuitive reasoning from (B) for Test 1. CSC and MS stand for complete serial compound and microstimulus, respectively [one sample t test against a null of zero; t(99) = RPE (CSC), −65.74; RPE (MS), −27.57; ANCCR, 18.60; two-tailed P values = RPE (CSC), 1.7×10^{-83}, RPE (MS), 3.0×10^{-48}, ANCCR, 4.5×10^{-34}; n = 100 simulations]. (**D**) Licking and dopamine response from two example mice (rewards with less than 3 seconds previous IRI were excluded to avoid confounding by ongoing licking responses). Though not our initial prediction, ANCCR can even account for the negative unpredicted sucrose response from Animal 2 (fig. S8). (**E**) Quantification of correlation between dopamine response and number of rewards. The left panel shows the data from an example animal and the right panel shows the population summary across all animals [one sample t test against a null of zero; t(7) = 4.40, two-tailed P = 0.0031; n = 8 animals]. Reward response was defined as the difference of area under the curve (AUC) of fluorescence trace between reward and baseline period (Methods). (**F**) Simulations confirming the intuitive reasoning from (B) for Test 2 [one sample t test against a null of zero; t(99) = RPE (CSC), -1.7×10^{3}, RPE (MS), −151.28, ANCCR, 335.03; two-tailed P values = RPE (CSC), 5.0×10^{-223}, RPE (MS), 6.3×10^{-119}, ANCCR, 4.8×10^{-153}, n = 100 iterations]. (**G**) Quantification of correlation between dopamine response and the previous IRI for an example session (left) and the population of all animals [one sample t test against a null of zero; t(7) = 5.95, two-tailed $P = 5.7 \times 10^{-4}$, n = 8 animals]. The average correlation across all sessions for each animal is plotted in the bar graph.

reward across species, and this paradigm has provided some of the strongest support for TDRL RPE coding (*4*, *5*, *42*–*45*). During cue-reward learning, both RPE and ANCCR predict that dopamine responses to the cue will be low early in learning and high late in learning. Thus, the increase in dopamine response to the cue can be used as a measure of dopaminergic learning (defined as dopaminergic signaling related to the external cue-reward association). The RPE hypothesis predicts a tight relationship between the dynamics of behavioral and dopaminergic learning (Fig. 4A). This is because TDRL RPE updates the value signal used for behavioral learning, and dopaminergic signaling in NAcc is necessary for the learning of anticipatory licking in head-fixed mice (*33*). By contrast, the ANCCR of the cue is a continuously evolving estimate of whether the cue is itself a meaningful causal target due to its association with reward and hence is not predicted to evolve in lockstep with the behavior. Indeed, in the ANCCR hypothesis, associations are learned first and timing second: behavioral learning requires the threshold crossing of ANCCR to learn a causal model of the world ("cue causes reward"), followed by the separate learning of the temporal delay between cue and reward ("cue causes reward after a 3 second delay"). Only then does a timed decision signal for behavior become available (fig. 4B and fig. S2). Thus, the ANCCR hypothesis predicts that the gradual dopaminergic learning of the cue response will significantly precede behavioral learning, and that behavioral learning will be much more abrupt than dopaminergic learning since it requires an internal threshold crossing of the net contingency between cue and reward (Test 3) (supplementary note 5). The observed dopaminergic dynamics during learning were consistent with ANCCR but not RPE: dopamine response to CS+ was evident long before animals showed anticipatory licking (fig. 4, B and F, and fig. S9). In fact, dopamine cue responses were at their peak by the time of behavioral acquisition (fig. S10).

Further, when a learned delay between cue onset and reward (3 seconds) is extended permanently to a new, longer delay (9 seconds), RPE predicts that as animals learn the longer delay and suppress anticipatory licking at the previous short delay, there will be a concomitant reduction in the dopamine cue response due to temporal discounting (*46*). By contrast, ANCCR predicts little to no change in the dopamine cue response as the structure of the task is largely unchanged (Test 4, Fig. 4G and figs. S9 and S10; intuitively, relative to the long intertrial interval, the cue-reward delay is still short). Experimentally, we observed that although animals learned the new delay rapidly, dopaminergic cue responses showed no significant change (Fig. 4, G to I). After the extension of the cue-reward delay, RPE predicts a suppression of dopamine after the old delay expires without reward. Because the increase in cue-reward delay is permanent [unlike in prior experiments (*45*)], ANCCR predicts that the delay representation in the internal causal model of the animal would be updated to reflect the new delay. This predicts no reward omission response at the old delay (3 seconds) after the increase in the delay (9 seconds). Thus, ANCCR predicts no negative omission response after the old delay expires without reward. (Test 5). Experimentally, we observed no suppression of dopamine response at 3 seconds in this experiment but did observe suppression in a separate experiment when the reward was indeed omitted (Fig. 4J and fig. S10).

Next, we tested extinction of a learned cue-reward association. Extinction of a learned association does not cause unlearning of the original association (*47*). However, TDRL learns a zero-cue value following extinction, thereby predicting that the dopaminergic cue response will reduce to zero concomitant with behavioral learning. However, ANCCR includes the measurement of a retrospective association between the cue and reward. This association does not update without rewards and hence does not degrade as a result of extinction. This "long-term memory" was observed previously in orbitofrontal neurons projecting to the ventral tegmental area, the region where the somata of the mesolimbic dopamine neurons reside (*19*). Hence, the ANCCR hypothesis predicts that dopamine responses will remain significantly positive long after animals learn to suppress anticipatory licking. This is because the cue remains a meaningful causal target despite extinction, even though animals can learn extinction by noting that the base rate of rewards in the context becomes zero. Thus, Test 6 investigated whether dopamine cue response remained positive long after extinction was behaviorally learned (Fig. 4, J to L). As predicted by ANCCR but not RPE, dopamine cue response remained significantly positive well after animals cease to behaviorally respond to the cues (Fig. 4, J to L), consistent with prior studies (*48*, *49*).

To test whether the significant positive dopamine responses following extinction reflect a retrospective association between the cue and reward, we selectively reduced the retrospective association without reducing the prospective association. We maintained the fixed reward following the cue but added unpredictable rewards during the intertrial interval. In this experiment, not all rewards are preceded by the cue (i.e., retrospective association is weak), but all cues are followed by reward (i.e., prospective association is high). ANCCR predicts a rapid drop in dopamine cue response whereas RPE predicts no change in cue response if TDRL only considers the cue-reward "trial period" (Test 7, fig. S10). The dopamine cue response remained significantly positive but decayed across trials faster than during extinction (Fig. 4, M to P).

Test 8 ("trial-less" cue-reward learning)

We performed another test related to the temporal scalability of TDRL versus retrospective causal inference (Test 8, Fig. 5). A key motivation for developing our model was that current TDRL models do not have a scalable representation of time and hence fail to learn the correct structure of even simple environments in which a cue predicts a reward at a fixed delay with 100% probability (fig. S6). We devised an experiment in which a single cue predicted the reward at a fixed delay with 100% probability, but the cue occurred unpredictably with an exponentially distributed intercue interval between 0 to 99 seconds. We reduced the cue duration to 250 ms to allow nearby occurrences of the cue to be separated in time and had a long trace interval (3 seconds) following cue offset until reward delivery. Animals learned the cue-reward association quickly in this modified "trial-less" task (fig. S11).

In this task, a cue will occasionally be presented during the wait from the previous cue to its associated reward (Fig. 5A). If the "trial period" for cue-reward tasks is considered as the interval between the cue and reward, the next "trial" can occasionally start before the previous trial is completed. During these "intermediate" cues, TDRL resets its prediction because it assumes a new trial has started without reward in the previous trial, thereby resulting in a negative RPE (i.e., the intermediate cue signals that the reward will now be further delayed; intuitively, the intermediate cue implies omission of reward after the previous cue). This results from the inability of TDRL to learn the correct structure of the task, which is that every cue occurrence causes a reward at a fixed delay (supplementary note 6).

On the other hand, ANCCR will learn that the intermediate cue is qualitatively similar to the previous cue because both predict reward, but because of a local increase in cue rate ANCCR predicts a lower but positive response to the intermediate cue (Fig. 5, A and B). We did not observe any negative dopamine response to the intermediate cue regardless of how the baseline was measured and instead observed a positive but weaker response, consistent with ANCCR but not RPE (Fig. 5, C and D, and fig. S11).

Tests 9 to 11 (backpropagation within a trial)

A critical postulate of the TDRL RPE account is that dopamine responses drive value learning of the immediately preceding state. We tested three predictions of this central postulate that are each inconsistent with ANCCR.

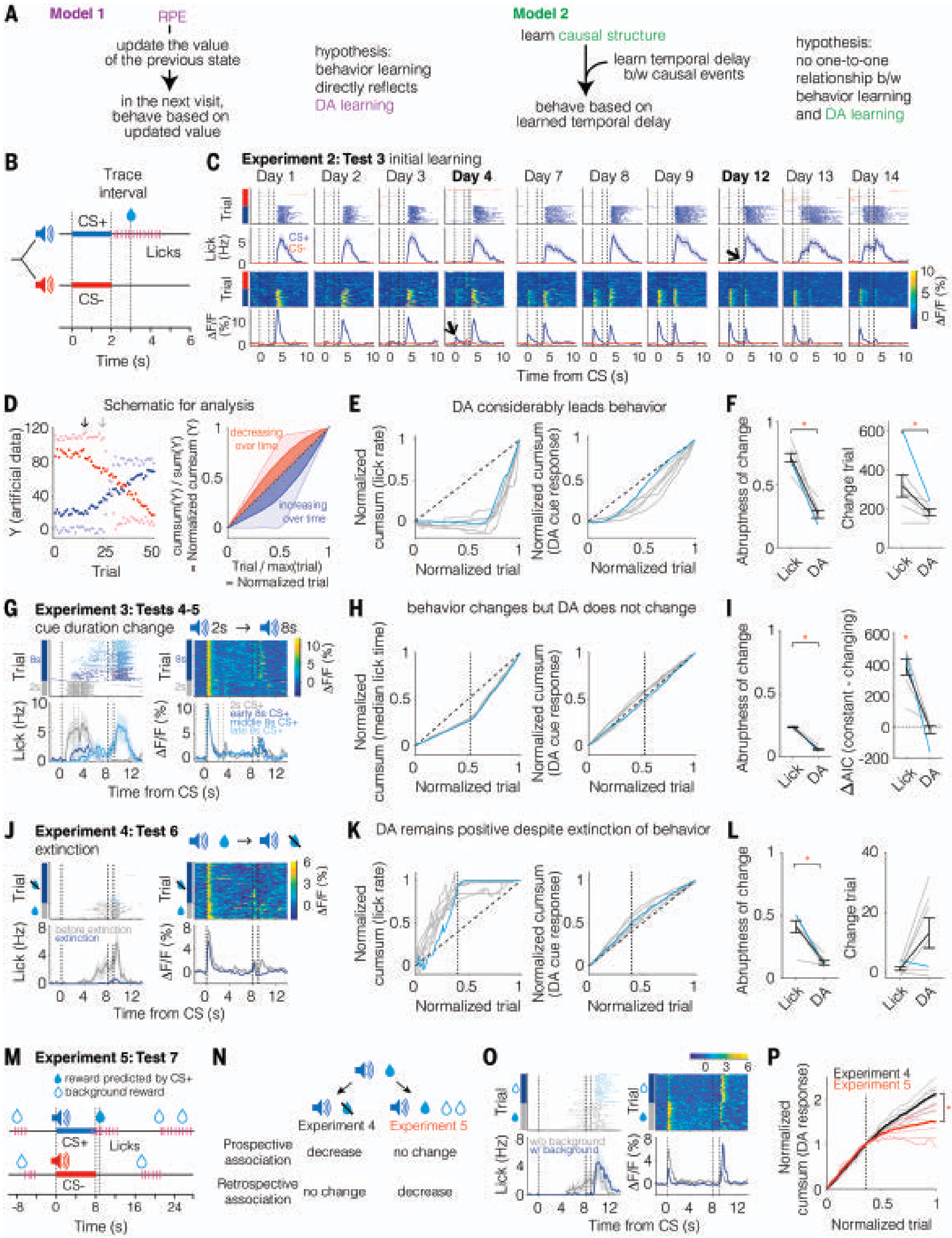


Fig. 4. The dynamics of dopamine responses during cue-reward learning are consistent with ANCCR, but not TDRL RPE. (**A**) TDRL predicts that dopaminergic and behavioral learning will be tightly linked during learning. However, the causal learning model proposes that there is no one-to-one relationship between behavioral and dopaminergic learning. (**B**) Schematic of a cue-reward learning task in which one auditory tone predicted reward (labeled CS+) while another had no predicted outcome (labeled CS−). (**C**) Licking and dopamine measurements from an example animal showing that the dopamine response to CS+ significantly precedes the emergence of anticipatory licking (day 4 versus 12 respectively, shown by arrows). (**D**) Schematic showing a cumulative sum (cumsum) plot of artificial time series data. A time series that increases over trials appears below the diagonal in the cumsum plot with an increasing slope over trials, and one that decreases over trials appears above the diagonal. Further, a sudden change in time series appears as a sudden change in slope in the cumsum plot. (**E** and **F**) Dopamine cue response evolution precedes behavior for all animals. Each line is one animal, with the blue line corresponding to the example from (C). Behavioral learning is much more abrupt than dopaminergic learning [paired t test for abruptness of change; $t(6) = 9.06$; two-tailed $P = 1.0 \times 10^{-4}$; paired t test for change trial; $t(6) = -2.93$; two-tailed $P = 0.0263$; $n = 7$ animals]. (**G**) Anticipatory licking and dopamine release in an example animal after increasing the cue duration from 2 to 8 seconds while maintaining a 1-second trace interval and a long ITI

(~33 seconds). Trials are shown in chronological order from bottom to top. The three vertical dashed lines indicate cue onset, cue offset, and reward delivery [also in (**J** and **O**)]. (**H** and **I**) Behavior is learned abruptly by all animals, but the dopaminergic cue response shows little to no change. The dashed vertical line is the trial at which the experimental condition transitions [in (**H**, **K**, and **P**)]. We tested for the lack of change by showing that the Akaike Information Criterion (AIC) is similar between a model assuming change and a model assuming no change. Paired *t* test for abruptness of change; t(6) = 22.92; two-tailed *P* = 4.52 × 10^{-7}; one-sample *t* test for ΔAIC against a null of zero; t(6) = 7.49 for lick, −0.86 for dopamine; two-tailed *P* = 2.9 × 10^{-4} for lick, 0.4244 for dopamine (*n* = 7 animals). (J) The dopaminergic cue response of an example animal remains positive well after it learns extinction of the cue-reward association. (**K** to **L**) Across all animals, the dopaminergic cue response remains significantly positive despite abrupt behavioral learning of extinction [paired *t* test for abruptness of change; t(6) = 5.67; two-tailed *P* = 0.0013; paired *t* test for change trial; t(6) = −2.40; two-tailed *P* = 0.0531; *n* = 7 animals]. (**M**) Experiment to reduce retrospective association while maintaining prospective association. (**N**) Two experiments that show specific reduction in either prospective or retrospective association. (**O**) Licking and dopamine release from an example animal. (**P**) Dopamine cue response reduces more rapidly during the background reward experiment in which the cue is followed consistently by a reward than during extinction in which there is no reward [paired *t* test; t(6) = −3.51; two-tailed *P* = 0.0126; *n* = 7 animals].

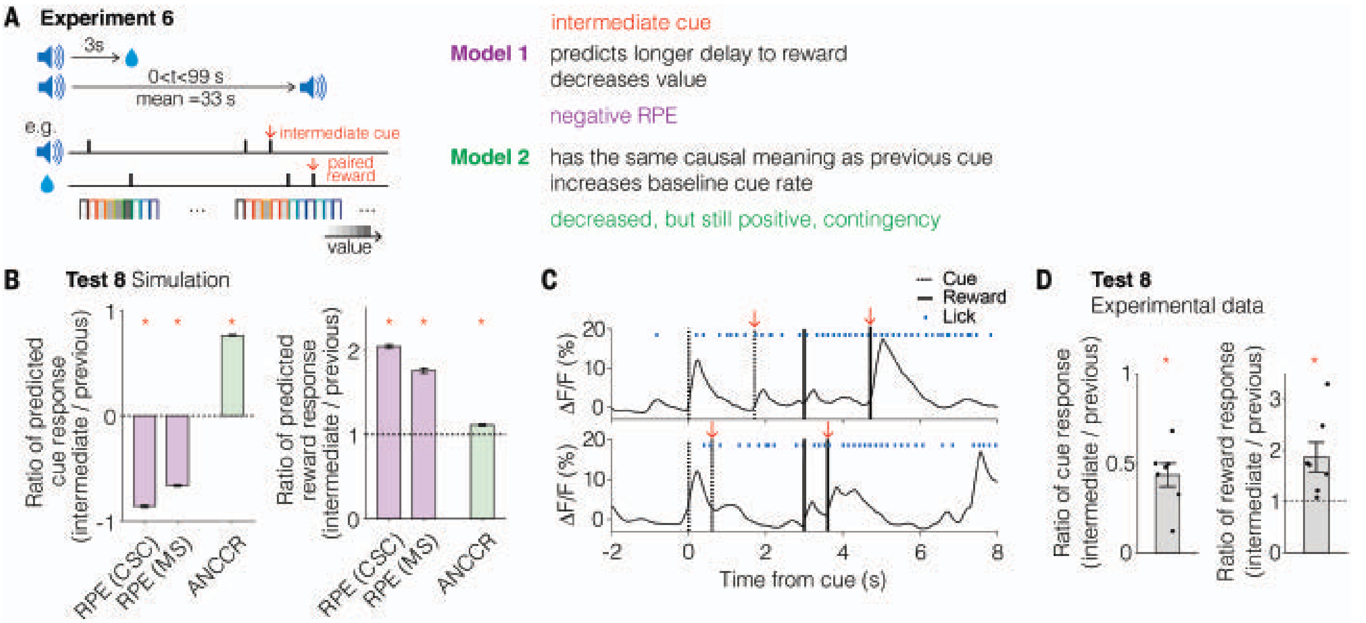


Fig. 5. Dopamine responses in a "trial-less" cue-reward task reflect causal structure like ANCCR but unlike TDRL RPE. (**A**) A "trial-less" cue-reward learning task. Here, a cue (250-ms duration) is consistently followed by a reward at a fixed delay (3-second trace interval). However, the cues themselves occur with an exponential intercue interval with a mean of 33 seconds. (**B**) Confirmation of these intuitions based on simulations (Methods) [One sample *t* test against a null of zero; t(99) = RPE (CSC), −114.74; RPE (MS), −181.32; ANCCR, 322.53; two-tailed *P* values = RPE (CSC), 4.1 × 10^{-107}; RPE (MS), 1.1 × 10^{-126}; ANCCR, 2.1 × 10^{-151}; *n* = 100 iterations]. Reward responses are predicted to be positive by both models [One sample *t* test against a null of one; t(99) = RPE (CSC), 87.67; RPE (MS), 62.86; ANCCR, 16.78; two-tailed *P* values = RPE (CSC), 1.2 × 10^{-95}; RPE (MS), 1.3 × 10^{-81}; ANCCR, 1.1 × 10^{-30}; *n* = 100 iterations]. (**C**) Example traces from one animal showing that the dopamine response to the intermediate cue is positive. (**D**) Quantification of the experimentally observed ratio between the intermediate cue response and the previous cue response [One sample *t* test against a null of zero; t(6) = 6.64, two-tailed *P* value = 5.6 × 10^{-4}; *n* = 7 animals], and reward response [One sample *t* test against a null of one; t(6) = 2.95; two-tailed *P* value = 0.0256; *n* = 7 animals].

The first is that during the acquisition of trace conditioning, dopamine response systematically backpropagates from the moment immediately prior to reward to the cue onset (*50*) (Test 9, Fig. 6A). Unlike TDRL RPE, ANCCR does not make such a prediction since delay periods are not broken into states in ANCCR. The second is that during sequential conditioning (cue1 predicts cue2 predicts reward), dopamine response first increases to cue2 and then increases to cue1 (Test 10, Fig. 6C). ANCCR instead predicts that dopamine responses to both cues will increase together and later diverge when cue2 is learned to be caused by cue1. The third is that artificially suppressing dopamine release from cue2 to reward during sequential conditioning will prevent learning of cue1 responses (Test 11, Fig. 6, E to H). By contrast, suppressing cue2 response in ANCCR only prevents the learning of the cue1→cue2 association and does not prevent the learning of the cue1 response.

We tested the first prediction using the animals that underwent the previous cue-reward learning. Our observations were not consistent with a backpropagating bump of activity and were instead consistent with an increase in cue response over trials of learning (Fig. 6B) (see supplementary note 9 for potential reasons for discrepancy with a recent study). To test the second and third predictions, we performed sequential conditioning with an experimental group receiving inhibition of dopaminergic cell bodies from cue2 to reward, and a no-opsin control group that received the same laser but no inhibition of dopamine neurons. We measured NAcc dopamine release in both groups. The control group allowed us to test the dynamics of dopamine responses during sequential conditioning in the absence of dopamine neuron inhibition (i.e., the second prediction). Consistent with ANCCR, we experimentally found that cue2 and cue1 responses increased together early in learning prior to separating later in learning (Fig. 6D).

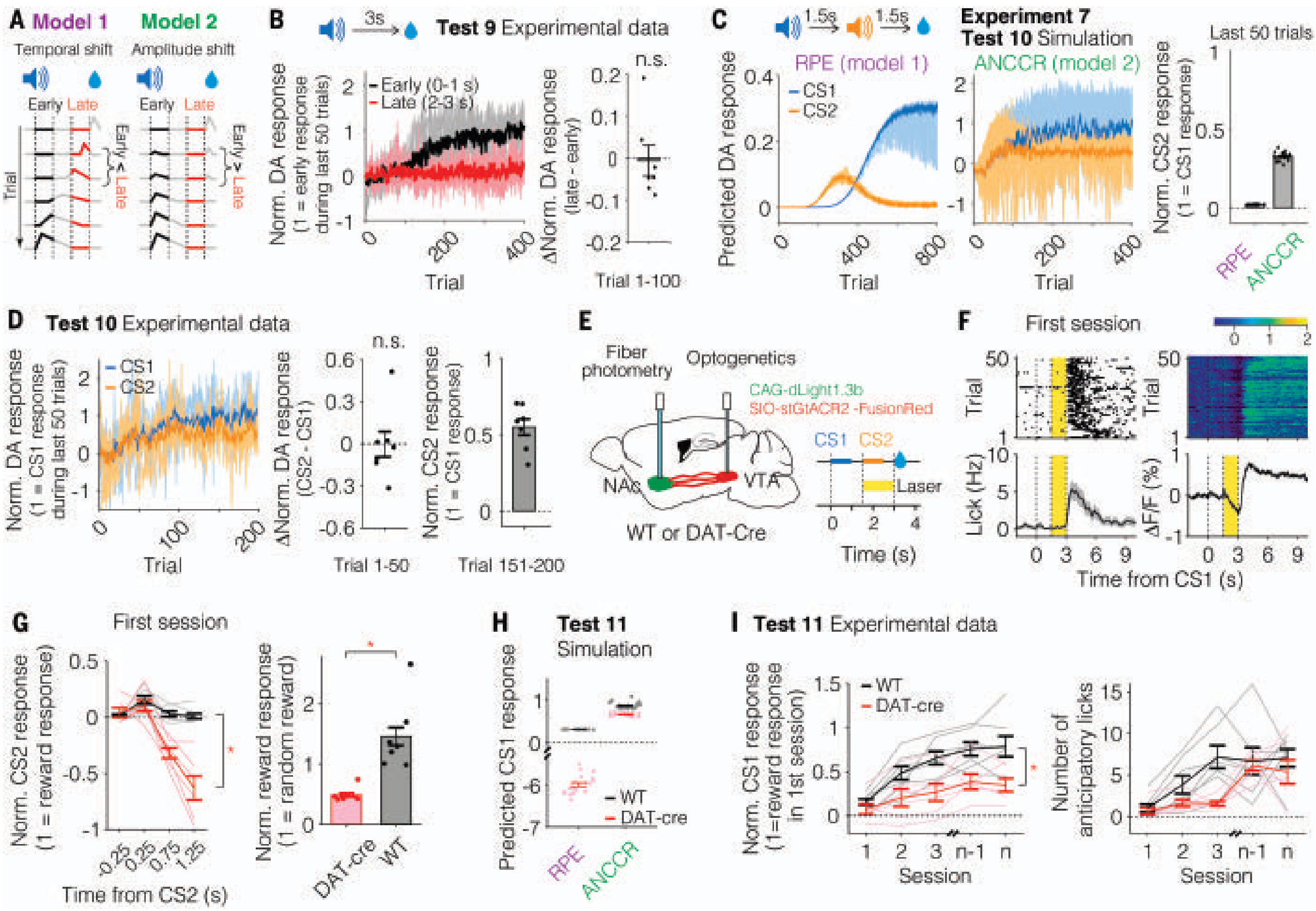


Fig. 6. No backpropagation of dopamine signals during learning. (**A**) Schematic of learning dynamics for pre-reward dopamine dynamics based on RPE or ANCCR signaling. Schematic was inspired from (*50*). If there is a temporal shift, the difference in dopamine response between early and late phases of a trial will be negative in the initial trials. (**B**) Dynamics of dopamine response during early and late periods within a trial over training (left), and their difference during the first 100 trials. (**C**) Simulated dynamics for dopamine responses to cues (CS1 and CS2) during sequential conditioning (left), and averaged CS2 response during the last 50 trials (right). (**D**) Experimental data showing dynamics of dopamine responses to cues (left). Response difference between two cues during early phase of learning (middle; similar to Fig. 6B, right) and CS2 response during late phase of learning (right; similar to Fig. 6C, right). (**E**) Schematic of optogenetic inhibition experiment during sequential conditioning for both experimental DAT-Cre animals receiving inhibition and control wild type animals receiving light but no inhibition. Animals received laser from CS2 until reward throughout conditioning. (**F**) Measured licking and dopamine responses on the first session of conditioning from an example experimental animal, showing robust inhibition. (**G**) Quantification of magnitude of inhibition during CS2 presentation prior to reward, and reward response. Both responses are measured relative to pre-CS1 baseline. (**H**) Predicted dopamine responses using simulations of RPE or ANCCR. (**I**) Experimental data showing CS1 response (left) and anticipatory licking (right) across sessions. Here, n represents the last session.

To test the third prediction, we first verified robust inhibition of mesolimbic dopamine release during the cue2→reward delay in the experimental group (~0.6 times the reward response on day 1 of conditioning) (supplementary note 10). With such strong inhibition, TDRL RPE predicted no behavioral learning in this experiment and a strong negative cue1 dopamine response (Fig. 6H and fig. S12). By contrast, ANCCR predicted largely intact learning of cue1 but with slower behavioral learning and reduced cue1 response (see supplementary note 10 for explanation). Consistent with ANCCR, we observed that every experimental animal learned the task and that mesolimbic dopamine acquired positive responses to cue1 in all experimental animals (Fig. 6I).

Discussion

The dynamics of mesolimbic dopamine release in NAcc were inconsistent with TDRL RPE across a multitude of experiments but remained consistent with a causal learning algorithm. The algorithm proposed here operates by testing whether a stimulus precedes reward beyond that expected by chance and by converting this association to a prospective prediction (supplementary note 7). Using this prediction, the algorithm learns a causal map of associations and signals whether a stimulus has become a meaningful causal target following such learning. Though our data are inconsistent with encoding of TDRL RPE by mesolimbic dopamine release, our framework is not inconsistent with prediction errors in general. Indeed, "prediction errors" related to event rates are a part of our framework (supplementary note 4).

The algorithm and results presented here provide a unified account of numerous published observations. Evidence across multiple species and brain regions shows that in addition to prospective associations, the brain stores memories of retrospective associations (*19*, *51*, *52*). Behavioral learning is also guided by retrospective associations (*18*, *53*). Dopamine responses remain significantly positive even for

fully predicted, delayed rewards (4, 46, 54–56). This is usually explained by appealing to an internal uncertainty about the delay (46) but occurs without any accounting of temporal uncertainty in our theory (Fig. 2A). Consistent with our theory, a previous study observed no correlation between temporal uncertainty of an animal and the dopaminergic response to a fully predicted, delayed reward (57). Under some settings, dopamine reward responses during cue-reward conditioning have been observed to increase during initial learning, before decreasing back (54). While this observation is not consistent with RPE, it naturally results from our algorithm if the animal had no exposure to the reward in the experimental context before conditioning, as was the case here (fig. S13). This might also explain why NAcc dopamine response to a predicted punishment might increase in some scenarios whereas the responses to repeated punishments at fixed intervals decrease (34) (punishments are also meaningful causal targets; see supplementary note 8). ANCCR also explains recent observations of dopamine ramps used in favor of the RPE hypothesis (58) (fig. S13). Our explanation is also consistent with dopamine ramps in the striatum reflecting a causal association between an action and reward (59). Finally, dopamine responses guide learning in a way that sometimes violates the predictions of model-free TDRL (17, 60–63). Our proposal that the dopaminergic system conveys whether cues are meaningful causal targets, thereby promoting the learning of their causes, explains these results (fig. S13).

Our work raises several questions for which reports in the literature suggest answers: First, how is retrospective cue-reward information conveyed to the dopaminergic system? Prior work suggests the orbitofrontal cortex as a source of this information (19) (fig. S14). Second, how do animals infer the appropriate timescales in the world? Currently, we simply assume that animals set the appropriate timescale of an environment based on knowledge of the inter-reward interval. As a more principled solution, recent work has suggested that multiple parallel systems with different time constants exist in the brain and can learn a timescale invariant representation of past time (64–67). Third, are there as-yet unknown state space assumptions that make TDRL RPE fit our data? We cannot rule out all possible assumptions of TDRL state spaces because there is unlimited flexibility in assuming the state space used by animals, thereby making them currently unfalsifiable (though see fig. S15). In the absence of such falsifiable assumptions, our work demonstrates that the TDRL algorithm with conventional state space assumptions does not explain the dynamics of dopamine release in NAcc. Fourth, does dopamine release in regions other than NAcc signal RPE? As mentioned in the introduction, we studied dopamine release in NAcc precisely because it is the region with the strongest support for the RPE hypothesis. Considering the theoretical advantages of ANCCR compared with TDRL RPE in learning associations between rates of events (figs. S6 and S15B), we believe that dopamine release in other regions might also be inconsistent with TDRL RPE, although this remains to be tested. Finally, since it has been demonstrated that animal behavior and neural activity for even simple Pavlovian associations may be explained by the learning of causal cognitive maps (68–71), is all associative learning, including for action-conditional cognitive maps (56, 59, 72–76), the product of causal inference? This remains to be addressed. Collectively, our data demonstrate that mesolimbic dopaminergic signaling in NAcc is inconsistent with the dominant theory of TDRL RPE signaling and instead guides a causal learning algorithm.

REFERENCES AND NOTES

1. R. A. Rescorla, A. R. Wagner, "A theory of Pavlovian conditioning: Variations in the effectiveness of reinforcement and nonreinforcement" in *Classical conditioning II: Current Research and Theory*, pp. 64–99 (Appleton-Century-Crofts, 1972).
2. Y. Niv, G. Schoenbaum, Dialogues on prediction errors. *Trends Cogn. Sci.* **12**, 265–272 (2008). doi: 10.1016/j.tics.2008.03.006; pmid: 18567531
3. Y. Niv, Reinforcement learning in the brain. *J. Math. Psychol.* **53**, 139–154 (2009). doi: 10.1016/j.jmp.2008.12.005
4. J. Y. Cohen, S. Haesler, L. Vong, B. B. Lowell, N. Uchida, Neuron-type-specific signals for reward and punishment in the ventral tegmental area. *Nature* **482**, 85–88 (2012). doi: 10.1038/nature10754; pmid: 22258508
5. W. Schultz, P. Dayan, P. R. Montague, A neural substrate of prediction and reward. *Science* **275**, 1593–1599 (1997). doi: 10.1126/science.275.5306.1593; pmid: 9054347
6. Y. K. Takahashi *et al*., Expectancy-related changes in firing of dopamine neurons depend on orbitofrontal cortex. *Nat. Neurosci.* **14**, 1590–1597 (2011). doi: 10.1038/nn.2957; pmid: 22037501
7. A. Mohebi *et al*., Dissociable dopamine dynamics for learning and motivation. *Nature* **570**, 65–70 (2019). doi: 10.1038/s41586-019-1235-y; pmid: 31118513
8. A. S. Hart, R. B. Rutledge, P. W. Glimcher, P. E. M. Phillips, Phasic dopamine release in the rat nucleus accumbens symmetrically encodes a reward prediction error term. *J. Neurosci.* **34**, 698–704 (2014). doi: 10.1523/JNEUROSCI.2489-13.2014; pmid: 24431428
9. J. J. Day, M. F. Roitman, R. M. Wightman, R. M. Carelli, Associative learning mediates dynamic shifts in dopamine signaling in the nucleus accumbens. *Nat. Neurosci.* **10**, 1020–1028 (2007). doi: 10.1038/nn1923; pmid: 17603481
10. P. E. M. Phillips, G. D. Stuber, M. L. A. V. Heien, R. M. Wightman, R. M. Carelli, Subsecond dopamine release promotes cocaine seeking. *Nature* **422**, 614–618 (2003). doi: 10.1038/nature01476; pmid: 12687000
11. M. P. Saddoris, F. Cacciapaglia, R. M. Wightman, R. M. Carelli, Differential Dopamine Release Dynamics in the Nucleus Accumbens Core and Shell Reveal Complementary Signals for Error Prediction and Incentive Motivation. *J. Neurosci.* **35**, 11572–11582 (2015). doi: 10.1523/JNEUROSCI.2344-15.2015; pmid: 26290234
12. M. P. Saddoris *et al*., Mesolimbic dopamine dynamically tracks, and is causally linked to, discrete aspects of value-based decision making. *Biol. Psychiatry* **77**, 903–911 (2015). doi: 10.1016/j.biopsych.2014.10.024; pmid: 25541492
13. H. M. Bayer, P. W. Glimcher, Midbrain dopamine neurons encode a quantitative reward prediction error signal. *Neuron* **47**, 129–141 (2005). doi: 10.1016/j.neuron.2005.05.020; pmid: 15996553
14. E. E. Steinberg *et al*., A causal link between prediction errors, dopamine neurons and learning. *Nat. Neurosci.* **16**, 966–973 (2013). doi: 10.1038/nn.3413; pmid: 23708143
15. C. Y. Chang *et al*., Brief optogenetic inhibition of dopamine neurons mimics endogenous negative reward prediction errors. *Nat. Neurosci.* **19**, 111–116 (2016). doi: 10.1038/nn.4191; pmid: 26642092
16. H.-C. Tsai *et al*., Phasic firing in dopaminergic neurons is sufficient for behavioral conditioning. *Science* **324**, 1080–1084 (2009). doi: 10.1126/science.1168878; pmid: 19389999
17. E. J. P. Maes *et al*., Causal evidence supporting the proposal that dopamine transients function as temporal difference prediction errors. *Nat. Neurosci.* **23**, 176–178 (2020). doi: 10.1038/s41593-019-0574-1; pmid: 31959935
18. C. R. Gallistel, A. R. Craig, T. A. Shahan, Contingency, contiguity, and causality in conditioning: Applying information theory and Weber's Law to the assignment of credit problem. *Psychol. Rev.* **126**, 761–773 (2019). doi: 10.1037/rev0000163; pmid: 31464474
19. V. M. K. Namboodiri *et al*., Single-cell activity tracking reveals that orbitofrontal neurons acquire and maintain a long-term memory to guide behavioral adaptation. *Nat. Neurosci.* **22**, 1110–1121 (2019). doi: 10.1038/s41593-019-0408-1; pmid: 31160741
20. V. M. K Namboodiri, G. D. Stuber, The learning of prospective and retrospective cognitive maps within neural circuits. *Neuron* **109**, 3552–3575 (2021). doi: 10.1016/j.neuron.2021.09.034; pmid: 34678148
21. V. M. K. Namboodiri, How do real animals account for the passage of time during associative learning? *Behav. Neurosci.* **136**, 383–391 (2022). doi: 10.1037/bne0000516; pmid: 35482634
22. J. R. Platt, Strong Inference: Certain systematic methods of scientific thinking may produce much more rapid progress than others. *Science* **146**, 347–353 (1964). doi: 10.1126/science.146.3642.347; pmid: 17739513
23. G. Heymann *et al*., Synergy of Distinct Dopamine Projection Populations in Behavioral Reinforcement. *Neuron* **105**, 909–920.e5 (2020). doi: 10.1016/j.neuron.2019.11.024; pmid: 31879163
24. W. Menegas *et al*., Dopamine neurons projecting to the posterior striatum form an anatomically distinct subclass. *eLife* **4**, e10032 (2015). doi: 10.7554/eLife.10032; pmid: 26322384
25. W. Menegas, K. Akiti, R. Amo, N. Uchida, M. Watabe-Uchida, Dopamine neurons projecting to the posterior striatum reinforce avoidance of threatening stimuli. *Nat. Neurosci.* **21**, 1421–1430 (2018). doi: 10.1038/s41593-018-0222-1; pmid: 30177795
26. S. Lammel, B. K. Lim, R. C. Malenka, Reward and aversion in a heterogeneous midbrain dopamine system. *Neuropharmacology* **76**, 351–359 (2014). doi: 10.1016/j.neuropharm.2013.03.019; pmid: 23578393
27. A. Lutas *et al*., State-specific gating of salient cues by midbrain dopaminergic input to basal amygdala. *Nat. Neurosci.* **22**, 1820–1833 (2019). doi: 10.1038/s41593-019-0506-0; pmid: 31611706
28. B. T. Saunders, J. M. Richard, E. B. Margolis, P. H. Janak, Dopamine neurons create Pavlovian conditioned stimuli with circuit-defined motivational properties. *Nat. Neurosci.* **21**, 1072–1083 (2018). doi: 10.1038/s41593-018-0191-4; pmid: 30038277
29. A. A. Hamid *et al*., Mesolimbic dopamine signals the value of work. *Nat. Neurosci.* **19**, 117–126 (2016). doi: 10.1038/nn.4173; pmid: 26595651
30. A. Lak, K. Nomoto, M. Keramati, M. Sakagami, A. Kepecs, Midbrain Dopamine Neurons Signal Belief in Choice Accuracy during a Perceptual Decision. *Curr. Biol.* **27**, 821–832 (2017). doi: 10.1016/j.cub.2017.02.026; pmid: 28285994
31. J. A. Parkinson *et al*., Nucleus accumbens dopamine depletion impairs both acquisition and performance of appetitive Pavlovian approach behaviour: implications for mesoaccumbens dopamine function. *Behavioural Brain Research* **137**, 149–163 (2002).
32. M. Darvas, A. M. Wunsch, J. T. Gibbs, R. D. Palmiter, Dopamine dependency for acquisition and performance of Pavlovian conditioned response. *Proc. Natl. Acad. Sci. U.S.A.* **111**, 2764–2769 (2014). doi: 10.1073/pnas.1400332111; pmid: 24550305
33. K. Yamaguchi *et al*., A behavioural correlate of the synaptic eligibility trace in the nucleus accumbens. *Sci. Rep.* **12**, 1921 (2022). doi: 10.1038/s41598-022-05637-6; pmid: 35121769
34. M. G. Kutlu *et al*., Dopamine release in the nucleus accumbens core signals perceived saliency. *Curr. Biol.* **31**, 4748–4761.e8 (2021). doi: 10.1016/j.cub.2021.08.052; pmid: 34529938

35. T. Patriarchi *et al*., Ultrafast neuronal imaging of dopamine dynamics with designed genetically encoded sensors. *Science* **360**, eaat4422 (2018). doi: 10.1126/science.aat4422; pmid: 29853555
36. N. D. Daw, A. C. Courville, D. S. Touretzky, D. S. Touretzky, Representation and timing in theories of the dopamine system. *Neural Comput.* **18**, 1637–1677 (2006). doi: 10.1162/neco.2006.18.7.1637; pmid: 16764517
37. H.-E. Tan *et al*., The gut-brain axis mediates sugar preference. *Nature* **580**, 511–516 (2020). doi: 10.1038/s41586-020-2199-7; pmid: 32322067
38. C. R. Gallistel, T. A. Mark, A. P. King, P. E. Latham, The rat approximates an ideal detector of changes in rates of reward: Implications for the law of effect. *J. Exp. Psychol. Anim. Behav. Process.* **27**, 354–372 (2001). doi: 10.1037/0097-7403.27.4.354; pmid: 11676086
39. R. A. Rescorla, Pavlovian conditioning and its proper control procedures. *Psychol. Rev.* **74**, 71–80 (1967). doi: 10.1037/h0024109; pmid: 5341445
40. R. A. Rescorla, Probability of shock in the presence and absence of CS in fear conditioning. *J. Comp. Physiol. Psychol.* **66**, 1–5 (1968). doi: 10.1037/h0025984; pmid: 5672628
41. C. R. Gallistel, Robert Rescorla: Time, Information and Contingency. *Rev. Hist. Psicol.* **42**, 7–21 (2021).
42. V. M. K Namboodiri *et al*., Relative salience signaling within a thalamo-orbitofrontal circuit governs learning rate. *Curr. Biol.* **31**, 5176–5191.e5 (2021). doi: 10.1016/j.cub.2021.09.037; pmid: 34637750
43. C. D. Fiorillo, W. T. Newsome, W. Schultz, The temporal precision of reward prediction in dopamine neurons. *Nat. Neurosci.* **11**, 966–973 (2008). doi: 10.1038/nn.2159; pmid: 18660807
44. A. Pastor-Bernier, A. Stasiak, W. Schultz, Reward-specific satiety affects subjective value signals in orbitofrontal cortex during multicomponent economic choice. *Proc. Natl. Acad. Sci. U.S.A.* **118**, e2022650118 (2021). doi: 10.1073/pnas.2022650118; pmid: 34285071
45. J. R. Hollerman, W. Schultz, Dopamine neurons report an error in the temporal prediction of reward during learning. *Nat. Neurosci.* **1**, 304–309 (1998). doi: 10.1038/1124; pmid: 10195164
46. S. Kobayashi, W. Schultz, Influence of reward delays on responses of dopamine neurons. *J. Neurosci.* **28**, 7837–7846 (2008). doi: 10.1523/JNEUROSCI.1600-08.2008; pmid: 18667616
47. M. E. Bouton, S. Maren, G. P. McNally, Behavioral and neurobiological mechanisms of pavlovian and instrumental extinction learning. *Physiol. Rev.* **101**, 611–681 (2021). doi: 10.1152/physrev.00016.2020; pmid: 32970967
48. W.-X. Pan, R. Schmidt, J. R. Wickens, B. I. Hyland, Tripartite mechanism of extinction suggested by dopamine neuron activity and temporal difference model. *J. Neurosci.* **28**, 9619–9631 (2008). doi: 10.1523/JNEUROSCI.0255-08.2008; pmid: 18815248
49. W. Zhong, Y. Li, Q. Feng, M. Luo, Learning and Stress Shape the Reward Response Patterns of Serotonin Neurons. *J. Neurosci.* **37**, 8863–8875 (2017). doi: 10.1523/JNEUROSCI.1181-17.2017; pmid: 28821671
50. R. Amo *et al*., A gradual temporal shift of dopamine responses mirrors the progression of temporal difference error in machine learning. *Nat. Neurosci.* **25**, 1082–1092 (2022). doi: 10.1038/s41593-022-01109-2; pmid: 35798979
51. K. E. Bouchard, M. S. Brainard, Neural encoding and integration of learned probabilistic sequences in avian sensory-motor circuitry. *J. Neurosci.* **33**, 17710–17723 (2013). doi: 10.1523/JNEUROSCI.2181-13.2013; pmid: 24198363
52. Y. Komura *et al*., Retrospective and prospective coding for predicted reward in the sensory thalamus. *Nature* **412**, 546–549 (2001). doi: 10.1038/35087595; pmid: 11484055
53. H. E. Manzur, K. Vlasov, S.-C. Lin, A retrospective and stepwise learning strategy revealed by neuronal activity in the basal forebrain. bioRxiv 2022.04.01.486795 [Preprint] (2022); doi: 10.1101/2022.04.01.486795v1
54. L. T. Coddington, J. T. Dudman, The timing of action determines reward prediction signals in identified midbrain dopamine neurons. *Nat. Neurosci.* **21**, 1563–1573 (2018). doi: 10.1038/s41593-018-0245-7; pmid: 30323275
55. K. Lee *et al*., Temporally restricted dopaminergic control of reward-conditioned movements. *Nat. Neurosci.* **23**, 209–216 (2020). doi: 10.1038/s41593-019-0567-0; pmid: 31932769
56. B. Engelhard *et al*., Specialized coding of sensory, motor and cognitive variables in VTA dopamine neurons. *Nature* **570**, 509–513 (2019). doi: 10.1038/s41586-019-1261-9; pmid: 31142844
57. R. N. Hughes *et al*., Ventral Tegmental Dopamine Neurons Control the Impulse Vector during Motivated Behavior. *Curr. Biol.* **30**, 2681–2694.e5 (2020). doi: 10.1016/j.cub.2020.05.003; pmid: 32470362
58. H. R. Kim *et al*., A Unified Framework for Dopamine Signals across Timescales. *Cell* **183**, 1600–1616.e25 (2020). doi: 10.1016/j.cell.2020.11.013; pmid: 33248024
59. A. A. Hamid, M. J. Frank, C. I. Moore, Wave-like dopamine dynamics as a mechanism for spatiotemporal credit assignment. *Cell* **184**, 2733–2749.e16 (2021). doi: 10.1016/j.cell.2021.03.046; pmid: 33861952
60. M. J. Sharpe *et al*., Dopamine transients are sufficient and necessary for acquisition of model-based associations. *Nat. Neurosci.* **20**, 735–742 (2017). doi: 10.1038/nn.4538; pmid: 28368385
61. M. J. Sharpe *et al*., Dopamine transients do not act as model-free prediction errors during associative learning. *Nat. Commun.* **11**, 106 (2020). doi: 10.1038/s41467-019-13953-1; pmid: 31913274
62. B. M. Seitz, I. B. Hoang, L. E. DiFazio, A. P. Blaisdell, M. J. Sharpe, Dopamine errors drive excitatory and inhibitory components of backward conditioning in an outcome-specific manner. *Curr. Biol.* **32**, 3210–3218.e3 (2022). doi: 10.1016/j.cub.2022.06.035; pmid: 35752165
63. I. Trujillo-Pisanty, K. Conover, P. Solis, D. Palacios, P. Shizgal, Dopamine neurons do not constitute an obligatory stage in the final common path for the evaluation and pursuit of brain stimulation reward. *PLOS ONE* **15**, e0226722 (2020). doi: 10.1371/journal.pone.0226722; pmid: 32502210
64. W. Z. Goh, V. Ursekar, M. W. Howard, Predicting the Future With a Scale-Invariant Temporal Memory for the Past. *Neural Comput.* **34**, 642–685 (2022). doi: 10.1162/neco_a_01475; pmid: 35026027
65. K. H. Shankar, M. W. Howard, A scale-invariant internal representation of time. *Neural Comput.* **24**, 134–193 (2012). doi: 10.1162/NECO_a_00212; pmid: 21919782
66. A. Tsao *et al*., Integrating time from experience in the lateral entorhinal cortex. *Nature* **561**, 57–62 (2018). doi: 10.1038/s41586-018-0459-6; pmid: 30158699
67. W. Wei, A. Mohebi, J. D. Berke, Striatal dopamine pulses follow a temporal discounting spectrum. bioRxiv 2021.10.31.466705 [Preprint] (2021); doi: 10.1101/2021.10.31.466705
68. T. J. Madarasz *et al*., Evaluation of ambiguous associations in the amygdala by learning the structure of the environment. *Nat. Neurosci.* **19**, 965–972 (2016). doi: 10.1038/nn.4308; pmid: 27214568
69. S. J. Gershman, Y. Niv, Exploring a latent cause theory of classical conditioning. *Learn. Behav.* **40**, 255–268 (2012). doi: 10.3758/s13420-012-0080-8; pmid: 22927000
70. P. D. Balsam, C. R. Gallistel, Temporal maps and informativeness in associative learning. *Trends Neurosci.* **32**, 73–78 (2009). doi: 10.1016/j.tins.2008.10.004; pmid: 19136158
71. S. J. Gershman, D. M. Blei, Y. Niv, Context, learning, and extinction. *Psychol. Rev.* **117**, 197–209 (2010). doi: 10.1037/a0017808; pmid: 20063968
72. E. C. J. Syed *et al*., Action initiation shapes mesolimbic dopamine encoding of future rewards. *Nat. Neurosci.* **19**, 34–36 (2016). doi: 10.1038/nn.4187; pmid: 26642087
73. A. L. Collins *et al*., Dynamic mesolimbic dopamine signaling during action sequence learning and expectation violation. *Sci. Rep.* **6**, 20231 (2016). doi: 10.1038/srep20231; pmid: 26869075
74. A. Guru *et al*., Ramping activity in midbrain dopamine neurons signifies the use of a cognitive map. bioRxiv2020.05.21.108886 [Preprint] (2020), doi: 10.1101/2020.05.21.108886
75. N. G. Hollon *et al*., Nigrostriatal dopamine signals sequence-specific action-outcome prediction errors. *Curr. Biol.* **31**, 5350–5363.e5 (2021). doi: 10.1016/j.cub.2021.09.040; pmid: 34637751
76. W. van Elzelingen *et al*., Striatal dopamine signals are region specific and temporally stable across action-sequence habit formation. *Curr. Biol.* **32**, 1163–1174.e6 (2022). doi: 10.1016/j.cub.2021.12.027; pmid: 35134325
77. J. P. Gavornik, M. G. H. Shuler, Y. Loewenstein, M. F. Bear, H. Z. Shouval, Learning reward timing in cortex through reward dependent expression of synaptic plasticity. *Proc. Natl. Acad. Sci. U.S.A.* **106**, 6826–6831 (2009). doi: 10.1073/pnas.0901835106; pmid: 19346478
78. V. M. K. Namboodiri, S. Mihalas, T. M. Marton, M. G. Hussain Shuler, A general theory of intertemporal decision-making and the perception of time. *Front. Behav. Neurosci.* **8**, 61 (2014). doi: 10.3389/fnbeh.2014.00061; pmid: 24616677
79. P. N. Tobler, C. D. Fiorillo, W. Schultz, Adaptive coding of reward value by dopamine neurons. *Science* **307**, 1642–1645 (2005). doi: 10.1126/science.1105370; pmid: 15761155
80. N. F. Parker *et al*., Reward and choice encoding in terminals of midbrain dopamine neurons depends on striatal target. *Nat. Neurosci.* **19**, 845–854 (2016). doi: 10.1038/nn.4287; pmid: 27110917
81. H. Jeong *et al*., Mesolimbic dopamine release conveys causal associations, Version 1, Zenodo (2022); https://zenodo.org/record/7302777#.Y4j503bMI2w

ACKNOWLEDGMENTS

We thank S. Gu for suggesting that successor representation may relate to predecessor representation by Bayes' rule, an insight critical to this formulation. We thank A. Mohebi for advice on the initial photometry setup. We thank J. Berke, M. Frank, L. Frank, M. Andermann, K. Wassum, M. Brainard, M. Stryker, A. Nelson, V. Sohaal, M. Kheirbek, H. Fields, Z. Knight, H. Shouval, J. Johansen, A. Kepecs, A. Lutas, M. Hussain Shuler, G. Stuber, M. Howard, A. Mohebi, T. Krausz, R. Gowrishankar, I.Trujillo-Pisanty, J. Levy, J. Rodriguez-Romaguera, R. Simon, M. Hjort, Z.C. Zhou, V. Collins, T. Faust, M. Duhne, and other Nam lab members for comments on the general conceptual framework, experiments and/or the manuscript/figures. **Funding:** This work was funded by the following: National Institute of Mental Health grant R00MH118422 (to V.M.K.N.); National Institute of Mental Health grant R01MH129582 (to V.M.K.N.); Scott Alan Myers Endowed Professorship (to V.M.K.N.) **Author contributions:** H.J. and V.M.K.N. designed the study. H.J., V.M.K.N., A.T., and M.L. performed simulations with input from S.M. H.J., M.Z., and V.M.K.N. set up instrumentation for behavior control and photometry. H.J., J.R.F., B.W., and D.A.B. performed experiments. H.J. performed analysis. H.J., A.T., and V.M.K.N. wrote the paper with help from all authors. V.M.K.N. supervised all aspects of the study. **Competing interests:** Authors declare that they have no competing interests. **Data and materials availability:** All data from this study are publicly available on NIH DANDI at https://dandiarchive.org/dandiset/000351. The codes for analysis and simulation are available publicly on Github (https://github.com/namboodirilab/ANCCR) and on Zenodo (*81*).

License information: Copyright © 2022 the authors, some rights reserved; exclusive licensee American Association for the Advancement of Science. No claim to original US government works. https://www.sciencemag.org/about/science-licenses-journal-article-reuse

SUPPLEMENTARY MATERIALS

https://science.org/doi/10.1126/science.abq6740
Materials and Methods
Supplementary Notes 1 to 10
Figs. S1 to S15
Table S1
References (*82*–*96*)

Submitted 22 April 2022; accepted 25 November 2022
10.1126/science.abq6740

RESEARCH ARTICLES

SOLAR CELLS

Compositional texture engineering for highly stable wide-bandgap perovskite solar cells

Qi Jiang[1], Jinhui Tong[1]*, Rebecca A. Scheidt[1], Xiaoming Wang[2,3], Amy E. Louks[4], Yeming Xian[2,3], Robert Tirawat[1], Axel F. Palmstrom[4], Matthew P. Hautzinger[1], Steven P. Harvey[4], Steve Johnston[4], Laura T. Schelhas[1], Bryon W. Larson[1], Emily L. Warren[1], Matthew C. Beard[1,5], Joseph J. Berry[4,5,6], Yanfa Yan[2,3], Kai Zhu[1]*

The development of highly stable and efficient wide-bandgap (WBG) perovskite solar cells (PSCs) based on bromine-iodine (Br–I) mixed-halide perovskite (with Br greater than 20%) is critical to create tandem solar cells. However, issues with Br–I phase segregation under solar cell operational conditions (such as light and heat) limit the device voltage and operational stability. This challenge is often exacerbated by the ready defect formation associated with the rapid crystallization of Br-rich perovskite chemistry with antisolvent processes. We combined the rapid Br crystallization with a gentle gas-quench method to prepare highly textured columnar 1.75–electron volt Br–I mixed WBG perovskite films with reduced defect density. With this approach, we obtained 1.75–electron volt WBG PSCs with greater than 20% power conversion efficiency, approximately 1.33-volt open-circuit voltage (V_{oc}), and excellent operational stability (less than 5% degradation over 1100 hours of operation under 1.2 sun at 65°C). When further integrated with 1.25–electron volt narrow-bandgap PSC, we obtained a 27.1% efficient, all-perovskite, two-terminal tandem device with a high V_{oc} of 2.2 volts.

The bandgap tunability of organic-inorganic hybrid perovskites makes them a suitable candidate for applications in both single-junction and multijunction solar cells (*1*–*3*). Perovskite-based tandem solar cells have demonstrated rapid improvements in power conversion efficiencies (PCEs) for multiple tandem configurations (*4*–*6*). As the top subcell for an efficient tandem device, the wide-bandgap (WBG) perovskite (about 1.7 eV or higher) harvests high-energy photons, contributes to high open-circuit voltage (V_{oc}), and enables stable operation of the tandem stack by filtering harmful ultraviolet radiation from reaching the bottom cell (*7*).

For state-of-the-art perovskite tandem devices, WBG perovskites are normally based on bromine-iodine (Br–I) mixed halides with a range of high Br contents (*4*, *5*). In principle, adding more Br should make the perovskite absorber more stable, given the strength of the lead (Pb)–Br bond relative to the Pb–I bond. This effect is associated with the smaller radius of Br^- (1.96 Å) compared with that of I^- (2.20 Å) and the higher electronegativity of Br (*3*, *8*, *9*).

[1]Chemistry and Nanoscience Center, National Renewable Energy Laboratory, Golden, CO 80401, USA. [2]Department of Physics and Astronomy, University of Toledo, Toledo, OH 43606, USA. [3]Wright Center for Photovoltaics Innovation and Commercialization, University of Toledo, Toledo, OH 43606, USA. [4]Materials Science Center, National Renewable Energy Laboratory, Golden, CO 80401, USA. [5]Renewable and Sustainable Energy Institute, University of Colorado Boulder, Boulder, CO 80309, USA. [6]Department of Physics, University of Colorado Boulder, Boulder, CO 80309, USA.
***Corresponding author. Email: tongjinhui1@gmail.com (J.T.); kai.zhu@nrel.gov (K.Z.)**

However, perovskites with mixed halides are prone to phase segregation under operating conditions (exposure to light and heat) and limit WBG perovskite solar cell (PSC) performance (*10*–*12*) by creating a large V_{oc} deficit and poor operational stability in comparison with those of mid-bandgap (~1.5 to 1.6 eV) perovskites (*13*, *14*).

A high Br content causes more rapid crystallization of the perovskite film that often creates defects associated with structure and composition nonuniformity and high density of grain boundaries (GBs) (*15*–*17*). Various strategies have been proposed to mitigate these issues, such as composition engineering (*18*–*22*), additive engineering (*23*–*29*), and interface engineering (*30*–*34*). Despite these efforts, the stability of WBG PSCs is still inadequate, especially for devices under illumination or operation at elevated temperatures (table S1).

Here, we report a rational strategy to drastically enhance 1.75-eV Br–I mixed WBG PSC operational stability with high PCE and low V_{oc} deficit. Our design strategy is based on a few principles for Br–I mixed WBG perovskite thin films: (i) Br–I phase segregation is the main limitation on Br-rich WBG PSC performance (that is, operational stability and efficiency), (ii) Br–I phase segregation is facilitated by defective sites, and (iii) reducing the density of defective sites can suppress Br–I phase segregation. We hypothesized that a high-quality WBG perovskite thin film in which the bulk and surface defects are minimized could suppress Br–I phase segregation in a device under operational conditions.

We leveraged the rapid crystallization characteristics of Br^- (relative to I^-) by using a gas-quenching process that was amenable to the Br-rich WBG perovskite precursors. In comparison with the conventional antisolvent approach, the gentler gas-quench method first produced a Br-rich surface layer that then induced top-down columnar growth to form a gradient structure, which had less Br in the bulk than in the near-surface region. The resulting WBG perovskite film had improved structural and optoelectronic properties, such as larger grain size, fewer GBs, longer diffusion length, and reduced defect density. We achieved 1.75-eV WBG PSCs with >20% PCE, ~1.33-V V_{oc}, and excellent operational stability (retaining >95% maximum PCE over 1100 hours of operation under 1.2 sun at 65°C). When coupling the 1.75-eV WBG PSC with the 1.25-eV tin (Sn)–Pb PSC, we obtained a 27.1% all-perovskite two-terminal tandem cell with a high V_{oc} of 2.2 V.

WBG PSC characteristics

We first illustrate the value of the gas-quench method for processing the high-Br-content perovskite to simultaneously achieve high PCE—especially high V_{oc}—and excellent operational device stability. In this study, the WBG perovskite is based on $Cs_{0.3}FA_{0.6}DMA_{0.1}Pb(I_{0.7}Br_{0.3})_3$. We highlight the gas-quench method by comparing it with the conventional antisolvent approach (supplementary materials, materials and methods). We used nitrogen (N_2) gas for most gas-quench studies unless otherwise stated. In comparison with the antisolvent sample, the gas-quench sample exhibited a slight redshift of the absorption onset, corresponding to a 10- to 20-meV decrease in bandgap (fig. S1). We used a typical inverted (or p-i-n) device structure: glass/ITO/SAM/perovskite/LiF/C_{60}/bathocuproine (BCP)/Ag, where ITO is indium tin oxide, and SAM denotes a self-assembled monolayer (LiF, lithium fluoride; Ag, silver). The SAM layer consists of mixed MeO-2PACz and Me-4PACz, where MeO-2PACz is [2-(3,6-dimethoxy-9H-carbazol-9-yl)ethyl]phosphonic acid and Me-4PACz is [4-(3,6-dimethyl-9H-carbazol-9-yl)butyl]phosphonic acid.

The device characteristics of gas quench–based WBG PSCs are described here (Fig. 1). The current density-voltage (*J-V*) curves under reverse and forward voltage scans exhibited negligible hysteresis (Fig. 1A), with reverse- and forward-scan PCEs of 20.3 and 20.0%, respectively; the detailed photovoltaic (PV) characteristics are tabulated in table S2. The highest V_{oc} values reached ~1.33 V, and fill factor (FF) reached 85% (fig. S2), both of which are among the best reported for 1.75-eV WBG PSCs (*35*). The stable power output (SPO) efficiency reached 20.1% (Fig. 1A, inset). The corresponding external quantum efficiency (EQE)

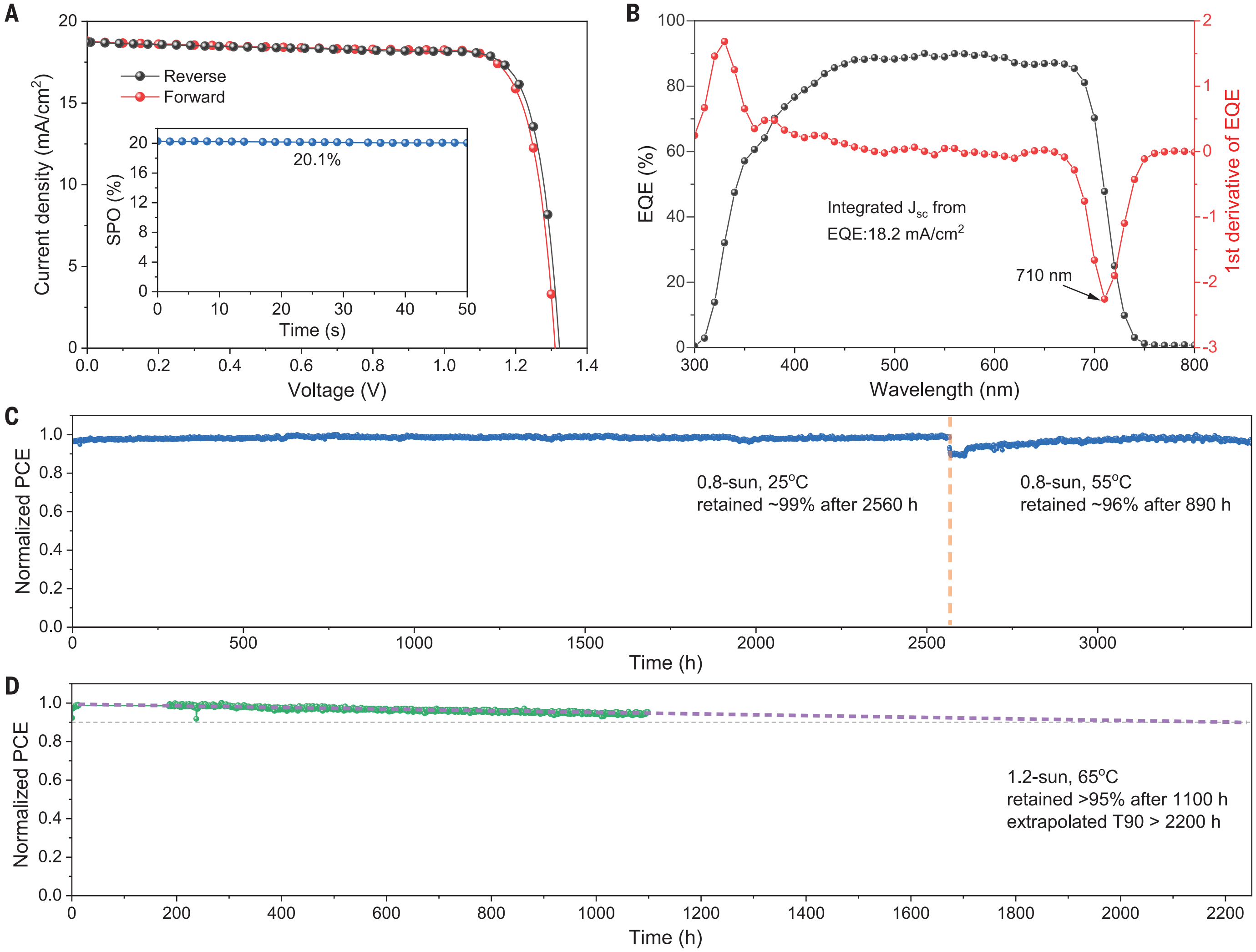


Fig. 1. Device characteristics of 1.75-eV WBG PSCs made by means of gas-quench processing. (**A**) *J-V* curves of a WBG PSC under reverse and forward scans. (Inset) The SPO efficiency. (**B**) The corresponding EQE with determination of the bandgap. (**C** and **D**) Long-term device operational stability under continuous light illumination in N_2 at different temperatures. (C) A cell aged under 0.8 sun for 2560 hours at 25°C followed by 890 hours at 55°C. (D) A cell aged under 1.2 sun at 65°C for 1100 hours, with a linear extrapolation to estimate T90 (purple dashed line).

spectrum (Fig. 1B) yielded an integrated current density of 18.2 mA/cm^2, which is consistent with the *J-V* curves.

Compared with the antisolvent method, the gas quench–based WBG PSCs displayed enhancements in all PV parameters, especially in V_{oc} (by ~30 mV) and short-circuit photocurrent density (J_{sc}) (by ~1 mA/cm^2) (figs. S2 and S3). The enhanced J_{sc} was partially attributed to the slightly reduced bandgap produced by the gas-quench method (figs. S1 and S4). The gas-quench method was also statistically more reproducible than the antisolvent approach (fig. S2), which is consistent with the wider perovskite active layer processing window associated with the gas-quench approach (fig. S5). We found that the gas-quench method also worked when argon (Ar) or air was used as the drying gas, indicating that the gas-quench method is a general way for improving the performance of WBG PSCs (fig. S6).

In addition to the PCE enhancement, the gas-quench method led to excellent operational stability from 25° to 65°C. The gas quench–based WBG PSC exhibited minimal changes in device efficiency, retaining ~99% of the maximum PCE under continuous 0.8-sun light soaking from a sulfur plasma lamp near the maximum power point (MPP) at ~25°C over 2560 hours in an N_2 atmosphere (Fig. 1C). By contrast, the antisolvent-based control device showed a dramatic PCE drop when tested under the same operation condition (fig. S7). For the same gas quench–based device, we further tested the stability at 55°C (Fig. 1C, right half, separated by vertical dashed line). The same cell retained about 96% of its maximum PCE during aging under 0.8-sun illumination at 55°C over 890 hours.

We also examined another gas-quench device under 1.2-sun light-soaking, illuminated by white light–emitting diodes near MPP at 65°C in N_2 (Fig. 1D). This device retained >95% of its maximum PCE over 1100 hours of aging, with a linear extrapolation to a T90 > 2200 hours (T90 means the time for a solar cell to degrade to 90% of its maximum efficiency). These stability results substantially surpassed other reports for Br–I mixed WBG PSCs (table S1), and this level of performance exceeds our previously reported state-of-the-art 1.53-eV p-i-n PSCs (*14*).

Structural and optoelectronic properties

In the next several sections, we discuss the key features that led to our highly stable and efficient WBG PSCs. First, we compared the structural properties of WBG perovskite films prepared with antisolvent and gas-quench methods. The surface and cross-section scanning electron microscopy (SEM) images showed several differences between these two methods. For the antisolvent approach, the grain morphology

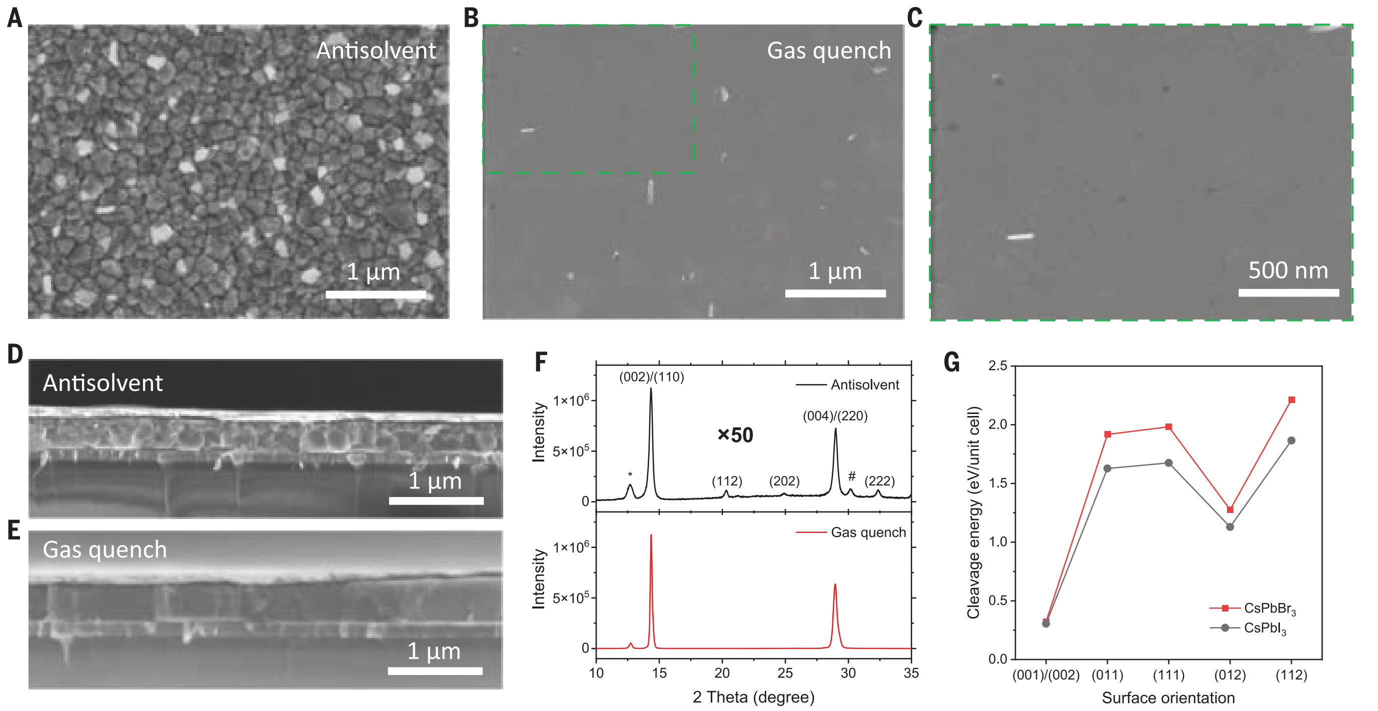


Fig. 2. Structural properties of WBG perovskite. (**A** to **C**) Top-view SEM images of $FA_{0.6}Cs_{0.3}DMA_{0.1}Pb(I_{0.7}Br_{0.3})_3$ perovskite thin films made with (A) antisolvent and [(B) and (C)] gas-quench methods. (C) The magnified image of the selected region in (B). (**D** and **E**) Cross-section SEM images of WBG perovskite films made with (D) antisolvent and (E) gas-quench methods. (**F**) XRD patterns of WBG perovskite films made with antisolvent and gas-quench methods. The peak labeled with an asterisk denotes PbI_2, and the peak labeled with a pound sign (#) denotes ITO. (**G**) Calculated cleavage energies of common surfaces, as indicated.

appeared rough, and the apparent perovskite grain size was small (150 to 200 nm) (Fig. 2A), which is common for Br-rich perovskite thin films because of the rapid crystallization rate associated with Br^- (*36*, *37*). In general, this Br^--related challenge (relative to the I^- counterpart) can be attributed to two factors: (i) the lower solubility of Br^-, which leads to rapid nucleation, and (ii) the smaller ionic radius of Br^-, which leads to faster ion diffusion and grain coarsening (*38*). These issues are further exacerbated by the rapid solvent extraction during the antisolvent process. Thus, Br-rich perovskite thin films tend to grow with a disordered and nonuniform morphology in comparison with that of I-rich ones.

Gas quench—often based on N_2 or air—is generally regarded as a gentler process than the antisolvent quench. The gas-quench approach was initially reported around the same time as the antisolvent method (*39*) but has only recently received more attention, given its advantages for scalable deposition (*40*–*44*). For gas quench, the structure and morphology data indicated that the perovskite nucleation and grain growth dynamics were distinct from what occurs during the antisolvent approach. The gas-quench film exhibited dense, closely packed morphology with a flat, smooth surface and nearly invisible GBs (Fig. 2, B and C). The morphology difference between the two methods was also evident in the corresponding cross-section SEM images (Fig. 2, D and E).

Gas quenching also led to an enhanced (by 50×) main x-ray diffraction (XRD) diffraction peak ($2\theta = 14.2°$, where 2θ is the angle between the x-ray detector and incident x-ray beam) and a reduced full width at half maximum (FWHM) (from 0.29° to 0.17°) (Fig. 2F), which suggests enhanced ordering in the perovskite film. The gas-quench sample exhibited much stronger texturing (fig. S8). The textured columnar grains suggest that the vertical GBs are mostly low-angle GBs, which in general have much lower densities of defects than those of normal GBs (*45*). The morphology contrast was more pronounced for higher concentrations of the Br-rich perovskite precursor (fig. S9). By contrast, when a pure I-based perovskite precursor was used, the morphology difference was substantially reduced, with both gas-quench and antisolvent samples showing multiple apparent grains across the film thickness (fig. S10). These results support the rationale for coupling the gas-quench process with a high-Br-content precursor for generating highly textured, top-down columnar growth of WBG perovskite films.

Our density functional theory (DFT) calculation revealed that the top-down growth with high texturing was governed by the surface energy difference caused by the high Br concentration in the surface region. During film growth, surfaces with smaller surface energies are expected to form with a higher preference. For ionic crystals such as halides, surface energy is dominated by the cleavage energies that do not undergo surface reconstruction. We calculated the cleavage energies of the most common surfaces, including (001)/(002), (011), (111), (012), and (112). The cleavage energy is the same for the (001) and (002) surfaces because they have the same atomic structure. Incorporating Br promoted the preferred growth along the (001)/(002) surface (Fig. 2G). As discussed above, the gas-quench method results in a surface region that is more Br rich. Thus, gas quench of mixed-halide perovskites can be anticipated to promote enhanced textured growth in the surface region. We expected the highly preferred (001)/(002) and top-down growth to form perovskite films with textured columnar grains that have fewer GBs and a low density of defects.

For the high-Br-content perovskite composition in this study, gas-quench and antisolvent methods were also expected to produce different composition profiles along the vertical growth direction. Crystallization and growth take place simultaneously across the film thickness in the antisolvent approach, and consistent with a rapid uniform quench, we expected to see a relatively uniform distribution of the perovskite composition along the vertical direction.

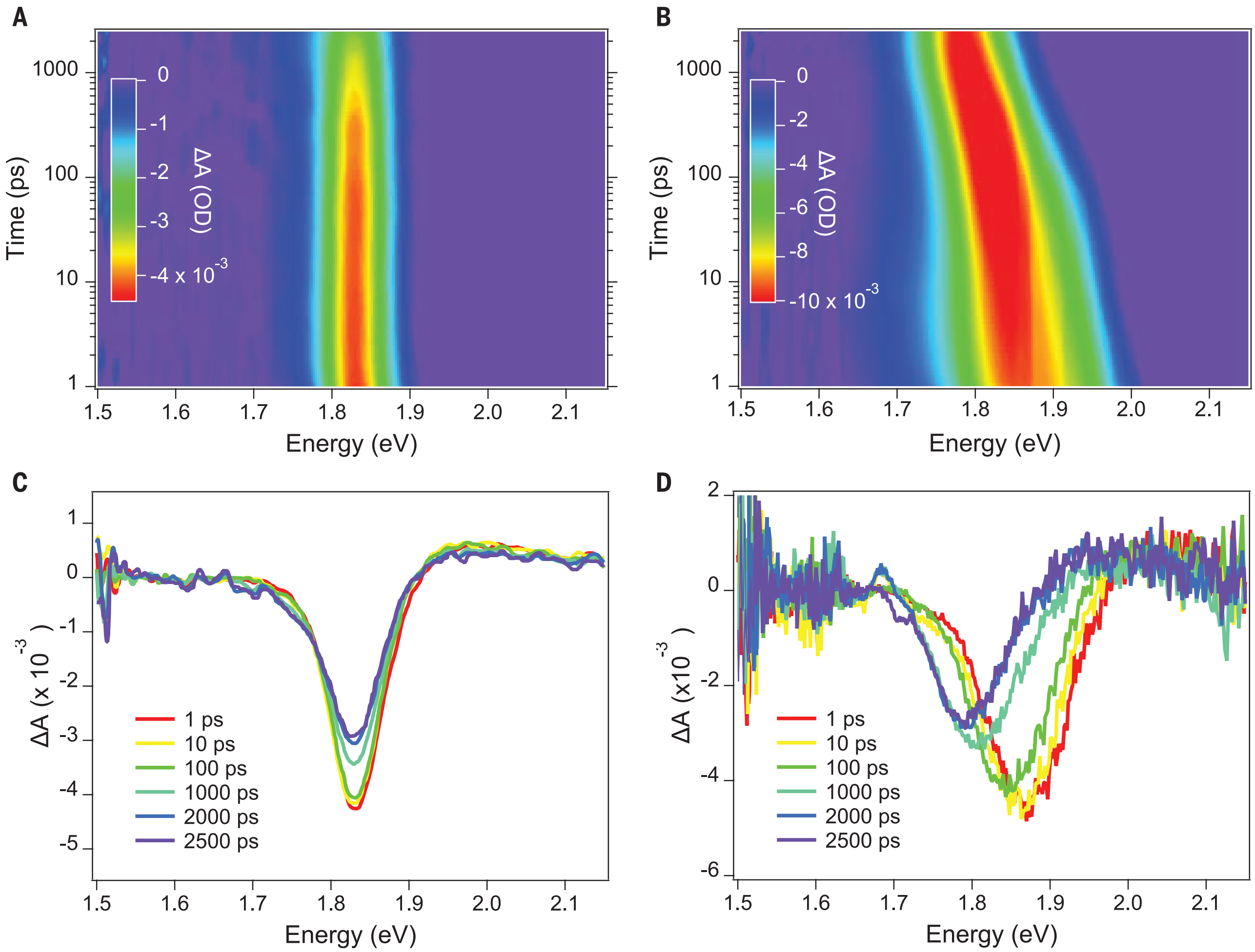


Fig. 3. TA measurements. (**A** and **B**) Pseudocolor representation of the TA results and (**C** and **D**) TA spectra at various post-pump delay times of WBG perovskite thin films prepared with antisolvent [(A) and (C)] and gas-quench [(B) and (D)] methods. The pump excitation energy is 3.1 eV (400 nm) incident from the top of the perovskite samples.

By contrast, the gas-quench approach appears to act more slowly and induces Br-rich nucleation in the surface layer, followed by a gradient structure along the vertical direction, resulting in columnar growth. Transient absorption (TA) measurements of the antisolvent sample showed a single ground-state bleach peak during the carrier's lifetime, indicating a uniform composition within the sample as carriers diffuse across the film and sample the energetic landscape before relaxing back to their ground state (Fig. 3, A and C).

However, the gas-quench sample showed a distinct shifting of the ground-state bleach as a function of time after excitation. At early times, the bleach occurred at a higher energy, corresponding to carriers residing in a Br-rich (higher energy) region, and then the bleach slowly shifted to a lower energy, corresponding to carriers moving toward the region with reduced Br content. The ground-state bleach shifted by ~0.1 eV, over a time scale of hundreds of picoseconds (Fig. 3, B and D). When the gas-quench sample was excited from the back side, we observed no evolution of the TA spectrum (fig. S11). Thus, the evolution in the TA spectrum for the gas-quench sample indicates that there is a gradient in the Br content, where the higher bandgap (more Br) lies at the surface of the film, and the lower bandgap (less Br) is deeper into the film. The gradient structure is consistent with the time-of-flight secondary-ion mass spectroscopy results (fig. S12). At the early pump-probe times, only the high-bandgap, Br-rich perovskite at the surface of the film was excited because of Beer's law absorbance of the pump pulse into the film surface, and the TA spectrum showed its spectral signature. After hundreds of picoseconds, the photoexcited charge carriers that initially resided near the top surface diffused into the perovskite film, and thus the TA spectrum evolved to the spectral signature of the lower-bandgap, more I-rich perovskite. The gradient composition created an energy cascade structure that is beneficial for solar cell operation because it repels carriers away from defective surfaces (*46*–*50*).

We conducted time-resolved microwave conductivity (TRMC) and dark *J-V* measurements to examine the impact of growth methods on optoelectronic properties. Analysis of typical TRMC transients revealed that the yield-mobility product $\phi\Sigma\mu$ value (where ϕ is free-carrier generation yield and $\Sigma\mu$ is the sum of carrier mobilities of holes and electrons) and free carrier lifetime were 4.9 cm^2 V^{-1} s^{-1} and 426 ns for antisolvent samples but 20.8 cm^2 V^{-1} s^{-1} and 355 ns for gas-quench samples, respectively (Fig. 4A). We observed the relative change in $\phi\Sigma\mu$ over a wide range of excitation intensities (Fig. 4B). The carrier diffusion lengths, determined by the product of carrier mobility and lifetime, were 2.3 μm for the antisolvent sample and 4.4 μm for the gas-quench sample.

The suppressed gigahertz mobility value for the antisolvent sample was consistent with greater structural disorder indicated in the XRD data and the morphology and apparent-grain nonuniformities observed in the SEM images (*51*). For the gas-quench sample, the longer carrier diffusion length, which is often

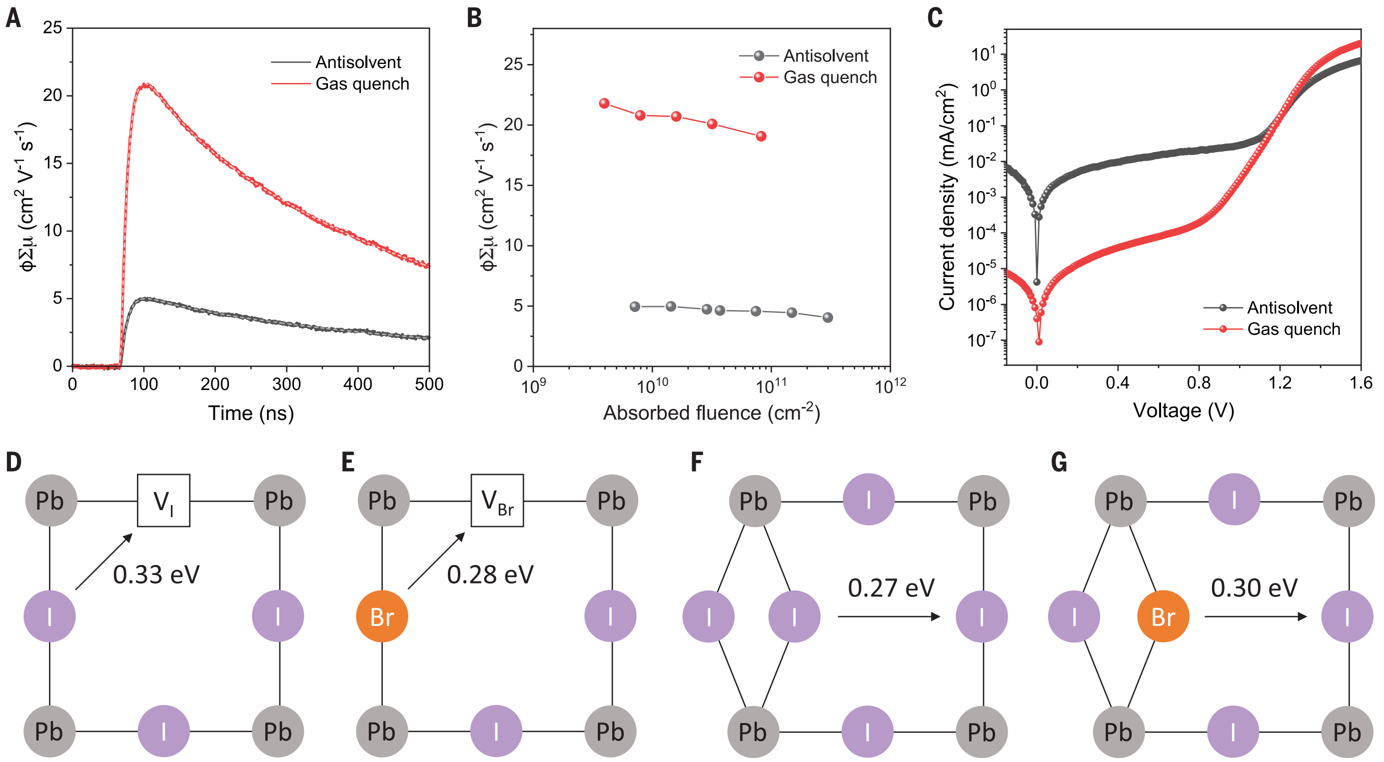


Fig. 4. Optoelectronic properties and calculation of defect-assisted diffusion barriers. (**A**) Photoconductivity ($\phi\Sigma\mu$) transients for the lowest absorbed pump fluence, obtained with TRMC measurement. Pulsed (10 Hz) optical excitation at 1.93 eV (643 nm) was used, with an absorbed fluence range over about two orders of magnitude. (**B**) Excitation intensity dependence of photoconductivity as a function of excitation intensity. (**C**) Dark *J-V* curves for PSCs based on perovskite films prepared with antisolvent and gas-quench methods. (**D** to **G**) Calculations of diffusion energy barriers for several common defects. (D) Iodine vacancy, V_I. (E) Bromine vacancy, V_{Br}. (F) Iodine interstitial, I_i. (G) Bromine interstitial, Br_i.

associated with enhanced material quality (degree of crystallinity) and reduced defect density, was consistent with the improved device characteristics. The comparison of the dark *J-V* curves (Fig. 4C) showed an increase in shunt resistance greater than two orders of magnitude that reduced leakage current and was suggestive of a lower defect density for gas quench–based PSCs (*52*), which is consistent with the deep-level transient spectroscopy (DLTS) results (fig. S13).

We attributed the improved structural and optoelectronic properties and enhanced operational stability with gas quench to suppression of halide phase separation, which involves halide exchange. Our DFT calculations revealed that halide exchange requires the assistance of a halide vacancy. The energy needed to diffuse a halide atom from its lattice to a nearby interstitial site was as high as 1.4 eV for I and 1.3 eV for Br (figs. S14 and S15). However, these energies were reduced to 0.33 and 0.28 eV for I and Br, respectively (Fig. 4, D and E, and figs. S16 and S17), when a halide vacancy was nearby. Additionally, I and Br interstitials diffused easily, with energy barriers of 0.27 and 0.30 eV, respectively (Fig. 4, F and G, and figs. S18 and S19). Our calculation confirmed that reducing the density of defects (halide vacancies and interstitials) helped suppress halide phase separation.

All-perovskite tandem solar cell characteristics

To exploit the effectiveness of our optimized WBG perovskites, we fabricated monolithic all-perovskite tandem solar cells by integrating 1.25-eV $FA_{0.6}MA_{0.4}Sn_{0.6}Pb_{0.4}I_3$ narrow-bandgap PSC with our optimized 1.75-eV WBG PSC. The tandem device stack consisted of glass/ITO/SAM/1.75-eV perovskite/LiF/C_{60}/33-nm SnO_x/1-nm Au/PEDOT:PSS/1.25-eV perovskite/C_{60}/BCP/Ag, where PEDOT:PSS is poly(3,4-ethylenedioxythiophene):polystyrene sulfonate (Au, gold). The fabrication of the Sn-Pb perovskite and the tandem structure is detailed in (*53*). The *J-V* curves of the tandem device (Fig. 5A) showed negligible hysteresis between reverse and forward scans. The reverse scan yielded a PCE of 27.1%, with a J_{sc} of 15.3 mA cm^{-2}, V_{oc} of 2.20 V, and FF of 80.8%; the forward scan showed a PCE of 27.2%, with a J_{sc} of 15.1 mA cm^{-2}, V_{oc} of 2.20 V, and FF of 81.6%. The corresponding SPO efficiency reached 27.1% (Fig. 5B). The tandem V_{oc} of 2.2 V is the highest reported (*53*). The EQE spectra for the corresponding top and bottom subcells are shown in fig. S20. We also examined the operational stability of the tandem devices. The unencapsulated tandem cell retained ~81% of its maximum PCE after 1825 hours under continuous ~0.8-sun illumination from a sulfur plasma lamp at ~35°C in N_2 (Fig. 5C). The encapsulated tandem cell exhibited a T84 of 763 hours when tested at ~50°C in air (fig. S21).

Discussion

We report a simple strategy to control the growth of WBG perovskite thin films by applying a gentle gas-quench method to high-Br-content perovskite. With this approach, the WBG perovskite films showed improved structural and optoelectronic properties with longer diffusion length and reduced defect density. As a result, we obtained efficient and stable WBG PSCs and all-perovskite tandem solar cells. This study not only demonstrates the potential of high-performance, all-perovskite tandem devices but is also a valuable advance for the development of other perovskite-based tandem architectures, such as perovskite-silicon tandems that use mixed-halide WBG perovskites (*54*–*56*). The conversion efficiency and long-term stability of these devices support our hypothesis that suppression of Br–I phase segregation by enhancing perovskite crystallization quality and

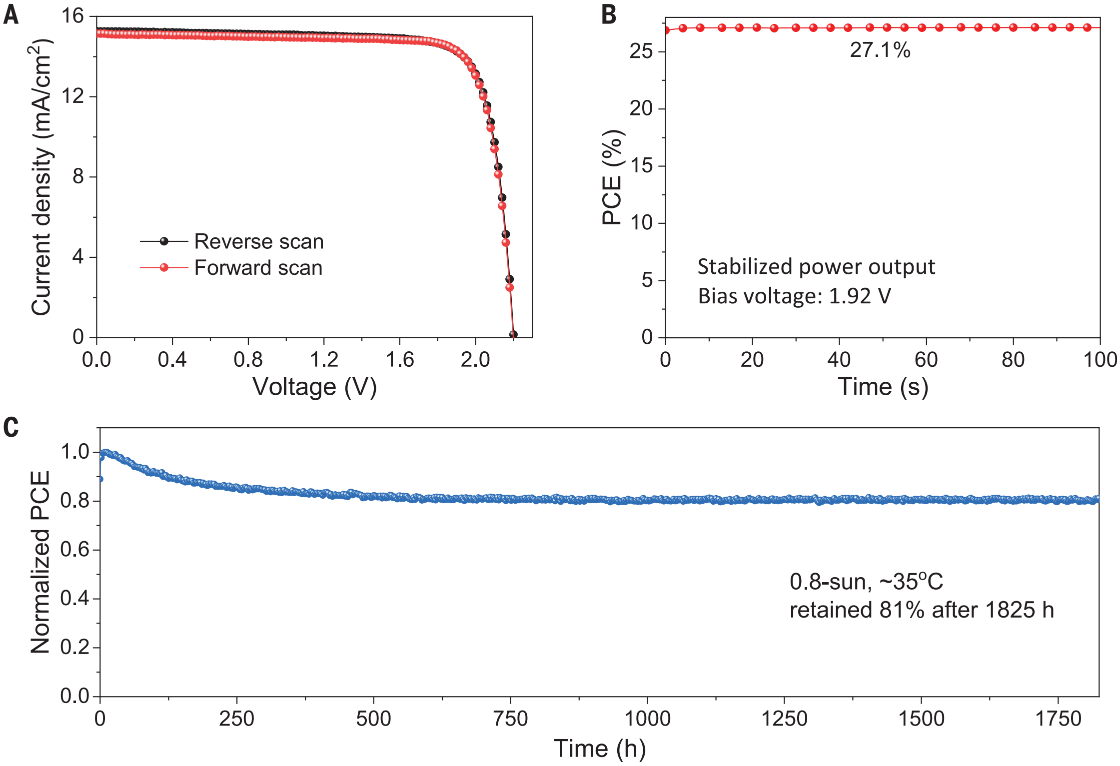


Fig. 5. Tandem device. (**A**) *J-V* curves of an all-perovskite tandem solar cell incorporating the gas quench–based 1.75-eV WBG PSC. The device area was 0.059 cm^2 as defined by a metal aperture. (**B**) The corresponding SPO efficiency near the MPP. The narrow-bandgap bottom cell is based on 1.25-eV Sn–Pb perovskite ($FA_{0.6}MA_{0.4}Sn_{0.6}Pb_{0.4}I_3$), as detailed in (*53*). (**C**) Long-term stability of the tandem device under continuous ~0.8-sun illumination at ~35°C in N_2. The tandem device retained ~81% of its maximum efficiency after 1825 hours.

minimizing defects can improve WBG perovskite PV performance.

REFERENCES AND NOTES

1. Y. Zhao, K. Zhu, *Chem. Soc. Rev.* **45**, 655–689 (2016).
2. G. E. Eperon, M. T. Hörantner, H. J. Snaith, *Nat. Rev. Chem.* **1**, 0095 (2017).
3. J. H. Noh, S. H. Im, J. H. Heo, T. N. Mandal, S. I. Seok, *Nano Lett.* **13**, 1764–1769 (2013).
4. R. Lin *et al.*, *Nature* **603**, 73–78 (2022).
5. A. Al-Ashouri *et al.*, *Science* **370**, 1300–1309 (2020).
6. M. Jošt *et al.*, *ACS Energy Lett.* **7**, 1298–1307 (2022).
7. J. Tong *et al.*, *ACS Energy Lett.* **6**, 232–248 (2021).
8. J. Wang, W. Li, W.-J. Yin, *Adv. Mater.* **32**, 1906115 (2020).
9. K. Li *et al.*, *Mater. Chem. Front.* **3**, 1678–1685 (2019).
10. E. T. Hoke *et al.*, *Chem. Sci.* **6**, 613–617 (2015).
11. R. A. Kerner, Z. Xu, B. W. Larson, B. P. Rand, *Joule* **5**, 2273–2295 (2021).
12. M. C. Brennan, S. Draguta, P. V. Kamat, M. Kuno, *ACS Energy Lett.* **3**, 204–213 (2018).
13. Y. Zhao *et al.*, *Science* **377**, 531–534 (2022).
14. Q. Jiang *et al.*, *Nature* **611**, 278–283 (2022).
15. S. J. Yoon, M. Kuno, P. V. Kamat, *ACS Energy Lett.* **2**, 1507–1514 (2017).
16. P. S. Mathew, G. F. Samu, C. Janáky, P. V. Kamat, *ACS Energy Lett.* **5**, 1872–1880 (2020).
17. A. J. Barker *et al.*, *ACS Energy Lett.* **2**, 1416–1424 (2017).
18. R. J. Stoddard *et al.*, *ACS Energy Lett.* **3**, 1261–1268 (2018).
19. H. Tan *et al.*, *Nat. Commun.* **9**, 3100 (2018).
20. G. E. Eperon *et al.*, *ACS Energy Lett.* **5**, 1856–1864 (2020).
21. S. Gholipour *et al.*, *Adv. Mater.* **29**, 1702005 (2017).
22. D. P. McMeekin *et al.*, *Science* **351**, 151–155 (2016).
23. Y. Zhou *et al.*, *Adv. Funct. Mater.* **28**, 1803130 (2018).
24. J. Kim *et al.*, *Adv. Mater.* **30**, e1706275 (2018).
25. M. Abdi-Jalebi *et al.*, *Nature* **555**, 497–501 (2018).
26. D. Kim *et al.*, *Science* **368**, 155–160 (2020).
27. D. H. Kim *et al.*, *Joule* **3**, 1734–1745 (2019).
28. Y. Yu *et al.*, *ACS Energy Lett.* **2**, 1177–1182 (2017).
29. F. Yu *et al.*, *Sol. RRL* **6**, 2100906 (2022).
30. C. Chen *et al.*, *ACS Energy Lett.* **5**, 2560–2568 (2020).
31. T. Bu *et al.*, *Nano Energy* **75**, 104917 (2020).
32. S. Gharibzadeh *et al.*, *Adv. Energy Mater.* **9**, 1803699 (2019).
33. Z. Liu, J. Siekmann, B. Klingebiel, U. Rau, T. Kirchartz, *Adv. Energy Mater.* **11**, 2003386 (2021).
34. C. Chen *et al.*, *Nano Energy* **61**, 141–147 (2019).
35. Y. Tong *et al.*, *Adv. Sci.* **9**, e2105085 (2022).
36. M. I. Saidaminov *et al.*, *Nat. Mater.* **19**, 412–418 (2020).
37. H. S. Jung, N.-G. Park, *Small* **11**, 10–25 (2015).
38. Y. Tidhar *et al.*, *J. Am. Chem. Soc.* **136**, 13249–13256 (2014).
39. F. Huang *et al.*, *Nano Energy* **10**, 10–18 (2014).
40. Y. Deng *et al.*, *Sci. Adv.* **5**, eaax7537 (2019).
41. Y. Deng *et al.*, *Joule* **4**, 1949–1960 (2020).
42. X. Dai *et al.*, *Adv. Energy Mater.* **10**, 1903108 (2020).
43. A. S. Subbiah *et al.*, *ACS Energy Lett.* **5**, 3034–3040 (2020).
44. J. Ding *et al.*, *Joule* **3**, 402–416 (2019).
45. S. Pouladi *et al.*, *Sol. Energy Mater. Sol. Cells* **199**, 122–128 (2019).
46. Z. Yu *et al.*, *Adv. Mater.* **34**, e2110351 (2022).
47. Y. Wu *et al.*, *Nat. Energy* **1**, 16148 (2016).
48. Q. Zhao *et al.*, *Nat. Commun.* **10**, 2842 (2019).
49. G. Tong *et al.*, *Sol. RRL* **3**, 1900030 (2019).
50. K. T. Cho *et al.*, *Energy Environ. Sci.* **10**, 621–627 (2017).
51. O. G. Reid, M. Yang, N. Kopidakis, K. Zhu, G. Rumbles, *ACS Energy Lett.* **1**, 561–565 (2016).
52. C. Li *et al.*, *Adv. Energy Mater.* **9**, 1803135 (2019).
53. J. Tong *et al.*, *Nat. Energy* **7**, 642–651 (2022).
54. J. Wang, H. Liu, Y. Zhao, X. Zhang, *Joule* **6**, 509–511 (2022).
55. Y. Li, Y. Peng, F. Hou, S. Ren, H. Tan, D. Zhao, in *Perovskite Materials and Devices*, L. Ding, Ed. (Wiley, 2022), pp. 303–334.
56. R. Wang *et al.*, *Nat. Photonics* **15**, 411–425 (2021).

ACKNOWLEDGMENTS

Funding: This work was partially supported by the US Department of Energy (DOE) under contract DE-AC36-08GO28308 with Alliance for Sustainable Energy, the manager and operator of the National Renewable Energy Laboratory. The authors acknowledge the support with first-principle calculations and optoelectronic characterizations (such as TA and TRMC) from the Center for Hybrid Organic-Inorganic Semiconductors for Energy (CHOISE), an Energy Frontier Research Center funded by the DOE Office of Basic Energy Sciences, Office of Science. The first-principles calculations were performed by using computational resources sponsored by the DOE Office of Energy Efficiency and Renewable Energy and located at the National Renewable Energy Laboratory. The authors also acknowledge the support on WBG perovskite device fabrication and characterizations from Tandem Photovoltaics DE-00038266 and the support on the all-perovskite tandem device fabrication and characterization and general stability evaluation from the Advanced Perovskite Cells and Modules program of the National Center for Photovoltaics, funded by the DOE Office of Energy Efficiency and Renewable Energy, Solar Energy Technologies Office. Y.Y. acknowledges the support from DOE Office of Energy Efficiency and Renewable Energy (EERE) under the Hydrogen and Fuel Cell Technologies Office Award DE-EE0008837. The views expressed in the article do not necessarily represent the views of the DOE or the US government. **Author Contributions:** Q.J. and K.Z. conceived the idea. K.Z. and J.T. supervised the projects. Q.J. fabricated perovskite films and devices, conducted scanning electron microscopy, θ-2θ XRD, and ultraviolet-visible measurements. J.T. and Q.J. fabricated and characterized tandem solar cells and contributed to device design and analysis. R.A.S. conducted TA measurements and analysis, under the guidance of M.C.B.; X.W. and Y.X. carried out the DFT calculations, under the supervision of Y.Y.; A.E.L. and R.T. worked on device stability test and analysis, under the supervision of J.J.B.; B.W.L. conducted the TRMC measurements and analysis. A.F.P. conducted atomic layer deposition. M.P.H. helped crystallographic analysis of perovskite structures. S.P.H. conducted the time-of-flight secondary-ion mass spectrometry study and analysis. S.J. conducted the deep-level transient spectroscopy measurement and analysis. L.T.S. and J.J.B conducted 2D XRD measurements and analysis. E.L.W. contributed to helpful discussions on WBG perovskite development for tandem applications. Q.J. and K.Z. wrote the first draft of the manuscript. All authors discussed the results and contributed to the revisions of the manuscript. **Competing interests:** Q.J., J.T., and K.Z. are inventors on a provisional patent (US patent application number 63/315,834) related to the subject matter of this manuscript. **Data and materials availability:** All data needed to evaluate the conclusions in the paper are present in the paper or the supplementary materials. **License information:** Copyright © 2022 the authors, some rights reserved; exclusive licensee American Association for the Advancement of Science. No claim to original US government works. https://www.science.org/content/page/science-licenses-journal-article-reuse

SUPPLEMENTARY MATERIALS

science.org/doi/10.1126/science.adf0194
Materials and Methods
Figs S1 to S21
Tables S1 and S2
References (*57*–*69*)

Submitted 23 September 2022; accepted 22 November 2022
10.1126/science.adf0194

QUANTUM SENSING

Nanoscale covariance magnetometry with diamond quantum sensors

Jared Rovny[1], Zhiyang Yuan[1], Mattias Fitzpatrick[1]†, Ahmed I. Abdalla[1]‡, Laura Futamura[1]§, Carter Fox[2], Matthew Carl Cambria[2], Shimon Kolkowitz[2], Nathalie P. de Leon[1]*

Nitrogen vacancy (NV) centers in diamond are atom-scale defects that can be used to sense magnetic fields with high sensitivity and spatial resolution. Typically, the magnetic field is measured by averaging sequential measurements of single NV centers, or by spatial averaging over ensembles of many NV centers, which provides mean values that contain no nonlocal information about the relationship between two points separated in space or time. Here, we propose and implement a sensing modality whereby two or more NV centers are measured simultaneously, and we extract temporal and spatial correlations in their signals that would otherwise be inaccessible. We demonstrate measurements of correlated applied noise using spin-to-charge readout of two NV centers and implement a spectral reconstruction protocol for disentangling local and nonlocal noise sources.

Correlated phenomena play a central role in condensed matter physics and have been studied in many contexts, including phase transitions (*1*, *2*), many-body interactions and entanglement (*3*, *4*), and magnetic ordering (*5*, *6*), as well as in the context of fluctuating electromagnetic fields, where two-point correlators are central to characterizing field statistics (*7*, *8*). Recent efforts toward improving quantum devices have also explored correlated noise in superconducting quantum interference devices (*9*) and qubits (*10*–*12*). Nitrogen vacancy (NV) centers in diamond are a promising sensing platform for detecting correlations because they are robust, noninvasive, and capable of measuring weak signals with nanoscale resolution (*13*). These advantages have made them a useful tool for studying many condensed matter systems, including magnetic systems such as two-dimensional (2D) van der Waals materials (*14*, *15*), magnons (*16*), and skyrmions (*17*, *18*); and transport phenomena such as Johnson noise (*19*), hydrodynamic flow (*20*–*22*), and electron-phonon interactions in graphene (*23*). These applications are powerful but have so far been limited to signals that are averaged over space or time—more information is potentially available by studying spatial and temporal correlations in the system. Advances in nanoscale spectroscopy have already been made by studying correlations from a single NV center at different points in time (*24*–*26*), where temporal correlations are calculated between subsequent measurements before signal averaging. Here, we extend this technique to measuring correlations in both space and time between individual measurements with pairs of NV centers before signal averaging; measuring correlated dynamics between two different NV centers provides simultaneous information at length scales ranging from the diffraction limit to the full field of view (~0.1- to 100-μm length scales) and at two different sensing times limited only by the experimental clock cycle (~1-ns resolution). Measurements of spatiotemporal correlations at these length and time scales would provide useful information about the dynamics of the target system, including the electron mean free path, signatures of hydrodynamic flow (*27*), or the microscopic nature of local NV center noise sources such as surface spins (*28*, *29*).

[1]Department of Electrical and Computer Engineering, Princeton University, Princeton, NJ 08544, USA.
[2]Department of Physics, University of Wisconsin–Madison, Madison, WI 53706, USA.
*Corresponding author. Email: npdeleon@princeton.edu
†Present address: Thayer School of Engineering, Dartmouth College, Hanover, NH 03755, USA.
‡Present address: Department of Electrical Engineering, Stanford University, Stanford, CA 94305, USA.
§Present address: Department of Physics, Stanford University, Stanford, CA 94305, USA.

Determining correlations between NV centers

We consider two NV centers that do not directly interact with each other but experience a shared classical magnetic field, whose amplitude is correlated at the locations of the two NV centers (Fig. 1A). Each NV center also sees a distinct local magnetic field that is uncorrelated between the two locations. These fields are detected using a Ramsey-type experiment that addresses the $m_s = 0$ and $m_s = +1$ (or −1) spin sublevels of the NV center (referred to as states 0 and 1, respectively) (Fig. 1, B to D). After many repeated measurements, we accumulated a list of signals $S_1 = \{s_{1,i}\}$ and $S_2 = \{s_{2,i}\}$ from NV1 and NV2, respectively, where s is the number of photons detected in a single experiment and $i = 1 \ldots N$ indexes the N total experiments.

Though similar to a typical Ramsey-type variance detection sequence (*30*), we emphasize two modifications for covariance detection. First, despite detecting zero-mean noise, we chose a final pulse that is 90° out of phase with the initial pulse, such that for high-frequency noise detection, the final spin state is equally likely to be 0 or 1 (Fig. 1, B and C), which maximizes our sensitivity to correlations. This is not done in conventional noise detection using variance magnetometry, because straightforward signal averaging would then always produce the same result $\langle m_{s_i} \rangle = 0.5$. Second, we did not compute the average value of this signal but rather computed the shot-to-shot cross-correlation between the raw signals S_1 and S_2 (Fig. 1D).

Whereas conventional variance measurements provide spectral densities with no spatial information (top row of Fig. 1E), the addition of covariance information allows us to identify which spectral components are common between two NV centers and which are specific to each (bottom row of Fig. 1E). Throughout this work, we focus on the measured Pearson correlation $r = \mathrm{Cov}(S_1, S_2)/(\sigma_1\sigma_2)$, where Cov is the covariance and σ_1 and σ_2 are the standard deviations of S_1 and S_2.

Experimental implementation of covariance measurements

To demonstrate our protocol, we used an external radiofrequency coil or stripline to apply a global, random phase ac signal to two shallow NV centers ~10 nm from the diamond surface. Here, the two NV centers share the same magnetic resonance frequency, so that all microwave pulses address both. They are spatially resolved, which allows for separate excitation and readout using two independent optical paths (*31*). To boost the sensitivity of our readout, we used a simultaneous spin-to-charge conversion (SCC) protocol (*32*, *33*) on each NV center separately. We used an XY8 sensing protocol for each NV center to maximize sensitivity to the applied ac signal (*34*) (Fig. 2A). We observed correlations that are maximized when the interpulse spacing matches the frequency of the global signal (blue circles in Fig. 2B). The correlations are apparent in the photon count statistics [bottom panel (ii) of Fig. 2B]; when one or more photons are detected from NV1, we observed a higher likelihood of also detecting a photon from NV2. To confirm that we were indeed detecting correlations in the spin state of the NV centers rather than spurious technical correlations (*31*), we could also initialize the two NV centers on opposite sides of the Bloch sphere before applying the XY8 sequence (Fig. 2A). The phase accumulation step then results in a final state that is anticorrelated between the two NV centers (red squares in Fig. 2B).

The sensitivity of a covariance measurement differs from that of a traditional magnetometry measurement because it requires simultaneous signals from two NV centers. Assuming that the detected phases are statistically even, as for a noisy or random-phase signal, we find (*31*) the Pearson correlation

$$r = \frac{e^{-[\chi_1(t_1) + \chi_2(t_2)]}}{\sigma_{R_1}\sigma_{R_2}} \left\langle \sin\left[\phi_{C_1}(t_1)\right] \sin\left[\phi_{C_2}(t_2)\right] \right\rangle \quad (1)$$

where the subscripts 1 and 2 denote NV1 and NV2, respectively; the decoherence function $\tilde{\chi}_{1,2}(t)$ describes the "typical" coherence decay of the NV centers due to the local fields (*35*); $\phi_{C_{1,2}}$ are the phases accumulated by the NV centers due to the correlated field; and the readout noise $\sigma_{R_{1,2}} = \sqrt{1+2(\alpha_0+\alpha_1)/(\alpha_0-\alpha_1)^2}$ characterizes the fidelity of a photon-counting experiment with mean detected photon numbers α_0 and α_1 for spin states 0 and 1, respectively (*30*). For thresholding, the readout noise instead depends on the fidelity of the spin-state assignment. Readout noise may be generalized to include non-Poisson statistics that result from errors in charge-state initialization or ionization (*31*).

Note that the detectable correlation depends quadratically on the readout noise, which makes readout fidelity especially important for detecting correlations; this key fact is implicit in prior calculations of single-NV center two-point correlators derived in the context of repeated weak measurements (*25*). This may be intuitively understood from Fig. 2C, which shows the raw photon counts for conventional versus SCC readout methods. Using conventional readout, only ~0.01 photons are detected per measurement, such that detecting simultaneous counts from both NV centers is extremely unlikely. Using SCC readout substantially increases our ability to detect coincident events and has a greater effect on covariance measurements than on conventional single–NV center measurements. From the independently measured values for each term on the right-hand side of Eq. 1 (*31*), we expect the detectable correlation in our experiment to be approximately bounded by $r \approx 0.01$, in good agreement with the maximum correlation $r \approx 0.008$ that we detect here (Fig. 2B). The remaining discrepancy is likely due to experimental imperfections such as sample drift or pulse miscalibration over time.

Because readout noise plays an amplified role in covariance detection, covariance measurements can become prohibitively long without optimizing sensitivity, for which we require a detailed understanding of the signal-to-noise ratio (SNR). The sensitivity (minimum noise amplitude $\sigma_{B_{min}}$ with SNR = 1) of an experiment that detects Gaussian noise is given by (*31*)

$$\sigma^2_{B,min} = \frac{-\pi\cdot Hz}{4{\gamma_e}^2 t}\ln\left(1-\frac{2{\sigma_R}^2 e^{2t/T_2}}{\sqrt{T/(t+t_R)}}\right) \quad (2)$$

where γ_e is the electron gyromagnetic ratio, t is the phase integration time, T_2 is the coherence time, t_R is the readout time, and $T \approx (t + t_R)N$ is the total experiment time ignoring initialization. This is shown in the bottom graph of Fig. 2C for three different readout methods: conventional (σ_R = 35), SCC (σ_R = 4), and single-shot readout with perfect fidelity (σ_R = 1), which is ultimately limited by quantum projection noise. Achieving an SNR equal to 1 for these three scenarios when σ_B = 1 nT requires total experiment times on the order of 300 hours, 3 hours, and 10 s, respectively. Whereas detecting correlations is extremely inefficient using conventional readout, enhanced readout protocols like SCC (*32*, *36*) allow for substantially lower readout noise, making covariance magnetometry possible to implement in practice.

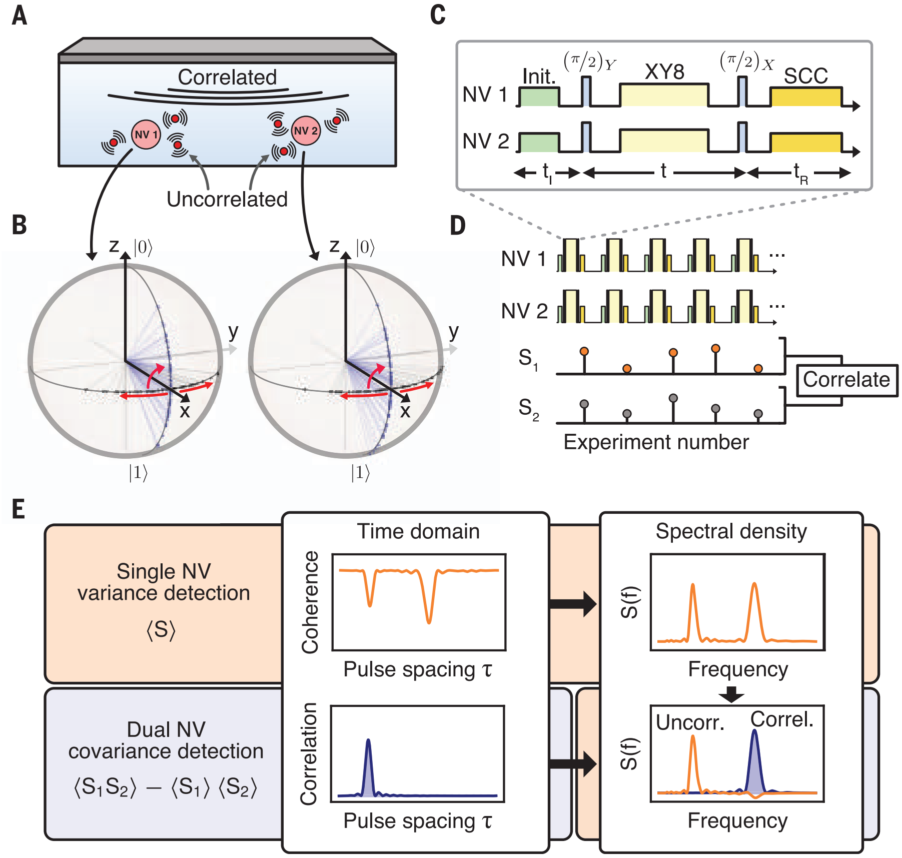


Fig. 1. Covariance noise sensing. (**A**) Diagram of a diamond with two near-surface NV centers that are experiencing uncorrelated local fields and a correlated common field. (**B**) Bloch sphere representations of each qubit state during sensing, with the states prepared along *x* followed by a phase accumulation that will be different in each experiment, resulting in a distribution of phases. At the end of each experiment, a final π/2 pulse maps these phases to populations. (**C** and **D**) Pulse sequence diagrams showing the sensing (XY8) and measurement (SCC) sequence for each NV center. The measurement is repeated many times, retaining the photon counts from each measurement without signal averaging; we instead measured the correlation between the resulting lists S_i. (**E**) Using conventional detection of single NV centers (top row), the coherence decay gives access to the noise spectral density $S(f)$ but provides no spatial information. Covariance magnetometry measuring two NV centers (bottom row) provides information about which spectral features are correlated and which are uncorrelated.

Disentangling correlated and uncorrelated noise sources

Detecting cross-correlations in pure noise reveals previously hidden information about the spatial structure of the noise, which we now demonstrate using two NV centers that sense both local and nonlocal magnetic fields. We first measured the spectral density $S(f)$, where f is frequency, using a conventional variance magnetometry measurement of two different NV centers (Fig. 3A, top). These individual spectra reveal that there are two frequencies where signals are seen by both NV centers but cannot provide simultaneous nonlocal spatial information about that signal. Using covariance magnetometry over the same frequency range (Fig. 3A, bottom) shows only the higher-frequency feature, which clearly reveals that the higher-frequency feature is caused by a noise signal common to each NV center, whereas the lower-frequency feature is instead caused by local noise sources specific to each NV center.

This ability to distinguish correlated and uncorrelated features enables spatially resolved spectral decomposition, which allows us to distinguish spectral components that are shared from those that are local. For phases that are

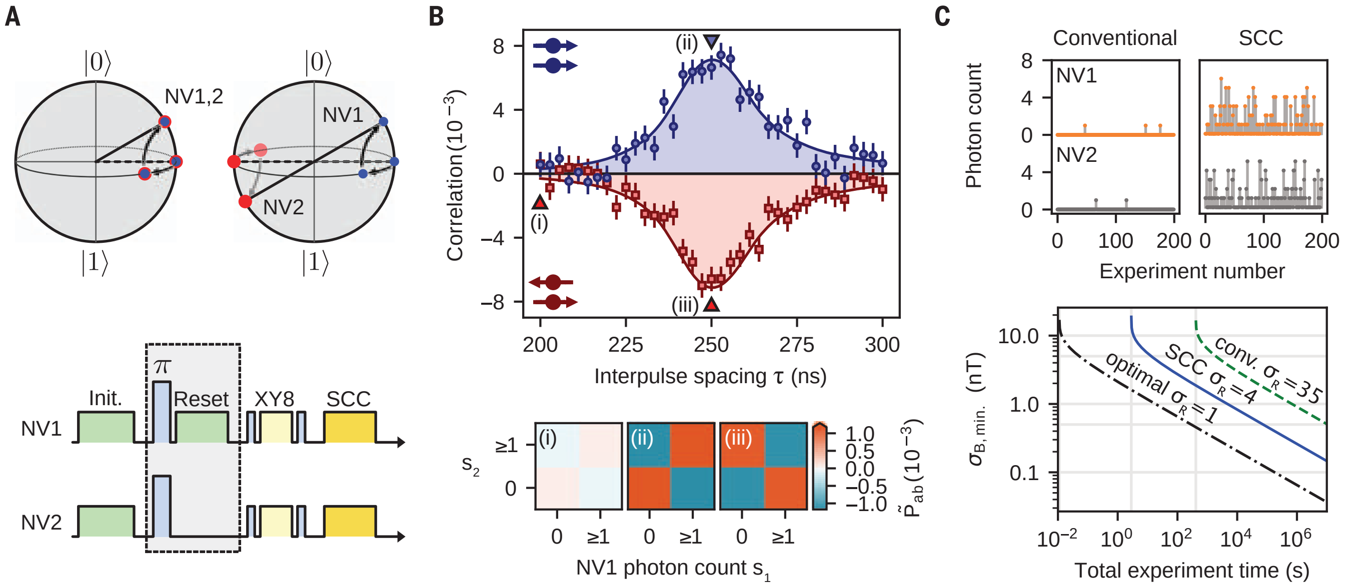


Fig. 2. Detecting correlations and anticorrelations. (**A**) Pulse sequence and final Bloch sphere mapping for correlation (top left) or anticorrelation (top right) measurements using global microwave control. For anticorrelations, an extra π pulse and spatially selective NV polarization optical pulse ("reset") are added during initialization (bottom, gray box). (**B**) Correlation detected from a 2-MHz ac signal whose phase is randomized with 1-MHz bandwidth Gaussian noise. The measured correlations are positive when the NV centers are initialized parallel to one another (blue circles) and negative when they are initialized antiparallel to one another (red squares). Lines indicate the predicted correlation shape (*31*). Raw photon count statistics (bottom) taken from the marked data points in the top panel show no correlation (i), positive correlation (ii), or negative correlation (iii), where the color indicates the joint detection probability $\tilde{P}_{ab} \equiv P(s_1 = a, s_2 = b) - P(s_1 = a)P(s_2 = b)$. (**C**) Comparison of shot-to-shot photon counts during averaging for conventional readout (top left) and SCC readout (top right). Minimum magnetic field amplitude to detect correlations with SNR = 1 for Gaussian noise is shown at the bottom. Here, we have assumed T_2 = 100 μs and the phase integration time $t = T_2/2$ = 50 μs, as well as a readout time of 300 ns for conventional readout and 1 ms for SCC and optimal readout. Initialization time was ignored. The horizontal and vertical gray lines are guides to the eye.

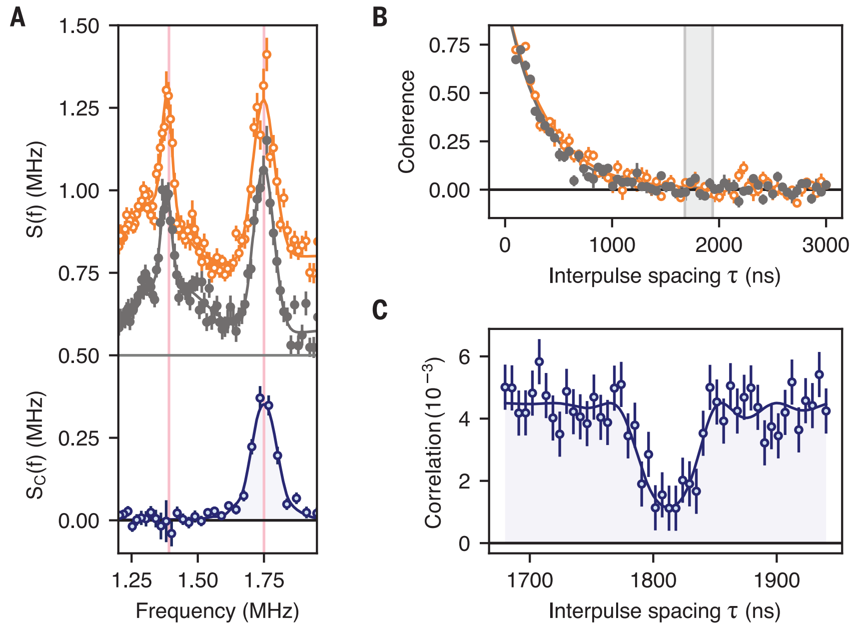


Fig. 3. Disentangling correlated and uncorrelated signals. (**A**) Single-NV noise spectra derived from conventional XY8 variance magnetometry (top) of two NV centers (orange open markers and gray filled markers with Gaussian fit lines, arbitrarily offset). Each NV center detects signals at two common frequencies, but it is impossible to directly determine whether the sources are local or nonlocal. Spectral decomposition (bottom) using covariance magnetometry (Eq. 3) reveals that the higher-frequency peak is caused by a shared noise source. Here, the shared noise feature is engineered using an applied global 1.75-MHz ac signal, whereas the local feature is caused by the ^{15}N nuclear spin intrinsic to each NV center. The line indicates the predicted correlation shape. The light red vertical lines indicate the expected peak locations (*31*). (**B**) In a broadband correlated noise environment, the two NV centers rapidly decohere (orange open markers and gray filled markers). Lines are exponential fits. (**C**) Covariance magnetometry for evolution times indicated by the gray region in (B) reveals a dip in the Pearson correlation around τ = 1800 ns that arises from the uncorrelated ^{15}N nuclear spins intrinsic to each NV center. The line indicates the predicted correlation shape. The broadband noise is correlated, which allows for the observation of spectral features from local signals even at evolution times beyond the coherence time of both NV centers.

Gaussian-distributed or small ($\phi \ll \pi$), we can find (*31*) the correlated noise spectrum $S_C(f)$ if we have access to both the two-NV correlation r as well as each NV center's coherence decay $C_i(t) = e^{-\chi(t)}$ [note that $C_i(t)$ includes both the correlated and uncorrelated noise sources]:

$$S_C(f) = \frac{\pi}{2t}\sinh^{-1}\left(\frac{\sigma_R{}^2 r}{C_1(t)C_2(t)}\right) \qquad (3)$$

where $t = n/(2f)$ and n is the total number of applied XY8 pulses. This equation is used to obtain the correlated spectrum from the measured correlation and single–NV center coherence decays, as shown in Fig. 3A. The

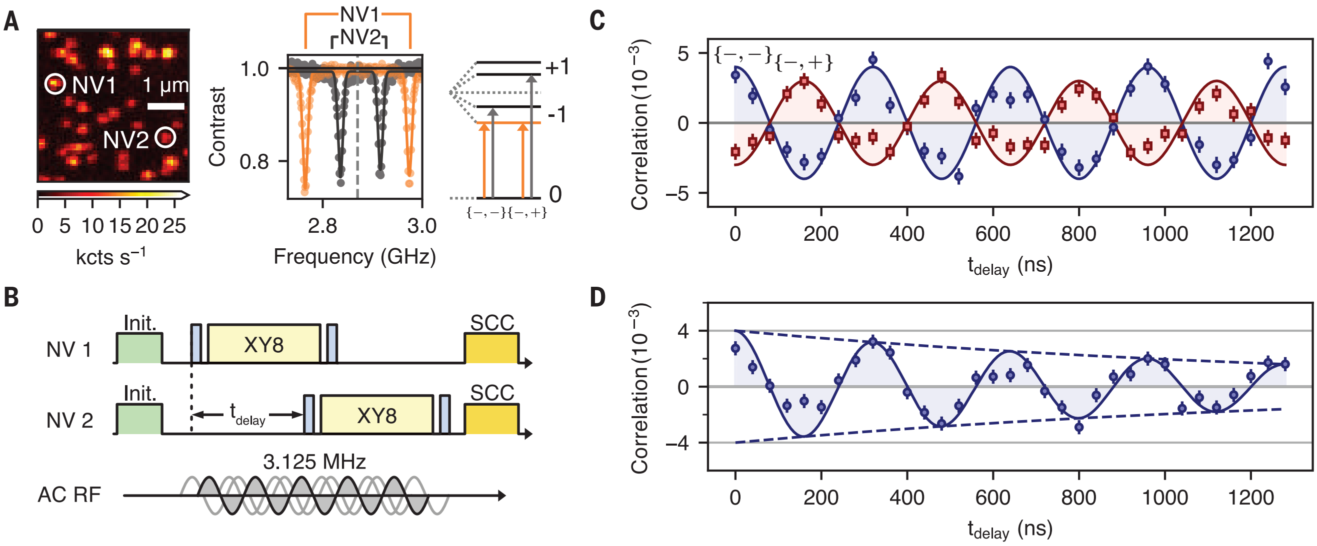


Fig. 4. Temporal structure in correlations using independent control. (**A**) Confocal image showing the two NV centers used for these experiments (left). Optically detected magnetic resonance spectrum (middle) showing optical contrast as a function of microwave drive frequency displays two distinct sets of transitions corresponding to NV1 and NV2, with assignments (right). The NV centers are driven independently on either the (0, −1) transitions for both NVs, labeled {−, −}, or the (0, −1) and (0, +1) transitions for NV1 and NV2, respectively, labeled {−, +}. (**B**) Diagram of the pulse sequence used to probe temporal correlations. After initialization, the start of the XY8 pulse sequence applied to NV2 is delayed by time t_{delay} from the start of the pulses on NV1. A f_0 = 3.125 MHz global ac signal is applied, making the resonant XY8 interpulse spacing τ = 160 ns. (**C**) Correlations for the case in which the NV centers are addressed on the same transitions ({−, −}, blue circles) oscillate as a function of t_{delay} at the ac signal frequency of 3.125 MHz. The correlations invert (red squares) when the two NV centers are addressed on different transitions ({−, +}), because they now accumulate opposite phases for the same signal. (**D**) With added phase noise, the time-domain dephasing of the ac signal is resolvable, despite having a short coherence time (less than 2 μs) compared with the XY8 sequence time.

local spectrum for each NV center $S_{L_{1,2}}(f)$ may also be found from each individual NV center's total spectrum $S_{L_{1,2}}(f) = S_{1,2}(f) - S_C(f)$.

So far, we have analyzed the case where shared and local features are spectrally resolved, but an interesting scenario arises when a shared signal decoheres each NV center at frequencies coincident with local noise sources. To probe this case, we applied a global broadband Gaussian noise signal, decohering both NV centers while inducing broadband correlations in their phases (Fig. 3, B and C). Beyond the coherence time of each NV center, conventional variance detection cannot reveal any information (gray region in Fig. 3B). However, covariance magnetometry (Fig. 3C) measures the broadband correlation in the random phases of the decohered NV centers; this correlation will dip if either NV center interacts with a local noise source in its vicinity, because the local signal induces a phase that is specific to that NV center. The covariance magnetometry spectrum therefore reveals a feature that is hidden in the single-NV spectra.

Temporal structure of correlations

Covariance magnetometry also enables measurements of the temporal structure of the two-point correlator $\langle B(r_1, t_1)B(r_2, t_2)\rangle$ separated in time as well as space for short time scales where $t_2 - t_1 < t + t_R$, which is not possible with single–NV center correlation measurements (*24*–*26*). To perform this measurement, independent control of each NV center is required. We accomplished this by choosing two NV centers with different orientations at low magnetic fields (Fig. 4A), such that the 0→−1 transition of the NV center that is aligned with the magnetic field is detuned by 70 MHz from that of the misaligned NV center. We then offset the beginning of the XY8 sequence applied to NV2 by time t_{delay} (Fig. 4B) and measured an applied ac field at frequency f_0 = 3.125 MHz. As we swept t_{delay}, the correlations oscillated at frequency f_0 (Fig. 4C), as expected for a random-phase ac signal (*26*, *37*). Independent control also allowed us to simultaneously address opposite spin transitions for each NV center (Fig. 4A, right). Because the two NV centers then accumulate opposite phases from the ac field, we observed anticorrelations with the same frequency (red squares in Fig. 4C).

Because the two NV centers are manipulated independently, there are no fundamental constraints on the length of t_{delay}. This allowed us to directly measure time-domain structure on the nanosecond time scale at two points in space, despite using π pulses with 60-ns duration. When we measured the correlations between two NV centers experiencing a shared ac signal with added phase noise (Fig. 4D), we could directly resolve the temporal structure of the ac signal despite its short coherence time of less than 2 μs, without making use of spectral deconvolution. We emphasize that this technique is very general and is thus applicable to any time-varying signal with a nonzero correlation time that can be detected with NV centers. Correlations will remain detectable on the time scale of the underlying signal correlation time, even when the signal phase is completely random from one experiment to the next (as in Fig. 3C).

Concluding remarks

Our demonstration of simultaneous control and readout of two spatially resolved NV centers shows that nanoscale magnetometry of two-point spatiotemporal field correlators that would normally be discarded using conventional NV center magnetometry is possible. Spatiotemporal correlations of any signal that can be imprinted as a phase on the NV centers can be sensed with this technique, provided that the statistics of the signal remain sufficiently stationary over the course of the experiment. Our approach has many potential applications; measurements of these two-point correlators can reveal the underlying length and time scales of fluctuating electromagnetic fields near surfaces (*7*, *8*), which provides information about nonequilibrium transport dynamics (*38*) and condensed matter phenomena like magnetic ordering in low-dimensional systems (*5*, *15*). For example, there has been considerable recent interest in studying hydrodynamic flow in 2D materials (*20*–*22*), but it

is challenging to directly observe the hydrodynamic transition—covariance noise sensing could provide new quantitative information about these dynamics. Also, magnetic excitations such as magnons can have micron-scale dynamics, a natural length scale for covariance magnetometry with pairs of NV centers. Future extensions of the current demonstration include using photonic structures to improve photon collection efficiency (*33*), applying different pulse sequences to each NV center to probe the correlations between signals at different frequencies or phases (*39*), measuring more NV centers to measure higher-order joint cumulants (*31*), and using detector arrays to perform simultaneous readout of many pairs of NV centers.

REFERENCES AND NOTES

1. H. Bernien *et al.*, *Nature* **551**, 579–584 (2017).
2. J. Zhang *et al.*, *Nature* **551**, 601–604 (2017).
3. X.-L. Deng, D. Porras, J. I. Cirac, *Phys. Rev. A* **72**, 063407 (2005).
4. M. L. Baez *et al.*, *Proc. Natl. Acad. Sci. U.S.A.* **117**, 26123–26134 (2020).
5. A. Mazurenko *et al.*, *Nature* **545**, 462–466 (2017).
6. J. Simon *et al.*, *Nature* **472**, 307–312 (2011).
7. V. N. Premakumar, M. G. Vavilov, R. Joynt, *Quantum Sci. Technol.* **3**, 015001 (2017).
8. K. Agarwal *et al.*, *Phys. Rev. B* **95**, 155107 (2017).
9. S. Gustavsson *et al.*, *Phys. Rev. B* **84**, 014525 (2011).
10. C. D. Wilen *et al.*, *Nature* **594**, 369–373 (2021).
11. U. von Lüpke *et al.*, *PRX Quantum* **1**, 010305 (2020).
12. P. Szańkowski, M. Trippenbach, Ł. Cywiński, *Phys. Rev. A* **94**, 012109 (2016).
13. F. Casola, T. van der Sar, A. Yacoby, *Nat. Rev. Mater.* **3**, 17088 (2018).
14. Q.-C. Sun *et al.*, *Nat. Commun.* **12**, 1989 (2021).
15. L. Thiel *et al.*, *Science* **364**, 973–976 (2019).
16. E. Lee-Wong *et al.*, *Nano Lett.* **20**, 3284–3290 (2020).
17. A. Jenkins *et al.*, *Phys. Rev. Mater.* **3**, 083801 (2019).
18. Y. Dovzhenko *et al.*, *Nat. Commun.* **9**, 2712 (2018).
19. S. Kolkowitz *et al.*, *Science* **347**, 1129–1132 (2015).
20. M. J. H. Ku *et al.*, *Nature* **583**, 537–541 (2020).
21. U. Vool *et al.*, *Nat. Phys.* **17**, 1216–1220 (2021).
22. A. Jenkins *et al.*, *Phys. Rev. Lett.* **129**, 087701 (2022).
23. T. I. Andersen *et al.*, *Science* **364**, 154–157 (2019).
24. J. M. Boss, K. S. Cujia, J. Zopes, C. L. Degen, *Science* **356**, 837–840 (2017).
25. M. Pfender *et al.*, *Nat. Commun.* **10**, 594 (2019).
26. A. Laraoui *et al.*, *Nat. Commun.* **4**, 1651 (2013).
27. L. Levitov, G. Falkovich, *Nat. Phys.* **12**, 672–676 (2016).
28. B. L. Dwyer *et al.*, arXiv:2103.12757 [quant-ph] (2021).
29. S. Sangtawesin *et al.*, *Phys. Rev. X* **9**, 031052 (2019).
30. J. M. Taylor *et al.*, *Nat. Phys.* **4**, 810–816 (2008).
31. See supplementary materials.
32. B. J. Shields, Q. P. Unterreithmeier, N. P. de Leon, H. Park, M. D. Lukin, *Phys. Rev. Lett.* **114**, 136402 (2015).
33. J. F. Barry *et al.*, *Rev. Mod. Phys.* **92**, 015004 (2020).
34. T. Gullion, D. B. Baker, M. S. Conradi, *J. Magn. Reson.* **89**, 479–484 (1990).
35. Ł. Cywiński, R. M. Lutchyn, C. P. Nave, S. Das Sarma, *Phys. Rev. B* **77**, 174509 (2008).
36. D. A. Hopper, H. J. Shulevitz, L. C. Bassett, *Micromachines* **9**, 437 (2018).
37. C. L. Degen, F. Reinhard, P. Cappellaro, *Rev. Mod. Phys.* **89**, 035002 (2017).
38. P. E. Dolgirev *et al.*, *Phys. Rev. B* **105**, 024507 (2022).
39. P. Szańkowski, G. Ramon, J. Krzywda, D. Kwiatkowski, Ł. Cywiński, *J. Phys. Condens. Matter* **29**, 333001 (2017).
40. J. Rovny *et al.*, Nanoscale covariance magnetometry with diamond quantum sensors, *Harvard Dataverse* (2022); https://doi.org/10.7910/DVN/XMEIHR.

ACKNOWLEDGMENTS

We acknowledge helpful conversations with A. Burgers, S. Gopalakrishnan, and J. Thompson. **Funding:** This work was funded by NSF CAREER grant DMR-1752047; the Princeton Catalysis Initiative; the US Department of Energy, Office of Science, Office of Basic Energy Sciences, under award no. DE-SC0018978; the US Department of Energy Office of Science National Quantum Information Science Research Centers; a Princeton Quantum Initiative Postdoctoral Fellowship (J.R.); and the Intelligence Community Postdoctoral Research Fellowship Program by the Oak Ridge Institute for Science and Education (ORISE) through an interagency agreement between the US Department of Energy and the Office of the Director of National Intelligence (ODNI) (M.F.). **Author contributions:** Theoretical framework: J.R., M.F., A.I.A., C.F., M.C.C., S.K., N.P.d.L.; Experiment: J.R., Z.Y., L.F.; Sensing technique, experimental design, data analysis: J.R., C.F., M.C.C., S.K., N.P.d.L.; Writing: J.R., C.F., M.C.C., S.K., N.P.d.L. **Competing interests:** The authors declare that they have no competing interests. **Data and materials availability:** All data needed to evaluate the conclusions in this paper are present in the paper or the supplementary materials and are publicly available at Harvard Dataverse (*40*).

License information: Copyright © 2022 the authors, some rights reserved; exclusive licensee American Association for the Advancement of Science. No claim to original US government works. https://www.science.org/about/science-licenses-journal-article-reuse

SUPPLEMENTARY MATERIALS

science.org/doi/10.1126/science.ade9858
Materials and Methods
Figs. S1 and S2
References (*41*–*45*)

Submitted 20 September 2022; accepted 25 November 2022
10.1126/science.ade9858

DEVELOPMENT

Zygotic genome activation by the totipotency pioneer factor Nr5a2

Johanna Gassler[1,2]†, Wataru Kobayashi[1]†, Imre Gáspár[1]†, Siwat Ruangroengkulrith[1]†, Adarsh Mohanan[1], Laura Gómez Hernández[1], Pavel Kravchenko[1], Maximilian Kümmecke[2], Aleksandar Lalic[1], Nikita Rifel[1], Robert John Ashburn[1], Maciej Zaczek[2], Antoine Vallot[2], Laura Cuenca Rico[2], Sabrina Ladstätter[2], Kikuë Tachibana[1,2]*

Life begins with a switch in genetic control from the maternal to the embryonic genome during zygotic genome activation (ZGA). Despite its importance, the essential regulators of ZGA remain largely unknown in mammals. On the basis of de novo motif searches, we identified the orphan nuclear receptor Nr5a2 as a key activator of major ZGA in mouse two-cell embryos. Nr5a2 is required for progression beyond the two-cell stage. It binds to its motif within *SINE B1/Alu* retrotransposable elements found in cis-regulatory regions of ZGA genes. Chemical inhibition suggests that 72% of ZGA genes are regulated by Nr5a2 and potentially other orphan nuclear receptors. Nr5a2 promotes chromatin accessibility during ZGA and binds nucleosomal DNA in vitro. We conclude that Nr5a2 is an essential pioneer factor that regulates ZGA.

The discovery that oocyte cytoplasm can reprogram somatic nuclei to totipotency has given rise to the idea that maternally provided factors reprogram and trigger zygotic genome activation (ZGA) in the embryo (*1*). This transcriptional awakening of the embryonic genome in mice occurs in at least two waves—minor ZGA in the zygote and major ZGA (hereafter referred to as just ZGA) in the two-cell embryo (fig. S1A) (*2*, *3*). Zygotic transcription is required for progression beyond the two-cell stage (*4*).

The transcription factors that initiate ZGA appear to be poorly conserved between species. During *Drosophila* embryogenesis, transcription factors including the diptera-specific Zelda, GAGA factor (GAF), and chromatin-linked adaptor for male-specific lethal protein (CLAMP) are essential for ZGA (*5*–*7*). In zebrafish and frogs, pluripotency factors belonging to the POU and Sox families as well as Nanog are required for ZGA (*8*–*10*). By contrast, the pluripotency factor Oct4 is not essential for murine ZGA (*11*). Nfya, Yap1, Dux, Rarg, Dppa2, and Dppa4 have been linked to mammalian ZGA (*12*–*17*) but are not required for progression beyond the two-cell embryo in knockdown or genetic knockout models (*12*, *18*–*22*). The essential transcription factors that activate mammalian zygotic genomes therefore remain largely unknown.

Transcription factors bind to regulatory elements in the genome to control gene expression and cell fate. Genomic DNA is wrapped around a histone octamer in the nucleosome, which is a barrier to transcription factor occupancy. Pioneer transcription factors (hereafter referred to as pioneer factors) have the capacity to bind their (partial) motif on nucleosomal DNA in vitro and to be recruited to closed chromatin in vivo, eliciting local chromatin opening by diverse mechanisms (*23*). Pioneer factors cooperatively open the fruit fly and zebrafish genomes during ZGA (*6*–*9*, *24*, *25*). Whether pioneer activities initiate mammalian ZGA is not known. In this work, we identified

[1]Department of Totipotency, Max Planck Institute of Biochemistry (MPIB), Munich, Germany. [2]Institute of Molecular Biotechnology of the Austrian Academy of Sciences (IMBA), Vienna Biocenter (VBC), Vienna, Austria.
***Corresponding author. Email: tachibana@biochem.mpg.de**
†These authors contributed equally to this work.

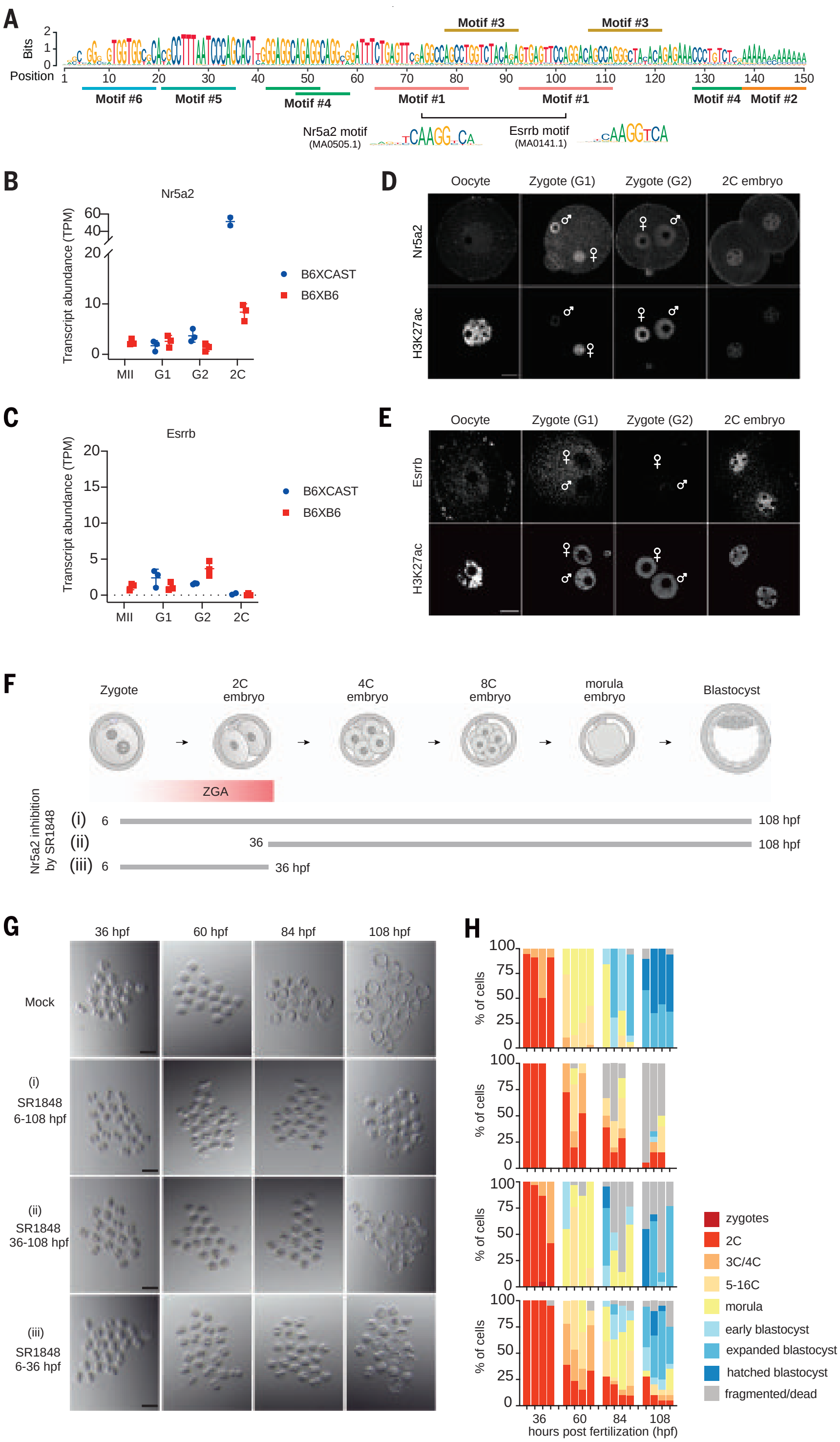


Fig. 1. Nr5a2 is required for early embryonic development. (**A**) Sequence logo of the identified super motif with individual motifs highlighted. Motif 1 resembles the cognate binding sequence of Nr5a2 or Esrrb. (**B** and **C**) Transcript abundance of main protein-coding isoforms of Nr5a2 (B) and Esrrb (C) during the oocyte–to–two-cell (2C) embryo transition from pure B6 (B6xB6) and B6CASTF1 (B6xCAST) mice (see materials and methods). TPM, transcripts per million. (**D** and **E**) Representative immunofluorescence images depicting Nr5a2 (D) and Esrrb (E) in embryonic stages. Maternal and paternal zygotic nuclei are indicated by the respective symbols. H3K27ac immunofluorescence is shown to indicate proper antibody penetration and to outline the nuclei. Depicted are single *z* slices. Scale bars, 20 μm. (**F**) Schematic of early embryo stages, including timing and length of inhibitor treatment. (**G**) Stereomicroscopic representative images of the embryonic stages observed at the indicated time points in different conditions. Mock control embryos were treated with DMSO. Scale bars, 150 μm. (**H**) Quantification of four replicate experiments of embryonic development. Sample sizes are as follows: mock, *n* = 19, 23, 16, and 33 cells; SR1848 (6 to 108 hpf), *n* = 18, 20, and 21; SR1848 (6 to 36 hpf), *n* = 18, 20, 20, and 30; SR1848 (36 to 108 hpf), *n* = 20, 21, 17, and 29. Each experiment comprised 6 to 12 females.

the orphan nuclear receptor Nr5a2 as a pioneer factor that activates genome-wide gene expression in mouse embryos.

Nr5a2 is required for early embryonic development

We hypothesized that motifs of transcription factors regulating ZGA are enriched in the cis-regulatory regions of ZGA genes. To define ZGA genes, we compared transcription profiles of two mouse strains during the oocyte-to-embryo transition. A total of 2508 extended ZGA genes were up-regulated more than fourfold in two-cell embryos of the two strains. The 985 genes common to both were classified as core ZGA genes (fig. S1). Using de novo motif searches, we found a consensus sequence, comprising six motifs, that is enriched within 8 kb upstream of ~70% of core and extended ZGA genes (compared with 31% of non-ZGA genes) (Fig. 1A and fig. S2, A and B). The sequence has 90% similarity to the *short interspersed nuclear element* (*SINE*) *B1* family of retrotransposons, which are related to the human *Alu* family (Fig. 1A). A CA version of a variable pyrimidine-purine stretch (*YR5*) within the sequence is correlated with higher chromatin accessibility and histone acetylation during

major ZGA (fig. S2, C and E), which implies a functional relevance. *YR5* is located in motif 1, which shows a high frequency and mean occurrence upstream of ZGA genes (fig. S2D). The CA version of motif 1 contains the consensus sequences for orphan nuclear receptors Nr5a2 (TCAAGGCCA, hereafter Nr5a2 motif) and Esrrb (TCAAGGTCA, hereafter Esrrb motif) and nuclear hormone receptor retinoic acid receptor gamma (Rarg) (AGGTCAAGGTCA) (*26*, *27*). Given that Rarg is not essential for ZGA because *Rarg*$^{-/-}$ females are fertile (*18*), we focused on the orphan nuclear receptors. *Nr5a2*$^{-/-}$ and *Esrrb*$^{-/-}$ embryos produced from heterozygote intercrosses die around implantation (*28*, *29*). Because at least transcripts for both transcription factors are maternally provided (see below), it is conceivable that maternal proteins enable progression beyond ZGA in homozygous knockout embryos. It is therefore unknown whether these transcription factors have functions during ZGA.

To assess whether Nr5a2 and Esrrb are ZGA regulators, we examined their expression during the oocyte-to-embryo transition. Both are maternally deposited as transcripts in metaphase II eggs and zygotes, and Nr5a2 is strongly expressed in two-cell embryos (Fig. 1, B and C). Nr5a2 protein is present in oocytes and enriched in the nuclei of zygotes and two-cell embryos (Fig. 1D). Esrrb protein becomes detectable in two-cell embryos (Fig. 1E). Because Nr5a2 protein is present before ZGA, we focused on this transcription factor as a candidate regulator of zygotic gene expression.

To determine whether Nr5a2 has an early embryonic function that would be consistent with regulating ZGA, we tested whether Nr5a2 perturbation affects development (Fig. 1F). Nr5a2 can be inhibited by the chemical compound SR1848 (*30*, *31*). To evaluate its specificity, we expressed orphan nuclear receptor family members and performed a luciferase reporter assay in HEK293T cells. SR1848 inhibited Nr5a2, as expected, as well as Nr5a1 and Nr2c2, but the latter two were undetectable as transcripts before ZGA (fig. S3); Nr5a1 remained largely undetectable throughout preimplantation development, and Nr2c2 is transcribed during ZGA. SR1848 did not inhibit Esrrb and Esrrg, which were both present before ZGA (fig. S3). These results suggest that the main target of SR1848 in early embryos is Nr5a2.

Embryos that were constitutively cultured with SR1848 failed to form blastocysts and fragmented or died at 108 hours postfertilization (hpf) [Fig. 1, G and H, condition (i)]. This is consistent with a function of Nr5a2 in maintaining naïve pluripotency in mouse embryonic stem (ES) cells (*26*) and suggests that it is also required for pluripotency establishment in vivo. Embryos treated with SR1848 from the two-cell stage (36 hpf) onward had a less severe phenotype than those treated from 6 hpf [Fig. 1, G and H, condition (ii)], which suggests that Nr5a2 activity is required not only after but also before the two-cell stage. Transient inhibition of Nr5a2 from 6 to 36 hpf caused either an immediate two-cell arrest or a >24-hours developmental delay [Fig. 1, G and H, condition (iii)]. Overall, these findings suggest that Nr5a2 plays multiple roles in development, including a hitherto unknown function between fertilization and the two-cell stage, when ZGA occurs.

Nr5a2 and Esrrb contribute to ZGA

To monitor ZGA directly, we visualized nascent ZGA transcripts by single-molecule fluorescence in situ hybridization (ZGA-FISH) (fig. S4A). Two sets of FISH probes were designed for robustness, and each detected ~80 nascent ZGA transcripts that were quantified by single-molecule FISH analysis algorithms (*32*–*34*). The lower threshold was determined by triptolide treatment to degrade RNA polymerase II in embryos. The total copy number of nuclear transcripts was reduced by ~62% in triptolide-treated two-cell embryos compared with dimethyl sulfoxide (DMSO)–treated controls (fig. S4, B and C).

Treatment of zygotes with SR1848 resulted in a dose-dependent reduction of nascent ZGA transcripts (~20 and ~40% for 5 and 10 μM SR1848, respectively) (fig. S5, A and B), which suggests that Nr5a2 regulates ZGA. To determine whether this effect could be rescued by overexpression of transcription factors, SR1848-treated embryos were microinjected with mRNA encoding orphan nuclear receptors (fig. S5C). Esrrb–green fluorescent protein (GFP) was ineffective in rescuing ZGA (fig. S5D). By contrast, Nr5a2-GFP, Nr5a1-GFP, and Nr2c2-GFP rescued ZGA to nearly control levels (Fig. 2A and fig. S5, E and F). This shows that the inhibitor is not a generic suppressor of transcription and supports the notion that SR1848 inhibits ZGA by inactivating Nr5a2 (because the other two are not detectable in early embryos). Moreover, Nr5a2-GFP but not Esrrb-GFP overexpression in otherwise unperturbed zygotes was sufficient to significantly increase transcription during ZGA in two-cell embryos (Fig. 2B). These results suggest that multiple orphan nuclear receptor family members have the ability to activate ZGA genes, presumably by recognizing the same motif. However, because only Nr5a2 can be detected in early embryos, these results suggest that Nr5a2 is required for ZGA.

To directly test whether Nr5a2 is involved in ZGA, we used Trim-Away (*35*, *36*) to target endogenous Nr5a2 for degradation. *Trim21-mCherry* mRNA and nonspecific immunoglobulin G (IgG) or two different Nr5a2 antibodies were microinjected into zygotes, and the resulting two-cell embryos were analyzed by ZGA-FISH. Nr5a2 targeting resulted in ~43% reduction of ZGA transcripts, which suggests that Nr5a2 is required for ZGA (Fig. 2C and fig. S5, G and H). In an orthogonal approach, we performed small interfering RNA (siRNA)–mediated knockdown of Nr5a2 in oocytes and analyzed two-cell embryos by ZGA-FISH (Fig. 2D). Nr5a2 knockdown had a negligible effect on ZGA in late two-cell embryos (34 hpf) (fig. S6), which could be the result of zygotic transcription of *Nr5a2* overcoming the knockdown effect (Fig. 1B). To overcome this potential rescue, we examined early two-cell embryos (26 hpf) and found that Nr5a2 knockdown reduced nascent ZGA transcripts by ~27% compared with controls (Fig. 2D). Expression of *Nr5a2* mRNA under these conditions rescued ZGA, demonstrating knockdown specificity (fig. S5, I and J). Using a similar approach in early two-cell embryos, Esrrb knockdown repressed ZGA by ~18% (Fig. 2D). These data suggest that Nr5a2 and, to some extent, Esrrb contribute to efficient ZGA.

To examine ZGA genome-wide, we performed single-embryo RNA sequencing (RNA-seq) of two-cell embryos (Fig. 2, E to G). Nr5a2 perturbation resulted in up- and down-regulation of transcripts, including a strong decrease in *Nr5a2* abundance in SR1848-treated embryos and a moderate decrease in siRNA-treated embryos at this time point (Fig. 2, E and F). Because the knockdown efficiency varied between cells (fig. S7, A and B), the analysis focused on embryos with the fewest *Nr5a2* transcripts as strong knockdown embryos (fig. S7B). Nr5a2 knockdown resulted in repression of *Nr2c2* transcription at ZGA, and Nr5a2 inhibition by SR1848 also resulted in down-regulation of several orphan nuclear receptors including its own gene, which suggests that Nr5a2 is required for their expression during ZGA (fig. S8).

Overall, Nr5a2 inhibition resulted in down-regulation of 5891 genes, including 1809 of the strictly defined ZGA genes, corresponding to 72% of ZGA genes (Fig. 2G and fig. S7F). By contrast, Nr5a2 knockdown resulted in down-regulation of only 448 genes, including 197 ZGA genes (Fig. 2G and fig. S7F). There are at least two non–mutually exclusive explanations for the greater genome-wide effects seen by chemical inhibition. One possibility is that Nr5a2 depletion by siRNA is incomplete because of maternal protein contributions and/or *Nr5a2* transcription during ZGA, whereas SR1848 directly inhibits the Nr5a2 protein. Another possibility is that the inhibitor targets multiple transcription factors. Although this is difficult to exclude, the luciferase assay combined with RNA-seq of embryos suggests that the main target for SR1848 present in early embryos is Nr5a2 (fig. S3). Consistent with this, Nr5a2 expression in SR1848-treated embryos largely rescued transcription of down-regulated genes (fig. S9). Hence, we conclude

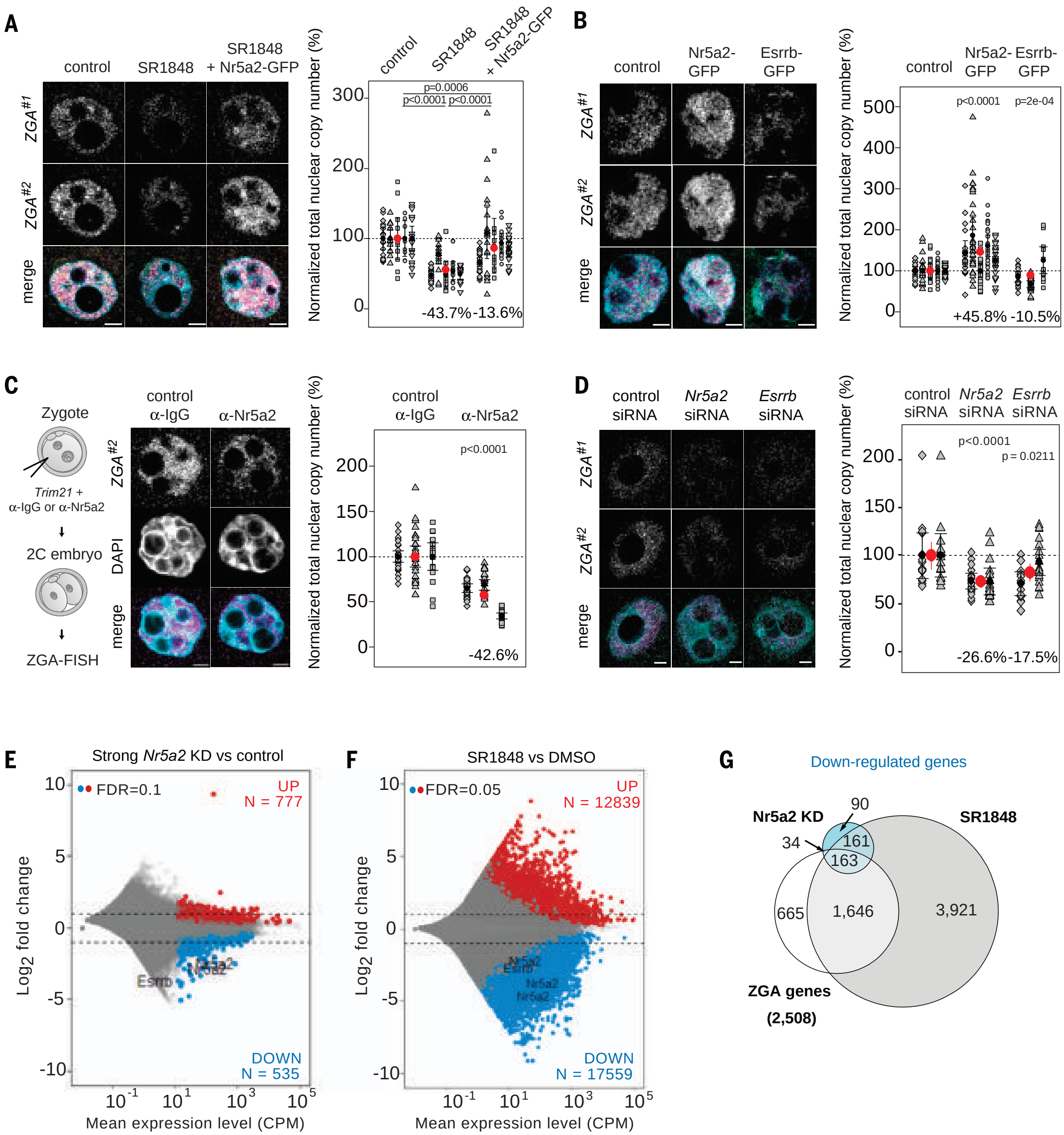


Fig. 2. Nr5a2 and Esrrb are required for efficient ZGA. (**A**) Representative nascent ZGA-FISH images of DMSO control, SR1848-treated, and SR1848-treated and Nr5a2-GFP mRNA microinjected two-cell embryos. (Right) Quantification of total nascent ZGA-FISH signal within the nuclei of two-cell embryos. Biological replicates are shown with different bullet styles. Black dots and bars show the means and 95% confidence intervals, respectively, per replicate, and red dots and bars indicate the means and 95% confidence intervals, respectively, of the experimental condition with all replicates merged [also for (B) to (D)]. Sample sizes are as follows: control, n = 16, 13, 13, 9, and 19 nuclei; SR1848, n = 21, 18, 12, 16, and 13; SR1848+Nr5a2-GFP, n = 28, 20, 12, 16, and 20. Scale bars, 5 μm. (**B**) Representative nascent ZGA-FISH images of two-cell embryos microinjected with Nr5a2-GFP or Esrrb-GFP mRNA. (Right) Quantification of total nascent ZGA-FISH signal within nuclei of two-cell embryos. Sample sizes are as follows: control, n = 20, 22, 19, 34, and 24 nuclei; Nr5a2-GFP, n = 21, 30, 23, 29, and 24; Esrrb-GFP, n = 23, 18, and 23. Scale bars, 5 μm. (**C**) Illustration showing Trim-Away–mediated Nr5a2 depletion in two-cell embryos. Representative nascent ZGA-FISH images of two-cell embryos microinjected with control IgG or Nr5a2 antibodies. (Right) Quantification of total nascent ZGA-FISH signal within nuclei of two-cell embryos in the respective conditions. Sample sizes are as follows: control IgG, n = 35, 31, and 18 nuclei; anti-Nr5a2, n = 28, 26, and 22. Scale bars, 5 μm. DAPI, 4′,6-diamidino-2-phenylindole. (**D**) Representative nascent ZGA-FISH images of *Esrrb*- and *Nr5a2*-siRNA embryos and controls during early ZGA (26 hpf). (Right) Quantification of total nascent ZGA-FISH signal within nuclei of *Nr5a2*-siRNA, *Esrrb*-siRNA, and control two-cell embryos in early ZGA in two replicates. Sample sizes are as follows: control, n = 15 and 15; *Esrrb*-siRNA, n = 19 and 16; *Nr5a2*-siRNA, n = 16 and 18. Scale bars, 5 μm. (**E**) Bland–Altman (MA) plot comparing strong Nr5a2-knockdown (KD) embryos with control by DESeq2. (**F**) MA plot comparing chemically inhibited two-cell embryos with control by DESeq2. (**G**) Euler diagrams showing the overlap of major ZGA genes with down-regulated genes in strong Nr5a2-knockdown and in SR1848-treated two-cell embryos.

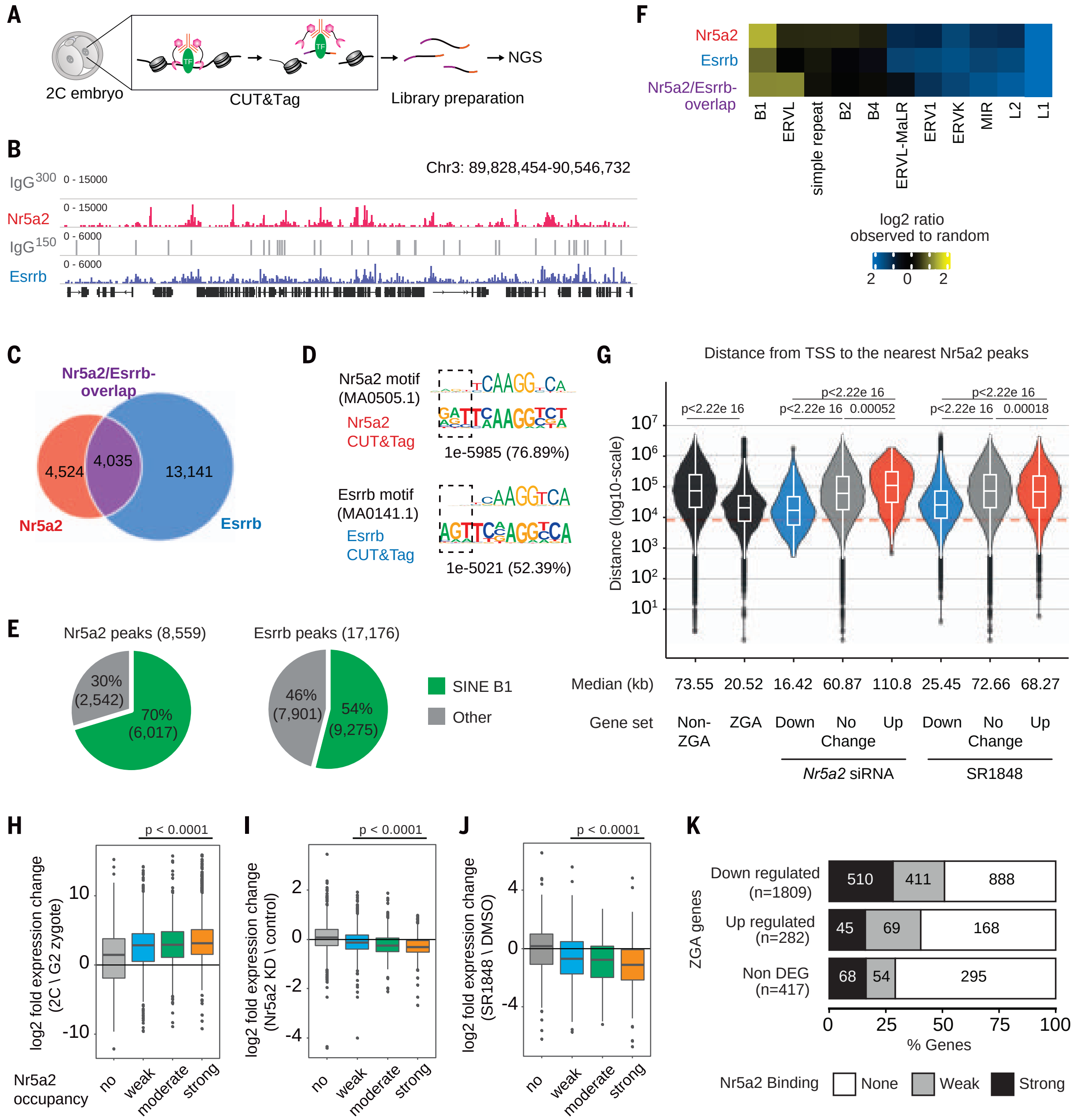


Fig. 3. Genomic binding sites of Nr5a2 and Esrrb during ZGA. (**A**) Illustration of CUT&Tag on two-cell embryos. NGS, next-generation sequencing. (**B**) Representative integrative genomics viewer (IGV) snapshot showing enrichment of IgG control (gray), Nr5a2 (red), and Esrrb (blue) within the indicated region on chromosome 3 (Chr3). The CUT&Tag signal for each transcription factor was merged from two replicates. (**C**) Euler diagram showing overlap between Nr5a2 and Esrrb peaks in two-cell embryos. (**D**) DNA sequence identified by Homer de novo motif analysis from Nr5a2 and Esrrb peaks compared with Nr5a2 (MA0505.1) and Esrrb (MA0141.1) motifs reported in the JASPAR database. The *P* value of the motif comparison and the percent of peaks containing de novo motifs are indicated. Black dashed squares show three extended nucleotides that are identified from CUT&Tag in two-cell embryos. (**E**) Pie chart showing the percentage of peaks with *SINE B1*. (**F**) Heatmaps showing the enrichment of repeats (subfamily) in Nr5a2-specific, Esrrb-specific, and Nr5a2-Esrrb–overlap peaks in two-cell embryos. (**G**) Violin plots showing the distance from TSS to the nearest Nr5a2 peaks between down-regulated, up-regulated, and unaffected genes in Nr5a2-knockdown and SR1848-treated embryos, ZGA genes, and non-ZGA genes. Red dashed line shows 8 kb. (**H** to **J**) Box plots showing the expression change of genes with no, weak, moderate, or strong Nr5a2 CUT&Tag signal at Nr5a2 motifs in their 8-kb upstream regions between G2 zygotes and two-cell embryos (H), in *Nr5a2*-knockdown (I), and in SR1848-treated two-cell embryos (J). Bonferroni-corrected *P* values of pairwise Mann-Whitney *U* tests against genes with no Nr5a2 occupancy are shown. (**K**) Bar chart representing the extended ZGA genes according to their expression changes upon chemical inhibition of Nr5a2 (*y* axis) and the total Nr5a2 CUT&Tag signal measured in their 8000-bp upstream regions (black indicates strong, gray indicates weak, and white indicates no occupancy). DEG, differentially expressed gene.

that Nr5a2 is required for the expression of major ZGA genes.

Nr5a2 binds near transcription start sites of Nr5a2-regulated ZGA genes

To determine whether Nr5a2 binds in the vicinity of ZGA genes in two-cell embryos, we adapted cleavage under targets and tagmentation (CUT&Tag) for ultralow-input samples and compared the results with published data on histone modifications (*37–39*) (Fig. 3A and fig. S10, A to C). We optimized conditions for Nr5a2 and Esrrb and obtained transcription factor binding profiles using 300 two-cell embryos. These showed an enrichment for specific and overlapping genomic regions that were not observed with IgG controls (Fig. 3B and fig. S10, D and E). We identified 4035 peaks enriched for both Nr5a2 and Esrrb, 4524 peaks specific to Nr5a2, and 13,141 peaks specific to Esrrb (Fig. 3C).

De novo motif analyses revealed that Nr5a2 motifs were enriched in 77% of all Nr5a2 CUT&Tag peaks, whereas Esrrb motifs were enriched in 52% of all Esrrb CUT&Tag peaks (Fig. 3D). The motifs that emerged from the detected peaks contained (A/G)(A/G)T upstream of the consensus sequences (Fig. 3D), which was also detected in motif 1 in the *SINE B1/Alu YR5* upstream of ZGA genes (Fig. 1A and fig. S2D). In fact, 70% of Nr5a2 peaks and 54% of Esrrb peaks overlapped with *SINE B1/Alu* (Fig. 3, E and F), which suggests that *SINE B1/Alu* retrotransposons are major targets for Nr5a2 and Esrrb in two-cell embryos. We cannot exclude that Nr5a2 recruitment outside canonical *SINE B1/Alu* (30% of the peaks) also contributes to ZGA regulation. However, these isolated Nr5a2 motifs also show signatures of degenerate *SINE B1/Alu* elements, which implies that most Nr5a2 motifs are derived from retrotransposon propagation (fig. S2F).

We examined the distance from the transcription start sites (TSSs) of ZGA genes to the nearest Nr5a2 peak. Nr5a2 peaks were substantially closer to ZGA genes (median: 20.52 kb) than to non-ZGA genes (median: 73.55 kb) (Fig. 3G). Nr5a2 peaks were also much closer to the TSSs of genes that were down-regulated versus those that were up-regulated in Nr5a2-knockdown two-cell embryos. Focusing on down-regulated genes, we found that the distances for knockdown-sensitive (median: 18.73 kb) and SR1848-sensitive genes (25.57 kb) were much closer than those for nondifferentially regulated genes (median: 72.3 kb) (fig. S7G). These findings suggest that the inhibitor-sensitive genes

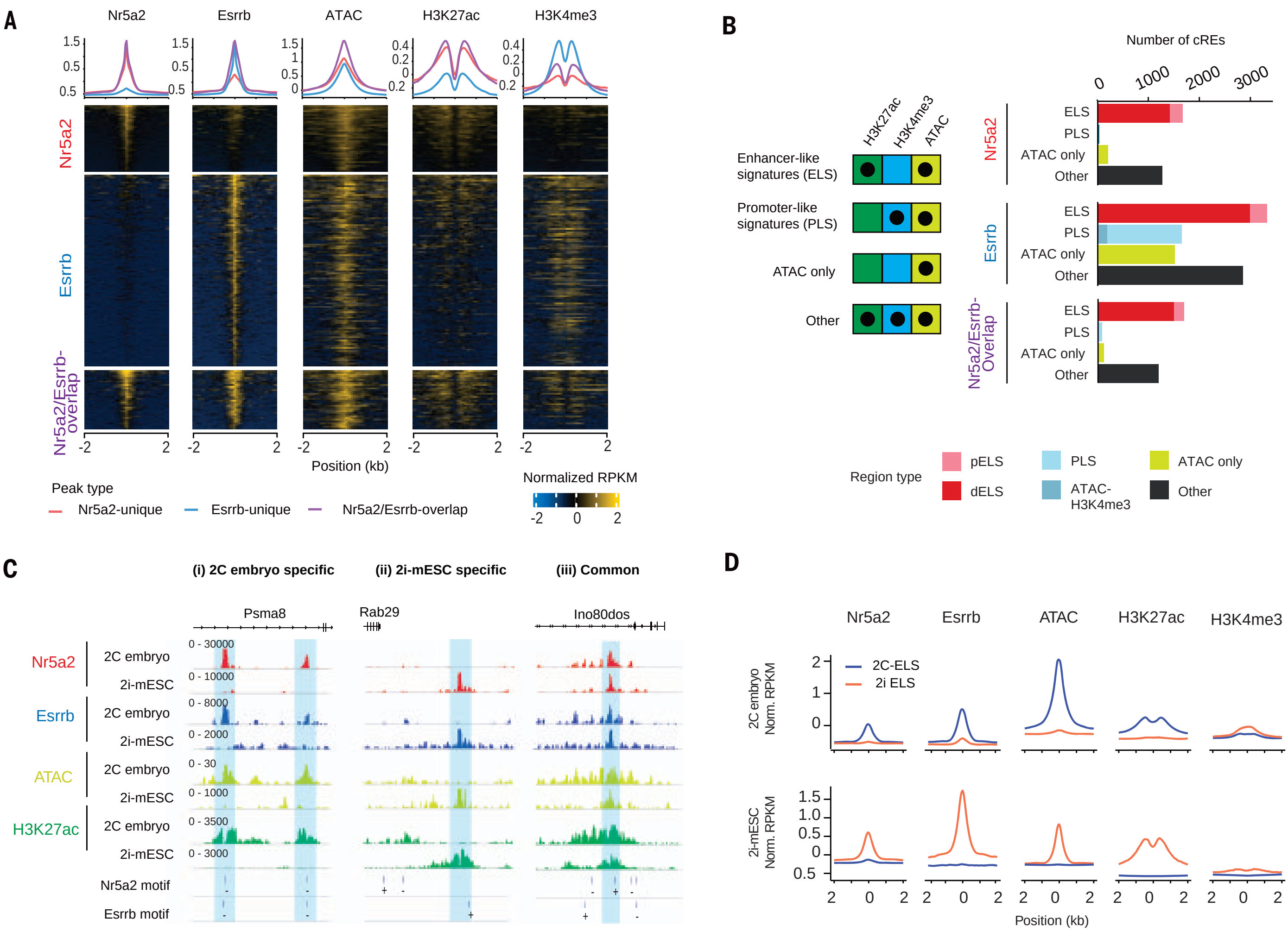


Fig. 4. Cell type–specific distribution of Nr5a2 and Esrrb. (**A**) Line plots (above) and heatmaps (below) of Nr5a2, Esrrb, ATAC-seq, H3K27ac, and H3K4me3 enrichments in two-cell embryos [*Z*-score–normalized RPKM (reads per kilobase per million reads mapped) value]. Each row is classified by Nr5a2-specific, Esrrb-specific, and Nr5a2-Esrrb–overlap regions. (**B**) Classification of cREs bound by Nr5a2 and Esrrb according to epigenetic signatures. We defined four major groups: ELSs, PLSs, ATAC-only, and other. Number of cREs bound by Nr5a2 and Esrrb are shown as bar graphs. The criteria of proximity are described in the materials and methods section. pELS, proximal ELS. (**C**) Representative IGV snapshots show the enrichment of Nr5a2 (red), Esrrb (blue), ATAC-seq (yellow), and H3K27ac (green) in two-cell embryos and 2i-mESCs. Nr5a2 and Esrrb peaks are highlighted in blue. (**D**) Average profiles of Nr5a2, Esrrb, ATAC-seq, H3K27ac, and H3K4me3 in 2C-ELSs and 2i-ELSs. The signal in a ±2-kb window flanking the peak center is shown. Blue and orange lines indicate peaks on 2C-ELSs and 2i-ELSs, respectively.

are similar to knockdown-sensitive genes with respect to the distance of Nr5a2 binding to TSS and imply that the former are unlikely to be off-target effects (fig. S7G).

To analyze the correlation between gene expression changes during ZGA and Nr5a2 occupancy, we conservatively defined occupancy as the sum of Nr5a2 CUT&Tag signals over Nr5a2 motifs in the 8-kb upstream region of genes (fig. S10F). The gene expression changes between G2-phase zygotes and two-cell stages were significantly higher for genes with higher Nr5a2 occupancy, and stronger gene expression changes correlated with increased Nr5a2 occupancy (Fig. 3H and fig. S10G). We further examined the correlation between gene expression changes in *Nr5a2*-siRNA and SR1848-treated embryos and Nr5a2 occupancy. Genes with Nr5a2 occupancy were significantly more down-regulated by Nr5a2 perturbation compared with unoccupied genes. Among genes occupied by Nr5a2, down-regulation of gene expression was also inversely correlated with Nr5a2 occupancy (Fig. 3, I and J, and fig. S10, H and I). Further analysis showed that >50% (921/1809) of ZGA genes down-regulated by SR1848 treatment showed some Nr5a2 CUT&Tag signal in their extended promoter regions, whereas both the number and proportion of Nr5a2-occupied regions were lower for unchanged or up-regulated ZGA genes (Fig. 3K). On the basis of these data, we propose that Nr5a2 binding close to ZGA genes promotes their transcriptional activation at ZGA, although it cannot be excluded that distant binding of Nr5a2 also contributes to ZGA regulation. These data also indicate that Nr5a2 controls expression of many ZGA genes directly.

Nr5a2 and Esrrb target cell type–specific enhancers

To analyze whether the regions bound by Nr5a2 and Esrrb in two-cell embryos could be cis-regulatory elements (cREs), we compared our CUT&Tag binding profiles with published assay for transposase-accessible chromatin using sequencing (ATAC-seq) and histone modification chromatin immunoprecipitation sequencing (ChIP-seq) data from two-cell embryos (*40*, *41*) and found that these transcription factors bind to open chromatin (Fig. 4A). We classified enhancer-like signatures (ELSs) as regions with high H3K27ac and ATAC-seq and low H3K4me3 signals versus promoter-like signatures (PLSs) with high H3K4me3 and ATAC-seq and low H3K27ac signals (*42*) (fig. S11, A and B). Nr5a2 binding was enriched at distal enhancer-like signatures (dELSs) (Fig. 4B), whereas Esrrb binding was detected at ELSs, PLSs, and other regions (Fig. 4B). These findings suggest that Nr5a2 and Esrrb target common and distinct loci, and Nr5a2 preferentially binds enhancers in two-cell embryos.

Esrrb, and to a lesser extent Nr5a2, are also expressed in ES cells (*26*). We examined published data to determine whether these transcription factors are recruited to distinct cREs in totipotent two-cell embryos versus pluripotent ES cells (*43*, *44*). This comparison suggests that Nr5a2 and Esrrb bind to prominent ATAC-seq and H3K27ac peaks (ELSs) that are present (i) in two-cell embryos only, (ii) in 2i medium-cultured ES cells only, or (iii) in both two-cell embryos and ES cells (Fig. 4C). We identified 9099 two-cell embryo–specific ELSs (2C-ELSs), 6460 2i–mouse embryonic stem cell (mESC)–specific ELSs (2i-ELSs), but only 110 common ELS sites (fig. S11C). Aggregation plot analysis showed that both Nr5a2 and Esrrb are specifically bound to each cell type–specific ELS with H3K27ac enrichment and chromatin accessibility (Fig. 4D and fig. S11, D and E). These data suggest that Nr5a2 and Esrrb are involved in setting up largely distinct gene-regulatory networks during different stages of embryogenesis by defining development (cell type)–specific enhancers.

Nr5a2 directly promotes chromatin accessibility

To test whether Nr5a2 and Esrrb are required for chromatin accessibility in two-cell embryos, we developed a microscopy-based approach to quantify open chromatin in single cells, which we termed ChARM (chromatin accessibility revealed by microscopy). Similar to assay of transposase-accessible chromatin with visualization (ATAC-see) (*45*), ChARM uses Tn5-mediated insertion of adaptor DNA into accessible chromatin but uses hybridization chain reaction (HCR) to amplify signals of the inserted adaptor DNA. This approach generated quantifiable spot-like patterns rather than the diffusive signals observed by ATAC-see (fig. S12, A and B). As a proof of concept, we examined bromodomain 4 (Brd4)–dependent open chromatin. Two-cell embryos treated with the Brd4 inhibitor JQ-1 showed reduced H3K27 acetylation, as expected (fig. S12, C and D), and significantly reduced ChARM signal (fig. S12, C and E).

To test whether Nr5a2 and Esrrb promote chromatin accessibility, we performed knockdown in oocytes and analyzed two-cell embryos by ChARM at 26 hpf. Chromatin accessibility was reduced in *Nr5a2*- and *Esrrb*-siRNA embryos compared with controls, which suggests that both transcription factors contribute to chromatin accessibility (Fig. 5, A and B). Similar results were obtained for two-cell embryos treated with SR1848 (fig. S12F). Together, these findings suggest that these transcription factors promote chromatin accessibility.

To determine whether Nr5a2 functions as a pioneer factor, we tested whether Nr5a2 is required for chromatin opening at sites where it is bound. SR1848 was used to inhibit Nr5a2 and obtain sufficient cell numbers to perform Omni ATAC-seq (fig. S13, A to C) (*46*). Changes in accessibility at TSSs were significantly correlated with gene expression changes (fig. S13, D and E), which suggests that changes in chromatin accessibility reflect gene expression changes that depend on Nr5a2.

By comparing ATAC-seq peaks from SR1848- versus DMSO-treated embryos, we identified 492 differentially accessible regions (DARs) that all showed loss of accessibility [10% false discovery rate (FDR); Fig. 5C]. Nearly half of the DARs overlapped with Nr5a2 CUT&Tag peaks in two-cell embryos (Fig. 5D). To determine whether the DARs are dependent on Nr5a2, we performed motif enrichment analysis and examined Nr5a2 occupancy. Although Nr5a2 and similar motifs occurred with similar frequencies in non-DAR and DAR regions (42 and 56%; fig. S13F), DARs showed higher occupancy of Nr5a2 in two-cell embryos (Fig. 5E). These regions are largely inaccessible in zygotes (fig. S13G), which suggests that their opening occurs in two-cell embryos.

We also investigated whether accessibility changes in CREs are related to Nr5a2 binding. Chromatin accessibility of PLSs and ELSs occupied by Nr5a2 is more reduced by SR1848 treatment than in unbound regions (Fig. 5F). These results suggest that Nr5a2 binding promotes opening of chromatin, which is a hallmark of pioneer factors.

Nr5a2 and Esrrb bind nucleosomal DNA in vitro

Another hallmark of pioneer factors is the ability to target their (partial) motif on nucleosomal DNA (*23*). To test whether Nr5a2 and Esrrb have this ability, we purified full-length and DNA binding domains (DBDs) of mouse Nr5a2 and Esrrb as well as mouse histones as recombinant proteins (fig. S14, A to D). Mass photometry showed that Nr5a2 forms a monomer, whereas Esrrb forms a dimer or multimer in solution (fig. S14E).

To examine the binding specificity to naked DNA, we performed fluorescence polarization measurements and electrophoretic mobility shift analysis (EMSA). Because Esrrb showed promiscuous binding to DNA (fig. S14F), we performed experiments in the presence of low concentrations of competitor DNA. Nr5a2 bound to its own motif and the Esrrb motif with comparable affinity (dissociation constant K_d of 5.62 ± 1 nM and 6.49 ± 0.35 nM, respectively). By contrast, Esrrb bound to its own motif with a higher affinity than the Nr5a2 motif (K_d of 8.56 ± 0.69 nM and 625.53 ± 133 nM, respectively) (Fig. 6A and fig. S14G). The same motif specificity was observed by EMSA (fig. S6, H and I).

To test whether Nr5a2 and Esrrb bind nucleosomal DNA, we performed SeEN-seq (selected engagement on nucleosome sequencing), in which motifs are tiled throughout the Widom

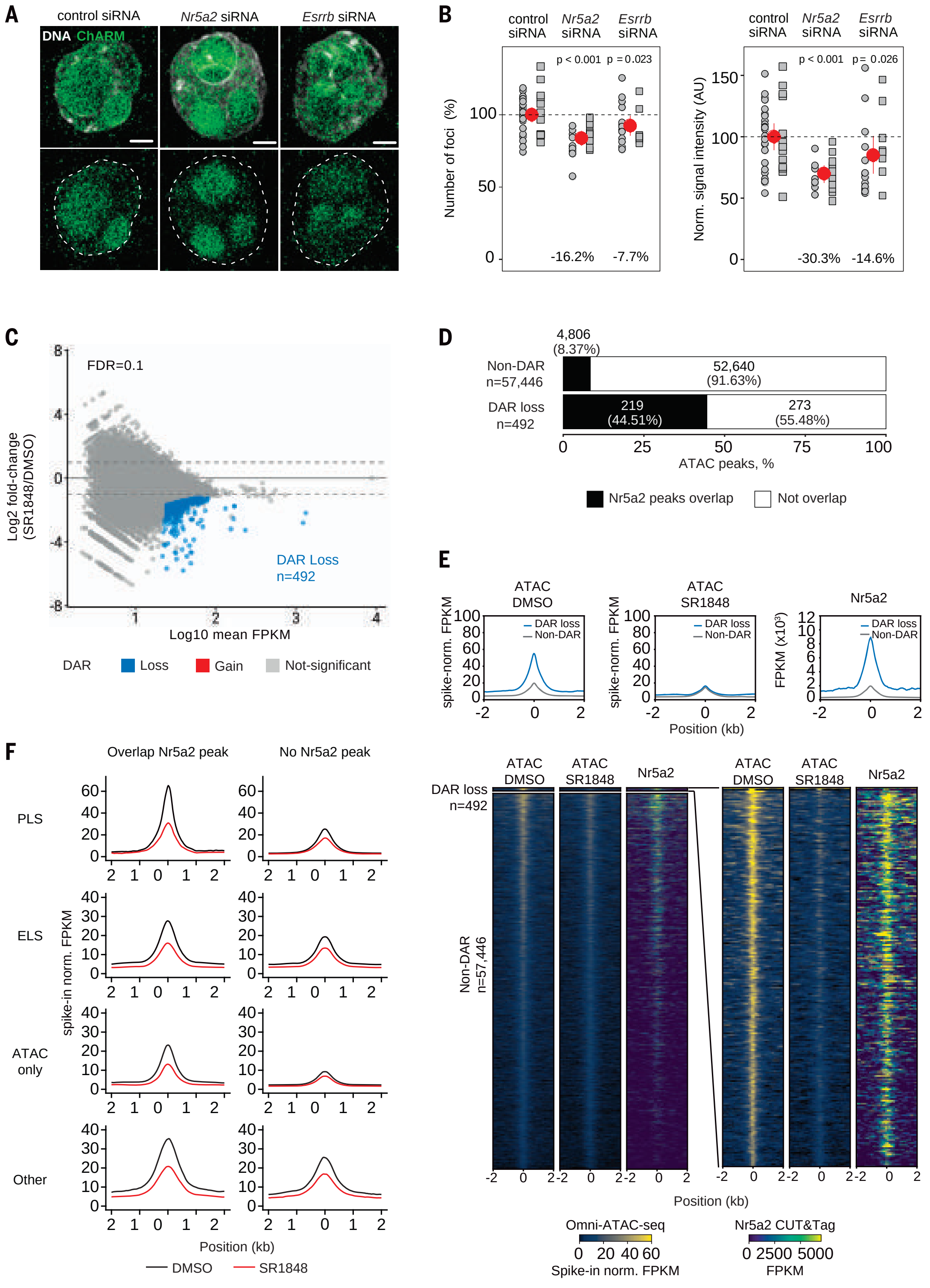


Fig. 5. Nr5a2 regulates chromatin accessibility during ZGA. (**A**) Representative images of ChARM (green) in two-cell embryos. (Top) Merged signal between ChARM (green) and DNA labeled by DAPI (gray). (Bottom) Only ChARM channel with the nuclear outlines (dashed line). Scale bars, 5 μm. (**B**) Scatter plots show the relative percentage of the number of ChARM foci per nucleus and normalized signal intensity. Experimental replicates are shown with different bullet styles. Red dots and bars indicate the means and 95% confidence intervals, respectively, of the experimental condition with all replicates merged. The number of nuclei analyzed in the replicates are as follows: control, n = 24 and 13; *Nr5a2*-siRNA, n = 9 and 12; Esrrb-siRNA, n = 14 and 9. (**C**) MA plot showing DAR analysis between SR1848-treated versus DMSO (control) two-cell embryos (FDR < 10%). Loss DARs are shown in blue. (**D**) Bar chart representing the ratios of DAR loss and non-DAR that overlap with Nr5a2 peaks from CUT&Tag. (**E**) Aggregation plots and heatmap comparing accessibility [omni-ATAC, DMSO (control), and SR1848] and Nr5a2 signal at regions that lost and showed no change in accessibility upon chemical inhibitor treatment. (**F**) Aggregation plot comparing accessibility at different classes of CREs with and without Nr5a2 peaks.

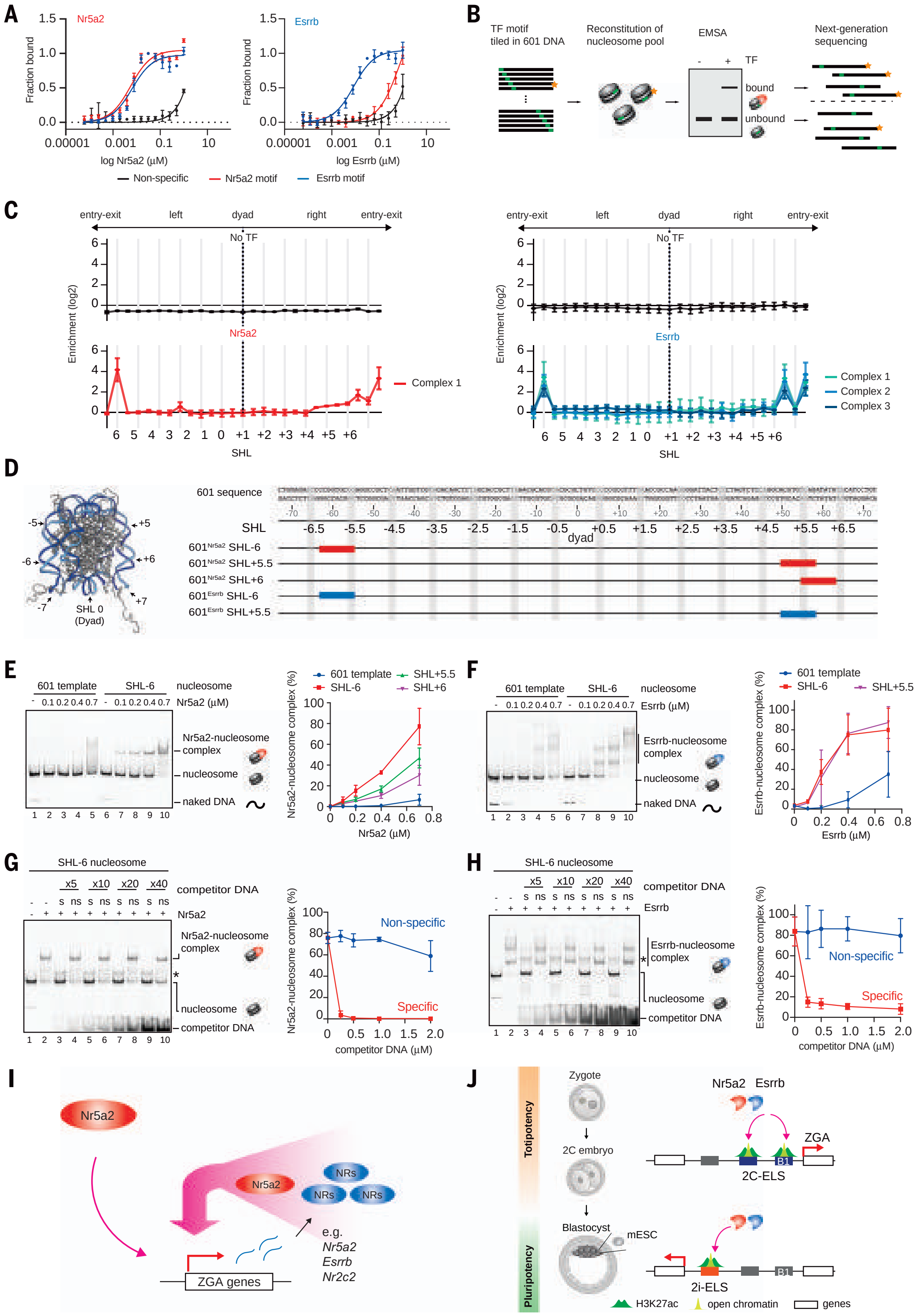


Fig. 6. Nr5a2 and Esrrb specifically recognize nucleosomal target DNA. (**A**) DNA binding measured by fluorescence polarization (FP) for Nr5a2 (left) and Esrrb (right) using DNA with nonspecific (black lines), Nr5a2 motif (red lines), and Esrrb motif (blue lines). The average values of three independent experiments are shown with the SD values. (**B**) Illustration of SeEN-seq. Nucleosome libraries were reconstituted with transcription factor (TF) motif (green) tiled in 601 DNA. TF-bound and -unbound fractions were recovered and sequenced to reveal position-specific enrichments. Stars indicate a sequence of specific enrichment as an example. (**C**) SeEN-seq enrichment profiles of Nr5a2 (left) and Esrrb (right). The enrichments (log_2) were plotted against each SHL (from SHL −6.5 to SHL +6.5). The average values of two independent experiments are shown with the SD values. (**D**) (Left) Schematic of SHL positions on nucleosome (Protein Data Bank ID: 1KX5). (Right) The location where the Nr5a2 (red) or Esrrb (blue) motif is inserted on 601 DNA sequence. (**E** and **F**) Nucleosome binding assays with Nr5a2 (E) or Esrrb (F). (Left) Representative data of EMSA with the 601 template nucleosome and SHL −6 nucleosome. (Right) Graphical representation. The average values of three independent experiments are shown with the SD values. (**G** and **H**) Competition assays with Nr5a2 (G) and Esrrb (H). Nr5a2 or Esrrb (0.5 μM) was incubated with SHL −6 nucleosome containing their own motifs (50 nM) in the presence of 5-, 10-, 20-, and 40-fold molar excess of specific competitor DNA ("s" lanes) or nonspecific DNA ("ns" lanes). Asterisks indicate the competitor DNA-bound complex. (Right) Quantification of the results. The average values of three independent experiments are shown with the SD values. (**I**) Model of Nr5a2-dependent ZGA regulation in mouse embryos. (**J**) Model of Nr5a2's distinct regulation of totipotency and pluripotency networks during mammalian development.

601 nucleosome positioning sequence (Fig. 6B) (*47*). We prepared nucleosome libraries with 5–base pair (bp) shifts in the position of each motif (fig. S15, A and C, and table S13). EMSA showed a shift of Nr5a2 with the nucleosome library but not with the 601 "template" nucleosome lacking a motif, which suggests that the Nr5a2-nucleosome complex forms in a motif-dependent manner (fig. S15B). Similarly, Esrrb showed specific band shifts with the nucleosome library (fig. S15D). Transcription factor–bound and –unbound fractions were purified and sequenced. SeEN-seq revealed that Nr5a2 and Esrrb preferentially bound at the entry-exit sites on the nucleosome (Fig. 6C), reminiscent of how the pioneer factors Oct4-Sox2 and GATA3 bind to nucleosomal DNA (*47*, *48*).

To investigate Nr5a2 and Esrrb binding at specific motif positions on nucleosomes, we selected high-enrichment sites and reconstituted

nucleosomes with motifs at superhelical locations (SHLs) −6, +5.5, and +6 for Nr5a2 and at SHLs −6 and +5.5 for Esrrb (Fig. 6D and fig. S15E). Consistent with the SeEN-seq results, a band shift was detected for Nr5a2 binding to nucleosomes containing the motif at SHL −6, SHL +5.5, and SHL +6 (Fig. 6E and fig. S15F). Motif-specific binding was also detected for the Nr5a2 DBD (fig. S15H). Esrrb full-length and DBD showed similar nucleosome binding efficiencies (Fig. 6F and fig. S15, G and I). A stronger band shift was detected for Esrrb binding to nucleosomes with motifs at SHL −6 and SHL +5.5 than for the 601 template (Fig. 6F and fig. S15G). Because it is conceivable that the binding to entry-exit sites of nucleosomal DNA is the result of the tight binding of 601 DNA to histones, we also tested whether Nr5a2 could bind to an endogenous sequence in which the motif was closer to the dyad axis. We found that Nr5a2 could also bind nucleosomes containing this endogenous sequence (fig. S15, J and K), which suggests that Nr5a2 can recognize its motif in different SHLs.

To test the specificity of the transcription factor–nucleosome interactions, we performed competition assays with naked DNA. Specific but not nonspecific DNA outcompeted binding of Nr5a2 and Esrrb to nucleosomes (Fig. 6, G and H). Thus, both Nr5a2 and Esrrb directly engage with their own motifs on nucleosomal DNA. Overall, our data show that Nr5a2 and Esrrb have properties consistent with pioneer factor activity in vivo and in vitro.

Discussion

We provide evidence that the orphan nuclear receptor Nr5a2 is a pivotal pioneer factor that activates up to 72% of major ZGA genes in mouse embryos. Nr5a2 binds to *SINE B1/Alu* retrotransposable elements in the cis-regulatory regions of nearly half of all ZGA genes, and this binding correlates with transcriptional changes. The genome-wide regulation of ZGA by Nr5a2 and potentially other orphan nuclear receptors exceeds that of Nfya, which affects ~15% of ZGA genes (*13*) and is comparable to Zelda in *Drosophila* (~75% of ZGA genes) (*5*) and the collective activity of three pluripotency factors in zebrafish (>75% of ZGA genes) (*8*, *9*). Based on genome-wide binding profiles, chromatin accessibility, and in vitro nucleosome binding assays, we propose that Nr5a2 acts locally to promote chromatin opening and functions as a pioneer factor to initiate ZGA in mouse embryos.

The classification of Nr5a2 and Esrrb as pioneer factors suggests that the mechanism of multiple pioneer factors triggering ZGA is evolutionarily conserved from fly to mouse and possibly to human, despite differences in transcription factor identities. The species-specific regulation of some ZGA genes is supported by the recent finding that human-specific TPRXs contribute to ZGA (*49*). However, ZGA is a fundamental process that initiates control of the zygotic genome for all multicellular organisms. It is therefore important to note that Nr5a2 is conserved in all taxa of metazoa that we examined and is maternally provided in embryos of model organisms and humans, which implies an ancestral function in early development (fig. S16) (*50*, *51*). Although *SINE B1* are murine specific, the human genome harbors the related *Alu* retrotransposable elements that also originated from 7SL RNA. *Alu* elements contain two full and one degenerated Nr5a2 motifs (fig. S16B). We speculate that the regulation of ZGA by orphan nuclear receptors such as Nr5a2 is a conserved mechanism, at least among mammals.

Our work provides a conceptual “ex uno plura” (many from one) framework for ZGA activation based on three findings: (i) Nr5a2 directly activates transcription of many ZGA genes; (ii) Nr5a2 is required for transcription of its own gene, *Nr2c2*, and other orphan nuclear receptors during ZGA (fig. S8); and (iii) orphan nuclear receptors that are normally expressed during ZGA, such as Nr2c2, can principally activate ZGA genes when overexpressed at an earlier stage (fig. S5F). We therefore propose that Nr5a2 activates transcription of ZGA genes, which includes orphan nuclear receptors that can recognize motif 1 and potentiate the activation of ZGA genes (Fig. 6I). Current data do not allow us to distinguish whether Nr5a2 cooperates with newly synthesized transcription factors or whether each functions redundantly after ZGA initiation by Nr5a2. Whether transcription factors that bind to the other motifs in *SINE B1/Alu* contribute to ZGA also remains to be elucidated.

A notable finding is that the same transcription factors are important for totipotency and later for pluripotency during mammalian development. Nr5a2 and Esrrb target distinct enhancer-like sequences in two-cell embryos and 2i-ES cells. How these transcription factors selectively establish cell type–specific enhancers remains to be determined. Because *SINE B1/Alu* elements contain several motifs, it is conceivable that cooperative binding of multiple transcription factors, including Nr5a2 and Esrrb, establishes two-cell embryo–specific active enhancers (Fig. 6J). Our findings imply that maternally provided Nr5a2 initiates a cascade of transcription factor bindings that lead to the transcriptional waves at the start of life.

Materials and methods summary

A detailed materials and methods section is provided in the supplementary materials. Briefly, the care and use of the mice at IMBA were carried out in agreement with the authorizing committee according to the Austrian Animal Welfare law and the guidelines of the International Guiding Principles for Biomedical Research Involving Animals [Council for International Organizations of Medical Sciences (CIOMS)]. All animals housed at MPIB were euthanized before the removal of organs, in accordance with the European Commission Recommendations for the euthanasia of experimental animals (Part 1 and Part 2). Breeding and housing as well as the euthanasia of the animals are fully compliant with all German (e.g., German Animal Welfare Act) and European Union (e.g., Directive 2010/63/EU) applicable laws and regulations concerning the care and use of laboratory animals.

In vitro maturation and fertilization were performed as described previously (*52*) with some changes. For siRNA knockdown, isolated germinal vesicle–stage (GV) oocytes were microinjected with sets of two siRNAs against targets or control. Trim-Away was performed according to the published method (*35*, *36*). For single-embryo RNA-seq, sequencing libraries were prepared using the SmartSeq2 protocol described in (*53*).

For the ZGA-FISH, FISH probes were designed as three (ZGA$^{\#1}$, ZGA$^{\#2}$, and ZGA$^{\#3}$) categories based on their transcript abundance in two-cell embryos. Embryos at the appropriate developmental time were fixed with 4% paraformaldehyde. Prehybridization was done in 1× pre-HYBEC supplemented with 50 μg/ml heparin by placing the embryos into a humid chamber in a water bath. Preheated hybridization mixture was applied to the embryos. For ChARM, split-initiator oligonucleotides were applied to prehybridized embryos. Excess initiator molecules were washed away, and prepared hairpins were applied to the embryos to initiate HCR.

CUT&Tag was performed as described previously (*37*) with a few modifications. Briefly, cells with intact zona pellucida were incubated with ice-cold extraction buffer. Pre-extracted cells were lightly fixed by Dulbecco’s phosphate-buffered saline with 0.1% formaldehyde for 2 min at room temperature. Cells were incubated with appropriate antibodies, and prepared DNA libraries were sequenced on a NextSeq 500. Omni ATAC-seq was performed as described previously (*46*).

The recombinant Nr5a2 and Esrrb were bacterially expressed and purified. Mouse histones H2A, H2B, H3.3, and H4 were expressed and purified according to published protocols (*54*). The nucleosomes were reconstituted by salt dialysis method and were further purified by polyacrylamide gel electrophoresis using a Prep Cell apparatus. SeEN-seq assay was performed as described previously with a few modifications (*47*). Nr5a2 motif (TCAAGGCCA) or Esrrb motif (TCAAGGTCA) was tiled in 5-bp intervals across the entire

Widom 601 DNA sequence (*55*). DNA libraries were prepared as described previously (*47*).

REFERENCES AND NOTES

1. J. B. Gurdon, *Development* **10**, 622–640 (1962).
2. F. Aoki, D. M. Worrad, R. M. Schultz, *Dev. Biol.* **181**, 296–307 (1997).
3. G. Flach, M. H. Johnson, P. R. Braude, R. A. Taylor, V. N. Bolton, *EMBO J.* **1**, 681–686 (1982).
4. K. I. Abe *et al*., *Proc. Natl. Acad. Sci. U.S.A.* **115**, E6780–E6788 (2018).
5. H. L. Liang *et al*., *Nature* **456**, 400–403 (2008).
6. M. M. Gaskill, T. J. Gibson, E. D. Larson, M. M. Harrison, *eLife* **10**, e66668 (2021).
7. J. Duan *et al*., *eLife* **10**, e69937 (2021).
8. M. T. Lee *et al*., *Nature* **503**, 360–364 (2013).
9. M. Leichsenring, J. Maes, R. Mössner, W. Driever, D. Onichtchouk, *Science* **341**, 1005–1009 (2013).
10. G. E. Gentsch, T. Spruce, N. D. L. Owens, J. C. Smith, *Nat. Commun.* **10**, 4269 (2019).
11. G. Wu *et al*., *Nat. Cell Biol.* **15**, 1089–1097 (2013).
12. C. Yu *et al*., *Cell Res.* **26**, 275–287 (2016).
13. F. Lu *et al*., *Cell* **165**, 1375–1388 (2016).
14. A. De Iaco *et al*., *Nat. Genet.* **49**, 941–945 (2017).
15. P. G. Hendrickson *et al*., *Nat. Genet.* **49**, 925–934 (2017).
16. J. L. Whiddon, A. T. Langford, C. J. Wong, J. W. Zhong, S. J. Tapscott, *Nat. Genet.* **49**, 935–940 (2017).
17. A. Iturbide *et al*., *Nat. Struct. Mol. Biol.* **28**, 521–532 (2021).
18. D. Lohnes *et al*., *Cell* **73**, 643–658 (1993).
19. A. De Iaco, S. Verp, S. Offner, D. Grun, D. Trono, *Development* **147**, dev.177725 (2020).
20. Z. Chen, Z. Xie, Y. Zhang, *Development* **148**, dev200178 (2021).
21. O. Kubinyecz, F. Santos, D. Drage, W. Reik, M. A. Eckersley-Maslin, *Development* **148**, dev200191 (2021).
22. Z. Chen, Y. Zhang, *Nat. Genet.* **51**, 947–951 (2019).
23. M. Iwafuchi-Doi, K. S. Zaret, *Genes Dev.* **28**, 2679–2692 (2014).
24. K. N. Schulz *et al*., *Genome Res.* **25**, 1715–1726 (2015).
25. Y. Sun *et al*., *Genome Res.* **25**, 1703–1714 (2015).
26. N. Festuccia, N. Owens, A. Chervova, A. Dubois, P. Navarro, *Development* **148**, dev199604 (2021).
27. Y. Wang *et al*., *Nat. Commun.* **12**, 1247 (2021).
28. J. Luo *et al*., *Nature* **388**, 778–782 (1997).
29. C. Labelle-Dumais, M. Jacob-Wagner, J. F. Paré, L. Bélanger, D. Dufort, *Dev. Dyn.* **235**, 3359–3369 (2006).
30. S. Busby *et al*., in *Probe Reports from the NIH Molecular Libraries Program* (National Center for Biotechnology Information, 2010).
31. C. A. Corzo *et al*., *Mol. Pharmacol.* **87**, 296–304 (2015).
32. A. Raj, P. van den Bogaard, S. A. Rifkin, A. van Oudenaarden, S. Tyagi, *Nat. Methods* **5**, 877–879 (2008).
33. S. C. Little, K. S. Sinsimer, J. J. Lee, E. F. Wieschaus, E. R. Gavis, *Nat. Cell Biol.* **17**, 558–568 (2015).
34. I. Gaspar, F. Wippich, A. Ephrussi, *RNA* **23**, 1582–1591 (2017).
35. D. Clift *et al*., *Cell* **171**, 1692–1706.e18 (2017).
36. D. Clift, C. So, W. A. McEwan, L. C. James, M. Schuh, *Nat. Protoc.* **13**, 2149–2175 (2018).
37. H. S. Kaya-Okur *et al*., *Nat. Commun.* **10**, 1930 (2019).
38. B. Zhang *et al*., *Nature* **537**, 553–557 (2016).
39. W. Xia *et al*., *Science* **365**, 353–360 (2019).
40. J. A. Dahl *et al*., *Nature* **537**, 548–552 (2016).
41. J. Wu *et al*., *Nature* **534**, 652–657 (2016).
42. ENCODE Project Consortium *et al*., *Nature* **583**, 699–710 (2020).
43. Y. Atlasi *et al*., *Nat. Cell Biol.* **21**, 568–578 (2019).
44. C. Galonska, M. J. Ziller, R. Karnik, A. Meissner, *Cell Stem Cell* **17**, 462–470 (2015).
45. X. Chen *et al*., *Nat. Methods* **13**, 1013–1020 (2016).
46. M. R. Corces *et al*., *Nat. Methods* **14**, 959–962 (2017).
47. A. K. Michael *et al*., *Science* **368**, 1460–1465 (2020).
48. H. Tanaka *et al*., *Nat. Commun.* **11**, 4136 (2020).
49. Z. Zou *et al*., *Science* **378**, abo7923 (2022).
50. Z. H. Zhao *et al*., *BMC Genomics* **21**, 475 (2020).
51. W. Hu *et al*., *Nat. Commun.* **13**, 5114 (2022).
52. J. Gassler *et al*., *EMBO J.* **36**, 3600–3618 (2017).
53. S. Picelli *et al*., *Nat. Protoc.* **9**, 171–181 (2014).
54. T. Kujirai *et al*., *Methods Mol. Biol.* **1832**, 3–20 (2018).
55. P. T. Lowary, J. Widom, *J. Mol. Biol.* **276**, 19–42 (1998).

ACKNOWLEDGMENTS

We thank B. Kunkel, R. Hornberger, K. Straßer, H. Jung, and E. Krstevska-Vulic for technical assistance. We thank all members of K.T.'s laboratory, including B. J. Dequeker, E. E. Chatzidaki, S. Feng, and H. Marvanova, for assistance with oocyte isolation. We thank L. Zeitler (Murray laboratory, MPIB) for technical assistance with the luciferase assay. HEK293T cells were a gift from R. Fässler (MPIB). Expression vectors used in the luciferase reporter assay were a gift from P. R. Griffin (Scripps Research Institute). JQ-1 was a gift from J. Zuber (IMP). We thank R. S. Grand (Schübeler laboratory, FMI) for advice on SeEN-seq analysis. We thank R. H. Kim for sequencing single-embryo samples at the NGS facility in the Department of Totipotency, MPIB. Illumina sequencing of the developmental transcriptome analysis was performed by the NGS facility at Vienna BioCenter Core Facilities (VBCF). We thank M. Novatchkova (IMP) for RNA-seq analysis of maternal-to-zygotic transition (MZT) data. We thank J.-M. Peters and Life Science Editors for critical reading of the manuscript. **Funding:** This study was supported by a L'Oréal Austria Fellowship for Women in Science (J.G.), the Austrian Science Fund (FWF), DK Chromosome Dynamics grant W1238-B20 (K.T. and J.G.), a JSPS Overseas Research Fellowship (W.K.), European Research Council grant ERC-CoG-818556 TotipotentZygotChrom (K.T.), Human Frontier Science program RGP0057-2018 (K.T.), the Austrian Academy of Sciences (K.T.), and the Max Planck Society (K.T.). **Author contributions:** J.G. collected MZT samples for developmental RNA-seq. J.G., A.M., A.V., L.C.R., and L.G.H. performed oocyte microinjections and collected samples for FISH and RNA-seq analyses. J.G. performed Esrrb and Nr5a2 immunofluorescence assays. J.G. carried out embryo developmental competence assays. I.G. designed and I.G. and L.G.H. carried out the ZGA-FISH experiments. I.G. and N.R. analyzed the ZGA-FISH experiments. I.G., P.K., and S.R. analyzed single-embryo RNA-seq data. W.K. and S.L. established the method of CUT&Tag. W.K. performed CUT&Tag and Omni ATAC-seq using mouse oocytes and embryos. S.R., I.G., and P.K. analyzed CUT&Tag data. I.G. and J.G. performed ChARM and analyzed data. S.R., I.G., and P.K. analyzed Omni ATAC-seq data. W.K., M.K., and M.Z. performed protein purification, SeEN-seq, and biochemical analyses. S.R. analyzed SeEN-seq data. A.L., R.J.A., and N.R. carried out the luciferase reporter assay. K.T. conceived the project and supervised the work. W.K., I.G., J.G., S.R., and K.T. planned the project, designed the experiments, and wrote the manuscript. All authors discussed the results and commented on the manuscript. **Competing interests:** The authors declare that they have no competing interests. **Data and materials availability:** Requests for plasmids generated in this study should be directed to the corresponding author. All RNA-seq data have been deposited to the Gene Expression Omnibus (GEO) under accession no. GSE178661. All CUT&Tag and Omni ATAC-seq data have been deposited to the GEO under accession no. GSE178234. ATAC-seq and histone modification ChIP-seq in two-cell embryo datasets were downloaded from GEO accession nos. GSE66390 and GSE72784, respectively. For the dataset in mESCs, ChIP-seq data of Nr5a2, Esrrb, and H3K27ac were obtained from GSE92412. H3K4me3 ChIP-seq was obtained from GSE56312. MNase-seq (micrococcal nuclease digestion with deep sequencing) data in mESCs were obtained from GSE82127.

License information: Copyright © 2022 the authors, some rights reserved; exclusive licensee American Association for the Advancement of Science. No claim to original US government works. https://www.science.org/about/science-licenses-journal-article-reuse

SUPPLEMENTARY MATERIALS

science.org/doi/10.1126/science.abn7478
Materials and Methods
Figs. S1 to S16
Tables S1 to S14
References (*56*–*82*)
MDAR Reproducibility Checklist

Submitted 16 December 2021; resubmitted 28 September 2022
Accepted 15 November 2022
Published online 24 November 2022
10.1126/science.abn7478

REPORTS

PHYSIOLOGY

Glassfrogs conceal blood in their liver to maintain transparency

Carlos Taboada[1,2]*†, Jesse Delia[2,3,4]*†, Maomao Chen[2]†, Chenshuo Ma[2], Xiaorui Peng[2], Xiaoyi Zhu[2], Laiming Jiang[5], Tri Vu[2], Qifa Zhou[5,6,7], Junjie Yao[2]*, Lauren O'Connell[3], Sönke Johnsen[1]

Transparency in animals is a complex form of camouflage involving mechanisms that reduce light scattering and absorption throughout the organism. In vertebrates, attaining transparency is difficult because their circulatory system is full of red blood cells (RBCs) that strongly attenuate light. Here, we document how glassfrogs overcome this challenge by concealing these cells from view. Using photoacoustic imaging to track RBCs in vivo, we show that resting glassfrogs increase transparency two- to threefold by removing ~89% of their RBCs from circulation and packing them within their liver. Vertebrate transparency thus requires both see-through tissues and active mechanisms that "clear" respiratory pigments from these tissues. Furthermore, glassfrogs' ability to regulate the location, density, and packing of RBCs without clotting offers insight in metabolic, hemodynamic, and blood-clot research.

Transparency is a form of whole-body camouflage that is common in aquatic ecosystems but rare on land (*1*). In contrast to other forms of camouflage, transparency requires complex specializations that minimize light scattering and absorption throughout the entire animal (*2*–*4*). These include a range of cell- and tissue-specific mechanisms, from those that facilitate light transmission through functional tissues, to active processes that conceal or minimize intrinsically pigmented tissues (*1*). Such mechanisms are poorly understood despite decades of biomedical interest in developing transparent model organisms (*5*–*7*).

In vertebrates, achieving transparency is challenging because their circulatory system is full of hemoglobin-containing red blood

cells (RBCs) that strongly absorb blue and green light (*8–10*). Thus, even if tissues themselves are highly transparent, their metabolic requirements render them opaque through the hemoglobin oxygen-transport system. Transparent ice fish and larval eels have apparently overcome this blood problem by not producing hemoglobin and RBCs (*11–13*). Here, we document that glassfrogs use an alternative strategy to overcome this challenge, by essentially hiding RBCs from view.

Glassfrogs are well known for their highly transparent muscles and ventral skin, through which their bones and other organs are visible (*14–16*) (Fig. 1 and figs. S1 and S2). We found that these tissues transmit more than 90 to 95% of visible light while maintaining functionality (e.g., locomotion, vocalization) (fig. S2, E to F). This transparency is adaptive because it camouflages glassfrogs from predators while they sleep on vegetation during the day (*17*) (Fig. 1, A to F, and fig. S1). However, circulating RBCs could compromise leaf camouflage, as they strongly absorb light in regions that are transmitted and reflected by living vegetation (i.e., green light) (Fig. 1, A and B, and fig. S1). Outside of unpigmented tissues, almost nothing is known about the mechanisms of vertebrate transparency (*1*, *2*).

We found that the glassfrog *Hyalinobatrachium fleischmanni* actively maintains high levels of transparency while it sleeps during the day (Fig. 1 and movie S1). We used calibrated color photography to measure transparency of 11 frogs repeatedly while they were asleep, awake, calling to mates, after exercise, and under anesthesia. While sleeping, glassfrogs transmitted on average 34 to 61% more light compared to all other conditions (post hoc comparisons $P < 0.0001$), whereas they transmitted similar levels of light while in all other nonsleeping states ($P \geq 0.22$) (Fig. 1D; fig. S2, A to D; and table S1). Offering a potential explanation for the reduction in transparency, we observed that sleeping frogs circulate plasma with sparse RBCs, and that RBC concentration increased sharply as they awoke (Fig. 1C and movies S2 and S3).

Using optical spectroscopy, we confirmed that a reduction in circulating RBCs was responsible for the increase in transparency during sleep. We measured the diffuse reflectance and transmittance of 13 individuals repeatedly while they slept and after induced exercise. Within seconds after exercise, their leaf-like dorsal reflectance changed markedly and light transmittance dropped two- to threefold across the visible portion of the spectrum (Fig. 1, E to F, and fig. S1). When comparing spectral changes between states, we found a clear and strong hemoglobin signal that was primarily attributed to increased absorption by both oxy- and deoxyhemoglobin (Fig. 1G and fig. S3A). A clear and strong hemoglobin signal was evident in attenuation spectra for exercised frogs (hemoglobin Q-band 500 to 600 nm), whereas the hemoglobin signal was barely detectable while they were sleeping (fig. S3B). Using a simplified optical model, we confirmed that increased RBC density very closely predicts the empirical reduction in transparency (fig. S3, C to E, and table S2). These results show that glassfrog transparency involves active processes that reduce the concentration of circulating RBCs in otherwise transparent tissues.

Understanding the physiological mechanisms of vertebrate transparency requires a strict in vivo approach, as transparency is often lost in death and during stress (*1*). In glassfrogs, we found that RBC perfusion—and hence their transparency—is easily disrupted by activity, stress, anesthesia, and most forms of euthanasia (Fig. 1, figs. S1 and S3, and movies S1 and S2). Therefore, we required an imaging technique that could (i) capture spatial hemodynamics deep within sleeping frogs without inducing RBC perfusion; (ii) specifically target hemoglobin in RBCs without using any contrast agents; and (iii) image through opaque organs, which might store RBCs during rest. This last requirement is important because *H. fleischmanni* heart, liver, and digestive organs are within mirrored sacs that contain reflective guanine crystals and attenuate over 80% of the incident visible light (fig. S2E) (*16*).

To meet these imaging requirements, we used photoacoustic microscopy (PAM) (*18*, *19*) (fig. S4A and table S3). This hybrid imaging technique relies on the photoacoustic effect—essentially, when light is absorbed by molecules, some of the absorbed energy is converted into ultrasonic waves. By optically inducing and then acoustically measuring ultrasonic-wave production, PAM can image deeper than pure optical modalities, as biological tissue is far more transparent to ultrasonic waves than light. Furthermore, PAM can be optimized to detect light absorption by hemoglobin and quantify its oxygenation level, without the need for contrast agents (*20*).

First, we imaged the whole body of glassfrogs to determine where RBCs aggregate during sleep by using two PAM systems optimized for either resolution or depth (Fig. 2 and fig. S4, A to E). Whole-body imaging requires hours of scanning, which cannot capture exercise-level perfusion as frogs quickly conceal RBCs after exercise (see below). Therefore, we imaged three frogs while they were asleep and again under anesthesia—the latter condition resulted in extensive RBC perfusion and allowed us to determine where sleeping frogs store RBCs (Fig. 1D, Fig. 2A, table S1, and movie S1). While frogs were asleep, circulating RBCs decreased by 80 to 90% and RBC signal was largely restricted to the liver (Fig. 2 and fig. S4, F to H).

To test whether glassfrogs actively store RBCs in their liver while asleep and release them back into circulation when active, we performed an exercise assay and measured specific anatomical regions at the single-vessel level using high-resolution PAM (Fig. 3 and fig. S4, A to G). First, we repeatedly imaged the liver of 12 individuals and found that RBCs are aggregated in this organ while frogs rest, flow out of the liver and back into the vasculature during exercise, and then reaggregate in the liver after recovery ($P < 2.2e^{-16}$; Fig. 3, A and B, and table S4). RBC signal in the liver declined on average by 83% after exercise and then again increased by similar levels after recovery (post hoc comparisons with the exercised state $P < 0.0001$). RBC signal in the liver was similar during rest and after recovery from exercise ($P = 0.67$). Frogs can store RBCs in large, distensible sinusoids of the liver (*21*, *22*). Our histological examination showed that glassfrogs also pack RBCs in these sinusoids during rest (Fig. 3G and fig. S5), which confirms our results using three different PAM systems.

Next, we imaged skin and muscle tissue of the abdomen and proximal region of the thighs in 13 glassfrogs. We found that RBC signal within the vasculature of these tissues decreased on average by 89% while frogs rested [generalized linear mixed model (GLMM): $\chi^2 = 634.7$, $P < 2.2e^{-16}$; Fig. 3, C and D]. Furthermore, the percentage of oxygenated hemoglobin (sO_2) decreased on average by 31% during sleep ($\chi^2 = 522.09$, $P < 2.2e^{-16}$; Fig. 3E). Accounting for the difference in overall RBC perfusion between states, frogs had on average 96.6% less oxygenated hemoglobin in circulation while at rest than after exercise. Finally, we continually tracked the temporal dynamics of RBC perfusion and light transmittance during recovery by combining calibrated photography with a high-speed PAM system (Fig. 3F; fig. S4, A to E and I; and movie S4). Increases in light transmittance closely corresponded with a decrease in relative RBC signal over time—frogs recovered baseline levels of transparency within ~60 min after exercise.

In glassfrogs, many visceral organs are enclosed within sacs that contain highly reflective guanine crystals (*16*) that attenuate over 80% of incident light (fig. S2E and fig. S5).

[1]Biology Department, Duke University, Durham, NC, USA. [2]Department of Biomedical Engineering, Duke University, Durham, NC, USA. [3]Department of Biology, Stanford University, Stanford, CA, USA. [4]Division of Vertebrate Zoology and Richard Gilder Graduate School, American Museum of Natural History, New York, NY, USA. [5]Department of Biomedical Engineering, University of Southern California, Los Angeles, CA 90089, USA. [6]Department of Ophthalmology, University of Southern California, Los Angeles, CA 90033, USA. [7]USC Ginsburg Institute for Biomedical Therapeutics, University of Southern California, Los Angeles, CA 90033, USA.
***Corresponding author. Email: carlos.taboada@duke.edu (C.T.); jdelia@amnh.org (J.D.); junjie.yao@duke.edu (J.Y.)**
†These authors contributed equally to this work.

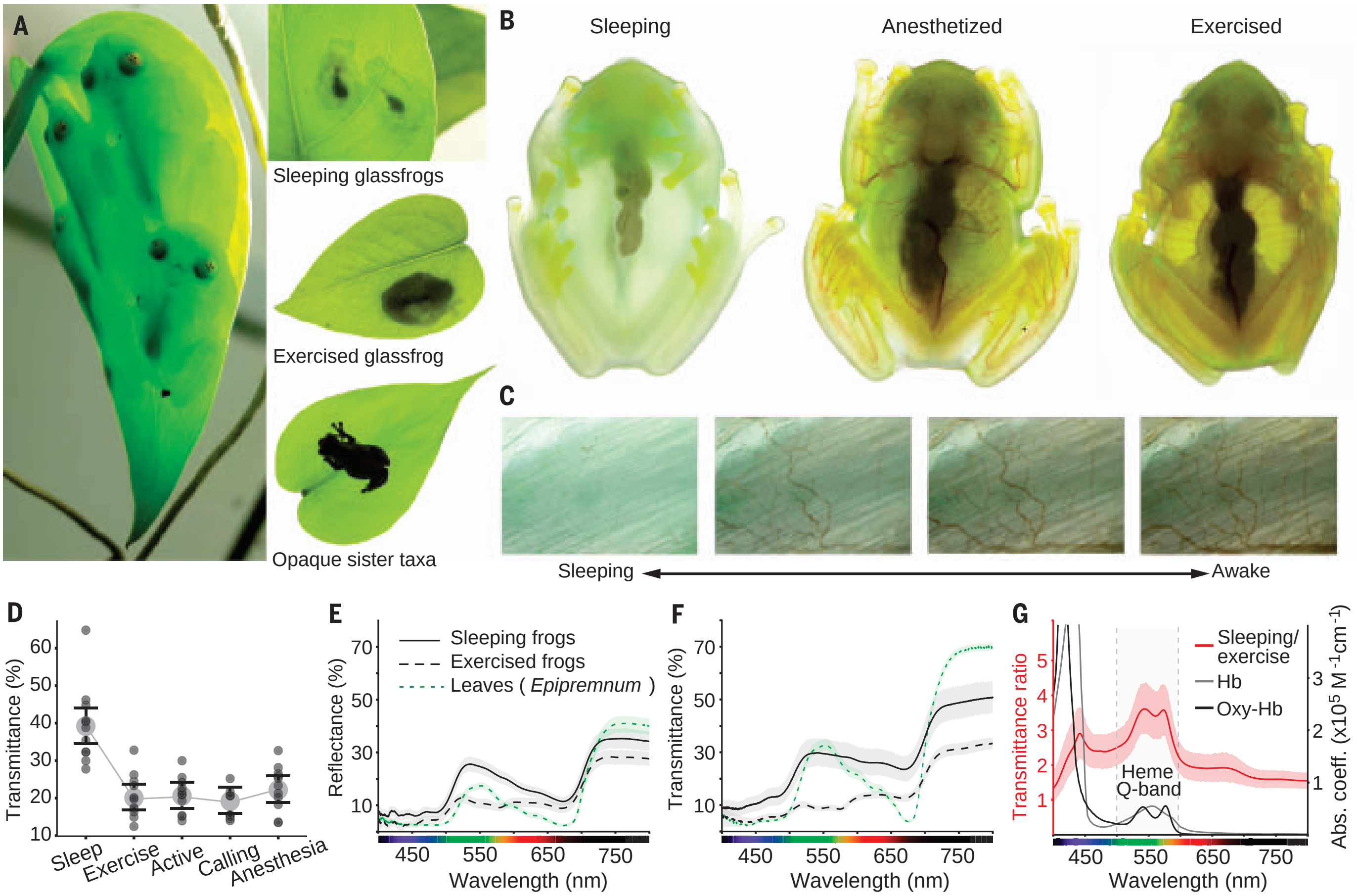


Fig. 1. Glassfrog transparency and leaf-like coloration changes with activity. The leaf-dwelling glassfrog *Hyalinobatrachium* ("*Centrolenella*") *fleischmanni* forages and breeds on vegetation at night along forested streams (occurring from southern Mexico to northwestern South America) (*33*–*36*). During the day, *Hyalinobatrachium* frogs sleep upside on broadleaf vegetation, where a combination of green leaf-like dorsal coloration and transparency could provide camouflage on translucent leaves (*17*–*38*) (fig. S1). (**A** and **B**) Frogs photographed in transmitted light (backlit). (**C**) RBC perfusion in abdominal tissues (skin and muscle) (backlit). (**D**) Calibrated transmittance photography of the same 11 frogs measured across activity levels. Small dark gray circles show individual frog measurements; larger light gray circles and error bars show mean ± 95% confidence interval of transmittance (green channel; for all color channels, see fig. S2 and table S1). (**E** and **F**) Diffuse reflectance and transmittance of 13 frogs during sleep and immediately after exercise, and five leaves where they sleep. (**G**) Ratio of transmittance between states (sleeping/exercise). The reduction in transparency during exercise is largely due to increased absorption by oxygenated (oxy-Hb) and deoxygenated (Hb) hemoglobin (hemoglobin Q-band 500 to 600 nm) (fig. S3 and table S2). Absorption spectra for hemoglobin were obtained from (*39*).

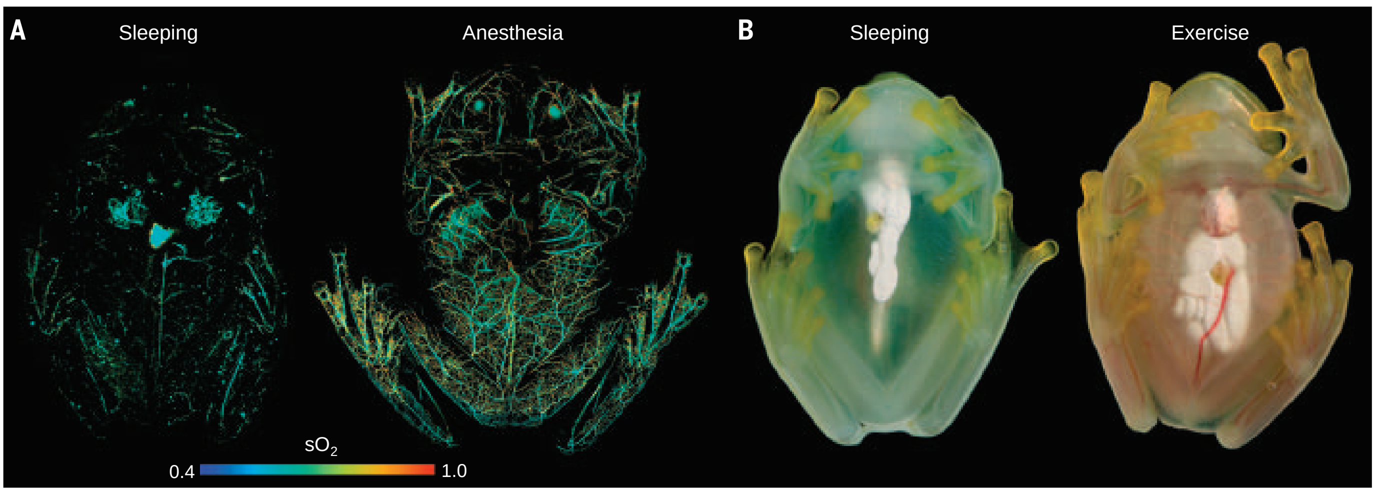


Fig. 2. Glassfrogs remove RBCs from circulation while sleeping. (**A**) High-resolution PAM showing RBC perfusion within the vasculature of the same frog while asleep and under anesthesia. This PAM technique can capture the location of RBCs within single vessels, as well as the oxygen saturation of hemoglobin (sO_2). (**B**) Flash photography showing the visible change in RBC perfusion between activity levels.

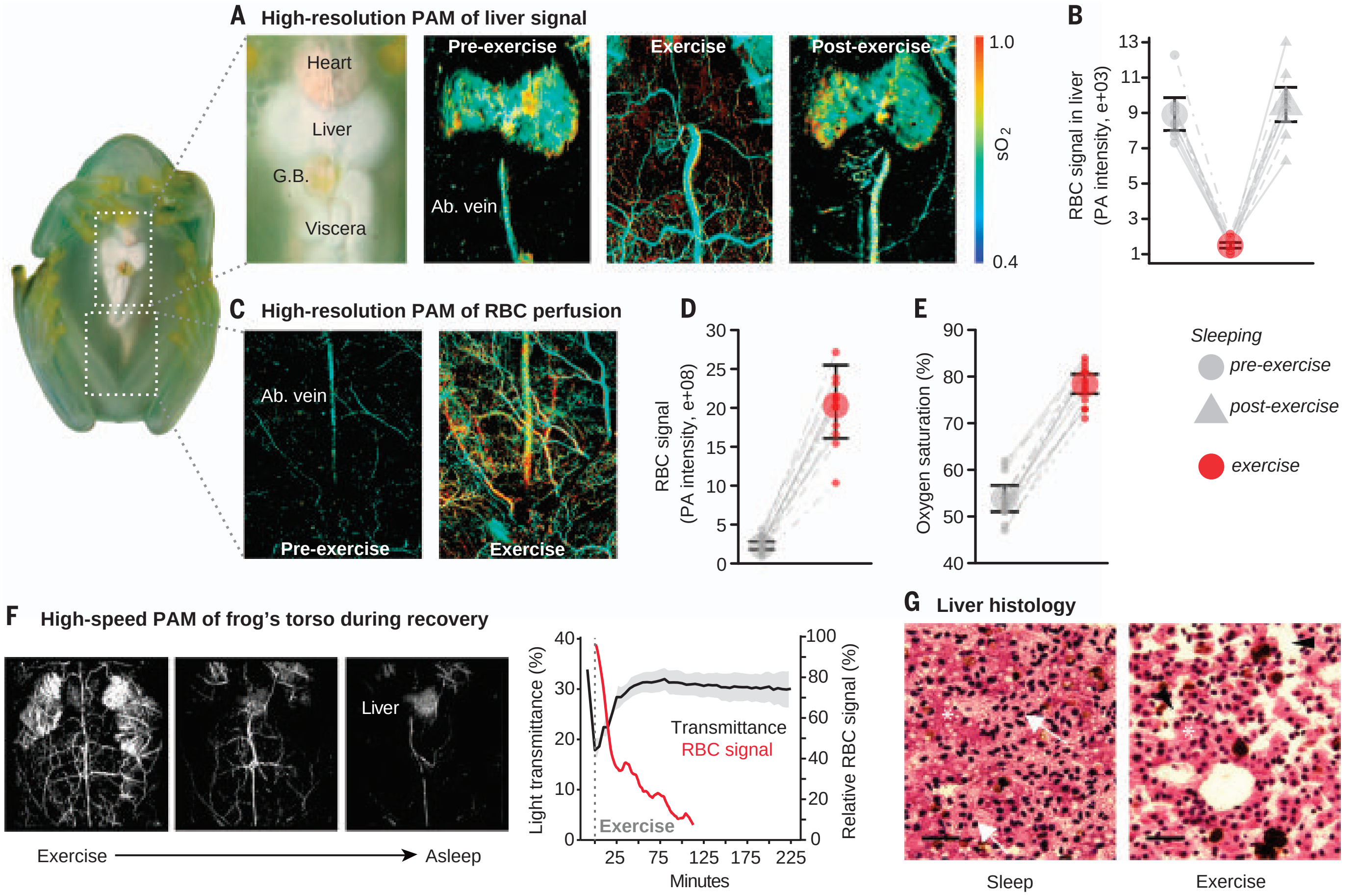


Fig. 3. Glassfrogs store RBCs in their liver while asleep. Hemodynamics of targeted anatomical regions using high-resolution PAM. (**A** and **B**) RBC signal in the liver declined after exercise and then increased by similar levels after recovery. (**C** to **E**) RBC signal (D) and the fraction of oxygenated hemoglobin (sO_2) (E) in abdominal tissues declined during sleep. (**F**) Temporal dynamics of RBC perfusion (*n* = 1) and associated changes in light transmittance during recovery (*n* = 10), using calibrated photography and high-speed PAM (movie S4). (**G**) Hematoxylin and eosin–stained sections of livers from sleeping and exercised glassfrogs. Frog RBCs have oblong nuclei and appear light pink inside the hepatic sinusoids. Hepatocytes (asterisk) are darker round cells with round nuclei and they are arranged in plates that line the sinusoids. Sinusoids are expanded and packed with RBCs (arrows) during sleep, and largely empty and compressed during exercise (arrowheads) (fig. S5). Liver volume changes by 40% between exercise and sleep (see Fig. 4). Scale bars, 30 μm.

We confirmed that this crystal layer attenuates photoacoustic signal to below a detection threshold during anesthesia and exercise by comparing transparent versus crystallized lobes of livers of individual froglets—conveniently, crystal development on the liver peritoneum occurs just after metamorphosis, during which the peritoneum is transparent in one lobe and covered in crystals in the other (fig. S6). Altogether, our results indicate that sleeping glassfrogs remove most RBCs from systemic circulation and conceal them within their mirrored liver during periods when transparency is important for camouflage (Figs. 1 to 3 and figs. S1 to S7).

Glassfrog transparency appears to build on a preexisting respiratory property of frog livers. In the European frog *Pelophylax* "*Rana*" *esculentus*, the liver regulates respiration by storing excess RBCs in sinusoids and releasing them back into circulation as metabolic demand increases (*21*, *22*). These frogs can store up to 44% of their RBCs while under a chemically induced coma at low temperatures (6°C) in well-oxygenated conditions (presumably mimicking cold season torpor) (*21*, *22*). However, by 18°C their liver no longer stores RBCs; all are in circulation, owing to temperature effects on cell respiration. Notably, glassfrogs store 82 to 93% of their RBCs while sleeping at temperatures at least as high as 25° to 27°C, and then mobilize them nightly during activity.

These results raise the question of whether other tropical, nontransparent frogs can store high levels of RBCs while resting. We compared RBC perfusion between states for three species from three tropical families of opaque, arboreal frogs using high-resolution PAM (Fig. 4, A to C, and fig. S8). While resting, circulating RBCs decreased on average by or below 12% among the opaque species versus 89% in glassfrogs (GLM: $\chi^2 = 730.76$, $P < 2.2e^{-16}$, $n = 22$), and their vasculature remained perfused with RBCs while resting at 25° to 27°C (Fig. 4, B and D).

To quantify changes in liver size associated with RBC packing, we used high-frequency ultrasound tomography to repeatedly measure the liver volume of 10 glassfrogs and 8 *Allophryne ruthveni*—a species from the most closely related nontransparent taxa of glassfrogs. The liver volume of glassfrogs increased on average by 40% while their livers were packed with RBCs during sleep (post hoc comparisons $P < 0.0001$), whereas the liver volume of *A. ruthveni* did not change significantly between activity levels (post hoc comparisons $P = 0.78$, $\overline{x} = 1.2\%$ increase during rest; Fig. 4E and table S6).

Our results have three major implications. First, we discovered that a vertebrate can actively regulate the location and density of its

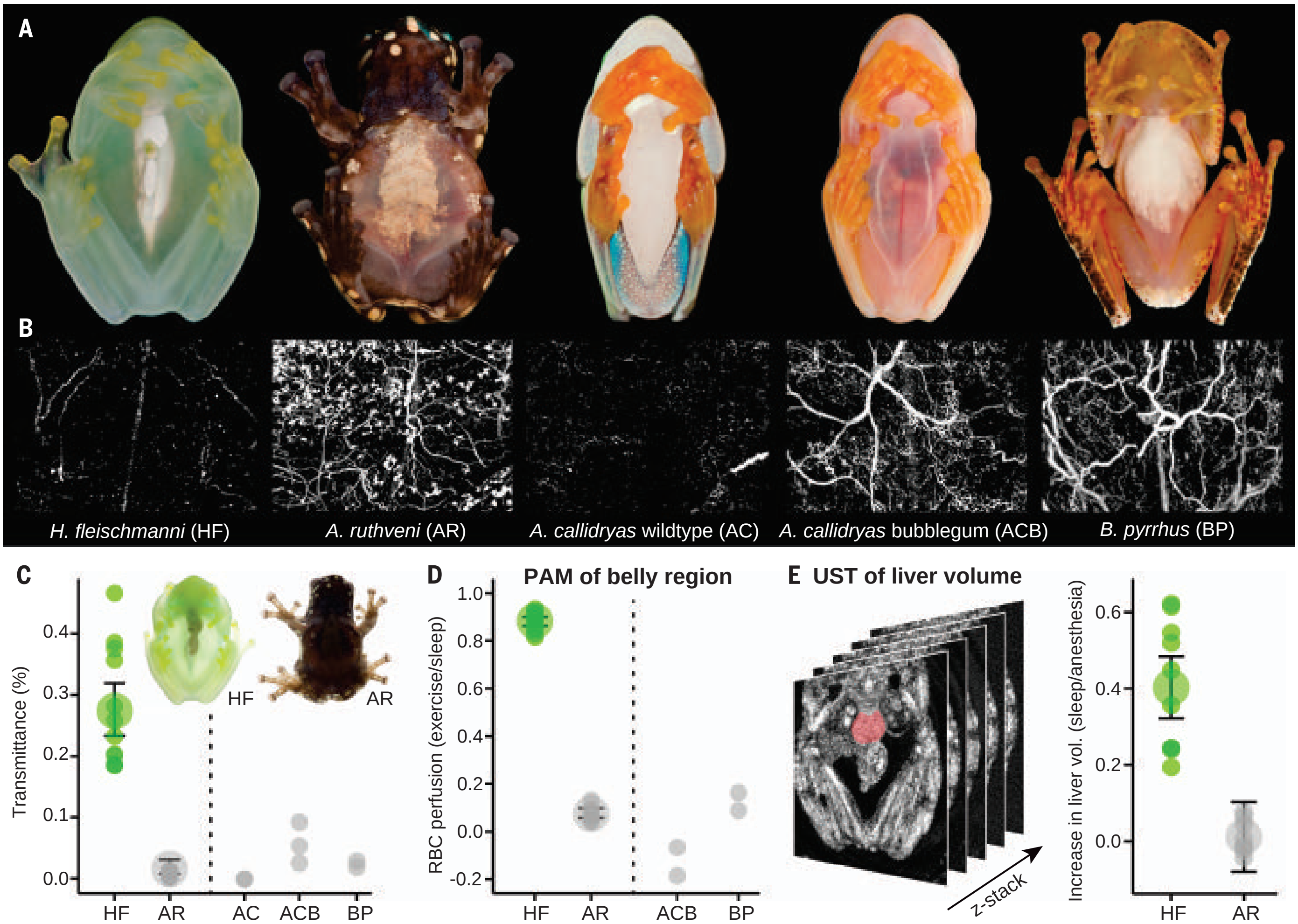


Fig. 4. Opaque tropical frogs do not store high levels of RBCs during rest. Light transmittance and RBC storage across three independent origins of arboreality—in *Allophryne ruthveni* from the enigmatic sister family of glassfrogs (Allophrynidae), the sympatric leaf-dwelling treefrog *Agalychnis callidryas* (Hylidae), and the Malagasy "treefrog" *Boophis pyrrhus* (Mantellidae) (fig. S8). (**A**) Flash photography of resting frogs. (**B**) RBC signal in abdominal tissues (skin and muscle) of sleeping frogs (using PAM). The wild type of *A. callidryas* cannot be imaged with PAM because their abdomen tissue is wrapped in reflective crystals. The "bubblegum" morph largely lacks pigmentary cells, which permits mapping RBCs by PAM. (**C**) During rest, these species transmit much lower levels of visible light compared to *H. fleischmanni* ($P < 2.2e^{-16}$, $n = 22$; table S5). Inset: Frogs in transmitted light (backlit). (**D**) RBC storage (%) during exercise and rest. (**E**) Liver volume associated with RBC packing during sleep.

RBCs in ways that improve transparency. Previous research found that transparency camouflages glassfrogs while they sleep on vegetation during the day (*17*) (Fig. 1). We found that blood storage increases transparency two- to threefold but results in an extreme daily reduction in circulating RBCs. Just 3.4% of their total hemoglobin is bound with oxygen during this transparent state, indicating that glassfrogs likely exhibit depressed metabolic activity or nonoxidative metabolic processes (*21*–*25*). Research on transparent shrimp has also shown that stress and/or activity can result in hemolymph perfusion that opacifies the animals, which could have consequences for predation (*4*, *26*). Taken together, transparency camouflage in complex animals requires physiological specializations that can remove respiratory pigments from transparent tissue, as well as those that compensate for the resulting respiratory constraint.

Second, glassfrogs likely offer insight into the mechanisms involved in preventing vascular pathologies. In most vertebrates, local RBC aggregations cause thromboses (*27*). Notably, glassfrogs are capable of packing and unpacking 82 to 93% of their RBCs in their liver on a daily basis without triggering vaso-occlusive or clotting (thrombotic) events. Concentrating RBCs in this fashion would presumably require biochemical factors and/or physical modifications (e.g., structural changes of packed RBCs) that ultimately interact with clotting factors (*28*). Glassfrogs may be particularly useful for blood-clot research. Compared to fish models, frogs share the same genetic and physiological factors that regulate hemostasis as those in mammals [e.g., upstream coagulation factor XII (*29*)]. Finally, these naturally transparent vertebrates are an excellent animal for in vivo physiology research. Their entire body can be imaged with cellular resolution to capture natural hemodynamic processes without restraint or contrast agents (movie S5). Measuring the cardiovascular physiology of vertebrates in vivo is challenging and has been largely limited to anesthetized, restrained, and/or surgically altered animals. Furthermore, transparent tetrapod models are basically unpigmented mutants that are not transparent [e.g., (*30*–*32*)]. Glassfrogs may provide a solution

to these challenges and offer insight into biological mechanisms of vertebrate transparency.

REFERENCES AND NOTES

1. S. Johnsen, *Biol. Bull.* **201**, 301–318 (2001).
2. S. Johnsen, E. A. Widder, *J. Theor. Biol.* **199**, 181–198 (1999).
3. L. Zueva *et al.*, *Microsc. Microanal.* **22**, 379–386 (2016).
4. L. E. Bagge, S. T. Kinsey, J. Gladman, S. Johnsen, *J. Exp. Biol.* **220**, 4225–4233 (2017).
5. Y. Wakamatsu, S. Pristyazhnyuk, M. Kinoshita, M. Tanaka, K. Ozato, *Proc. Natl. Acad. Sci. U.S.A.* **98**, 10046–10050 (2001).
6. R. M. White *et al.*, *Cell Stem Cell* **2**, 183–189 (2008).
7. M. Inyushin, D. Meshalkina, L. Zueva, A. Zayas-Santiago, *Molecules* **24**, 2388 (2019).
8. R. E. Dickerson, I. Geis, *Hemoglobin: Structure, Function, Evolution, and Pathology* (Benjamin-Cummings Publishing Company, Menlo Park, CA, 1983).
9. R. C. Hardison, *Proc. Natl. Acad. Sci. U.S.A.* **93**, 5675–5679 (1996).
10. R. Hardison, *J. Exp. Biol.* **201**, 1099–1117 (1998).
11. F. Garofalo, D. Pellegrino, D. Amelio, B. Tota, *Comp. Biochem. Physiol. A Mol. Integr. Physiol.* **154**, 10–28 (2009).
12. M. J. Miller, *Aqua-Biosci. Monogr.* **2**, 1–94 (2009).
13. J. T. Ruud, *Nature* **173**, 848–850 (1954).
14. P. A. Schwalm, J. A. McNulty, *J. Morphol.* **163**, 37–44 (1980).
15. J. W. Streicher *et al.*, *Mol. Phylogenet. Evol.* **119**, 128–143 (2018).
16. D. F. Cisneros-Heredia, R. W. Mcdiarmid, *Zootaxa* **1572**, 1–82 (2007).
17. J. B. Barnett *et al.*, *Proc. Natl. Acad. Sci. U.S.A.* **117**, 12885–12890 (2020).
18. W. Liu, J. Yao, *Biomed. Eng. Lett.* **8**, 203–213 (2018).
19. L. V. Wang, J. Yao, *Nat. Methods* **13**, 627–638 (2016).
20. J. Yao, K. I. Maslov, Y. Zhang, Y. Xia, L. V. Wang, *J. Biomed. Opt.* **16**, 076003 (2011).
21. G. Frangioni, G. Borgioli, *J. Zool.* **230**, 483–493 (1993).
22. G. Frangioni, G. Borgioli, *J. Zool.* **234**, 601–611 (1994).
23. K. B. Storey, J. M. Storey, *Q. Rev. Biol.* **65**, 145–174 (1990).
24. T. J. Park *et al.*, *Science* **356**, 307–311 (2017).
25. P. E. Bickler, L. T. Buck, *Annu. Rev. Physiol.* **69**, 145–170 (2007).
26. A. Bhandiwad, S. Johnsen, *J. Exp. Biol.* **214**, 709–716 (2011).
27. F. T. Yu, J. K. Armstrong, J. Tripette, H. J. Meiselman, G. Cloutier, *J. Thromb. Haemost.* **9**, 481–488 (2011).
28. D. B. Cines *et al.*, *Blood* **123**, 1596–1603 (2014).
29. M. B. Ponczek, D. Gailani, R. F. Doolittle, *J. Thromb. Haemost.* **6**, 1876–1883 (2008).
30. K. Nakajima, M. Shimamura, N. Furuno, *Dev. Dyn.* **250**, 1420–1431 (2021).
31. M. Sumida *et al.*, *Sci. Rep.* **6**, 24431 (2016).
32. S. Castroviejo-Fisher, I. De la Riva, C. Vilà, *Nature* **449**, 972 (2007).
33. AmphibiaWeb, https://amphibiaweb.org (accessed July 2021).
34. S. K. Jacobson, *Herpetologica* **41**, 396–404 (1985).
35. J. R. Delia, A. Ramírez-Bautista, K. Summers, *Behav. Ecol. Sociobiol.* **67**, 557–569 (2013).
36. J. Delia, L. Bravo-Valencia, R. W. McDiarmid, *Phyllomedusa* **16**, 101–107 (2017).
37. P. A. Schwalm, P. H. Starrett, R. W. McDiarmid, *Science* **196**, 1225–1227 (1977).
38. C. Taboada *et al.*, *Proc. Natl. Acad. Sci. U.S.A.* **117**, 18574–18581 (2020).
39. S. Prahl, Optical absorption of hemoglobin. http://omlc.ogi.edu/spectra/hemoglobin (1999).

ACKNOWLEDGMENTS

We thank S. Solie, A. Davis, C. Raxworthy, E. Twomey, K. Warkentin, A. Wolberg, and M. Ryan for comments that improved this manuscript. We also thank H. Sheng, J. P. Gibert, G. Silva, and V. Simoes for lab space and reagents. **Funding:** This study was supported by National Geographic Society grant NGS-65348R-19 (J.D., C.T.); Human Frontier Science Program postdoctoral fellowship LT 000660/2018-L (C.T.); Gerstner Scholars Fellowship provided by the Gerstner Family Foundation and the Richard Gilder Graduate School at the American Museum of Natural History (J.D.); start-up funds from Stanford University (L.O.); start-up funds from Duke University (S.J.); National Institutes of Health grant R01 EB028143 (J.Y.); National Institutes of Health grant R01 NS111039 (J.Y.); National Institutes of Health grant RF1 NS115581 BRAIN Initiative (J.Y.); Duke Institute of Brain Science Incubator award (J.Y.); American Heart Association Collaborative Sciences award 18CSA34080277 (J.Y.); Chan Zuckerberg Initiative grant 2020-226178 (J.Y.); and National Science Foundation CAREER award 2144788 (J.Y.). **Author contributions:** Biological discovery and conceptualization: C.T., J.D. Methodology: C.T., J.D., M.C., C.M., X.P., X.Z., L.J., T.V., Q.Z., J.Y., S.J. Investigation: C.T., J.D., M.C., X.Z., C.M. Formal Analysis: C.T., J.D., M.C., C.M. Visualization: C.T., J.D., M.C., J.Y. Funding acquisition: C.T., J.D., J.Y., L.O., S.J. Mentorship: J.Y., S.J. Writing – original draft: C.T., J.D. Writing – review and editing: C.T., J.D., M.C., C.M., X.P., X.Z., L.J., T.V., Q.Z., J.Y., L.O., S.J. **Competing interests:** The authors declare that they have no competing interests. **Data and materials availability:** All data and code are available in the supplementary materials.

License information: Copyright © 2022 the authors, some rights reserved; exclusive licensee American Association for the Advancement of Science. No claim to original US government works. https://www.science.org/about/science-licenses-journal-article-reuse

SUPPLEMENTARY MATERIALS

science.org/doi/10.1126/science.abl6620
Materials and Methods
Figs. S1 to S9
Tables S1 to S7
References (*40–71*)
MDAR Reproducibility Checklist
Movies S1 to S5
Data and code

Submitted 28 July 2021; resubmitted 10 June 2022
Accepted 8 November 2022
10.1126/science.abl6620

BATTERIES

High-entropy mechanism to boost ionic conductivity

Yan Zeng[1]†, Bin Ouyang[1,2,3]*†, Jue Liu[4], Young-Woon Byeon[1], Zijian Cai[1,2], Lincoln J. Miara[5]‡, Yan Wang[5], Gerbrand Ceder[1,2]*

Advances in solid-state batteries have primarily been driven by the discovery of superionic conducting structural frameworks that function as solid electrolytes. We demonstrate the ability of high-entropy metal cation mixes to improve ionic conductivity in a compound, which leads to less reliance on specific chemistries and enhanced synthesizability. The local distortions introduced into high-entropy materials give rise to an overlapping distribution of site energies for the alkali ions so that they can percolate with low activation energy. Experiments verify that high entropy leads to orders-of-magnitude higher ionic conductivities in lithium (Li)–sodium (Na) superionic conductor (Li-NASICON), sodium NASICON (Na-NASICON), and Li-garnet structures, even at fixed alkali content. We provide insight into selecting the optimal distortion and designing high-entropy superionic conductors across the vast compositional space.

A critical advancement in the development of superionic conductors for solid-state batteries has been the discovery of structural frameworks that provide connected low-barrier diffusion channels for facile ion migration (*1*–*6*). Recent progress in the development of Li-ion conductors has been largely driven by searching for frameworks with the right Li coordination environment (*1*, *2*), Li site connectivity (*3*), distortion tolerance of the anion framework (*4*, *5*), or crystalline symmetry (*6*). Several basic concepts have emerged to increase the alkali ion conductivity in compounds: (i) A percolating pathway of sites needs to exist along which coordination change is minimized. This is particularly important for sulfides in which the S^{2-} ion screens much of the electrostatic interaction between the carrier and the other cations. (ii) Raising the energy of the carrier ions increases their mobility. This can be achieved by increasing the amount of alkali ions in the compound (Li or Na "stuffing"), which forces the alkali to occupy higher-energy sites and/or raises their energy by increasing alkali-alkali repulsion. Alkali stuffing has been applied successfully to increase conductivity in $Li_{1+x}Al_xTi_{2-x}(PO_4)_3$ (*7*) and $Na_{3+x}Zr_2(SiO_4)_{2+x}(PO_4)_{1-x}$ in the Na superionic conductor (NASICON) framework (*8*) and $Li_7La_3Zr_2O_{12}$ (LLZO) in the garnet framework (*9*). Although these concepts are valuable, the charge compensation needed to achieve a high alkali concentration may be associated with a limited selection of possible dopants (*10*), complicated synthesis (*3*), and pronounced Li loss during heat treatment (*11*). We combined ab initio modeling and experiments to unveil how high entropy can affect ionic conductivity using nonstuffed common oxide-based frameworks.

Figure 1A illustrates our hypothesis of how local structural distortions can enhance alkali ion mobility. Consider a well-ordered structure with two distinct sites: Whereas site 1 has

[1]Materials Sciences Division, Lawrence Berkeley National Laboratory, Berkeley, CA 94720, USA. [2]Department of Materials Science and Engineering, University of California Berkeley, Berkeley, CA 94720, USA. [3]Department of Chemistry and Biochemistry, Florida State University, Tallahassee, FL 32304, USA. [4]Neutron Scattering Division, Oak Ridge National Laboratory, Oak Ridge, TN 37831, USA. [5]Advanced Materials Lab, Samsung Advanced Institute of Technology–America, Samsung Semiconductor Inc., Cambridge, MA 02138, USA.
*Corresponding author: Email: bouyang@fsu.edu (B.O.); gceder@berkeley.edu (G.C.)
†These authors contributed equally to this work.
‡Present address: Pure Lithium Corporation, Charlestown, MA 02129, USA.

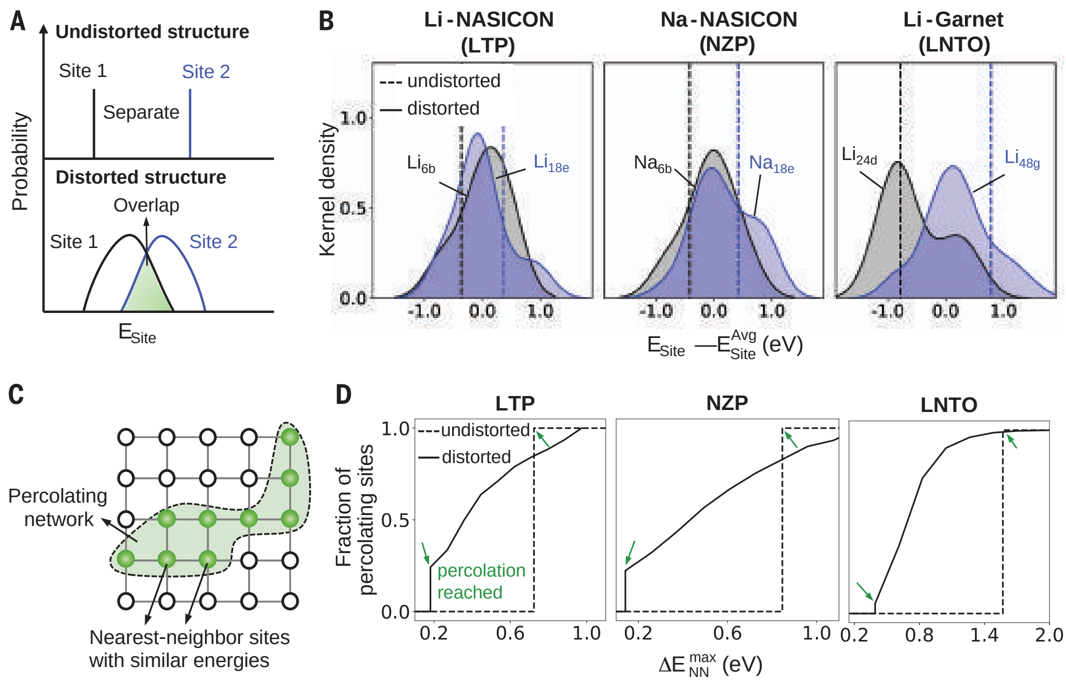


Fig. 1. Effect of structural distortions on alkali site energies and percolation. (**A**) Schematic showing how local distortions create overlapping site-energy distributions. (**B**) Calculated site energies before (dashed vertical lines) and after introducing a standard deviation of 0.1 Å to the metal-oxygen bond lengths in three baseline materials. (**C**) Schematic of percolation defined as the network of sites in which the maximum nearest-neighbor site-energy difference is ΔE_{NN}^{max}. (**D**) Calculated fraction of percolating Li or Na sites as a function of ΔE_{NN}^{max} in distorted (solid lines) and undistorted (dashed lines) structures. The arrows point out the lowest ΔE_{NN}^{max} at which percolation occurs.

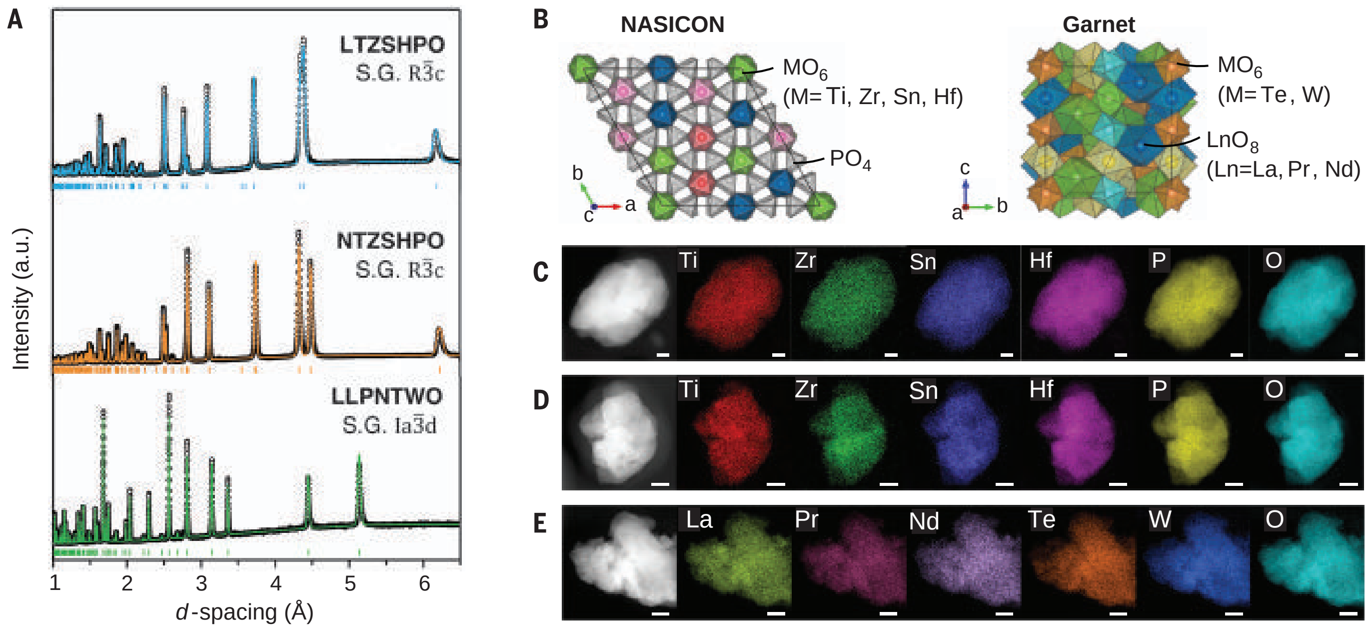


Fig. 2. Synthesis and structures of three high-entropy oxides. (**A**) XRD patterns (open circles, observed; solid lines, calculated; sticks, Bragg positions) of NASICON and garnet-based high-entropy materials. a.u., arbitrary units. (**B**) Schematics of the NASICON and garnet structures with multiple elements substituting on one site. Li and Na are not shown. (**C** to **E**) HAADF-STEM images and elemental mappings of LTZSHPO (C), NTZSHPO (D), and LLPNTWO (E), showing that the elements are homogeneously distributed. Scale bars are 50 nm.

the lowest energy, site 2 can be an alkali-metal site within the diffusion network where the alkali ion has higher energy or it can be a high-symmetry saddle point along a hopping path. Introducing chemical disorder and its resulting distortions will locally perturb the site energy, creating a distribution of site energies. When this distribution is wide enough for the energy of neighboring sites to overlap, ion hopping between them will be promoted. If such a network of sites with similar energy percolates, macroscopic diffusion is enhanced by the disorder.

Using density functional theory (DFT), we quantified how structural distortions modify the energy of the alkali-metal sites in three common oxide-based ion conducting frameworks: Li-NASICON, Na-NASICON, and Li-garnet, starting from the baseline compounds $LiTi_2(PO_4)_3$ (LTP), $NaZr_2(PO_4)_3$ (NZP), and $Li_3Nd_3Te_2O_{12}$ (LNTO). Gaussian-distributed local distortions with a standard deviation (d_σ) of 0.1 Å were applied to the metal-oxygen bond length in LTP (Ti–O), NZP (Zr–O), and LNTO (Nd–O and

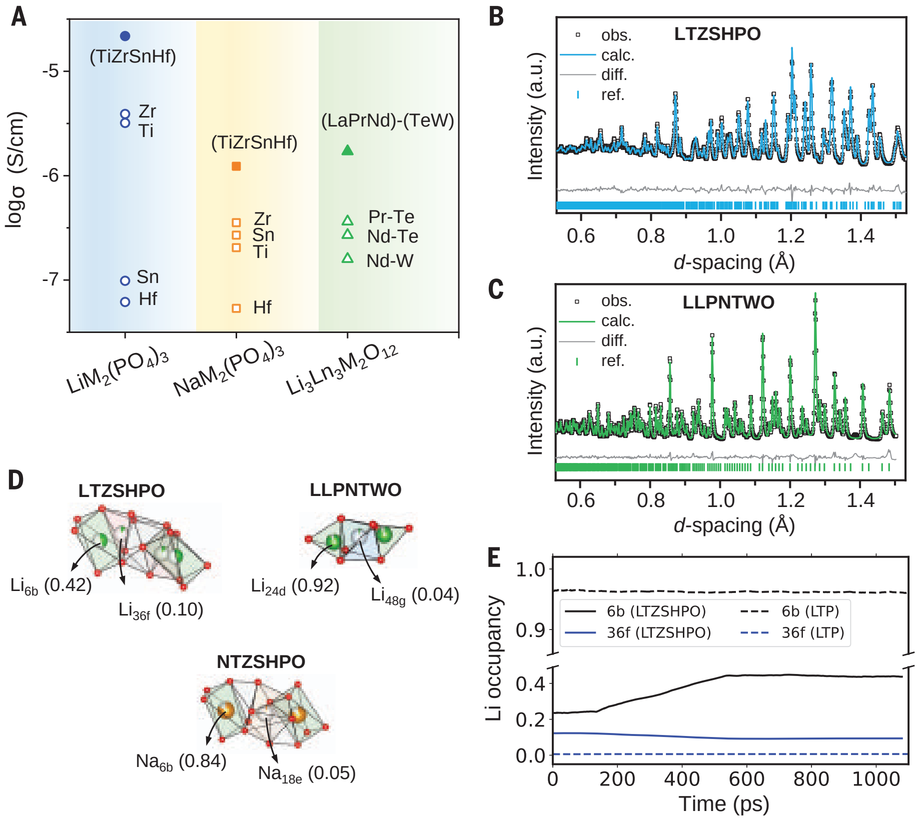


Fig. 3. Ionic conductivities and Li or Na occupancies for the high-entropy materials. (**A**) Ionic conductivities of LTZSHPO, NTZSHPO, and LLPNTWO and their single-metal counterparts measured at room temperature. (**B** and **C**) Neutron diffraction patterns and refinements of LTZSHPO (B) and LLPNTWO (C). obs., observed; calc., calculated; diff., difference; ref., reference. (**D**) Schematics of Li or Na partial occupancies determined from neutron diffraction or XRD refinements. Li_{6b} (0.42) designates that the occupancy factor of Li on 6b sites is 0.42. (**E**) AIMD-simulated Li-site occupancy evolution in LTZSHPO (solid lines) and LTP (dashed lines) at 300 K.

Te–O) at fixed supercell volume. A Gaussian was chosen for convenience, but any distribution that perturbs the site energy is expected to give qualitatively similar results. The site energy was probed by inserting a single alkali at the different sites of the framework and was properly charge-compensated with background charge (see materials and methods). Figure 1B shows the resulting energy distributions for the lowest- and highest-energy sites in each structure, with the site energy in the undistorted structure indicated by the dashed vertical lines. Taking LNTO as an example, the energy difference between the Li_{24d} and Li_{48g} sites is 1.57 eV, which establishes the minimum energy barrier for percolating ion hopping. The black and purple curves in Fig. 1B represent the site energies of these two sites in the distorted structures, showing a notable overlap between the energy distributions of both sites. This overlap is even more substantial in distorted LTP and NZP. Additional percolation analysis, including the Li_{36f} site in LTP, is shown in fig. S1.

We anticipate that the overlap in site energies provides a diffusion pathway along which the site-energy varies minimally (Fig. 1C). The connectivity of the pathway depends on the maximum site-energy difference that one allows between nearest neighbors (ΔE_{NN}^{max}). Figure 1D shows the fraction of alkali sites that are part of the percolating trajectory for a given value of ΔE_{NN}^{max}. In the undistorted (ordered) LTP, percolation cannot occur until ΔE_{NN}^{max} reaches the energy difference between the 6b and 18e site (0.72 eV). For NZP and LNTO, the ΔE_{NN}^{max} are 0.85 and 1.57 eV, respectively. By contrast, when local bond distortion (d_σ = 0.1 Å) is introduced, percolation can occur at a much smaller ΔE_{NN}^{max}. Specifically, in distorted LTP, percolation with 24.2% of Li sites participating begins at $\Delta E_{NN}^{max} = 0.18$ eV, and more sites can percolate at higher ΔE_{NN}^{max}. In distorted NZP, 22.3% of Na sites form a percolation network at $\Delta E_{NN}^{max} = 0.14$ eV. In distorted LNTO, 5.2% of Li sites percolate at $\Delta E_{NN}^{max} = 0.39$ eV. Diffusion will occur through these percolation networks with a minimal activation energy equal to ΔE_{NN}^{max}. Hence, this basic analysis shows that disorder can result in a dramatic lowering of the alkali ion diffusion activation energy by creating a percolation network of sites with small energy differences.

We designed three nonstuffed high-entropy materials—$Li(Ti,Zr,Sn,Hf)_2(PO_4)_3$ (LTZSHPO), $Na(Ti,Zr,Sn,Hf)_2(PO_4)_3$ (NTZSHPO), and $Li_3(La,Pr,Nd)_3(Te,W)_2O_{12}$ (LLPNTWO)—to represent the Li-NASICON, Na-NASICON, and Li-garnet frameworks, respectively. Higher-entropy materials enable the joint solubility of ions with a large ionic radius difference, which will create the bond-length deviations that are shown by our analysis to enhance diffusion.

Figure 2A shows the x-ray diffraction (XRD) patterns of LTZSHPO, NTZSHPO, and LLPNTWO that were synthesized by a solid-state reaction. By indexing to the reference patterns, we find that LTZSHPO and NTZSHPO form the rhombohedral $R\bar{3}c$ NASICON structure, whereas LLPNTWO forms the cubic $Ia\bar{3}d$ garnet structure. There are no visible impurity peaks in the three patterns, which indicates single-phase samples. Rietveld refinements indicate a good fit when Ti, Zr, Sn, and Hf are distributed on the octahedral MO_6 site (Fig. 2B). For LLPNTWO, La, Pr, and Nd are confirmed to share the dodecahedral LnO_8 site, whereas Te and W share the octahedral MO_6 site (Fig. 2B). Energy-dispersive x-ray (EDX) spectroscopy from a high-angle annular dark-field scanning transmission electron microscope (HAADF-STEM) (Fig. 2, C to E) shows that each element is uniformly distributed, which provides further evidence that no impurity phases exist.

The ionic conductivities of the three high-entropy materials were determined by electrochemical impedance spectroscopy (Fig. 3A). The overall room-temperature conductivities are 2.2×10^{-5} S/cm for LTZSHPO (15% porosity), 1.2×10^{-6} S/cm for NTZSHPO (20% porosity), and 1.7×10^{-6} S/cm for LLPNTWO (27% porosity). Figure 3A also presents the conductivities of the single-metal analog compounds that were synthesized and measured using the same approaches as the high-entropy samples. The ionic conductivities of all three high-entropy materials surpass those of their single-metal counterparts by several orders of magnitude (figs. S2 to S5 and table S1).

We attribute the enhancement of ionic conductivity in the high-entropy materials to the cation disorder that creates site-energy overlap and promotes ion percolation (Fig. 1). To acquire more explicit experimental evidence of Li disorder across sites, we assessed the Li site occupancies through refinement of time-of-flight neutron diffraction patterns (Fig. 3, B and C). In LTZSHPO, the site occupancy factors (SOF) found are SOF(Li_{6b}) = 0.4182 and SOF(Li_{36f}) = 0.0970 (illustrated

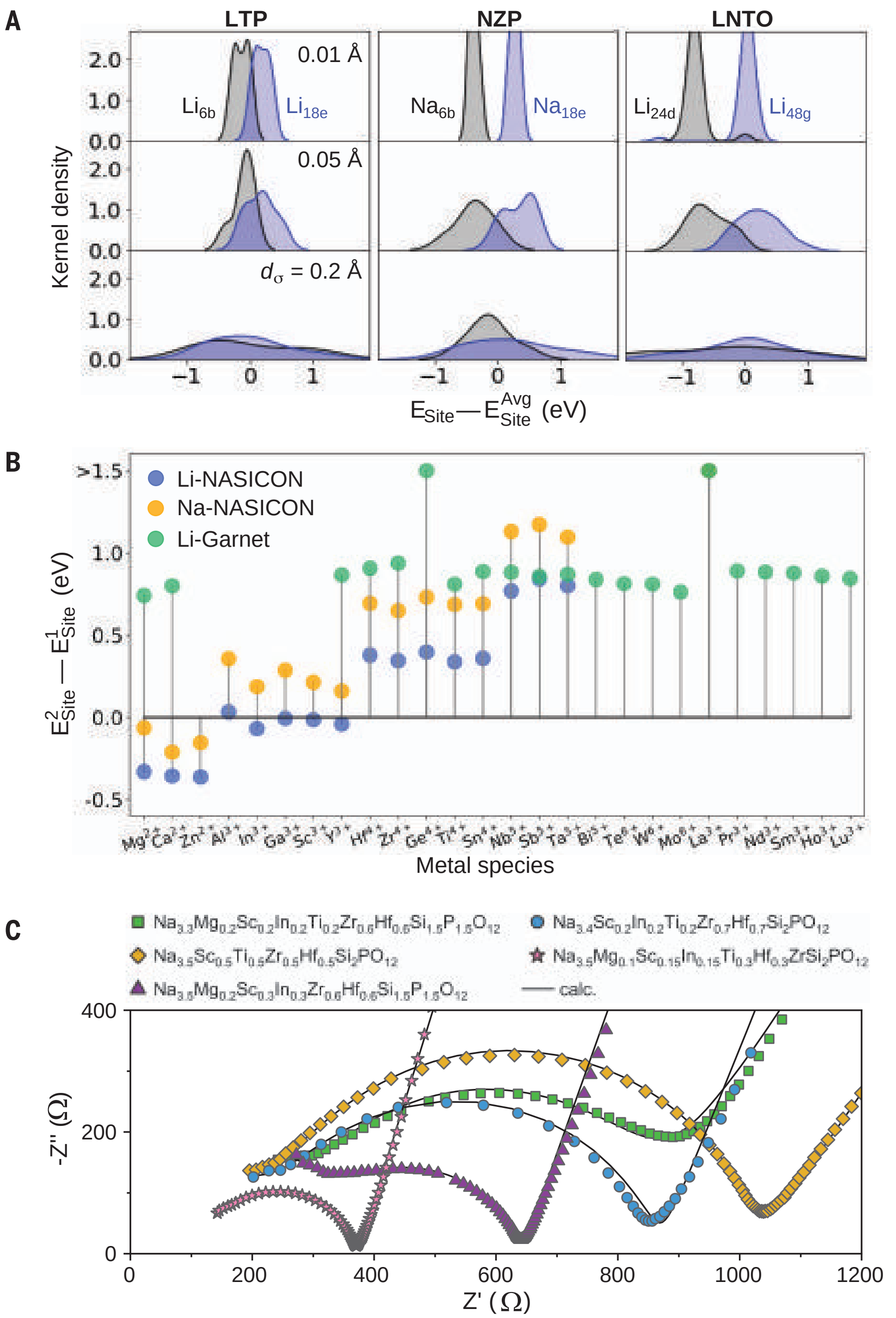


Fig. 4. Design guidelines for optimal distortion and effect of metal chemistry. (**A**) Calculated site-energy distributions in LTP, NZP, and LNTO with small (0.01 Å), medium (0.05 Å), and large (0.2 Å) distortions. (**B**) Calculated site-energy difference with various metal species in Li-NASICON, Na-NASICON, and Li-garnet. For Li- and Na-NASICONs, site 1 refers to 6b sites and site 2 refers to 18e sites. For Li-garnet, site 1 refers to 24d sites and site 2 refers to 48g sites. (**C**) Nyquist plots of Na-stuffed high-entropy compounds. Z′, the real part of the impedance; -Z″, the imaginary part of the impedance.

in Fig. 3D). As a comparison, LTP contains Li exclusively on 6b sites (fig. S6). Moreover, other single-metal $LiM_2(PO_4)_3$ have not been observed to exhibit Li partial occupancy at room temperature (*12*–*14*). We also observed partial occupancies in the garnet LLPNTWO with SOF(Li_{24d}) = 0.9196 and SOF(Li_{48g}) = 0.0402 (Fig. 3D). In comparison, LNTO contains Li exclusively on 24d sites (fig. S6). Other low-entropy Li_3-garnets also only accommodate Li on 24d sites (*15*). We obtained the Na site occupancy factor for NTZSHPO from XRD to be SOF(Na_{6b}) = 0.8383 and SOF(Na_{18e}) = 0.0539 (Fig. 3D). Again, single-metal $NaM_2(PO_4)_3$ only accommodates Na on 6b sites (*16*, *17*). The detailed Rietveld refinements are presented in tables S2 to S4. These observations confirm that multiple metals on cation sites create Li- or Na-site disorder, which can only arise when their otherwise distinct sites become more similar in energy.

To further validate that high-entropy materials have a stronger tendency to create Li-site disorder than their single-metal analogs, we performed ab initio molecular dynamics (AIMD) simulations to compare LTZSHPO and LTP in the canonical ensemble at 300 K (see methods). The site occupancy evolution along a 1.1-ns trajectory of AIMD simulations is demonstrated in Fig. 3E. The occupancy versus time shown in Fig. 3E was calculated by averaging the occupancies in a trajectory during the past 100 ps. Figure 3E shows that the average Li occupancies in LTZSHPO gradually converge to 0.40 on 6b sites and 0.09 on 36f sites after around 0.6 ns, close to the experimental observations (Fig. 3B). By contrast, there is barely any site occupancy change for LTP. This simulation confirms the higher disordering tendency in LTZSHPO compared with that in LTP.

Unlike many other physical properties of materials, diffusivity is not an "averaged" property over the structure. The ionic conductivity in materials does not depend on the average migration rate between all pairs of sites but rather depends on the fastest percolating pathway the ions can take through the system. Because of the very high connectivity of sites in a typical crystal structure (many paths can be created between two distant sites), ion transport is not sensitive to some of these paths being very high in energy, because an ion variationally picks the path of lowest resistance. This explains why the site-energy distributions that are created through the high-entropy metal cation disorder are so effective for promoting percolation. It creates a sufficient probability that some neighboring sites are close in energy, making it easier for ions to jump between them. At a critical level of such close-energy neighbors, the system percolates and has high conductivity. The fact that disorder may also create nearest-neighbor site pairs with an increased energy difference does not matter because their participation in transport is not required.

A small fraction of conductors may not benefit from high-entropy optimization. Purely one-dimensional (1D) conductors only have a single path available between two sites in the same channel (*18*), and perturbations to the site-energy landscape can lower conductivity by creating some high-energy barriers that need to be crossed. But for most materials that have 2D and 3D site connectivity, high entropy is a valid strategy to increase conductivity.

With these insights, we anticipate three scenarios for the site-energy distributions that arise from different degrees of distortion. When the distortion is minimal, or the site energies are too far apart, the dispersion of site energies created by local distortions is too narrow to create overlap between the two sites. Consequently, the alkali metals' percolation can barely occur. At the other extreme, overly large distortions lead to a very broad dispersion of site energies, which increases the probability for neighboring sites to have a higher energy difference, thereby limiting ion percolation. Between these two extremes, there is an optimal range of distortion that creates a percolating network of sites that are all within a narrow energy range.

To put this in the context of real materials, Fig. 4A shows the calculated site-energy distributions in distorted LTP, NZP, and LNTO with small (0.01 Å), medium (0.05 Å), and large (0.2 Å) distortions, in addition to the 0.1 Å that was used to generate Fig. 1B. We find that with d_σ = 0.01 Å, the energy of the two sites has no (e.g., NZP) or scarce (e.g., LTP and LNTO) overlap, whereas larger d_σ values (0.05 Å in Fig. 4B and 0.1 Å in Fig. 1B) create more overlap. However, a further increase of distortion (0.2 Å) spreads out the site energies too much, making percolation difficult (percolation analysis in fig. S7). These results indicate that there is an optimal distortion for good ionic conductivity due to the trade-off between site-energy overlap and the amount of accessible percolating sites. Using DFT on a large supercell (fig. S8) with a random arrangement of the nonalkali metals, we found the bond-length deviation to be 0.067 Å in LTZSHPO, 0.065 Å in NTZSHPO, and 0.054 Å in LLPNTWO (fig. S9), which creates overlapping site-energy distributions that are consistent with our explanation for the improved conductivity (fig. S10).

In addition to the structural distortions that can influence the alkali energy landscape, a direct interaction between the metal cations and the alkali ion may also modify the site energies (*19*). To probe this effect, we calculated how the site-energy difference varies with chemistry by substituting nonalkali metal cations in LTP, NZP, and LNTO. In this calculation, the atomic positions and lattice constants are fixed to separate the effect of chemistry from that of the distortion that was previously discussed. Figure 4B depicts the calculated site-energy difference in the presence of different metal species. Note that there are two different metal sites in Li-garnet, and the values in Fig. 4B are averaged from all compositions that have the targeted metal cation. Calculations for each individual composition are demonstrated in fig. S11. In Li-NASICON and Na-NASICON, the nonalkali metal cations can change the site-energy difference. In general, lower-valent metals (e.g., Mg^{2+}) prefer the alkali in 18e sites, whereas higher-valent metals (e.g., Zr^{4+}) in the compound stabilize the alkali in 6b. For garnets, although 24d sites are always preferred, the site-energy difference still varies. For example, the site-energy difference in garnet with Pr^{3+} or Nd^{3+} is more than 500 meV less than that with La^{3+}.

The entropy-stabilization mechanism of high-entropy compounds enables the solubility of more and different cations than would be possible under low-entropy conditions (*20*). This can be used to create site-energy distributions that lead to percolating transport networks with much higher ionic conductivity than those achieved with a single-metal cation component. Although in our work only a few compositions were tested, the high-dimensional nature of the high-entropy systems creates a vast opportunity space for compositional tuning and makes it more likely to stay within the space of earth-abundant and inexpensive elements. As demonstrated in our experiments and computations, high-entropy materials do not necessarily need an excess concentration of Li or Na to improve ionic conductivity, which may in turn help overcome the Li loss issues observed during the sintering of Li-stuffed ionic conductors (*11*) (also see table S5 for Li-loss in Li-garnets). To further this field, understanding is needed on which elements can form a compatible high-entropy ensemble through high-throughput modeling (*10*, *21*) and rapid experimenting (*22*). For example, we found that the NASICONs with five equimolar M^{4+} metal cations (Ge, Ti, Zr, Sn, Hf) could not be synthesized, probably because of the large size mismatch of Ge^{4+} with the other metal cations. Similarly, garnets with three equimolar M^{6+} (Mo, W, Te) were attempted but did not lead to phase-pure samples.

The high-entropy strategy can potentially be combined with the alkali metal–stuffing strategy to further optimize the ionic conductivity. To support this idea, we designed and synthesized five Na-stuffed high-entropy NASICON compounds (XRD in fig. S12). The measured impedance spectra are plotted in Fig. 4C, with detailed information provided in fig. S13 and table S1. All five compounds exhibit bulk room-temperature ionic conductivities that exceed 1 mS/cm. $Na_{3.5}Mg_{0.1}Sc_{0.15}In_{0.15}Ti_{0.3}Hf_{0.3}ZrSi_2PO_{12}$, even with 7% pellet porosity, shows a total conductivity of 1.1 mS/cm and a bulk conductivity of 3.3 mS/cm, which is comparable to that of the fastest Na-ion conductors (*10*, *23*).

We demonstrate that the local disorder in high-entropy materials can effectively promote site percolation and enhance ionic conductivity through the creation of overlapping site-energy distributions. This work paves the way for developing high-entropy superionic conductors and a pathway to achieve high ionic conductivity in solid electrolytes and other applications involving ion diffusion.

REFERENCES AND NOTES

1. X. He *et al.*, *Adv. Energy Mater.* **9**, 1902078 (2019).
2. Y. Wang *et al.*, *Nat. Mater.* **14**, 1026–1031 (2015).
3. Y. Xiao *et al.*, *Adv. Energy Mater.* **11**, 2101437 (2021).
4. D. Di Stefano *et al.*, *Chem* **5**, 2450–2460 (2019).
5. K. Jun *et al.*, *Nat. Mater.* **21**, 924–931 (2022).
6. Y. Zhang *et al.*, *Nat. Commun.* **10**, 5260 (2019).
7. H. Aono, E. Sugimoto, Y. Sadaoka, N. Imanaka, G. y. Adachi, *J. Electrochem. Soc.* **137**, 1023–1027 (1990).
8. H. Y. P. Hong, *Mater. Res. Bull.* **11**, 173–182 (1976).
9. M. P. O'Callaghan, A. S. Powell, J. J. Titman, G. Z. Chen, E. J. Cussen, *Chem. Mater.* **20**, 2360–2369 (2008).
10. B. Ouyang *et al.*, *Nat. Commun.* **12**, 5752 (2021).
11. A. Paolella *et al.*, *ACS Appl. Energy Mater.* **3**, 3415–3424 (2020).
12. E. R. Losilla, M. A. G. Aranda, M. Martínez-Lara, S. Bruque, *Chem. Mater.* **9**, 1678–1685 (1997).
13. M. Catti, S. Stramare, R. Ibberson, *Solid State Ion.* **123**, 173–180 (1999).
14. E. I. Morin *et al.*, *ChemInform* **29**, 1 (1997).
15. M. P. O'Callaghan, D. R. Lynham, E. J. Cussen, G. Z. Chen, *Chem. Mater.* **18**, 4681–4689 (2006).
16. J. Alamo, J. L. Rodrigo, *Mater. Res. Bull.* **27**, 1091–1098 (1992).
17. G. Pang *et al.*, *Nanoscale* **6**, 6328–6334 (2014).
18. D. Morgan, A. Van der Ven, G. Ceder, *Electrochem. Solid-State Lett.* **7**, A30 (2004).
19. D. A. Kuznetsov *et al.*, *Joule* **2**, 225–244 (2018).
20. C. Oses, C. Toher, S. Curtarolo, *Nat. Rev. Mater.* **5**, 295–309 (2020).
21. Z. Lun *et al.*, *Nat. Mater.* **20**, 214–221 (2021).
22. N. J. Szymanski *et al.*, *Mater. Horiz.* **8**, 2169–2198 (2021).
23. Y. Tian *et al.*, *Chem. Rev.* **121**, 1623–1669 (2021).

ACKNOWLEDGMENTS

Funding: This work was supported by the Assistant Secretary for Energy Efficiency and Renewable Energy, Vehicle Technologies Office, of the US Department of Energy under contract no. DE-AC02-05CH11231. The computational analysis was performed using Eagle and Swift at the National Renewable Energy Laboratory, Extreme Science and Engineering Discovery Environment, supported by NSF ACI1053575; and the National Energy Research Scientific Computing Center. Neutron diffraction was conducted at the NOMAD beamlines at Oak Ridge National Laboratory's Spallation Neutron Source, which was sponsored by the Scientific User Facilities Division, whereas STEM was performed at the National Center for Electron Microscopy (NCEM) at Lawrence Berkeley National Laboratory (LBNL). Both facilities are supported by the Office of Science of the US Department of Energy. We also appreciate K. Bustillo from NCEM at LBNL for her technical assistance in STEM. **Author contributions:** Y.Z., B.O., and G.C. planned this work. G.C. supervised all aspects of the research. Y.Z. synthesized, characterized, and tested the proposed materials. Y.Z. and B.O. proposed and designed the theoretical calculations. B.O. performed the calculations and analyzed the results with help from Y.W. J.L. collected and helped Y.Z. analyze the neutron diffraction data. Y.-W.B. performed STEM. Z.C. performed inductively coupled plasma. Y.Z., B.O., and G.C. wrote the paper with help from L.J.M. All authors contributed to discussions and writing. **Competing interests:** None declared. **Data and materials availability:** All data are available in the paper and the supplementary materials. **License information:** Copyright © 2022 the authors, some rights reserved; exclusive licensee American Association for the Advancement of Science. No claim to original US government works. https://www.science.org/about/science-licenses-journal-article-reuse

SUPPLEMENTARY MATERIALS

science.org/doi/10.1126/science.abq1346
Materials and Methods
Figs. S1 to S13
Tables S1 to S5
References (*24–27*)

Submitted 20 March 2022; accepted 28 October 2022
10.1126/science.abq1346

3D PRINTING

Three-dimensional nanofabrication via ultrafast laser patterning and kinetically regulated material assembly

Fei Han[1,2]*, Songyun Gu[1]*, Aleks Klimas[3], Ni Zhao[2,4], Yongxin Zhao[3]†, Shih-Chi Chen[1,2,5]†

A major challenge in nanotechnology is the fabrication of complex three-dimensional (3D) structures with desired materials. We present a strategy for fabricating arbitrary 3D nanostructures with a library of materials including metals, metal alloys, 2D materials, oxides, diamond, upconversion materials, semiconductors, polymers, biomaterials, molecular crystals, and inks. Specifically, hydrogels patterned by femtosecond light sheets are used as templates that allow for direct assembly of materials to form designed nanostructures. By fine-tuning the exposure strategy and features of the patterned gel, 2D and 3D structures of 20- to 200-nm resolution are realized. We fabricated nanodevices, including encrypted optical storage and microelectrodes, to demonstrate their designed functionality and precision. These results show that our method provides a systematic solution for nanofabrication across different classes of materials and opens up further possibilities for the design of sophisticated nanodevices.

In the field of nanotechnology, multimaterial three-dimendional (3D) fabrication at nanoscale has been a long sought-after goal (*1*, *2*). Most 3D nanofabrication techniques rely on lithographic methods to create complex structures with nanoscale resolution, in which photoinitiated chemical reactions such as photopolymerization (*3*–*5*) and photoreduction (*6*–*8*) are critical. Despite many previous attempts, material choices for nanofabrication are still largely limited to polymeric materials or metals. A fabrication solution for a wider class of materials without compromising existing structural complexity, nanoscale feature sizes, and material functions remains a critical challenge.

Fabrication of designed 3D nanostructures through direct assembly of materials has become an effective nanofabrication strategy. A prerequisite of the method is to selectively control the movement and subsequent integration of the material building blocks, such as nanoparticles (NPs) or macromolecules, with nanoscale precision. To this end, the driving force that governs the material assembly is critically important. Recent advances have demonstrated assembling charged metal particles with electrical fields (*9*–*11*), stacking blocks of nucleic acid with base pairings (*12*–*14*), or covalently linking dye molecules to a hydrogel, followed by attaching materials to the dyes (*15*). In principle, such bottom-up processes should be generally applicable in growing nanostructures of any material. Despite the straightforward strategy, none of the existing methods offer a generalizable solution. Particles from different materials always have distinctively different physical or chemical properties, and to systematically manipulate their assembly within a singular system is impossible due to the lack of suitable driving forces.

A hydrogel can capture a variety of materials through their different interactions, such as hydrogen bonds, charge effects, covalent bonds, or through their dense scaffolds. Thus, hydrogels can be used to form composites with different nanomaterials for 3D printing (*16*), or to support in situ photoreduction of metal NPs for nanopatterning (*17*). Moreover, by exposing a hydrogel with femtosecond (fs) laser, designed patterns can be labeled on the gel with two-photon reactions and additional photoreactive molecules (*18*–*20*). By engineering the molecular structures of these molecules in combination with the shrinking of gel substrates (implosion fabrication), certain functional materials can be bridged to the patterned gel through the coordination effect or hydrogen bonds with resolution beyond the optical diffraction limit (*15*).

We report a strategy to directly create arbitrary 3D patterns of various materials in hydrogel through the kinetic effects enabled by programmable fs light sheets (*21*, *22*). Previously, the optical system was used for two-photon lithography to generate 3D polymeric micro- and nanostructures. In this work, we found that its ultrahigh peak intensity (> 1 TW/cm^2) can directly modify the polymeric network of a polyacrylate-polyacrylamide hydrogel (*15*, *23*) in pure water (Fig. 1B), leading to reduced scaffold density and improved capability of forming hydrogen bonds at the exposed site. We exploited this phenomena to pattern the gel with designed 3D geometries and then selectively assembled material particles to the sites through regioselectivity induced by the size-dependent steric effect, or by the increasing density of hydrogen bonds. As this method uses kinetic factors to directly assemble materials (instead of tailored bridging molecules or conjugation reactions), our strategy can be extended to water-dispersible materials with suitable sizes (table S1) or hydrophilicity. To verify this point, we fabricated various 3D structures with a library of materials including metals, alloys, 2D materials, upconversion materials, diamond, molecular crystals, oxides, semiconductors, biomaterials, polymers, fluorescent species, and even inks from fountain pens. In addition, features of the patterned gels can be preadjusted before material deposition to achieve sub–diffraction limit resolution (20 to 35 nm). The assembled material particles were densely packed to form 3D structures with an exterior surface roughness of < 5 nm and a material filling ratio of ~60% by volume, which is suitable for nanodevice fabrication.

Schematics illustrating the fabrication steps are shown in Fig. 1, A to D, and fig. S1 (*24*). We first patterned an expanded hydrogel with our fs light sheet patterning system (*21*). A 100-fs laser beam from a 1-kHz regenerative amplifier is shaped and dispersed through a digital micromirror device (DMD), and then projected to the gel as a temporally focused light sheet for rapid patterning (Fig. 1E and fig. S2). The patterned gel was then incubated in the solution of the target material for 2 hours. This allowed for volumetric self-assembly of material particles onto the predefined patterns, generating 3D structures with submicrometer resolution (Fig. 1G).

Alternatively, as acrylic acid–based hydrogels shrink in acid, the patterned gel can be preshrunk in hydrochloric acid (4 mM) before material deposition, and then air-dried to create small features below the diffraction limit (Fig. 1C). Isotropic substrate shrinkage can be achieved by affixing the gel on a thin copper wire (fig. S3); the lateral and axial contraction ratios are measured to be 12.8 ± 0.4 and 12.7 ± 0.7 (mean ± SD, n = 10), respectively (fig. S4). After material deposition and dehydration, the small features can be characterized by scanning electron microscopy (SEM) (Fig. 1, H and I). Although the hydrogel scaffolds were kept for structural support in our demonstrations, cleavable crosslinkers (*25*), sintering (*26*), or chemical etching (*27*) may be used to remove the gel in some applications where a permanent scaffold is not desired.

Different from previous methods that pattern hydrogels through two-photon reactions with certain organic molecules (*15*, *18*–*20*), the

[1]Department of Mechanical and Automation Engineering, The Chinese University of Hong Kong, Shatin, Hong Kong. [2]Oxford-CityU Centre for Cerebro-Cardiovascular Health Engineering (COCHE), Shatin, N.T., Hong Kong. [3]Department of Biological Sciences, Carnegie Mellon University, Pittsburgh, Pennsylvania 15213-3815, United States. [4]Department of Electronic Engineering, The Chinese University of Hong Kong, Shatin, Hong Kong. [5]Centre for Perceptual and Interactive Intelligence (CPII), Shatin, N.T., Hong Kong.
*These authors contributed equally to this work.
†Corresponding author. Email: scchen@mae.cuhk.edu.hk (S.-C.C.); yongxinz@andrew.cmu.edu (Y.Z.)

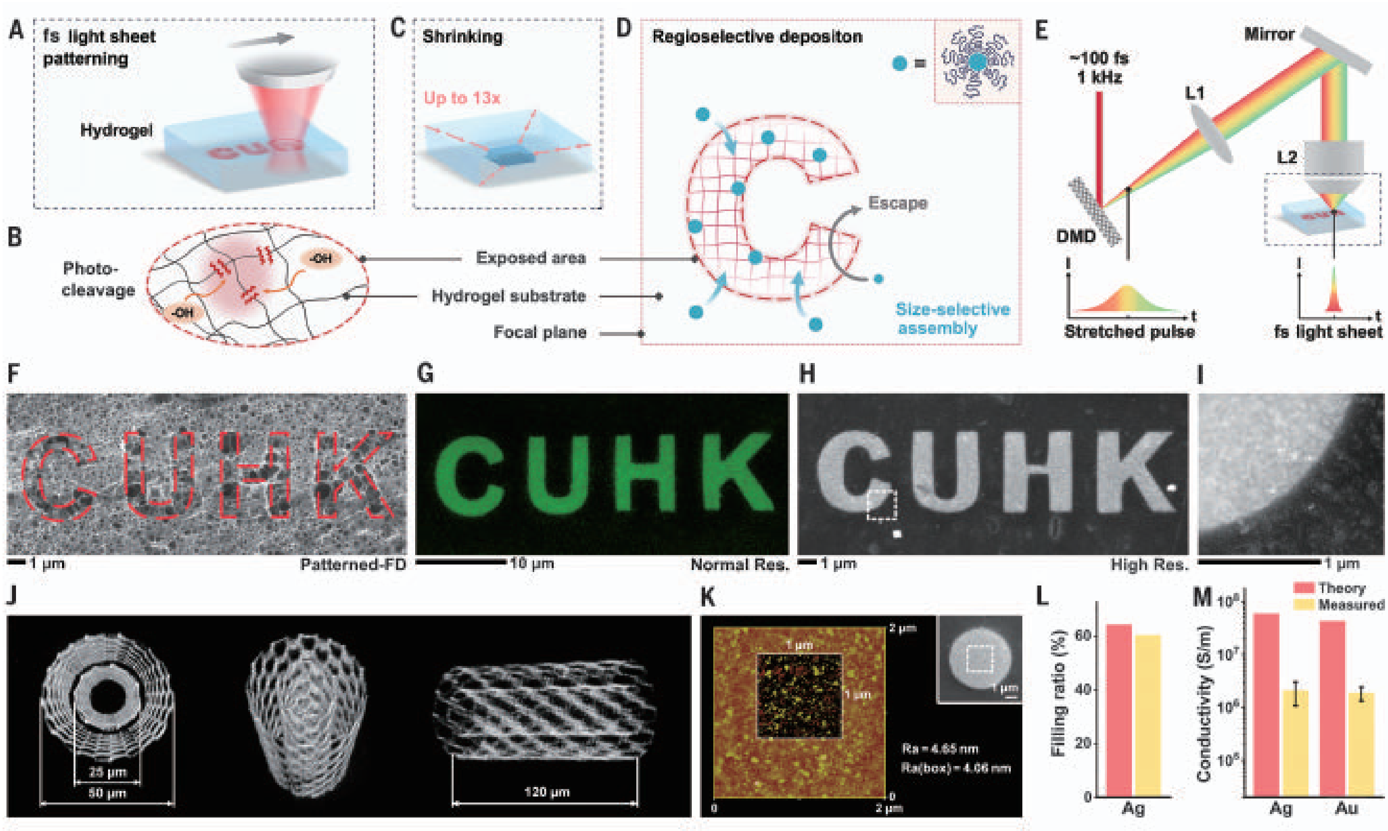


Fig. 1. Fabrication setup, process, and results. Schematics illustrating (**A**) the patterning process, in which complex patterns can be defined with a single exposure; (**B**) photocleavage of the polymer network of a hydrogel during patterning; (**C**) shrinkage of the patterned gel to reduce the feature size; and (**D**) regioselective deposition of materials in a shrunk gel through size selective assembly. (**E**) Configuration of the fs light sheet patterning system. L1: collimating lens; L2: objective lens. (**F**) SEM image of a fully shrunk and freeze-dried (FD) gel showing network structures on the "CUHK" pattern. (**G**) Fluorescent image of the "CUHK" pattern deposited with graphene QDs without preshrinking. SEM images of (**H**) the "CUHK" pattern deposited with Ag NPs (15 nm) after preshrinking the gel. (**I**) Zoomed in view of (G). (**J**) Top, tilted, and side views of a double-walled carbon nanotube structure assembled by fluorescein. (**K**) Atomic force microscopy measurements of a silver disk (shown in the inset). (**L**) Volume filling ratio of Au, TiO_2, and Fe_3O_4 in a 3×3×3 μm^3 cube; the theoretical value refers to random close packing (~64%). (**M**) Conductivity of the fabricated metal structures after laser sintering; error bars indicate mean ± SD (n = 8).

average light intensity (300 to 1000 W/cm^2) of the fs light sheets is high enough to directly modify the gel network in pure water for pattern definition. To explore how laser irradiance modified its microstructures, we characterized a patterned gel with SEM. The gel was shrunk and freeze-dried to remove the retention water. The results showed that the hydrogel substrate was partially etched at the patterned sites (Fig. 1F), leaving more porous network structures than the unexposed region. As its degree of porosity roughly increases with increasing laser doses (fig. S5), and the system contains no photosensitive species, it is possible that the gel scaffolds were partially removed through direct photodisruption (*28*) of its polymeric chains under the high-power laser.

X-ray photoelectron spectroscopy measurements indicated that the ratio of oxygen to carbon increased for ~49% after patterning (fig. S6), suggesting that the chemical components were modified. Interestingly, both Fourier-transform infrared (FTIR) spectroscopy and Raman spectroscopy indicated that the major chemical bonds of the gel remained unchanged (fig. S7). Only the FTIR spectrums showed a new peak at 1294 cm^{-1}, possibly corresponding to the stretching of C–O–H bonds. We further found that the laser for patterning is strong enough to directly excite the exposed water molecules (*29*, *30*), which can dissociate them into hydroxyls and free protons by 12% or more (*29*). As the photoexcited species should be highly reactive, we speculate that during the cleavage of hydrogel scaffolds, the simultaneously excited hydroxyls may connect to the partially disrupted polymer network (Fig. 1B), thereby contributing to the new peak in FTIR.

The addition of hydroxyls is expected to increase the formation of hydrogen bonds at the exposed sites. We exploited this effect to selectively attach suitable materials to construct 3D nanostructures. We designed a set of Chinese zodiac animals as test patterns to examine our method (fig. S10A). Six of the patterns were deposited with different hydrophilic materials to promote the formation of hydrogen bonds, including two dragons of CdSe quantum dots (QDs) (Fig. 2A), where the stripes show a feature size of 200 nm, a tiger of graphene QDs, a goat of fluorescent gold, a horse of fluorescent polystyrene spheres, a rooster of fluorescein, and a mouse of protein (Fig. 2, I-M). By tuning the laser dosage, the density of hydrogen bonds can be fine-tuned to achieve precise grayscale control (fig. S8). The fluorescent imaging results indicate that these photoluminescent materials retain their functions after deposition, which suggests that the chemical structures of the QDs or macromolecules were not modified.

By contrast, we used the porous network to kinetically regulate the assembly of materials in a preshrunk hydrogel. As the patterned sites have reduced densities of polymer networks, NPs of suitable sizes can be selectively trapped there to form defined patterns (Fig. 1D). For example, we patterned a gel with a laser dose

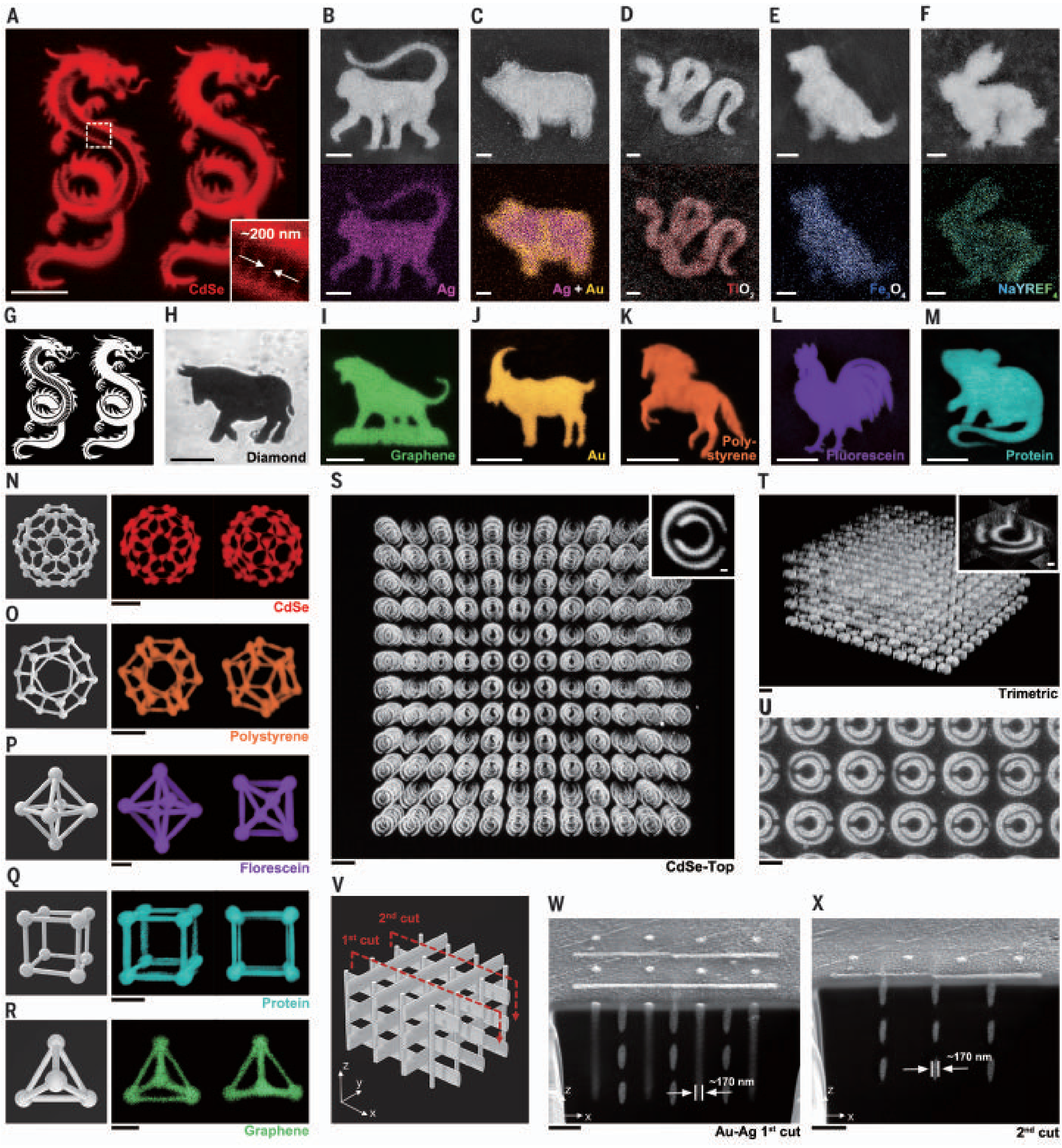


Fig. 2. Demonstration of material variety. (**A**) Fluorescent image of two dragons of CdSe QDs without shrinking; the inset shows a resolution of ~200 nm. (**B** to **F**) SEM (top) and EDX (bottom) images of a monkey of Ag, pig of Au-Ag alloy, snake of TiO_2, dog of Fe_3O_4, and rabbit of $NaYREF_4$, respectively. (**G**) Designed dragon patterns in (A). (**H**) Optical microscopy image of an ox of diamond. (**I** to **M**) Fluorescent images of a tiger of graphene QDs, a goat of fluorescent Au, a horse of polystyrene, a rooster of fluorescein, and a mouse of fluorescent protein, respectively. (**N** to **R**) 3D models and fluorescent images (maximum intensity projection) of the fabricated structures in shapes of a C_{60} molecule, regular dodecahedron, regular octahedron, cube, and regular tetrahedron of different materials, respectively. (**S**) Top view of a five-layer split ring resonator (SRR) structure; inset: SRR unit. (**T**) Trimetric view of the SRR structure in (S); inset: slice view of an SRR unit. (**U**) SEM image of the top layer of an SRR structure after shrinking and dehydration. (**V**) 3D model of a woodpile structure containing 16 vertical rods along the z axis. (**W** and **X**) SEM cross-sectional images of the fabricated woodpile at the two cut planes in (V), respectively. (Substrate tilt angle: 52°). Scale bars are 1 μm for (B to F, U, W, X, and the insets of S and T), and 10 μm for (A, H to M, and N to T).

of 600 W/cm^2 and 50 ms, into which we deposited gold NPs of different sizes. SEM images (fig. S9, A to F) showed that the 15- and 30-nm NPs were densely packed on the patterns to form designed geometries, whereas the 5-nm NPs failed to fill the patterns due to their much smaller size and limited steric hindrance. These results suggest that for a given laser dose, the deposition quality critically depends on the size of the NPs (see notes of fig. S9 for details). Additionally, as the porosity of the patterned network is determined by the laser dose, one may deposit smaller NPs with reduced doses (for example, 3 nm) (table S5). To precisely control the assembly toward ordered patterns, we varied the kinetic barrier of NP migration from the perspectives of entropy, restricting Brownian motion, and the repulsive surface charges. Specifically, the hydrogen bonds and steric effect were exploited to selectively reduce the barrier by providing adhesive forces to overcome electrostatic repulsion, or to suppress random aggregation elsewhere by trapping the NPs in the network, promoting selective assembly at the patterned sites. Notably, the steric effect can be further strengthened to improve the fabrication; encapsulating NPs with bulky ligands can increase selectivity during assembly (*31*, *32*) by introducing additional steric hindrance. For example, comparing with small-molecule ligands like citrate, functionalizing the gold NPs with polyvinylpyrrolidone (PVP) results in better structures with well-defined boundaries, smooth surfaces, and fewer background particles (fig. S9, E to G). PVP is a sizable ligand with long chains and multiple binding sites (Fig. 1D, inset); therefore, the interior NPs can be readily tethered to the porous network or each other (*33*), kinetically promoting their assembly and subsequent integration. The other kinetic factor, hydrogen bonding, still affects the process, and highly hydrophilic ligands such as hydroxyls should be avoided to prevent the retention of NPs on the substrate (fig. S9, F to I).

To demonstrate that steric control is generally applicable to materials of different chemical or physical properties, we deposited different NPs into the remaining six zodiac animals (see table S5 for detailed fabrication parameters), including a monkey of silver (Fig. 2B), a snake of TiO_2, a dog of Fe_3O_4, a rabbit of upconversion material [$NaYREF_4$ (RE: Yb, Er, Tm, Gd, Mn, Lu)], and an ox of diamond (Fig. 2, D to F and H, respectively). The method also allows for fabrication of alloy structures, such as gold-silver alloy (Fig. 2C) and TiO_2-Fe_3O_4 alloy (fig. S10F), by directly incubating the gel with a mixed solution of two NPs. The SEM images show that the structures do not have visible distortion at high shrinkage ratios, producing patterns of the designed shapes. The fabrication results were further confirmed by energy-dispersive x-ray (EDX) mappings (fig. S10 and S11). Notably, such kinetic control is not limited to the aforementioned species. Fabrication of other materials, such as sulfur, platinum, zinc sulfide, and even fountain pen inks, can generally be achieved by choosing appropriate combinations of particle sizes and laser doses (fig. S12).

Next, we demonstrate our capability in fabricating complex 3D structures of different materials and feature sizes. First, a series of polyhedrons were sequentially patterned and deposited with different materials without preshrinking the gel, including a C_{60} model of CdSe, a regular dodecahedron of fluorescent polystyrene, a regular octahedron of fluorescein, a cube of protein, and a regular tetrahedron of graphene (Fig. 2, N to R). As the materials are assembled volumetrically, when combined with the fs light sheet system, the method allows rapid fabrication of large-area 3D structures, such as a five-layer, spatially separated split ring resonator array with 720 individual units in a volume of 1.44×10^7 µm^3 (Fig. 2, S to U). Notably, the patterning process was completed in only 0.18 seconds with our system [patterning rate of ~300 mm^3/hour or ~1.6×10^8 voxel/sec (*21*)], which usually needs minutes to hours in a conventional point-scanning system (*3*, *15*). Aside from the high patterning rate, our method also realizes self-alignment for multilayer printing. This enables the creation of arbitrary, unconnected 3D structures, which could not be readily achieved previously. Examples of millimeter-scale complex 3D structures are presented in fig. S13.

To verify that the morphology of the fabricated structures can be retained in all three dimensions in preshrunk hydrogels, we fabricated a modified woodpile structure of gold-silver alloy, which contains 16 vertical rods along the z axis (Fig. 2V). Our SEM images showed that the structure has a well-defined top surface without visible distortion (fig. S14E). We applied a focused ion beam (FIB) to section and evaluate the interior of the structure, which confirmed that the materials were densely packed inside the woodpile structure with good geometric accuracy (Fig. 2, W and X, and fig. S13, B to D). More results of woodpile structures of different scales are presented in fig. S14 and S15.

To investigate the fabrication resolution, we designed a series of 2D and 3D nanostructures. First, we fabricated arrays of four nanowires with projected widths of 7, 5, 3, and 2 pixels (px) on the DMD, respectively (Fig. 3C). The DMD pixel has a pitch of 7.56 µm, which maps to 94.5 nm in the build plane. Because the diffraction limit of the patterning system is 340 nm (calculated with the Rayleigh criterion), and the hydrogel has a shrinkage ratio of ~13, the corresponding minimal feature size after preshrinking is estimated to be ~25 nm. To match the scale, 5-nm silver NPs were used in the fabrication in combination with lower laser doses (500 W/cm^2 and 5 ms) (Fig. 3E). Figures 3, A and B, presents a representative nanowire array. We measured the widths of the wires (A to C) from both the SEM images and the gray level profiles (Fig. 3F), in which their full widths at half maximum (FWHMs) were 19.0, 23.5, and 39.0 nm, respectively. The top wire in Fig. 3A, which was defined by only 2 px, shows uneven width. We attribute this potentially to insufficient laser intensity: As the width of the projected wires reduces, their FWHM at the focal plane converges to the diffraction limit, and the corresponding intensity decreases (Fig. 3, D and E). Thus, the simulated intensity of the thinnest wire is approximately one-half of that of wire A, and only approximately one-quarter of that of wire C, which is too weak for uniform pattern creation. A survey that we performed of 10 groups of such arrays shows the widths of the wires (A to C) are 21.1 ± 5.0, 29.2 ± 3.0, and 37.7 ± 2.8 nm (mean ± SD), respectively, indicating that the fabrication is highly reproducible even at its limit.

We designed and fabricated a nonconnected 3D "NANO" structure consisting of arrays of parallel nanowires (Fig. 3H) to examine whether the same small feature size can be achieved in a complex 3D structure. Each nanowire had a projected width of 6 px on the DMD, and thus we estimated the final feature size to be ~35 nm. After fabrication with 5-nm silver NPs, we applied the FIB to section and evaluate the "NANO" structure (Fig. 3, I to K), where we found that the nanowires were accurately positioned without distortion. Our FWHM measurements of the linewidth produced an average lateral and axial resolution of 36.0 ± 5.1 and 148.4 ± 19.2 nm (mean ± SD, n = 20), respectively (Fig. 3L). This is consistent with the fabrication results of a 16-layer woodpile structure [with the same designed linewidth as the "NANO" structure (fig. S15)] and agrees with the simulation (fig. S2C), in which one may observe that the voxel aspect ratio increases with increasing projected linewidths.

The density of the deposited material is an important metric in evaluating the fabricated structures. We first performed AFM measurements on the exterior surface of the dehydrated material-deposited gels. The results showed high levels of smoothness, such that the mean surface roughness of the gold and silver structures only measured 4.69 and 4.06 nm, respectively (Fig. 1K and fig. S18), which suggests high material density. This smoothness is among the best reported results across all 3D printing and nanofabrication methods (See discussions in fig. S18). To characterize the material density in a 3D structure, we next fabricated a 3 µm^3 cube with 15-nm silver NPs, to which FIB was applied to section and examine the interior (fig. S16, B to D). The results confirm that the silver NPs

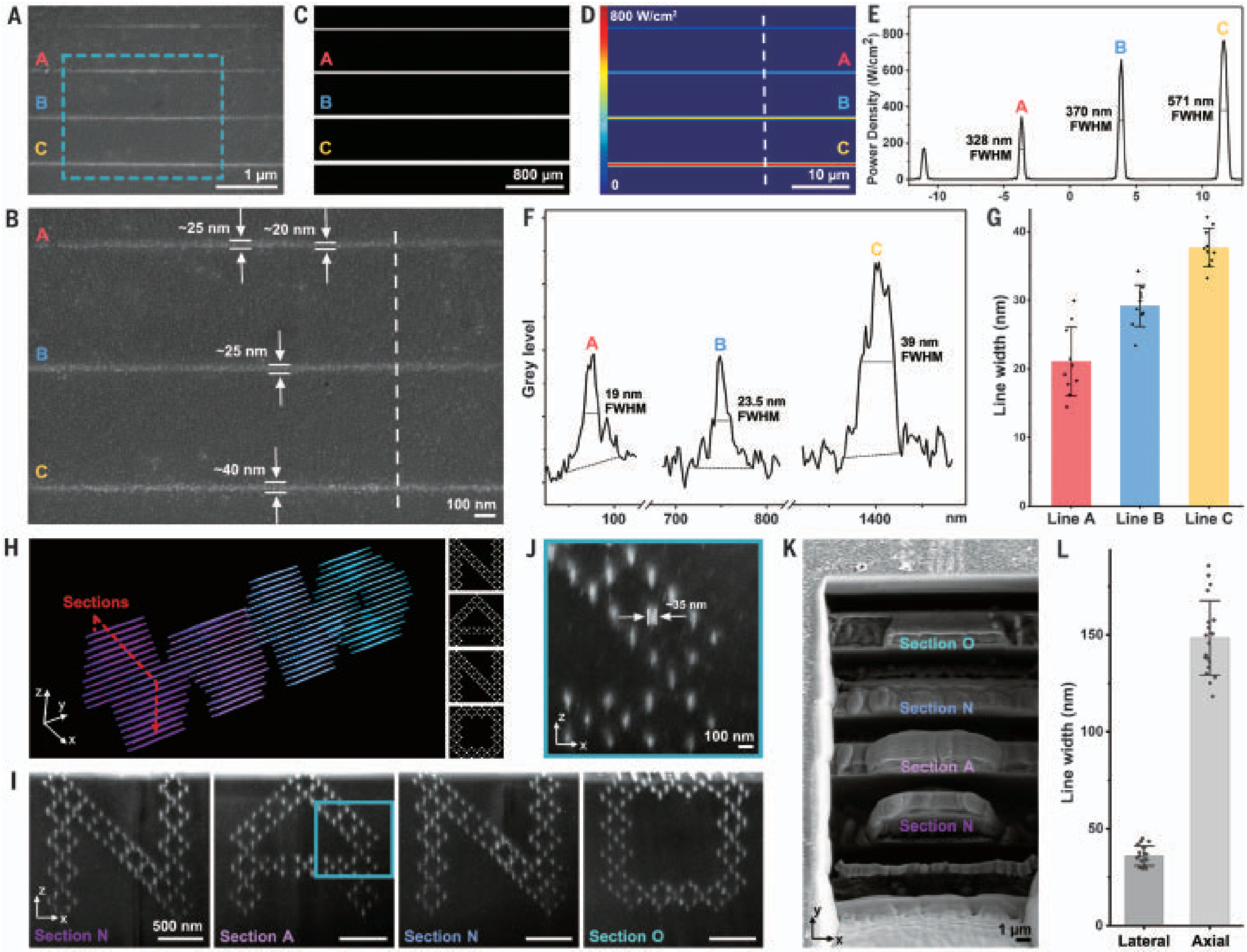


Fig. 3. Nanostructures demonstrating minimum feature sizes. SEM images of (**A**) an array of nanowires fabricated with 5-nm silver NPs, and (**B**) a zoomed-in view of (A). (**C**) Pattern displayed on the DMD. (**D**) Simulated intensity distribution at the build plane. (**E**) Cross-sectional profiles showing the intensity distribution in (D). (**F**) Grey level profiles of nanowires A to C across the dashed line in (B), which provide more accurate measurements. (**G**) Measurements of the linewidths in ten nanowire arrays. (**H**) 3D model of a nonconnected "NANO" structure comprised of arrays of parallel nanowires; and its four cross-sectional patterns (on the *x*-*z* plane). (**I**) SEM cross-sectional images of the "NANO" structure cut by FIB; and (**J**) a zoomed-in view of the letter "A" in (I). (**K**) SEM images showing the trenches of the gel sample opened by the FIB cut, in which the positions of each letter are labeled. All cross-sectional images were taken at a substrate tilt angle of 52°. (**L**) Survey of 20 different linewidths in 3D structures measured from (I) and fig. S15; error bars indicate mean ± SD.

are highly uniform and densely packed inside the cube. EDX mapping of a 1 μm^2 area of the section showed that the volume fraction of silver is 60.2% (fig. S16E), which reached ~94% of the theoretical density, assuming random close packing. Further experiments show that our method can also achieve high volume-filling ratio for non-metal materials, such as 61.3% and 58.3% for TiO_2 (5 nm) and Fe_3O_4 (10 nm), respectively (Fig. 1L and fig. S17).

Because the target materials are only applied in the last fabrication step, their original properties and functions can be preserved. We investigated the properties of fabricated metal structures, which are widely used in nanoscience, and demonstrated their potential applications. We tested the conductivity of different metals in preshrunk hydrogels, such as silver, gold, and gold-silver alloy (atomic ratio of 1:1). After material dehydration, an 80-MHz fs laser was applied to sinter the assembled NPs and to remove any ligands that may influence conductivity (fig. S19). The sintered structures were highly conductive, possibly owing to the high material-filling fraction. The silver, gold, and gold-silver alloy achieved conductivity of 2.06×10^6, 1.86×10^6, and 2.16×10^4 S/m, respectively, which allowed for the fabrication of conductive microelectrodes (fig. S20). The high conductivity was also evidenced by the highly linear current-voltage (*I-V*) curves [coefficient of determination (R^2) > 0.999]. Such high conductivity levels are ideal for applications in sensors, catalysis, and microelectronics.

Because the hydrogels are optically transparent, our method can directly fabricate various optical microdevices, such as diffractive optical elements (DOEs). We designed a 200 by 200 px binary hologram (fig. S21A) that encodes a pair of symmetric smileys (Fig. 4B). The hologram was first projected to the hydrogel for pattern definition. The gel was then shrunk, followed by the deposition of silver (15 nm). After dehydration, the device was completed and had a pixel size of 500 nm (Fig. 4A and fig. S21, B to D). The hologram is binarized through the different optical densities; the silver-deposited sites represent "0" and the empty sites represent

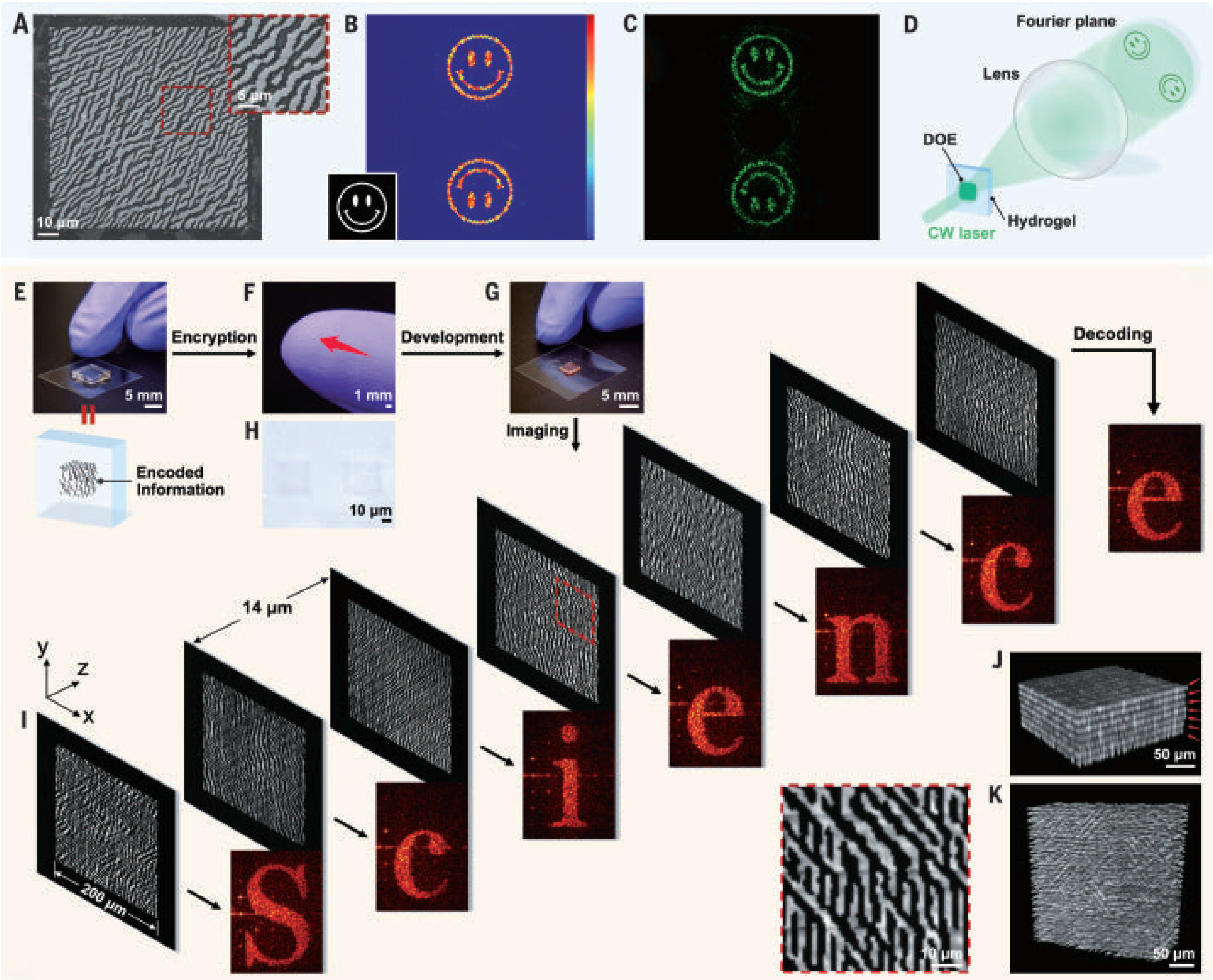


Fig. 4. Fabrication of DOE and applications in 3D optical storage and encryption. (**A**) SEM image and a zoomed-in view of a fabricated DOE. (**B**) Simulated intensity distribution at the Fourier plane of the DOE; inset: the encoded smiley. (**C**) Image recorded from the fabricated DOE in (A). The 0th order is spatially blocked to avoid camera damage. (**D**) Schematic of the optical setup to record the encoded image. (**E** to **G**) Demonstration of optical storage and encryption: (E) an expanded hydrogel patterned with designed information; (F) the gel in (E) after full shrinkage and dehydration to realize physical encryption; (G) the re-expanded gel deposited with CdSe and developed to decrypt the stored patterns. (**H**) Optical image showing two encrypted seven-layer hologram patterns in (F). (**I**) Fluorescent images of the decrypted holograms, in which "Science" is decoded; and (**J** and **K**) 3D views of the decrypted holograms.

"1" with a much higher transmission ratio. We collimated a 532 nm continuous wave laser to fully fill the aperture of the hologram, and recorded the reconstructed patterns on the observation screen (Fig. 4C). The reconstructed patterns show that the spatial frequency information of the device is well preserved during the large-area fabrication.

By exploiting the nanometer-level feature size and high laser patterning rate, we demonstrate an optical storage and encryption method by physically shrinking the optically written information in a 3D nanostructure. As a proof-of-concept demonstration, we designed and fabricated a seven-layer 3D structure that encodes "Science," where each layer contains a 200 by 200 px hologram that is encoded with a letter (pixel size 2000 nm) (fig. S23). The designed holograms were patterned in a fully expanded gel by means of the fs light sheet (Fig. 4E). After full shrinkage, each pixel of the structure was reduced to ~150 nm with a storage density of 20 terabits (Tb)/cm^3. Because the feature size was then below the diffraction limit and 3D in nature, information stored in the structure was effectively encrypted. When structures with reduced thickness are patterned, they are completely invisible (fig. S24C). Only a translucent rectangle without structural details could be observed under an optical microscope (Fig. 4H). Additionally, the shrunk and dehydrated hydrogels are chemically stable and can be stored over long periods of time.

To decrypt the structure, the device was re-expanded in a solution of NaOH (0.5 mM aq.) and deposited with CdSe QDs (or other fluorescent materials) to read out the stored holograms by confocal microscopy, which were subsequently decoded into "Science" (Fig. 4I). From these results, we confirmed that the stored holograms can be retrieved with high fidelity (Fig. 4, I to K, and fig. S23). Considering the high pattern rate of the fs light sheet, this approach has enabled an optical writing

speed of up to 84 megabits (Mbit)/s and a theoretical storage density of ~5 petabits (Pbit)/cm^3 (by setting the pixel size to ~40 nm). The fs patterning system can be modified into a temporal focusing microscope (*34*) to achieve an optical reading speed of ~84 Mbit/s, which may create opportunities in the field of digital data storage. For example, in fig. S25, we demonstrated a storage density of 1.14 Pbit/cm^3, reaching the same order of magnitude of the theoretical limit.

In traditional nanoscience, direct assembly of materials into complex 3D structures requires complicated chemistry and/or a tailored printing setup. Our work demonstrates the delicate use of kinetic control in manipulating the assembly of a wide range of materials. In principle, the method can be readily extended to other water-soluble or -dispersible materials without further chemistry design. With advanced nanosynthesis methods (*35*), such as creating core-shell or composite structures, our method may work for materials that are unstable in water, such as perovskite. Its application scope may be further expanded by applying the strategy to other high-throughput optical platforms (*36*, *37*) or polarization optimizations (*38*). With the demonstrated throughput, resolution, and material generality, our new fabrication platform presents a disruptive solution in creating new functional and biocompatible microdevices, optical metamaterials, and flexible electronics that may impact the fields of photonics, nanotechnology, and biotechnology.

REFERENCES AND NOTES

1. H. Zhao *et al*., *Nano Today* **30**, 100825 (2020).
2. D. A. Walker, J. L. Hedrick, C. A. Mirkin, *Science* **366**, 360–364 (2019).
3. E. Skliutas *et al*., *Nanophotonics* **10**, 1211–1242 (2021).
4. J. F. Xing, M. L. Zheng, X. M. Duan, *Chem. Soc. Rev.* **44**, 5031–5039 (2015).
5. Y. L. Zhang, Q. D. Chen, H. Xia, H. B. Sun, *Nano Today* **5**, 435–448 (2010).
6. Y. Chen *et al*., *Nat. Commun.* **11**, 5334 (2020).
7. C. Barner-Kowollik *et al*., *Angew. Chem. Int. Ed.* **56**, 15828–15845 (2017).
8. J. Li, E. H. Hill, L. Lin, Y. Zheng, *ACS Nano* **13**, 3783–3795 (2019).
9. W. Jung *et al*., *Nature* **592**, 54–59 (2021).
10. M. S. Saleh, C. Hu, R. Panat, *Sci. Adv.* **3**, e1601986 (2017).
11. H. Lee *et al*., *Nano Lett.* **11**, 119–124 (2011).
12. L. L. Ong *et al*., *Nature* **552**, 72–77 (2017).
13. D. Han *et al*., *Science* **332**, 342–346 (2011).
14. S. Dey *et al*., *Nat. Rev. Methods Primers* **1**, 1–24 (2021).
15. D. Oran *et al*., *Science* **362**, 1281–1285 (2018).
16. S.SoleymaniEilBakhtiari *et al*., *Adv. Eng. Mater.* **23**, 2100477 (2021).
17. S. Kang, K. Vora, E. Mazur, *Nanotechnology* **26**, 121001 (2015).
18. C. A. DeForest, K. S. Anseth, *Angew. Chem. Int. Ed.* **124**, 1852–1855 (2012).
19. M. A. Skylar-Scott, M.-C. Liu, Y. Wu, A. Dixit, M. F. Yanik, *Adv. Healthc. Mater.* **5**, 1233–1243 (2016).
20. C. A. DeForest, K. S. Anseth, *Nat. Chem.* **3**, 925–931 (2011).
21. S. K. Saha *et al*., *Science* **366**, 105–109 (2019).
22. D. Kim, P. T. C. So, *Opt. Lett.* **35**, 1602–1604 (2010).
23. F. Chen, P. W. Tillberg, E. S. Boyden, *Science* **347**, 543–548 (2015).
24. Materials and methods are available as supplementary materials.
25. J. B. Chang *et al*., *Nat. Methods* **14**, 593–599 (2017).
26. L. R. Meza, S. Das, J. R. Greer, *Science* **345**, 1322–1326 (2014).
27. X. Zheng *et al*., *Nat. Mater.* **15**, 1100–1106 (2016).
28. S. Pradhan, K. A. Keller, J. L. Sperduto, J. H. Slater, *Adv. Healthc. Mater.* **6**, 1700681 (2017).
29. J. Xu, D. Chen, S. Meng, *J. Am. Chem. Soc.* **143**, 10382–10388 (2021).
30. M. F. Lin *et al*., *Science* **374**, 92–95 (2021).
31. Y. Wang, J. He, C. Liu, W. H. Chong, H. Chen, *Angew. Chem. Int. Ed.* **54**, 2022–2051 (2015).
32. F. Han *et al*., *J. Am. Chem. Soc.* **142**, 15396–15402 (2020).
33. H. Sun *et al*., *J. Am. Chem. Soc.* **135**, 9099–9110 (2013).
34. J. Jiang *et al*., *Opt. Express* **23**, 24362–24368 (2015).
35. H. Wang, L. Chen, Y. Feng, H. Chen, *Acc. Chem. Res.* **46**, 1636–1646 (2013).
36. M. Ren *et al*., *Opt. Express* **29**, 44250–44263 (2021).
37. L. Jonušauskas *et al*., *Opt. Express* **27**, 15205–15221 (2019).
38. S. Rekštytė *et al*., *Adv. Opt. Mater.* **4**, 1209–1214 (2016).

ACKNOWLEDGMENTS

We thank Dongmeng Su from the Nanyang Technological University for providing the Au NPs for initial experiments; X. Han for obtaining Raman spectrums; S. Liu for accessing the confocal microscope; H. Chen and Y. Zhu for the helpful discussions; X. Xu for information on preparing the hydrogels; and J. Yang for accessing the sourcemeter for conductivity measurements. **Fundings:** We acknowledge funding support from the HKSAR Research Grants Council, General Research Fund 14203020; Innovation and Technology Commission, Innovation Technology Fund ITS/178/20FP; Carnegie Mellon University faculty startup fund; and InnoHK Centre projects funded by the Innovation and Technology Commission A-CUHK-16-5-14 and COCHE-1.5. **Author contributions:** S.-C.C., Y.Z., and F.H. conceived the study. S.G. set up the fs light sheet patterning system and patterned the hydrogels. Y.Z. and A.K. prepared the hydrogels for the initial studies. F.H. and S.G. performed material deposition, characterization, and other experiments together. F.H. investigated the mechanism of material assembly. Y.Z., N.Z., A.K., S.G., and S.-C.C discussed and improve the mechanism. F.H. and S.G. optimized fabrication protocols. F.H. and S.G. prepared the manuscript with revisions from S.-C.C., N.Z., and Y.Z. **Competing interests:** A US patent application related to this work has been filed with S.-C.C., S.G., F.H., Y.Z., and A.K. as coinventors. All authors declare that they have no other competing interests. **Data and materials availability:** All data are available in the manuscript or the supplementary materials.

License information: Copyright © 2022 the authors, some rights reserved; exclusive licensee American Association for the Advancement of Science. No claim to original US government works. https://www.science.org/about/science-licenses-journal-article-reuse

SUPPLEMENTARY MATERIALS

science.org/doi/10.1126/science.abm8420
Materials and Methods
Figures S1 to S25
Tables S1 to S5
Movie S1
References (*39*–*42*)

Submitted 15 October 2021; resubmitted 7 June 2022
Accepted 21 November 2022
10.1126/science.abm8420

ORGANIC CHEMISTRY

Transition metal–free ketene formation from carbon monoxide through isolable ketenyl anions

Mike Jörges†, Felix Krischer†, Viktoria H. Gessner*

The capacity of transition metals to bind and transform carbon monoxide (CO) is critical to its use in many chemical processes as a sustainable, inexpensive C1 building block. By contrast, only few s- and p-block element compounds bind and activate CO, and conversion of CO into useful carbonyl-containing organic compounds in such cases remains elusive. We report that metalated phosphorus ylides provide facile access to ketenyl anions ($[RC{=}C{=}O]^-$) by phosphine displacement with CO. These anions are very stable and storable reagents with a distinctive electronic structure between that of the prototypical ketene ($H_2C{=}C{=}O$) and that of ethynol ($HC{\equiv}C{-}OH$). Nonetheless, the ketenyl anions selectively react with a range of electrophiles at the carbon atom, thus offering high-yielding and versatile access to ketenes and related compounds.

Carbon monoxide (CO) is an inexpensive C1 source that is available from fossil resources and biomass in large quantities and is therefore a sustainable building block for synthetic chemistry (*1*). Today, CO is the key component in many transition metal–catalyzed reactions conducted on bulk scale in industry (*1*, *2*), such as the Fischer-Tropsch process (*3*) or the Monsanto/Cativa process (*4*). Similar to other small molecules, productive activation of CO was long thought to require transition metal mediation or catalysis. However, recent success in the activation of small molecules such as H_2 or CO_2 by main group element compounds (*5*) has also sparked interest in the transition metal–free activation of CO. This led to the isolation of carbonyl complexes (**I** and **II**; Fig. 1) (*6*–*8*) and the reduction or reductive coupling of CO with low-valent group 13 (*9*–*11*) and 14 (*12*–*15*) or s-block metal compounds (*16*, *17*) (**III** to **VI**). However, only in very few cases could the CO-containing compounds be liberated (*18*–*20*), and as of yet, no selective synthetically useful protocol to a single carbonyl compound using CO as a C1 building block has been developed.

Ketenes **3** are versatile carbonyl-containing compounds with interesting properties and reactivity modes. Because of their intrinsic reactivity, they are usually generated in situ and directly converted to the final products. The most common preparation methods are stoichiometric reactions above all from carboxylic acids and their derivatives, from α-diazoketones,

Faculty of Chemistry and Biochemistry, Ruhr-University Bochum, 44801 Bochum, Germany.
*Corresponding author. Email: viktoria.gessner@rub.de
†These authors contributed equally to this work.

or through pyrolysis (Fig. 1B) (*21*). These methods, however, usually involve unstable starting materials, are limited to few substrates, require specialized equipment, or are low yielding and poorly selective. The preparation of ketenes from metal carbenes and CO is a more robust method but usually uses stoichiometric amounts of transition metals, requires high temperatures, and also often suffers from low yields (*22*). Therefore, new strategies for ketene formation are required to further exploit their utility in synthesis. Ketenyl anions **2** [RC(M)C=O with M = Li, Na, or K] and their subsequent reaction with different electrophiles offer such an alternative (Fig. 1D). However, no efficient synthesis from simple starting reagents has been reported, and no ketenyl anion has yet been isolated and structurally elucidated (*23*, *24*). Thus, it remains unclear whether these species can be regarded as ketenyl anions **2** or if they would be better described as ynolates **2′**. Prior reports often referred to these compounds as ynolates even though the protonated ketene structure is significantly more stable than the ethynol isomer (Fig. 1C). The latter has so far only been detected under matrix isolation conditions or in interstellar ices (*25*, *26*). However, recent reports made us confident that their anionic congeners should indeed be isolable. For example, Stephan and co-workers very recently reported on the intermediate formation of an anionic ketene, $Ph_2P(S)C(Li)CO$, from the reaction of a dilithiomethandiide with CO and N_2O (*9*). The anion could be characterized by nuclear magnetic resonance (NMR) spectroscopy, but only its decomposition product **V** was isolated.

Building on the distinctive transition metal–like behavior of carbon compounds in unusual bonding situations (*27*, *28*), we hypothesized that ketenyl anions should be accessible from the reaction of CO and alkali metalated ylides (*29*, *30*). These s-block metal reagents can be regarded as phosphine-stabilized carbynyl anions **1′** (Fig. 1D), which, in analogy to transition metal carbynes, should be able to form ketenes by phosphine displacement with CO (*31*). As a starting point for our investigations, we selected the metalated ylide **1a**, which is readily accessible from its corresponding ylide because of the anion-stabilizing thiophosphinoyl group (*32*). The potassium salt was chosen because of its higher solubility and solution stability compared with the lithium and sodium compound, respectively. Monitoring of the reaction of **1a** with 1 atm of CO led to the selective liberation of the phosphine, as judged by $^{31}P\{^1H\}$ NMR spectroscopy, with appearance of a signal at 63.2 ppm. Ketenyl anion **2a** precipitated from the reaction mixture in toluene and could easily be isolated as a colorless solid (Fig. 2). For a more convenient synthesis, **2a** can also be generated in gram scale (88% yield) from ylide **4a** by in situ sulfuration, deprotonation with benzyl potassium, and carbonylation. The ketenyl anion exhibits an unexpectedly high stability under inert atmosphere, thus allowing its storage for weeks and enabling further applications (see below), as well as its structure elucidation. In tetrahydrofuran solution, **2a** shows a doublet at 2.4 ppm in the ^{13}C NMR spectrum, with a large $^1J_{CP}$ coupling constant of 174.5 Hz corresponding to the former ylidic carbon atom C1, whereas the carbonyl carbon atom resonates at 142.7 ppm ($^2J_{PC}$ = 40.3 Hz). Both signals are comparable to those previously reported for in situ–prepared anionic ketenyl species (*9*, *33*), but are clearly high-field shifted compared with neutral ketenes (*34*–*36*). The infrared spectrum of **2a** showed a characteristic C=C=O stretching vibration at 2086 cm^{-1}, which is in the range of ketenes [e.g., 2096 cm^{-1} for $(Trip)_2CCO$] (*37*), and clearly points toward a strong C–O interaction.

Single-crystal x-ray diffraction analysis revealed that the potassium salt **2a** forms a polymeric structure in the solid state (Fig. 2), with two molecules in the asymmetric unit, which both feature coordination of the metal by the C1 carbon atom as well as the oxygen atom of the newly formed C=C=O linkage. The C–C bond length in the ketene moiety (~1.245 Å) is slightly shorter than the average C–C double bond, including those reported for neutral ketenes, e.g., 1.298(3) Å for $(Trip)_2C=C=O$ (*15*, *34*–*36*). By contrast, the C=O distances in **2a** (~1.215 Å) are slightly longer than in typical ketenes, thus indicating a weakening of the C=O double bond, consistent with a contribution of the ynolate

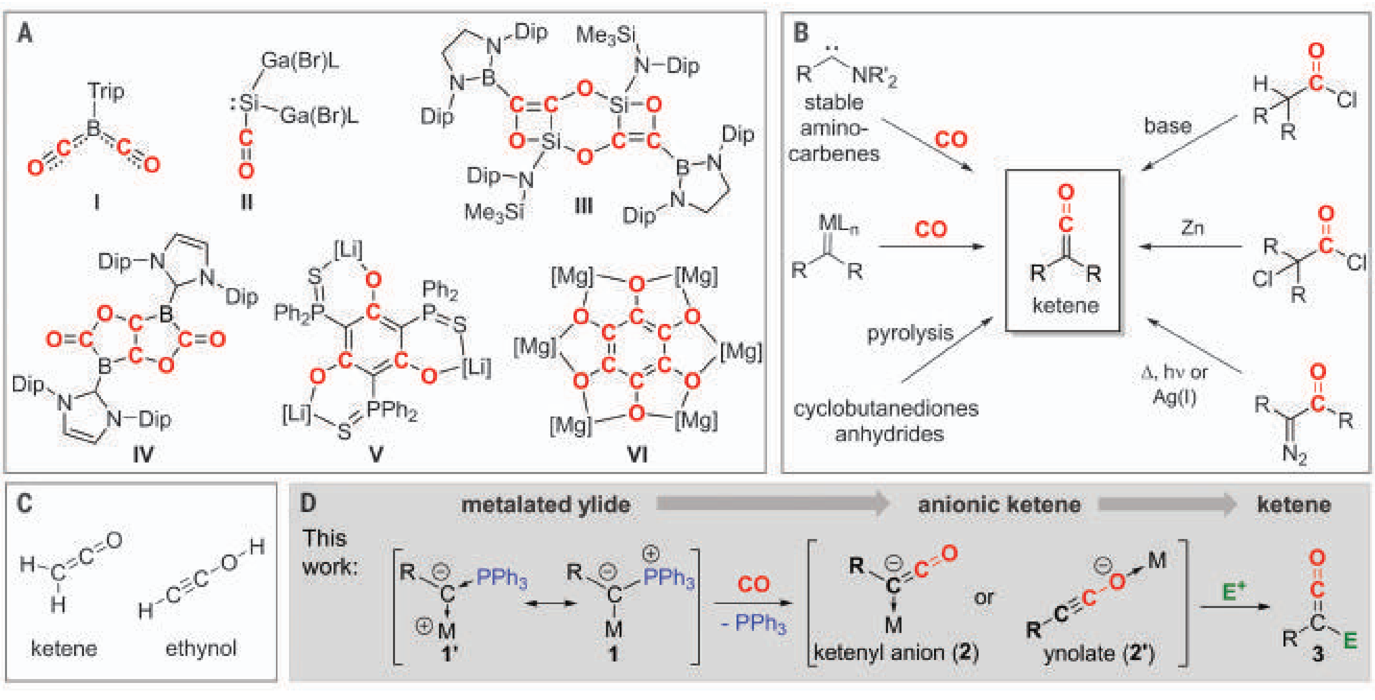


Fig. 1. Examples of main group element compounds derived from CO and synthetic strategies for ketene formation. (**A**) Main group element CO complexes and CO coupling products of s- and p-block element compounds. Dip, 2,6-diisopropylphenyl; Trip, 2,4,6-triisopropylphenyl. (**B** to **D**) Reported pathways to ketenes (B), tautomers of C_2H_2O (C), and synthetic strategy to ketenes through ketenyl anions formed from metalated ylides and CO (C).

form. However, the P–C–C angles of ~147.5(7)° clearly deviate from linearity, arguing for the ketenyl anion form. To break up the polymeric structure of **2a**, the 18-crown-6 complex of the potassium salt was prepared and isolated. The monomeric complex [**2a**·(18-crown-6)] features only a metal–carbon interaction, but no metal–oxygen interaction in the solid state, with similar bond lengths and angles in the ketenyl unit as found in the polymeric structure. Overall, the structural parameters argue for an intermediate structure between a ketenyl anion and the ynolate form.

Computational studies provided further insights into the bonding situation in **2a** (*37*).

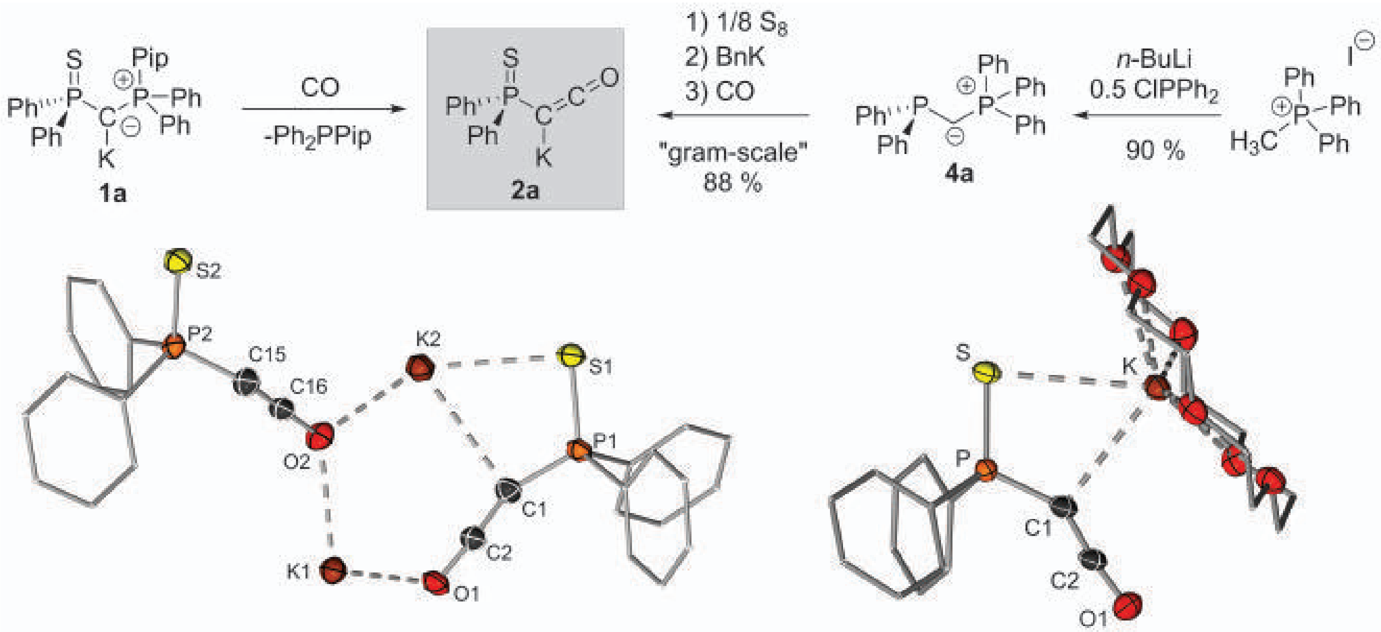


Fig. 2. Synthesis and structures of ketenyl anion 2a. (Top) Synthesis of ketenyl anion **2a** by carbonylation of the isolated metalated ylide **1a** or through ylide **4a**. Pip, piperidyl. Bottom left, asymmetric unit of the molecular structure of polymeric [**2a**]$_\infty$. Bottom right, structure of the monomeric 18-crown-6 complex. Hydrogen atoms and disordered segments are omitted for clarity. Important bond lengths and angles: [**2a**]$_\infty$: C1–C2 1.240(8), C2–O1 1.216(7), C1–P1 1.695(6), C15–C16 1.248(8), C16–O2 1.214(7), C15–P2 1.689(6) Å; P1–C1–C2 145.6(6), C1–C2–O1 175.0(7), P2–C15–C16 149.7(5), C15–C16–O2 175.0(7)°; [**2a**·(18-crown-6)]: C1–C2 1.178(8), C2–O1 1.248(8), C1–P1 1.698(3) Å; P1–C1–C2 146.2(5), C1–C2–O1 174.5(11)°.

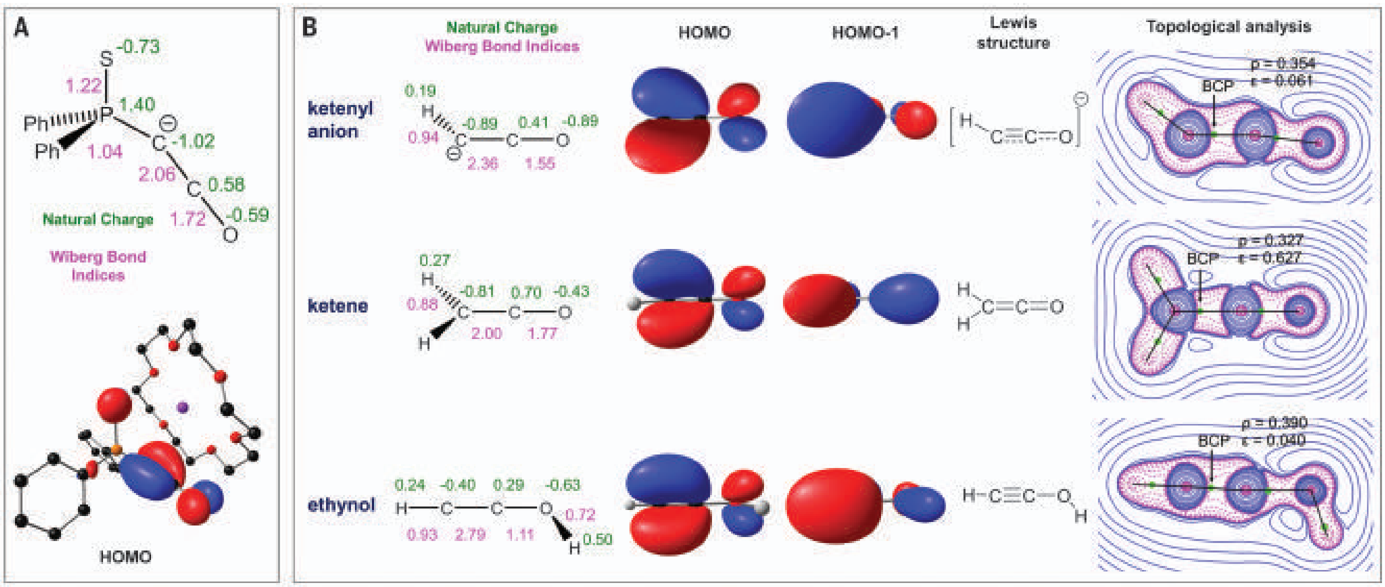


Fig. 3. Electronic structure of the ketenyl anion, ketene, and ethynol. (**A**) Calculated natural charges (in [e]), WBIs, and representation of the HOMO of [**2a**·(18-crown-6)] (PBE1PBE/def2tzvpp). (**B**) Comparison of the charges, WBIs, two HOMOs, canonical form, and contour plots of the Laplacian of the electron density in anion $[HC{=}C{=}O]^-$, ketene $H_2C{=}C{=}O$, and ethynol HC≡C–OH.

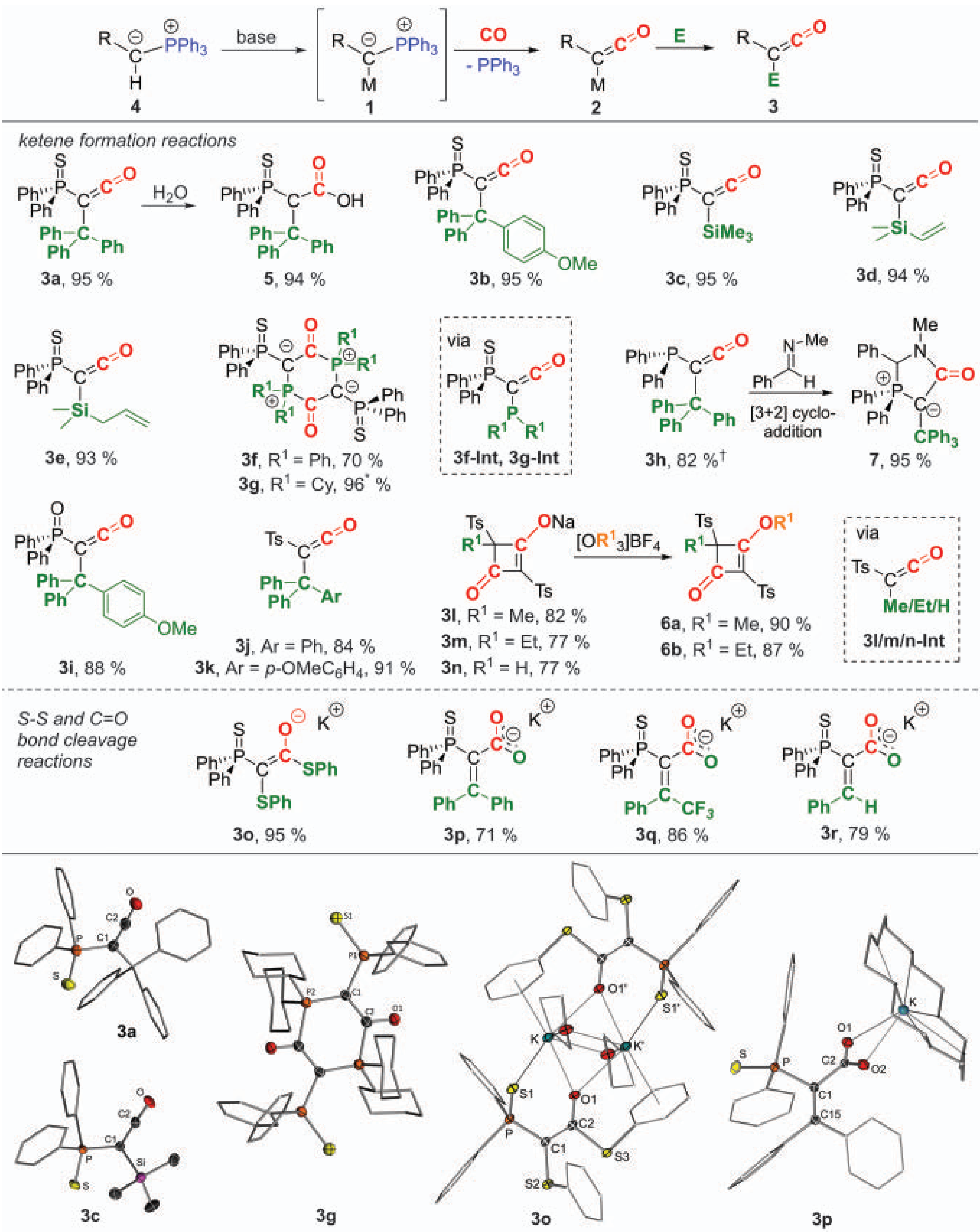


Fig. 4. Scope of ketene formation through carbonylation of metalated ylides. (Top) Scope of the carbonylation reaction. Conditions: metalated ylides are generated in situ from ylides **4** [base is BnK or MHMDS; solvent is toluene or tetrahydrofuran; for the (thio)phosphinoyl anion, the potassium salt was used; for the tosyl (Ts) compound, the sodium compound was used], room temperature, 1 atm. CO, E, chlorosilanes, trityl chlorides, disulfides, ketones, methyl iodide, ethyl bromide, and hydrochloric acid. Yields refer to isolated products. *NMR yield. †Synthesized from **3a** with $PtBu_3$ as reductant. (Bottom) Crystal structures of the carbonylation products **3a**, **3c**, **3g**, **3o**, and **3p**.

Natural bond orbital calculations of [**2a**·(18-crown-6)] yielded a Wiberg bond index (WBI) of 2.06 for the C–C bond and 1.72 for the C–O bond (Fig. 3A) (*38*), but with a higher negative charge at the carbon atom (–1.02 e) compared with the oxygen atom (–0.59 e). This bonding situation is not exclusive to the thiophosphinoyl-substituted anion, but is also found for the parent ketenyl anion $[HC{=}C{=}O]^-$ (Fig. 3B). Comparison of the anion with its protonated forms, ketene $H_2C{=}C{=}O$ and ethynol HC≡C–OH, demonstrates that ketene deprotonation results in the strengthening of the C–C bond and the weakening of the C–O bond, as indicated by the changes in the WBIs. The additional negative charge in the anion is delocalized toward the C–O end rather than being localized at the C1 carbon atom. Nonetheless, a higher negative charge remains at the C1 carbon atom. The positive charge at C2 significantly decreases from +0.70 e in the ketene to +0.41 e in the anion, thus resulting in a reduced amphiphilicity that presumably contributes to the substantial stability of the anion. The weakening of the C–O bond in the anion compared with the ketene, and thus the importance of the ynolate form of the anion, becomes evident from the molecular orbitals. The highest occupied molecular orbital (HOMO) and HOMO-1 of the ketenyl anion show nodal planes between C2 and O. This distribution is similar to ethynol but in contrast to the structure of ketene, in which the HOMO-1 features a nodal plane between C1 and C2. The topological analysis of the electron density using Bader's atoms in molecules further confirmed this bonding situation (*39*). Whereas the ketene features an ellipticity value larger than zero for the C–C bond (ε = 0.627), this value is close to zero (ε < 0.07) for ethynol and the ketenyl anion, thus being consistent with a change from a C–C double bond to a triple bond in the anion. Likewise, the electron denzsity at the bond critical point of the C–C bond continuously increases from ketene to ketenyl and ethynol. Taken together, the x-ray diffraction analysis, infrared spectroscopic analysis, and computational studies argue for an intermediate electronic structure between the ketenyl anion and the ethynolate form. Nonetheless, the simple anion features a clearly bent structure and, more importantly, the protonation of the anion is clearly thermodynamically favored at the carbon atom, with the resulting ketene $H_2C{=}C{=}O$ being 140.9 kJ/mol more stable than the alcohol HC≡C–OH. This is consistent with the higher C=C and C=O bond strengths and the reported fleeting character of ethynol (*25*, *26*).

The facile isolation of ketenyl anion **2a** and its stability led us to investigate its use in the formation of ketenes by reaction with different electrophiles. Initially, we focused on the introduction of bulky and electropositive substituents to enable isolation of the thus stabilized ketenes. To our delight, **2a** exhibited exclusive reactivity at the carbon site. Treatment with different trityl chlorides and chlorosilanes selectively furnished the corresponding ketenes **3a** to **3e**, which could be isolated in excellent yields of >90% as stable solids and unambiguously characterized by different spectroscopic methods. The *para*-methoxy-functionalized compound **3b** was accessible in high yields under the same reaction condition, showing no signs of competing *ortho*-metalation reaction. In addition, reaction of **2a** with primary chlorophosphines gave rise to the phosphorus heterocycles **3f** and **3g** formed through the dimerization of the intermediate phosphino-substituted ketenes **3f/g-Int**. The versatility of the protocol is furthermore demonstrated by reduction of the thiophosphinoyl group to form a stable phosphino-substituted ketene **3h** and the high-yielding formation of the phosphinoyl-substituted (**3i**) and tosyl-substituted (**3j** and **3k**) ketenes through the corresponding ketenyl anions. The tosyl compounds offer further follow-up chemistry through nucleophilic substitution. It is noteworthy that these ketene formation reactions do not necessarily require the isolation of the reactive ketenyl anion but can be performed starting from stable ylides **4** by in situ metalation with benzyl potassium or common MHMDS bases and one-pot carbonylation and substitution reactions. In addition to stable ketenes, reactive species can also be accessed by treatment of the ketenyl anions with small electrophiles such as MeI, EtI, or even HCl. These ketenes undergo a follow-up reaction with the still present ketenyl anion to form cyclic ketones such as **3l** to **3n** and the corresponding enolethers **6** after methylation. The cyclic structures are presumably formed through initial carbometallation of the ketene followed by a [2+2] cycloaddition, thus confirming the ketene reactivity of the products **3**. The ketene reactivity of the more stable compounds is also proven by the reaction of **3d** with water, giving the corresponding acid **5**, and by the cycloaddition reaction of **3h** with (*E*)-*N*-methyl-1-phenylmethanimine to lactam **7**. Because of the steric shielding of the C1 carbon atom, the phosphino group acts as nucleophilic site, thus resulting in a [2+3] cycloaddition reaction.

The ketenyl anions not only provide simple and efficient access to ketenes and their follow-up products, but also enable new reactivity patterns. Therefore, reaction with diphenylsulfide led to the formation of the thioester enolate **3q**, presumably by initial S–S bond cleavage through nucleophilic attack of **2a** at the sulfur, followed by addition of the thiolate at the C2 atom of the ketene moiety. Furthermore, treatment with ketones and aldehydes led to the unusual cleavage of the C=O double bond with concomitant formation of a new C=C double bond to give acrylates **3p**, **3q**, and **3r** in 71 to 86% yields, thus representing an alternative to the transition metal–catalyzed Reppe synthesis of acrylic acids from CO. These reactions proceed in a stereoselective manner, with the smaller alkene substituents pointing toward the acid moiety. Overall, these reactivities clearly demonstrate that ketenyl anions not only serve as valuable reagents to ketenes and their follow-up products, but present new reactivity patterns for the formation of a variety of CO-containing organic compounds starting from metalated ylides and CO.

We have developed a highly efficient process to produce ketenes and related compounds from the reaction of ylides with CO as C1 source under basic conditions. The key to the efficiency of this protocol is the high-yielding formation of ketenyl anions as entry points into ketene chemistry. These anions exhibit an electronic structure between that of a ketenyl anion and ethynolate, but also have enhanced stability, which makes them valuable reagents in organic synthesis.

REFERENCES AND NOTES

1. X.-F. Wu *et al.*, *Acc. Chem. Res.* **47**, 1041–1053 (2014).
2. R. Franke, D. Selent, A. Börner, *Chem. Rev.* **112**, 5675–5732 (2012).
3. A. Y. Khodakov, W. Chu, P. Fongarland, *Chem. Rev.* **107**, 1692–1744 (2007).
4. P. M. Maitlis, A. Haynes, G. J. Sunley, M. J. Howard, *J. Chem. Soc., Dalton Trans.* (11): 2187–2196 (1996).
5. P. P. Power, *Nature* **463**, 171–177 (2010).
6. H. Braunschweig *et al.*, *Nature* **522**, 327–330 (2015).
7. C. Ganesamoorthy *et al.*, *Nat. Chem.* **12**, 608–614 (2020).
8. D. Reiter, R. Holzner, A. Porzelt, P. Frisch, S. Inoue, *Nat. Chem.* **12**, 1131–1135 (2020).
9. M. Finze *et al.*, *J. Am. Chem. Soc.* **124**, 15385–15398 (2002).
10. H. Braunschweig *et al.*, *Nat. Chem.* **5**, 1025–1028 (2013).
11. R. Y. Kong, M. R. Crimmin, *J. Am. Chem. Soc.* **140**, 13614–13617 (2018).
12. A. V. Protchenko *et al.*, *Angew. Chem. Int. Ed.* **58**, 1808–1812 (2019).
13. V. Lavallo, Y. Canac, B. Donnadieu, W. W. Schoeller, G. Bertrand, *Angew. Chem. Int. Ed.* **45**, 3488–3491 (2006).
14. M. Majumdar *et al.*, *Angew. Chem. Int. Ed.* **54**, 8746–8750 (2015).
15. Y. Wang *et al.*, *J. Am. Chem. Soc.* **141**, 626–634 (2019).
16. M. Xu, T. Wang, Z.-W. Qu, S. Grimme, D. W. Stephan, *Angew. Chem. Int. Ed.* **60**, 25281–25285 (2021).
17. T. J. Hadlington, T. Szilvási, *Nat. Commun.* **13**, 461 (2022).
18. M. D. Anker, M. S. Hill, J. P. Lowe, M. F. Mahon, *Angew. Chem. Int. Ed.* **54**, 10009–10011 (2015).
19. M. Xu *et al.*, *Angew. Chem. Int. Ed.* **60**, 16965–16969 (2021).
20. M. Xu, Z. W. Qu, S. Grimme, D. W. Stephan, *J. Am. Chem. Soc.* **143**, 634–638 (2021).
21. A. D. Allen, T. T. Tidwell, *Chem. Rev.* **113**, 7287–7342 (2013).
22. Z. Zhang, Y. Zhang, J. Wang, *ACS Catal.* **1**, 1621–1630 (2011).
23. R. P. Woodbury, N. R. Long, M. W. Rathke, *J. Org. Chem.* **43**, 376 (1978).
24. H. Kai, K. Iwamoto, N. Chatani, S. Murai, *J. Am. Chem. Soc.* **118**, 7634–7635 (1996).
25. R. Hochstrasser, J. Wirz, *Angew. Chem. Int. Ed.* **28**, 181–183 (1989).
26. A. M. Turner *et al.*, *Astrophys. J.* **896**, 88–96 (2020).
27. G. D. Frey, V. Lavallo, B. Donnadieu, W. W. Schoeller, G. Bertrand, *Science* **316**, 439–441 (2007).

28. M. Alcarazo, C. W. Lehmann, A. Anoop, W. Thiel, A. Fürstner, *Nat. Chem.* **1**, 295–301 (2009).
29. T. Scherpf, R. Wirth, S. Molitor, K.-S. Feichtner, V. H. Gessner, *Angew. Chem. Int. Ed.* **54**, 8542–8546 (2015).
30. T. X. Gentner, R. E. Mulvey, *Angew. Chem. Int. Ed.* **60**, 9247–9262 (2021).
31. L. T. Scharf, D. M. Andrada, G. Frenking, V. H. Gessner, *Chemistry* **23**, 4422–4434 (2017).
32. M. Jörges *et al*., *ChemistryOpen* **10**, 1089–1094 (2021).
33. J. A. Buss, T. Agapie, *J. Am. Chem. Soc.* **138**, 16466–16477 (2016).
34. H. Hörnig, E. Walther, U. Schubert, *Organometallics* **4**, 1905–1906 (1985).
35. W. Huang, D. Fang, K. Temple, T. T. Tidwell, *J. Am. Chem. Soc.* **119**, 2832–2838 (1997).
36. J. Frey, Z. Rappoport, *J. Am. Chem. Soc.* **118**, 5169–5181 (1996).
37. M. J. Frisch *et al*., "Gaussian 16, revision C.01" (Gaussian, Inc., 2019).
38. E. D. Glendening *et al*., "NBO 7.0" (Theoretical Chemistry Institute, University of Wisconsin, 2018).
39. R. F. W. Bader, *Chem. Rev.* **91**, 893–928 (1991).

ACKNOWLEDGMENTS

Funding: This work was supported by RESOLV, which is funded by the Deutsche Forschungsgemeinschaft (DFG, German Research Foundation) under Germany's Excellence Strategy (EXC-2033 Projektnummer 390677874 to V.H.G.) and by the European Research Council (ERC Starting Grant YlideLigands 677749 to V.H.G.). **Author contributions:** M.J. performed most of the synthetic work with the thiophosphinoyl compound. F.K. performed the synthetic work with the tosyl and the thiophosphinoyl compounds, isolated some of the compounds shown in Fig. 4, and performed computational studies. V.H.G. assisted with data analysis and directed the research. V.H.G. wrote the manuscript with input from all authors. **Competing interests:** The authors declare no competing interests. **Data and materials availability:** Crystallographic data for compounds [**2a**]$_\infty$, [**2a**·(18-crown-6)], **3a**, **3c**, **3g**, **3o**, **3p**, and **5** are available free of charge from the Cambridge Crystallographic Data Centre under references CCDC-2201263, CCDC-2201261, CCDC-2201267, CCDC-2201262, CCDC-2201268, CCDC-2201264, CCDC-2201265, and CCDC-2201266, respectively. Additional spectroscopic, crystallographic, and computational data are included in the supplementary materials. **License information:** Copyright © 2022 the authors, some rights reserved; exclusive licensee American Association for the Advancement of Science. No claim to original US government works. https://www.science.org/about/science-licenses-journal-article-reuse

SUPPLEMENTARY MATERIALS

science.org/doi/10.1126/science.ade4563
Materials and Methods
Figs. S1 to S28
Tables S1 to S24
References (*40*–*64*)

Submitted 17 August 2022; accepted 30 November 2022
10.1126/science.ade4563

NEUROSCIENCE

Layer-specific pain relief pathways originating from primary motor cortex

Zheng Gan[1], Vijayan Gangadharan[1]†, Sheng Liu[1], Christoph Körber[2], Linette Liqi Tan[1], Han Li[1], Manfred Josef Oswald[1], Juhyun Kang[1], Jesus Martin-Cortecero[3], Deepitha Männich[1], Alexander Groh[3], Thomas Kuner[2], Sebastian Wieland[2,4], Rohini Kuner[1]*

The primary motor cortex (M1) is involved in the control of voluntary movements and is extensively mapped in this capacity. Although the M1 is implicated in modulation of pain, the underlying circuitry and causal underpinnings remain elusive. We unexpectedly unraveled a connection from the M1 to the nucleus accumbens reward circuitry through a M1 layer 6-mediodorsal thalamus pathway, which specifically suppresses negative emotional valence and associated coping behaviors in neuropathic pain. By contrast, layer 5 M1 neurons connect with specific cell populations in zona incerta and periaqueductal gray to suppress sensory hypersensitivity without altering pain affect. Thus, the M1 employs distinct, layer-specific pathways to attune sensory and aversive-emotional components of neuropathic pain, which can be exploited for purposes of pain relief.

The primary motor cortex (M1) controls voluntary motor behaviors and has been extensively studied with respect to the physiological processes and neuronal circuitry underlying initiation of movement (*1*). Unexpectedly, the percept of pain also evokes responses in the human primary motor cortex in intracortical recordings and functional neuroimaging studies (*2*). The M1 undergoes plasticity in chronic pain (*3*) and interactions between pain and motor functions are exploited in exercise therapies. However, very little is known about the neurobiological basis for this putative, unconventional role for the M1 in modulating pain perception. Neurostimulation therapies involving transcranial magnetic stimulation or transcranial direct current stimulation (tDCS) over primary motor areas are emerging as attractive alternatives to drug therapy (*4*). However, these are limited in clinical utility by high variability in efficacy, which has been ascribed to a fundamental lack of understanding of the underlying circuitry (*5*, *6*). As observed in human studies, application of anodal tDCS over the M1 alleviates neuropathic hypersensitivity in mice (fig. S1, A and B) (*7*), but does so in a broad manner because diverse adjoining sensory and prefrontal cortical areas that are implicated in pain are also vividly coactivated (fig. S1C).

With the goal of specifically dissecting the role of the M1 in pain relief and elucidating its neurobiological underpinnings, we employed layer- and cell type–specific optogenetic (*8*) and chemogenetic approaches (*9*) for temporally controlled and reversible manipulation of M1 microcircuitry. In mice virally expressing either the excitatory chemogenetic Designer Receptor Exclusively Activated by Designer Drugs (DREADD) hM3Dq (Gq) or mCherry (as control), the DREADD-stimulating ligand Clozapine-N-oxide (CNO) (*9*) was applied before or after induction of neuropathic pain in the spared nerve injury (SNI) model (*10*) (Fig. 1A and fig. S2A; validation and specificity of M1 activation shown in Fig. 1B and fig. S2B). Spatially restricted activation of the M1 hindlimb cortex across all cellular layers, driving hM3Dq expression from the murine synapsin promoter, significantly suppressed peak nociceptive hypersensitivity toward non-noxious mechanical stimulation (0.07 to 0.6 g; mechanical allodynia; Fig. 1C), whereas similar manipulations in non-neuropathic mice led to no changes in nociception (fig. S2C, left panel). Chemogenetically stimulating M1 excitatory neurons specifically, using the murine CamkIIα promoter (validation of specificity and efficacy shown in fig. S2, D and E, respectively), recapitulated the specific and beneficial effects on mechanical allodynia and alleviated hypersensitivity toward 5°C cooling, another hallmark of neuropathic pain disorders (*10*) (Fig. 1D and fig. S2F) without affecting motor behaviors (fig. S2, G and H). Suppression of mechanical allodynia was robustly preserved when neuropathic pain was chronically maintained at 8 weeks post-SNI (Fig. 1D). By contrast, chemogenetically stimulating the adjoining somatosensory hindlimb cortex (S1HL) had no impact on neuropathic pain-related behavior (fig. S3A).

Whether M1 stimulation operates through modulation of excitatory or inhibitory neurons has been a topic of much debate (*11*). Signal processing and output of cortical microcircuits is determined by the interplay between excitatory pyramidal neurons and diverse classes of GABAergic interneurons. Parvalbumin-expressing neurons (PV), the largest class of neocortical GABAergic neurons, inhibit deep pyramidal cell layers at the soma, while their distal dendrites are inhibited by Somatostatin-type

[1]Pharmacology Institute, Medical Faculty Heidelberg, Heidelberg University, Heidelberg, Germany. [2]Department of Functional Neuroanatomy, Institute for Anatomy and Cell Biology, Medical Faculty Heidelberg, Heidelberg University, Heidelberg, Germany. [3]Institute for Physiology and Pathophysiology, Medical Faculty Heidelberg, Heidelberg University, Heidelberg, Germany. [4]Department of General Internal Medicine and Psychosomatics, Medical Faculty Heidelberg and University Clinic Heidelberg, Heidelberg, Germany.
***Corresponding author. Email: rohini.kuner@pharma.uni-heidelberg.de** †Present address: Institute for Vascular and Islet Cell Biology, German Diabetes Center, Leibniz Center for Diabetes Research at Heinrich Heine University Düsseldorf, Düsseldorf, Germany.

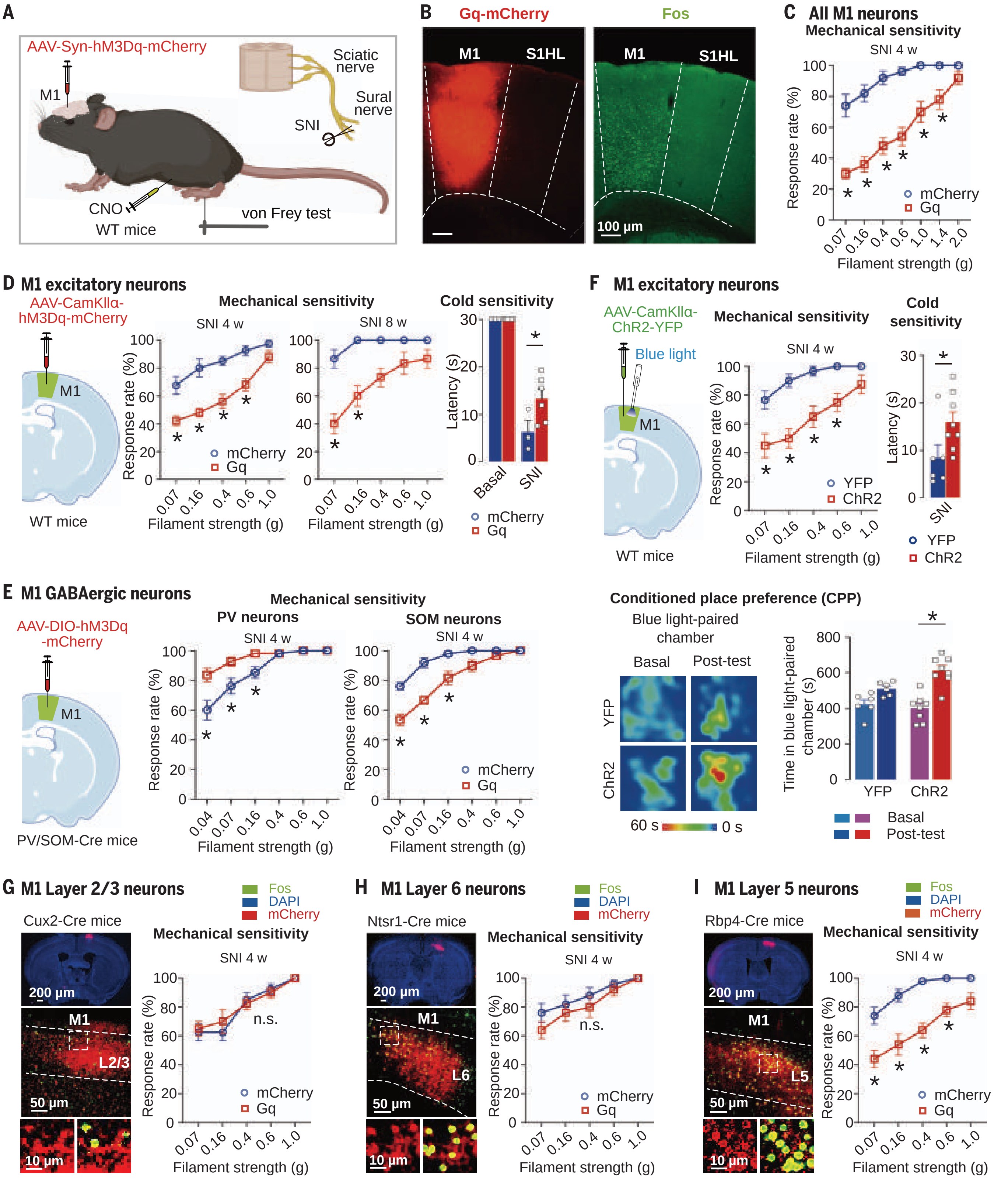


Fig. 1. M1-restricted activation leads to pain relief in neuropathic mice and reversal of allodynia occurs through layer 5. (**A**) Chemogenetic activation strategy for the M1 cortex through hM3Dq (Gq) expression and Clozapine-N-oxide (CNO) application with spared nerve injury (SNI). (**B**) M1 chemogenetic targeting (left) and activation (right; anti-Fos immunohistochemistry). S1HL, primary somatosensory hindlimb cortex. (**C**) Mechanical hypersensitivity to von Frey filament force at 4 weeks (4 w) post-SNI (n = 10 mice per group) in CNO-treated Gq- or mCherry-injected mice (control). (**D**) Chemogenetic activation strategy for M1 excitatory neurons (left) and reversal of mechanical allodynia (middle) (at SNI 4 w, mCherry: n = 8, Gq: n = 10 mice; at SNI 8 w: n = mCherry: n = 3, Gq: n = 6 mice) and cold allodynia (mCherry: n = 3, Gq: n = 6 mice, F = 1.268, P = 0.0362). (**E**) Chemogenetic activation strategy for M1 GABAergic populations

(left) and effect on mechanical allodynia (right) upon activation of PV neurons (n = 11 mice per group) or SOM neurons (mCherry: n = 10, Gq: n = 12 mice). (**F**) Optogenetic activation strategy for M1 excitatory neurons (left), reversal of mechanical allodynia (top middle; YFP: n = 6, ChR2: n = 6 mice) and cold allodynia (top right; n = 8 mice per group); CPP to a chamber paired with optogenetic stimulation (bottom), shown as heat plots (bottom left, below) and cumulative time (bottom right; YFP: n = 6, ChR2: n = 8 mice). (**G**, **H**, and **I**) Layer-specific chemogenetic M1 activation using transgenic mice targeting layer 2/3 [(G) Cux2-Cre, n = 8 mice per group], layer 6 [(H) Ntsr1-Cre, n = 10 mice per group), and layer 5 [(I) Rbp4-Cre, n = 10 mice per group], expression areas [(left panels in (G) to (I)] and mechanical allodynia [(right panels in (G) to (I)]; $P < 0.05$ for Gq curves for layer 5 versus layer 2/3 and layer 6. Analysis of variance (ANOVA) for random measures followed by post-hoc Sidak's test. * represents $P < 0.05$; exact F and P values for all groups are given in table S1. Data are shown as mean ± standard error of the mean (SEM).

(SOM) GABAergic neurons that also limit the activity of PV neurons (*12*). Using cell type–specific transgenic mouse lines, we observed that chemogenetic activation of PV neurons in the M1 markedly exacerbated neuropathic hypersensitivity (Fig. 1E and fig. S3, B and C), whereas chemogenetically activating SOM neurons significantly reduced mechanical allodynia (Fig. 1E and fig. S3, B and D). Because DREADD-based cortical activation spans several hours at a time and could thus potentially lead to widespread downstream changes, we also performed temporally restricted optogenetic manipulations using CamkIIα promoter–driven expression of Channelrhodopsin (ChR2) (Fig. 1F). Blue light–induced activation of excitatory M1 neurons precisely coinciding with the time frame of sensory stimulation acutely suppressed both mechanical and cold allodynia in neuropathic mice (Fig. 1F and fig. S4A). Temporally limited optogenetic activation of the M1 also enabled us to conduct experiments in a real time paradigm in which different operant chambers with contextual cues were longitudinally paired with either M1 or sham stimulation (fig. S4B). Neuropathic—but not naïve—mice showed real-time conditioned place preference (CPP) for the chamber paired with M1 stimulation (Fig. 1F, bottom panels). Locomotion was not hampered by M1-specific manipulations (fig. S3C).

Which M1 cortical layers deliver the required excitatory output? By employing transgenic mice for layer-specific chemogenetic manipulations, we observed that selective activation of neither layer 2/3 (Fig. 1G and fig. S4D) or layer 6 (Fig. 1H and fig. S4E) influenced nociceptive behaviors in neuropathic mice. By contrast, selectively activating M1 layer 5 recapitulated the anti-hyperalgesic effects seen with whole M1 activation (Fig. 1I and fig. S4F). No sex differences were observed with anti-hyperalgesic effects of activation of M1 or of the individual layers or downstream pathways.

We studied acute changes in expression of the activity marker Fos in neuropathic mice upon chemogenetic activation of M1 excitatory neurons (fig. S5A) and matched this information to the known salient projections of the M1 (*13*, *14*). Amongst the 15 pain-related target regions analyzed, the periaqueductal gray (PAG) and the zona incerta (ZI) stood out. Although the midcingulate and prelimbic cortices also showed changes in Fos, we observed in anterograde viral tracing experiments that they do not receive direct projections from the M1 (fig. S5B), suggesting indirect downstream modulation. We therefore first expressed ChR2 in all excitatory neurons of the hindlimb M1 cortex and optogenetically stimulated M1 projections to the ZI (electrophysiological validation in Fig. 2A and fig. S6, A and B) or the lateral and ventrolateral PAG (lPAG/vlPAG, electrophysiological validation in Fig. 2B and fig. S6, C and D), and observed that each can significantly—but only partly—suppress neuropathic allodynia. Moreover, each was weaker than stimulation of either the whole M1 or layer 5 alone, suggesting that these two pathways act independently and additively. The ZI is a subthalamic nucleus that receives dense nociceptive input through the spinothalamic tract (*15*). However, very little is known about the underlying cellular circuitry and modulation of the ZI by the M1 remains largely unexplored. ZI neurons are not homogenous in function but show a high level of specificity in modulating defensive behaviors, binge eating, hunting, and sleep, depending upon their neurochemical identity and subdivision into distinct anatomical sectors (*16*, *17*). We observed that hindlimb M1 neurons project to the dorsal (ZId) and ventral (ZIv) sectors (Fig. 2A), but not to the rostral and caudal sectors. Tracing analyses using layer-specific transgenic mice revealed that hindlimb M1 layer 5 but not layer 6 neurons project to the ZI (fig. S7, A and B), consistent with dye labeling analyses in vibrissae M1 (*17*). Keeping tracer bias and limitations related to viral tropism in mind, we performed retrograde labeling with Fluorogold (fig. S7B) or retrograde AAV-YFP virus (Fig. 2C) injected in the ZI and found labeled layer 5, but not layer 6, neurons in the M1. The dorsal sector of the ZI predominantly harbors excitatory neurons, e.g., nNos-expressing neurons, that send excitatory projections to the midbrain and brainstem nuclei, such as the PAG and raphe nuclei, which gate the modulation of pain. By contrast, ZIv is overwhelmingly GABAergic in nature, including PV, SOM, and Tac1 subclasses, and exerts feedforward inhibition in projection areas, particularly the thalamus (*15*, *18*). A number of our observations collectively revealed that M1 activation preferentially fosters output of the ZI to the midbrain and brainstem. First, employing a viral strategy that specifically enables trans-synaptic labeling of projection targets with a fluorescent reporter (validated in fig. S8A) in combination with viral labeling of GABAergic neurons (Fig. 2D), we observed that most ZI neurons receiving M1 monosynaptic inputs comprise non-GABAergic neurons. Coimmunohistochemistry with marker proteins for the PV, SOM, and Tac1 populations further revealed that most of the neurons receiving M1 inputs in the ZId and ZIv, respectively, do not belong to the aforementioned GABAergic neuron categories (Fig. 2E). Second, optogenetic M1 stimulation in mice with SNI increased the activity marker Fos in neurons of the ZId but not in the ZIv, and this increase was specific to non-GABAergic neurons (Fig. 2F). GABAergic neurons overall—particularly the PV-type GABAergic neurons—showed a decrease in Fos expression upon M1 stimulation post-SNI (Fig. 2G), suggesting modulation within local ZI microcircuits.

The PAG has been linked with motor cortex stimulation–induced analgesia (*6*). However, neither causality nor cellular connectivity has been addressed. We observed that the hindlimb M1 neurons project densely to the upper segment of the ventrolateral column (vlPAG) and the lower segment of the lateral column (lPAG) (Fig. 2B), but not the dorsal and medial columns of the PAG. Retrograde labeling from the lPAG and vlPAG using viral transfer- or Flurogold-labeled M1 neurons (Fig. 2H and fig. S8B, respectively) only in layer 5 and not layer 6, which was further validated through anterograde viral tracing in layer-specific transgenic mice (fig. S7A). Optogenetically activating projections of layer 5 M1 neurons to the lPAG and vlPAG robustly attenuated mechanical allodynia in neuropathic mice (Fig. 2I and fig. S9A). Optogenetic stimulation of the M1 layer 5-PAG pathway increased Fos expression significantly in both GABAergic neurons (fig. S9B) and non-GABAergic neurons (Fig. 2J) of the lPAG-vlPAG. Trans-synaptic labeling (see Fig. 2D) revealed that more than 80% of the lPAG-vlPAG neurons receiving direct synaptic inputs from the M1 are non-GABAergic in nature in SNI mice (Fig. 2K). In the vlPAG, chemogenetic activation of excitatory neurons inhibits nociception, whereas activation of GABAergic neurons facilitates nociception (*19*).

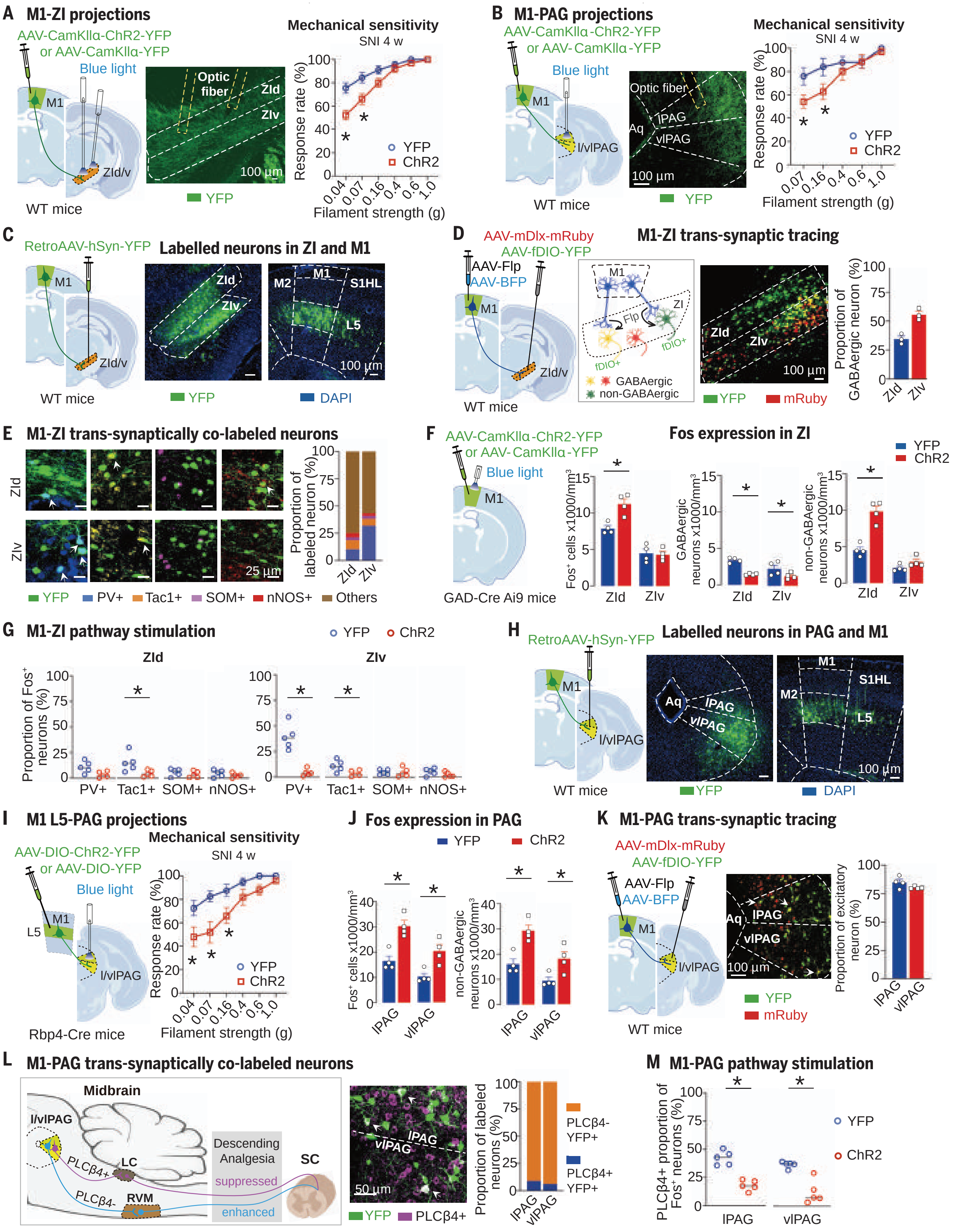

A M1-ZI projections
AAV-CamKIIα-ChR2-YFP
or AAV-CamKIIα-YFP
Blue light
M1
ZId/v
WT mice
Optic fiber
ZId
ZIv
100 µm
YFP
Mechanical sensitivity
SNI 4 w
Response rate (%)
YFP
ChR2
Filament strength (g)
B M1-PAG projections
AAV-CamKIIα-ChR2-YFP
or AAV-CamKIIα-YFP
Blue light
M1
l/vlPAG
WT mice
Optic fiber
Aq
lPAG
vlPAG
100 µm
YFP
Mechanical sensitivity
SNI 4 w
Response rate (%)
YFP
ChR2
Filament strength (g)
C
RetroAAV-hSyn-YFP
Labelled neurons in ZI and M1
M1
ZId/v
WT mice
ZId
ZIv
M2
M1
S1HL
L5
100 µm
YFP
DAPI
D
AAV-mDlx-mRuby
AAV-fDIO-YFP
M1-ZI trans-synaptic tracing
AAV-Flp
AAV-BFP
M1
ZId/v
WT mice
ZI
Flp
fDIO+
GABAergic
non-GABAergic
ZId
ZIv
100 µm
YFP
mRuby
Proportion of GABAergic neuron (%)
E M1-ZI trans-synaptically co-labeled neurons
ZId
ZIv
25 µm
Proportion of labeled neuron (%)
YFP
PV+
Tac1+
SOM+
nNOS+
Others
F
AAV-CamKIIα-ChR2-YFP
or AAV-CamKIIα-YFP
Blue light
M1
GAD-Cre Ai9 mice
Fos expression in ZI
YFP
ChR2
Fos+ cells x1000/mm3
GABAergic neurons x1000/mm3
non-GABAergic neurons x1000/mm3
ZId
ZIv
G M1-ZI pathway stimulation
YFP
ChR2
ZId
ZIv
Proportion of Fos+ neurons (%)
PV+
Tac1+
SOM+
nNOS+
H
RetroAAV-hSyn-YFP
Labelled neurons in PAG and M1
M1
l/vlPAG
WT mice
Aq
lPAG
vlPAG
M1
S1HL
M2
L5
100 µm
YFP
DAPI
I M1 L5-PAG projections
Mechanical sensitivity
SNI 4 w
AAV-DIO-ChR2-YFP
or AAV-DIO-YFP
Blue light
M1
L5
l/vlPAG
Rbp4-Cre mice
Response rate (%)
YFP
ChR2
Filament strength (g)
J Fos expression in PAG
YFP
ChR2
Fos+ cells x1000/mm3
non-GABAergic neurons x1000/mm3
lPAG
vlPAG
K M1-PAG trans-synaptic tracing
AAV-mDlx-mRuby
AAV-fDIO-YFP
AAV-Flp
AAV-BFP
M1
l/vlPAG
WT mice
Aq
lPAG
vlPAG
100 µm
YFP
mRuby
Proportion of excitatory neuron (%)
L M1-PAG trans-synaptically co-labeled neurons
Midbrain
l/vlPAG
PLCβ4+
LC
PLCβ4-
RVM
Descending Analgesia
suppressed
enhanced
SC
lPAG
vlPAG
50 µm
YFP
PLCβ4+
Proportion of labeled neurons (%)
PLCβ4- YFP+
PLCβ4+ YFP+
M M1-PAG pathway stimulation
PLCβ4+ proportion of Fos+ neurons (%)
YFP
ChR2
lPAG
vlPAG

Figure 2

Fig. 2. M1 layer 5 projections to specific neuronal populations in the ZI and PAG inhibit neuropathic mechanical allodynia. (**A** and **B**) Optogenetic stimulation of M1 excitatory neuron projections to ZI dorsal (ZId) and ventral (ZIv) domains (A) or to PAG lateral (lPAG) and ventrolateral (vlPAG) columns (B). Shown are schematics (left panels), labeled projections (middle panels), and impact on mechanical allodynia (right panels) for the ZI [(A) YFP: *n* = 9, ChR2: *n* = 13 mice] and PAG [(B) YFP: *n* = 5, ChR2: *n* = 7 mice]. (**C**) Strategy (left) for retrograde labeling of M1 layer 5 neurons (right) after injection in ZI (middle). (**D**) Strategy (left) for viral trans-synaptic YFP labeling of ZI neurons receiving M1 afferent projections (middle) and analysis of non-GABAergic neurons [(right) (*n* = 3 mice per group)]. (**E**) Immunohistochemical characterization of trans-synaptically YFP-labeled ZI neurons receiving M1 afferent inputs (*n* = 3 mice per group). (**F**) Fos expression in GABAergic neuron reporter mice in ZI domains (right) upon optogenetic activation of M1 excitatory neurons [(left) (*n* = 3 mice per group]. (**G**) Fos expression upon optogenetic stimulation of the M1-ZI projections (*n* = 3 to 4 mice per group). (**H**) Strategy [left for labeling of M1 layer 5 neurons (example on right)] retrogradely after viral injection in lPAG/vlPAG (example in middle). (**I** and **J**) Strategy [(I) (left)] for optogenetic stimulation of excitatory M1-lPAG/vlPAG projections and impact on mechanical allodynia [(I), right; YFP: *n* = 10, ChR2: *n* = 8 mice] and on Fos expression in lPAG/vlPAG [(J) *n* = 3 mice per group]. (**K**) Strategy [(left) viral trans-synaptic YFP labeling of PAG neurons receiving M1 afferent projections (middle) and proportion of non-GABAergic neurons (right)] (*n* = 4 mice per group). (**L** and **M**) Further characterization of trans-synaptically labeled PAG neuron populations receiving M1 afferent input using anti-PLCβ4 immunohistochemistry [(L) *n* = 3 mice per group] and Fos expression upon optogenetic stimulation of the M1-PAG pathway [(right) *n* = 3 mice per group]. In statistical analyses for [(A), (B), and (I)]: ANOVA for random measures followed by post-hoc Sidak's test was performed, for [(F), (G), (J), and (M)]: a two-tailed unpaired *t* test was performed. * represents $P < 0.05$.

Our data thus suggest that M1 layer 5 activation shifts the neuronal excitation-inhibition balance in the vlPAG toward increased activation. Optogenetic activation of the M1 layer 5-PAG pathway or the M1 layer 5-ZI pathway did not affect motor behaviors in neuropathic or uninjured mice (fig. S9, C to E, and movies S1 to S3) or elicit CPP in uninjured mice (fig. S9G). Retrograde viral labeling with dual constructs revealed that most M1 projections to the ZI and vlPAG are collaterals (fig. S10A) and transsynaptic anterograde tracing showed that both lPAG/vlPAG neurons and ZI neurons that receive M1 inputs project to areas such as the locus coeruleus (LC) and rostral ventromedial medulla (RVM) that are involved in descending modulation of spinal nociception, in addition to diverse other functions (fig. S10, B and C). It has been proposed that the PAG-RVM pathway enhances descending inhibition of nociception, whereas PAG neurons projecting to the locus ceruleus—which can be specifically identified through expression of the signaling enzyme PLCβ4—suppress descending analgesic pathways (*20*) (Fig. 2L, left panel). Although PLCβ4-expressing neurons were abundant in lPAG-vlPAG, they constituted less than 10% of neurons that were trans-synaptically labeled from incoming M1-PAG projections (Fig. 2L, middle and right panels). Furthermore, whereas optogenetic M1 stimulation in neuropathic mice led to a significant increase in Fos expression in PAG neurons receiving direct synaptic inputs from the M1 (Fig. 2J), the proportion of PLCβ4-expressing neurons showing Fos expression decreased significantly (Fig. 2M).

How does M1 activation reduce negative emotional valence in neuropathic pain? Optogenetic activation of the M1-ZI, M1-PAG, or M1 layer 5-PAG pathways did not reproduce the CPP phenotype (Fig. 3A) displayed by neuropathic mice with optogenetic stimulation of the entire hindlimb M1 (see Fig. 1F). Layer 6 of the M1 densely projects to diverse thalamic nuclei (*13*), and the mediodorsal thalamus (MD) is an important station that relays ascending sensory inputs related to the aversive component of pain to prefrontal and limbic cortices (*21*). We therefore studied M1 connectivity with the MD in detail using anterograde (Fig. 3B and fig. S11A) viral tracing experiments and noted that layer 6 of hindlimb M1 predominantly targets the lateral domain of the MD (MD_L). By contrast, the MD_L does not receive inputs from layer 5 of the M1 (fig. S11B). Upon expressing ChR2 in either the entire hindlimb M1 (Fig. 3C and fig. S11C) or selectively in layer 6 using a specific transgenic mouse line (Fig. 3D) and optogenetically activating projections specifically in the MD_L (electrophysiological validation in fig. S11D), neuropathic mice developed significant CPP without any change in sensory hypersensitivity (Fig. 3, C and D, and fig. S11, E and F).

Given that the rostral anterior cingulate cortex (rACC) plays a role in the aversive component of pain (*21*), it was reasonable to expect that the layer 6-MD_L pathway targets the rACC to alleviate pain affect in neuropathic mice. However, a number of observations revealed that this is unlikely to be the case. First, dual multisite labeling revealed that the M1 layer 6 projection zone in the MD and the MD domains retrogradely labeled from the rACC do not overlap with each other (Fig. 3E and fig. S12A). Secondly, anterograde labeling revealed that the MD_L domain of the MD makes denser connections with other neocortical domains, such as the M2, as compared with the rACC (fig. S12B). Third, trans-synaptic tracing in mice with virally labeled GABAergic neurons revealed that MD_L neurons receiving direct inputs from M1 layer 6 are almost exclusively non-GABAergic (Fig. 3F); in support, Fos mapping experiments indicated that optogenetic activation of M1 layer 6 enhances activity in non-GABAergic neurons of the MD_L (fig. S12B). However, optogenetic activation of excitatory connectivity from the MD to the rACC evokes aversion (*22*), as opposed to the anti-aversive effects upon activating M1 layer 6-MD connectivity.

We therefore further studied the projections emerging from the MD_L and found sparse termination zones in the prelimbic cortex and the basolateral amygdala (fig. S12C) and dense terminations in the nucleus accumbens (NAc) (Fig. 4A). In Fos labeling experiments, the NAc, but not the prelimbic cortex or basolateral amygdala, demonstrated changes upon optogenetic stimulation of layer 6 M1 neurons (fig. S12D). Thalamic control of the NAc from the paraventricular thalamus represents one of the most salient and functionally well-characterized input pathways into the NAc, which is linked to expression of aversive behaviors (*23*). By contrast, although large scale connectivity analyses on the NAc include inputs from the MD, they have not been functionally interrogated thus far. Our anterograde tracing experiments demonstrated that the MD_L robustly targets the core region of the NAc (NAcC) (Fig. 4A), with sparser connections to the shell (NAcSh) also noted in more medial areas (fig. S12E). More than 90% of NAc neurons are GABAergic medium spiny neurons (MSNs), with a much smaller proportion of local cholinergic interneurons. Using a combination of trans-synaptic viral labeling in transgenic mice with labeling of dopamine receptor D1- or D2-types of GABAergic MSNs using specific transgenic mouse lines (Fig. 4B and fig. S13A), we observed that the MD_L targets both D1- and D2-types of MSNs in the NAc, with a higher density of D2-type MSNs receiving MD_L inputs being observed (Fig. 4B). In patch clamp recordings on MSNs in NAcC, optogenetic terminal stimulation of MD_L-NAcC projections in the NAcC evoked excitatory glutamatergic currents, which are consistent with direct synaptic input (Fig. 4C), thus demonstrating that MD_L-NAcC connections are functional and capable of modulating the activity of NAcC MSNs. In vivo evidence for functionality of this pathway was given by fiber photometry imaging experiments, in which were expressed the genetically encoded calcium indicator GCaMP7.0f in NAc and red-shifted excitatory opsin ChrimsonR in the MD_L (Fig. 4D, left panel). In vivo optogenetic stimulation of MD_L neurons in awake mice induced acute bulk calcium transients in NAc (Fig. 4D,

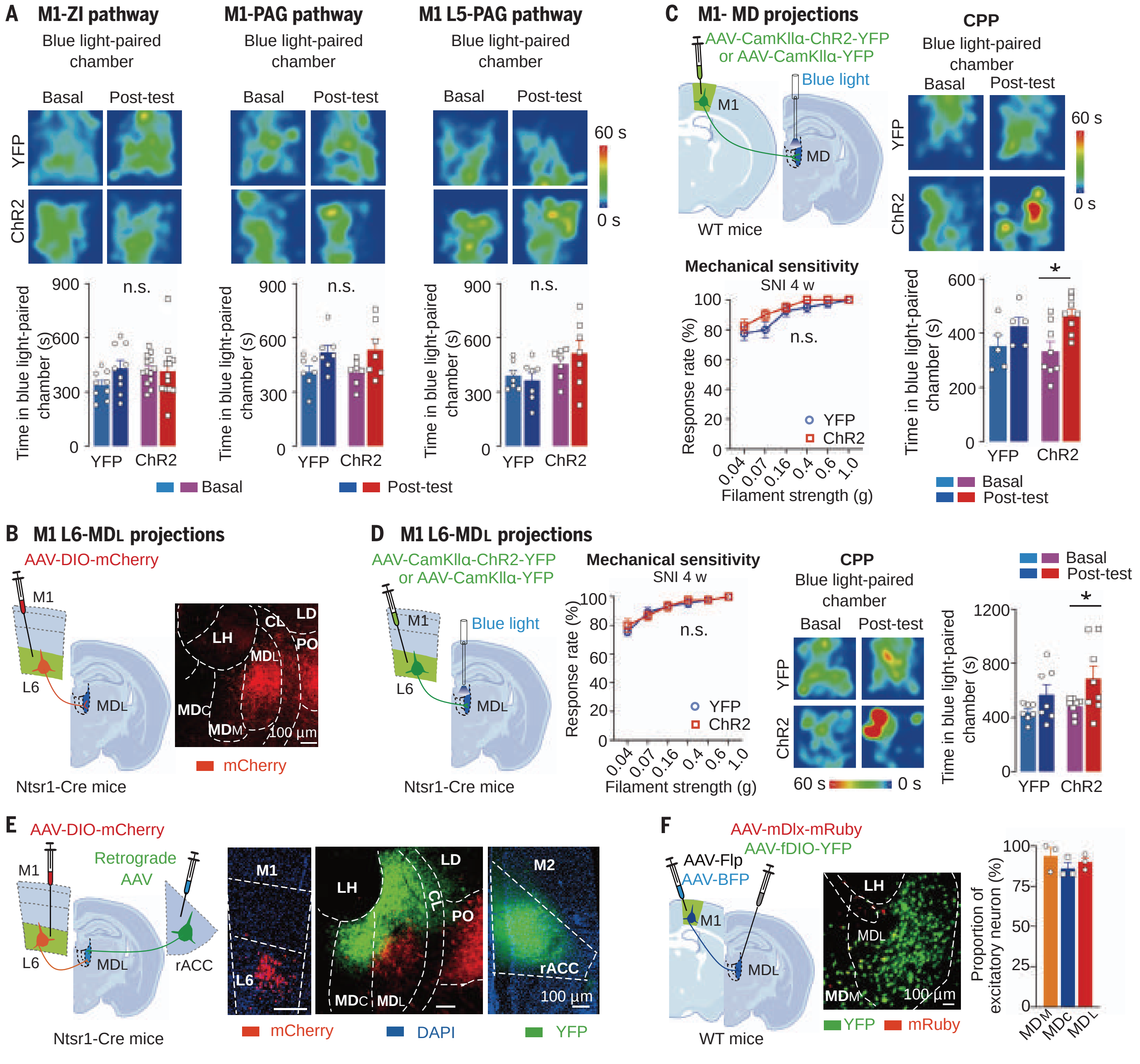


Fig. 3. Activation of M1 layer 6 neurons specifically reduces negative affective valence in neuropathic pain through projections to the mediodorsal thalamus. (**A**) Lack of CPP following optogenetic stimulation of M1-ZI projections, M1-PAG projections, or layer 5 M1-PAG projections. Shown are heat plots of time spent in an optogenetic stimulation-paired chamber (top) and the respective quantitative summary (bottom) [(left) YFP: n = 9, ChR2: n = 13 mice, (middle) n = 9 mice per group, (right) n = 7 mice per group). (**B**) Strategy (left) for viral anterograde tracing of M1 layer 6 projections to the lateral mediodorsal thalamus [MD_L (middle)] using Ntsr1-Cre mice. (**C** and **D**) Impact of optogenetic stimulation of M1 projections to the MD (C) or specifically of M1 layer 6 projections to the MD_L (D) on neuropathic mechanical allodynia (n = 8 to 9 mice per group) and CPP (YFP: n = 5 to 7, ChR2: n = 8 mice). (**E**) Schematic (left) and examples (right) demonstrating lack of convergence within the MD_L (middle) of M1-MD_L afferents labeled anterogradely from M1 layer 6 neurons (red in left image) and efferents from the MD to the rACC labeled retrogradely from the rACC (green in right image) (n = 4 mice). (**F**) Viral trans-synaptic YFP labeling of MD_L neurons receiving M1 afferent projections (middle) and analysis of non-GABAergic neurons [(right) n = 3 mice per group); AAV-BFP was injected as a local targeting control. ANOVA for random measures was performed followed by post-hoc Sidak's test. * represents P < 0.05.

middle panel, and fig. S13B). Upon longitudinal testing, all tested mice demonstrated a trend for decreased bulk calcium transients evoked by MD_L-NAc pathway stimulation 1-week post-SNI, when peak neuropathic pain is established. However, reduction in peak amplitude did not reach statistical significance (Fig. 4D, right panel). Finally, to test the in vivo functional significance of the MD_L-NAc pathway—particularly its relevance to alleviation of neuropathic pain upon M1 activation—we performed behavioral experiments integrating a trans-synaptic optogenetic approach enabling specific activation of terminations in the NAcC of only MD_L neurons receiving direct inputs from the M1

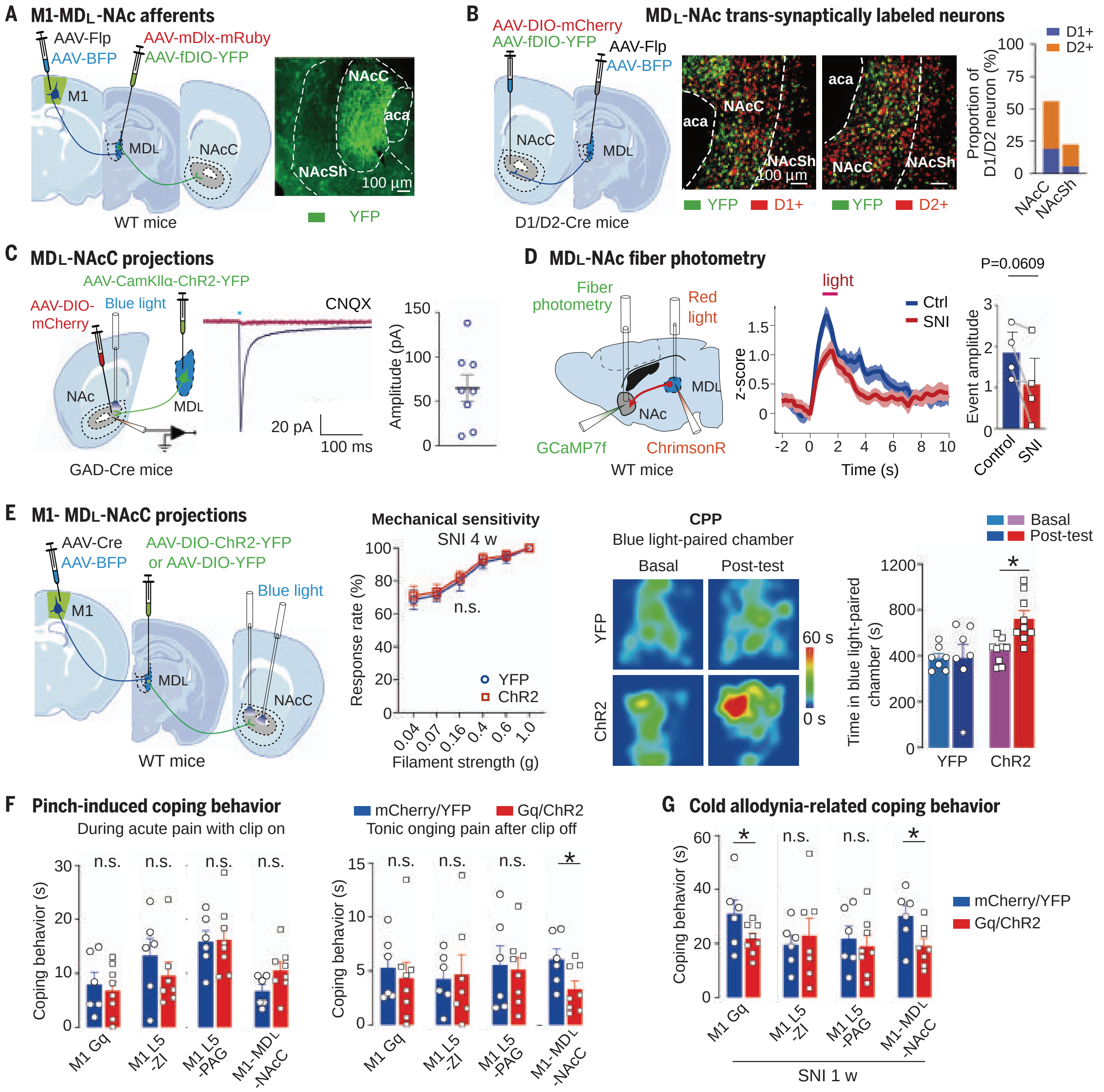


Fig. 4. Unraveling of a functional M1-MD_L-nucleus accumbens (NAc) pathway alleviating negative affective valence in neuropathic pain. (**A**) A trans-synaptic viral labeling approach for identifying efferent connections of MD_L neurons receiving direct input from M1 layer 6 neurons (schematic on the left), which reveal the NAc core (NAcC) as a major target and parts of the NAc shell (NAcSh) (example image on right). (**B**) Virally mediated trans-synaptic YFP labeling of neurons in the NAcC and NAcSh receiving afferent projections from the MD_L (left) and their subdivision into D1- and D2-expressing populations using D1-Cre and D2-Cre mice (middle) and quantification [(right) n = 5 sections per group]. (**C**) Patch clamp recordings of activity of NAc GABAergic MSNs in brain slices upon optogenetic stimulation of MD_L-NAcC projections with strategy (left), example traces [(middle) blocked by glutamate receptor channel antagonist CNQX] and quantification [(right) n = 8 cells from 3 mice.] (**D**) In vivo fiber photometry recordings of calcium transients through GCaMP7f imaging in the NAc upon ChrimsonR-mediated optogenetic stimulation of MD_L-NAc projections longitudinally across baseline (control) and post-SNI conditions with strategy (left), example traces (middle), and quantification [(right) n = 4 mice)]. (**E**) Optogenetic stimulation of MD_L-NAcC efferent projections specifically originating from MD_L neurons receiving M1 afferent inputs (left) and impact on mechanical allodynia (n = 7 mice in the YFP group and 9 mice in the ChR2 group) and CPP in neuropathic mice (YFP: n = 7, ChR2: n = 9 mice). AAV-BFP: injection control. (**F** and **G**) Changes in coping behaviors during [(F) left] and after [(F) right] prolonged pinch in uninjured mice and in relation to cold allodynia in neuropathic mice (G) upon chemogenetic M1 activation or optogenetic stimulation of M1 pathways as indicated. In [(E), (F), and (G)], ANOVA for random measures followed by post-hoc Sidak's test was performed; for (D), a one-tailed paired t test was performed. * represents $P < 0.05$.

(scheme shown in Fig. 4E, left panel, and fig. S13C). Activating this novel M1-MD_L-NAcC pathway led to CPP in neuropathic mice (Fig. 4E, middle panels), but not in baseline conditions in uninjured mice (fig. S13D), without affecting neuropathic sensory hypersensitivity (Fig. 4E, right panel, and fig. S13E) or motor behaviors (fig. S13, F and G). To consolidate these findings with additional analyses of pain-related negative valence, we performed prolonged application of a strong pinch stimulus in uninjured mice (Fig. 4F) (*24*) and studied coping behaviors comprising attending and escape-related behaviors in video monitoring experiments (movie S4). Chemogenetic activation of whole M1 or optogenetic activation of the M1 pathways to ZI, PAG, or MD_L-NAcC did not alter coping behavior during pinch application (clip on, Fig. 4F, left panel), whereas only activation of the M1-MD_L-NAcC pathway significantly reduced ongoing pain-related coping behaviors persisting after removal of the noxious stimulus (clip off, Fig. 4F, right panel, and movies S5 to S7). In mice with nerve injury, only activation of the M1-MD_L-NAcC significantly reduced cold allodynia-related coping behaviors to a 3°C cold stimulus (Fig. 4G and movies S8 to S10). Analysis of baseline and noxious stimulus–induced Fos expression in conjunction with cell type–selective neuronal markers (*24*, *25*) revealed that neurons involved in ascending relay of noxious information or descending modulation of spinal nociception are differentially affected by activation of the individual M1 pathways projecting to the ZI, PAG, or MD_L-NAcC (see Supplementary note 1 for details; figs. S14 and S15).

These results uncover a notable functional dichotomy of circuit connectivity of layer 5 and layer 6 pyramidal neurons of the hindlimb M1 in regulating two distinct components of pain (fig. S16). The study identifies the ZI as an important target of M1-mediated cortical control of nociceptive hypersensitivity, particularly by strengthening excitatory outputs to the descending nociceptive modulatory centers, such as raphe nuclei and the PAG. Neuropathic pain involves both a depletion of ZI activity (*26*) and a loss of descending bulbospinal inhibitory control of nociception through the PAG. The implication of our findings is that in neuropathic conditions M1 activation can restore balance in the ZI and the PAG through layer 5 pathways and thus aid in regaining normal nociceptive sensitivity by controlling both ascending and descending information flow in somatosensory nociceptive pathways (fig. S16). Confounding motor effects upon activation of M1 layer 5-corticospinal projections, which activate spinal motor neurons, are unlikely given lack of changes in motor behaviors in optogenetic/chemogenetic experiments and lack of effect on baseline paw withdrawal in the absence of neuropathy.

The elucidation of a previously unknown M1 layer 6-MD_L-NAcC pathway in this study demonstrates that modulation by the primary motor cortex is not restricted to sensory-motor circuitry controlling spinally mediated nociceptive reflexive behaviors but is also a major regulator of emotional processing. Although the classical view postulates antagonistic roles for D1 and D2 neurons in reward and aversion, more recent studies have revealed a more complex role for both D1 and D2-expressing NAc neurons in motivated behaviors depending upon context, early versus persistent phases, and type or origin of afferent input (*27*, *28*). D2-expressing MSNs undergo long-term depression through depletion of excitatory inputs in neuropathic pain conditions (*29*). There is mounting evidence for depletion of dopamine as well as disbalance between D1- and D2-MSN activity in the NAc in chronic pain states (*30*). Our observation that MD_L neurons receiving excitatory inputs from the M1 can stimulate D1 and D2 neurons through glutamatergic transmission thus opens up the possibility that M1 activation can bypass the accumbal dopamine deficit and restore balance in the dysregulated MSN circuitry in neuropathic pain conditions, a hypothesis which requires detailed testing. Both layer 5- and layer 6-derived pathways to the ZI/PAG or MD_L-NAcC did not impact normal nociception in the absence of injury, suggesting that this level of control specifically emerges in neuropathic pain conditions and will not hamper the protective function of physiological pain. These insights, coupled with our observation that chronically established neuropathic pain can be reversed by activation of layer 5/layer 6-dependent pathways, will help provide insights for developing and improving neurostimulation therapies for optimal pain control.

REFERENCES AND NOTES

1. C. L. Ebbesen, M. Brecht, *Nat. Rev. Neurosci.* **18**, 694–705 (2017).
2. M. Frot, M. Magnin, F. Mauguière, L. Garcia-Larrea, *Hum. Brain Mapp.* **34**, 2655–2668 (2013).
3. R. Peyron *et al.*, *Neurology* **63**, 1838–1846 (2004).
4. N. Attal *et al.*, *Brain* **144**, 3328–3339 (2021).
5. K. Gatzinsky *et al.*, *Scand. J. Pain* **21**, 8–21 (2020).
6. X. Moisset, D. C. de Andrade, D. Bouhassira, *Eur. J. Pain* **20**, 689–700 (2016).
7. Z. Gan, H. Li, P. V. Naser, M. J. Oswald, R. Kuner, *Sci. Rep.* **11**, 9735 (2021).
8. C. K. Kim, A. Adhikari, K. Deisseroth, *Nat. Rev. Neurosci.* **18**, 222–235 (2017).
9. S. M. Sternson, B. L. Roth, *Annu. Rev. Neurosci.* **37**, 387–407 (2014).
10. I. Decosterd, C. J. Woolf, *Pain* **87**, 149–158 (2000).
11. J. P. Nguyen, J. Nizard, Y. Keravel, J. P. Lefaucheur, *Nat. Rev. Neurol.* **7**, 699–709 (2011).
12. J. Cichon, T. J. J. Blanck, W.-B. Gan, G. Yang, *Nat. Neurosci.* **20**, 1122–1132 (2017).
13. M. Jeong *et al.*, *Sci. Rep.* **6**, 20072 (2016).
14. R. Muñoz-Castañeda *et al.*, *Nature* **598**, 159–166 (2021).
15. X. Wang, X. L. Chou, L. I. Zhang, H. W. Tao, *Trends Neurosci.* **43**, 82–87 (2020).
16. X. Zhang, A. N. van den Pol, *Science* **356**, 853–859 (2017).
17. N. Urbain, M. Deschênes, *Neuron* **56**, 714–725 (2007).
18. C. Kolmac, J. Mitrofanis, *Anat. Embryol.* **199**, 265–280 (1999).
19. V. K. Samineni *et al.*, *eNeuro* **4**, ENEURO.0129-16.2017 (2017).
20. J. H. Kim *et al.*, *Proc. Natl. Acad. Sci. U.S.A.* **115**, 11078–11083 (2018).
21. L. L. Tan, R. Kuner, *Nat. Rev. Neurosci.* **22**, 458–471 (2021).
22. K. S. Meda *et al.*, *Neuron* **102**, 944–959.e3 (2019).
23. Y. Zhu, C. F. Wienecke, G. Nachtrab, X. Chen, *Nature* **530**, 219–222 (2016).
24. T. Huang *et al.*, *Nature* **565**, 86–90 (2019).
25. A. François *et al.*, *Neuron* **93**, 822–839.e6 (2017).
26. H. C. Moon, Y. S. Park, *J. Pain Res.* **10**, 1125–1134 (2017).
27. C. Soares-Cunha *et al.*, *Cell Rep.* **38**, 110380 (2022).
28. A. Andrianarivelo *et al.*, *Sci. Adv.* **7**, eabg5970 (2021).
29. N. Schwartz *et al.*, *Science* **345**, 535–542 (2014).
30. E. Navratilova, C. W. Atcherley, F. Porreca, *Trends Neurosci.* **38**, 741–750 (2015).

ACKNOWLEDGMENTS

The authors sincerely thank M. Brecht and R.-R. Ji for providing insightful scientific feedback on an earlier version of the manuscript. The authors are grateful to C. Gartner for secretarial assistance, to N. Gehrig, D. Baumgartl-Ahlert, B. Zimmermann, and L. Wang for technical assistance, and D. Mittal for data management. The authors gratefully acknowledge the Interdisciplinary Neurobehavioral Core Facility of Medical Faculty Heidelberg for assistance with behavioral experiments. R.K. is an investigator in the Molecular Medicine Partnership Unit, Heidelberg. **Funding:** This work was funded by the following: German Research Foundation grant in Collaborative Research Center 1158 (to R.K., project B01, B06, Z01; T.K., project B08; A.G., project B10; S.W., project B04). Partial scholarship support was provided from Union Hospital, Tongji Medical college, and Huazhong University of Science and Technology (Z.G.) Partial scholarship support was also provided from China Scholarship Council (H.L.). **Author contributions:** Conceptualization: R.K. Methodology: Z.G., V.G., S.L., M.O., L.L.T., S.W., J.M.C., A.G., T.K. Investigation: Z.G., V.G., S.L., H.L., L.L.T., J.K., C.K., S.W. Visualization: Z.G., S.W., S.L., C.K., M.O. Funding acquisition: R.K., T.K., A.G., S.W. Project administration: R.K., Z.G. Supervision: R.K. Writing – original draft: R.K. Writing – review and editing: Z.G., T.K., S.W., A.G., C.K., M.O., L.L.T., V.G. **Competing interests:** Authors declare that they have no competing interests. **Data and materials availability:** All individual data points are available in the main text or the supplementary materials or stored and curated in public data repository (https://heibox.uni-heidelberg.de/d/c953c55267344092993c/). Code files for analysis of electrophysiological and calcium imaging data are also available at https://heibox.uni-heidelberg.de/d/c953c55267344092993c/. **License information:** Copyright © 2022 the authors, some rights reserved; exclusive licensee American Association for the Advancement of Science. No claim to original US government works. https://www.sciencemag.org/about/science-licenses-journal-article-reuse

SUPPLEMENTARY MATERIALS

science.org/doi/10.1126/science.add4391
Materials and Methods
Supplementary note 1
Figs. S1 to S16
Tables S1 to S4
References (*31*–*55*)
MDAR Reproducibility Checklist
Movies S1 to S10

Submitted 11 June 2022; accepted 21 November 2022
10.1126/science.add4391

CALORICS

Ionocaloric refrigeration cycle

Drew Lilley[1,2] and Ravi Prasher[1,2]*

Developing high-efficiency cooling with safe, low–global warming potential refrigerants is a grand challenge for tackling climate change. Caloric effect–based cooling technologies, such as magneto- or electrocaloric refrigeration, are promising but often require large applied fields for a relatively low coefficient of performance and adiabatic temperature change. We propose using the ionocaloric effect and the accompanying thermodynamic cycle as a caloric-based, all–condensed-phase cooling technology. Theoretical and experimental results show higher adiabatic temperature change and entropy change per unit mass and volume compared with other caloric effects under low applied field strengths. We demonstrated the viability of a practical system using an ionocaloric Stirling refrigeration cycle. Our experimental results show a coefficient of performance of 30% relative to Carnot and a temperature lift as high as 25°C using a voltage strength of ~0.22 volts.

Vapor-compression (VC) technology has dominated refrigeration for the past century by using hydrofluorocarbons (HFCs) as liquid refrigerants (*1*). HFCs, however, have global warming potential (GWP) greater than 2000 times that of CO_2, and by 2050, HFC emissions are predicted to account for up to 20% of equivalent CO_2 emissions because of rapidly growing demand for refrigeration in the world (*2*, *3*). Other liquid-based alternatives to HFCs, such as hydrofluoroolefins (HFOs), are being implemented in parts of the world, but these low-GWP refrigerants are still slightly flammable, have smaller power densities and coefficients of performance (COPs) compared with HFCs, and pose other environmental concerns (*4*–*6*). To overcome these challenges, researchers have turned to solid-state materials that provide a refrigeration effect upon the application of an external field (*7*, *8*). These materials—often referred to as caloric materials—generally require large field strengths, and their accompanying thermodynamic cycles have thus far yielded low COPs, small adiabatic temperature changes, and lower power outputs relative to those of a typical VC cycle (*8*–*14*). We report a different caloric effect that we refer to as the ionocaloric effect and demonstrate better performance than previously reported caloric materials.

In general, a caloric effect refers to an isothermal entropic response to an external field applied to its conjugated energetic variable, such as an electric polarization in response to an electric field. The magnetocaloric effect, for example, refers to a thermal response driven by a magnetic field (*15*); the electrocaloric effect refers to a thermal response driven by an electric field (*16*). Physically, the magnetic field induces an entropy change by aligning the material's magnetic dipoles, whereas the electric field aligns the electric dipoles. Likewise, we define the ionocaloric effect as the thermal response to a changing ionic environment surrounding a solid phase, driven by an electrochemical field. The ionocaloric effect induces an entropy change through the electrochemical mixing of species. As with other caloric effects, the isothermal entropy change (ΔS_T) and adiabatic temperature change (ΔT_s) can be well defined for the ionocaloric effect using Maxwell relations. Maxwell relations can be constructed for the electrochemical field and its corresponding conjugated quantity of chemical species [(*17*), section SI.1], which leads to $\Delta T_s = \int_{\Delta\mu} \frac{T}{C_\mu}\left(\frac{\delta n}{\delta T}\right)_\mu \delta\mu$ and $\Delta S_T = -\int_{\Delta\mu}\left(\frac{\delta n}{\delta T}\right)_\mu \delta\mu$, where μ is the electrochemical field, T is the temperature, C_μ is the constant electrochemical potential heat capacity, and n is the molar quantity.

Compared with conventional caloric effects, the ionocaloric effect presents a distinct thermodynamic nuance: In other caloric systems, the applied field induces an energetic response by interacting with its conjugate pair; the ionocaloric system operates in reverse. The electrochemical potential cannot be directly controlled in the way that an electric, magnetic, or pressure field can. Instead, the effect is calculated from the concentration of chemical species (conjugate variable) using $\mu = RT\ln(\gamma x)$, where γ is the activity coefficient of the species and x is the mole fraction. The chemical species, however, can be added or removed from the system through couplings to other field variables, such as temperature (e.g., distillation), pressure (e.g., reverse osmosis), and voltage. We use voltage in our demonstration for the coupling.

Physically, the ionocaloric effect manifests within first-order, solid-liquid phase boundaries by lowering the melting point of a solid below the ambient temperature upon the addition of ions to its surroundings (i.e., applying an electrochemical field). Under this field, the solid melts because the liquid phase becomes more stable, which requires energy. If the system is insulated from its surroundings (adiabatic), it must trade its own internal energy to melt the solid phase, at which point it lowers its own temperature by endothermically converting some solid to the liquid phase. This process will continue until the solid's temperature is equal to its new melting temperature, which is dictated both by the strength of the applied electrochemical field and the caloric material's solid-liquid phase boundaries. The reverse effect, observed by removing ions from the caloric material's surroundings (or, conversely, by adding more caloric material), will increase the melting point of the liquid phase. The liquid, which is now most stable as a solid, crystallizes—releasing energy to do so. Under adiabatic conditions, it will release energy to itself, increasing the temperature and exothermically converting some liquid to the solid phase. This process will continue until the liquid's temperature is equal to the new melting or crystallization temperature.

Because we are using ions to manipulate the electrochemical field, our approach can broadly be considered electrochemical refrigeration; however, the strategy is different from traditional electrochemical refrigeration. It aligns more closely with the caloric effects because the entropy change is achieved using a reversible phase transition and exhibits a field-induced phase transition temperature change enabled by the electrochemical field. In traditional electrochemical refrigeration, cooling is driven by the thermogalvanic effect, which uses the entropy change of ions participating in redox reactions to generate a temperature difference from applied work. In thermogalvanic cooling, ions participate in the cooling, and the liquid solvent serves to enable ion transport. Although the entropy change per unit ion is large, the entropy change per unit mass and volume is very low because of the large amount of liquid solvent present in the system. Therefore, the temperature lift is expected to be very small. Recent experimental demonstrations (*18*, *19*) have shown that the highest-temperature lift achieved to date is 0.15°C, with a relative Carnot COP (COP_C) < 0.002. In our proposed idea, the solvent is participating in a first-order phase transition, and very large isothermal entropy changes and adiabatic temperature changes can be achieved because the whole medium is participating in the entropy change.

The ionocaloric effect can cool or heat a material under an applied or removed electrochemical field, respectively, but to provide continuous refrigeration, it must be embedded into an appropriate thermodynamic cycle. In physical terms, this can be done in four steps (Fig. 1A): (i) mixing a salt with a solid, which cools the solid to its now-lower melting point; (ii) melting the solid at the lower melting point; (iii) separating the salt from the liquid, thereby heating the solution, and raising its melting

[1]Lawrence Berkeley National Laboratory, Berkeley, CA 94720, USA. [2]Department of Mechanical Engineering, University of California, Berkeley, CA 94720, USA.
*Corresponding author. Email: rsprasher@lbl.gov

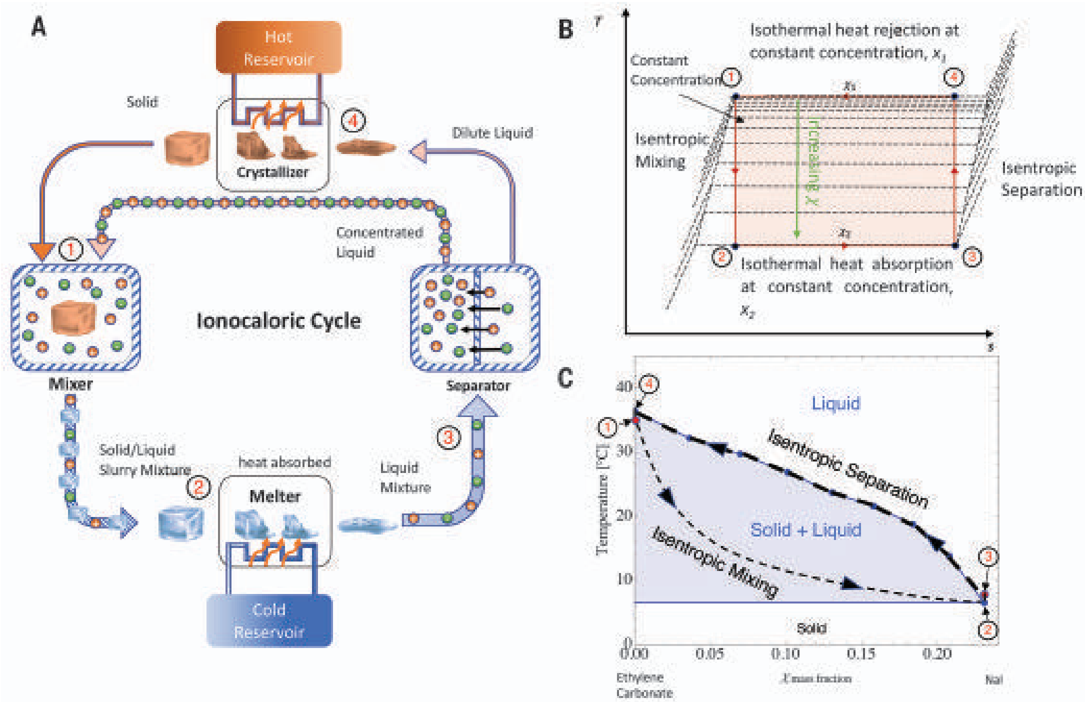


Fig. 1. Overview of the ionocaloric cycle. (**A**) Schematic of the four steps involved in ionocaloric refrigeration (separation, crystallization, mixing, and melting). (**B**) *T-S* diagram for an ideal, reversible ionocaloric cycle. (**C**) The *T*-X binary phase equilibria for the EC-NaI system along with state points corresponding to various points on the *T-S* diagram and schematic in (A).

point; and (iv) crystallizing the solid from the liquid at the now-higher melting point. To make this Carnot-like (Fig. 1B), this must be done through (i) isentropic (adiabatic and reversible) mixing, (ii) isocompositional and isothermal heat absorption, (iii) isentropic separation, and (iv) isocompositional and isothermal heat rejection. We depict the *T-S* diagram of the ionocaloric cycle along different lines of constant composition (Fig. 1B) and show the traversal of each step on the system's temperature-composition (*T*-X) phase boundaries at different electrochemical fields (mass fractions) (Fig. 1C). We determined the system's *T-X* phase equilibria (Fig. 1C) by differential scanning calorimetry [(*17*), section SI.3].

The maximum and minimum operating temperatures of the cycle are dictated by the pure caloric material's melting point and the lowest melting point of the binary salt mixture. The refrigeration capacity, or the amount of heat absorbed per cycle, is determined by the caloric material's enthalpy of fusion. The ideal ionocaloric material will have a melting point above room temperature, a eutectic (or some other invariant point) well below room temperature, and a high enthalpy of fusion. Ideal ionocaloric materials should also have high cryoscopic constants (*20*) so that large temperature changes can be achieved using small amounts of electrolyte. On the basis of these criteria, we identified the ethylene carbonate–sodium iodide (EC-NaI) system as a promising ionocaloric system [(*17*), section SI.2] with a pure melting point of T_{melt} = 36.4°C, a eutectic transition at $T_{eutectic}$ = 6.4°C, and a relatively high latent heat of fusion ΔH_{fus} = 204.6 J mL^{-1} (as compared with ΔH_{fusion} ≈ 330 J mL^{-1} for water, which has one of the highest entropies of fusion of known near–room temperature molecules). The EC-NaI system is a CO_2-negative, environmentally benign, nonhazardous, zero-GWP, nontoxic, and nonflammable mixture. EC is a common additive to battery electrolytes (e.g., lithium-ion), can be made stable over a long lifetime, and has shown good cyclability and stability; however, more studies are needed for cooling applications.

The ionocaloric effect, characterized by $\Delta S_{isothermal}$ and $\Delta T_{adiabatic}$ of the EC-NaI system, is better than other caloric effects reported in the literature (Fig. 2A) (*21*–*28*). We determined $\Delta S_{isothermal}$ = 802.08 J L^{-1} K^{-1} by calorimetry [(*17*), section SI.3], which is roughly twice as large as the neopentyl glycol–based barocaloric effect, which has one of the highest $\Delta S_{isothermal}$ reported (*22*). In addition, $\Delta S_{isothermal}$ per unit mass (Fig. 2, A and B) is more than 10 times the state of the art for magneto-, electro-, and elastocaloric effects (Fig. 2A). For the EC-NaI system, we directly measured a $\Delta T_{adiabatic}$ (Fig. 2C) of 28°C using an electrochemical potential of ~450 J mol^{-1} [i.e., at a NaI mass fraction of ~0.18 using $\mu = RT\ln(\gamma x)$]. This is larger than other caloric effects (Fig. 2A). Multicalorics is an emerging field in which entropy changes from multiple applied fields can potentially increase $\Delta T_{adiabatic}$ and $\Delta S_{isothermal}$; however, the reported performances (*29*) are still smaller than what has been found for the best caloric materials. Our theoretical model for $\Delta T_{adiabatic}$ [(*17*), sections SI.4 and SI.5] matches well with our data (Fig. 2C). To modulate the electrochemical potential in a real system, the ion concentration can be controlled by applying a voltage in an electrolytic cell (e.g., dual-ion battery), where the applied voltage is typically ~1 V. This stimulus is considerably milder than those used in magnetic, electric, and pressure-based caloric systems.

We determined the maximum $COP = \frac{Q_{cool}}{W_{in}}$ for the EC-NaI system by the minimum energy needed to reversibly separate the solution, which is given by the free energy of mixing, and the cooling energy, Q_{cool}, is related to the enthalpy of fusion of ethylene carbonate [(*17*), section SI.7]. Neglecting any work output available during the isentropic mixing step (analogous to using an expansion valve instead of a turbine in a VC cycle) and assuming perfect regeneration [(*17*), section SI.6], we compute the relative COP_C to be roughly 0.9 for temperature spans of 10° to 30°C [(*17*), section SI.7].

Although the theoretical reversible properties of the EC-NaI system are competitive with those of other caloric materials, and the theoretical performance in an ideal thermodynamic cycle can reach very high efficiencies, the performance in practice will be strongly affected by the details of the separation process, which can be viewed as a desalination step. Desalination technologies (*30*, *31*) are mature and plentiful and include thermal, mechanical, and electrochemical techniques. Thermal separation techniques are inherently less efficient than mechanical techniques because of second law penalties of three-temperature

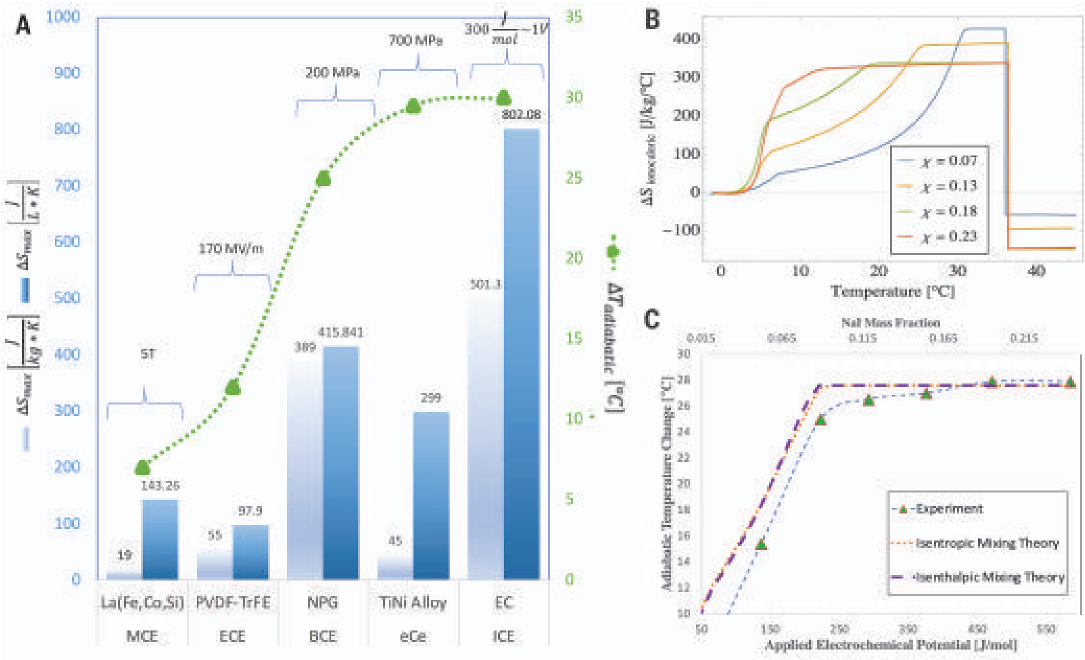


Fig. 2. The ionocaloric effect of the EC-NaI system. (**A**) Comparison of the maximum entropy change (per kilogram and liter) and adiabatic temperature change of EC-NaI to the state of the art in magnetocaloric (MCE), electrocaloric (ECE), elastocaloric (eCe), and barocaloric (BCE) literature (*21*–*24*), along with the applied field strengths to achieve the effect. The data shown for other caloric materials are typical values based on three criteria: (i) simultaneous measurement of entropy and adiabatic temperature change on the same system, (ii) measurement taken near room temperature, and (iii) reversible material changes. Detailed datasets for all other possible cases are available in (*25*, *27*, *28*). ICE, ionocaloric. (**B**) Ionocaloric entropy change for various mass fractions of NaI. (**C**) Directly measured adiabatic temperature change of EC as a function of the applied electrochemical potential (bottom axis) and mass fraction (top axis).

systems. Mechanical techniques (*32*), such as reverse osmosis, can operate at efficiencies as high as 50% of the theoretical limit of separation in commercial plants but require relatively high operating pressures. Electrochemical techniques, such as electrodialysis, also routinely operate at high efficiencies (~50%) but do not require high operating pressures or fields (*33*). For this reason, electrodialysis was used in the separation step in this study to show the feasibility of a practical system.

Electrodialysis separates ions by applying an electric field across permselective ion-exchange membranes. In our EC-NaI system, the electrodialysis process is a system broken up into the working fluid and electrode compartments (Fig. 3A). The electrode compartments are each filled with 0.5 M NaI_3 and 1.5 M NaI, forming a symmetric cell. Current is driven across the cell using an iodide-triiodide redox couple (well studied for applications in dye-sensitized solar cells). At the negative electrode, triiodide is reduced, following $I_3^- + 2e^- \rightarrow 3I^-$, and at the positive electrode, iodide is oxidized such that $3I^- \rightarrow I_3^- + 2e^-$. Because they are symmetric reactions, the change in Gibbs free energy between the oxidized and reduced states is zero, and the reaction proceeds at any nonzero voltage applied across the electrodes. At higher potentials [~1V higher than the iodide-triiodide couple versus saturated calomel electrode (SCE)] [(*17*), section SI.6], triiodide is further oxidized to pure iodine, $2I_3^- \rightarrow 3I_2 + 2e^-$. I_2 is soluble in EC, so it dissolves back into the electrode solution and, upon circulation, either combines with an I^- to reform I_3^- or gets reduced at the negative electrode to the same result. Positive ions (Na^+) will then be driven toward the negative electrode upon reduction of I_3^-. Na^+ can cross the cation-exchange membranes (Fig. 3A, red) but are prevented from crossing the anion-exchange membrane (Fig. 1A, green) by Donnan exclusion. Likewise, the negative I^- ions will be driven toward the positive electrode upon oxidation of I^- and may cross the anion-exchange membrane, but they are prevented from crossing the cation-exchange membranes. Because the membranes are selective to only one type of ion, one compartment will eventually become completely depleted of ions while the other becomes concentrated.

This cell setup was run until depletion of one compartment for various EC-NaI concentrations and current densities. These experiments assume a regenerative ionocaloric cycle [(*17*), section SI.6] so that the separation process was done isothermally instead of isentropically. As the concentration of the diluent is decreased, the melting point will increase until it is equal to the temperature of the external sink, at which point crystallization of the diluent rejects heat to the external sink. At the end of the separation process, the diluent is predominantly solid, whereas the concentrate is liquid [(*17*), section SI.10]. The work input into the separation process is directly calculated by the total electrical work into the system done at the electrodes. The temperature of the cold side is dictated by the final concentration of the two solutions when mixed such that all energy is absorbed at the system's liquidus temperature (solid-liquid phase boundary). The energy absorbed at the liquidus temperature is correlated to the amount of solid coming out of the electrodialysis cell [(*17*), section SI.10]. The experimental COP was then calculated from the work input measured and the cooling energy provided.

We show the relative COP_C versus temperature and cooling power of the ionocaloric device compared with the performance of devices made using other caloric effects (*14*, *18*, *19*, *34*–*39*) (Fig. 3, B and C). The performance of the ionocaloric device operated at a temperature span [$\Delta T_{span} = (T_{hot} - T_{cold})$] of 25.76°C is 29.5% relative to Carnot with a cooling power of 5.75 W L^{-1}. The best device-level performance using other caloric effects is reported at 7.4% relative to Carnot at a much smaller temperature span of 13°C (Fig. 3B). Compared with elastocaloric devices at 7% efficiency, the ionocaloric device's cooling power is at least an order of magnitude larger (Fig. 3C). However, an electrocaloric device operating at ΔT_{span} = 1.6°C has a cooling power more than an order of magnitude larger than that of the ionocaloric device. This difference is expected because the electrocaloric device operated at a much lower temperature span than the ionocaloric device.

The largest challenge to overcome using electrodialysis in the ionocaloric cycle is the cooling power output. The membrane resistance for the EC-NaI electrolyte is ~100 times as large as a typical membrane resistance in an aqueous system [(*17*), section SI.13], which poses a

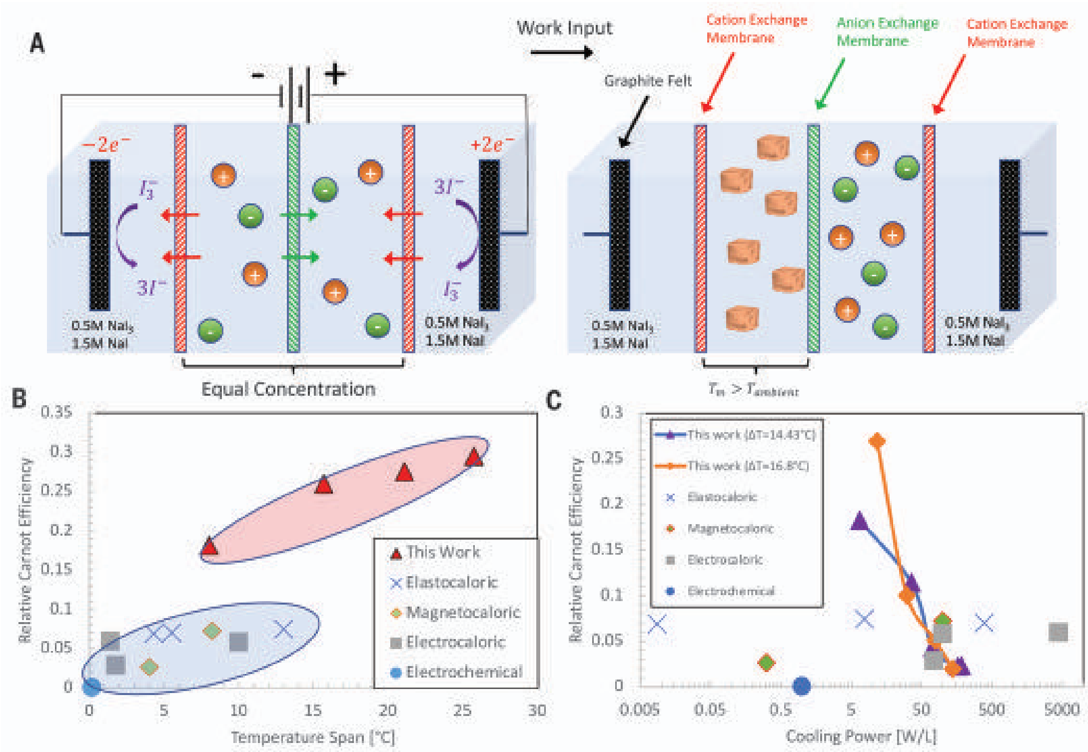


Fig. 3. Experimental setup and results. (**A**) Electrodialysis cell used for the separation process of the ionocaloric cycle. (**B** and **C**) Relative Carnot efficiency versus temperature span (B) and relative Carnot efficiency versus cooling power per liter (C) of the device compared against that of other elastocaloric, magnetocaloric, electrocaloric, and electrochemical prototypes reported in literature (*14*, *18*, *19*, *34*–*39*). The data shown were curated from the literature where COP, temperature span, and cooling power were simultaneously reported. Detailed datasets for other conditions can be obtained from (*28*).

hurdle for achieving high cooling power densities at high efficiencies. Most ion-exchange membranes are designed for aqueous systems, so developing low-resistance membranes specifically made for organic electrolytes would be needed to increase the cooling power density. For additional perspective, some high-efficiency aqueous vanadium redox flow batteries operate at 800 mA cm^{-2}; the ionocaloric device operated at ≈0.5 mA cm^{-2} for its highest-efficiency results. If, for example, it operated at 800 mA cm^{-2}, like in the aqueous system, the cooling power output would be equal to 9.2 kW L^{-1}.

The largest benefit of using electrodialysis in the separation step is in lowering the needed strength of the applied field. Magnetocaloric devices use incredibly strong magnetic fields (up to 5 T) (Fig. 2A), which are difficult to generate using permanent magnets alone. In electrocaloric devices, electric fields of ≈200 MV m^{-1} are common (more than 50 times as large as the dielectric strength of air) and can only be generated by applying voltages across micrometer-sized films in the kilovolt range. Elastocaloric devices with high ΔT_{span} operate at stresses of 800 MPa; barocaloric devices operate at stresses of ~200 MPa. For context, the yield strength of steel is 350 MPa. In the ionocaloric device, the applied field is ~0.22 V, which is relatively modest. As a comparison, a lithium-ion battery operates at ~4 V. Such lowering of the applied field will have a substantial effect on reducing the cost of refrigeration technology based on the ionocaloric cycle proposed here.

The experimental device demonstration is based on the regenerative system, which is completely analogous to the Stirling cycle [(*17*), section SI.6]. Therefore, we can name our experimentally demonstrated cycle an ionocaloric Stirling refrigeration cycle.

We have shown how the ionocaloric effect can lead to higher performance as compared with other caloric materials. Even higher COP, temperature lift (ΔT), and power density are possible with additional improvements. For example, the maximum adiabatic temperature change of ethylene carbonate is ~100°C $\left(\Delta T_{adiabatic} \approx \frac{\Delta H_{fus}}{C_p} \approx 100°C\right)$, but we were only able to achieve 30°C. This limitation comes from the phase boundaries (Fig. 1C). A ternary or quaternary eutectic system can push these phase boundaries to lower temperatures if a larger adiabatic temperature change is needed. Similarly, power density could potentially be increased by 100× if commercial membranes could be designed to have similar resistance values for EC as they do for water [(*17*), section SI.13]. As the resistance is decreased and the selectivity of the membranes improves, higher efficiencies can be achieved for the same power output, leading to increased COP.

REFERENCES AND NOTES

1. International Energy Agency (IEA), The Future of Cooling: Opportunities for energy-efficient air conditioning (IEA, 2018); https://www.iea.org/reports/the-future-of-cooling.
2. G. J. M. Velders, D. W. Fahey, J. S. Daniel, M. McFarland, S. O. Andersen, *Proc. Natl. Acad. Sci. U.S.A.* **106**, 10949–10954 (2009).
3. L. T. Biardeau, L. W. Davis, P. Gertler, C. Wolfram, *Nat. Sustain.* **3**, 25–28 (2020).
4. M. O. McLinden, J. S. Brown, R. Brignoli, A. F. Kazakov, P. A. Domanski, *Nat. Commun.* **8**, 14476 (2017).
5. D. Behringer *et al.*, "Persistent degradation products of halogenated refrigerants and blowing agents in the environment: Type, environmental concentrations, and fate with particular regard to new halogenated substitutes with low global warming potential" (German Environment Agency, report no. FB000452/ENG, 2021); https://www.umweltbundesamt.de/publikationen/persistent-degradation-products-of-halogenated.
6. M. O. McLinden, C. J. Seeton, A. Pearson, *Science* **370**, 791–796 (2020).
7. A. Kitanovski, U. Plaznik, U. Tomc, A. Poredoš, *Int. J. Refrig.* **57**, 288–298 (2015).
8. A. Greco, C. Aprea, A. Maiorino, C. Masselli, *Int. J. Refrig.* **106**, 66–88 (2019).
9. P. Lloveras, J.-L. Tamarit, *MRS Energy Sustain.* **8**, 3–15 (2021).
10. A. Chauhan, S. Patel, R. Vaish, C. R. Bowen, *MRS Energy Sustain.* **2**, 16 (2015).
11. A. Torelló *et al.*, *Science* **370**, 125–129 (2020).
12. X. Qian *et al.*, *Nature* **600**, 664–669 (2021).
13. C. Aprea, A. Greco, A. Maiorino, C. Masselli, *Energy* **165**, 439–455 (2018).
14. Y. Meng *et al.*, *Nat. Energy* **5**, 996–1002 (2020).
15. N. R. Ram *et al.*, *J. Supercond. Nov. Magn.* **31**, 1971–1979 (2018).
16. R. Ma *et al.*, *Science* **357**, 1130–1134 (2017).
17. See the supplementary materials.
18. I. S. McKay, L. Y. Kunz, A. Majumdar, *Sci. Rep.* **9**, 13945 (2019).
19. A. Rajan, I. S. McKay, S. K. Yee, *Nat. Energy* **7**, 320–328 (2022).
20. J. R. Rumble, *CRC Handbook of Chemistry and Physics* (CRC Press, ed. 102, 2021).
21. S. G. Lu *et al.*, *Appl. Phys. Lett.* **97**, 202901 (2010).
22. B. Li *et al.*, *Nature* **567**, 506–510 (2019).
23. V. K. Pecharsky, K. A. Gschneidner Jr., *Phys. Rev. Lett.* **78**, 4494–4497 (1997).
24. D. Cong *et al.*, *Phys. Rev. Lett.* **122**, 255703–255704 (2019).
25. A. Torelló, E. Defay, *Adv. Electron. Mater.* **8**, 2101031 (2022).
26. L. Mañosa, A. Planes, *Appl. Phys. Lett.* **116**, 050501 (2020).
27. J. Lyubina, *J. Phys. D Appl. Phys.* **50**, 053002 (2017).

28. H. Hou, S. Qian, I. Takeuchi, *Nat. Rev. Mater.* **7**, 633–652 (2022).
29. Z. Li *et al*., *Acta Mater.* **192**, 52–59 (2020).
30. A. T. Bouma, J. H. Lienhard, *Desalination* **445**, 280–291 (2018).
31. A. Campione *et al*., *Desalination* **434**, 121–160 (2018).
32. S. K. Patel, P. M. Biesheuvel, M. Elimelech, *ACS EST Eng.* **1**, 851–864 (2021).
33. H. Strathmann, *Desalination* **264**, 268–288 (2010).
34. F. Greibich *et al*., *Nat. Energy* **6**, 260–267 (2021).
35. F. Bruederlin, H. Ossmer, F. Wendler, S. Miyazaki, M. Kohl, *J. Phys. D Appl. Phys.* **50**, 424003 (2017).
36. S. Jacobs *et al*., *Int. J. Refrig.* **37**, 84–91 (2014).
37. P. Clot *et al*., *IEEE Trans. Magn.* **39**, 3349–3351 (2003).
38. U. Plaznik *et al*., *Int. J. Refrig.* **98**, 139–149 (2019).
39. Ž. Ahčin *et al*., *Joule* **6**, 2338–2357 (2022).

ACKNOWLEDGMENTS

Funding: This work was supported by the Office of Energy Efficiency and Renewable Energy's Building Technologies Program of the US Department of Energy under contract no. DEAC02-05CH11231. **Author contributions:** Conceptualization: D.L. and R.P. Methodology: D.L. Investigation: D.L. Formal analysis: D.L. Visualization: D.L. Funding acquisition: R.P. Project administration: D.L. and R.P. Supervision: R.P. Writing – original draft: D.L. and R.P. Writing – review & editing: D.L. and R.P. **Competing interests:** The authors have filed a US provisional patent application based on this work. The authors declare that they have no other competing interests. **Data and materials availability:** All data are available in the main text or the supplementary materials.

License information: Copyright © 2022 the authors, some rights reserved; exclusive licensee American Association for the Advancement of Science. No claim to original US government works. https://www.science.org/about/science-licenses-journal-article-reuse

SUPPLEMENTARY MATERIALS

science.org/doi/10.1126/science.ade1696
Supplementary Text
Figs. S1 to S23
Tables S1 to S6
References (*40*–*54*)

Submitted 28 July 2022; accepted 28 October 2022
10.1126/science.ade1696

東華大學
DONGHUA UNIVERSITY

Donghua University Global Recruiting Program



DHU (Donghua University) is the first textile institution of higher learning in the People's Republic of China. With having "Virtue, Erudition, Aspiration & Earnestness" as a motto, DHU is working to become a unique multidisciplinary, high-level institution with a focus on textile, material, as well as design. The university has trained more than 260,000 talents for the country. A large number of scientific research achievements are widely used in aerospace, major construction projects, environmental protection and other fields, making constructions to "Shenzhou", "Tiangong", "Beidou", "Chang'e".

DHU adheres to the core strategy of strengthening the university with talents, continuously optimizes the structure of the talent team, and strengthens the construction of the faculty. There are about 2,300 faculty members and staff and more than 1,400 full-time teachers, including more than 900 teachers with senior professional titles. It has gradually formed a group of teachers that includes high-level talents, such as academicians, recipients of National Science Fund for Distinguished Young Scholars, recipients of National Science Fund for Excellent Young Scientists, Chief Scientist of the National 973 Programme, Chief Scientist of National Key Research and Development program, and other high-level talents as well as outstanding young and middle-aged academic elites.

Colleges (Departments, Centers)

College of Textile
College of Fashion and Design
Glorious Sun School of Business and Management
College of Mechanical Engineering
School of Information Sciences and Technology
School of Computer Sciences and Technology
College of Chemistry and Chemical Engineering
College of Materials Science and Engineering
College of Environmental Science and Engineering
College of Biological Science and Medical Engineering
College of Humanities
College of Marxism Studies
College of Science
College of Foreign Languages
Department of Physical Education
Continuing Education College
International Cultural Exchange School
Shanghai International College of Fashion and Innovation
Innovation Center for Textile Science and Technology
Center for Civil Aviation Composites
Center for Advanced Low-dimension Materials
Shanghai International Fashion Innovation Center
Institute of Functional Materials
Institute of Artificial Intelligence

Listed into the Shanghai Universities First-Class Disciplines Project

Textile Science and Engineering
Materials Science and Engineering
Design
Mechanical Engineering
Control Science and Engineering
Environmental Science and Engineering
Chemistry

Recruitment Positions

Distinguished Young Professor:
1. Under the age of 35 for researchers in natural science and engineering, or under the age of 40 for researchers in humanities and social sciences.
2. Applicant should get PhD degree and have postdoctoral experience or obtained assistant professorship or above in overseas universities; or professors in domestic universities or institutions.

The 8th Donghua University Shangshi Forum for International Young Scholars will be held online on 23th Dec. 2022. Welcome young scholars to exchange latest research trends.
More information please contact us by email rcb@dhu.edu.cn or by telephone (+86)021-67792042.



Henan Laboratory of Advanced biomedical sciences (Tianjian laboratory)

Zhengzhou University, Zhengzhou, China

郑州大学
ZHENGZHOU UNIVERSITY

Mission

The Tianjian Laboratory aims to conduct groundbreaking research in chronic diseases such as obesity, diabetes, cancer and neurological diseases. With exceptional discovery, translational and clinical research, the Tianjian Laboratory is dedicated to rapidly advance novel diagnosis and life-changing therapies to address the unmet need of chronic diseases.

About Tianjian Laboratory

The Tianjian Laboratory is a new biomedical research institute located in Zhengzhou, Henan Province, China. It is founded by Henan Province and Zhengzhou University in 2022, and was supported by China-US (Henan) Hormel Cancer Institute, and other biotech companies.

About Zhengzhou University

Zhengzhou University, founded in 1928, has a long and distinguished history in China's higher education. Zhengzhou University is consistently ranked in China's top 30 universities. As an innovative and research-intensive university, it offers comprehensive academic programs spanning humanities, science, engineering and medicine. The top majors include clinical medicine, chemistry and material sciences, all of which rank top 1‰ globally.

Research directions

- Metabolic remodeling and related diseases
- Cell fate determination and related diseases
- New technologies for chronic disease diagnosis and treatment

Support

- 12 affiliated hospitals
- 95,000 square meters
- Core facilities

Leadership

- Peng Li, Ph.D. – Director

Exciting Job Opportunities

- We sincerely invites researchers, postdoctoral fellows and doctors engaged in metabolism, tumor biology, cell biology, genetics, immunology, metabolomics, bioinformatics, biological imaging, mathematics, physics, bioinformatics, and etc.
- We provide favorable salaries and benefits in accordance with the academic achievements

Contact information: Dr. Zhang (rctjlab@zzu.edu.cn)

ScienceCareers online @sciencecareers.org

OPPORTUNITIES IN CHINA



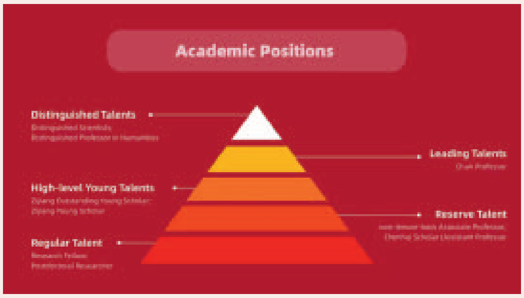
ECNU Seeking Global Talents

Founded in 1951, and based in Shanghai, East China Normal University (ECNU) is one of the top research universities in China. Directly under the Ministry of Education and sponsored by the national key university programs—"Project 211" and "Project 985"— our university is renowned for its teacher education and high-level research programs in both basic and applied sciences. In 2017, ECNU was selected into Class A of the "Double First-Class Program" (First Class University and First-Class Academic Discipline in the World), an education initiative launched by the Ministry of Education aiming at developing elite Chinese universities into world-class institutions by the end of 2050. Adhering to the strategy of pursuing interdisciplinary development, internationalization, and informatization, ECNU has made great achievements in teaching, scientific research, community service and international exchanges in the past few decades. In terms of international cooperation and exchange, we have established close partnership with world-renowned universities such as École Normale Supérieure de Lyon, New York University, University of Virginia, and The University of British Columbia, and signed academic collaboration and exchange agreements with more than 300 universities and research institutions across the world. With all these efforts, ECNU intends to fulfill its vision of Excellent Education, Excellent Research, Excellent Culture, Excellent Development and becomes a more prestigious university with global impact. Join ECNU and grow up with us together!

Job Opportunities and Qualifications

ECNU invites applications for tenure-track faculty positions in multiple disciplines in all ranks from assistant researcherThe positions of research scientists and postdoctoral fellowships are also open for application.

Applicants must hold a doctorate degree in a closely related field and show evidence of relevant teaching and research experience, including peer-reviewed publications. Applicants who has a professional record that proves their external funding history or potential.



Salary and Support

All of the above positions offer generous salary and support in accordance with the relevant policies of the Shanghai Municipality and we help solve your children's schooling based on the excellent education resources provided by our affiliated schools. Join us, enjoy competitive salary, and at the same time, let your children enjoy the city's high-quality education resources from kindergarten to high school.

How to Apply

If you are interested, please contact our HR office for more details regarding the applying process and application materials
Contact: Ms. Cai/Mr.Wang
E-mail: xmcai@sist.ecnu.edu.cn/cwang@bio.ecnu.edu.cn
Office Tel: 86-021-54836169
Personnel Department: http://hr.ecnu.edu.cn

WAYNE STATE UNIVERSITY

ASSISTANT / ASSOCIATE /FULL PROFESSOR
MEDICINAL CHEMISTRY/CHEMICAL BIOLOGY

The Department of Pharmaceutical Sciences in the Eugene Applebaum College of Pharmacy and Health Sciences invites applications for a **12-month tenure-track position at any academic level**. Applicants are expected to have earned a PhD, MD/PhD, PharmD/PhD or equivalent degree in pharmaceutical sciences, medicinal chemistry, chemistry, or a related discipline. Preference will be afforded to scientists with a record of high impact research in medicinal chemistry or chemical biology. Applicants that focus on drug design and discovery in the areas of metabolic disease, neurosciences, infectious disease, or oncology are especially desired, although other research areas will be considered. The finalists are expected to have or develop a vigorous externally funded research program and provide valued teaching in the PhD and PharmD programs. We offer an uncommonly collegial academic culture, extremely a competitive start-up and compensation package, generous benefits, excellent laboratory facilities and extensive research support. Submit applications via **http://jobs.wayne.edu** under Department H1822-Pharmaceutical Sciences posting Assistant/Associate/Full Professor in Medicinal Chemistry/Chemical Biology (req644). Further details are available by contacting Dr. Aloke Dutta at **adutta@wayne.edu** or (313) 577-1064.

Wayne State University is a Carnegie Highest Research Activity (R1) institution and a premier public, urban research university in the heart of Detroit where students from all backgrounds enjoy a rich, high-quality education. The College is located in midtown, one of the dynamic urban communities leading the Detroit renaissance. The cosmopolitan environment is rich in cultural offerings, strong schools, and outstanding affordable housing, all within the beautiful Great Lakes region. Our deep-rooted commitment to excellence, collaboration, integrity, diversity and inclusion creates exceptional educational opportunities that prepare students for success in a diverse and global society. We encourage applications from women, people of color, and other underrepresented groups.

Wayne State is an affirmative action/equal opportunity employer. All qualified applicants will receive consideration for employment without regard to race, color, religion, sex, national origin, age, disability, veteran status, or any other characteristic protected by law. Application review will begin immediately with a target faculty start date in **August 2023**. The positions will remain open until filled.



Who's the top employer for 2022?

Science Careers' annual survey reveals the top companies in biotech & pharma voted on by *Science* readers.

Read the article at sciencecareers.org/topemployers

Science 2022 TOP EMPLOYER



Apply to NIH FIRST at Northwestern University

Northwestern University is recruiting exceptional early career applicants in the biomedical sciences through the NIH Faculty Institutional Recruitment for Sustainable Transformation (FIRST) program.

Multiple positions at the tenure-track Assistant Professor level will be available across a broad range of scholarship in the areas of:

Cancer

Cardiovascular, and

Brain, Mind, and Behavior.

Cluster hiring of new faculty will take place over a period of three years.

Northwestern encourages applications by members of groups underrepresented in the biomedical, clinical, behavioral, engineering, physical, and social sciences.

To review our requirements and apply to open positions, please visit **www.nurture.northwestern.edu.**

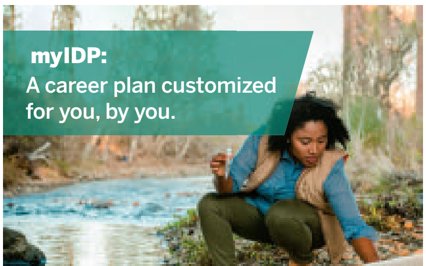
Northwestern University is an Equal Opportunity, Affirmative Action Employer of all protected classes, including veterans and individuals with disabilities. Women, racial and ethnic minorities, individuals with disabilities, and veterans are encouraged to apply.

Northwestern University

Successful candidates will possess a doctorate degree and should not have held a prior position at the tenure-track Assistant Professor (or equivalent) level.

Applicants should have a strong record demonstrating ability or potential for conducting high-level research and a commitment to promoting diversity and inclusive excellence.

For more information, contact **nurture@northwestern.edu**.



There's only one Science

Features in myIDP include:

- Exercises to help you examine your skills, interests, and values.
- A list of 20 scientific career paths with a prediction of which ones best fit your skills and interests.

Visit the website and start planning today!
myIDP.sciencecareers.org

Science Careers AAAS In partnership with:

UCSF University of California San Francisco · UIC · Burroughs Wellcome Fund · University of Massachusetts UMASS Medical School · FASEB Federation of American Societies for Experimental Biology

utmb Health

A postdoctoral position is available immediately in the laboratory of Dr. Thomas Geisbert to study the pathogenesis of Ebola, Marburg, Lassa, CCHF, Nipah, and/or Hendra viruses and to develop countermeasures against these agents. Applicants must have a Ph.D. or M.D. with a background in virology or pathology. The candidate must have experience working with infectious agents or laboratory experience working with animals. The candidate should be highly motivated and must be able to plan and perform experiments in an independent manner with minimal supervision. The applicant will also be responsible for writing papers, protocols, and lab reports associated with these projects. The applicant must meet all State and Federal requirements necessary for working with Select Agents.

ESSENTIAL JOB FUNCTIONS:

- Plan and perform experiments independently
- Prepare lab reports
- Writes protocol
- Interacts with graduate students
- Capable of presenting data at meeting

MARGINAL OR PERIODIC FUNCTIONS:

- Performs related duties as assigned.

KNOWLEDGE / SKILLS / ABILITIES:

- Ability to plan and perform experiments independently
- Ability to observe and record experiments/research and report accurately
- Writing skills for protocols, reports, journal manuscripts and funding applications
- Mentoring and teaching skills for interaction with graduate students
- Presentation skills

REQUIRED EDUCATION / EXPERIENCE:

Ph. D, M.D, D.O., or D.V.M in related field. Knowledge in the relevant scientific discipline with increasing professional achievement. Applicants should be highly motivated, able to conduct independent research.

PREFERRED EDUCATION / EXPERIENCE:

Experience in a BSL-3 or BSL-4 work environment is preferred but not required.

Hiring Manager: Thomas Geisbert, PhD, Professor/ Ann Higgins

Salary – Commensurate with experience: $54,840 or at the NIH Standard (based on experience)

WORKING ENVIRONMENT/LOCATION OF POSITION:

Standard office and laboratory environment at UTMB's main campus, Galveston National Laboratory.

EQUAL OPPORTUNITY STATEMENT

"UTMB Health strives to provide equal opportunity employment without regard to race, color, national origin, sex, age, religion, disability, sexual orientation, gender identity or expression, genetic information, veteran status, or any other basis protected by institutional policy or by federal, state or local laws unless such distinction is required by law. As a Federal Contractor, UTMB Health takes affirmative action to hire and advance women, minorities, protected veterans and individuals with disabilities."

UTMB has several highly interactive research centers, biomedical institutes, and a national biocontainment laboratory with excellent infrastructure to conduct research at BSL2, -3 and -4 on diverse animal models of infectious diseases. The Department, with 41 full-time faculty members, is ranked among the top of its peer departments in NIH funding.

Interested candidates should apply to **Requisition # 2202642**, Postdoctoral Fellow via the UTMB careers website at **https://www.utmb.edu/hr/careers/**

WORKING LIFE

By **Jacqueline Forson**

A break for my health

I should have been starting the second year of my Ph.D. Instead, I was at my parents' house, recently discharged from the hospital, logging into my graduate program director's personal Zoom room. Embarrassed by my condition, I sat uncomfortably in my childhood bedroom—my first time in weeks sitting upright in a chair—dressed in an oversize knit sweater I found in my dad's closet and pajama pants. I had taken Tylenol an hour before, hoping it would help me tolerate the use of my abdominal muscles to sit. What I needed to do felt equally painful: Discuss my new disability and possible accommodations with the director.

I had been ready for the inevitable failures of grad school—experiments, funding proposals, even classes. But I was caught off-guard when midway through my first year I began to face a different type of challenge. I felt fatigued every morning. My appetite decreased. I started to notice an increase in trips to the bathroom. Finally came the blood each time I went, which continued for more than a week and spurred me to go to the emergency department. Doctors ordered scans, ultrasounds, and blood work, but they found nothing. My symptoms were chalked up to stress.



"I learned to take solace in knowing that everyone's Ph.D. journey is unique."

Over the next few months, I visited the hospital often. Each time, the same tests were run, and the same question marks remained. I kept it a secret from my friends, family, and advisers until I finally broke down during a phone call with my parents. Within a day, they found a doctor who quickly scheduled me for an emergency colonoscopy in my hometown. When I was diagnosed with severe ulcerative colitis, it weirdly felt like a relief to know I had a disease—even one that repeatedly put me in the hospital, with abdominal pain that often rose to a 10 on the pain scale.

My doctors told me I needed to focus completely on my health for the next 6 months. I hoped I could keep up with my studies and take care of my health by switching projects from biochemistry to bioinformatics and attending classes virtually. That brought me to that Zoom call with my program director, explaining why I had been in and out of the hospital these past few months rather than in the lab and proposing my path forward. However, my graduate program wasn't keen on the idea—and my doctors weren't either. All said I had two options: a medical leave of absence or withdrawing from my program.

I had never taken a break before. I am the daughter of immigrants, and my parents believed breaks weren't an option for our family. I feared adding to the dropout statistic for students of color. I feared a leave of absence would be seen as a sign of weakness. Most of all, I feared I would simply be forgotten by the advisers I desperately wanted validation from. But I wasn't ready to give up on grad school, so the leave of absence seemed like the only option.

When I received the email notification that I would be taken off my training grant, I felt I had lost my identity. I was no longer a researcher or a student; I was a patient. When classmates swapped messages about assignments, experiments, and exams I felt I had nothing to add, so I stopped responding, and they stopped including me. The isolation fueled my fears, and then came the depression.

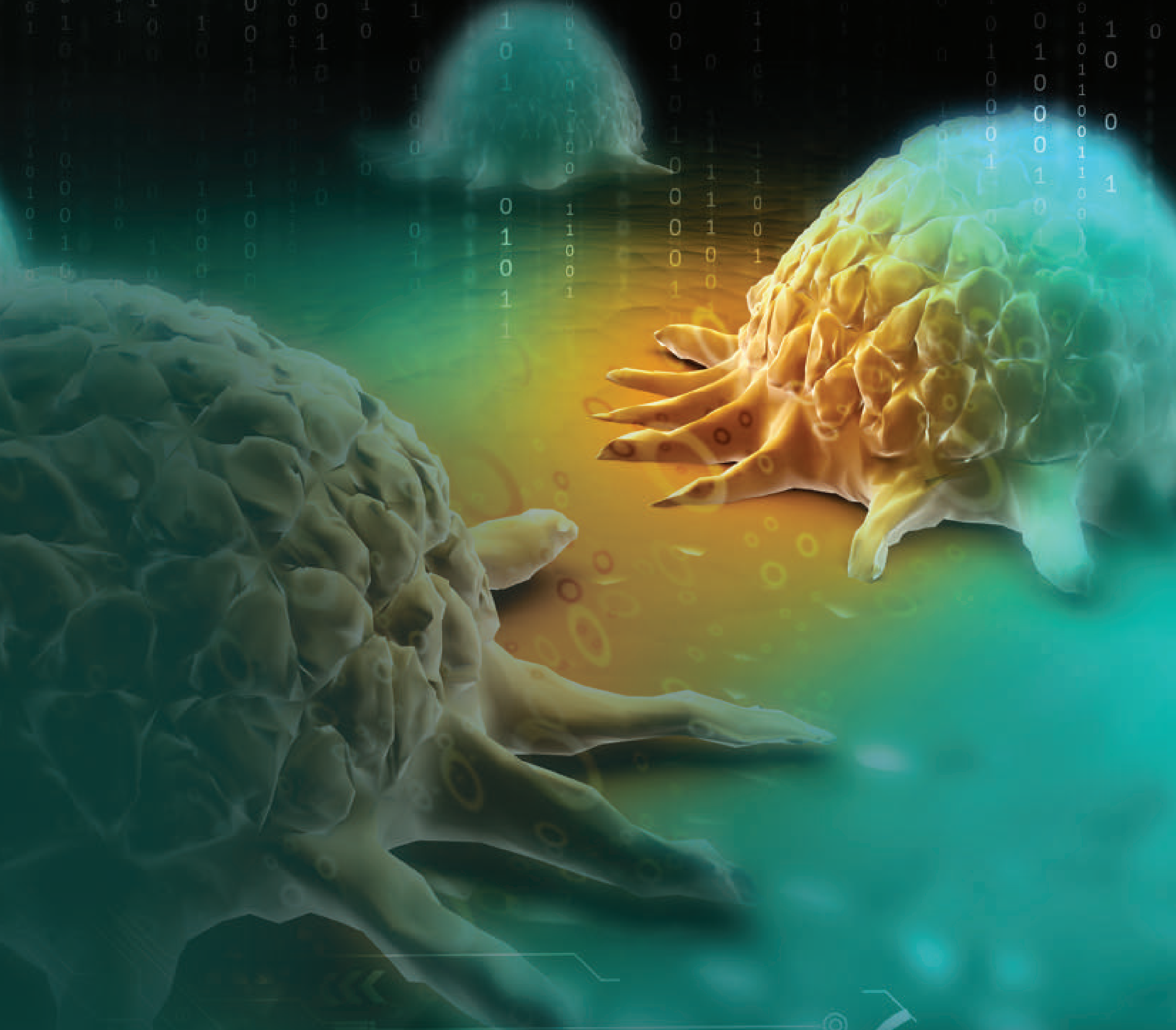
Still, I knew this leave of absence was essential. And with the help of my therapist, I learned to take solace in knowing that everyone's Ph.D. journey is unique, and mine was far from over.

I wish I could finish this story with a happy ending, but I have yet to reach that point. When I returned to my Ph.D. after 6 months, I had to relearn my project and how to be a graduate student. Over the next 5 months, I was admitted to the hospital three more times. I changed medications countless times and added numerous doctors to my care team. My Ph.D. journey will be a slow one, with more time away from thesis work than most.

I'm hopeful though. Over the past year, I connected with others who also took time away during graduate school. In hearing their stories, I learned that a leave of absence is perfectly OK, no matter the reason. There is bravery in taking the time to focus on yourself. ■

Jacqueline Forson is a Ph.D. student at the University of Michigan, Ann Arbor. Send your career story to SciCareerEditor@aaas.org.

ILLUSTRATION: ROBERT NEUBECKER



2023 AAAS MARTIN AND ROSE WACHTEL CANCER RESEARCH AWARD

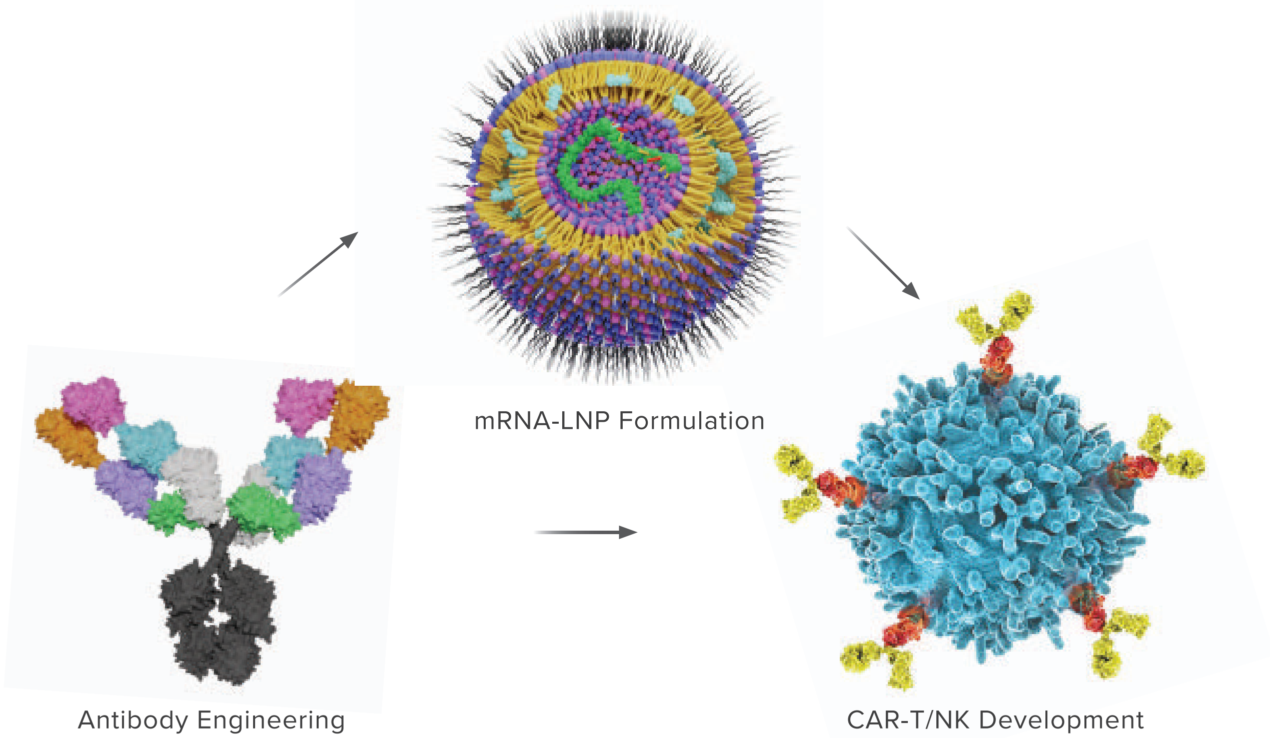
Recognizing the work of an early career scientist who has performed outstanding research in the field of cancer. Award nominees must have received their Ph.D. or M.D. within the last 10 years. The winner will deliver a public lecture on their research, receive a cash award of **$25,000**, and publish a Focus article on their award-winning research in *Science Translational Medicine*.

For more information visit
www.aaas.org/aboutaaas/awards/wachtel
or e-mail wachtelprize@aaas.org.
Deadline for submission: **February 1, 2023**.

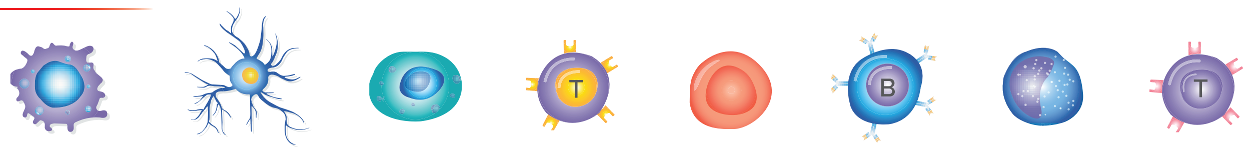
AAAS Science Translational Medicine

Immune Cell Engineering CRO Services

Advancing All Things Cell Therapy



Types of Cells



Antibody Services

- Monoclonal Ab Development
- Hybridoma Sequencing
- Human Antibody Screening
- Antibody Humanization
- Bispecific Antibody Engineering
- Stable Cell Line Generation

mRNA-LNP Services

- mRNA Design and Synthesis (IVT)
- mRNA Capping & Purification
- mRNA-LNP Encapsulation
- mRNA-LNP Scale Up and QC
- mRNA-LNP Validation In Vivo
- Ionizable Lipid Licensing

Immune Cell Services

- Lentivirus Production GMP
- CAR-T/NK Cell Generation
- CAR-T/NK Animal Model
- Immune Cell Engineering
- T/B/NK/Dendritic cell, Macrophages
- TCR knockout by CRISPR

All products are for research use only

Discover more | www.promab.com

ProMab Biotechnologies, Inc.
2600 Hilltop Dr, Building B, Richmond, CA 94806
1.866.339.0871 | info@promab.com

SCAN ME